Summer 8-31-2013

Exploitation of infrared polarimetric imagery for passive remote sensing applications

Joao Miguel Mendes Romano
New Jersey Institute of Technology

ABSTRACT

EXPLOITATION OF INFRARED POLARIMETRIC IMAGERY FOR PASSIVE REMOTE SENSING APPLICATIONS

by
João Miguel Mendes Romano

Polarimetric infrared imagery has emerged over the past few decades as a candidate technology to detect manmade objects by taking advantage of the fact that smooth materials emit strong polarized electromagnetic waves, which can be remotely sensed by a specialized camera using a rotating polarizer in front of the focal plate array in order to generate the so-called Stokes parameters: S_0, S_1, S_2, and DoLP. Current research in this area has shown the ability of using such variations of these parameters to detect smooth manmade structures in low contrast contrast scenarios.

This dissertation proposes and evaluates novel anomaly detection methods for long-wave infrared polarimetric imagery exploitation suited for surveillance applications requiring automatic target detection capability. The targets considered are manmade structures in natural clutter backgrounds under unknown illumination and atmospheric effects. A method based on mathematical morphology is proposed with the intent to enhance the polarimetric Stokes features of manmade structures found in the scene while minimizing its effects on natural clutter. The method suggests that morphology-based algorithms are capable of enhancing the contrast between manmade objects and natural clutter backgrounds, thus, improving the probability of correct detection of manmade objects in the scene. The second method departs from common practices in the polarimetric research community (i.e., using the Stokes vector parameters as input to algorithms) by using instead the raw polarization component imagery (e.g., 0°, 45°, 90°,

and 135°) and employing multivariate mathematical statistics to distinguish the two classes of objects. This dissertation unequivocally shows that algorithms based on this new direction significantly outperform the prior art (algorithms based on Stokes parameters and their variants). To support this claim, this dissertation offers an exhaustive data analysis and quantitative comparative study, among the various competing algorithms, using long-wave infrared polarimetric imagery collected outdoor, over several days, under varying weather conditions, geometry of illumination, and diurnal cycles.

EXPLOITATION OF INFRARED POLARIMETRIC IMAGERY FOR PASSIVE REMOTE SENSING APPLICATIONS

by
João Miguel Mendes Romano

A Dissertation
Submitted to the Faculty of
New Jersey Institute of Technology
in Partial Fulfillment of the Requirements for the Degree of
Doctor of Philosophy in Electrical Engineering

Department of Electrical and Computer Engineering

August 2013

.

APPROVAL PAGE

EXPLOITATION OF INFRARED POLARIMETRIC IMAGERY FOR PASSIVE REMOTE SENSING APPLICATIONS

João Miguel Mendes Romano

Dr. Edip Niver, Dissertation Co-Advisor — Date
Professor of Electrical and Computer Engineering, NJIT

Dr. Dalton Rosario Dissertation Co-Advisor — Date
Senior Researcher, Army Research Laboratory

Dr. Venkataraman Swaminathan, Committee Member — Date
Competency Manager, Acoustics and Network Division. US Army ARDEC

Dr. Alexander Haimovich, Committee Member — Date
Professor of Electrical and Computer Engineering, NJIT

Dr. Ali Abdi, Committee Member — Date
Associate Professor of Electrical and Computer Engineering, NJIT

BIOGRAPHICAL SKETCH

Author: João Miguel Mendes Romano

Degree: Doctor of Philosophy

Date: August 2013

Undergraduate and Graduate Education:

- Doctor of Philosophy in Electrical Engineering,
  New Jersey Institute of Technology, Newark, NJ, 2013

- Master of Science in Electrical Engineering,
  New Jersey Institute of Technology, Newark, NJ,2000

- Bachelor of Science in Electrical Engineering Technology,
  New Jersey Institute of Technology, Newark, NJ, 1999

Major: Electrical Engineering

Presentations and Publications:

Romano, Joao, Dalton Rosario, and Edip Niver, "Morphological operators for polarimetric anomaly detection," *Geoscience and Remote Sensing, IEEE Transactions on*, 2013. Accepted.

Romano, Joao, Dalton Rosario, and Edip Niver. "A novel approach to anomaly detection for manmade object detection in natural clutter backgrounds," *Optical Engineering and Applications, SPIE conference on*, 2013. Accepted.

Romano, Joao, Dalton Rosario, and James McCarthy, "Day/Night Polarimetric Anomaly Detection Using Spice Imagery," *Geoscience and Remote Sensing, IEEE Transactions on*, vol. PP, no. 99, pp. 1-10 December 2012.

Borel Christoph, Dalton Rosario and Joao Romano, "Range-invariant anomaly detection applied to imaging Fourier transform spectrometry data", *Proc. SPIE 8515, Imaging Spectrometry XVII*, 85150J, October 15, 2012.

Romano, Joao, Dalton Rosario, and Nasser Nasrabadi, "Covariance trace for polarimetric anomaly detection," *Geoscience and Remote Sensing Symposium (IGARSS)*, 2012 IEEE International, pp. 4233-4236, 22-27 July 2012.

Romano, Joao, Dalton Rosario, and Mark Woolley, "The spectral and polarimetric imagery collection experiment," *IEEE IGRSS Atmospheric Transmission Models Meeting Workshop*. Jun. 2011. Invited presentation

Rosario, Dalton, and Joao Romano, "Multidimensional image processing for remote applications," *IEEE Conf. Image Processing Theory, Tools, and Applications*. Jun 2010.

Romano, Joao, Dalton Rosario, and Luz Roth, "VNIR hyperspectral background characterization methods in adverse weather," *SPIE Defense, Security, and Sensing*. International Society for Optics and Photonics, 2009.

Rosario, Dalton, Joao Romano, and Rene Sepulveda. "Hyperspectral anomaly detection using Sony Playstation 3." *SPIE Defense, Security, and Sensing.* International Society for Optics and Photonics, 2009.

Romano, Joao, and Dalton Rosario "Analysis of an autonomous clutter background characterization method for hyperspectral imagery." *Proceedings of SPIE, the International Society for Optical Engineering.* Society of Photo-Optical Instrumentation Engineers, 2008.

Romano, Joao, and Dalton Rosario, "Random sampling statistics analysis for adaptive target-scale-invariant hyperspectral anomaly detection," *SPIE Defense and Security Symposium*. International Society for Optics and Photonics, 2007.

To my parents, Maria and Florival Romano; my wife, Bianca Romano;
and my two boys, Jon-Luc and Gian-Carlo Romano

ACKNOWLEDGMENT

Working on the Ph.D. has been a wonderful, insightful, and sometimes overwhelming experience in learning a new topic and writing papers, while trying to make a significant contribution in the field of polarimetry.

But regardless how turbulent the journey has been with the usual ups and downs of research, I will always be in debt to my Dissertation Co-Advisor, Dr. Edip Niver for his continuous support throughout my Ph.D. career. I am also in debt with my Dissertation Co-Advisor, Dr. Dalton Rosario, who has had a steady influence throughout this process. You have always been patient, encouraging, and most important of all listened to my ideas, which with your help, has led to the contributions presented in this work. Your ability to approach research problems, your insights to practical problems, and your hard work set an example to me. Finally, I can't thank you enough for continuously pressing me to do my best and keeping me focused.

I would also like to thank my Dissertation committee members, Dr. Venkataraman Swaminathan, Dr. Alexander Haimovich, and Dr. Ali Abdi for being a part of this process and their continuous help in improving the content presented in this dissertation through their comments and suggestions.

In addition, I have been very privileged to have known, worked and/or collaborated with many other individuals that have helped shape my thoughts and ideas as well as their contribution to the content of this dissertation. Firstly, I would like to thank Paul Granger for the almost daily conversations for many years on algorithm development, sensing modalities, lessons learned, and most importantly the need for continuous and/or adverse weather data collections. I also would like to thank Barbara

Machak for her many years of continued support for the hyperspectral and polarimetric science and technology program, which resulted in the development of many of the algorithms presented in this work.

Furthermore, I am very grateful to Glenn Miner, David Panhorst, and Bill Smith for allowing me to finish my dissertation this past year and for continuously supporting my research on advanced technologies that directly support our overall mission. I am also indebted to David Panhorst, Frank Loso, Stephen Leong, and Andrew Pskowski for helping me proofread the dissertation. I would also like to thank David Chenault and Larry Pezzaniti at Polaris Sensor Technologies for supporting the work presented in this dissertation through their help, expertize, and use of their cameras.

Finally, but definitely not least, I want to thank my team: Mark Woolley, Jacob Michalson, and Luz Roth, which without you none of this would have been possible. Your support in developing the necessary matlab codes for data calibration, Stokes parameters, polarization component separation, as well as maintaining the ongoing SPICE data collection was essential to the success of this dissertation.

TABLE OF CONTENTS

TABLE OF CONTENTS
(Continued)

Chapter **Page**

TABLE OF CONTENTS
(Continued)

TABLE OF CONTENTS
(Continued)

Chapter **Page**

LIST OF TABLES

LIST OF FIGURES

LIST OF FIGURES
(Continued)

Figure **Page**

LIST OF FIGURES
(Continued)

Figure **Page**

LIST OF FIGURES
(Continued)

Figure **Page**

LIST OF FIGURES
(Continued)

Figure **Page**

LIST OF FIGURES
(Continued)

Figure **Page**

LIST OF FIGURES
(Continued)

Figure **Page**

LIST OF FIGURES
(Continued)

Figure **Page**

LIST OF FIGURES
(Continued)

Figure **Page**

LIST OF FIGURES
(Continued)

Figure **Page**

LIST OF FIGURES
(Continued)

Figure **Page**

LIST OF FIGURES
(Continued)

Figure **Page**

LIST OF FIGURES
(Continued)

Figure **Page**

LIST OF FIGURES
(Continued)

Figure **Page**

LIST OF FIGURES
(Continued)

Figure **Page**

LIST OF FIGURES
(Continued)

Figure **Page**

LIST OF FIGURES
(Continued)

Figure **Page**

LIST OF FIGURES
(Continued)

Figure **Page**

LIST OF FIGURES
(Continued)

Figure **Page**

LIST OF FIGURES
(Continued)

Figure **Page**

LIST OF FIGURES
(Continued)

Figure **Page**

LIST OF FIGURES
(Continued)

Figure **Page**

LIST OF FIGURES
(Continued)

Figure **Page**

LIST OF FIGURES
(Continued)

Figure **Page**

LIST OF FIGURES
(Continued)

Figure **Page**

LIST OF FIGURES
(Continued)

Figure **Page**

LIST OF FIGURES
(Continued)

Figure **Page**

LIST OF FIGURES
(Continued)

Figure **Page**

LIST OF FIGURES
(Continued)

Figure **Page**

LIST OF FIGURES
(Continued)

Figure **Page**

LIST OF FIGURES
(Continued)

Figure **Page**

SYMBOLS AND ABBREVIATIONS

α	Radiance absorbance
ϵ	Radiance emittance
τ	Radiance transmittance
ρ	Radiance reflectance
ϕ	Radiant flux or radiant power
c	Speed of light $\left(3 \times 10^8 \frac{meters}{second}\right)$
E	Irradiance or radiant flux
EM	Electro-magnetic
FLIR	Forward looking infrared
FPA	Focal plane array
h	Plank's constant
H_0	Null hypothesis
H_1	Alternative hypothesis
HS	Hyperspectral
IR	Infrared
°K	Degrees in Kelvin
K	n-dimensional space for structuring element (Chapter 5.2), or degrees of freedom (Chapter 5.3)
L	Radiance
LUT	Look-up table
LWIR	Long-wave infrared

SYMBOLS AND ABBREVIATIONS

M	Radiance exitance
MAR	March
MM	Mathematical morphology
MWIR	Mid-wave infrared
PDF	Probability density function
P_d	Probability of detection
P_{fa}	Probability of false alarm
PI	Polarimetric imagery
PRS	Parallel Random Sampling
Q	Radiant energy
ROC	Receiver operating curves
RS	Random sampling
SCR	Signal-to-clutter ratio
SE	Structuring Element
SNR	Signal-to-noise ratio
SP	Spectral-polarimetric
SWIR	Short-wave infrared
T	Absolute temperature
TE	Transverse electrical
TM	Transverse magnetic

SYMBOLS AND ABBREVIATIONS

VLWIR	Very long-wave infrared
χ^2	Chi-square distribution

CHAPTER 1

INTRODUCTION

1.1 Objective

Remote sensing often refers to the use of aerial platforms with passive and/or active sensing devices that capture the information about an object of interest without any physical contact with the same object. This information is often captured by means of propagated electromagnetic signals through the atmosphere, which are then processed and analyzed by a man-in-the-loop or an autonomous system. Remote sensing sensor systems can be usually categorized as active or passive systems. An active system relies on the transmission of a signal directed toward the scene of interest, which is then reflected and captured by the same sensor and analyzed through a processing system. The advantages of using an active system include the ability to obtain measurements that are independent of time, season, or weather and to better control how the target is illuminated. On the other hand, the disadvantages of using active sensing platforms include the amount of energy necessary to adequately illuminate a scene under a variety of weather conditions and the fact that such systems can be easily detected by other sensors on the ground monitoring the skies.

Conversely, passive sensing devices can detect electromagnetic energy that is either emitted or reflected off a scene of interest without the use of a controlled source. In situations where the sensor captures reflective electromagnetic energy, a source is often needed to illuminate the scene. As an example, a visible camera system relies on sunlight to illuminate a scene, where the energy reflected from the scene is captured by the camera's RGB sensor. In contrast, emitted radiation is dependent on the emissivity

properties of the materials in the scene and their respective temperature. Passive systems are often desired because unlike active systems, they are not as easily detected since no active signal is being transmitted. The drawback is that their ability to detect and discriminate potential objects of interest is inherently dependent on weather and background effects on the target, the target state, and any available sources (e.g., sun) the sensor(s) can take advantage of.

In remote sensing applications, one can find a slew of different passive imaging sensors that operate in many regions of the spectrum such as visible, short-wave infrared (SWIR), mid-wave infrared (MWIR), and long-wave infrared (LWIR). Out of all the different modalities, LWIR is often the most sought after for surveillance applications, especially military, because 1) most materials at ambient temperature (250-300°K) and running vehicles (up to 373°K) tend to emit strongly (peak wavelength) between 7 and 11μm [1]; 2) all materials radiate thermal energy in the LWIR band day and night; and 3) the existence of a transmission window (greater than 65%) between 8 and 10μm allows the thermal energy to propagate through the atmosphere and be captured by a sensing device.

Electromagnetic waves, or light, can be described in terms of intensity, frequency, spectral characteristics, and polarization [2, 3, and 22]. Normally, remote sensing applications rely on the use of intensity and spectral based imagery exploitation for target detection, recognition, and identification, change detection, material classification, and anomaly detection [4-8].

Passive polarimetric imagery (PI), on the other hand, is attractive because it has shown the ability to enhance contrast over intensity imagery in situations where target

and background temperature contrast is often negligible [9], in addition it also can be used as a conventional and polarimetric infrared imagery depending on how the Stokes information is combined. Because manmade materials polarize strongly with respect to natural clutter, infrared polarimetric sensors can be used as an additional modality that together with existing sensing devices can dramatically improve important aspects of remote sensing applications such as enhanced target detection, classification, and recognition. As a result of the limited number of available databases and algorithm development activities that exploit target and background polarization feature diversity, polarimetric imagery has not been a technology of choice for remote sensing applications (compared to other technologies such as hyperspectral imaging). Nonetheless, in recent years there has been a significant amount of work accomplished that has demonstrated the potential of polarimetric imagery for applications such as anomaly detection [10, 11], target classification [12], material classification and clustering [13, 14] and more recently, detection of disturbed earth for improvised explosive devices (IEDs) [15].

Unlike target and material classification algorithms, anomaly detection algorithms (the focus of this dissertation) are quite useful in situations where *a priori* knowledge on the target and clutter distributions and atmospheric and illumination effects (altitude, sensor angle, etc.) are usually not available to the system. Such algorithms involve measuring the "distance" between an unknown sample and a known reference sample, where a cutoff threshold is applied as part of the test to determine whether the test sample is also controlled by the same PDF; if the latter is not true, the test sample is labeled as an anomaly relative to the reference sample.

The objective of this work is to develop novel anomaly detection algorithms for PI that can discriminate manmade objects from natural clutter for a variety of weather conditions, target state, and throughout the diurnal cycle while operating at very low false rates.

1.2 Work Overview

This dissertation specifically focuses on providing solutions to air-to-ground applications, where no *a priori* information on the target, background, weather, sensor angle (among other sources of variability) is available to the algorithm. In these applications, a target is any manmade object in a natural cluttered background whose scale and polarization information in the imagery is unavailable or deemed unreliable and as a result will not be used by the algorithm. The proposed algorithms consist of a series of techniques with the overall goal of autonomously detecting the presence of manmade objects in the scene, as polarization anomalies, while holding down the probability of false alarms. A manmade object present in the scene is assumed to be represented by multiple pixels with a total area that can be slightly smaller or greater than the size of a moving window, which is much smaller than the size of the test image.

This dissertation proposes multiple solutions to the problem of autonomous anomaly detection problem, requiring daytime-nighttime capability, using passive remote sensory long-wave infrared polarimetric imagery, to include the use of morphological filters to enhance manmade object features found in conventional Stokes imagery, while at the same time mitigating natural clutter attributes. This process increases the signal-to-noise ratio between manmade objects and background clutter more significantly than

found in Stokes imagery. An adaptive threshold based *a priori* on a chosen Gaussian probability density function is employed where the estimated mean and variance from the enhanced image are used to standardize the output surface. A criteria based on the desired TYPE I error is applied to reject pixels (i.e., anomalies) that fall outside the imposed criteria. In order to show a fair comparison between the proposed and currently employed methods, 72-hour polarimetric imagery (over 300 images), where the target satisfies the assumptions stated previously in this section, is used to evaluate and quantify the performances of the algorithms. In conclusion, the dissertation establishes that the use of morphological operations plays an important role in PI exploitation.

The dissertation recommends exploiting a novel use of polarimetric imagery yielding features never before used capable of discriminating manmade objects from natural clutter backgrounds more effectively than Stokes parameters can. The dissertation proposes to stack each of the raw polarimetric angle measurements imagery (0°, 45°, 90°, and 135°) captured by the camera to create a polarimetric data cube or PC. The work focuses on the bivariate space 0° and 90° where a significant effort of this dissertation is then devoted on the exploitation of the novel data in ways never done before in the scientific community, as validated by the Institute of Electrical and Electronic Engineers (IEEE) reviewers for the IEEE Transactions on Geoscience and Remote Sensing (TGRS) as they reviewed and accepted for publication the submitted manuscript reporting a portion of the new approach [75 and 76]. The analysis in the PC data space using multivariate higher order statistics demonstrate that covariance difference tests are effective in separating manmade objects from natural clutter backgrounds over a variety of weather patterns, target state, and diurnal cycle.

The result is the proposal of an anomaly detection algorithm based on a covariance difference test known in the literature as the M-Box covariance test [69] that exploits this new feature space by taking advantage of the variability difference between the two classes (manmade objects and natural clutter).

Two variations of the proposed algorithm are also proposed in order to make the solution more robust to range and target size variations. The performance of the three proposed covariance test variations were evaluated against a 72-hour database comprised of more than 300 polarimetric images and compared against conventional Stokes parameters and between the different covariance tests proposed in the dissertation.

Finally, the key differences between the covariance difference test anomaly detectors and the morphological filter based method proposed in this dissertation is twofold:

1) The morphologic filter based method is directly applied to conventional Stokes imagery, while the covariance test uses the raw angle measurements (0°, 45°, 90°, and 135°) captured by the sensor as input. The motivation in here is to leverage the fact that most, if not all, of fielded polarimetric sensors in the market today yield Stokes vector as output data.

2) The covariance difference test assumes that the data has a Wishart distribution and the resulting distribution from the test is defined by the χ^2 distribution with K degrees of freedom when the null hypothesis cannot be rejected; whereas for the case of the morphological filters, no assumption is made on the input data prior to the filters implementation.

1.3 Contributions of Proposed Work

To date a significant amount of research focused on manmade object detection using polarimetric imagery can be found in the literature [9-15], but little has been done to address some of the fundamental problems that affect anomaly detection algorithms using polarization features. For example, the input imagery common for much of the work in anomaly detection algorithms in literature is the Stokes vector parameters. As it will be

shown later on, the Stokes imagery features are unreliable due to their dependency on the angle between the sensor's line of sight and objects' surfaces, causing major degradation on algorithm performance. Although, it is beyond the scope of this dissertation to address all of the fundamental problems in anomaly detection algorithms for PI, the most important ones are addressed in this work.

In summary, this dissertation presents the following contributions:

1) An extensive analysis of polarization theory, concepts, and limitations supported by field data collections using multiple targets over different weather conditions, target state, and diurnal cycle.

2) Introduction of a novel algorithm suite based on morphological filters, which is tailored to enhance manmade objects found in Stokes imagery, while significantly suppressing the background clutter.

3) Introduction of a new data space, a data cube consisting of spatial information and radiometrically calibrated measurements of polarization components, in order to exploit potential discriminant features between manmade and natural object classes.

4) The first to study the proposed data space as input to multivariate algorithms for the purpose of manmade object detection, which allowed for the discovery of a key feature that distinguishes the two object classes in the scene. This feature – the second order statistics – seems reliable over the diurnal cycle and under variations due to changing atmospheric conditions and geometry of illumination.

5) Introduction of three algorithms specifically designed to exploit the discovered discriminant feature in the new data space, where the trade-off between algorithmic speed and added robustness can be weighted by potential users. The algorithms have demonstrated exceptional performance testing an example database, consisting of daytime and nighttime imagery.

6) The first to demonstrate an extensive performance comparison between all of the algorithms proposed in this dissertation for manmade object detection and the prior art using over 300 polarization images taken over the course of a 72-hour period of different weather conditions, target states, and diurnal cycle.

1.4 Dissertation Outline

The remainder of this dissertation is organized as follows:

Chapter 2 presents a brief introduction to infrared radiation theory and concepts followed by a discussion on the challenges of conventional broadband LWIR imagery for surveillance applications. Descriptions of different sensing modalities in the LWIR region of the spectrum that take advantage of different attributes found in light are assessed on their advantages and disadvantages relative to conventional broadband LWIR on a variety of topics.

Chapter 3 provides an extensive overview on the theory of polarimetry with the introduction of the Stokes parameters followed by a brief analysis on the reflection and transmission of electromagnetic waves through different mediums and experimental data collected using a polarimetric sensor is also presented to substantiate the theory. Finally, an extensive in-depth analysis, which to the best of our knowledge has never been shown before, presents the limitations on the use of Stokes parameters for manmade object detection in a natural clutter background for air-to-ground applications.

Chapter 4 introduces the data collection effort and database used for the dissertation. This chapter describes the facility used to collect the data, the LWIR polarimetric sensor, the surrogate targets, data acquisition and resulting products, and the meteorological data captured by the data collection facility that characterizes all of the different aspects of the weather conditions that occurred during the data collection effort.

Chapter 5 presents the proposed contributions for anomaly detection using polarimetric imagery. Firstly, this chapter introduces a procedure that applies morphologic-based filters, as a sequential set of image processing operations, to Stokes

imagery to enhance manmade object features while mitigating natural clutter attributes. This procedure demonstrates the capability in enhancing the signal-to-noise ratio of the manmade objects relative to natural clutter, which when combined with an adaptive threshold technique yields an efficient anomaly detection algorithm.

Subsequently, a novel concept is introduced that proposes the notion of a polarimetric datacube (PC) assembled from independent angle measurement imagery which then is used as input to multivariate detectors. Using this PC, an extensive data analysis is performed for the different classes (manmade and natural clutter), determines the inherent features that separate them, and a multivariate detector based on covariance-difference test is proposed for anomaly detection applications. Two variations of the detector are also introduced that permit the covariance-difference test to be range invariant.

Chapter 6 summarizes and concludes the work for the proposed procedures and presents some ideas for future work.

CHAPTER 2

INTRODUCTION TO INFRARED

2.1 Introduction

All objects continuously emit and absorb electromagnetic radiation as a consequence of the constant motion of charged particles within the material. A fundamental law of classical electromagnetics states that accelerated charged particles radiate energy, and as the motion of electrons and protons within a sample increases with temperature, then the amount of continuous radiation from the sample must also increase with temperature. [1] From this process, electromagnetic waves are radiated at all wavelengths which can be detected by a variety of sensors tuned to specific regions of the spectrum.

Historically, the spectrum has been divided into several regions, which are differentiated by the processes used to produce and detect the radiation. These regions can be divided into radio waves, microwaves, infrared, visible, ultraviolet, X rays, and gamma rays as seen in Figure 2.1.

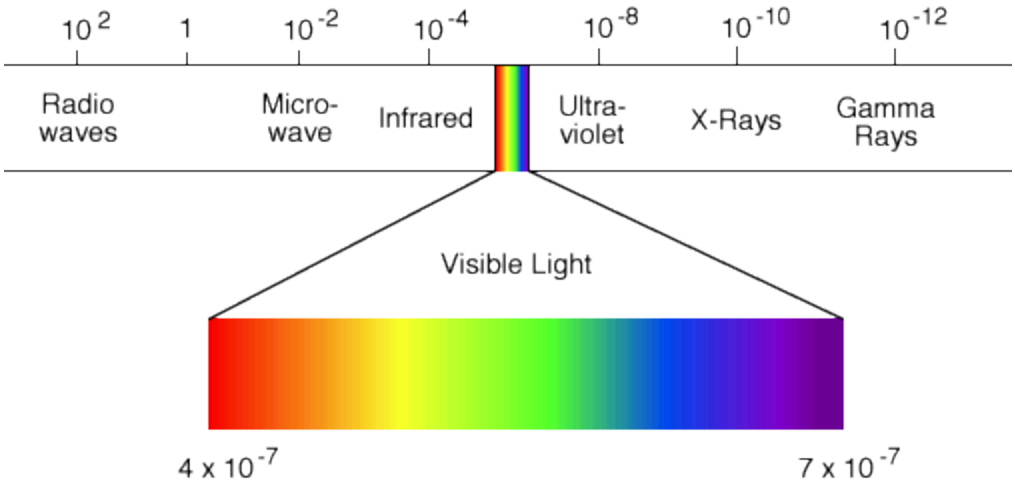

Figure 2.1 The electromagnetic spectrum as it is divided into the several regions.

Source: http://glossary.periodni.com/image/electromagnetic_radiation_spectrum_en.gif

The infrared (IR) spectrum is considered to be between 0.72 μm to approximately 1,000 μm and is divided into three distinct regions as defined by the international Commission on Illumination standard [17]: 1) IR-A (0.72 to 1.5 μm), 2) IE-B (1.5 to 3 μm), and 3) IR-C (3 to 1,000 μm). Other fields such as meteorology and climatology divide the infrared region into Near (0.7 to 4 μm), Mid (4 to 50 μm), and Far infrared (50 to 1,000 μm). No matter what standard one uses, several key points are important to underline with respect to the infrared band. For example, about 99% of the sun's output is accounted for by the ultraviolet (UV), visible, and near infrared bands. The range between 4 and 50 μm is often referred as the thermal IR band, while in other fields (for different types of applications) can reference the thermal IR as low as 14 μm. Interestingly, thermal radiation exchanges in the atmosphere tend to occur up to about 50 μm, conversely, for the band region from 50 to 1,000 μm the energy transfers in the

atmosphere is almost negligible when compared to the regions spanning from the visible to the thermal infrared.

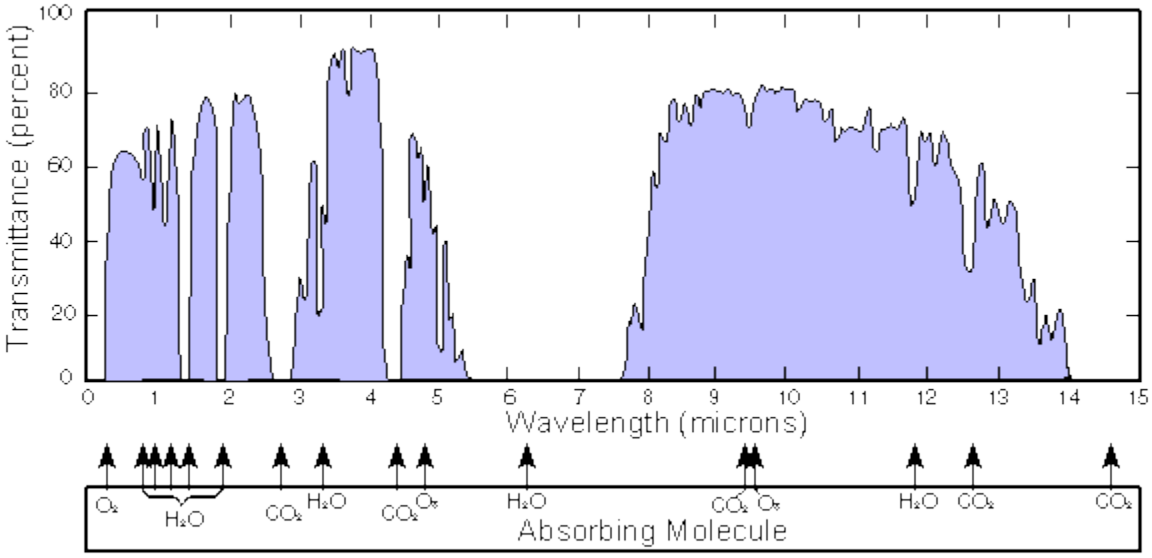

Figure 2.2 Transmittance (in percent) of EM energy per wavelength

Source:http://theboresight.blogspot.com/2009/07/airborne-infrared-andsupersonic.html#!/2009/07/airborne-infrared-and-supersonic.html

Another approach widely used by the engineering community working in remote sensing applications, and the one that shall be used in this dissertation, divides the infrared spectrum based on the response of various detectors [16] and their applications as follows: 1) Near infrared (0.72 to 1 μm) for silicon based detectors, which are widely used for night vision goggles; 2) Short-wave infrared (1 to 3 μm) for InGaAs based detectors and used for laser designation systems operating at 1064nm and 1550nm as well as visual systems that need to see through obscurants such as fog and smoke; 3) Mid-wave infrared (3 to 5 μm) which is covered by InSb and HgCdTe based detectors have applicability to anti-aircraft missile systems; 4) Long-wave infrared (7 to 14 μm) covered by HgCdTe and microbolometers are widely used in forward looking infrared (FLIR) systems that can be found in remote sensing applications as well as targeting

systems; and 5) Very long-wave infrared (14 to 30 μm) which can be detected using doped silicon.

2.2 Blackbody Radiation

In 1860, Kirchhoff [18] introduced a famous law that became the keystone in radiation transfer theory which stated, a good absorber must also be a good radiator. Kirchhoff then proposed the term blackbody to describe a body that would absorb all incident radiant energy, and as a result of his law, it would then have to be the most efficient radiator. Kirchhoff concluded that since a blackbody is defined as a perfect thermal radiator, it could also be used as a standard by which any other source should be compared to.

In 1879 Stefan, and later in 1884 Boltzmann, both reached the same conclusion that the total amount of energy radiated per unit surface by a blackbody per unit time is proportional to the fourth power of its absolute temperature [19]. In 1894, Wien published the displacement law, which describes the spectral radiation distribution of a blackbody. However, his equation only agreed with experimental data at short wavelengths and at low temperature. Nonetheless, Wien displacement law yields an important relationship between maximum amounts of radiated energy, temperature, and wavelength [20]. Six years later, Rayleigh would derive an expression that fitted experimental results at long wavelengths and at high temperatures but, this expression predicted that the energy increased without limits as a function of decreasing wavelength [21], see Figure 2.3.

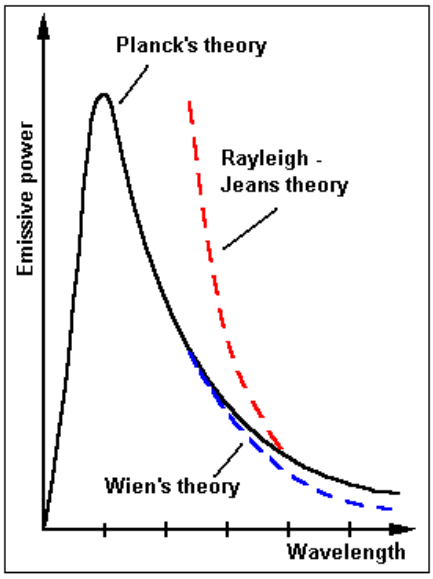

Figure 2.3. Comparison of the Wien and Rayleigh-Jeans theories to that of Planck

Source: http://library.thinkquest.org/28383/grafika/1/aczarnecialo2.gif

Plank observing that Rayleigh-Jeans law and Wien law were valid at the long and short wavelengths respectively, successfully formulated an expression that correctly interpolated the two laws at all wavelengths. Planck introduced the idea that amplitudes of oscillating electric charges, hence energy, could only increase in discrete steps by a quantity described by hv. The constant h, known today as Planck's constant is a physical constant ($h = 6.6256 \times 10^{-34}\ W\ sec^2$) which defines the sizes of energy quanta (q) of a photon and the frequency (v) of its associated wave. [22]

$$q = h\,v\ \text{[Joules]}. \tag{2.1}$$

In 1900, Planck, using his law, formulated the derivation of the radiation law that describes the spectral exitance radiation distribution from a blackbody source as, [1, 22, and 23]

$$M_\lambda = \frac{2h\pi c^2}{\lambda^5}\frac{1}{e^{ch/\lambda kT}-1}\ [W/m^2\mu m], \tag{2.2}$$

where, M_λ is the spectral exitance radiation in W/(m^{2}μm), λ the wavelength, h the Planck's constant, T the absolute temperature in °K, c the velocity of light, and k the Boltzmann's constant (1.38054x10^{-23} [W sec °K^{-1}].)

Figure 2.4 illustrates the blackbody exitance radiation at all wavelengths using the Planck's equation for different absolute temperatures. It is important to emphasize two key facts from Figure 2.4; first, Wien's displacement law describes the relationship between temperature and the wavelength of maximum spectral exitance radiation as follows, [1 and 23]

$$\lambda = \frac{A}{T}\ [\mu m], \tag{2.3}$$

where A = 2897.8 μm°K. This equation can be achieved by differentiating Planck's law and solving for the maximum. Wien's law states the wavelength were the maximum spectral radiant exitance is found decreases as a function of increasing T. As an example, Wien's equation predicts that for the sun, which its temperature is about 6000°K, the peak radiance, as per Equation (2.3), occurs within the visible portion of the spectrum at about 0.5μm. Furthermore, Figure 2.4 also illustrates Stefan-Boltzmann law, which states that the total amount of radiation emitted by a blackbody is proportional to the fourth power of its absolute temperature. The Stefan-Boltzmann law can be derived by integrating Planck's equation from zero to infinity yielding, [1 and 23]

$$M = \sigma T^4 \, [W/m^2], \tag{2.4}$$

where σ, also known as Stefan-Boltzmann constant, is defined as 5.6697x10^{-12} $[W/m^2K^4]$.

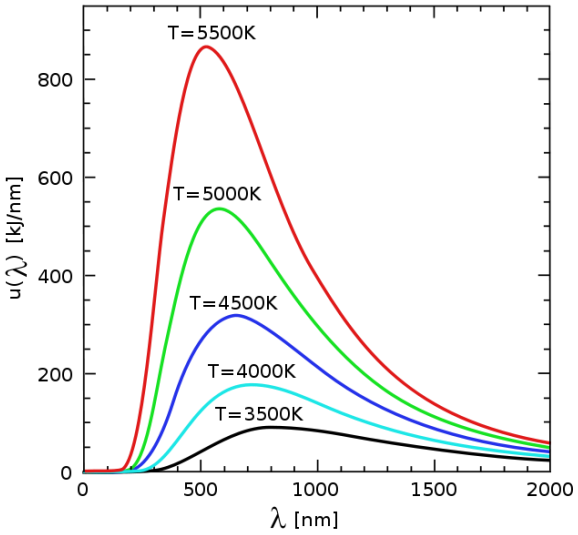

Figure 2.4 Blackbody spectral exitance radiation for different temperatures.

Source: http://www.flickr.com/photos/mitopencourseware/3681748795/

2.3 Infrared Radiometry

This section reviews the radiometric terms and definitions used to measure the amount of electromagnetic energy present in some location in space. To accomplish this, one can use ray/particle simplification of optics by assuming that light travels in straight lines and energy is transferred in discrete energy elements or packets also knows as quanta. The discussion that follows is based on material found in [1, 19, 22, and 23]

Electromagnetic radiation can be theorized as a flow of photons or discrete packets of energy, see Equation (2.1), where the total *radiant energy* (Q) can be defined as the energy carried by these same photons over all frequencies of interest,

$$Q = \sum q_i \text{ [Joules]}, \tag{2.5}$$

where, q_i is defined as,

$$q_i = n_i h v_i, \tag{2.6}$$

and h is known as *Plank's constant* with a constant value of 6.6256×10^{-34} [Joules sec] and n_i is an integer value describing the number of photons present at each of the frequencies.

A more commonly used metric is the *flux* (Φ), also known as *power*, *radiant flux*, or *radiant power*, and is defined as the rate at which the electromagnetic energy is propagating per unit time in Watts, or

$$\Phi = \frac{\partial Q}{\partial t} \text{ [W]}. \tag{2.7}$$

The rate at which electromagnetic energy is radiating onto a surface per unit area is defined as *irradiance* (E) or also known as *radiant flux density*,

$$\mathrm{E} = \frac{\partial \Phi}{\partial A} \left[\frac{\mathrm{W}}{m^2}\right]. \tag{2.8}$$

Radiant exitance (M) is defined as the flux per unit area radiated by a surface.

$$\mathrm{M} = \frac{\partial \Phi}{\partial A} \left[\frac{\mathrm{W}}{m^2}\right]. \tag{2.9}$$

Finally, *radiance* (L), one of the most important terms in radiation theory, defines the total amount of power/flux being emitted or reflected from a surface within a solid angle at a given direction. As an example, it indicates the amount of power emitted or reflected from a surface measured by an optical sensor system at an angle normal to the surface, or

$$\mathrm{L} = \frac{\partial^2 \Phi}{\partial A \, cos\theta \, \partial \Omega} \left[\frac{\mathrm{W}}{m^2 \mathrm{sr}}\right]. \tag{2.10}$$

Equations (2.7) through (2.10) have ignored the spectral response of the radiometric terms [22]. In fact, the amount of flux varies depending as a function of the wavelength of the radiating electromagnetic wave. If one is to describe flux in terms of wavelength response, Equations (2.7) through (2.10) are usually re-written as:

$$\Phi_\lambda = \frac{\partial Q(\lambda)}{\partial t} \ [\mathrm{W}], \tag{2.11}$$

$$\mathrm{E}_\lambda = \frac{\partial \Phi(\lambda)}{\partial A} \left[\frac{\mathrm{W}}{m^2}\right], \tag{2.12}$$

$$\mathrm{M}_\lambda = \frac{\partial \Phi(\lambda)}{\partial A} \left[\frac{\mathrm{W}}{m^2}\right], \tag{2.13}$$

$$\mathrm{L}_\lambda = \frac{\partial^2 \Phi(\lambda)}{\partial A \, cos\theta \, \partial \Omega} \left[\frac{\mathrm{W}}{m^2 \mathrm{sr}}\right]. \tag{2.14}$$

Where the subscript λ indicates the flux spectral response was taken into consideration in the calculations.

2.4 Emittance and Kirchhoff Law

Section 2.2 used the term blackbody to describe a body that absorbed all energy and as a result, it must also be the perfect emitter. The term blackbody followed from Kirchhoff's law, in 1860, that stated all good absorbers are also good radiators and such bodies would be, theoretically, the standard by which all other sources should be compared to. Planck's equation (Equation (2.2)) provides the limiting spectral distribution envelope of such body. This subsection will review and define the terms emittance, transmittance, absorbance, and reflectance as they are related to blackbodies, followed by brief explanation on the difference between blackbodies, graybodies, and selective radiators. The information in this subsection can be found in [1, 19, 22, and 23].

The term *emittance*, usually denoted by ϵ in the literature, is a unitless value from 0 to 1 that describes how well an object radiates with respect to a blackbody at the same temperature. A $\epsilon = 0$ implies that the object is a nonradiating body while $\epsilon = 1$ indicates that the object is radiating just like a blackbody would for some temperature T in Kelvin. *Absorbance* (α) is also an unitless value that describes the ability of an object to absorb energy relative to a blackbody at the same temperature. As mentioned in the first paragraph in this subsection, under Kirchhoff's law, all good absorbers are also good radiators and under this assumption one can state that for a blackbody emittance equals to absorbance as it shall be soon demonstrated. *Transmittance* (τ) is described as the ability of a material to allow energy to propagate through and is defined as an unitless ratio

between radiant energy transmitted through a body to that incident upon it. Finally, *reflectance* (ρ) is the ability of a material to reflect energy back to the source and is defined as the unitless ratio between radiant energy reflect by a body to that incident upon it.

Before continuing, it is important to distinguish the use of the words emissivity verses (vs) emitttance, (ϵ), absorptivity vs absorptance, (α), reflectivity vs reflectance, (ρ), and transmissivity vs transmitance, (τ), since these dual terms are widely and interchangeably used throughout the engineering community, employing the same notations but lacking any note on distinction. As per "The National Institute of Standards and Technology (NIST, formerly NBS) has recommended to reserve the ending "-ivity" for radiative properties of pure, perfectly smooth materials, and "-ance" for rough and contaminated surfaces" [24]. This dissertation follows the NIST convention and denotes α, ρ, τ, and ϵ as *absorptance*, *reflectance*, *transmittance*, and *emittance* respectively, since most real surfaces tend to fall into the latter category. Kirchhoff law can be described as follows,

$$\epsilon = \frac{M(T)}{M_{BB}(T)}, \tag{2.15}$$

where ϵ is the *radiant emittance*, $M(T)$ is the radiant exitance of the object in question and $M_{BB}(T)$ the radiant exitance of the blackbody at a given temperature T. Radiant emittance is an unitless value ranging from 0 to 1, where 0 implies a nonradiating source and 1 for a blackbody. As mentioned earlier, emittance describes how well an object can radiate energy relative to a blackbody at the same temperature. From Kirchhoff's law the

following is true: a good absorber is a good radiator, therefore, one can assume that under this assumption that

$$\alpha = \epsilon, \tag{2.16}$$

where α, known as *absorptance*, is defined as how well an object can absorb energy with respect to a blackbody at the same temperature.

When irradiance energy is incident upon a surface, the processes of absorption, reflection, and transmission must all add to 1, or

$$\alpha + \rho + \tau = 1. \tag{2.17}$$

For opaque materials where Kirchhoff's law applies, $\tau = 0$, therefore,

$$\alpha = 1 - \rho \text{ or } \epsilon = 1 - \rho. \tag{2.18}$$

When describing a blackbody, reflectance and transmittance must equal to zero, $\rho = \tau = 0$, in order to satisfy Kirchhoff's law that states all good absorbers are also good radiators, or in other words,

$$\alpha = \epsilon = 1. \tag{2.19}$$

Transmittance (τ) is often referred as the ability of a material to allow energy to propagate through and is defined as an unitless ratio between radiant energy transmitted (M_τ) through a body to that incident (E_i) upon it, or

$$\tau = \frac{M_\tau}{E_i}. \tag{2.20}$$

Reflectance (ρ) is the ability of a material to reflect energy back to the source and is defined as the unitless ratio between radiant energy reflect (M_ρ) by a body to that incident (E_i) upon it, or

$$\rho = \frac{M_\rho}{E_i}. \tag{2.21}$$

Absorbance (α) is a material's ability to convert irradiated energy into another form of energy (usually heat), and is defined as the unitless ratio between energy converted into another form of energy, M_α, to that incident (E_i) upon it, or

$$\alpha = \frac{M_\alpha}{E_i}. \tag{2.22}$$

If the material's emittance, reflectance, absorbance, and transmittance values fluctuate with respect to wavelength, the subscript λ should be used. Any source can be distinguished by the way the spectral emittance varies, for example, a blackbody emittance value is constant throughout all wavelengths ($\epsilon_\lambda = \epsilon = 1$), while for a graybody $\epsilon_\lambda = \epsilon = \text{constant} < 1$; and finally for a selective radiator, $\epsilon_\lambda$varies with wavelength as shown in Figure 2.5.

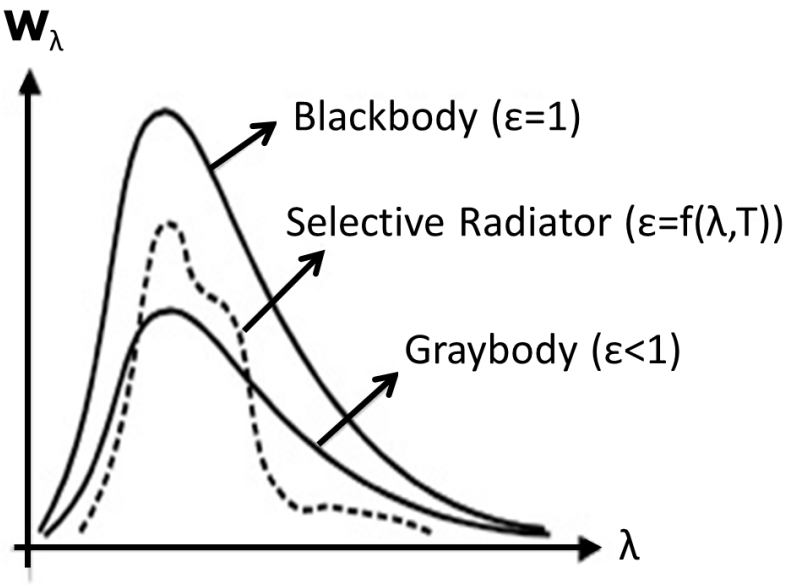

Figure 2.5 Comparison between Blackbody, Graybody, and Selective Radiator spectral response.

Source: [25]

Most materials types, independently whether they belong to natural or manmade objects, fall in the selective radiators category.

2.5 Challenges Using Conventional Infrared

Conventional LWIR sensors are widely used in commercial and military applications, and operate by integrating all the photons collected within the spectral response of the FPA. A picture of a FLIR Tau uncooled LWIR microbolometer and its typical spectral response can be seen in Figures 2.6 and 2.7, respectively.

Figure 2.6 Conventional LWIR microbolometer sensor manufactured by FLIR©, designated as Tau 640 camera engine.

Source: http://www.flir.com/

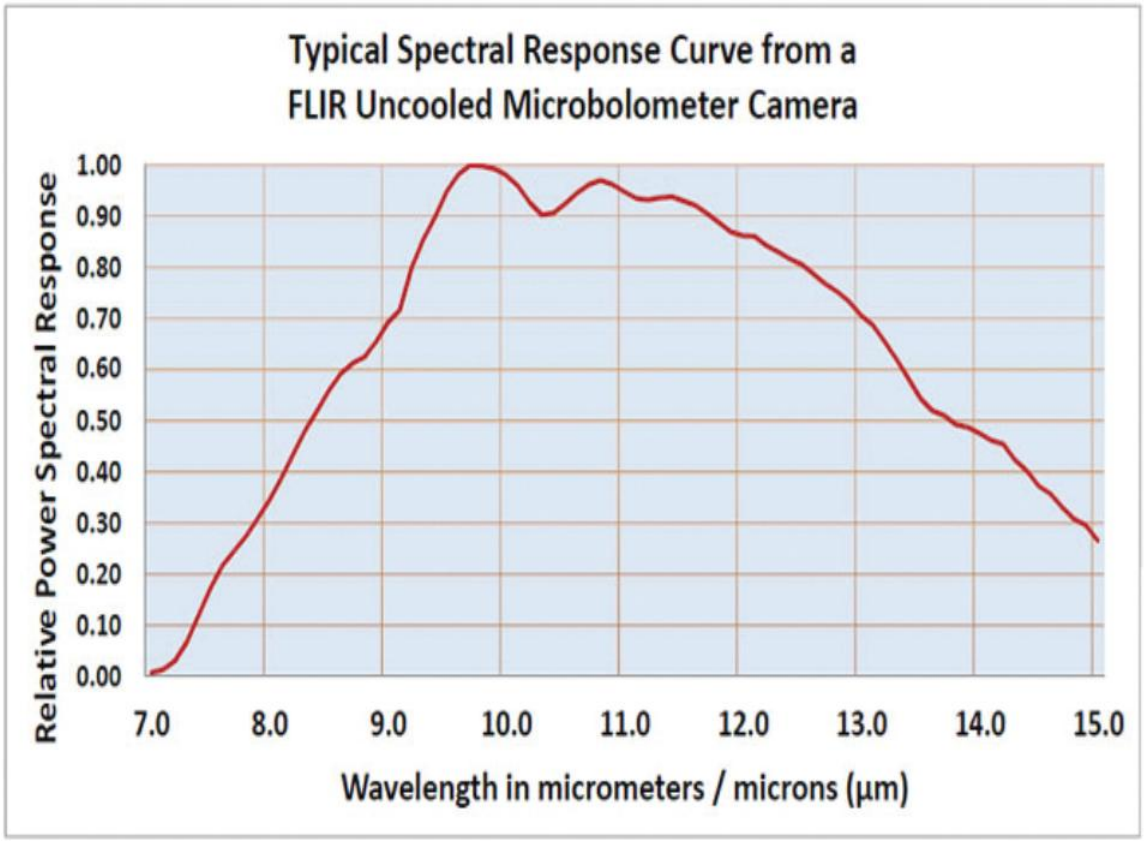

Figure 2.7 Typical spectral response curve for FLIR© Tau microbolometer cores.

Source:http://www.flir.com/uploadedFiles/CVS_Americas/Cores_and_Components_NEW/TauResponseCurve.pdf

In broadband imagery one can find two types of imagery, *low contrast* and *high contrast*. Low contrast imagery is usually defined as an image where the object of interest exhibits the same or very similar radiance values to that of clutter. In such situations, the object cannot be successfully detected without a high number of false alarms making the imagery unusable for detection applications. High contrast imagery is defined as a scene where the target exhibits significantly higher or lower radiance values, most cases the former is true, than existing clutter, therefore, the detection of the target is easily accomplished with very few false alarms.

Low contrast scenes are, of course, not desirable because targets (manmade objects in this case) in the LWIR region of the spectrum in particular are not very distinct relative to natural objects composing the background scene, thus making it extremely difficult for an operator to find these targets in a natural clutter environment. Ditto for an algorithm expected to perform this task automatically, without human intervention. Such low contrast conditions can be found during certain times of the day depending on the object temperature and meteorological conditions one may encounter.

Figure 2.8 illustrates a target site where surrogate targets were placed at about 550m from the sensor. In this image one can observe three surrogate targets at three different aspect angles denoted as T_0, T_{90}, and T_{135} referencing their aspect angles. An external blackbody covered by a black canvas and a concrete metal hut can also be observed on the left side of Figure 2.8, with the exception of the metal plates (shown in the middle of the figure) which were not present during the data collection.

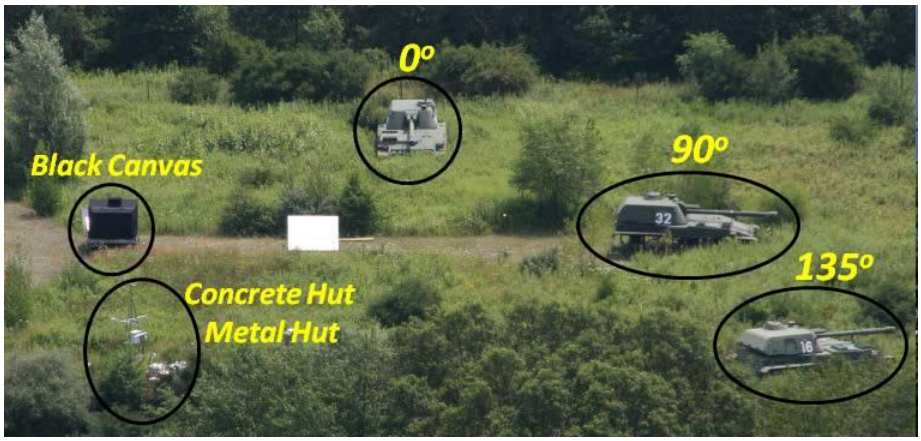

Figure 2.8 Target site depicts three surrogate targets and other manmade objects in a natural clutter background (trees, trunks, soil, grass) setting. Manmade objects that were present in the scene during the actual data collection are circled, with the tank surrogates' aspect angles labeled immediately above corresponding circles.

Figure 2.9 illustrates several hand-picked scenarios from 6 March (MAR) 2010 SPICE database (Chapter 4 introduces the SPICE data collection), where low contrast between the target and clutter was present using conventional (broadband) LWIR imagery. The targets used were self-propelled howitzers surrogates that had their heating elements turned *off* during this experiment, where the only possible source of heat would be the sun during daylight hours, as well as an outdoor blackbody system covered by a black canvas, see Figure 2.8,. A detailed description of the targets can be found in Chapter 4 in addition to details on the SPICE data collection.

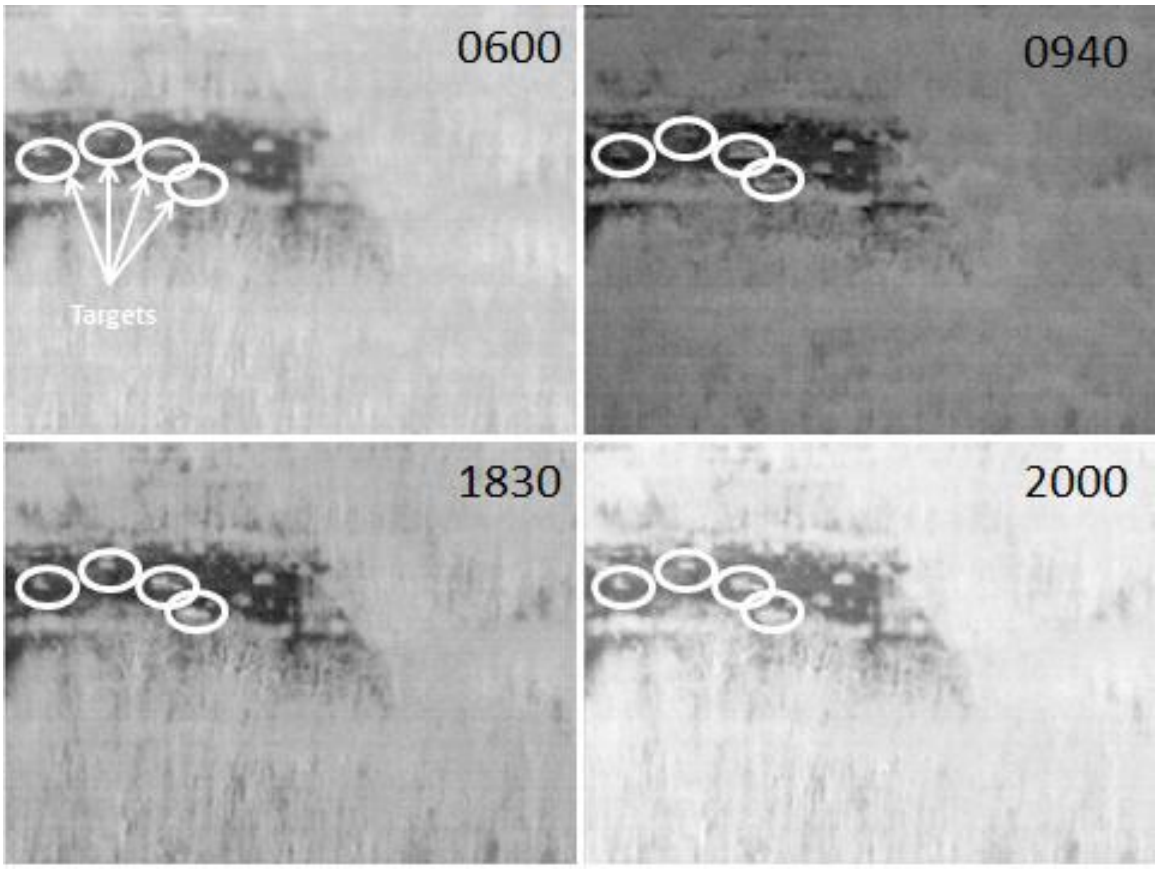

Figure 2.9 Example of low contrast scenarios using conventional broadband LWIR imagery at different times in the day for 6 MAR 2010. Targets in the scene had the heating elements turned *off*, and as a result, the targets temperature was similar to the surrounding clutter.

Each sub-figure in Figure 2.9 illustrates handpicked timestamps that represent low contrast imagery where dark tones represent low radiance values while bright tones represent high radiance values. Circles were used to aid the reader in locating the four targets in each of the sub-figures.

As shown in Figure 2.9 none of the manmade objects of interest can be successfully discerned from the background due their similar radiance values. This similarity is a result of the lack of solar loading on the manmade objects since the sunrise and sunset for 6 MAR 2010 was around 0625h and 1754h, respectively. Interestingly, one can observe that even at 0940h, more than three hours after sunrise, the target

radiance values are still very close to that of clutter. This very slow rise of the target temperature even after sunrise is the result of two key factors: 1) the manmade objects are located within a valley, therefore, the solar loading effect only happens after 0800h-0830h and 2) the surrogate targets used for this experiment are an empty shell, as one can see from Figure 2.8 for the target at 90° for example. Therefore, because of the constant flow of air surrounding the surrogate's shell, more time is needed, under the solar loading effect, for the target temperature to rise above clutter.

The top images in Figure 2.10 demonstrates an example of a low contrast scene (left side) and a binary image (right) representing the low contrast image thresholded using $\pm 3\sigma$ value. Pixel values that fall in the closed interval $[-3\sigma, 3\sigma]$ are represented by black pixels in the binary image in Figure 2.10 (top right side), and those that fall outside the interval are represented by white pixels in the same image, i.e., anomalies.

The plot in Figure 2.10 illustrates the kernel probability density estimation of each of the surrogates and clutter for the test image where the x-axis represent the range of radiance values that can be found in the test image while the y-axis represent the estimated PDF result from radiance values of the different object classes in the scene (natural background, T_0, T_{90}, T_{135}). Kernel density estimation techniques are non-parametric methods used to estimate the probability density function of observed data that cannot be readily apparent to the user.

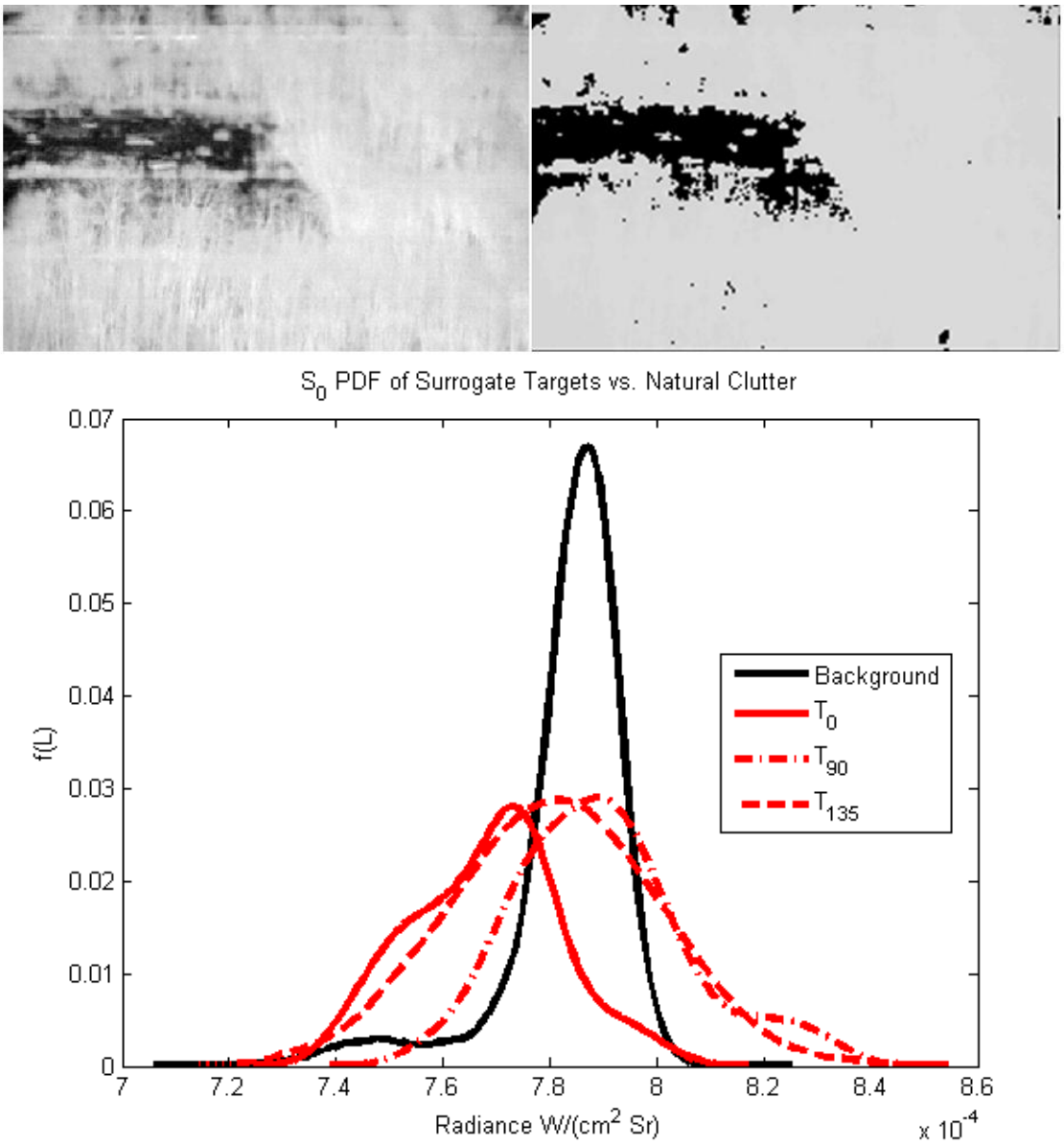

Figure 2.10 Example of a low contrast scene, top left, and the threshold (binary) image located top right. Bottom image illustrates the estimated PDF of the targets and background using a kernel method for the estimation. The PDF of the targets is clearly within the background distribution.

Where for a random variable $x = \{x_1, x_2, \dots, x_n\}$ drawn from an unknown density function f, the kernel density estimate of f is defined as,

$$\hat{f}_h(x) = \frac{1}{n}\sum_{1}^{n} K_h(x - x_i) = \frac{1}{nh}\sum_{1}^{n} K_h\left(\frac{x - x_i}{h}\right), \tag{2.23}$$

where the $K(\cdot)$ is the kernel , n the number of samples in x, h the smoothing parameter called the bandwith which is a free parameter that directly affects the estimation of f, see [26-28] for more information on the kernel density estimation and smoothing parameter. Matlab® function *ksdensity* [29] was used to determine the shape of distribution of all the classes shown on the plot in Figures 2.10 and 2.12 by using the Gaussian Kernel function, with 100 (default) equally spaced bins, and the default bandwidth parameter which is considered optimal for estimating normal densities. It is important to note that any changes in the Kernel function, bin spacing, or bandwidth parameter used has a direct influence on the resulting shape of the observed data and may result in a different shape than the ones presented in this dissertation.

As mentioned earlier, the plot in Figure 2.10 illustrates the estimated density of each of the surrogates compared to background clutter. One can observe that the distributions of the surrogate targets are within the clutter distribution and as a result the ability to discriminate each of the objects of interest (especially using features as the mean value from sampled radiance) from clutter is virtually impossible without allowing a tremendously high number of false alarms to pass through, which makes the resulting output surface impractical for any manned or unmanned system to use (see top right image of Figure 2.10 as an example).

Low contrast scenarios can happen or be achieved by several means other than as having sources of heat turned off (e.g., engine) as demonstrated in this example. Unfavorable meteorological conditions (e.g., rain, fog, etc.) that limit the system

detection range and the deployment of effective countermeasures such as fitted camouflaged nets also create situations where the target may not be readily visible with respect to the surrounding clutter. Consequently, one can conclude that low contrast conditions demonstrate a challenge for anomaly and target detection using conventional infrared imagery as both the target and clutter PDFs are not easily separable.

In contrast to the conditions shown in Figures 2.9 and 2.10, *high contrast* scenes are found when the object of interest temperature is higher, or sometimes lower, than background clutter, for example a tank with the engine running or the effect of solar loading on the target. Figure 2.11 demonstrates four timestamps of high contrast imagery where the temperature of the target is considerably higher than the surrounding clutter. One can also observe, as expected, that the difference between the target and clutter is more accentuated for timestamps 1320h and 1440h during which the sun is the strongest. Figure 2.12 illustrates a high contrast image (top left) and the resulting binary imagery (top right) when the top left image is thresholded using the same $\pm 3\sigma$ threshold value as before. As it can be observed, the three surrogate targets are clearly identified in the binary (threshold) imagery with very few false alarms. The bottom image in Figure 2.12 demonstrates, as expected for high contrast imagery, that a good portion of the probability density function of the surrogate targets is outside of the clutter density function. One can, therefore, conclude that broadband LWIR systems, cooled or uncooled, are extremely useful in discriminating objects from clutter in situations where the target temperature is significantly higher or lower than the temperature of the objects composing the background clutter. Regardless of the low contrast imagery problem,

broadband infrared is a very useful and widely used modality that can be found in many remote sensing applications.

Figure 2.11 Example of high contrast scenarios using conventional LWIR imagery at different times in the day for 6 MAR 2010. Targets in the scene had the heating elements turned off. Continuous solar loading allowed the target plates to reach temperatures higher than the surrounding clutter.

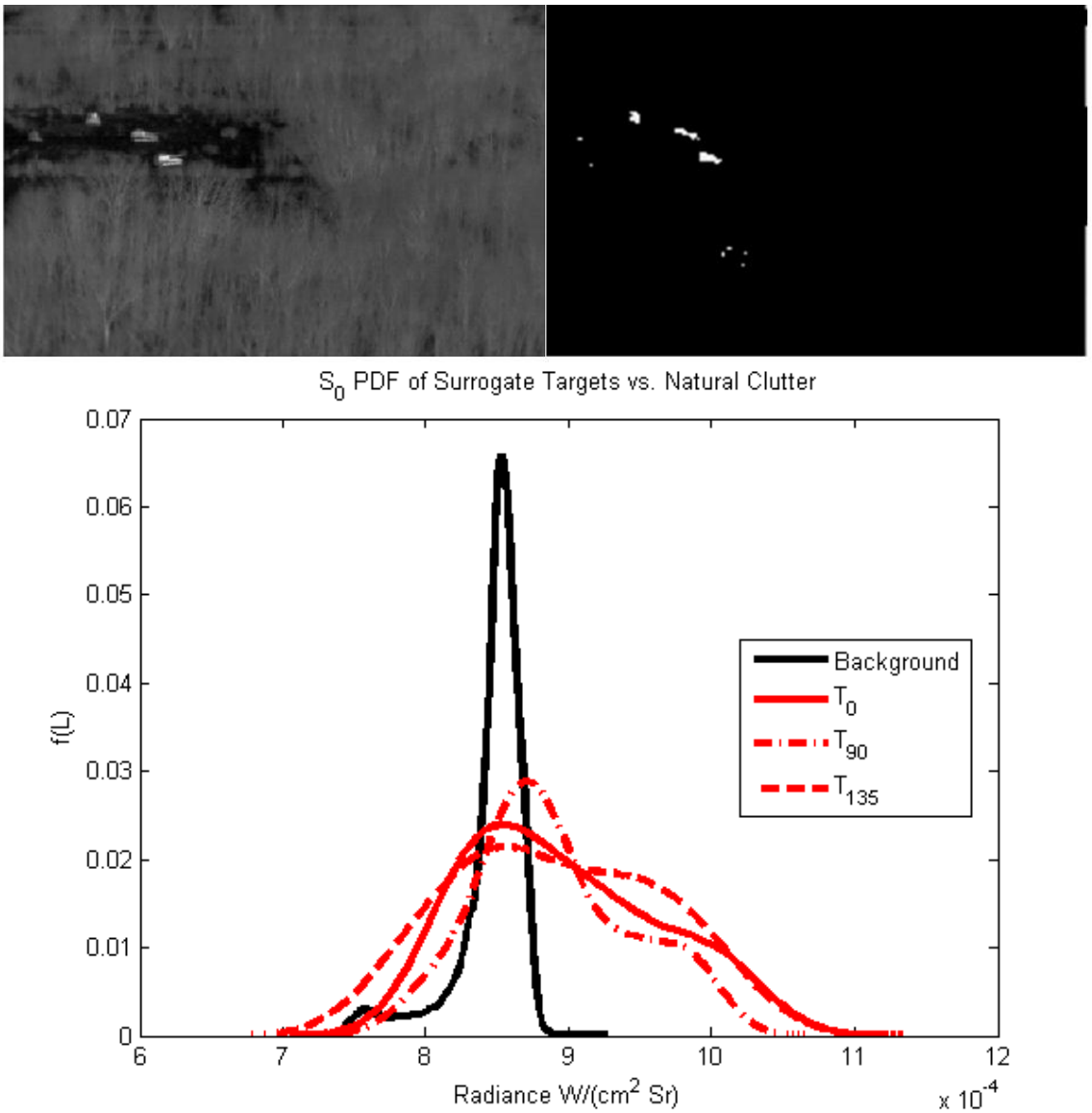

Figure 2.12 Example of a high contrast scene (top left) and binary image (top right). Bottom image illustrates the estimated PDF of the targets and background using a kernel density estimator. In contrast to Figure 2.10, portions of the target are separable from the natural clutter due to their significantly higher temperature compared to the background clutter.

Broadband LWIR imagery is quite useful in detecting targets if their distributions lie outside of the background clutter PDF as it was shown in Figures 2.11 and 2.12. Although the targets in the scene, Figure 2.11, were hotter than the background, it is also important to understand that high contrast imagery can also be represented by the opposite, a scene where the background is hotter than the targets.

In conclusion, broadband LWIR imagery performed very poorly in detecting the targets in low contrast imagery where the clutter and target PDFs aren't easily separable as shown in Figure 2.10. In this case many false alarms are detected prior to successfully detecting the intended targets, which make such imagery (see images in Figure 2.10) useless for an autonomous or aided system to successfully discriminate the intended target(s). Therefore, it is the conclusions of this subsection that LWIR broadband imagery, although extremely useful, has serious limitations for real world applications when encountering low contrast imagery.

2.6 Sensing Modalities in the LWIR Region

The focus of Section 2.5 illustrated the advantages and disadvantages of broadand infrared relative to high and low contrast scenes. Low contrast scenes, as demonstrated earlier, make it difficult to deploy conventional infrared system for the detection of potential manmade objects of interest. As highlighted earlier, low contrast can be achieved by 1) deploying infrared countermeasures such as camouflage nets, thereby reducing the target's infrared signature; 2) eliminating or turning off potential heat sources such as the engine; or 3) through adverse meteorological weather conditions. The third condition is often outside anyone's ability to control, unlike the first two. Giving that conventional infrared can be easily countermeasured by the use of camouflaged nets and flares or by turning off target engines and let the target cool off to ambient temperature; other modalities within the LWIR infrared region of the spectrum began to emerge that take advantage of other attributes found in light which are useful in discriminating potential targets from the background. These attributes, wavelength and polarization diversity, have been exploited using hyperspectral and polarimetric sensing

modalities, and more recently the spectral-polarimetric sensing modality. These three sensing modalities will be briefly discussed in the following subsections with a summary on their advantages and disadvantages.

2.6.1 Hyperspectral Imagery

Hyperspectral (HS) imaging sensors collect the electromagnetic radiation that each material reflects, absorbs, and emits by sampling the spectrum into tens or hundreds of bands, which in turn allows for the generation of spectral signatures that in theory should be unique to each material in the scene. Airborne platforms are often referenced as the platforms of choice for hyperspectral sensors for remote sensing applications due to their size, weight, and power capabilities, which is needed to operate such HS cameras.

A remote sensing hyperspectral sensor records the reflected or emitted electrogmagnetic radiation by dividing the bandwidth into many adjacent bands, each with a different spectral value. As the sensor flies over an area of interest, it records the radiation over an area in many different wavelengths (see Figure 2.13) with a ground sampling distance corresponding to less than one to many squared meters of the scene depending on the resolution of the FPA and its altitude to the ground.

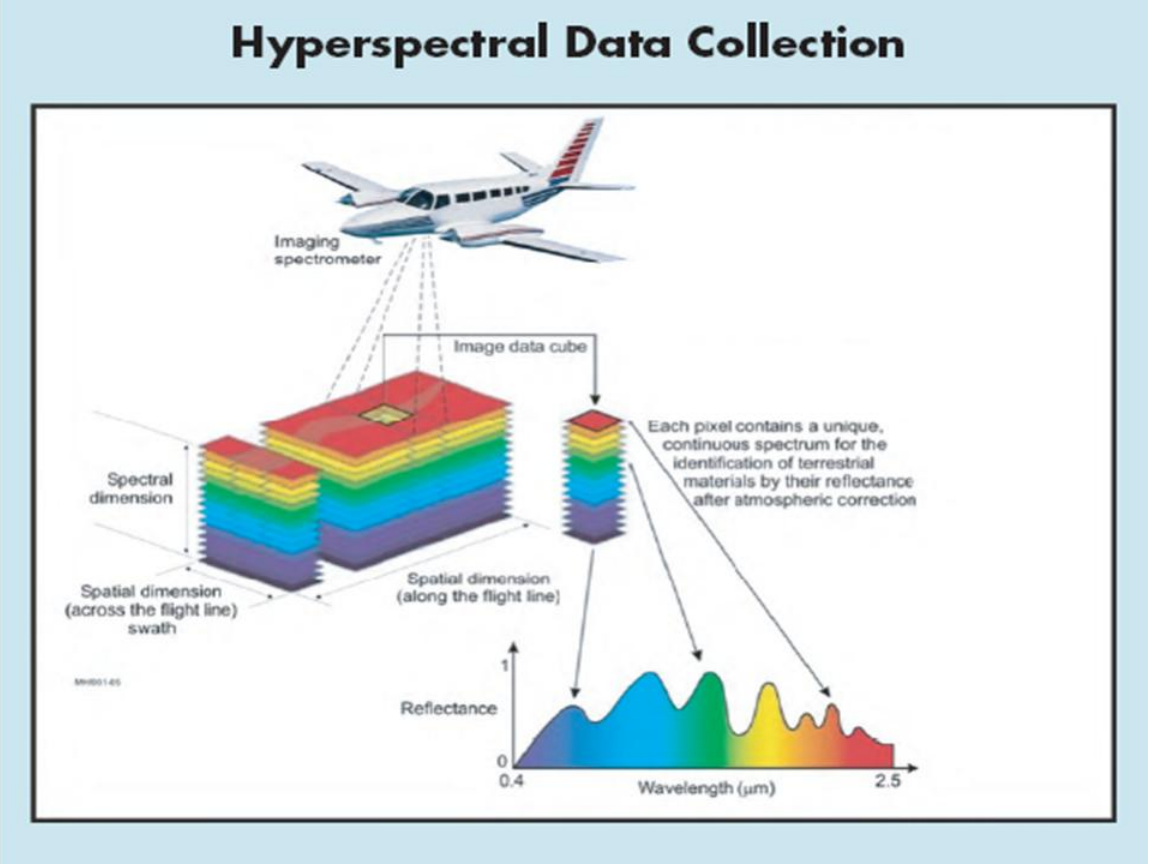

Figure 2.13 Hyperspectral cubes and material spectral sample. Hyperspectral cubes are representations of a scene at different wavelengths where the x and $y-axis$ represent the spatial information of the scene while the $z-axis$ represents the spatial area at different wavelengths. A pixel in a HS data cube is, therefore, a vector of wavelength information of a physical material present at a specific (x, y) location in the scene.

Source: http://www.hyvista.com/wp_11/wp-content/uploads/2008/08/hdc.png

The spatial-spectral information is then compiled into what is known as HS data cube where the length and width represent the spatial dimension and the depth the spectral dimension. Each pixel along the depth of the HS cube is defined by a spectral signature representative of the material(s) in that spatial area. In theory, each spectral signature should be unique to the properties of the material it represents, however, in practice, atmospheric conditions, sensor noise, sensor artifacts, illumination effects,

attenuation, etc., play a significant role in distorting the materials "pure" spectral signature causing the materials to exhibit high spectral variability.

Algorithm development for HS imagery can be divided into three categories: 1) *anomaly detection*, the identification of pixel locations anomalous to the scene; 2) *target detection*, the identification of objects by correlating known spectral signatures to pixels in the HS cube; and 3) *atmospheric correction* which corrects HS cubes for path losses by transforming the input cube into an observation of the materials in the scene as if no path losses were observed by the sensor.

As mentioned earlier, anomaly detection refers to the identification of "rare" pixels that fall outside the overall distribution of the majority of the pixels in the image. Anomaly detection usually has no *a priori* knowledge about any targets in the scene and it generally utilizes all the pixels in the scene in order to predict its global statistical distribution to identify pixels in the image that may fall outside the global distribution.

Target detection, on the other hand, is used to identify pixels of interest by matching the pixels in the scene to a look-up table (LUT) of spectra. This LUT is composed of materials that the user or system is trying to detect in the scene, however as previously mentioned, spectral variability due to a variety of factors is a major concern in hyperspectral target detection as one needs to have a tremendous amount of spectral signatures for a given material that incorporates all the possible variability that may be seen by the platform. A variety of target detection algorithms such as support vector machine, support vector data description, and sparsity [6, 8, 7, and 30] based target detectors are currently being used by the scientific community to identify materials of interest in HS imagery.

The third category on algorithm development is the use of atmospheric correction codes to revert, using atmospheric models, the spectral signatures in the HS data cube as if the sensor was collecting the data up close without any atmospheric path losses. In this construct, reversing the signatures to their "pure" state (eliminating the path loss observed by the sensor), target detection LUTs would only need to have one signature per material of interest, thus simplifying the complexity of the algorithm as well as processing time.

Software programs such as QUAC [31] and FLAASH-IR [32] by Spectral Sciences Inc. (SSI) attempt to correct each pixel in the HS cube for atmospheric effects/attenuations in order to retrieve the original spectral signature of each material in the scene, where QUAC is used for imagery collected in the VNIR region and FLAASH-IR is used for imagery collected in the LWIR region.

In the state of practice, HS systems often employ a system consisting of anomaly detection, atmospheric correction followed by target detection or identification, using retrieved reflectance (in the VNIR) or retrieved emissivity (in the LWIR region) for the test. This composite capability is particularly important for applications such as chemical plume detection, disturbed earth detection (as a precursor to finding IEDs) which need to rely on highly effective algorithms.

As advantageous as HS imagery may seem to be for detecting and identifying pixels of interest using spectral signatures, which cannot be accomplished in conventional infrared systems, it also comes with some noticeable drawbacks that need to be addressed. For example, the amount of processing required to load and process each HS cube, often composed of hundreds of images, is a lot higher than processing a 2-

dimension conventional infrared imagery. Parallel processing methods or high power processors are needed in order to process HS imagery in a timely manner thus, restricting the use of HS sensors and its processing to large aerial platforms that have the necessary real estate for the sensors and computing power needed.

Cost is another key disadvantage of HS sensors as they require the use of very sensitive detectors when compared to conventional infrared sensors. The need for higher sensitivity FPAs is the result of slicing the number of available photons within the response of the FPA by a very large number of bands captured by the sensor, thus reducing the signal-to-noise ratio of each spectral image. Finally, the size and weight of these systems make them too bulky to be hand carried by an operator and the power requirements needed for HS imagers limit how far these systems can be placed away from power generators (vehicle, airplane, or grid).

2.6.2 Polarimetric Imagery

Polarimetry imaging sensors, the modality in focus in this dissertation, capture the changes in the polarization state of incoming electromagnetic waves by, one method, rotating a polarizer in front of the optics. Such imaging sensors record the reflected or emitted electromagnetic radiation (intensity) as it passes through a polarizer at deterministic angles to form an p-dimensional polarimetric cube, where p is determined by the number of angles measured for each data cube, which for most cases, these measurements are accomplished at four distinct angles such as 0°, 45°, 90°, and 135°. By adding or subtracting specific images in the p-dimensional polarimetric cube, one can form a Stokes polarimetric image cube as shown in Figure 2.14.

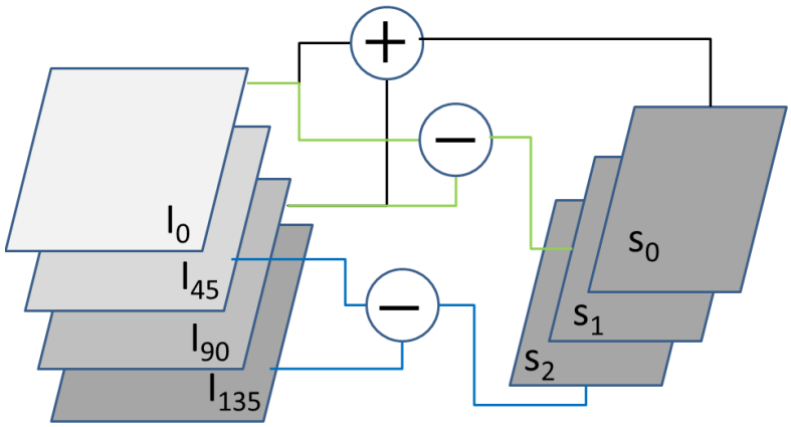

Figure 2.14 Generation of the Stokes vector parameters using polarization measurements (0°, 45°, 90°, and 135°).

Each image in the Stokes image cube is usually processed and analyzed independently from all others, as each image represents a measure on the state of the electromagnetic wave for a particular spatial location of the scene. The first image, denoted as S_0, is defined as the total intensity of the scene as if the polarizer was absent from the system. The second image S_1, represents the difference between the horizontal and vertical polarization measured by the camera, while S_2 represents the difference between +45° and -45° polarization. As a sensor flies over a scene, depending of the values of S_1 and S_2, smooth manmade object can be discriminated from the background as such materials tend to emit or reflect highly polarized electromagnetic radiation, while conversely, natural clutter often exhibits very low polarization content. As a result of this polarization difference between clutter and smooth surfaces, Stokes images S_1 and S_2 are widely used for the detection of manmade objects, as anomalies, in the context of natural clutter. In addition, it has been claimed by [14 and 33] that multi-view Stokes information could be used for material classification by estimating the complex index of

refraction of all the materials in the scene, however, such work has only been validated in laboratory environments at this time.

During the past decade, polarimetry has seen tremendous advancements especially in the field of sensor development with sensors that are light with low power consumption, and the methods/techniques by which the Stokes vector measurements are captured satisfy a variety of different applications. Polarization imagers can be divided into four very different techniques with each one of them having advantages and disadvantages and their applicability to certain applications.

The most straight forward and simple to manufacture polarimetric camera is the *Step Rotating Element Polarimetric Imager*. This method records polarization measurements by rotating a polarization element (polarizer) in front of the camera at specific angles from where the Stokes vector imagery are then calculated by adding or subtracting the collected imagery. The disadvantage of such system is that both the scene and the camera must be stationary in order to avoid the introduction of artifacts due to motion. Another technique called *Division of Amplitude* consists of a sensor that employs four separate FPAs combined with a common objective lens and polarizing beam splitters and retarders to produce a polarimetric image. By employing such methodology, one is able to measure the complete Stokes information from the four images captured simultaneously, reducing or eliminating any artifacts due to scene/platform movement. The obvious drawback of such system is the correct alignment of each of the FPAs that minimizes potential misregistration issues as well as the cost of the components, especially the FPAs and the electronics needed to support them. *Division of Aperture* uses a single FPA that is divided into, usually, four areas

where each one of those areas represents a polarization angle (see Figure 2.15). The principal advantage of this technique is the "instantaneous" collection of the four polarization images necessary to calculate the Stokes imagers. Cost, is another advantage, which unlike Division of Amplitude, only utilizes one FPA to collect the information. However, the disadvantages of using such system are: 1) the loss of FPA spatial resolution by a factor of two and 2) volume and weight of additional reimaging optics needed to co-bore sight all polarization channels.

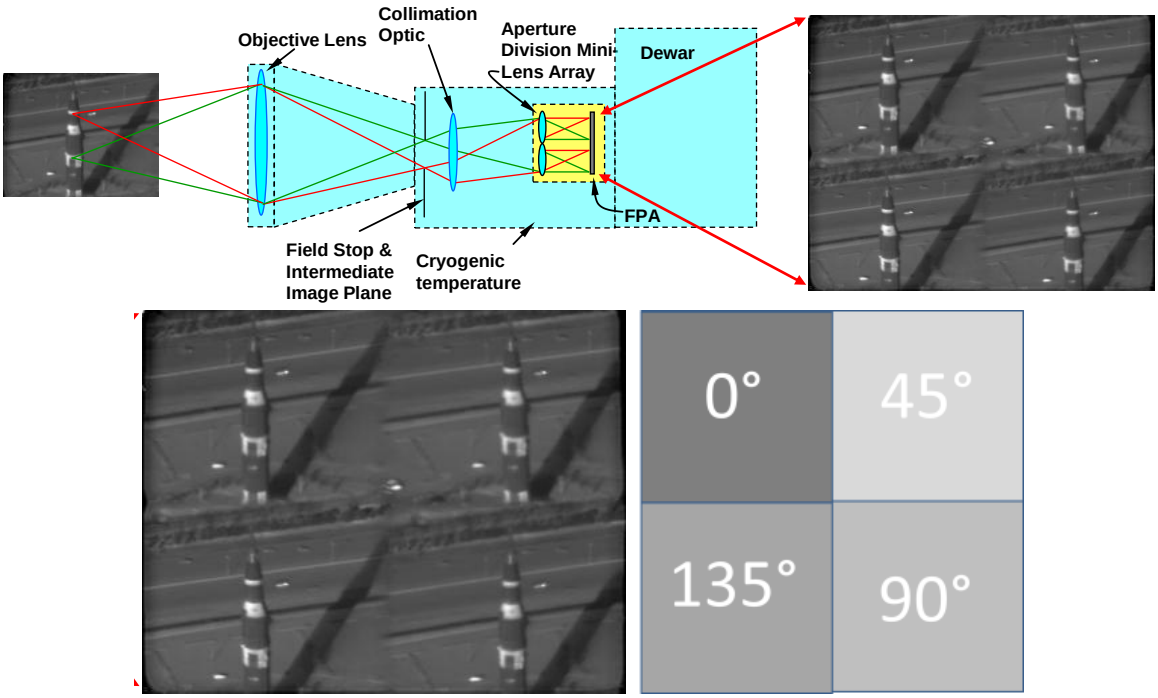

Figure 2.15 Schematic of a Mid-Wave infrared Division of Aperture imaging polarimeter.

Source: [34]

Finally, *Division of Focal-Plane Array* polarimeters use micro-optical polarization elements directly integrated onto the FPA such that each pixel sees a different polarization angle measurement and a group of 2×2 pixels may be used to

estimate the Stokes vector at each pixel by interpolating points in the FPA (see Figure 2.16).

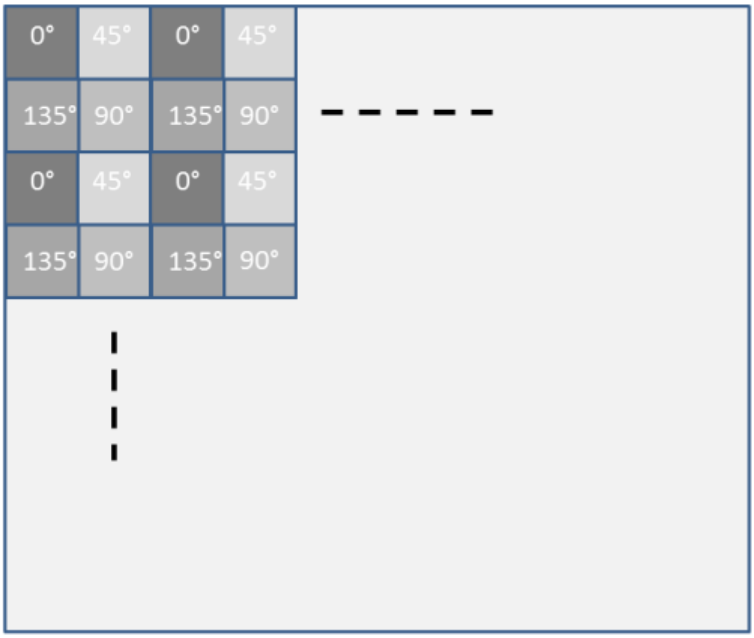

Figure 2.16 DoFP FPA divided into micro-optical polarization elements.

Division of Focal Plane Array sensors have the same advantages as Division of Aperture systems as they collect simultaneous measurements for every pixel in the scene while using only one FPA. However the disadvantages result from pixel-to-pixel crosstalk, which is unwanted information captured by a given pixel due to interferences from other neighboring pixels, and a one pixel misregistration when computing the Stokes vector information as a result of the division of FPA. For more information about each of the sensors please refer to [2].

Algorithm development for polarimetric imagery falls into three categories much like hyperspectral imagery: 1) anomaly detection, 2) object orientation, and 3) material classification. Polarimetric anomaly detection algorithms often refer to the identification of “rare” pixels that exhibit a preferred polarization orientation of the radiation that is

common to manmade materials. More often than not, this information can be easily extracted from either S_1 or S_2, however there have been cases where both S_1 and S_2 are fused in order to enhance the detection of manmade objects from a scene. Regardless of the methods one uses to extract the locations of rare pixels, anomaly detection is still one of the most widely used approaches in detecting manmade objects in natural clutter background. Surface orientation is another method where the use of polarimetric information allows in determining the orientation of optically smooth surfaces relative to the viewing perspective of the sensor. Such information has not been widely exploited in practical scenarios since one must be sure the test pixels do in fact represent the intended object of interest and not false alarms that may be present in the image. On the other hand, material classification using polarimetric imagery is accomplished by observing materials at different viewing camera angles and calculating the complex index of refraction for each material in the scene [35]. Although the work has shown promising results, some drawbacks of using such methodology include: 1) misregistration of collected imagery as the platform moves across the scene; and 2) lack of consideration for atmospheric effects on the propagation of the electromagnetic wave that may limit the ability in successfully classifying a material.

Several advantages in using polarimetric imagery are: 1) the cost of the sensors which can go from tens of thousands to hundreds of thousands of dollars depending of the application and sensitivity required; for example $40k for a LWIR polarimetric sensor versus a $200k or greater hyperspectral sensor; 2) the hardware complexity of such devices compared to hyperspectral sensors; 3) and the small size of the sensors, again depending of the application.

One key disadvantage is the lack of interest by the engineering community due to the difficulty of using polarization information to discriminate manmade objects in a variety of backgrounds as it shall be demonstrated in Chapter 3. The cost is another disadvantage of polarimetric sensing technology compared to broadband LWIR sensors. Moreover, using a polarimeter in front of the lens cuts the available light reaching the FPA by as much as 60%, which for certain applications, may require FPAs with higher sensitivity thus increasing the sensor's overall cost.

2.6.3 Spectro-Polarimetric Imagery

Spectro Polarimetric (SP) imagery which started in late 90s and early 2000s as a research topic has developed into a field of its own. The idea behind using such sensors is that it brings all of the features (shown in Subsections 2.6.1 and 2.6.2) into one single datacube. Each spectral slice of the datacube collected by a SP sensor is composed of three, sometimes four, different images: $S_0^{\lambda i}$, $S_1^{\lambda i}$, $S_2^{\lambda i}$, and Degree of Linear Polarization ($DoLP^{\lambda i}$). $S_0^{\lambda i}$ represents the broadband image and $S_1^{\lambda i}$, $S_2^{\lambda i}$, and $DoLP^{\lambda i}$ represent the polarization information images for wavelength λ_i as shown in Figure 2.17.

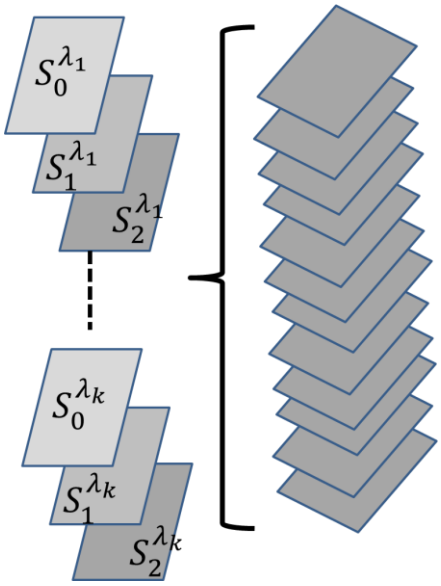

Figure 2.17 A spectral-polarimetric data cube. Each wavelength is represented by three measurements, the intensity (S_0), and S_1 and S_2 polarization measurement.

As such, if one were to stack all $S_0^{\lambda i}$ images into a cube, it would represent a hyperspectral data cube captured by a HS sensor. Conversely, if one would add up all of the individual $S_1^{\lambda i}$, $S_2^{\lambda i}$, or DoLP $^{\lambda i}$ images together it would represent the broadband polarization information captured by a conventional polarimeter. Finally, if one would integrate all $S_0^{\lambda i}$ images, then the output would be representative of a conventional broadband image. As one can observe, a SP sensor provides a lot of information that can be processed together or separately to provide enhanced detection and classification capabilities to a user. As advantageous as this technology may sound, its drawbacks are many, for example, if one of the drawbacks of hyperspectral was the SNR of each spectral image, now that a polarizer is introduced into the system, it would require a FPA with significantly higher sensitivity and, as a result, more expensive imagers need to be used with SP technology. The time that it takes to collect an image with tens of wavelengths was already difficult to accomplish in a dynamic environment using

hyperspectral imagery, adding another modality to the system, ultimately forces such systems to be used in stationary or in very low dynamic scenes.

2.7 Summary and Conclusions

Chapter 2 provided a brief introduction to infrared radiometry focused on conventional LWIR infrared imagery and the challenges LWIR imagery faces in situations where low contrast scenarios are observed by the sensor. During these situations, potential targets of interest are blended within the background making it very difficult for an autonomous algorithm to detect these targets from clutter. Three LWIR sensing modalities were introduced: hyperspectral, polarimetric, and spectral-polarimetric that take advantage of spectral and/or polarization aspects of reflected or emitted light and can be used to detect manmade objects (formed by a variety of material types) in natural clutter backgrounds under certain low contrast scenarios where broadband imagery fails. In particular, hyperspectral sensors divide the bandwidth into tens or hundreds of images each representing a different wavelength allowing for target and clutter spectral discrimination; and the polarization of reflected or emitted light, which can be collected using polarimetric sensors, is exploited for manmade object detection, since in principle optically smooth surfaces polarize differently from natural objects. Finally, the spectral-polarimetric sensor was briefly discussed in Subsection 2.6.3, which in essence combines the information captured by both hyperspectral and polarimetric sensors into one data cube, bringing along with it the advantages and disadvantages of both HS and polarimetric sensing modalities.

CHAPTER 3

OVERVIEW OF POLARIMETRY

3.1 Introduction

Properties of light can be placed into four distinct categories, intensity, wavelength, coherence, and polarization. Polarimetry is the science of measuring the nature of polarized light by specifying the orientation of the electric field. *Polarimetric imagery* (PI) focuses on the measurement of the polarization state across a scene of interest captured by a polarimetric sensor yielding one or more 2-dimensional images where each pixel contains the polarization information for the materials present in the image.

This chapter describes the nature of polarization by first reviewing the nature of EM wave energy, followed by a brief description on the interaction of the EM energy with two different media and the changes that occur as it is reflected and propagated between the two materials. The concept of polarization ellipse is introduced and determines the instantaneous polarization state of light followed by an introduction to the Stokes Vector, one of the cornerstones of PI remote sensing applications, which describes the polarization state of light in terms of intensity measurements. Exploitation techniques widely used in the research community will also be revisited in this chapter for a specific application: autonomous detection of manmade objects in the presence of a natural background scene. The information and equations presented in this chapter are based on material found in [1, 3, 22, and 36].

3.2 The Nature of Electromagnetic Waves and the Polarization Ellipse

This section introduces the electric field equations of a propagating electromagnetic wave, followed by the formulation of the polarization ellipse equation as a method to quantify the shifting of the x and y components of the electric field also known as polarization shift or rotation of the wave.

3.2.1 Derivation of the Polarization Ellipse

Polarization is a property of electromagnetic waves where the trajectory of the electric field vector is traced in the time domain at a fixed observation location. The *electric field* of a sinusoidal electromagnetic wave can be decomposed in terms of two orthogonal components with their respective amplitudes and phases:

$$E(z,t) = E_x(z,t) + E_y(z,t), \tag{3.1}$$

$$E_x(z,t) = E_{0x}\sin(\varpi t - kz + \delta_x), \tag{3.2}$$

$$E_y(z,t) = E_{0y}\sin\big(\varpi t - kz + \delta_y\big), \tag{3.3}$$

where E_x and E_y are the instantaneous amplitudes of the x and y components for a specific moment in time, while E_{0x} and E_{0y} are the peak amplitudes of the electric field at a fixed frequency. The angular frequency is denoted as $\varpi = \frac{2\pi c}{\lambda}$, where λ is the wavelength of the wave and c the speed of light in a vacuum. The variable t is time, followed by $k = \frac{\varpi}{c}$, which denotes the velocity of the wave in a particular medium, z the location along the propagation direction of the wave, and δ_y and δ_x are the relative phase shifts. It is important to emphasize that the initial reference phase shift of the waves is

irrelevant, however, the phase shift difference between the two waves (δ) is critical as it will determine the trajectory of the wave with respect to the x and y axis as one shall see very shortly.

Figure 3.1 illustrates such concept by demonstrating the phase shift between E_x and E_y as it propagates in the z-direction.

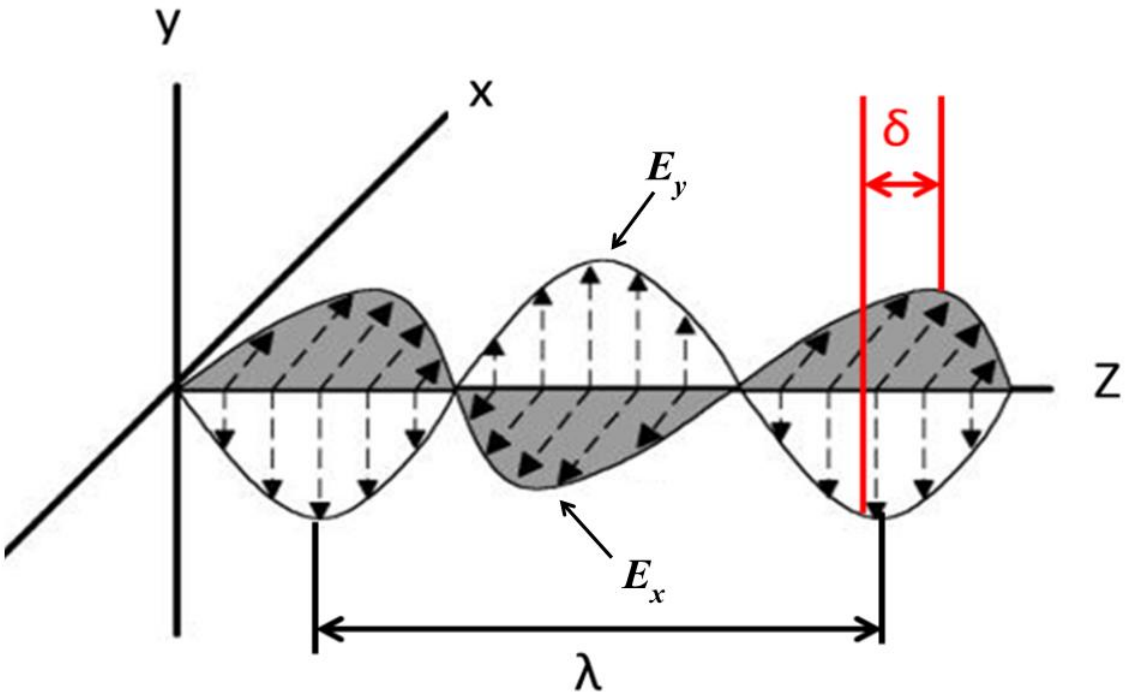

Figure 3.1 An electromagnetic wave with a phase shift of δ between the E_x and E_y components of the electric field.

The resulting locus accomplished by tracing Equation (3.1) over time, t, while propagating in the z-direction, see Figure 3.1, can be represented by Equation (3.4),

$$\frac{E_x^2}{E_{0x}^2} + \frac{E_y^2}{E_{0y}^2} - 2\frac{E_x E_y}{E_{0x}E_{0y}} cos\delta = sin^2\delta, \tag{3.4}$$

where $\delta = \delta_x - \delta_y$ is the phase difference between the x and y components. Equation (3.4), also known as polarization ellipse equation, describes an ellipse rotated at an angle ψ and represents the pattern traced by an EM wave over time on the z-plane as shown in Figure 3.2.

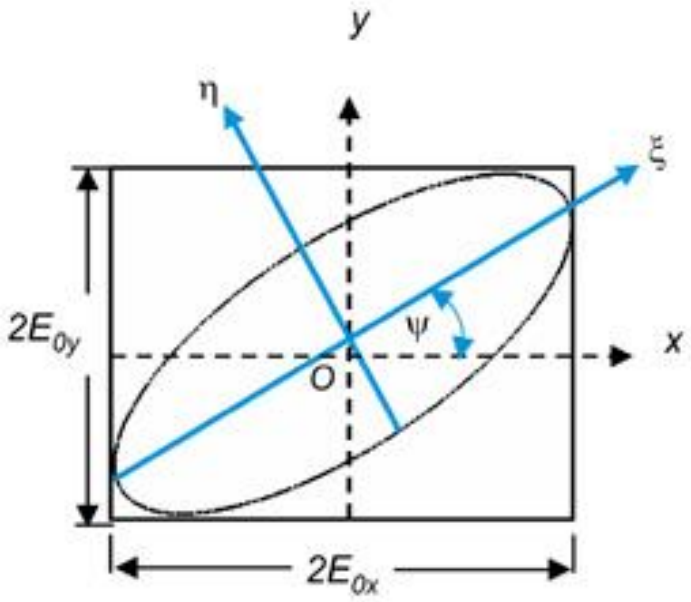

Figure 3.2 Polarization ellipse and the polarization angle (ψ).

Source: E. Collett. *Field Guide to Polarization*. Bellingham, WA: SPIE Press, 2005.

One can represent the angle at which the EM wave is shifted as follows,

$$\tan 2\psi = \frac{2E_{0x}E_{0y}\cos\delta}{E_{0x}^2 - E_{0y}^2}, \text{where } 0 \leq \psi \leq \pi. \tag{3.5}$$

Another well-known angle in polarization is the ellipticity angle, χ, and is defined by the ratio between the minor and major axis lengths,

$$\sin 2\chi = \frac{2E_{0x}E_{0y}\sin\delta}{E_{0x}^2 + E_{0y}^2}, \text{where } \frac{-\pi}{4} \leq \chi \leq \frac{\pi}{4}. \tag{3.6}$$

It is important to emphasize that polarized light often has a preferred orientation that can be distinguished from unpolarized EM waves. Randomly polarized or unpolarized EM waves, see Figure 3.3, are composed of many superimposed EM waves whose E field varies in orientation and, therefore, one cannot determine its orientation.

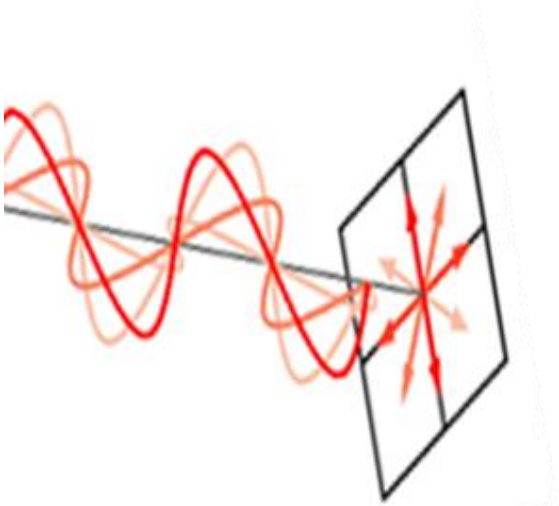

Figure 3.3 Unpolarized light is defined by an unspecified E-field direction as a function of time.

Source: http://electron6.phys.utk.edu/light/images7-10/polari1.gif

3.2.2 Degenerate Forms of the Polarization Ellispe

There are special forms derived from Equation (3.4) that categorizes polarization as linear or circular depending of the E field values and their respective angle shifts. Linear polarization can be further divided into four categories, horizontal, vertical, +45 and -45 degree. For the case of *linear horizontal polarization*, $E_x(z,t)$ is defined as,

$$E_x(z,t) = E_{0x}\sin(\varpi t - kz + \delta_x), \tag{3.7}$$

$$E_y(z,t) = 0, E_{0y} = 0.$$

Conversely, for linear vertical polarization,

$$E_y(z,t) = E_{0y}\sin(\varpi t - kz + \delta_y),$$
$$E_x(z,t) = 0, E_{0x} = 0. \tag{3.8}$$

Substituting $\delta = 0$ or π , Equation (3.4) reduces to

$$E_y = \pm\frac{E_{0y}}{E_{0x}}E_x. \tag{3.9}$$

Equation (3.9) represents the equation of a straight line with a zero intercept and a slope of $\frac{E_{0y}}{E_{0x}}$, where if $\delta = 0$ the slope is positive while for $\delta = \pi$, the slope is negative. For the case where $E_{0y} = E_{0x}$, the slope of Equation (3.9) is one which represents a EM wave polarized along the $\pm 45°$ for the respective phase shift difference, also known as $\pm 45°$ *linear polarization*.

Alternatively, when $\delta = \pm\frac{\pi}{2}$, Equation (3.4) reduces to

$$\frac{E_x^2}{E_{x0}^2} + \frac{E_y^2}{E_{y0}^2} = 1, \tag{3.10}$$

which is defined as the equation of an ellipse rotated at an angle $\psi = 0$. If $E_{0y} = E_{0x} = E_0$, then Equation (3.10) becomes,

$$\frac{E_x^2}{E_0^2} + \frac{E_y^2}{E_0^2} = 1. \tag{3.11}$$

Equation (3.11) represents the equation of a circle and is known as *circular polarization*. The rotation of the polarization is defined by the angle shift between the two components as *right* circular when $\delta = \frac{\pi}{2}$ and *left* circular for $\delta = \frac{-\pi}{2}$.

In this section, the polarization ellipse equation was presented, Equation (3.4), which is a very useful tool to describe the various polarization states of light in terms of a single equation. The polarization ellipse equation also demonstrated that for certain special cases, light can be described as linearly or circularly polarized light.

There are several limitations on the use of polarization ellipse equation for real world applications, for example, the polarization ellipse equation traces the EM wave ellipse or some special form of an ellipse in terms of amplitudes at a given moment in time. Given that the period of light is of the order of 10^{-15} seconds, it is impossible to observe the polarization ellipse in real time. Another limitation of the polarization ellipse is the fact that such an equation is only useful in describing light that is completely polarized, which in nature, light is often in an unpolarized or partially polarized state.

The following Subsection 3.3 presents the solution provided by Sir Georges Stokes to overcome the polarization ellipse equation limitations by introducing the Stokes parameters derived from measurable observables of the electric field.

3.3 Stokes Parameters

In 1852, Sir George Stokes (1819 – 1903) discovered that one could describe the behavior of polarized light in terms of four observable quantities, known today as the Stokes polarization parameters. The first parameter of the Stokes parameters reveals the total intensity of the optical field, while the remaining three parameters describe the

polarization state. Stokes demonstrated for the first time, that an observable such as intensity could describe light as unpolarized, partially polarized, or completely polarized. [37].

3.3.1 Derivation of the Stokes Parameters

Recall from Subsection 3.2.1 that for a completely polarized light beam, one can express the polarization ellipse, Equation (3.4), in terms of time as follows,

$$\frac{E_x^2(t)}{E_{0x}^2(t)} + \frac{E_y^2(t)}{E_{0y}^2(t)} - 2\frac{E_x(t)E_y(t)}{E_{0x}(t)E_{0y}(t)}cos\delta(t) = sin^2\delta(t), \tag{3.12}$$

where $\delta(t) = \delta_x(t) - \delta_y(t)$.

For monochromatic radiation, it is assumed that the amplitudes and phases are constant, which reduces Equation (3.12) to

$$\frac{E_x^2(t)}{E_{0x}^2} + \frac{E_y^2(t)}{E_{0y}^2} - 2\frac{E_x(t)E_y(t)}{E_{0x}E_{0y}}cos\delta = sin^2\delta. \tag{3.13}$$

Given that E_{x0}^2, E_{y0}^2, and δ are constants while $E_x^2(t)$and $E_y^2(t)$ vary with time as seen in Equations (3.2) and (3.3), in order to measure the intensity of the optical field one must take the time average over a single period of oscillation. Time averaging Equation (3.13) yields

$$\frac{\langle E_x^2(t)\rangle}{E_{0x}^2} + \frac{\langle E_y^2(t)\rangle}{E_{0y}^2} - 2\frac{\langle E_x(t)E_y(t)\rangle}{E_{0x}E_{0y}}cos\delta = sin^2\delta, \tag{3.14}$$

where the time average symbol is denoted as $\langle \ldots \rangle$. Sir Stokes demonstrated that with some algebraic manipulation one can express Equation (3.14) in terms of intensities, or

$$\left(E_{0x}^2 + E_{0y}^2\right)^2 = \left(E_{0x}^2 - E_{0y}^2\right)^2 + \left(2E_{0x}E_{0y}cos\delta\right)^2 + \left(2E_{0x}E_{0y}sin\delta\right)^2. \tag{3.15}$$

The term on the left side of the equal sign in Equation (3.15) is the sum of all the other terms, and as such it was termed as the total intensity of light. The first term on the right hand side of the equal sign is the difference between the horizontal and vertical intensities of the light beam and describes the amount of linear horizontal or vertical polarization, followed by a term which describes the total amount of linear +45° and -45° polarization, and finally the last term describes the amount of right or left circular polarization.

One can now write the quantities in Equation (3.15) as follows:

$$S_0 = E_{0x}^2 + E_{0y}^2, \tag{3.16}$$

$$S_1 = E_{0x}^2 - E_{0y}^2, \tag{3.17}$$

$$S_2 = 2E_{0x}E_{0y}cos\delta, \tag{3.18}$$

$$S_3 = 2E_{0x}E_{0y}sin\delta. \tag{3.19}$$

This leads to expressing Equation (3.15) in terms of the Stokes polarization parameters or,

$$S_0^2 = S_1^2 + S_2^2 + S_3^2. \tag{3.20}$$

Using Schwarz's inequality, it has been shown [3] that for any state of polarized light the Stokes parameters satisfy the following relation,

$$S_0^2 \geq S_1^2 + S_2^2 + S_3^2, \tag{3.21}$$

where the equality applies when completely polarized light is present, and the inequality when partially or unpolarized light is present.

The angle of the polarization field can be represented in terms of the Stokes parameters as

$$\tan 2\psi = \frac{S_2}{S_1}, \tag{3.22}$$

and the ellipticity angle χ can be represented as

$$\sin 2\chi = \frac{S_3}{S_0}. \tag{3.23}$$

One can define the *degree of polarization, P***,** of a light beam using the Stokes parameters as follows:

$$\mathrm{P} = \frac{\mathrm{I}_{pol}}{\mathrm{I}_{total}} = \frac{\sqrt{S_1^2 + S_2^2 + S_3^2}}{S_0}, 0 \leq \mathrm{P} \leq 1, \tag{3.24}$$

where if P = 1 corresponds to completely polarized light, P = 0 corresponds to unpolarized light, and when 0 < P < 1 corresponds to partially polarized light. It is worth noting that for passive systems circular polarization is often negligible ($S_3^2 \approx 0$), as shown in previous work [38], therefore, the degree of polarization becomes the *degree of linear polarization*, DoLP, and is defined as

$$\mathrm{DoLP} = \frac{\mathrm{I}_{pol}}{\mathrm{I}_{total}} = \frac{\sqrt{S_1^2 + S_2^2}}{S_0}, 0 \leq \mathrm{DoLP} \leq 1. \tag{3.25}$$

3.3.2 Degenerate Forms of the Polarization Ellipse using Stokes Parameters

The special cases of the polarization ellipse discussed in the Subsection 3.2.2 can be expressed in terms of the Stokes parameters in the following manner, for linear horizontally polarized light where $E_{0y} = 0$, Equations (3.16) through (3.19) become

$$S_0 = E_{0x}^2, \tag{3.26}$$

$$S_1 = E_{0x}^2, \tag{3.27}$$

$$S_2 = 0, \tag{3.28}$$

$$S_3 = 0. \tag{3.29}$$

While for linear vertically polarized light where $E_{0x} = 0$,

$$S_0 = E_{0y}^2, \tag{3.30}$$

$$S_1 = -E_{0y}^2, \tag{3.31}$$

$$S_2 = 0, \tag{3.32}$$

$$S_3 = 0. \tag{3.33}$$

For the case of linear +45° polarized light, where $E_{0y}^2 = E_{0x}^2 = E_0$ and $\delta = 0°$, the Stokes parameters convert to

$$S_0 = 2E_0^2, \tag{3.34}$$

$$S_1 = 0, \tag{3.35}$$

$$S_2 = 2E_0^2, \tag{3.36}$$

$$S_3 = 0. \tag{3.37}$$

For the case of linear -45° polarized light, where $E_{0y}^2 = E_{0x}^2 = E_0$ and $\delta = 180°$, the Stokes parameters become

$$S_0 = 2E_0^2, \tag{3.38}$$

$$S_1 = 0, \tag{3.39}$$

$$S_2 = -2E_0^2, \tag{3.40}$$

$$S_3 = 0. \tag{3.41}$$

When $E_{0y}^2 = E_{0x}^2 = E_0$ and $\delta = 90°$ right circular polarization occurs and in this case the Stokes parameters are defined as,

$$S_0 = 2E_0^2, \tag{3.42}$$

$$S_1 = 0, \tag{3.43}$$

$$S_2 = 0, \tag{3.44}$$

$$S_3 = 2E_0^2. \tag{3.45}$$

Finally, for left circular polarized light, where the amplitudes are the same except $\delta = -90°$, the Stokes parameters become,

$$S_0 = 2E_0^2, \tag{3.46}$$

$$S_1 = 0, \tag{3.47}$$

$$S_2 = 0, \tag{3.48}$$

$$S_3 = -2E_0^2. \tag{3.49}$$

3.3.3 The Stokes Vector Measurement using a Polarizer

It is common to arrange the Stokes parameter in a column matrix such as

$$S = \begin{pmatrix} S_0 \\ S_1 \\ S_2 \\ S_3 \end{pmatrix} = \begin{pmatrix} E_{0x}^2 + E_{0y}^2 \\ E_{0x}^2 - E_{0y}^2 \\ 2E_{0x}E_{0y}cos\delta \\ 2E_{0x}E_{0y}sin\delta \end{pmatrix}, \tag{3.50}$$

which is also known as the Stokes vector for a plane wave. The Stokes vector, mathematically is not a vector, but it has been called a vector for mathematical convenience. The parameter S_0 in Equation (3.50) represents the total intensity of light captured by the sensor and it can be defined as the total intensity captured by the system as if all polarization elements were removed from it. Conversely, Stokes vector parameters S_1, S_2, and S_3 represent the dominant orientation of the radiation (usually through the use of a positive or negative sign). When S_1, S_2, and S_3 are normalized by S_0, these parameters range from 0 to 1 indicating the extent (in percentage) by which the radiation is polarized with respect to the total intensity. If unpolarized light is encountered, due to the rapid varying field in random directions, S_1, S_2, and S_3 must, in theory, go to zero, yielding a Stokes vector represented by,

$$S = \begin{pmatrix} S_0 \\ S_1 \\ S_2 \\ S_3 \end{pmatrix} = \begin{pmatrix} S_0 \\ 0 \\ 0 \\ 0 \end{pmatrix}. \tag{3.51}$$

As previously mentioned for passive systems, Stokes parameter S_3 is often negligible ($S_3 \approx 0$) and more often than not it is not measured by such systems. Therefore, for the remainder of this work, when the words "Stokes vector parameters" are referred to, only the first three parameters S_0, S_1, and S_2 should be considered.

The measurement of the Stokes vector using a polarization camera is accomplished by measuring the intensity of a scene using a polarizer rotated at discretionary angles. Figure 3.4 illustrates the simplest polarimetric camera one can build by taking a camera with a polarizer in front of the lenses and by rotating the polarizer at specific angles one can measure the intensity of the scene as related to the polarization angle. One must emphasize that there are many different types of polarization cameras that collect the same information using different methodologies. A good explanation on the different types of polarization cameras can be found in Subsection 2.6.2 or in [2].

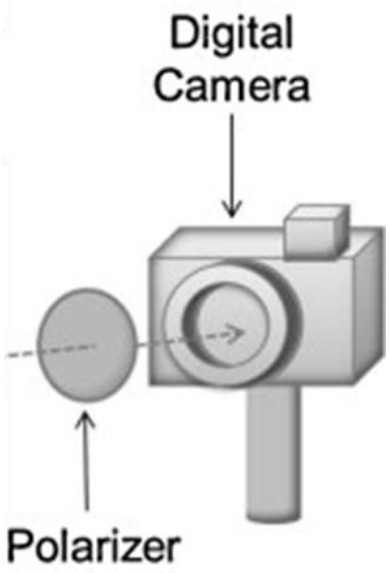

Figure 3.4 A a simple polarimetric camera using a polarizer in front of the lenses. By rotating the polarizer to 0°, 45°, 90°, and 135°, one can calculate the Stokes vector parameters.

Source: http://ars.els-cdn.com/content/image/1-s2.0-S030057121200108X-gr1.jpg

Stokes vector parameters (S_0, S_1, and S_2) can be easily estimated using the setup shown in Figure 3.4 by rotating the polarizer to specific angles (0°, 45°, 90°, and 135°) as discussed in Subsection 3.2.2 and taking into account that for passive remote systems S_3 is often not measured. In order to collect E_{0x}^2, the polarizer is rotated to 0°, also known as linear horizontal polarization using the ground plane as the reference. Consequently, E_{0y}^2 is measured by rotating the polarizer to 90° such that linear vertical polarization is captured by the sensor. Likewise, in order to measure the remainder degenerate cases for linear polarization, one must turn the polarizer to +45° and -45° (often called 135°) and measured their intensities. Equation (3.52) demonstrates how to describe the Stokes vector parameters in terms of observed intensities captured by sensor with a polarizer rotated at the specific angles in the following configuration, or

$$S = \begin{pmatrix} S_0 \\ S_1 \\ S_2 \end{pmatrix} = \begin{pmatrix} E_{0x}^2 + E_{0y}^2 \\ E_{0x}^2 - E_{0y}^2 \\ 2E_{0x}E_{0y}cos\delta \end{pmatrix} = \begin{pmatrix} I_{0^\circ} + I_{90^\circ} \\ I_{0^\circ} - I_{90^\circ} \\ I_{45^\circ} + I_{135^\circ} \end{pmatrix}. \quad (3.52)$$

It must be pointed out that the Stokes parameters were derived to a specific x and y coordinate system. When comparing polarimetric imagery, it is important that both datasets agree upon a common reference orientation from which the measurements are to be taken from. It is common to use the ground plane as the horizontal axis (parallel to the ground plane) from which one measures horizontal polarization, and use the vertical axis (perpendicular to the ground plane) to measure vertical polarization.

3.4 Reflection and Transmission of Electromagnetic Waves

This subsection reviews the behavior of reflected and transmitted polarized light through interactions with dielectric surfaces. This behavior is often expressed mathematically by a set of equations known as *Fresnel's* equations which can be derived from Maxwell's equations and describe the amount of light that is reflect and transmitted when light moves across two different mediums. Other important attributes such as Brewster angle, total internal reflection, and Snell's law will also be discussed since they too play an important role on the understanding of polarized light. Finally, data captured using a LWIR polarimetric camera is presented to link the theory presented in this section to actual measurements in the field.

Let's start by defining *Snell's law*, which is used to describe the relationship between the angle of incidence and transmission of EM waves as they pass from one medium to another with different indexes of refraction. Snell's law states that the ratio of sines of the angles of incident and transmission angle is equal to the ratio of the phase

velocities in the two media, or more commonly known, to the opposite ratio of the indices of refraction of each medium,

$$\frac{\sin\theta_1}{\sin\theta_2} = \frac{v_1}{v_2} = \frac{n_2}{n_1}, \tag{3.53}$$

where θ is the angle measured from the normal to the surface, v (m/s) the velocity of light inside the respective medium, and n the index of refraction of the respective medium.

Augustine-Jean Fresnel demonstrated that for an EM wave normally incident onto a planar dielectric surface, reflectivity is a function of the index of refraction of the two mediums defined as

$$r = \left(\frac{n_2 - n_1}{n_2 + n_1}\right)^2, \tag{3.54}$$

where n_1 and n_2 are the index of refraction of each of the mediums. However, for the case where the incident wave is at an arbitrary angle from the normal of the surface, the polarization of the wave must be taken into account.

3.4.1 $\bar{\mathbf{E}}$ is Perpendicular to the Plane of Incidence

For the case where the E field is perpendicular to the plane of incidence, also known as the *"s"-polarization* or *transverse electric* (TE), the amplitude reflection and transmission coefficients can be expressed in terms of the wave's incident angle and the index of refraction of each medium as follows

$$r_s = \frac{n_1\cos\theta_i - n_2\cos\theta_r}{n_1\cos\theta_i + n_2\cos\theta_r}. \tag{3.55}$$

Equation (3.55) can also be expressed in terms of Snell's law in order to eliminate the dependency on the indices of refraction,

$$r_s = -\frac{\sin(\theta_i - \theta_r)}{\sin(\theta_i + \theta_r)}. \tag{3.56}$$

The transmission coefficient can be derived as

$$t_s = \frac{2n_1 \cos\theta_i}{n_1 \cos\theta_i + n_2 \cos\theta_r}. \tag{3.57}$$

Similarly, it can be reduced in terms of θ_r and θ_i, or

$$t_s = \frac{2 \sin\theta_r \cos\theta_i}{\sin(\theta_i + \theta_r)}. \tag{3.58}$$

3.4.2 $\bar{\mathbf{E}}$ is Parallel to the Plane of Incidence

For the case where the E field is parallel to the plane of incidence, known as *"p"-polarization* or *transverse magnetic* (TM) polarization, the transmission and reflectance Fresnel's equations can be derived to be

$$r_p = \frac{n_2 \cos\theta_i - n_1 \cos\theta_r}{n_2 \cos\theta_i + n_1 \cos\theta_r}, \tag{3.59}$$

or, in terms of angle of incidence and reflection only,

$$r_p = \frac{\tan(\theta_i - \theta_r)}{\tan(\theta_i + \theta_r)}. \tag{3.60}$$

Furthermore, the transmission coefficient can be written as follows

$$t_p = \frac{2n_1 \cos\theta_i}{n_2 \cos\theta_i + n_1 \cos\theta_r}, \tag{3.61}$$

similarly, it can be reduced to

$$t_p = \frac{2 \sin\theta_r \cos\theta_i}{\sin(\theta_i + \theta_r)\cos(\theta_i - \theta_r)}. \tag{3.62}$$

More often than not, the reflectance and transmission are discussed in terms of power or intensity. In this case, one needs to square the absolute value of the amplitude reflection coefficients, $R = |r^2|$. The transmission coefficients can be calculated from the law of conservation of energy, as

$$T_s = 1 - R_s, \tag{3.63}$$

and,

$$T_p = 1 - R_p, \tag{3.64}$$

where R_s and T_s is the reflected and transmitted power for s −polarization and R_p and T_p the reflected and transmitted power for p −polarization.

It is important to emphasize that Equations (3.63) and (3.64) are only valid for power coefficients and should not be used for amplitude coefficients (Equations (3.55) through (3.62)).

Figure 3.5 illustrates, in a simplistic matter, some of the topics discussed above as an EM wave propagates from medium 1 having an index of refraction n_1 to medium 2 with an index of refraction n_2. The incident angle, $\Theta_{i,}$, and reflected angle Θ_r are equal to each other in a perfectly smooth material, the transmitted angle Θ_t is calculated from Equation (3.53) and the transmitted and reflected power from Equations (3.63) and (3.64).

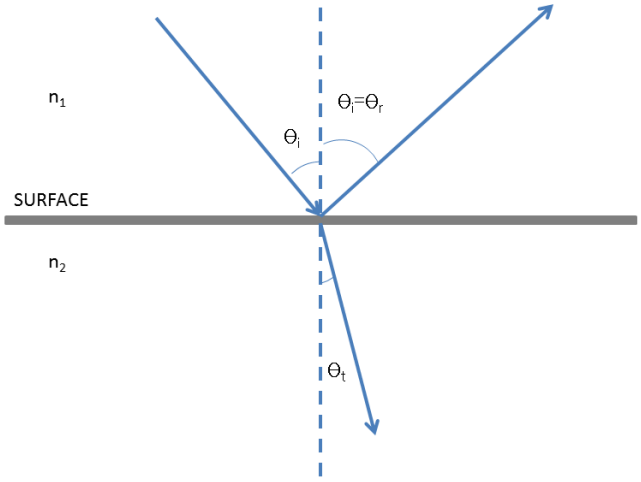

Figure 3.5 Reflectance and transmission of an incoming wave with angle Θ_i, a reflectance angle of Θ_r, and a transmission angle equal to Θ_t.

Let one consider what happens to the amplitude reflection coefficient in Equation (3.58) as the sum of the two angles equals to 90°. In the case when light is polarized parallel to the plane of incidence, the p polarization reflection coefficient vanishes, setting the total transmission to unity. The incident angle where the entire p-polarization power is transmitted into another medium is called the *Brewster angle*, and can be expressed in terms of the indices of refraction as follows,

$$\theta_{iB} = tan^{-1}\frac{n_2}{n_1} \tag{3.65}$$

Another important angle is the *critical angle* (θ_c), which defines a boundary where *total internal reflection* will occur if the incident angle is higher than the critical angle. When such occurs, no power will be transmitted to the other medium ($t = 0$). The critical angle can be found by solving the following equation,

$$\theta_c = sin^{-1}\frac{n_1}{n_2}. \tag{3.66}$$

Figures 3.6 through 3.9 present the key points described in this subsection which will be exploited in Subsections 3.5.1 and 3.5.2 for manmade object detection using Stokes parameters. Figure 3.6 and 3.7 demonstrate the reflected and transmitted power versus incident angle for an EM wave travelling from glass to air. The magnitude of reflected power of the s-polarization is higher than p-polarization around the Brewster angle, which results in an increase on the transmitted power for the the p-polarization with respect to s-polarization. At the Brewster angle, the reflective coefficient for p-polarization goes to zero meaning there is total transmitted power of p-polarization from glass to air. As the incident angle nears the critical angle, the reflective coefficient for both p and s polarization go to 1, and remains at 1, resulting in total internal reflection.

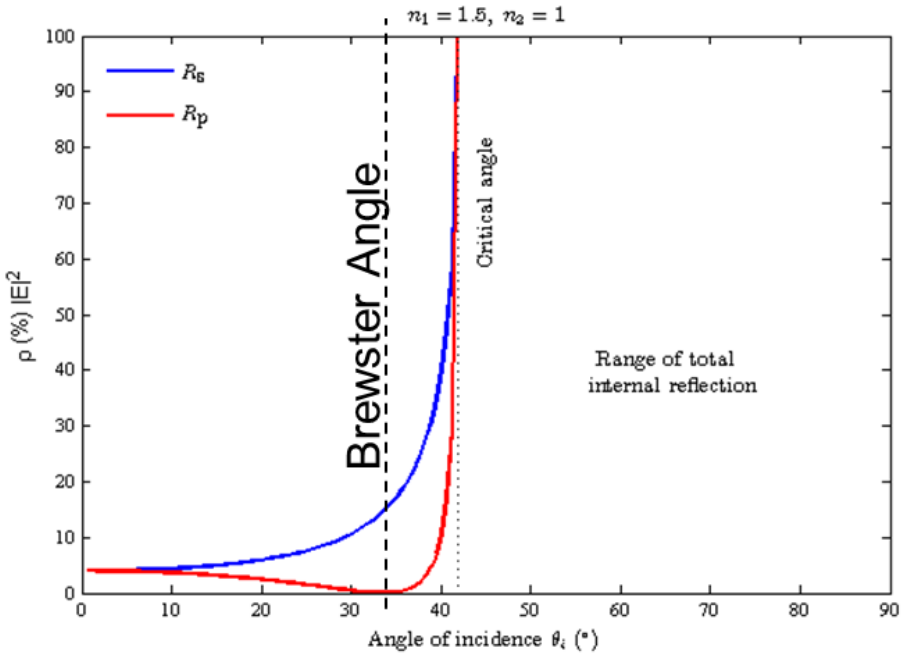

Figure 3.6 Reflectance percentage versus incident angle for $n_1 = 1$ and $n_2 = 1.5$ as a function of angle of incidence.

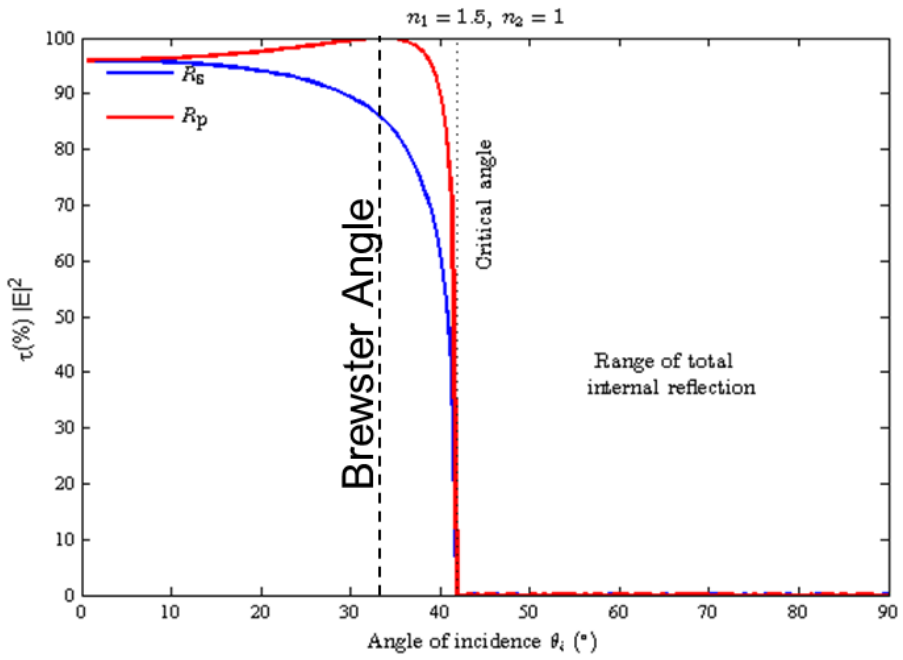

Figure 3.7 Transmission percentage versus incident angle for $n_1 = 1$ and $n_2 = 1.5$ as a function of angle of incidence.

Figures 3.8 and 3.9 illustrate the relationship between camera angle versus incident angle using Equations (3.53), (3.56), (3.60), (3.63), and (3.64) for $n_1 = 1$ and $n_2 = 1.5$. If the index of refraction of the material where the wave originates is higher than the material to which the wave is transmitted, the camera angle steps at a slower pace than the incident angle (Figure 3.8), however the opposite is true when n_1 is smaller than n_2 as shown in Figure 3.9 and in such scenarios total internal reflection often occurs.

From an exploitation point of view, which will be dealt in the Section 3.5, one way to discern manmade objects from natural clutter background is by looking at the difference between the s and p polarizations, the Stokes parameter S_1. One can immediately observe in Figure 3.7 that there is a limited range of angles from the sensor point of view that demonstrates high separability between s and p polarization; this is found in the vicinity of the Brewster angle. Given that a manmade object is a 3-

dimensional target composed of many surfaces at different angles relative to the sensor, one can conclude that only certain surfaces of the target (where $\Theta_t + \Theta_i \approx 90°$ suffices) will be clearly discernible when using the S_1 parameter as a discriminant factor, while the remaining surfaces will not be so easily detected. Subsection 3.4.3 demonstrates in more detail through experimentations the angle dependency of the *s* and *p*-polarization components and how this dependency affects the performance of S_1 and S_2 measurements.

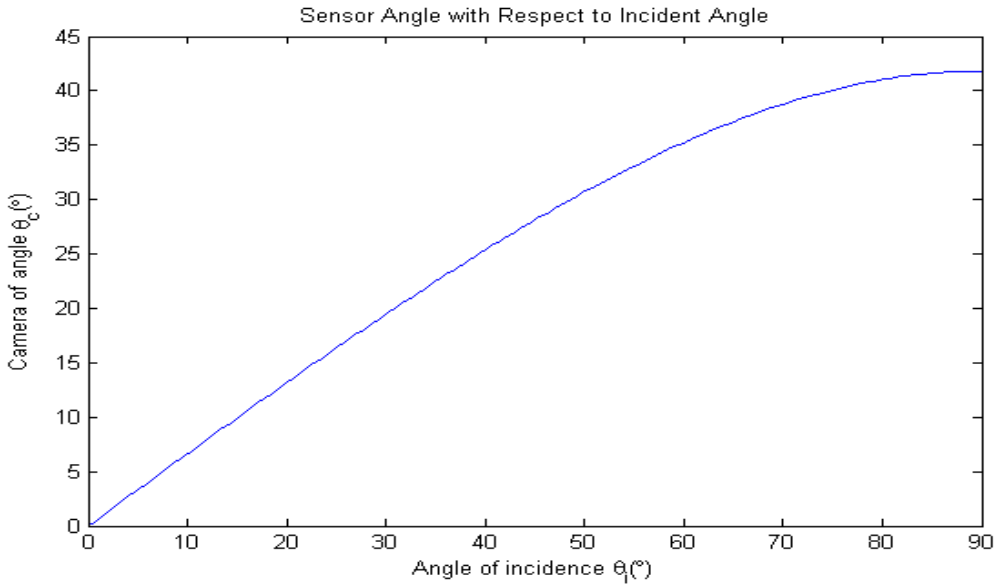

Figure 3.8 Relationship between angle of incidence and camera angle for $n_1 = 1.5$ and $n_2 = 1$.

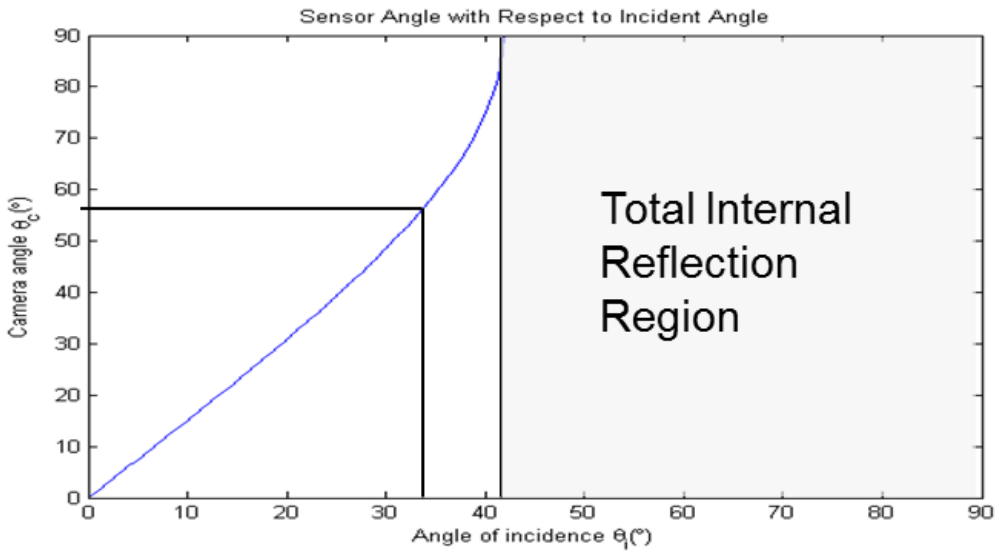

Figure 3.9 Relationship between angle of incident and camera angle for $n_1 = 1$ and $n_2 = 1.5$.

3.4.3 Emission from a Dielectric Surface

When dealing with remote sensing applications only the reflected or transmitted power is captured by the sensor of choice. Angles such as the Brewster angle, critical angle, and angle of incidence angle are not known to the passive remote systems, nor can be calculated without other *a priori* parameters such as the materials' indices of refraction. For LWIR polarimetric imagery, the modality of choice in this dissertation, only emitted energy, not reflected, is captured by the sensor. Figure 3.10 illustrates a simplified version of a wave being transmitted from a painted surface to the LWIR polarimetric sensor. In Figure 3.10, a wave originates from the metal due to the excitation of the atoms at a given temperature (in Kelvin) as a result of illumination by other sources, for example, the sun. The wave travels from the metal to the dielectric material, such as paint coating, at a given incident angle, and then into air, through the atmosphere, and finally arriving at the LWIR polarimetric sensor.

From a sensor point of view, one cannot see what happens prior to the wave being transmitted from the dielectric to the sensor. The only information that may be available is the sensor angle with respect to the normal of the surface. Without any further knowledge about the materials in question (n_1 and n_2) it is hard to identify empirically the Brewster angle, critical angle, and angle of incidence. However, Brewster angle can be identified if the sensor/plate can be tilted across a range of angles relative to the normal of the surface.

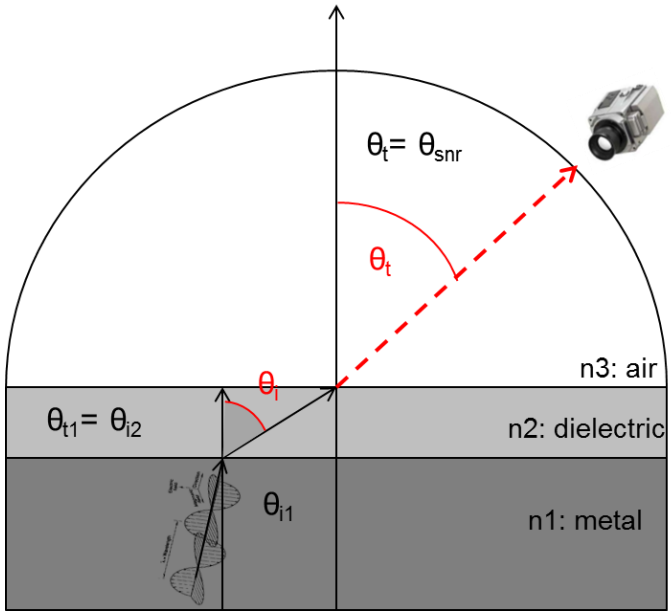

Figure 3.10 A simplistic model where an electromagnetic wave is transmitted from metal through dielectric material, such as paint on a target, travelling through the atmosphere to the sensor.

In order to illustrate the concepts in Sections 3.3 and Subsections 3.4.1 and 3.4.2 from an emittance (transmission) point of view, an experiment was performed which entailed a Polaris LWIR polarimetric sensor overlooking the scene about 20m from the ground, see Figure 3.11. In the scene, Figure 3.12, a plate painted with the color black was mounted on top of a pan and tilt system and positioned such that the camera was

normal to the plane (eyeballed). The camera collected both the vertical (p-polarization) and horizontal (s-polarization) polarization measurements as the plate tilt angle was increased every 5° until the plate was parallel to the camera (~90°). For reference, another black plate was left flat on the floor during the data collection period in order to confirm that the camera was working properly.

Figure 3.11 The Polaris LWIR polarimetric camera was located about 20 meters from the ground overlooking the test site. The test plate was placed on top of a pan and tilt system (QPT-500) and was tilted every five degrees from an initial position perpendicular to the camera (normal) to the final position parallel to the camera. The 0° and 90° intensity measurements were collected to represent the s and p-polarization components.

Figure 3.12 View of the plate on the pan and tilt system (QPT-500). In the test scene there are three manmade objects present, the test plate on the QPT-500, the reference plate on the floor, and the sidewalk. Grass is the predominant clutter class found in the sensor's field of view.

The collected imagery was then calibrated and an area of the plate was chosen and analyzed to demonstrate the changes in the p and s-polarization components relative to the viewing angle, see Figure 3.13.

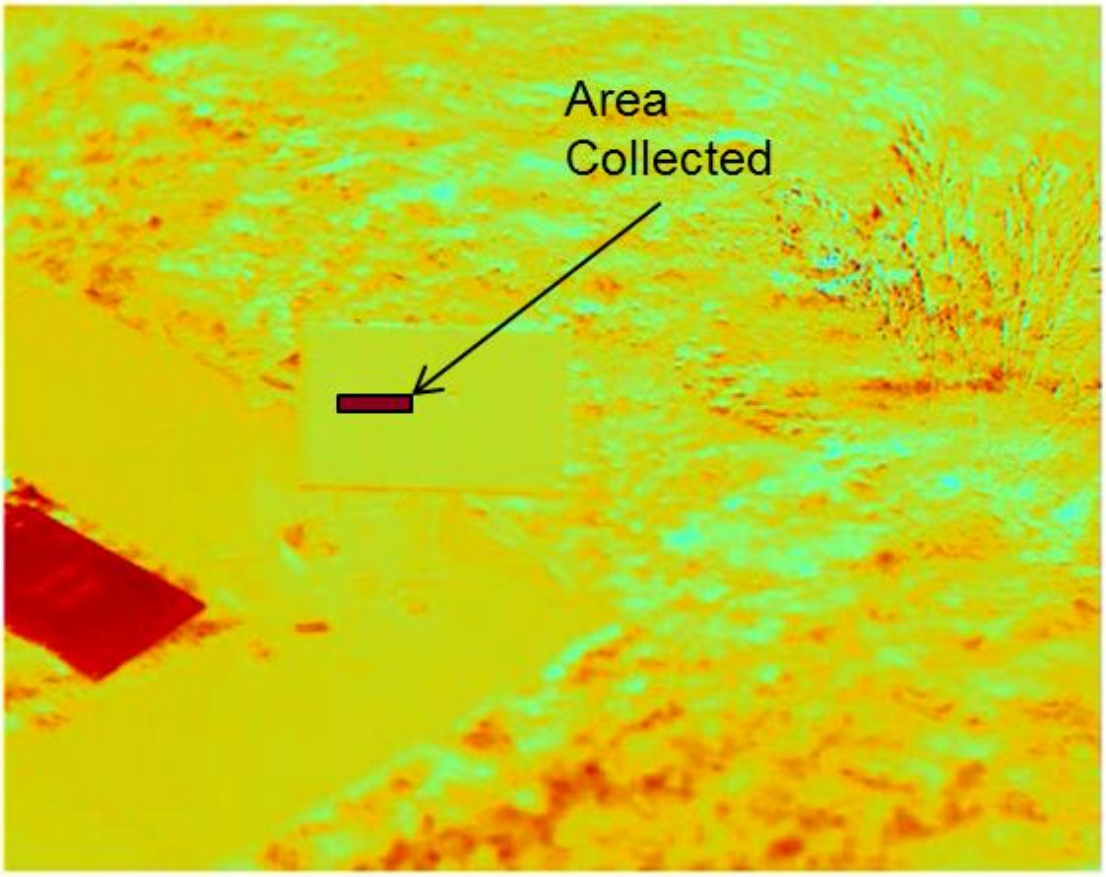

Figure 3.13 Image illustrates the difference between the p (90°) and s (0°)polarization images collected by the LWIR polarimetric sensor. A small area on top of the plate was collected for all the different angles for further analysis.

For example, the red color in Figure 3.13 represents pixels that exhibit a dominant p polarization component, while any other shades of yellow and orange illustrate pixels where p polarization is strong but not dominant. Conversely, dark blue represents pixels that exhibit a dominant s polarization component and different blue tones illustrate pixels where s polarization is the strong feature.

Figure 3.14 illustrates the intensities captured by the sensor for each degree the plate was tilted where, 0° means that the camera field of view is normal to the plate and 90°, the plate is parallel to the camera. The intensities within each polarization vary significantly as a result of the data collection being halted several times in order to let

clouds pass by. During this waiting period solar loading was not available, as represented by the vertical black lines in Figure 3.14 left side, and as a result the plate got colder compared to previous measurements. By taking the difference between the vertical and the horizontal polarization intensity, in other words, taking the horizontal polarization as the zero reference, one could relate the right side of Figure 3.14 to Figure 3.7. A caution to the reader as to realize that the x-axis in Figure 3.14 is the transmission angle while in Figure 3.7 the x-axis is defined as the incident angle.

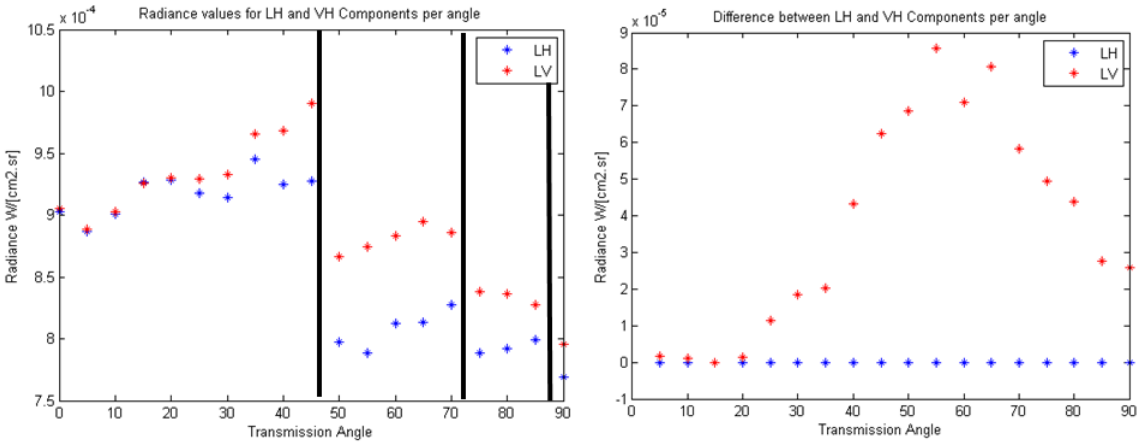

Figure 3.14 The plot on the left represents the horizontal and vertical polarization radiance collected by the Polaris camera as a function of the camera's viewing angle relative to the normal of the plate. While the plot on the right represents the difference between vertical and horizontal components using the horizontal values as the zero reference.

The data collection demonstrated three key points worth highlighting: 1) p-polarization is dominant in the emission part of the spectrum for dielectric materials; 2) The Brewster angle was shown to be around 55° where the difference between the p and s polarization is maximized; and 3) Fresnel's equations were verified through the data for the emittance portion of the spectrum.

3.5 Exploitation Techniques for Polarimetric Imagery

This section will explore the exploitation of PI when taking advantage of information learned from Section 3.3 such as the Stokes parameters as the discriminant function by which one can discern manmade objects from natural clutter backgrounds. First, using the tilting plate experiment, Subsection 3.5.1 will demonstrate the difficulty in discriminating manmade objects when the sensor angle relative to the normal of the plate does not lend itself to high polarization difference between vertical and horizontal measurements, S_1. Second, S_0, S_2, and DoLP measurements of the tilting plate experiment will also be presented followed by a performance comparison between the Stokes parameters and DoLP in discerning the manmade objects in the scene from the background clutter. Finally, using data collected of complex 3-dimensional targets at different aspect angles and different time periods in the day and using the lessons learned from previous examples, Subsection 3.5.2 will analyze the effectiveness of standard polarization exploitation methods, Stokes and DoLP, in detecting manmade objects in natural clutter backgrounds for a variety of weather events and diurnal changes of 3-dimensional manmade objects.

3.5.1 Exploitation of Polarimetric Imagery using Tilting Plate Data Collection

The goal of this subsection is twofold; first, to understand how each Stokes parameter and DoLP compares in detecting manmade objects in natural clutter backgrounds and secondly to examine the dependency of the Stokes components and DoLP to the camera viewing angle with respect to the normal of the plate. This comparison will be accomplished by utilizing a common threshold based on the image statistics in order to accurately compare each image as the angle of the plate changes relative to the camera.

The process by which the Stokes images are produced is accomplished by collecting the necessary imagery with the polarizer stationed at specific angles (0°, 45°, 90°, and 135°), see Equation (3.52), for each of the angles that the test plate was tilted to with respect to the camera. Stokes images were then generated by subtracting or adding the different combinations of the different polarization images into the S_0, S_1 and S_2 imagery (Equation (3.52)) and finally, the DoLP image is created (see Equation (3.25)) using the Stokes imagery.

Figure 3.15 shows the total intensity of light captured by the LWIR polarimetric sensor in terms of radiance $\left(\frac{W}{cm^2 sr}\right)$ for different tilt angles of the test plate with respect to the camera, as denoted on the top right corner of each sub-image. In each sub-image, the test plate is located in the center of the image, the reference plate on the left side of the image, the sidewalk where the pan and tilt system is located, and the remainder of the image is composed of small vegetation. Bright pixels indicate hot objects while dark pixels represent cold objects.

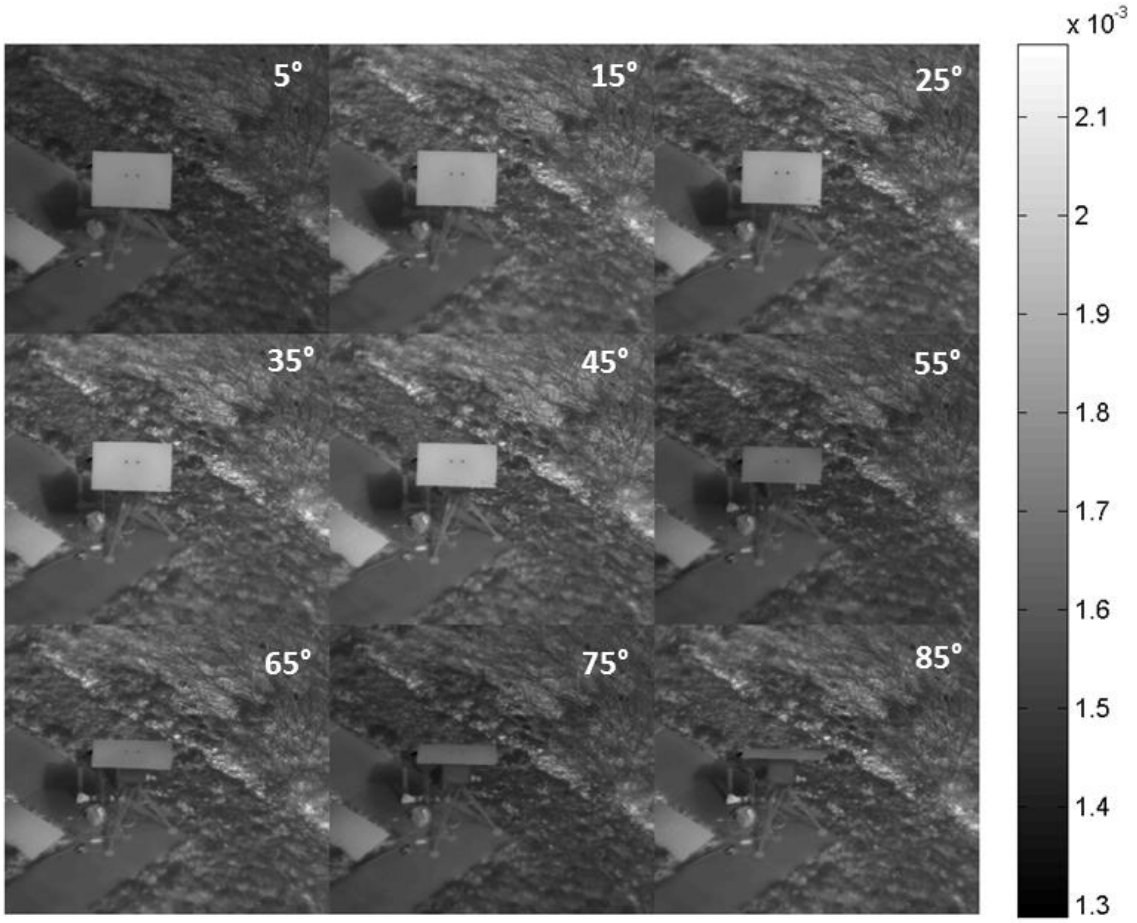

Figure 3.15 Intensity images (S_0) for the test plate at different angles relative to the sensor where S_0 is representative of the total radiance collected by the sensor as if the polarizing elements are removed from the system.

As it can be observed, the intensity of the plate varied throughout the data collection as a result of the sun's intensity, cloud cover, air flow, and small mass. Conversely, the reference plate holds its temperature longer because when sun is present, heat is transferred from the plate to the ground below it otherwise, when the sun is not available, the heat transfer is reversed from the ground back to the plate. Finally, looking at Figure 3.15, one can also observe two interesting details, first the sidewalk temperature is similar to that of clutter, and second, small portions of the background have similar or higher temperature relative to the test plate.

One effective way to compare the performance of different metrics is by thresholding the output of the algorithm using a common statistical threshold. In practice, anomaly detection algorithms usually rely on the background class to be modeled first and pixels in the image are compared to this model to determine if each particular pixel belongs to the clutter class. For this experiment, one shall assume that the background can be modeled using a Gaussian distribution where its parameters such as mean and variance can be easily estimated from the test image itself. The global mean value is then subtracted from all the pixels in the image and divided by the global standard deviation. The result is a standardized image where its values represent the number of standard deviations from the mean both in the positive and negative direction.

Figure 3.16 illustrates a PDF plot of a Gaussian (normal) distribution in terms of standard deviations (σ). The concept of using standard deviations is quite useful for thresholding imagery applicable to object detection applications when the image background clutter values follow a bell shaped curve. For example, if the target and clutter PDFs are separable (e.g., different means) and assuming that the clutter PDF is Gaussian, one can use the clutter distribution to set the desired Type I error (rejecting the null hypothesis when the null hypothesis is true). By setting a threshold of $\pm 3\sigma$, it suggests, as per the Figure 3.16, that 99.7% of all clutter pixels will be accepted as part of the null hypothesis while the remainder 0.3% of the image pixels will reject the null hypothesis and will be designated as anomalies. In theory, assuming that the target distribution has significantly different means and variances from background clutter, the result would entail that all target pixels would be rejected from the null hypothesis and identified as potential anomalies.

Finally, in order to use any type of statistical threshold, the background clutter must be modeled by a known family of distributions (e.g., Gaussian), and the target set must be distinct from clutter so that the researcher can develop an effective hypothesis test to find manmade objects in the scene.

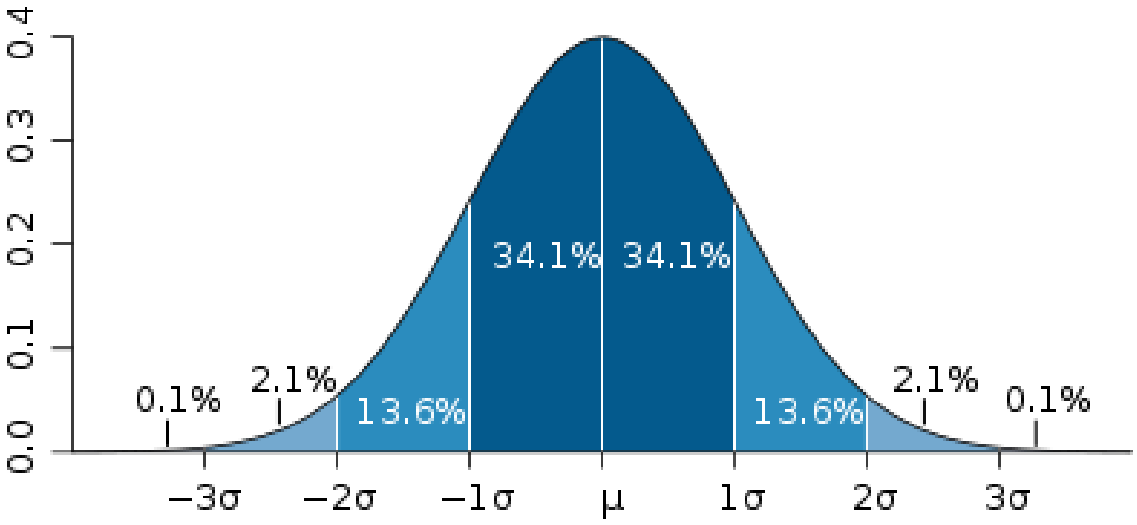

Figure 3.16 A plot of a normal distribution also known as bell shaped curve. Each band has a width of one standard deviation. For a normal distributed population about 68% of the values lie in 1σ, 95.5% at 2σ, and about 99.7% at 3σ (also known as the 68-95-99.7 rule.)

Source: http://en.wikipedia.org/wiki/Standard_deviation and http://en.wikipedia.org/wiki/68-95-99.7_rule

For the examples presented in this subsection, the assumption is that the clutter can be modeled by a Gaussian distribution and there is no *a priori* knowledge on the targets distribution.

In order to standardize an input image **X**, where $\boldsymbol{X} \in \boldsymbol{R}^{R\times C}$, R and C represent the number of rows and columns in the FPA respectively, and $x_{i,j}$ represents a pixel value (scalar) located at row i and column j in the image **X**. The global mean ($\mu_{\boldsymbol{X}}$) of **X** can be estimated as the sample mean using all pixel values in **X**, or

$$\mu_{\boldsymbol{X}} = \frac{1}{R \times C} \sum_{i=1}^{R} \sum_{j=1}^{C} x_{i,j}. \tag{3.67}$$

The global standard deviation, denoted as $\sigma_{\boldsymbol{X}}$, can be estimated by the sample variance, or

$$\sigma_X = \frac{\sum_{i=1}^{R} \sum_{j=1}^{C} \left(x_{i,j} - \mu_{\boldsymbol{X}}\right)^2}{n-1}. \tag{3.68}$$

Finally, in order to standardize the image **X**, one must remove the global mean from each pixel and divide the result by the global standard deviation, or

$$\boldsymbol{X}_{std} = \frac{\boldsymbol{X} - \mu_{\boldsymbol{X}}}{\sigma_{\boldsymbol{X}}}. \tag{3.69}$$

Figures 3.17 and 3.18 illustrate the intensity images S_0 using a $\pm 2\sigma$ and $\pm 3\sigma$ respectively, threshold based on the image statistics as demonstrated by Equations (3.67) through (3.69). Black pixels represent locations where the null hypothesis has been accepted while white pixels represent locations where the null hypothesis has been rejected. At this time a distinction must be made between statistics and engineering on the use of false alarm and true detection. In mathematics, when the null hypothesis is rejected when it should be accepted is often called probability of miss however, in engineering that's often called a false alarm (e.g., a clutter pixel was accepted as an anomaly), whereas a true detection is when the null hypothesis is successfully rejected and belongs to the object(s) one is trying to detect. In the engineering field of image processing the concept of probability of false alarms (P_{fa}) is defined as the probability of pixels belonging to the clutter class that pass the imposed threshold relative to all background pixels, while the probability of detection (P_d) is defined as the probability of

target pixels that were accepted above the threshold relative to all target pixels available in the test image. This notation of false alarm and true detection will be used throughout the dissertation.

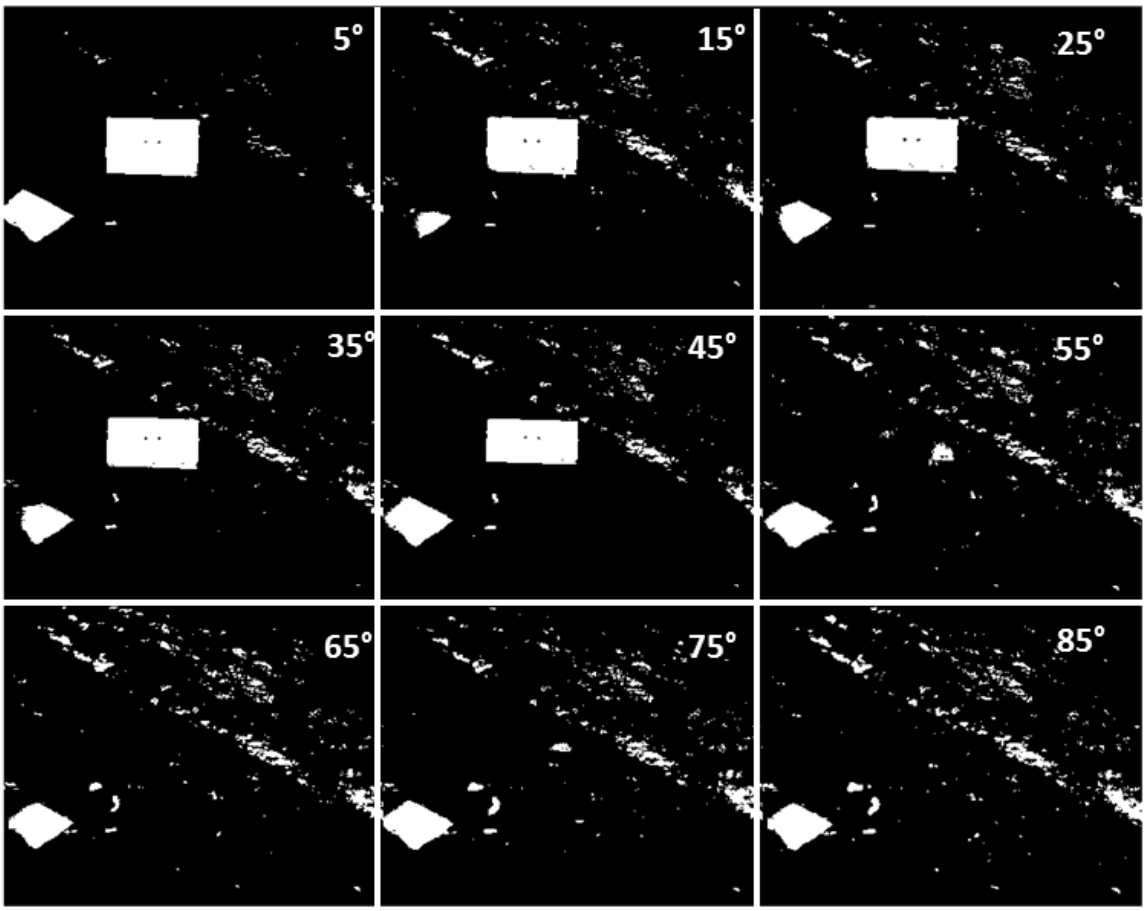

Figure 3.17 Intensity images with a threshold of $\pm 2\sigma$ based on the image global mean and variance. Black pixels represent locations where the null hypothesis has been accepted while white pixels represent locations where the null hypothesis was rejected. At $\pm 2\sigma$ there are plenty of false alarms showing up for most of the figures however, it becomes quite problematic after 55° and above where significant number of false alarms can be detected while the test plate cannot be discriminated successfully.

The thresholded images in Figure 3.17 demonstrate that for a $\pm 2\sigma$ the test plate, which is one of the targets, a manmade object, can be detected up to the 45° test image. From 55° image on, the lack of a constant available heating source (e.g., sun) resulted on the test plate getting colder relative to the background. As such, the test plate distribution

fell within the chosen threshold of $\pm 2\sigma$ resulting on its rejection as a potential anomaly. Conversely, the reference plate benefited from the warmed ground surface below as a result of the heat transfer between the two surfaces during the solar loading stage. During the periods where solar loading was absent, the heat transfer cycle reverses keeping the plate warm for a longer period of time than the test plate.

One can conclude that in order to detect the test plate successfully the threshold needs to be lowered resulting in the detection of more false alarms, which is an undesirable outcome. Intensity measurements, as explained in Subsection 2.5, is only a useful measure when the signal to noise ratio (in terms of radiance or temperature) between the target and background is high enough to be discriminatory with a minimum number of false alarms present. If such criteria is not met (see Figure 3.18, 15° image, for example) only false alarms are detected (background pixels) while the target is excluded from the thresholded image.

Figure 3.18 illustrates the intensity imagery using a $\pm 3\sigma$ threshold. The key point that needs to be addressed in this figure is that the reference plate, which did very well relative to the test plate in Figure 3.17, was only partially detected four out of nine images. On the other hand, the number of false alarms present in the image even at such high threshold remained quite high relative to $\pm 2\sigma$. In other words, the reference plate distribution is not very distinct from the background clutter distribution in this data collection example.

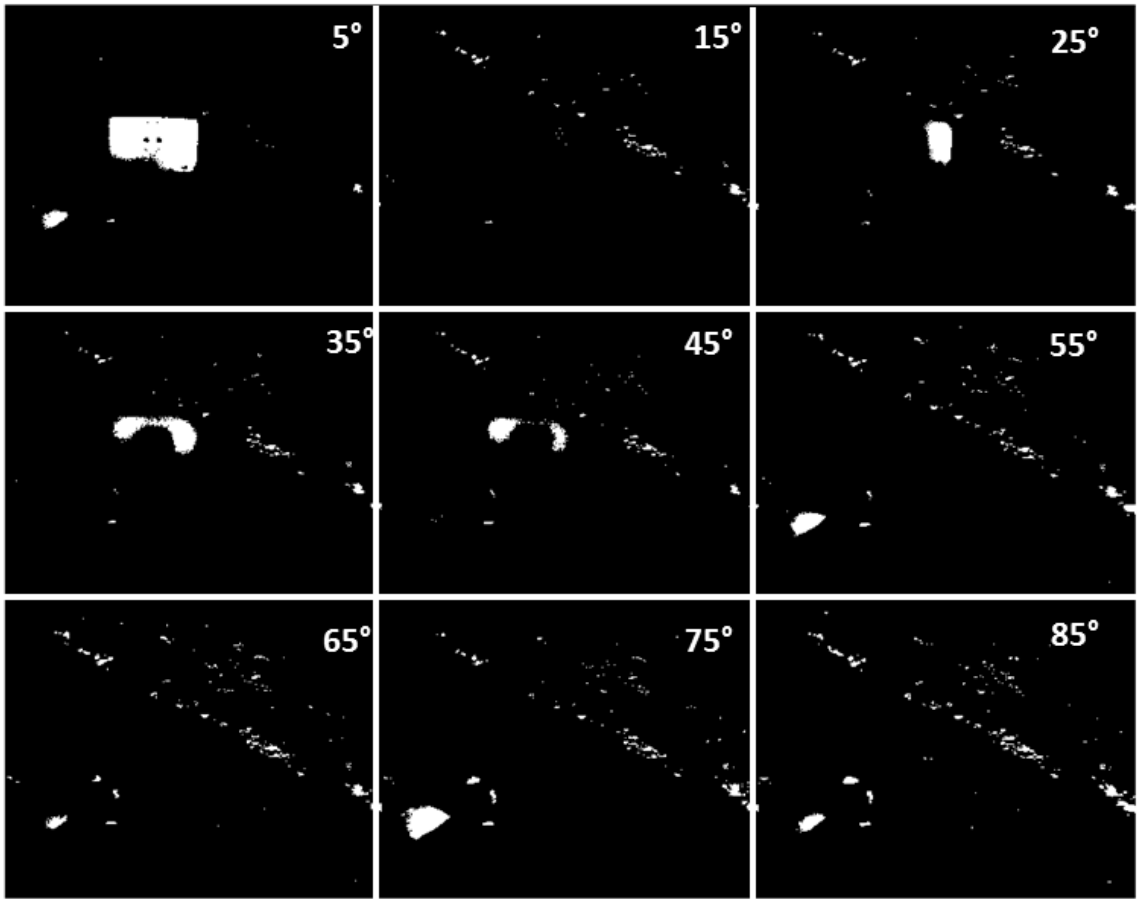

Figure 3.18 Intensity images with a threshold of $\pm 3\sigma$. In this figure the reference and test plate were only detected in a small number of images, while a significant number of false alarms were detected even at such high threshold.

Figure 3.19 illustrates the (-S1) image for each of the angles of the test plate. Since the preferred polarization orientation for manmade materials is often the vertical component, the negative sign was used to emphasize that preference (see Subsection 3.4).

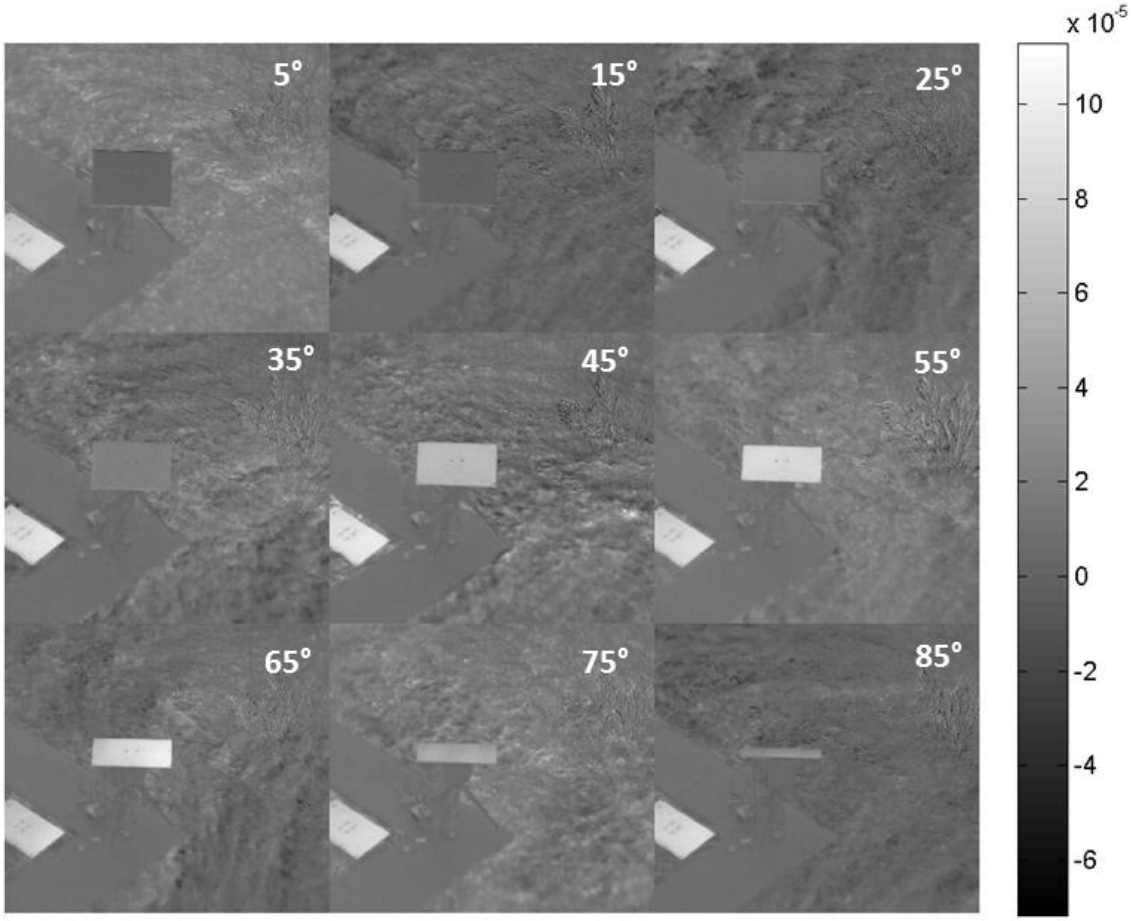

Figure 3.19 ($-S_1$) Stokes parameter for the test plate at different angles. The negative sign was applied to S_1 imagery to emphasize the vertical polarization component, which is the predominant feature when detecting polarized signals from dielectrically coated smooth surfaces. Therefore, dark pixels indicate horizontal component dominance while bright pixels represent vertical component dominance.

Figures 3.20 and 3.21 were thresholded using the same procedure used as in Figures 3.17 and 3.18 where the assumption is that the clutter in $-S_1$ is also Gaussian distributed. Therefore, using the estimated global mean and standard deviation one can standardized the images and apply $\pm 2\sigma$ and $\pm 3\sigma$ threshold.

The right side image of Figure 3.14 is a good reference to explain Figures 3.20 and 3.21. If one subtracts the horizontal from the vertical component as shown in Figure 3.14, one expects the result to be close to zero at incident angles between 0° and 20°,

with an increasing divergence with increasing angle up to a maximum point (Brewster angle, in this case 55°) and finally decreasing back to zero as the incident angle approaches 90°. The S_1 parameter behaves exactly as predicted in Figures 3.7 and 3.14, i.e., one would expect the start values from the test plate in S_1 imagery to be very small when the camera is normal to the surface and as the camera angle relative to the normal of the plate's surface increases up to the Brewster angle, the amount of radiance captured by the polarizer at the vertical position increases at a higher rate relative to the measured radiance of the polarizer at the horizontal position. As the angle between the tilting plate surface and the sensor increases from the Brewster angle to 90°, the divergence between the radiance values captured at horizontal and vertical positions diminishes, as depicted in Figures 3.7 and 3.14.

Using a threshold of $\pm 2\sigma$, the test plate was only detected for angles ranging from 45° through 85° while for the remaining angles the test plate pixel values were below the threshold. Conversely, the detection of the reference plate can be seen in all images because its angle relative to the sensor is beneficial to S_1 discrimination. When the threshold value was increased to $\pm 3\sigma$, Figure 3.21, the test plate can only be discriminated at 55° and 65° images in contrast to the five images in Figure 3.20. The reference plate can be easily identified in Figure 3.21 even with such high threshold value.

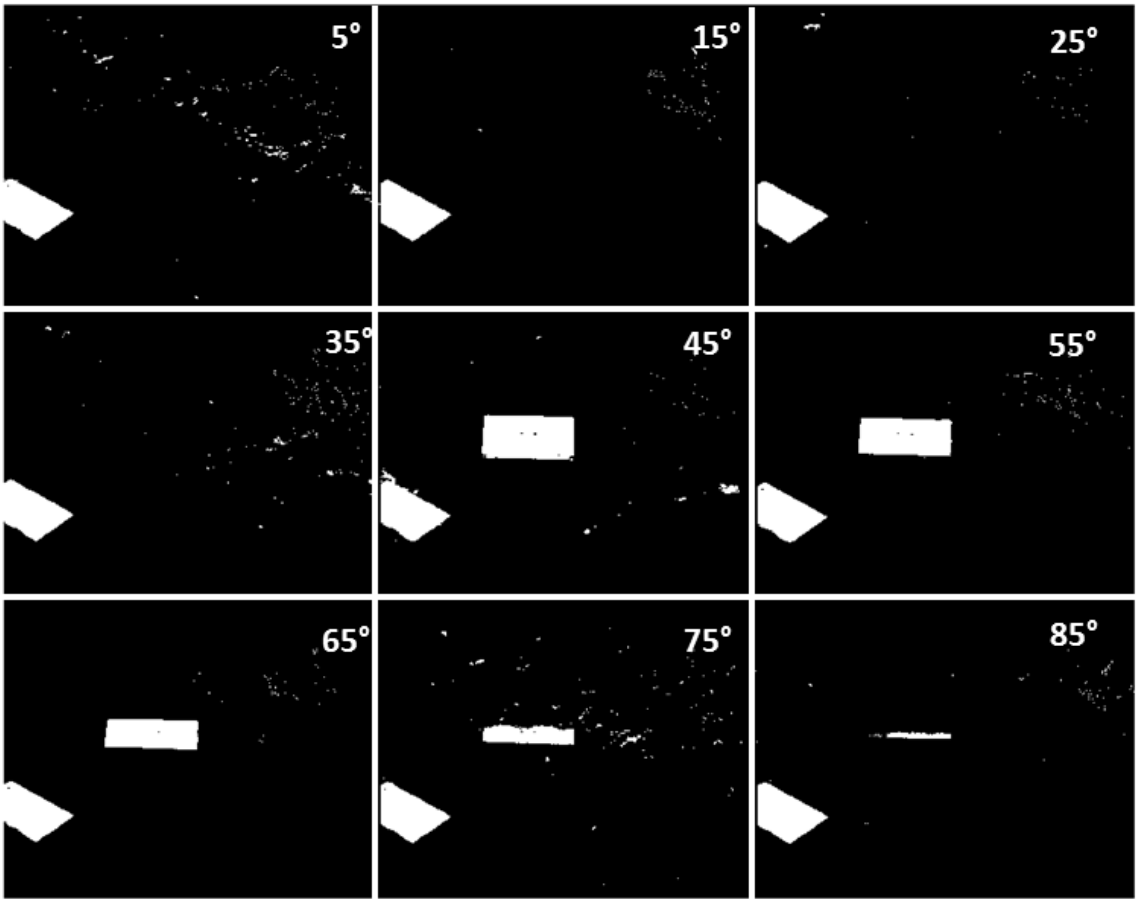

Figure 3.20 ($-S_1$) Stokes parameter images using a threshold of $\pm 2\sigma$. This experiment illustrates the S_1 angle dependency between the sensor and the test plate. The test plate is only detected at angles ranging from 45° through 85°. Conversely, because the reference plate remained at the same constant advantageous angle one was able to detect it for the entire experiment.

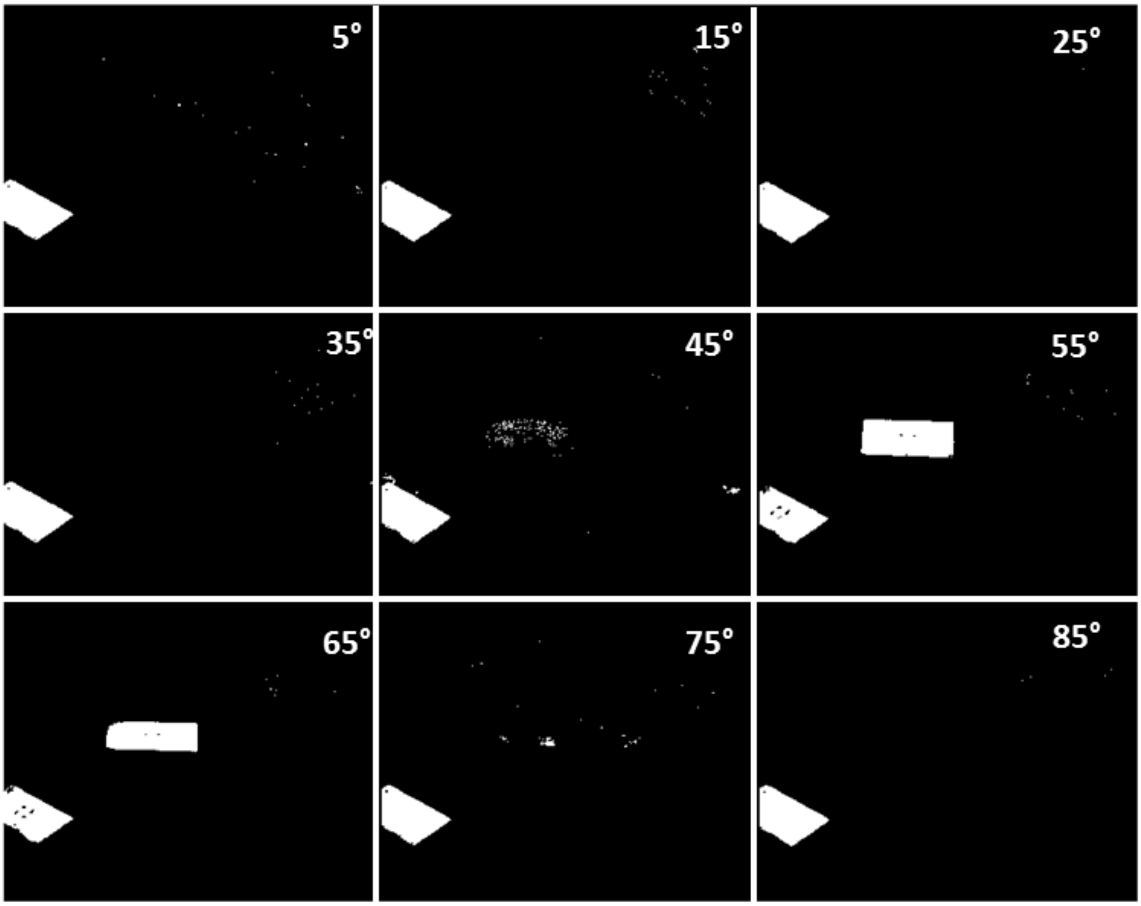

Figure 3.21 ($-S_1$) Stokes parameter images using a threshold of $\pm 3\sigma$. Here, as one expected, the number of images where the test plate was successfully detected diminished to only two, while the angle at which the reference plate was positioned relative to the camera allowed for its detection even at a higher threshold value.

Figures 3.20 and 3.21 demonstrate that the ability to detect the test plate is highly dependent on its angle relative to the sensor. The key message is that algorithm developers must be aware of this angle dependency as the target set transitions from a simple flat plane surface to complex multifaceted surfaces (see Subsection 3.5.2), having surfaces oriented at different angles. For example, if a target is composed several surfaces oriented at different angles, some of those surfaces may not favor high divergence between the horizontal and vertical components which would then result in

the inability of discriminating the whole target at a threshold level where false alarms are minimized.

Although angle dependency is a clear disadvantage with S_1 (as well as S_2 and DoLP, as it will be shown later) polarization brings an important feature which is the ability to detect smooth surfaces (if positioned correctly) even when their intensity values are within the clutter distribution. For example, observing Figure 3.17 where the test and reference plate were not detected for angles between 55° through 85°, Figure 3.20 shows that, using S_1 parameter, algorithms would have a better chance in detecting the smooth surfaces of both plates compared to using the S_0 parameter (broadband infrared). By subtracting both components (horizontal and vertical for S_1 and +45° and -45° for S_2), algorithms would focus on detecting the polarization orientation of the electromagnetic wave within each pixel of the image while disregarding the overall intensity information of each object relative to the background.

The reference plate, on the other hand, is always visible regardless of the threshold since it is placed at an optimum angle relative to the camera viewing angle, about 55°, naturally allowing a high SNR between horizontal and vertical polarization components.

Figure 3.22 demonstrates the S_2 polarization imagery for the different orientations of the test plate. As one can observe in this example, S_2 was not a very useful discriminating feature for detecting both plates from natural clutter background compared to S_1 and, as it will be shown later, DoLP imagery. Such performance degradation is a result of the orientation of the plates, relative to the sensor, which do not lend to any preferred orientation in the $\pm 45°$ relative to surrounding clutter.

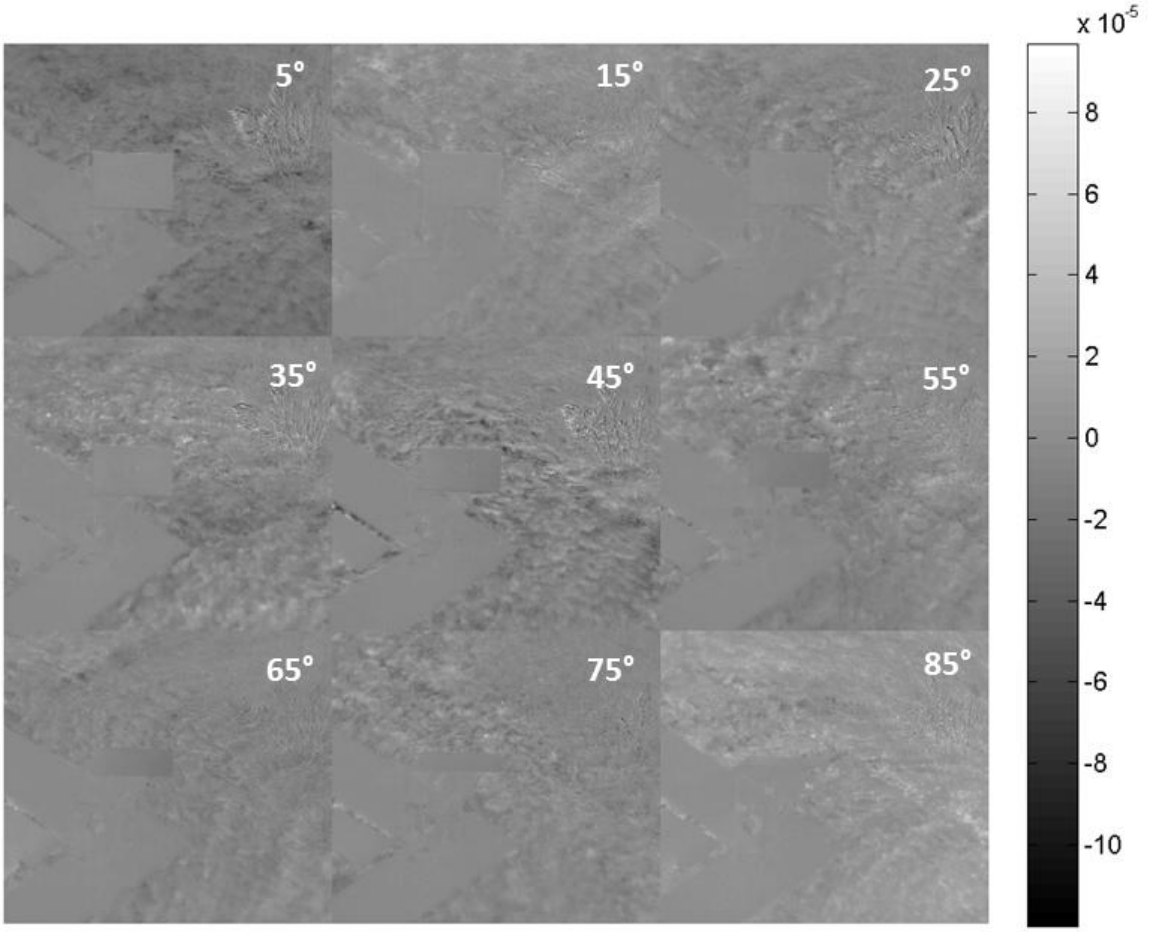

Figure 3.22 Measurement of the S_2 parameter images for the same scene depicted in Figure 3.12 as the angle of the test plate changes from 5° to 85°. The orientation of the plates demonstrate that the polarization of the incoming waves does not have a preferred polarization shift for either $\pm 45°$. As a result, there is no contrast between the manmade objects and the natural clutter. Bright pixels indicate a preferred $+45°$ orientation and dark tones indicates a preferred $-45°$ orientation.

Figures 3.23 and 3.24 present the S_2 imagery using $\pm 2\sigma$ and $\pm 3\sigma$ thresholds. As observed in Figure 3.22 the manmade objects present in the scene did not exhibit a preferred polarization orientation for either $\pm 45°$ and as a result their discernibility relative to the background is minimal, as validated by Figure 3.23, where none of the manmade objects in the scene were detected when using a low threshold value of $\pm 2\sigma$. Conversely, one can observe that some portions of the clutter exhibited a strong preferred

polarization orientation that is advantageous to S_2 detection and can be detected using a $\pm 2\sigma$ or $\pm 3\sigma$ threshold.

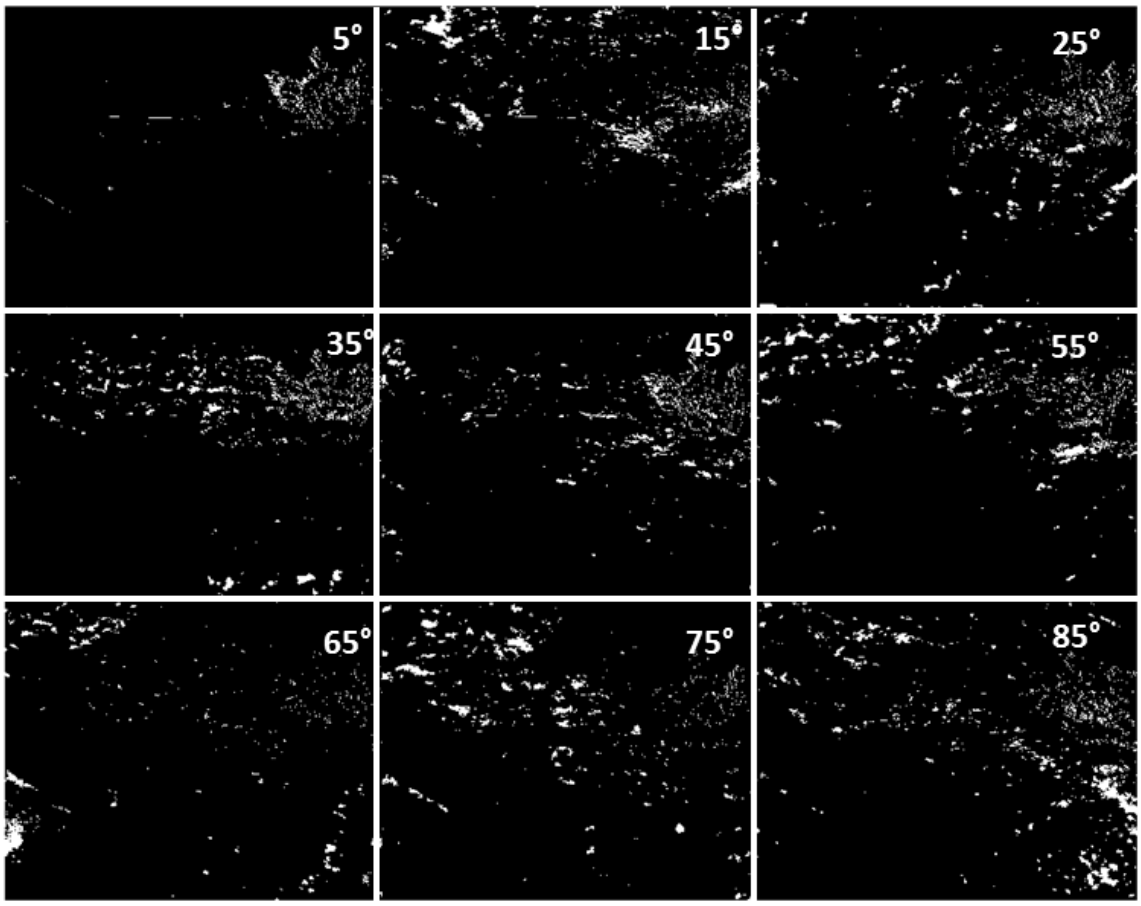

Figure 3.23 S_2 Stokes parameter images using a threshold of $\pm 2\sigma$. In this data collection scenario all manmade objects were not successfully discriminated from the background since their orientation did not lend to any preferred polarization for $\pm 45°$ that was substantially different from the surrounding clutter.

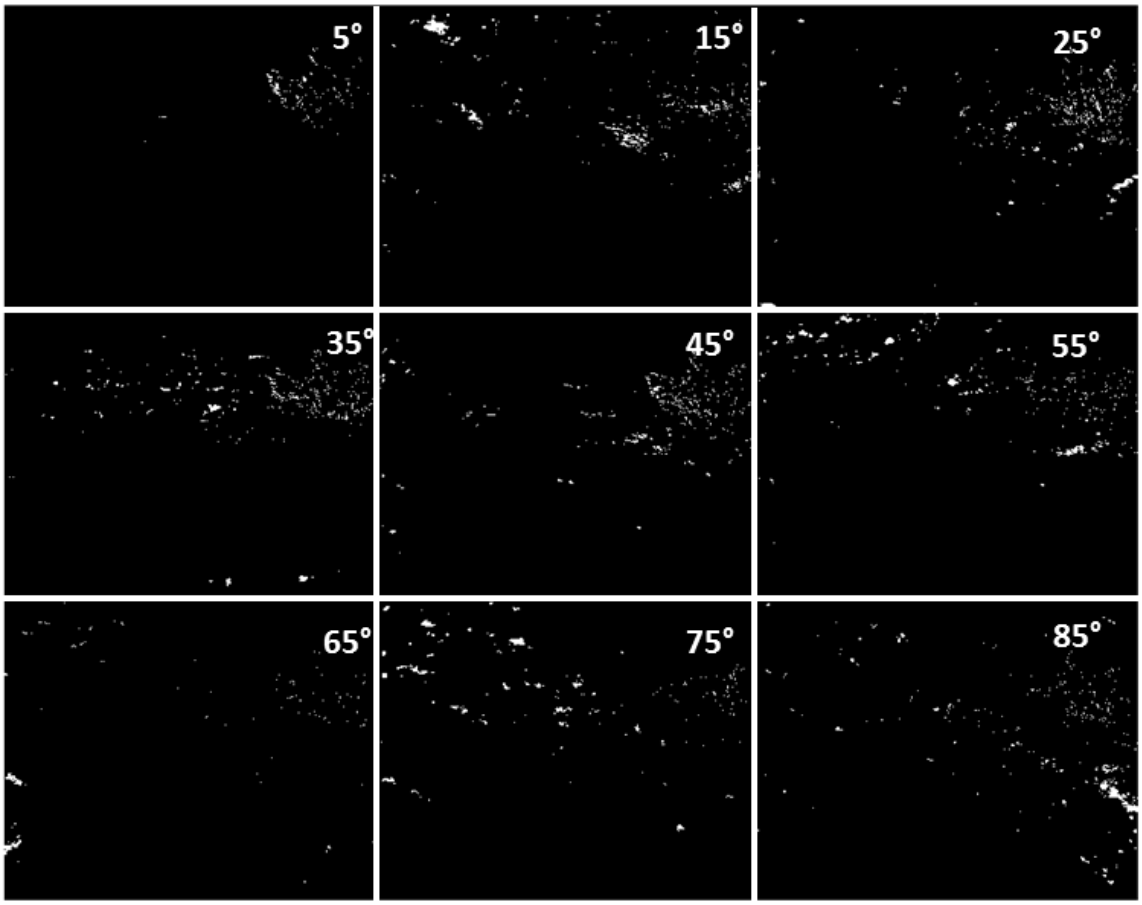

Figure 3.24 S_2 Stokes parameter images using a threshold of $\pm 3\sigma$ and as expected none of the manmade objects were found. However, it is interestingly to observe that some portions of the clutter are highly polarized in the S_2 domain and can still be detected using such high threshold value.

Figure 3.25 demonstrates DoLP imagery and its ability to discriminate the test and reference plate from natural clutter. DoLP values range from 0 to 1 where 0 indicates no polarization preference and 1 indicates fully polarized signal is detected. It will be shown in later chapters that DoLP imagery usually follows S_1 performance very closely and vice versa. Therefore, one can assume that in most cases, for the dataset used in this dissertation, S_2 imagery has little or no impact on the DoLP performance compared to S_1 influence. Such performance similarities can be readily observed in Figures 3.26 and

3.27, where the normalized images in Figure 3.25 are thresholded using $\pm 2\sigma$ and $\pm 3\sigma$ as the parameters of choice.

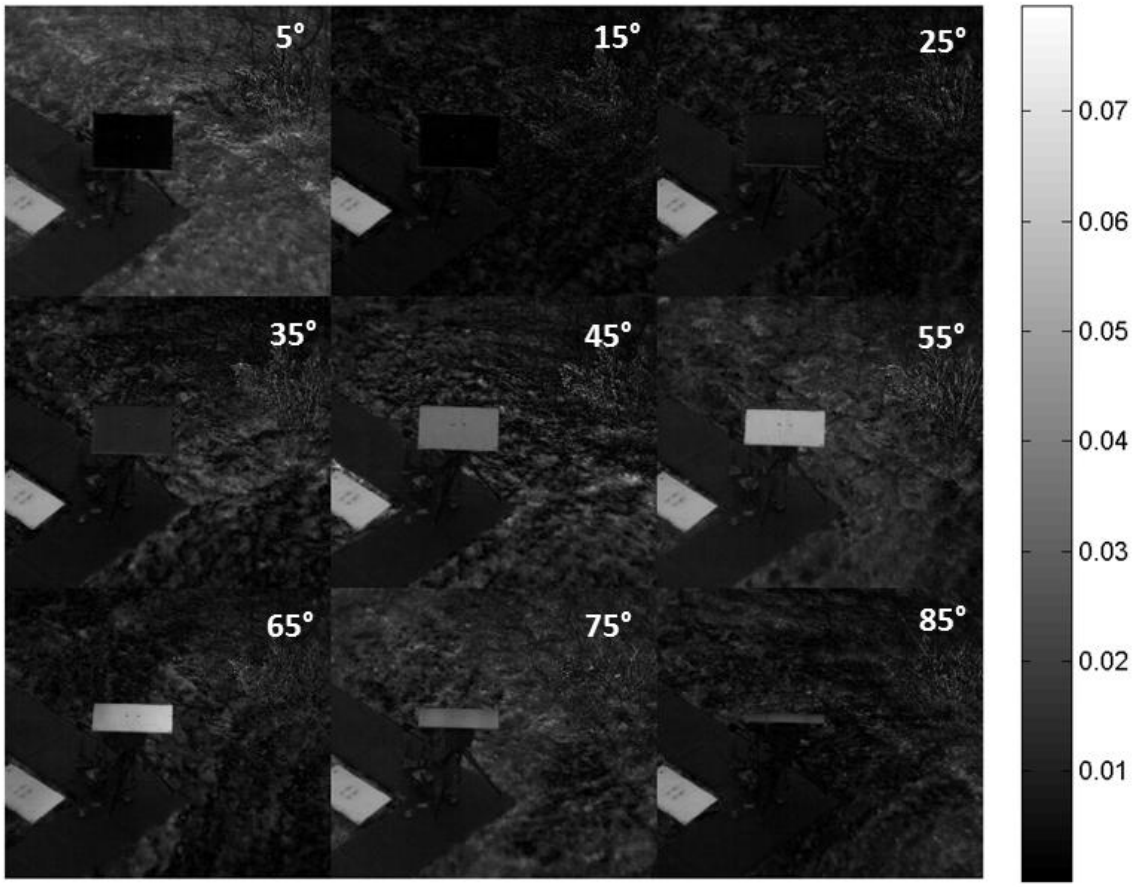

Figure 3.25 DoLP parameter for the test plate at different tilting angles. The plate exhibits no preferred orientation at the 5° and 15° angels, however as the angle between the camera and the plate increases the DoLP increases to a maximum of 0.075 at around 55° and decreases again to about 0.02 at 85°.

Comparing Figures 3.20 and 3.26 the following can be observed:

1) More false alarms can be found in DoLP images relative to S_1. This is a result of S_2 influence on DoLP where for the same threshold, S_2 demonstrated, see Figure 3.23, a high number of false alarms for all images compared to S_1.

2) The detection of the test plate using DoLP for $\pm 2\sigma$ is similar to S_1 with one exception where S_1 performs slightly better than DoLP for the 85° image.

3) The reference plate was successfully detected from natural clutter by both S_1 and DoLP using a $\pm 2\sigma$ threshold.

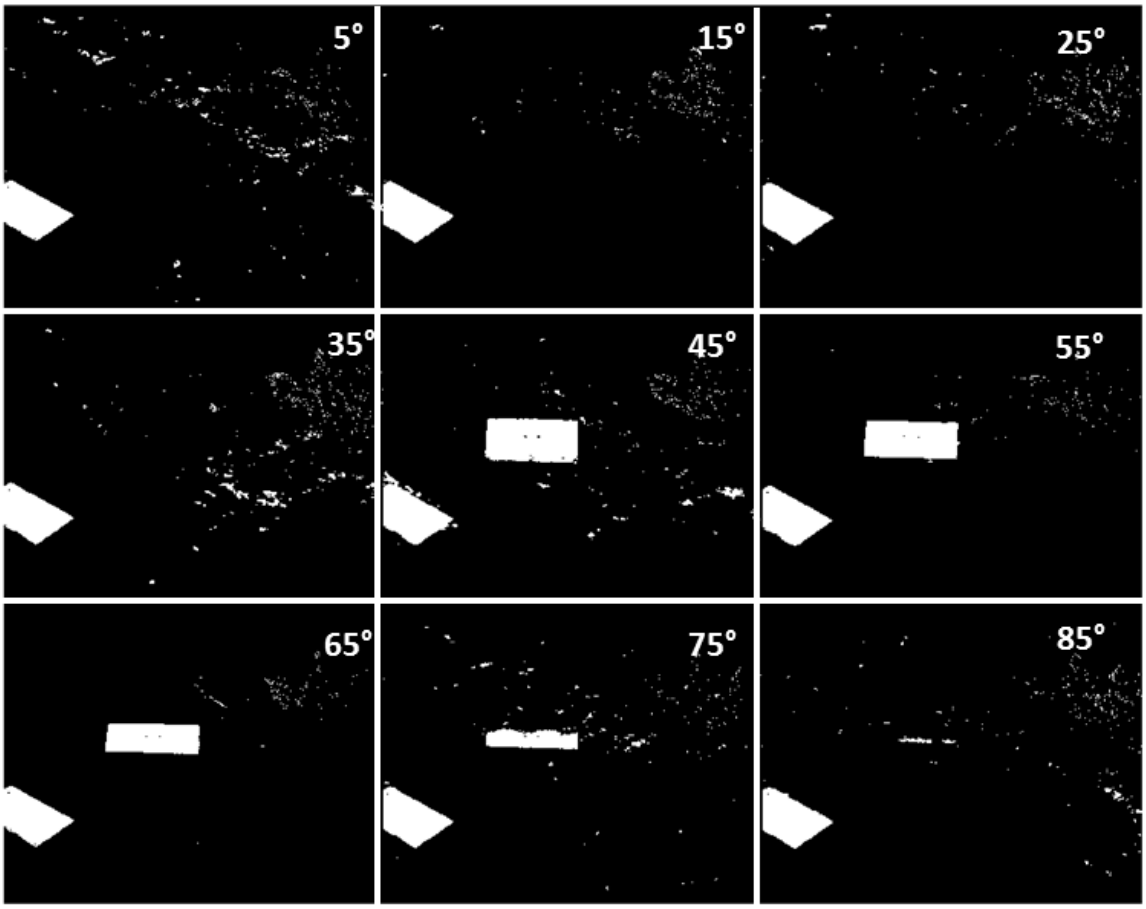

Figure 3.26 DoLP images with a threshold of $\pm 2\sigma$. DoLP performs very well in discriminating the reference plate from clutter, while the test plate is only detected for five images out of the nine taken. The number of false alarms present is significantly more than found in S_1 imagery which is a result of the S_2 term influence on DoLP.

Figure 3.27 depicts the detection of the reference and test plates using a $\pm 3\sigma$ threshold for different orientation angle of the test plate. In this example, DoLP experienced higher number of false alarms in all images relative to S_1 due to S_2 influence. DoLP is able to successfully discriminate the test plate for 55° and 65° imagery which is comparable to S_1; however S_1 was able to discriminate a higher number of pixels on the

test plate for the 45° image, which in contrast DoLP, wasn't able to discriminate any portion of the plate whatsoever.

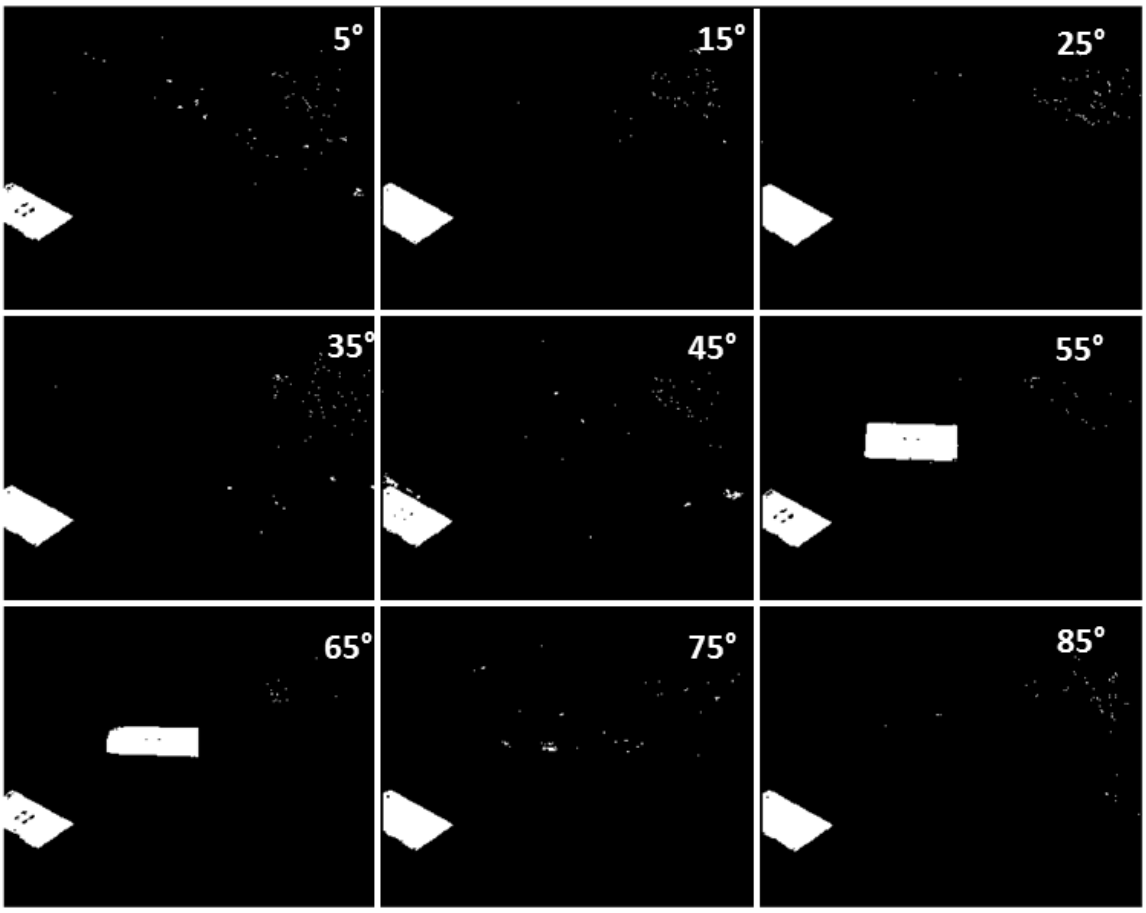

Figure 3.27 DoLP images with a threshold of $\pm 3\sigma$. In this example the DoLP performs very similarly to S_1 imagery with slightly more false alarms as a result of S_2 influence on DoLP. Furthermore, by comparing DoLP and S_1 parameters, one can observe that S_1 is able to identify a higher number of dispersed pixels on the test plate for the 45° image compared to DoLP, where the latter wasn't able to find any pixels on the test plate using the same threshold.

In summary, using measured data, this experiment demonstrated that the ability in discriminating manmade objects from clutter using S_1, S_2, and DoLP parameters is highly dependent on the angle of the manmade surfaces relative to the sensor position. Such dependency becomes problematic when many of the manmade objects facets may not be

oriented at angles (surface normal relative sensor) that are beneficial to separate manmade objects from clutter. As a result, as it will be demonstrated in Subsection 3.5.2, when detecting 3-dimensional manmade objects using Stokes information, only a very small number of facets are actually discriminated from clutter. Therefore, any algorithm that uses Stokes vector information as input is also susceptible to this angle dependency, which in turn affects its ability in discriminating 3-dimensional objects from complex natural clutter backgrounds.

3.5.2 Exploitation of Polarimetric Imagery for Discerning 3-D Objects from Clutter

Real operational scenarios which involve the detection of complex manmade objects in natural clutter environments with changing weather conditions will be examined in this subsection. Furthermore, in this subsection and the remainder of the dissertation, the SPICE data will be used to analyze existing and proposed algorithms. SPICE data was collected in Northern New Jersey, USA, using a Polaris LWIR microbolometer polarimeter camera, which will be described in Chapter 4 in more detail. Moreover, to facilitate the discussion on temporal changes within a diurnal cycle, this dissertation adopts a 24-hour time format (i.e., 0200h = 2:00AM, 1400h = 2:00 PM), which is observed as the standard format for most countries in the world.

The targets used for this data collection were surrogate self-propelled howitzers, placed at about 550m (slant range) from the sensor, and each of the three available targets were placed at different orientations (0°, 90°, and 135°) with respect to the sensor. The camera was located at a height of 55m on the data collection tower overlooking the scene with a depression angle of about 10°.

LWIR polarimetric images were collected every 5 minutes for a period of 72 consecutive hours of the mid-range target site (Figure 3.28) with the system pausing between the hours of 0300h and 0500h for sensor calibration. The sunrise and sunset for the data collection presented in the dissertation for MAR (MAR) 6th through 8th was around 0625h and 1754h. Four images were selected at specific times of the day illustrating, based on conventional thermal infrared which can be seen in Figure 3.29, the different thermal relationships between targets and background. For example, at 0710h, the targets and background have similar temperature (low contrast); around 0910h the targets are starting to warm up and as a result the temperature difference between the targets and clutter start to diverge. By 1310h, due to the continuous solar loading, the targets are hotter than the background and can be easily detected in the conventional infrared (high contrast), and finally by 2010h, about two hours after sunset, the targets are losing heat at a faster rate than the background as a result of their small thermal mass, therefore, their temperature relative to the surrounding background is once again very low (low contrast).

Figure 3.28 SPICE data collection surrogate targets placed at different viewing perspectives in relation to the data collection facility. The targets are designated by their respective angles (counterclockwise) as shown in the figure. The plates next to T_{90} were not present during the data collection presented in this dissertation.

Examining the S_0 output surfaces for the different times of the day on 6 MAR, 2010 in Figure 3.29, one can observe that the targets are not discriminatory against the background for the following timestamps: 0710h, 0910h, and 2010h. As a result of the lack of solar loading, and as explained in Subsection 2.5, this is often called a low contrast scene and it is not suitable for detection in broadband LIWR. Conversely, at 1310h, as the targets have been under the effect of solar loading for quite a long time, their temperatures are significantly higher than the surrounding background making them quite noticeable in conventional infrared imagery, also known as high contrast imagery.

During the early stages of solar loading, timestamp 0910h, one can observe slight differences in the target's temperature relative to clutter. However, such small

temperature difference is not suitable for anomaly detection using broadband infrared imagery, as the targets are still not very discriminatory relative to the background.

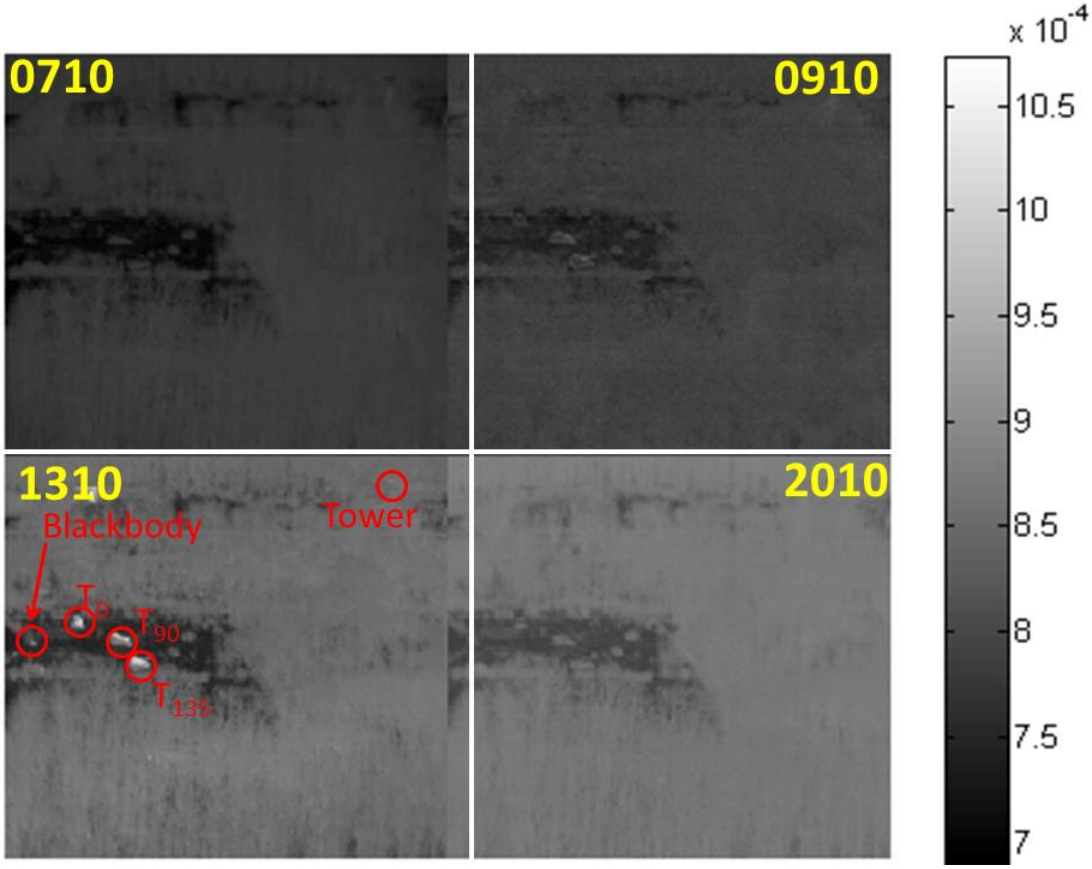

Figure 3.29 Output surfaces for S_0 for different times of the day (0710h, 0910h, 1310h, and 2010h) for 6 MAR 2010, illustrating low and high contrast imagery. As it is observed at timestamps 0710h and 2010h, the manmade objects in the scene are at similar temperature as the background making them very hard to be discriminated from clutter without any prior information. The image at 1310h depicts high contrast imagery where the manmade objects can be easily detected as a result of solar loading. At around 0910h the targets are at the early period of solar loading stage, and their temperatures are slightly more discriminatory than in 0710h and 2010h imagery.

Figure 3.30 depicts ($-S_1$) imagery for the same four timestamps as S_0. It is important to remember that dielectric surfaces usually emit vertically polarized imagery and in order to observe such phenomenon, negating S_1 imagery emphasizes such occurrence. Observing Figure 3.30, one can readily notice that most of the targets are quite obvious to the eye compared to S_0, especially when comparing low contrast

imagery. However, one can also observe that only small portions of the target (top surfaces) are discernible while the target side surfaces values are found to be within the natural clutter distribution. Moreover, also interesting is how grass, a natural material, exhibits slightly more vertically polarized information than trees. In fact, the amount of polarization found in grass for all timestamps is relatively similar to T_0. Such similarity may be the result that T_0 surfaces are oriented at angles that are unsuitable for polarization discrimination in the vertical/horizontal domain.

Figure 3.31 demonstrates the performance of S_2 imagery for the same timestamps as previous figures. Right away one notices that there is less contrast between manmade objects and natural clutter. Furthermore, natural clutter as a whole does not demonstrate a preferred orientation to $\pm 45°$, as seen in Figure 3.31, as its S_2 response seems to be very homogeneous regardless of material type and time of day.

Although most of the surrogate targets seem to be discriminatory to the eye, the blackbody is not easily detected in any of the S_2 imagery when compared to $-S_1$ imagery. Therefore, one can conclude that the orientation of the blackbody, for this experiment, does not exhibit a preferred $\pm 45°$ polarization. Moreover, as seen in $-S_1$ imagery, T_0 also lacks contrast relative to natural clutter for most timestamps but more significantly at 0910h, resulting in degraded performance regardless of the time period chosen.

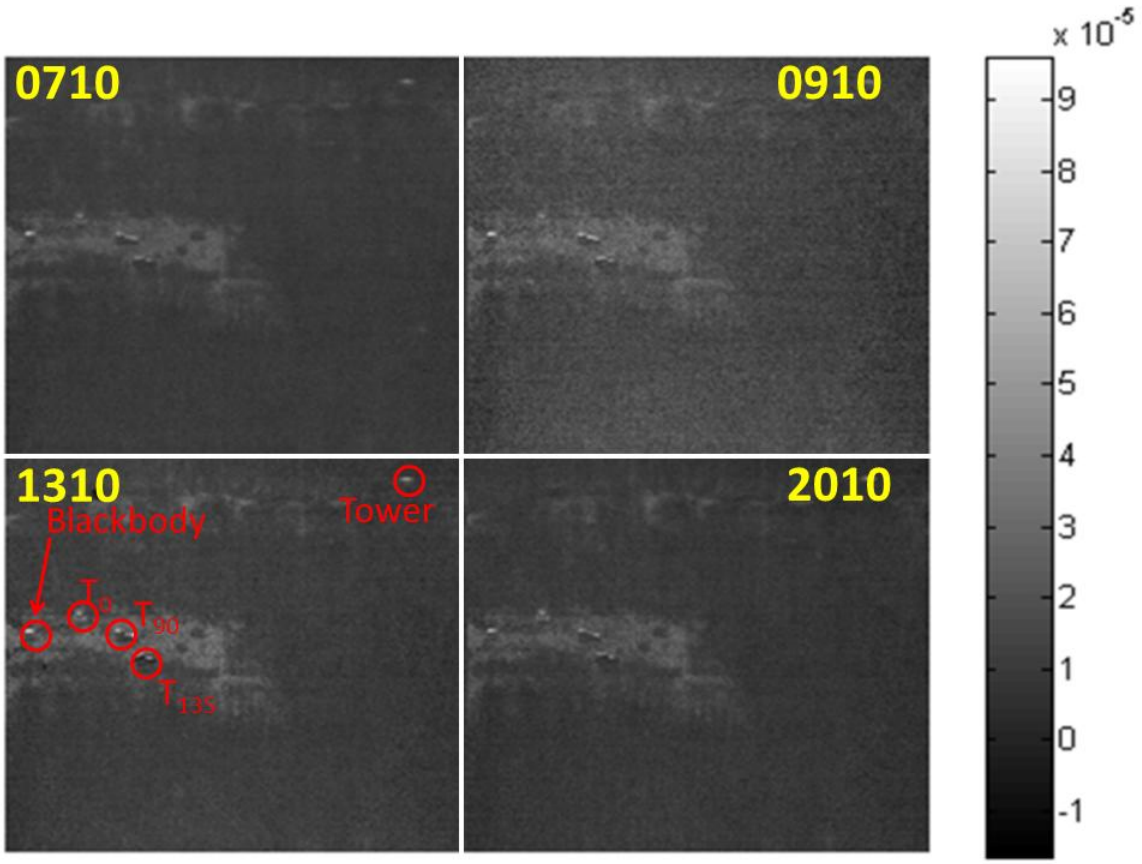

Figure 3.30 Output surfaces for ($-S_1$) for different times of the day (0710h, 0910h, 1310h, and 2010h) for 6 MAR 2010. In contrast to Figure 3.29, the manmade objects can be found relatively easy compared to S_0 imagery, especially for 0710h and 2010h. However, as one can observe in 0910h, T_0 is not as discriminatory compared to the remaining timestamps and other manmade objects in the scene for the same timestamp.

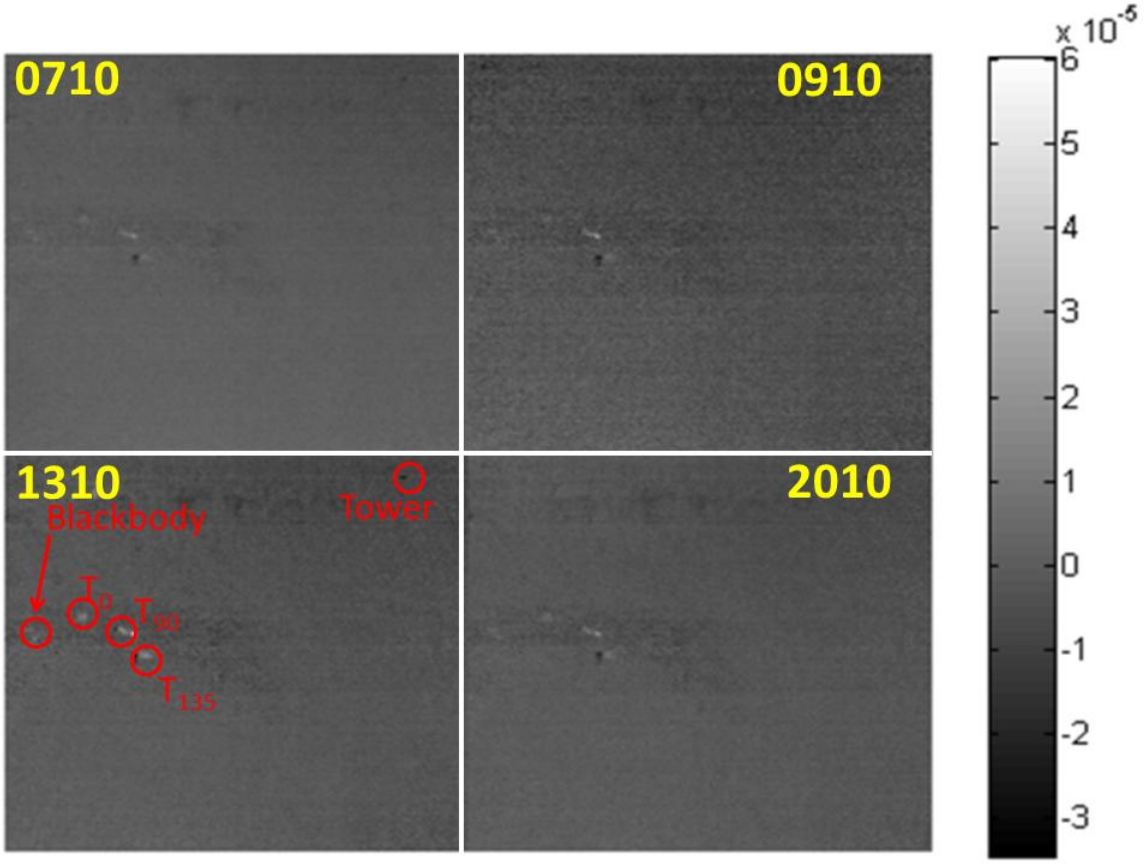

Figure 3.31 S_2 output surfaces for timestamps 0710h, 0910h, 1310h, and 2010h collected on 6 MAR 2010. Unlike previous Figure 3.30, natural clutter exhibits no preference for $\pm 45°$ polarization independent of natural material. The surrogate targets on the other hand, can be detected quite easily with the exception of the blackbody which does not have a noticeable preferred $\pm 45°$ polarization and as a result cannot be discriminated from natural clutter. T_0 once again exhibits the least amount of contrast relative to natural clutter of all three surrogate targets present in the scene.

Figure 3.32 demonstrates the performance of DoLP for the same four timestamps collected on 6 MAR 2010. As previously mentioned, DoLP is a combination of S_0, S_1, and S_2 imagery and as it was demonstrated in Figures 3.25, 3.26, and 3.27 DoLP suffered of performance degradation due to S_2 influence. In this experiment, however, by comparing Figures 3.32 and 3.30, one concludes that $-S_1$ and DoLP have similar results to each other. By examining S_2 imagery, one observes that natural clutter is quite homogeneous regardless of timestamp or natural material present on the scene, while most of the manmade objects can be easily distinguished from the background clutter.

Therefore, one can conclude that S_2, for this particular experiment, had little adverse influence on the number of false alarms present in DoLP imagery in contrast to what was shown for the tilting plate experiment, Figure 3.25.

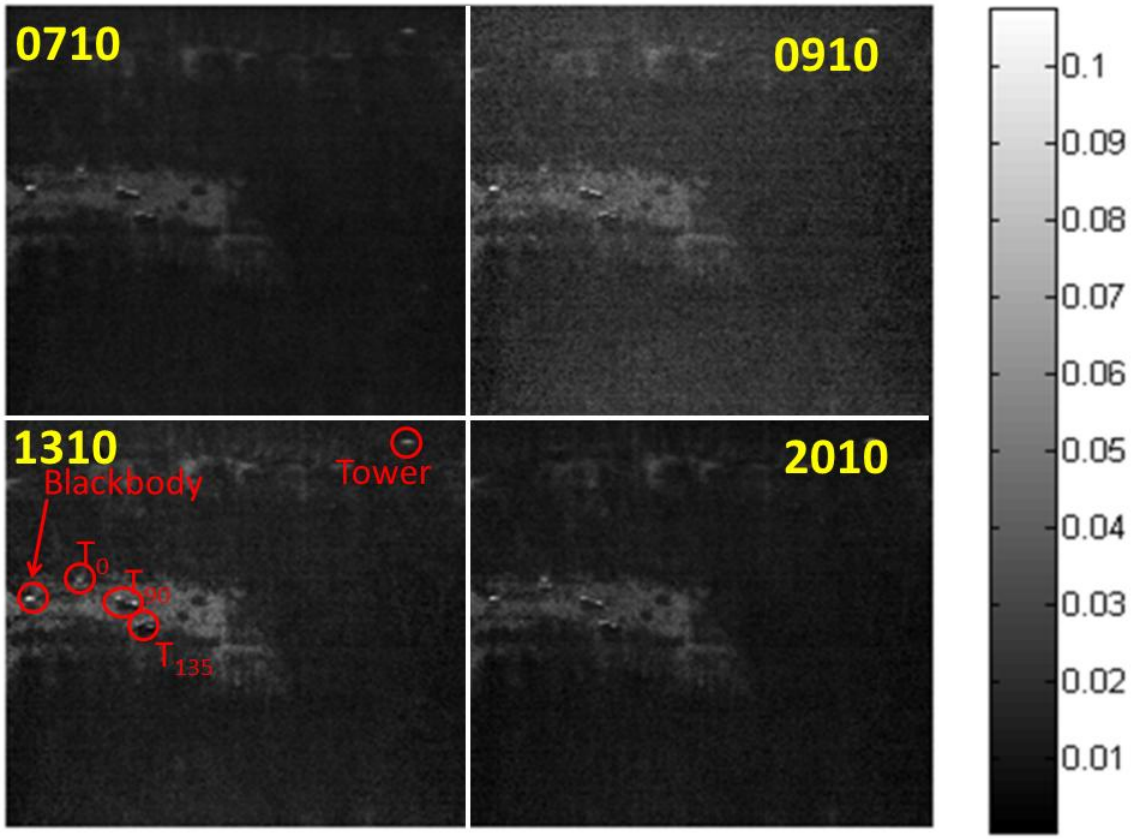

Figure 3.32 DoLP output surfaces for timestamps 0710h, 0910h, 1310h, and 2010h capture on 6 MAR 2010. The results demonstrated in this figure are quite similar to the results shown in Figure 3.30 for ($-S_1$) imagery. In contrast to what was concluded from Figure 3.25, S_2 parameter had negligible effect on the performance of DoLP. This can be traced to Figure 3.31 where all the natural materials present in the scene had no preferred $\pm 45°$ polarization.

A more useful measure and widely used in the community to compare different metrics or algorithms is the *Receiver Operating Curve* also known as *ROC* curve. This performance metric is calculated by varying the threshold of an output surface over all possible combinations and calculating the fraction of true positives (correct detection)

versus false positives (false alarms) according to the available ground truth. A good reference source discussing the use of ROC curves can be found in [39].

The ROC plots in Figures 3.33, 3.34, 3.35, and 3.36 illustrate the performance of each of the Stokes parameters and DoLP for each of the surrogate targets for timestamps 0710h, 0910h, 1310h, and 2010h. Furthermore, for each timestamp, the ROC curves are broken down by target aspect angle to emphasize some of the concerns demonstrated in Subsection 3.5.1 such as the Stokes parameters dependency on surface angle orientation. By imaging the same target type at three different orientation angles relative to the sensor, the goal is also to demonstrate the Stokes performance variability as a function of target aspect angle.

Figure 3.33 illustrates the ROC performance curves for 0710h for T_0, T_{90}, and T_{135}. The following conclusions are drawn from the ROC curves:

1) Polarimetric information appears to be useful in detecting small portions of the targets in low contrast scenarios at extremely low false alarm rates regardless of metric used.

2) The trends in performance between S_1 and DoLP are very similar with respect to each other for all targets with the exception where DoLP performs slightly better than S_1 for T_{135} at higher false alarm rates.

3) Overall, S_1 and DoLP perform better than S_2 regardless of the target angle indicating, as shown in Figures 3.30, 3.31 and 3.32, manmade objects exhibit more vertically polarized signals rather than $\pm 45°$ polarization.

4) S_2 performs better than S_0 for false alarm rates less than 0.005, which is expected since the temperature of the targets is similar to the surrounding background and broadband imagery does not perform very well in low contrast imagery.

5) S_0 performs better than S_1 or DoLP in some instances for a $P_{fa} \sim 0.05$, where $\sim$ denotes approximately. However, such high false alarm rates are impractical for real world applications since the number of false alarms present in the image will be too great to successfully discriminate the manmade objects from clutter.

6) Stokes and DoLP performances worsen as the target aspect angle changes relative to the sensor. Nonetheless, S_1, S_2, and DoLP performances are still higher than conventional infrared (S_0) at low false alarm rates $P_{fa} < 0.005$. As shown in Subsection 3.5.1, the Stokes vector parameters performance are highly dependent to sensor and target aspect angle, which is quite problematic for anomaly detection applications.

7) S_1 and S_2 have similar performance at extremely low false alarm rates indicating that similar features are available in both metrics. As a result, DoLP also follows S_1 and S_2 performance.

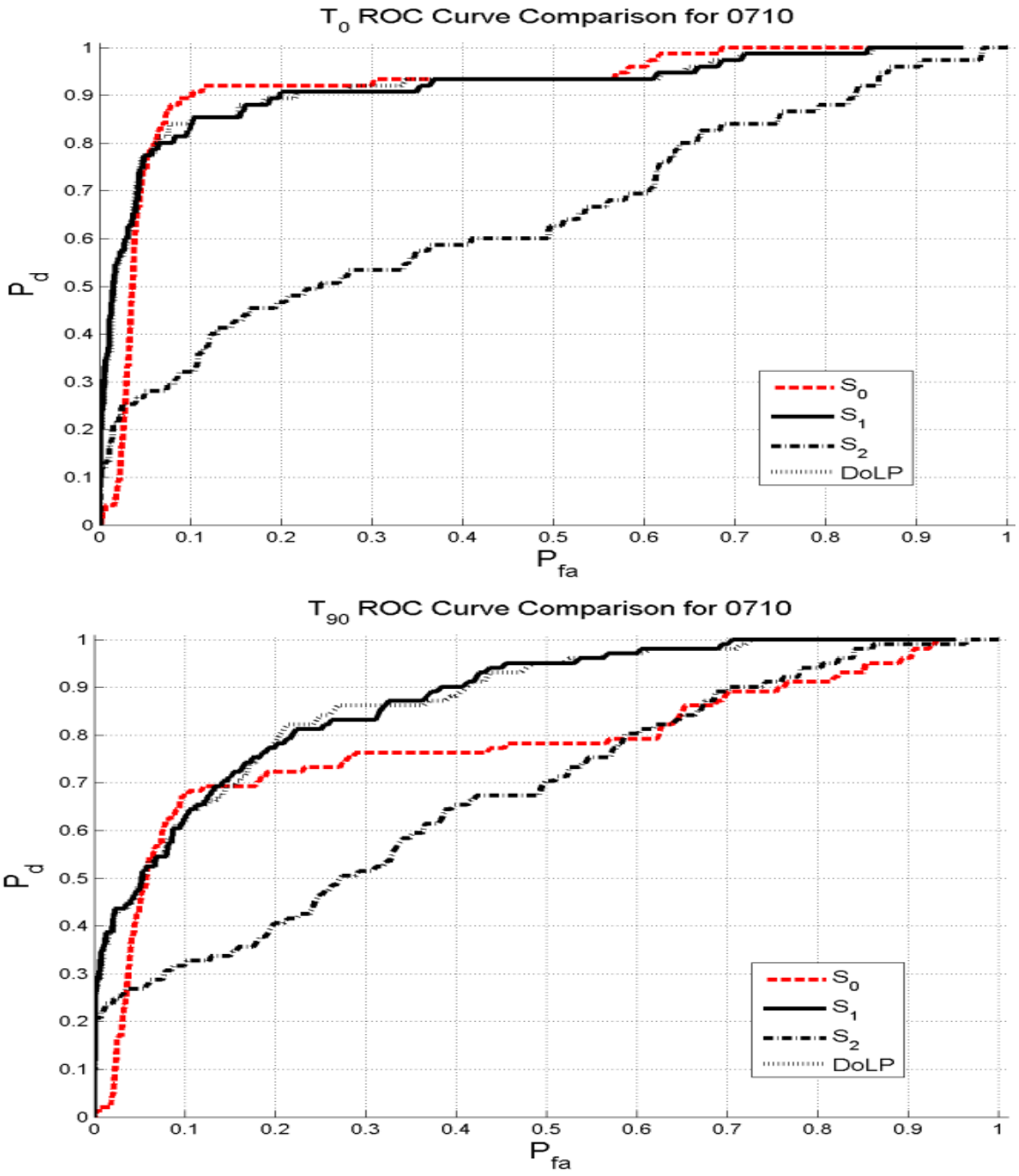

Figure 3.33 ROC curve comparison for each of the surrogate targets for S_0, S_1, S_2, and DoLP for timestamp 0710h. DoLP and S_1 performed better than S_2 and S_0 for most of the ROC curve PFA range. S_1 and S_2 have similar performance at extremely low false alarm rates indicating that similar features are available to both metrics. As a result, DoLP also follows S_1 and S_2 performance. However, as S_2 performance degrades quite significantly relative to S_1 and the performance of DoLP and S_1 continue to remain similar, one can conclude that DoLP performance becomes primarily a function of S_1 performance rather than S_2. Conversely, for T_{135}, DoLP actually performs better than S_1 as a result of better performance from S_2 which is the result of the orientation of the surfaces relative to the sensor.

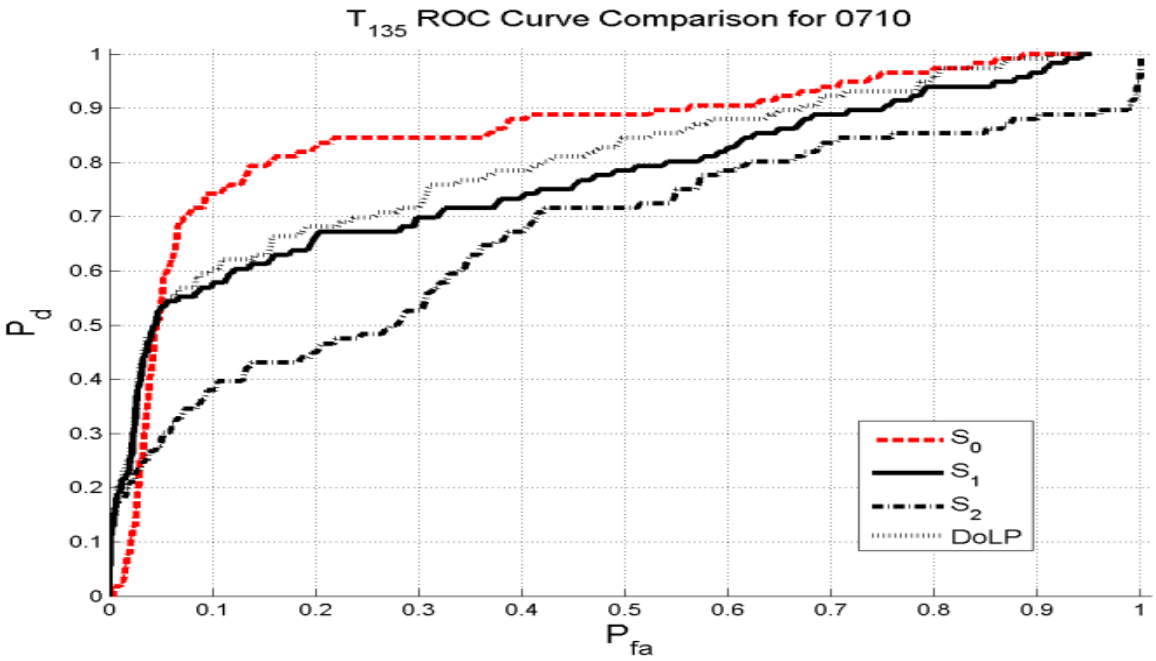

Figure 3.33 ROC curve comparison for each of the surrogate targets for S_0, S_1, S_2, and DoLP for timestamp 0710h. DoLP and S_1 performed better than S_2 and S_0 for most of the ROC curve PFA range. S_1 and S_2 have similar performance at extremely low false alarm rates indicating that similar features are available to both metrics. As a result, DoLP also follows S_1 and S_2 performance. However, as S_2 performance degrades quite significantly relative to S_1 and the performance of DoLP and S_1 continue to remain similar, one can conclude that DoLP performance becomes primarily a function of S_1 performance rather than S_2. Conversely, for T_{135}, DoLP actually performs better than S_1 as a result of better performance from S_2 which is the result of the orientation of the surfaces relative to the sensor. (Continuation)

Figure 3.34 demonstrates the Stokes vector output surfaces using a $\pm 5\sigma$ threshold for 0710h. The white pixels refer to known manmade object pixels that are above the threshold, for example, on the top right S_1 image, an observation deck of a data collection tower can be found. On the far left is the blackbody followed by, from left to right, T_0, T_{90}, and $T_{135,}$ respectively. On the contrary, red pixels indicate natural material locations where the values where higher than the chosen threshold, i.e., false alarms. Before examining the individual performances, it is important to emphasize a critical point illustrated by Figure 3.34. If one refers back to Figure 3.33, one observes that S_1, S_2, and

DoLP performed quite similarly to each other; however when the same threshold is applied to the three metrics only S_1 and DoLP demonstrate similar performance, with some false alarms present, while S_2 only detects a few pixels belonging to T_{90} and T_{135} with no false alarms. This indicates that a 5σ is a relative good threshold for S_2 but not so useful for S_1 and DoLP. As a result, such discrepancy reveals the intricacies of choosing a threshold for real applications where the same threshold yields different results for different metrics. Such discrepancy can be primarily traced to the use of threshold values based on Gaussian distributions on non-Gaussian data such as Sokes vector output surfaces. It is important to emphasize that the distribution of natural objects distribution is unknown, and clearly not Gaussian, and the distribution of manmade objects distribution is highly dependent on the viewing angle. Nonetheless, Figure 3.34 is still a useful comparison between the four Stoke vector parameters using a similar threshold in order to visually compare the different performances.

As seen in Figure 3.34, S_0, as expected, does not perform very well for a high threshold as the temperature values in both target and clutter classes are very similar. S_1 and DoLP perform similarly in finding all manmande objects present in the scene with few false alarms. As previously mentioned in Figure 3.30, grass exhibited a preferred vertical polarization similarly to that of manmade objects. As shown in Figure 3.34, that preference is shown in terms of false alarms. S_2 performs very well for T_{90}, T_{135}, and the observation tower, with the exception of T_0. As described in Figure 3.31, because T_0 had a very low contrast relative to the surrounding clutter, the use of a high threshold where low or no false alarms are detected also meant the elimination of low contrast manmade objects present in the imagery.

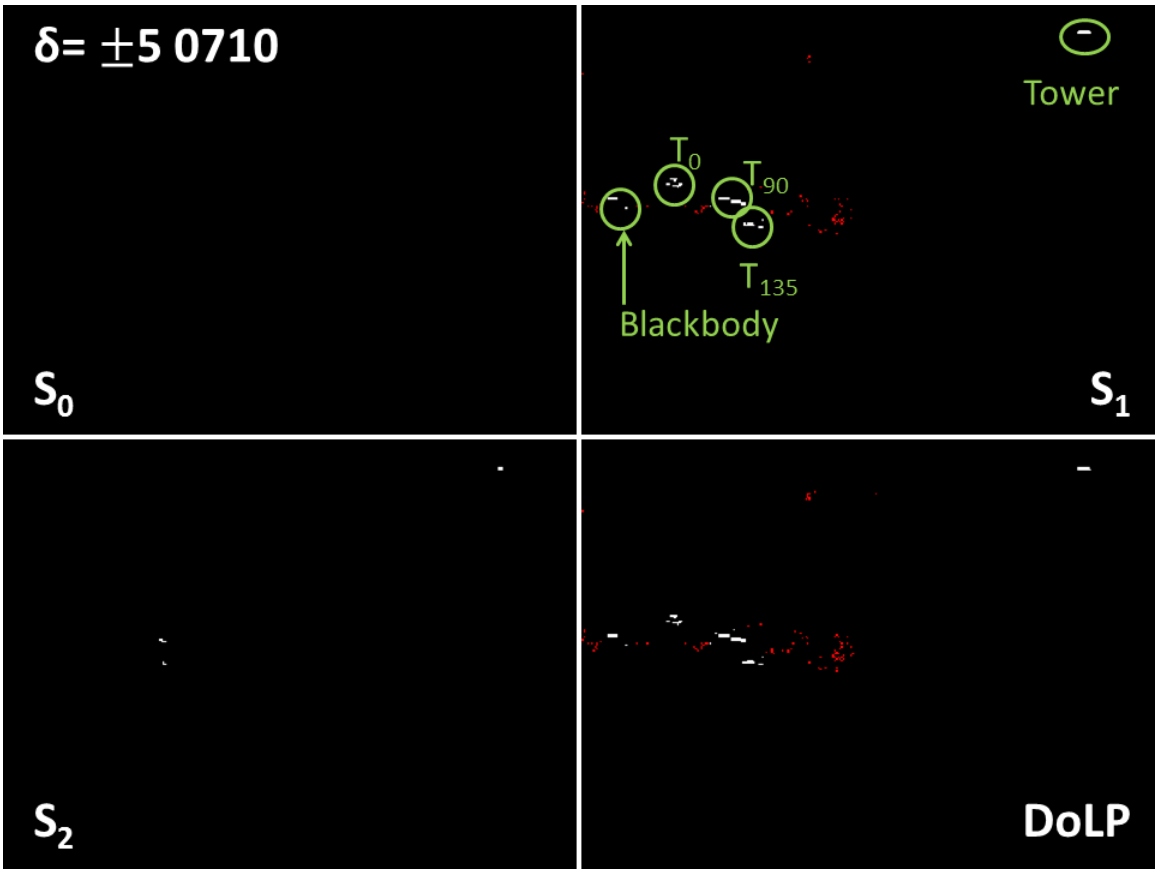

Figure 3.34 Output surfaces for Stokes and DoLP parameters using a ±5σ threshold value for imagery collect at 0710h. S_1 and DoLP imagery reveal some false alarms within the grass area of the image, with DoLP having slightly more false positives than S_1 imagery as a result of S_2 influence. S_2 imagery performed better than the remaining Stokes parameters by detecting small portions of T_{90}, T_{135}, and the observation tower with no false alarms. S_0, as expected, performed very poorly as a consequence of a very small temperature differential between the clutter and manmade objects.

Figure 3.35 depicts the ROC curves for timestamp 0910h for all four timestamps and surrogate targets. Some differences can be observed when comparing the ROC curves in Figure 3.33 that need to be emphasized:

1) The performances of S_1 and DoLP are relatively similar regardless of target aspect angle. Such performance similarity indicates that S_2 had very little influence in DoLP for timestamp 0910h.

2) S_1, DoLP, and S_2 performances degraded quite significantly with respect to Figure 3.33 for high false alarm rates, but with comparable results for the low false alarm rate region, which is the area of interest for real applications.

3) S_0 performs similarly to DoLP and S_1 for T_{135}, however S_0 performs quite poorly for T_0 and T_{90}. Such performance degradation can be the result of increasing clutter temperature relative to the targets. The reader is reminded that T_0, T_{90} and T_{135} are hollow shells and the low ambient temperature (2-3° Celsius) compounded by the small amount of time of solar loading did not increase the temperature differential between the clutter and the targets.

Figure 3.36 demonstrates the Stokes parameters output surfaces using a common $\pm 5\sigma$ threshold for comparison. Unlike Figure 3.34, S_0 was able to successfully detect portions of the external blackbody and T_{90} with some false alarms around the transition area between the grass and tree line. S_1 and DoLP continued to perform very similarly with some very small differences in the number of false alarms detected. These two parameters were able to detect all five manmade objects in the scene while S_2 was only able to detect T_{90} and T_{135} with no false alarms.

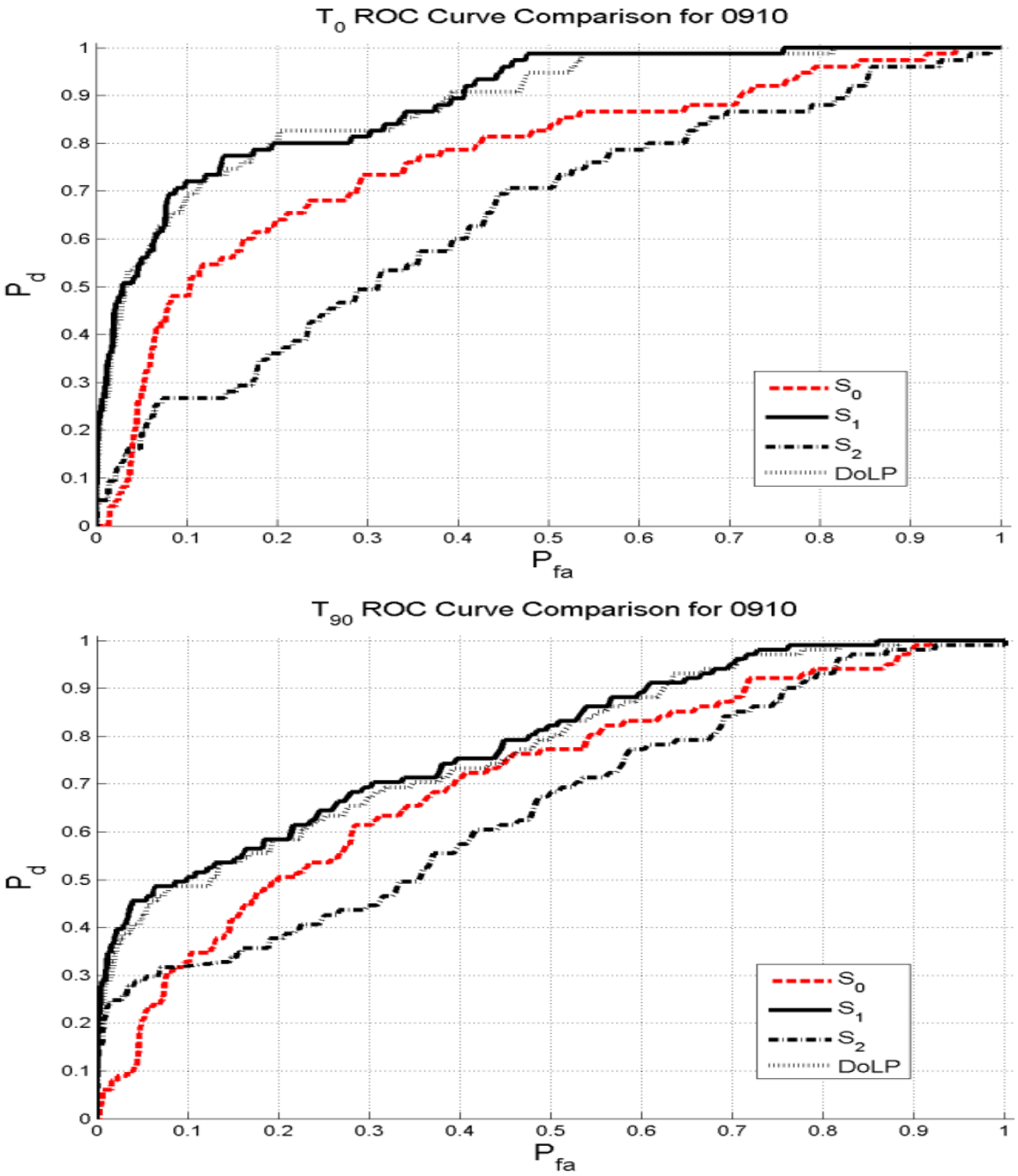

Figure 3.35 ROC curve comparison for each of the surrogate targets for S_0, S_1, S_2, and DoLP for timestamp 0910h. S_0 performance is slightly degraded with respect to previous Figure 3.33 from clutter temperature rising slightly above the manmade objects temperature. S_1 and DoLP performed very similarly for all manmade objects. Therefore, one can conclude that during this time period, the DoLP performance was a function of S_1 performance in contrast to what was observed in Figure 3.33 for T_{135}.

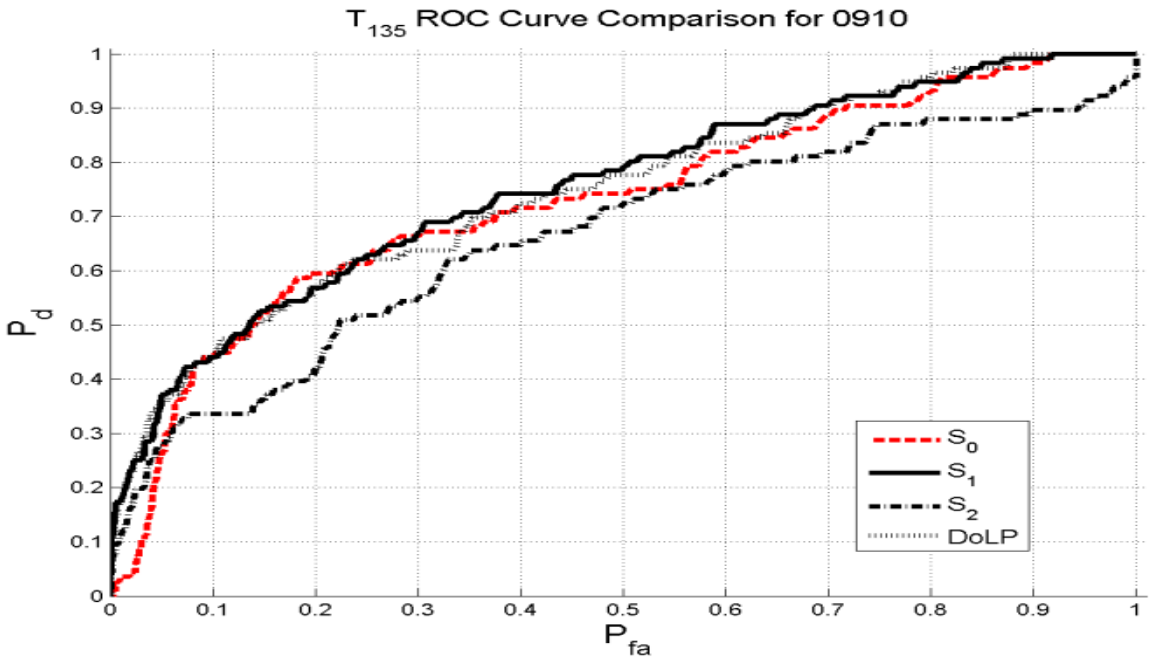

Figure 3.35 ROC curve comparison for each of the surrogate targets for S_0, S_1, S_2, and DoLP for timestamp 0910h. S_0 performance is slightly degraded with respect to previous Figure 3.33 from clutter temperature rising slightly above the manmade objects temperature. S_1 and DoLP performed very similarly for all manmade objects. Therefore, one can conclude that during this time period, the DoLP performance was a function of S_1 performance in contrast to what was observed in Figure 3.33 for T_{135}. (Continuation)

Figure 3.36 Output surfaces for the different Stokes and DoLP parameters using a $\pm 5\sigma$ threshold. In contrast to Figure 3.34, using a $\pm 5\sigma$ S_0 detects a small portion of the external blackbody and T_{90} as well as false alarms along the grass-tree transition area. S_1 and DoLP performed very well for 0910h by detecting all five manmade objects with very small number of false positives. S_2, on the other hand, continued to detect T_{90} and T_{135} with no false alarms, however it fails to detect T_0 and the observation.

The ROC curves for timestamp 1310h are shown in Figure 3.37 where several key points need to be emphasized, such as:

1) S_0 performs better than previously demonstrated in Figures 3.33 (0710h) and 3.35 (0910h) with somewhat similar performance to S_1, S_2, and DoLP at low false alarm rates. This performance increase is a consequence of the continuous solar loading effect throughout the day on the surrogate targets resulting in a higher temperature differential between clutter and manmade objects.

2) S_1 and DoLP performed very similarly in detecting T_0 at extremely small and high P_{fa} rates. S_2 performed better than S_1 and DoLP for T_{90} and T_{135} at small P_{fa} rates.

3) S_2 performed extremely well in detecting T_{135}, Figure 3.37, for low false alarm rates which was better than S_1 and DoLP throughout the ROC curve. Only S_0 performed better than S_2 for T_{135}. The only discrepancy between S_1 and DoLP happens at $0.5 \leq P_{fa} \leq 0.8$ where S_1 performance is increasing at a slower rate than S_2. During this range of false alarm values, S_2 influence is clearly demonstrated by a slight increase in DoLP performance relative to S_1.

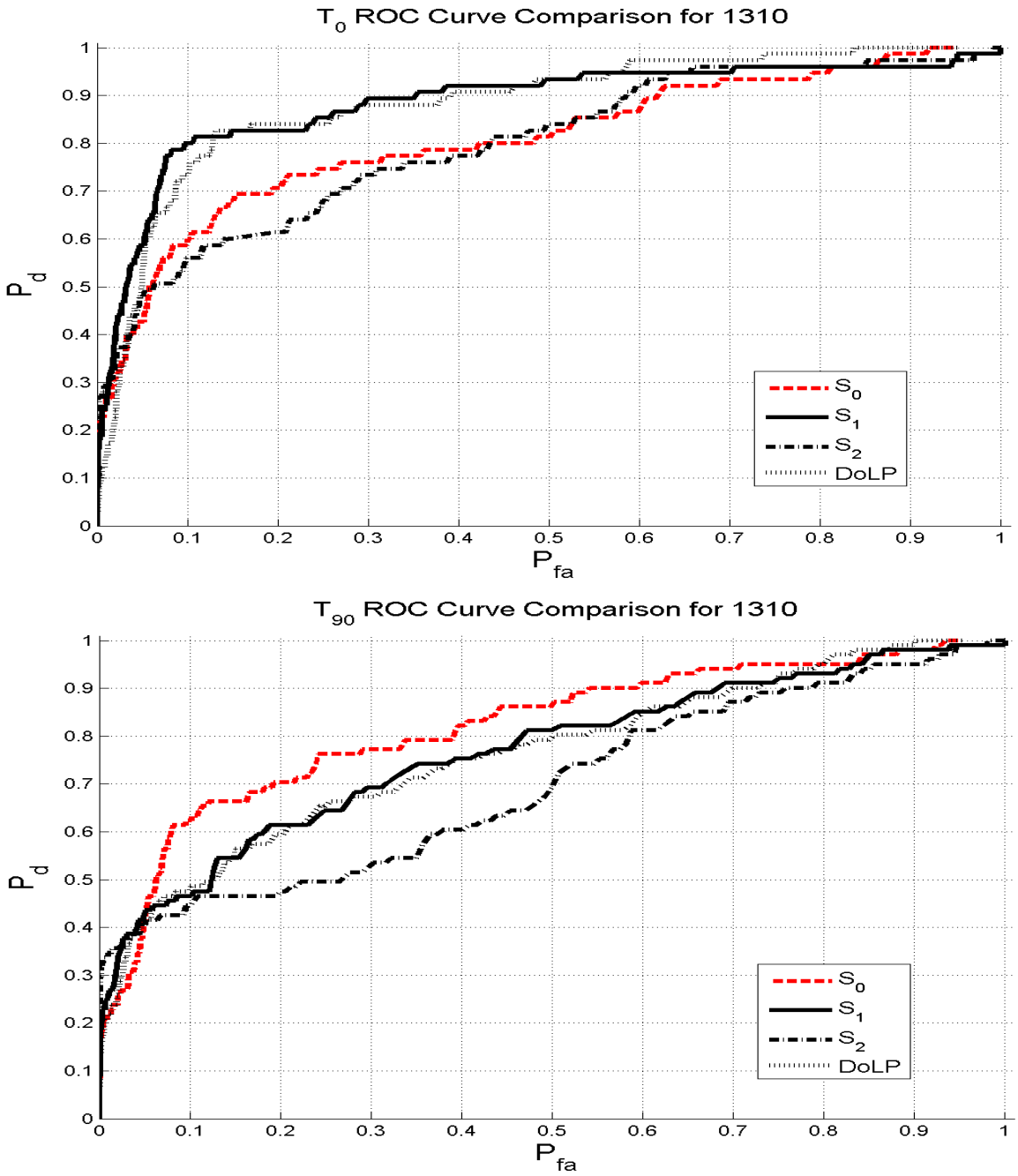

Figure 3.37 ROC curve comparison for each of the surrogate targets for S_0, S_1, S_2, and DoLP for timestamp 1310h. S_0 performance was significantly better than timestamps 0710h and 0910h as a consequence of continuous solar loading effect on the surrogate targets. S_1, S_2, and DoLP performed similarly for T_0 at low false alarm rates, however S_1 and DoLP outperformed S_2 for the remaider of the ROC curve. Conversely, S_2 performed better than S_1 and DoLP for low false alarm rates for T_{90} as well as for the full ROC curve for T_{135}.

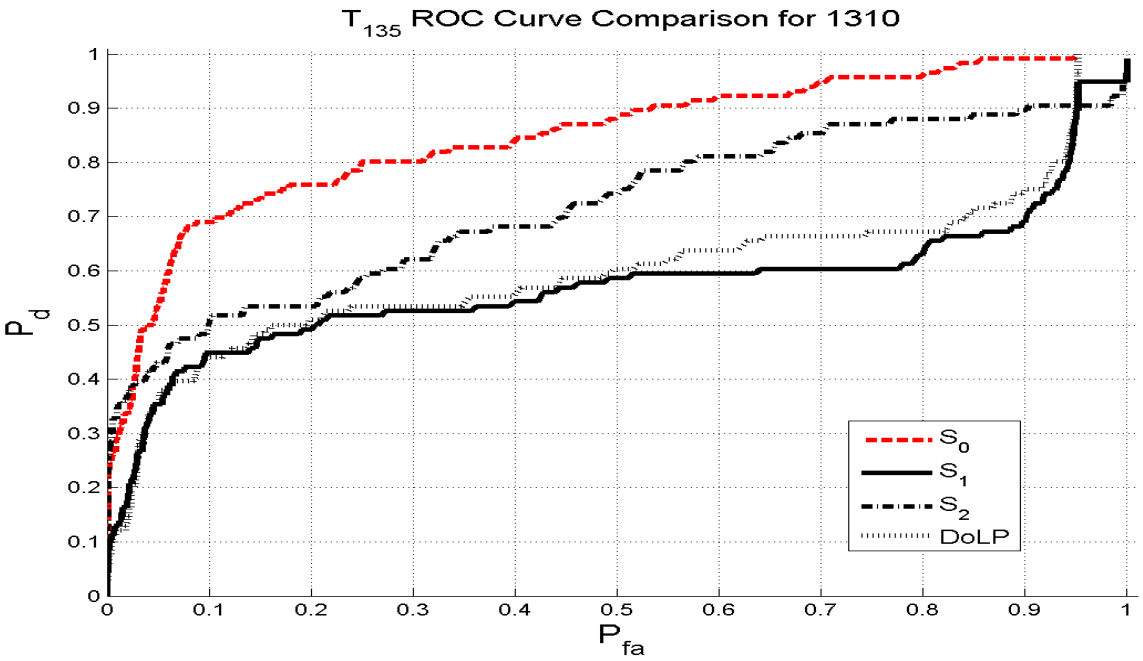

Figure 3.37 ROC curve comparison for each of the surrogate targets for S_0, S_1, S_2, and DoLP for timestamp 1310h. S_0 performance was significantly better than timestamps 0710h and 0910h as a consequence of continuous solar loading effect on the surrogate targets. S_1, S_2, and DoLP performed similarly for T_0 at low false alarm rates, however S_1 and DoLP outperformed S_2 for the remaider of the ROC curve. Conversely, S_2 performed better than S_1 and DoLP for low false alarm rates for T_{90} as well as for the full ROC curve for T_{135}. (Continuation)

The output surfaces for timestamp 1310h using a common $\pm 5\sigma$ threshold is demonstrated in Figure 3.38. The key points to emphasize in Figure 3.38 are as follows:

1) As a result of solar loading effect the temperature differential between the surrogates and clutter is significantly higher making the targets more discriminative in S_0 imagery. Conversely, both the external and the observation tower were not successfully detected.

2) S_2 demonstrates the best performance relative to previous Figures 3.34 and 3.36 by detecting all three surrogate targets and the observation tower with no apparent false alarms.

3) S_1 and DoLP are able to detect all manmade objects in the scene but at the expense of also detecting a significant number of false alarms as well.

4) The threshold value of $\pm 5\sigma$ chosen for S_1 and DoLP was not as useful as in previous timestamps 0710h and 0910h (Figures 3.34 and 3.36) since the

number of false alarms detected were significantly higher than previously seen.

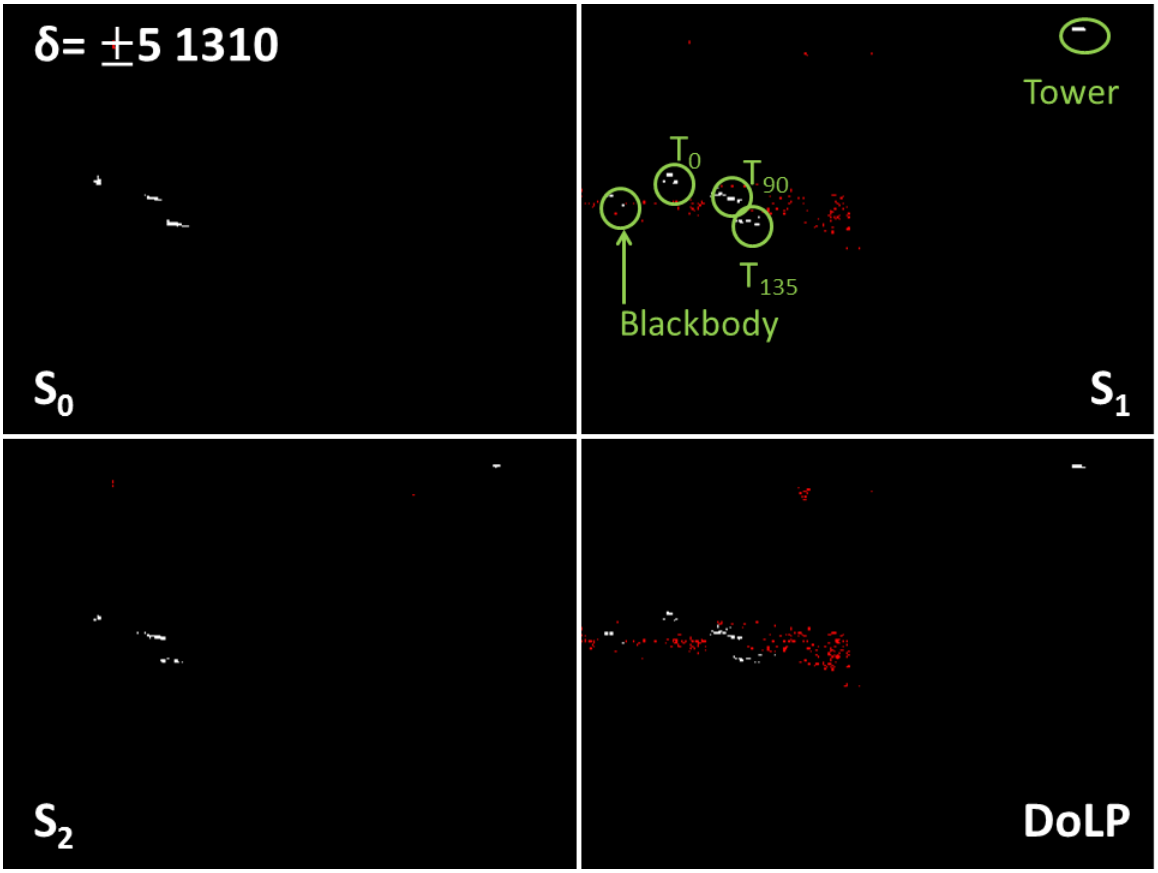

Figure 3.38 Output surfaces for S_0, S_1, S_2, and DoLP using a common threshold value of $\pm 5\sigma$. As a result of solar loading the surrogate targets are at a higher temperature than natural clutter allowing for their detection with no false alarms in S_0 imagery. However, the external blackbody and the observation tower were not successfully detected for the same threshold value. S_2 performs the best when compared to timestamps 0710h and 0910h (Figure 3.34 and 3.36) by detecting all three surrogate targets including the observation tower with no false alarms. Contrariwise, S_1 and DoLP performed very poorly compared to S_0 or S_2. Both metrics are able to find the all manmade objects but at the expense of detecting a large number of false alarms as well.

Finally, the ROC curves for timestamp 2010h shown in Figure 3.39 demonstrate a similar trend as previously observed in Figure 3.33 with S_0 underperforming S_1, S_2, and DoLP metrics for the low false alarm region where most systems like to operate. S_1 and DoLP performed very similarly for T_0 and T_{90} for most of the ROC curve with the

exception of T_{135} where DoLP performed better than S_1 as a result of S_2 influence where S_2 enhanced performance can be attributed to the orientation of the surfaces in T_{135}. Finally, at low false alarms rates, one can observe that all polarization metrics (S_1, S_2, and DoLP) performed similarly with a $P_d = 0.18, 0.20, \text{and } 0.10$ for T_0, T_{90}, and T_{135}, respectively.

Figure 3.40 illustrates the output surfaces for Stokes parameters and DoLP with a $\pm 5\sigma$ threshold at 2010h for 6 MAR 2010. The reader is reminded that white pixels indicate correct detections; red pixels indicate false alarms; and black pixels indicate locations where the values were below the threshold value. The following key points can be observed from Figure 3.40:

1) As a result of lack of solar loading, S_0 once again performs very poorly relative to the other metrics where no target pixels were detected using the $\pm 5\sigma$ threshold.

2) S_1 performs very well in detecting all four manmade objects in the scene with some false alarms found in the grass area. Thus, one can conclude that the grass exhibits strong vertical polarization features that are very similar to the features demonstrated by the manmade objects.

3) S_2 performs very well in detecting T_{90}, and a very small portion of T_{135} and the observation tower in the upper right corner with no false alarms present. T_0 and the external blackbody exhibited no strong S_2 features that could be successfully detected using the chosen threshold value.

4) Using DoLP, one was able to detect the same target pixels as S_1 for T_0, T_{90}, T_{135}, and the external blackbody system but with a significant higher number of false positives. Conversely, DoLP was able to detect a higher number of pixels on the observation tower relative to S_1 and S_2 imagery which one can conclude that S_0, S_1, and S_2 imagery together contributed enough information to make the observation tower more discriminatory than their individual output surfaces.

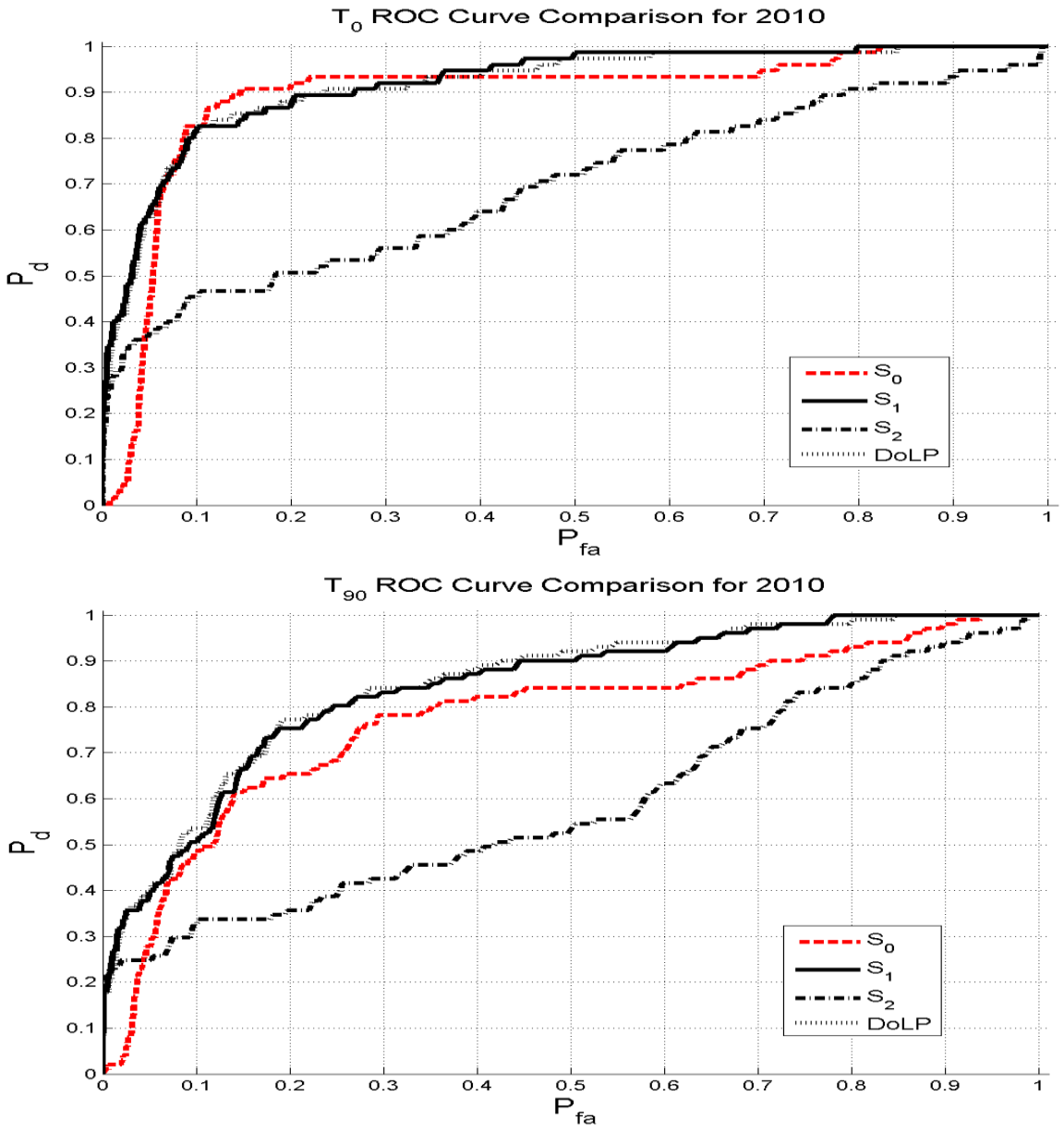

Figure 3.39 ROC curve comparison for each of the surrogate targets for S_0, S_1, S_2, and DoLP for timestamp 2010h. With no solar loading available as in Figure 3.33, S_0 performance was significantly reduced at the lower false alarm rates making S_0 imagery useless for an automated/aided systems. DoLP and S_1 performed better than S_2 and S_0 for most of the ROC curve PFA range for T_0 and T_{90}. Furthermore, one can observe that S_1 and S_2 have similar performance at extremely low false alarm rates indicating that similar features are available to both metrics. As a result, DoLP also follows S_1 and S_2 performance. However, as S_2 performance degrades quite significantly relative to S_1 and the performance of DoLP and S_1 continue to remain similar, one can conclude that DoLP performance becomes primarily a function of S_1 performance rather than S_2. Conversely, for T_{135}, DoLP performs better than S_1 as a result of better performance from S_2 parameter.

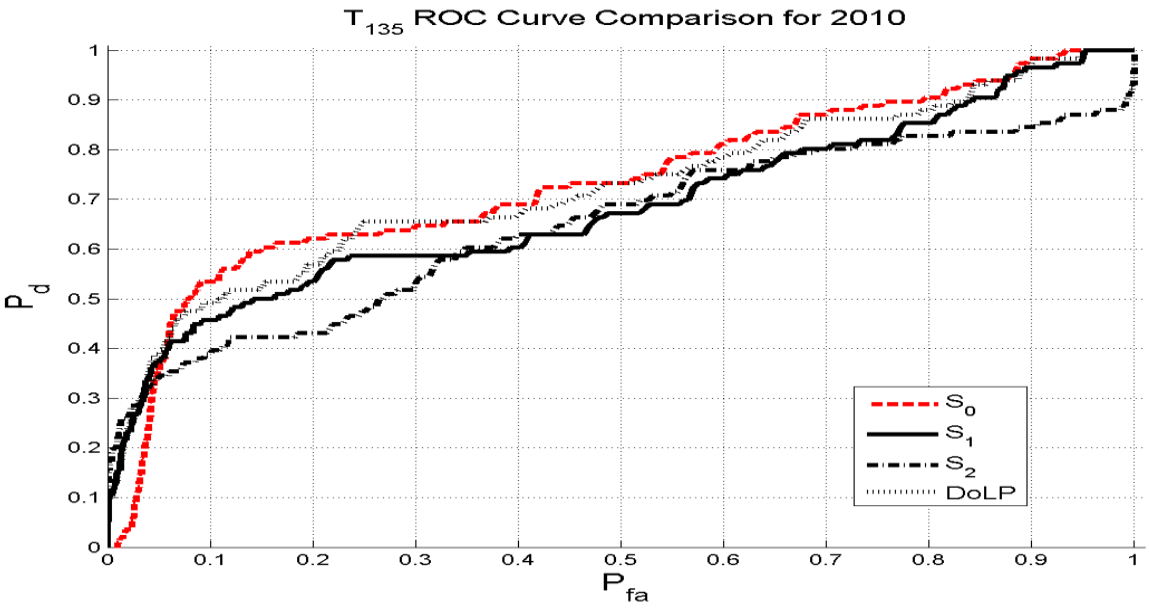

Figure 3.39 ROC curve comparison for each of the surrogate targets for S_0, S_1, S_2, and DoLP for timestamp 2010h. With no solar loading available as in Figure 3.33, S_0 performance was significantly reduced at the lower false alarm rates making S_0 imagery useless for an automated/aided systems. DoLP and S_1 performed better than S_2 and S_0 for most of the ROC curve PFA range for T_0 and T_{90}. Furthermore, one can observe that S_1 and S_2 have similar performance at extremely low false alarm rates indicating that similar features are available to both metrics. As a result, DoLP also follows S_1 and S_2 performance. However, as S_2 performance degrades quite significantly relative to S_1 and the performance of DoLP and S_1 continue to remain similar, one can conclude that DoLP performance becomes primarily a function of S_1 performance rather than S_2. Conversely, for T_{135}, DoLP performs better than S_1 as a result of better performance from S_2 parameter. (Continuation)

Figure 3.40 Output surfaces for S_0, S_1, S_2, and DoLP using a common threshold value of $\pm 5\sigma$. As a result of the lack solar loading S_0 once again performed very poorly with virtually no manmade object detected for timestamp 2010h. S_1, on the other hand, was able to identify all manmade objects in the scene with a lesser number of false alarms than DoLP. Conversely, DoLP was able to detect more pixels on the observation tower than S_1 imagery. S_2 successfully identified T_{90} and very small portions of T_{135} and the observation tower with no false alarms. However, T_0 and the external blackbody exhibited no strong S_2 polarization features that could be easily detected using the chosen threshold value.

In this subsection the performance of the Stokes and DoLP parameters was presented for the detection of three surrogate targets placed at three different aspect angles from the sensor perspective. As previously mentioned in Chapter 2, conventional infrared (S_0) had serious limitations in detecting the three targets of interest during the time periods where the engines were *off* and solar loading was not available.

In such low contrast scenarios, the target temperature is often similar to that of the background making it difficult for algorithms to discern target from clutter. In contrast,

S_1, S_2, and DoLP performed better than S_0 for low contrast situations, and with good enough performance for high contrast scenes within the desired low false alarm region of the ROC curves. However, these parameters were not very useful in detecting the whole target, rather only pixels where target surfaces exhibited strong polarization features because of their orientation angle relative to the sensor (see Subsection 3.5.1 for a more detailed explanation). Interestingly, one could also observe S_1 and DoLP performances behaving quite similarly throughout the ROC curve and usually over performing S_2 for T_0 and T_{90} independently of timestamp. The exception was observed in the detection of T_{135} where S_2 performed better than with previous targets, which facilitated DoLP in outperforming S_1 for most of the T_{135} ROC curve.

3.6 Summary and Conclusions

Chapter 3 presented the building blocks of PI exploitation by introducing the derivation of Stokes parameters, followed by an explanation of the polarized emission properties of smooth plane materials using the tilting plate data collection. In this data collection, it was shown that S_0, intensity, had difficulty in detecting the test plate during the time periods where the test plate and natural clutter had similar temperature values. Conversely, S_1 and DoLP demonstrated the capability of detecting manmade objects regardless of their temperature difference relative to the background clutter.

The caveat of using polarization as detection metrics is their dependency of surface orientation angle, as it was observed in Subsection 3.5.1, where, for example, S_1 and DoLP did not perform very well in discriminating the test plate at any angles below 45°. In conclusion the test in Subsection 3.5.1 demonstrated two key points worth mentioning:

1) In order to detect a potential manmade object, the surfaces need to be at favorable angles relative to the sensor in order to display a significant polarization difference.

2) The polarization metrics such as S_1, S_2, and DoLP are independent of the target temperature.

A second data collection was then presented where real data of three surrogate self-propelled howitzers was shown in Subsection 3.5.2. The data demonstrated that many of the target facets were not detectable as a result of their orientation relative to the sensor. Furthermore, it was also observed that for the chosen threshold of $\pm 5\sigma$, the number false alarms present in the scene varied depending of the time of day. For example, in S_1 the number of false alarms increased as the scene got hotter. As a result, the data collection from Subsection 3.5.2 demonstrated that the use of the Stokes parameters in detecting complex 3-dimensional manmade objects in an outdoor environment was quite problematic for anomaly detection applications for the following reasons:

1) As a result of the Stokes angle dependency, only a small number of pixels for each manmade object were significantly divergent from the clutter's distribution.-Portions of the grass, a natural clutter class, exhibited strong vertical polarization which increased the number of false alarms shown in S_1 and DoLP imagery.

2) Number of false alarms in S_1 and DoLP imagery increased as a function of temperature.

3) DoLP exhibited more false alarms than S_1 imagery alone, which one may conclude that the influence of S_2 degraded DoLP performance. Conversely, DoLP detected more pixels on the observation tower than S_1.

4) Due to factor 1, 2, and 3 the ability to discriminate manmade targets from natural clutter decreased significantly as the temperature increased since the small number of disjointed target pixels could be mistaken for false alarms or vice-versa.

In conclusion, Stokes and DoLP parameters are not good metrics for 3-dimensional object detection as per the reasons above. There is a need to develop algorithms that are diurnal cycle and surface orientation invariant to successfully detect potential manmade objects from clutter while at the same time reducing significantly the number of false alarms detected by the Stokes parameters and DoLP.

CHAPTER 4

SPECTRAL AND POLARIMETRIC DATA COLLECTION EXPERIMENT

4.1 Introduction

This dissertation uses the Spectral and Polarimetric Imagery Collection Experiment (SPICE) database for algorithm development and testing of PI. The goal of Chapter 4 is to describe the data collection conducted at a data collection facility located in Northern New Jersey. The data collection and its setup are discussed first, followed by details on the targets used, sensor specifications, and data products of the SPICE effort.

The objective of SPICE is to collect a comprehensive database of calibrated measurements of hyperspectral, polarimetric, and broadband images during a period of a full year to capture all kinds of weather conditions and target states. Such measured information can be utilized to develop and validate sensors, algorithms, and modeling and simulation programs. The SPICE data collection distinguishes from previous data acquisitions in that it autonomously collects and stores data of two target sites at 549m and 1280m from the sensors. Since the data acquisitions cover an entire year, the database holds a wide variation captured in the data ranging from changing weather conditions, environment (e.g., trees with leaves and tress without leaves depending on the season), geometry of illumination, and full diurnal cycles.

By collecting such comprehensive database, the intent of such effort allows the scientific community to: 1) Understand signature variability under the different weather patterns; 2) Develop robust algorithms; 3) Develop new sensors; 4) Improve high fidelity modeling and simulation programs; 5) Evaluate the different technologies (hyperspectral

and polarimetric) under adverse weather conditions; and 6) Evaluate the possible fusion of the different sensor systems.

The proposed chapter is organized as follows: Section 4.2 describes the location and facility where the SPICE collection was performed; Section 4.3 details the polarimetric sensor deployed; Section 4.4 explains the type of targets used; Section 4.5 describes the autonomous data collection system; Section 4.6 details the SPICE data products and presents LWIR polarimetric imagery collected before, during, and after an adverse weather event; Section 4.7 details the dataset used in the dissertation, and finally Section 4.8 concludes the chapter.

4.2 Data Collection Tower

The data collection facility, located in Northern New Jersey, USA, is specifically dedicated to the testing of sensors under adverse weather conditions. The laboratory consists of a base building and a 65 m data collection tower with two external elevators capable of serving as test beds for radars, electro-optic, or other sensors under test (see Figure 4.1). The data collection tower overlooks three instrumented target site areas (46m, 549m, and 1280m from base) as well as a mid-range meteorological instrumentation site (642m from base). The facility has automated collection of ground truth information to accurately determine and characterize meteorological conditions, measure the propagation path loss, perform the required measurements, and characterize the clutter background and target effects.

Figure 4.1 The data collection facility is a 65m tower located in Northern New Jersey, USA. The data collection tower is specifically dedicated to the testing and evaluation of sensors under adverse weather conditions.

The effective height of the tower is 126m as it was specifically positioned atop a 61m ridge, thus providing access to a vast portion of the area around it for data collection purposes.

Polarimetric imagery propagation under adverse weather conditions is certainly affected by the meteorological conditions present during testing and, therefore, precise knowledge of the actual meteorological conditions is vital to provide quantifiable results. Listed in Table 4.1 are a number of standard meteorological sensors that are deployed during adverse weather testing at the data collection.

Available standard meteorological instrumentation includes wind speed and direction, temperature, humidity, and barometric sensors. Recording of wind speed and direction is important since it can affect the shape of the raindrops and snow crystals and

their orientation with respect to the polarimetric sensors. The size of the raindrops or snow crystals can affect the emission and reflection signal propagation since in most cases their size is in the Rayleigh scattering region. Thus, emitted and reflected energy is greatly reduced in proportion to drop size. Humidity and temperature sensors indicate moisture content in the air, which affects the propagation attenuation.

Table 4.1 Meteorological Instrumentation used in SPICE Data Collection

Sensor	***Measures***	***Comments***	***Units***
Thermometer	Temperature		Celsius
Humidity Sensor	Humidity		Percentage
Snow/Rain Tipping Bucket	Rain rate	Also melted snow liquid rate	mm/hr
Optical Rain Gauge	Rain rate	Possibly snow rate	mm/hr
Visibility Meter	Visibility	Smoke, fog, haze	Km
Pyranometer	Sun and sky radiation	Visible	W/m^2
Pryheliometer	Solar radiation direction	Required tracking mount	W/m^2
Pyrgeometer	Sun and Sky radiation	Infrared	W/m^2
Ceileometer	Cloud range and thickness	Range and thickness of up to four layers of clouds	Meters
Total Sky Imager	Cloud Cover	Cloud cover estimation	Percentage

Other standard instrumentation includes rain gauges, a heated tipping bucket type that provides information on the liquid water content of the snow, as well as that for rain. By connecting the meteorological instrumentation to a network data logger located at the base building, meteorological information is autonomously collected and stored for further analysis.

Advanced meteorological sensors available at the data collection facility include an optical rain gauge, distrometers, snow depth gauge, soil moisture blocks, ceileometer, and a total sky imager. Optical rain gauges have the capability of performing more precise measurements at low rain rates, and at extremely high rain rates. Distrometers provide measurement of precipitation sizes. Since solar radiation can potentially affect the performance of the infrared imagery due to thermal effect or possible inversion layer effects, pyranometers are deployed to measure the total sun and sky radiation. Normal incidence pryheliometer along with a solar tracking mount were deployed to provide the measurement of the direct beam solar irradiance. Ceileometer provides range and thickness information up to four cloud layers and up to a distance of 30,000 feet. Such information is crucial since low cloud ceilings adversely affect polarimetric and hyperspectral infrared imagery. Finally, a total sky imager is a visual based system for sky imaging that allows for automated report on cloud cover within an area of interest. Cloud cover and cloud height information along with Pyrgeometer measurements allow researchers to measure the amount of downwelling energy being reemitted back to ground and how it affects target and background signatures. For the work in this dissertation, the amount of radiance being emitted from the sky is a very important measurement, because as the amount of radiation from the sky increases, features that once could be detected easily in a sunny clear day would be diminished quite significantly when downwelling values are extremely high.

Figures 4.2 through 4.6 illustrate some of the meteorological measurements that are available with the SPICE database. For example, Figures 4.2 and 4.5 illustrate a sunny day while Figures 4.3 and 4.6 represent a cloudy day. Figure 4.2, black curve,

illustrates the solar irradiance power captured by the pyrheliometer. The smooth shape reveals that very few clouds were present at the scene for most of the day, except around 1700 where one can observe a deep dip in the irradiance values as a consequence of a cloud blocking the sunlight. One can clearly observe the difference between a cloudy and sunny day by comparing Figures 4.2 and 4.3. In Figure 4.3, sun rays were diffused due to cloud cover and as a result the amount of direct sun radiation is highly attenuated. As previously mentioned, downwelling radiation (as well as other factors such as rain rate, humidity, and visibility) is often associated with decreased detection in polarization. If no clouds are present in the scene, one can observe that there is a clear difference between the upwelling and downwelling radiation values especially during the daylight periods.

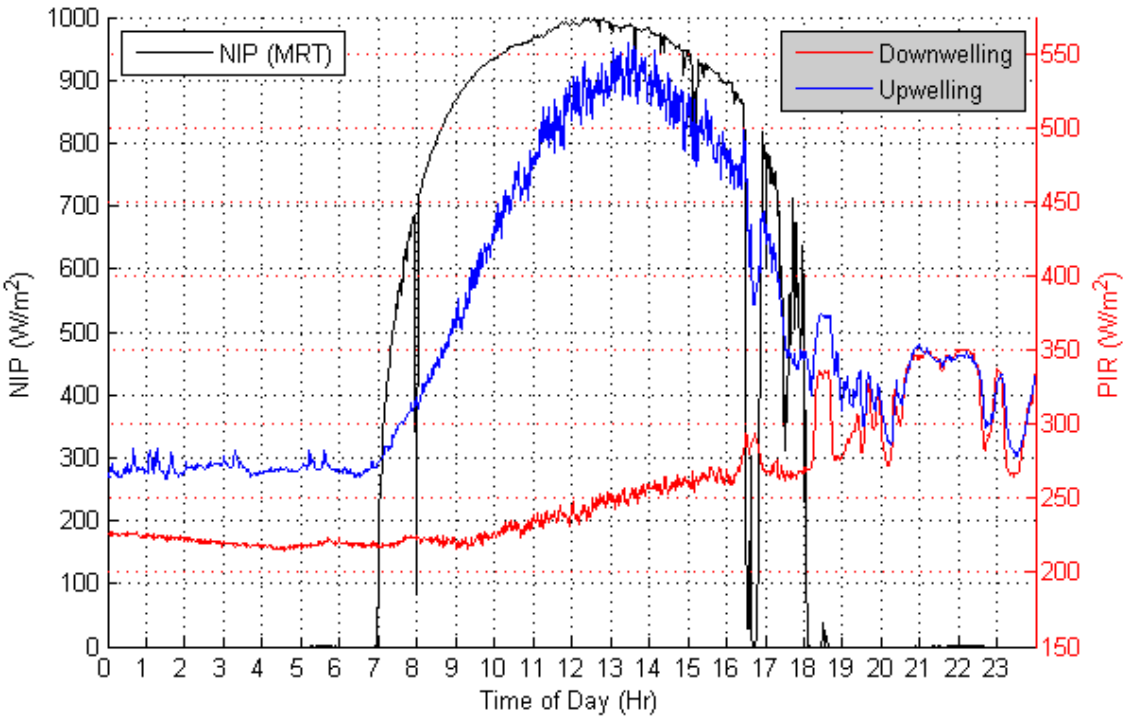

Figure 4.2 Plot showing the radiance values for a sunny day on 3 April (APR) 2012. The black curve represents the total incident power from the sun within the 200 and 4000nm region of the spectrum. The blue curve represents the amount of radiance being emitted by the background, while the red curve represents the amount of energy being reflected back to the ground from the sky. The pergyometers work within the IR region (4 to 1000 μm) of the spectrum.

Comparing these same parameters to Figure 4.3, one can observe that the difference between upwelling and downwelling is very small. The reason is that cloud cover absorbs the radiation being emitted by the earth and re-radiates it back to the scene. The amount of re-emitted radiation is a function of cloud cover and cloud height.

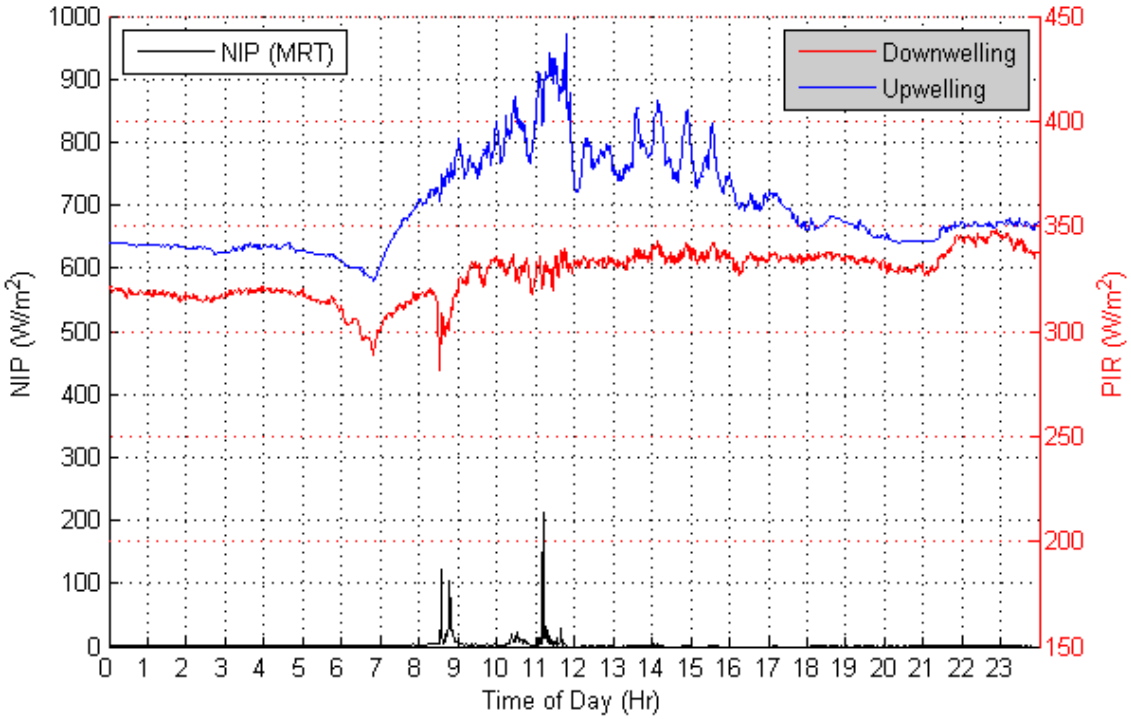

Figure 4.3 Plot showing the radiance values for cloudy day on 1 APR 2012, measured by the pergyometers and the Pryheliometer. During cloudy days the amount of direct solar radiation is very low as it is diffused by the clouds above. The difference between the upwelling and downwelling radiance values is small compared to a good day because clouds become good radiators by re-emitting radiation back to scene.

Figure 4.4 demonstrates the information captured and processed by the total sky imager equipment. The total sky imager works by capturing full color sky images using a visual camera which are then processed by software using a filter. Blue sky will be designated by blue color while clouds will be designated by white color. The amount of cloud cover is computed by taking the ratio of white versus blue pixels in the captured imagery.

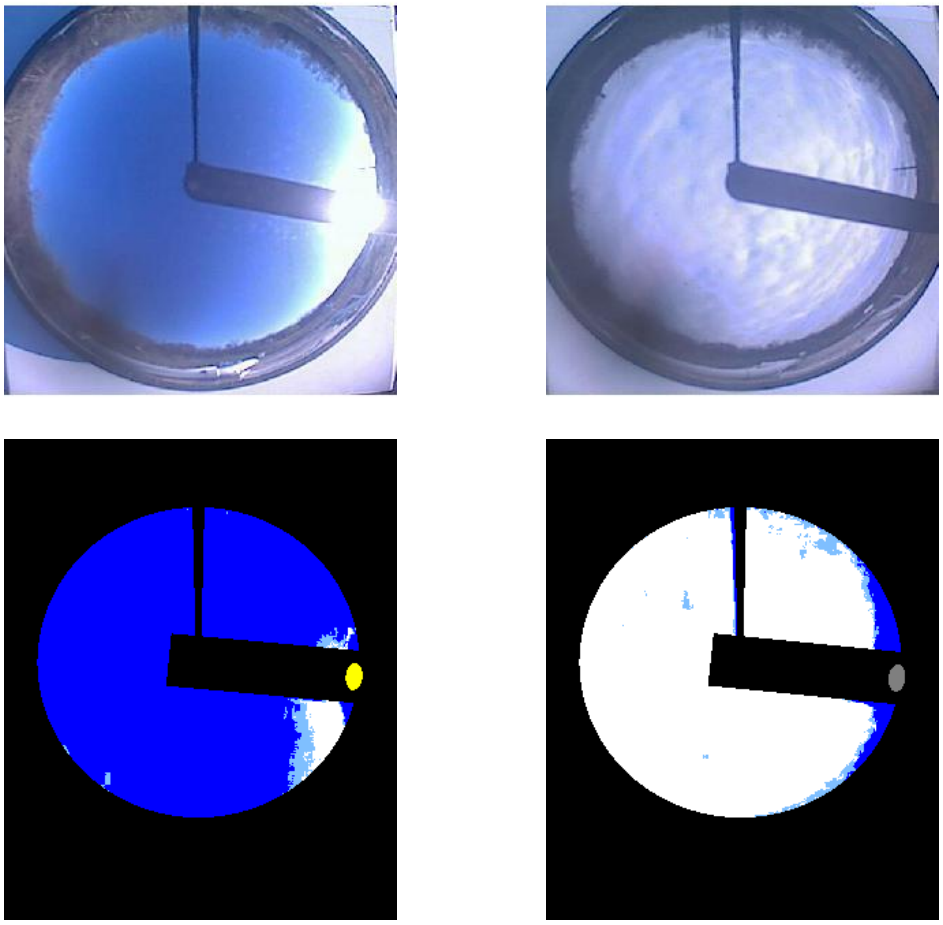

Figure 4.4 Total Sky Imager pictures and processed images illustrating the amount of cloud cover for 3 APR 2012 (left side) and 1 APR 2012 (right side). The top row represents the images taken by the Total Sky Imager, while the bottom row represents the processed images where the blue represents blue sky while white represents cloud cover.

Figures 4.5 and 4.6 illustrate the 12 hour percentile cloud cover plot for 3 and 4 APR 2012 respectively, captured by the total sky imager. This plot gives a better understanding of the cloud cover in the scene in terms of time throughout the daylight hours. The yellow bar on the top represents periods of time where sunshine was detected. As previously mentioned, one can see very clear that on 3 APR the amount of cloud cover was minimal for most of the day (<10%) compared to >95% for 4 APR 2012.

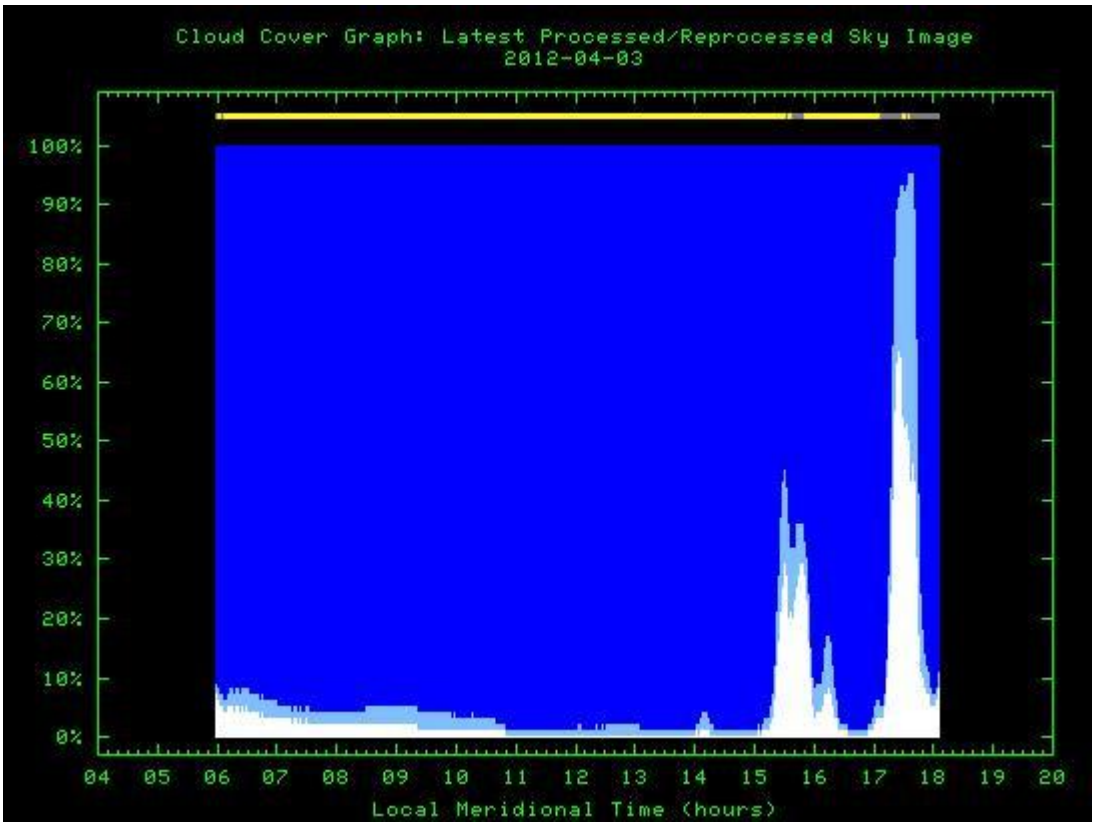

Figure 4.5 A 12-hour percentile cloud cover plot captured by the Total Sky Imager for 3 APR 2012 where white indicates opaque clouds, light blue thin clouds, dark blue clear sky. The yellow color across the plot represents periods where sunshine was detected while the gray color indicates no sunshine. In this chart one can observe that for most of the day very little cloud cover was detected across the 12 hour with some periods where high percentage of opaque cloud cover was detected between 1500 and 1600 and again for 1700 through 1800 hours.

In conclusion, meteorological data is of extreme importance to characterize the environment the target and sensor operate and aids in performance comparison of different systems for different weather events. During the course of the SPICE data collection several sensors were added to continuously improve the quality of the meteorological data collected. For example, during the 2010 data collection all sensors in Table 4.1 were available with the exception of the Total Sky Imager and the upwelling sensor, shown in Figures 4.2, 4.3, 4.5, and 4.6, which were added in mid-2012.

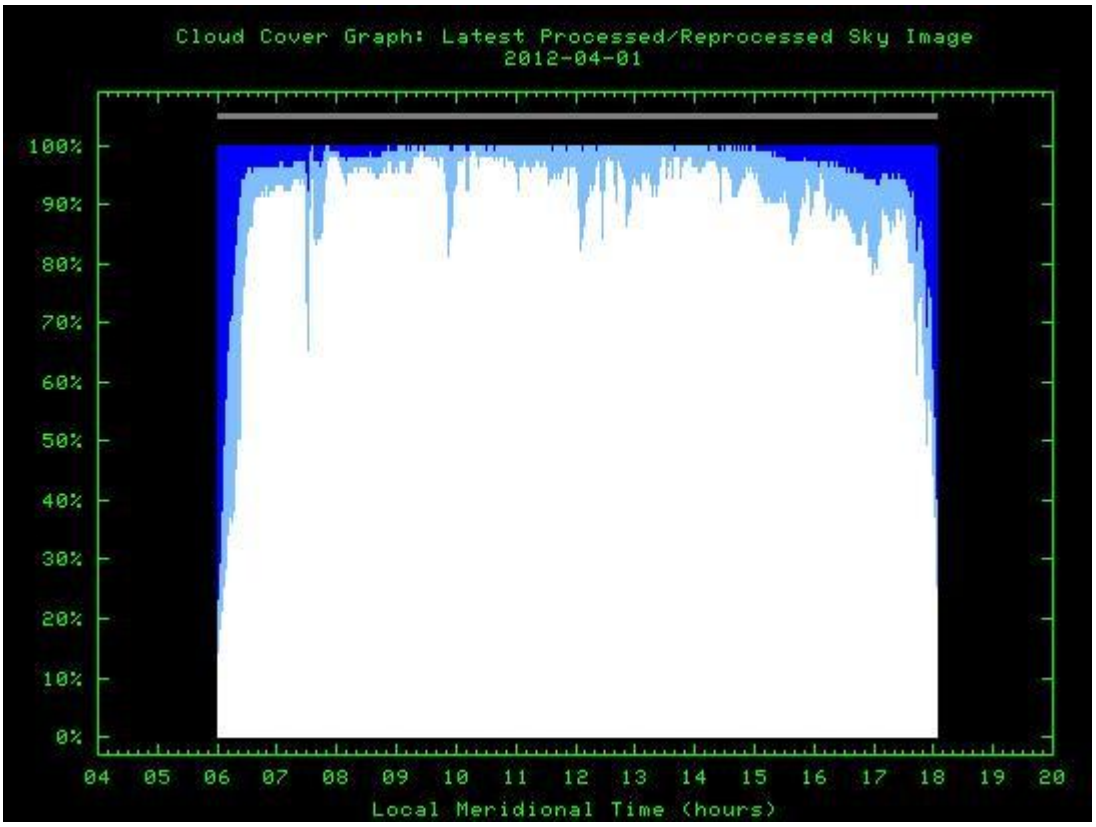

Figure 4.6 A 12-hour percentile cloud cover plot captured by the Total Sky Imager for 4 APR 2012 where white indicates opaque clouds, light blue thin clouds, dark blue clear sky. The yellow color across the plot represents periods where sunshine was detected while the gray color indicates no sunshine. For this day, there were no periods of sunshine detected by the Total Sky Imager (see bar graph on top) and a large percentage of opaque could cover was detected throughout the day which supports the conclusions from Figure 4.3.

4.3 Long-Wave Infrared Polarimetric Sensor

The LWIR imaging polarimeter used in SPICE data collection is a microbolometer-based rotating retarder imaging polarimeter developed by Polaris Sensor Technologies, Inc., Huntsville, AL (Figure 4.7). It operates by capturing up to 12 images sequentially in time, each at a different orientation of the rotating retarder. Together, the retarder and linear polarizer act as a polarization state analyzer for the light forming the image. Using the data reduction matrix method, the Stokes vectors are calculated, which completely

characterizes the polarization states of the light from the scene. Table 4.2 lists the sensor specifications.

Table 4.2 Specifications for the LWIR Imaging Polarimeter

Parameter	Value
FOV	13.7x11.0 degrees
Objective Focal Length	50mm
f/#	0.87
Total FPA pixels	324x256
Pixel size	38x38 um
Max Frame Rate (stream to disk)	30 fps
Sensor Dimensions (inches)	10”L x 6”W x 7.5”H
Sensor weight	12 lbs
Power	15V; 1.2 A

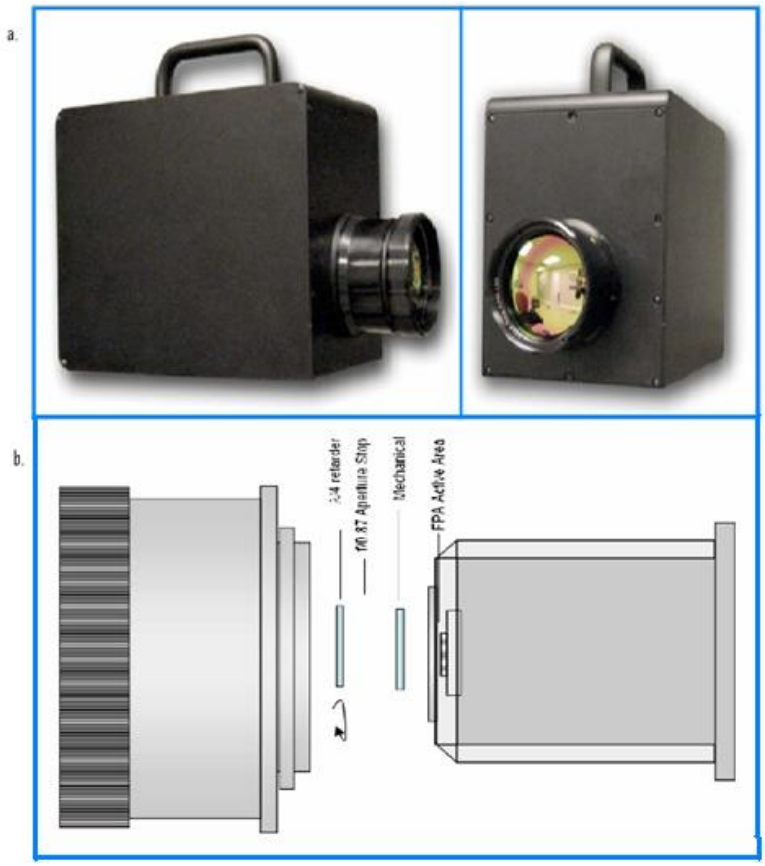

Figure 4.7 Polaris Long-Wave infrared polarimetric imaging sensor used in SPICE and optical layout of the spinning retarder microbolometer-based sensor.

4.4 Targets

The use of actual operational military vehicle as targets to support the continuous and automatic nature of data collection at the facility proved to be unaffordable. Thus, an alternative target approach had to be found. The solution came in the form of a surrogate military vehicle in the form of a self-propelled howitzer.

The surrogates, pictured in Figure 4.8, provide validated vehicle signatures in the 35GHz radio frequency (RF) and MWIR regions of the electromagnetic spectrum. This was accomplished by producing a physical replication of the actual vehicle (RF region), by its metallic construction (RF and IR region), and the use of supplemental heated surfaces (IR region).

Figure 4.8 Surrogate target used in the SPICE data collection. At each of the mid and long range target sites, three targets were placed in different orientations, 0°, 90°, and 135° with respect to the sensor.

In the IR region, the metallic construction properly produces the correct solar loading characteristics. The supplemental heated areas provide an approximate

characteristics of the actual vehicle in operation. The heated areas are shown in Figure 4.9.

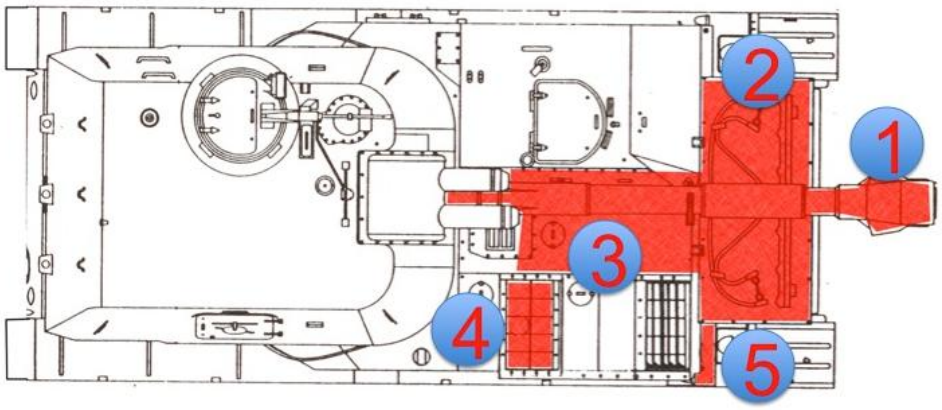

Figure 4.9 The surrogate target can be heated at different temperatures as per user needs to simulate a cold, idle, or running target. Table 4.3 designates the maximum Δt allowed for each of the surfaces.

Figure 4.9 depicts the most important parts of the target: the engine area, exhaust areas, gun barrel and replica road wheels can be independently heated and controlled. Table 4.3 shows the temperature range available for each heated element. All target heating elements are programmable and can be automatically controlled; a valuable capability for the data collection.

Table 4.3. Maximum Temperature Delta Values for Each of the Different Surfaces of the Surrogates

#	Area	Maximum Δt (Celsius from Ambient)
1	Gun Tube	70
2	Front T	30
3	Back T	30
4	Overhead Compartment	40
5	Exhaust (not used)	-
6	Wheels (not shown)	30

4.5 Autonomous Data Collection

Collection of imagery during adverse weather can be a hit or miss event. The use of test personnel for a long-term effort can be quite expensive and unproductive if waiting for a certain weather event to occur. Furthermore, what may be construed at first as the required weather events needed for algorithm development, other events may be required long after the data collection effort has ended. Obviously to pre-plan a list of events that is required for a complete data analysis, algorithm development, and technology evaluation can be quite difficult as one needs to anticipate the most important factors for such activities. Prediction of when such events may occur in order to have the right personnel on-site is not only difficult but also quite expensive to maintain.

To answer the difficulties in collecting a comprehensive database of a variety of weather patterns, the data collection facility has assembled a selection of polarimetric, hyperspectral, and broadband sensors into an autonomous data collection effort to collect a database of calibrated measurements of all atmospheric events, which includes the hit or miss adverse weather events. By using an autonomous data collection system, one is able to collect the necessary data while keeping the data collection cost at a manageable level.

To accomplish the autonomous polarimetric data collection where the sensors need to collect images from the mid and long range target sites at pre-defined time periods and be able to self-calibrate, required a collaborative effort between Invoke LLC, Polaris, and the data collection facility personnel.

The polarimetric sensors were placed inside the facility laboratory elevator on top of a Quickset QTP-500 Pan & Tilt positioner (Figure 4.10). The QTP-500 can handle

payloads up to 500 foot-pounds of torque, and the rugged design allows it to be in direct contact with the elements.

Figure 4.10 SPICE setup inside the facility elevator. Shown in the image is: 1) Mikron blackbody M350, 2) Quickset QTP-500 series, 3) Mid-Wave infrared hyperspectral Telops camera, 4) Long-Wave infrared hyperspectral Telops camera, 5) Long and Mid-Wave infrared polarimetric cameras from Polaris, 6) Blowers to protect sensors from rain and snow.

The Pan & Tilt system positions the sensors to collect data of the mid and long range sites by receiving positioning instructions through the network using a custom made control software developed by Invoke LLC. The control software reads a user defined excel spreadsheet (script file), which is divided into five columns (time, horizontal and vertical position, blackbody on/off setting, and blackbody temperature). The control program reads the script file and sends position instructions to QTP-500 at a specified time period. The Pan&Tilt system script is written as to position the sensors to view the mid and long range target sites every 5 minutes, only interrupting this cycle

when the polarimetric sensors need to be calibrated. The positioner software also communicates with a Mikron Blackbody source when needed by placing the Mikron blackbody on standby or automatic mode and setting the required blackbody temperature. Currently the system only communicates one-way with the Mikron blackbody, but development of a more sophisticated 2-way communication system is currently under way.

The autonomous acquisition software for the LWIR camera was developed by Polaris for the SPICE data collection. Both cameras can use a weekly or monthly script broken down by hour (0000h – 2300h), which instructs the computers on the data acquisition interval. Currently, the LWIR polarimetric camera acquisition computer runs a script that captures one image every 2:30 minutes.

In order to calibrate the polarimetric cameras, calibration segments are allocated during the course of day. For each of the calibration segments: 1) the Invoke software sends signals to the blackbody to go into automatic mode and transmits the first temperature. 2) The system waits 15 minutes prior to the first calibration session in order to stabilize the temperature in the blackbody. 3) Once the temperature of the blackbody stabilizes, the pan and tilt camera tilts downward in order to place the polarimetric camera in front of the blackbody. 4) Once the camera is calibrated with the first set of temperatures, the Invoke software tilts the camera back to a resting position and sends a new temperature value to the blackbody. The calibration segments repeat the above mentioned steps until all the temperature values are executed.

To minimize power consumption inside the elevator, the LWIR polarimetric computer was placed on a remote location of the data collection tower, outside the

elevator, where raw imagery and communication signals are transmitted and received using the data collection facility network.

In order to collect this massive database, the data collected by the computer is immediately transferred from the sensor directly to networked storage devices that give the ability to hot swap hard drives when storage space becomes limited. The hot-swapping feature is totally transparent to the acquisition software and allows for continuous data acquisition.

4.6 Data Collection Products

In order to evaluate sensor technology, algorithm performance, and fusion of different modalities when encountering adverse weather conditions, the instrumentation must record the necessary data from the sensor under test and the meteorological data. Since the data is obtained from different instrumentation and is recorded separately in different locations, accurate time tagging of the data is essential in order to enable correlation of the data on a post mission basis. To accomplish this, Inter Range Instrumentation Group (IRIG) time synchronization Global Positioning System (GPS) time is used to minimize drift errors of all instrumentation during the data collection.

The polarimetric data is recorded in its most basic format and it can be opened and calibrated using Polaris calibration software. Calibration of the data is accomplished by selecting a high and low calibration temperatures, from the calibration temperatures collected during sensor calibration, that best fits the target and background temperature values (air and ground) from the meteorological (MET) data for a particular date and period of time.

The calibrated data may be opened as a text image using Imagej [40], Mathworks Matlab [41], or any other program that can read text images for further processing and image analysis. The facility metrological database can also be opened and plotted using Microsoft Excel [42] or Mathworks Matlab program.

To illustrate the significance of collecting adverse weather data for data analysis, algorithm development, and technology evaluation, a set of images are shown below from the SPICE data collection. Figure 4.11 depicts some of the manmade objects found in the mid-range target site: T_0, T_{90}, and T_{135}, an external blackbody covered by a black canvas, a metal hut, and an observation tower (not shown). The plates found in the middle of the image were not present during the data collection period presented in this dissertation. The background clutter is mainly composed of leafless trees, with grass and a gravel road in the target area.

Figure 4.12 illustrates the S_0 image captured by the sensor of the mid-range target site. In this figure, one can observe that trees are the predominant natural clutter in the scene. For the data collected from 9-11 FEB 2010, T_0 and T_{90} heating plates were *on* throughout the three days.

The collected imagery shown in Figure 4.13 was collected on 9 – 11 FEB 2010 at 0600h, where in 10 FEB the data collection facility was hit by blizzard type conditions for 24 hours.

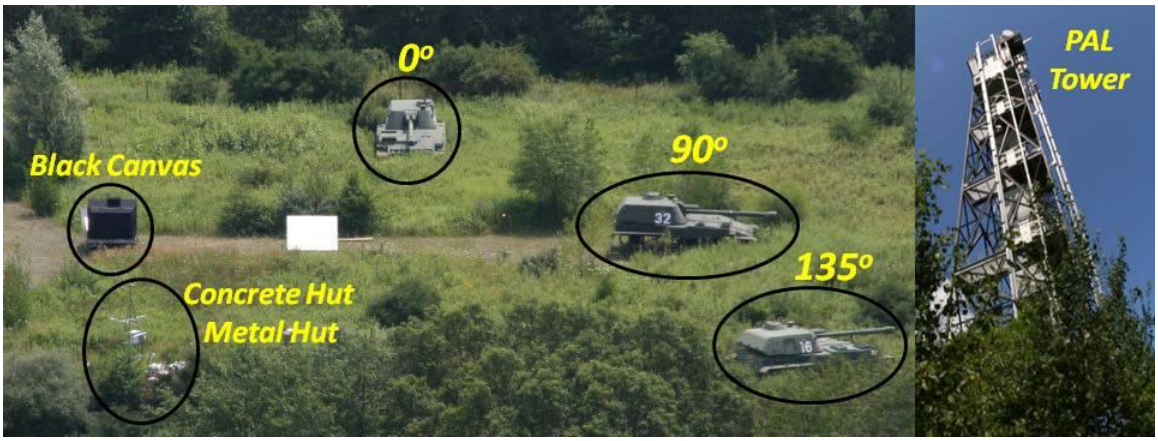

Figure 4.11 Mid-range target site has three surrogates targets and other manmade objects surrounded by natural clutter (trees, trunks, soil, grass) setting. Manmade objects present in the scene during the actual data collection are circled, with the surrogates' aspect angles labeled immediately above corresponding circles.

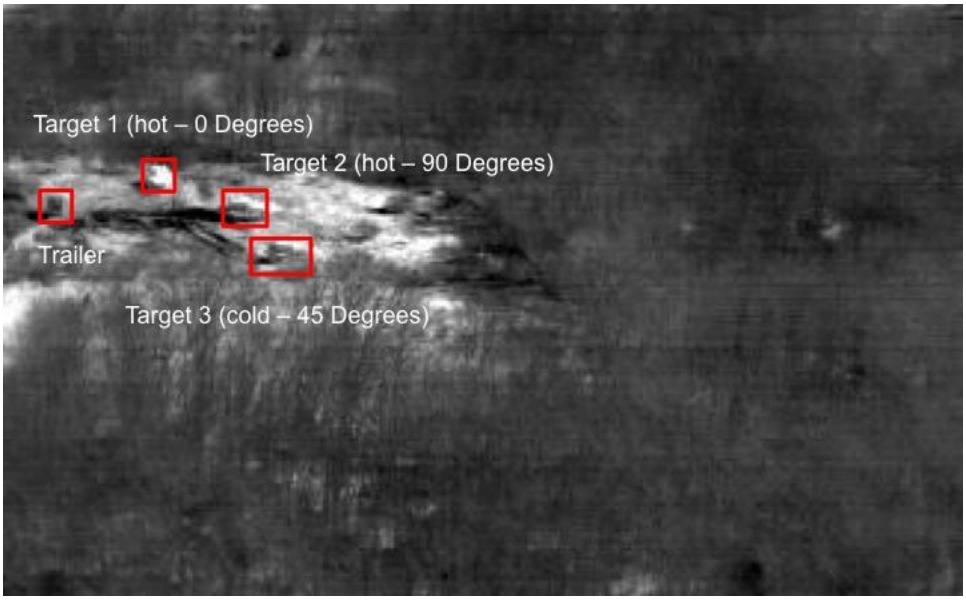

Figure 4.12 Long-Wave broadband infrared image collected by the LWIR polarimeter. The image is predominantly dominated by leefless trees. In the open area where the three targets are located, grass is the predominant natural clutter. A road made of gravel exists between the trailer and T_{90}.

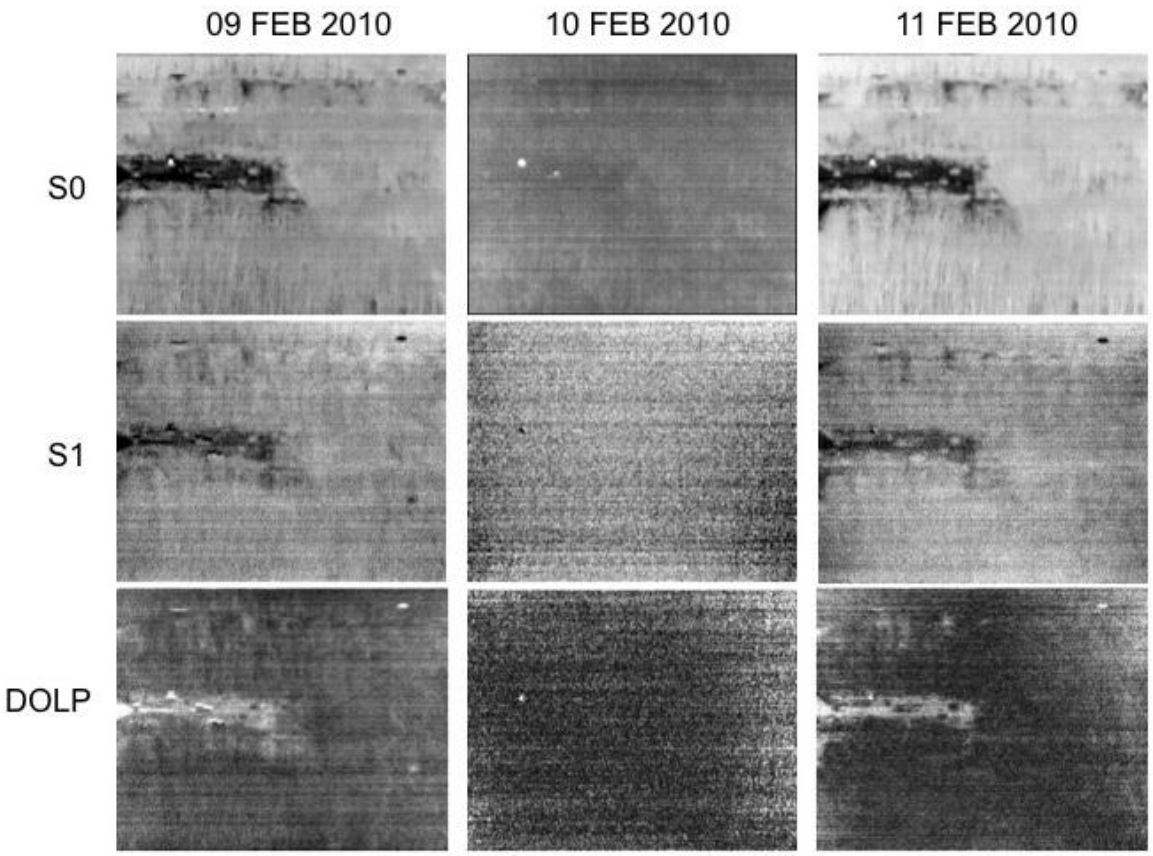

Figure 4.13 Imagery collected by the Long-Wave polarimetric sensor at 0600h on the day before, during, and after a snowstorm. Targets T_0 and T_{90} were running, while T_{135} was kept cold.

As Figure 4.13 demonstrates, S_0 clearly shows T_0 in all three days, however T_{90}'s (due to its orientation relative to the sensor) hot target surface cannot be observed on either 9 or 11 of FEB. On the other hand, due to the low background temperatures on 10 FEB, the surface of T_{90} can be distinguished from the surrounding clutter. T_{135} heating plates were off throughout the 3 days and as a result there is not enough contrast between the background and the target.

DoLP clearly discriminates all three targets (hot and cold) from the natural background for 9 and 11 of FEB. Conversely, for 10 FEB, only T_0 seems to be visible in contrast to T_{90} and T_{135}, which are not visible during the adverse weather event. The S_1

metric is not capable of discriminating all of the manmade objects from the background compared to DoLP for the same time period in Figure 4.13. For example, S_1 was only capable of distinguishing T_0 and T_{90} for 9 and 11 of FEB but not T_{135}, while during the adverse weather, 10 FEB, only T_0 was marginally detected.

4.7 Dissertation Dataset Description

As previously mentioned, the SPICE polarimetric data used in this dissertation was collected and recorded using a Polaris uncooled rotating polarizer LWIR microbolometer as described in Section 4.3. The LWIR polarimetric sensor, in particular, was placed near the top of data collection facility at a 550-m slant range from the target site, see Figure 4.11. The target site features three surrogate military targets posed at three aspect angles (0°, 90°, 135° counterclockwise) relative to the sensor's line of sight and depending on the collection day, some of the surrogates' *engines* were turned on. The scene is dominated by a natural clutter background (canopy trees, tree trunks, sparse grass, canopy bushes, and soil) and, in addition to the surrogates, there were also other manmade objects present in the scene, including an external blackbody completely covered by a black canvas and a observation tower, which the latter is not shown in Figure 4.11. Figure 4.11 shows the target site on 6 July (JUL) 2011, although the polarimetric data in reference were collected more than a year earlier on 6 MAR 2010. Note: the white metal plate in the scene reflecting the sky between the black canvas and the tank surrogate posed at $0^o$was not present in the scene during the data collection in MAR 2010.

The polarimetric dataset used to quantify the performance of algorithms in this dissertation were acquired continuously during a 72-hour time period between 6 and 8

MAR, 2010, starting at 0000h on 6 MAR with 10-minute intervals but excluding the time period between 0300h and 0500h for calibration each day which the sensor viewing direction would move to acquire data from an external blackbody—as a measurement reference—so at a later time radiometric calibration software could be applied to the data.

It is worth noting that, during the three day period, sunrise occurred at 0625h and sunset occurred around 1754h, hence, after 1800h the target site was completely dark to the naked eye. To assess the meteorological conditions during the entire 24-hour diurnal cycle for 6 through 8 MAR 2010, the following meteorological parameters are measured: direct solar irradiance, sky downwelling, visibility, temperature, and humidity levels (see Figures 4.14 through 4.16). The pyrheliometer is used to measure the direct solar irradiance and an infrared pyrgeometer to measure the average sky downwelling (see Section 4.2 for more information on the meteorological sensors). Observing Figure 4.14, the smooth curve shape and high value measured (>900 W/m^2) in the *Normal Incident Power* (NIP), also known as Pryheliometer, plot during the diurnal cycle, together with the low downwelling measurements from the sky ensured us that 6 MAR 2010 was characterized as a sunny day with no or very few clouds present in the sky. An *Optical Rain Gauge* (ORG) did not detect any precipitation for the duration of the day. Interpretation of the visibility data showed 6 MAR 2010 as a clear day with no fog or haze for the entire 24-hour cycle, using as a reference the high visibility values (>25km) as shown in Figure 4.14.

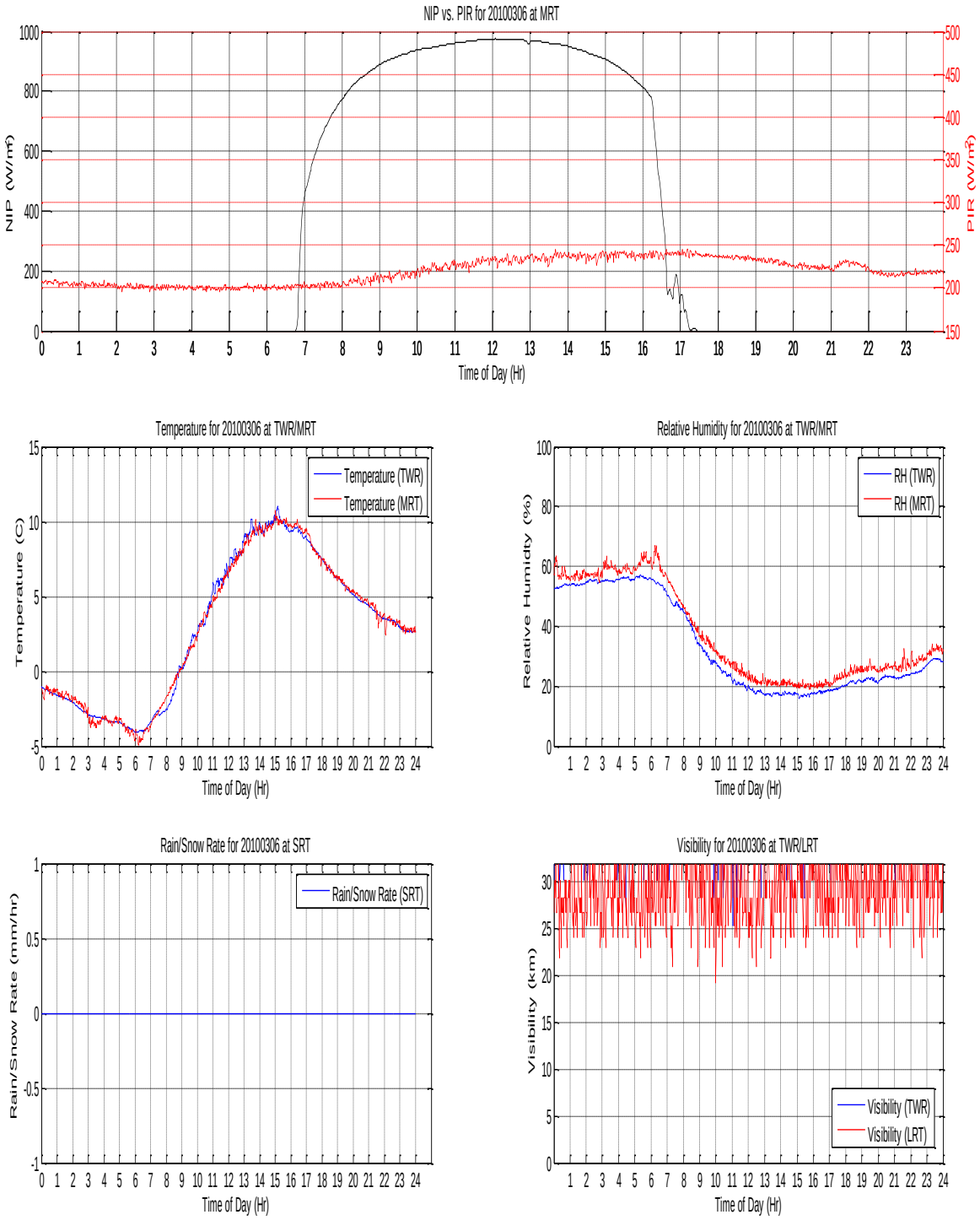

Figure 4.14 Meteorological information for 6 MAR 2010 captured by the data collection facility located in Northern NJ.

Humidity values were mostly low (about 60% and below) which correlates very well with the visibility meter of a clear sunny day. Temperature ranged from -4 to 10 degree Celsius (24.8 to 50 degrees Fahrenheit). Between 0000h and 0900h, air temperature values remained below zero degrees Celsius (32 degrees Fahrenheit) while for the time period between 2030h and 2350h the temperature values remained above two degrees Celsius (35.6 degree Fahrenheit) reaching the highest temperature of 10 degrees Celsius (50 degrees Fahrenheit) around 1500h. On the second day, Figure 4.15 7 MAR, one can observe that a sunny day was once again present (using pyrheliometer data) with temperatures ranging between zero and three degrees Celsius from 0000h and 0700h, and after sunrise the temperature increased from zero degrees Celsius to a maximum of 11 degrees Celsius at around 1500h. After sunset, around 1754h, the temperature dropped down to about -2 degrees Celsius. However, the temperature at the data collection tower dropped at a slower rate with its lowest temperature at around five degrees Celsius. The humidity levels for the time period between 0000h and 1800h hovered around 30% and 50%. A significant increase in humidity was detected at the mid-range target site after 1800h reaching a maximum of 90% humidity around 2300h. Again, the data collection tower instrumentation, where the camera was located, registered different values than what was recorded at mid-range target site with the humidity ranging between 40% and 50%. The ORG once again did not detect any precipitation during this 24-hour period. The visibility meter at the mid-range target site shows a slight decreasing trend from 25km starting at around 1000h reaching its lowest value of 20 km during the time period between 1900h and 2300h. Finally, on the 3rd day (Figure 4.16), the pyrheliometer data demonstrated, once again, a sunny day where very little or no clouds were detected. The

temperature in the mid-range target site ranged from zero to five degrees Celsius around 0000h and 0200h. The temperature stayed somewhat stable (within 1-2 degrees Celsius) up to sunrise with the temperature reaching a maximum of 13 degrees Celsius around 1500h. After sunset the temperature values captured at the mid-range dropped to about one degree Celsius at around 2200h. Once again the temperature values captured by the data collection tower instrumentation were different from the mid-range target site with its lowest value around 2300h of about seven degrees Celsius. The humidity recorded by the instrumentation at the mid-range target site shows that during the 0200h and 1800h time period, the humidity values remained around 35%-40%, while after 1800h humidity increased steadily to about 77% at 2200h, finally hovering around 65% for the remainder of the night. On the other hand, as seen in the previous day, the data collection tower humidity values stayed fairly consistent at around 40% for the entire day. The mid-range instrumentation recorded a visibility ranging from 20 Km and above for the 24-hour period, while the data collection tower visibility remained above 25 Km.

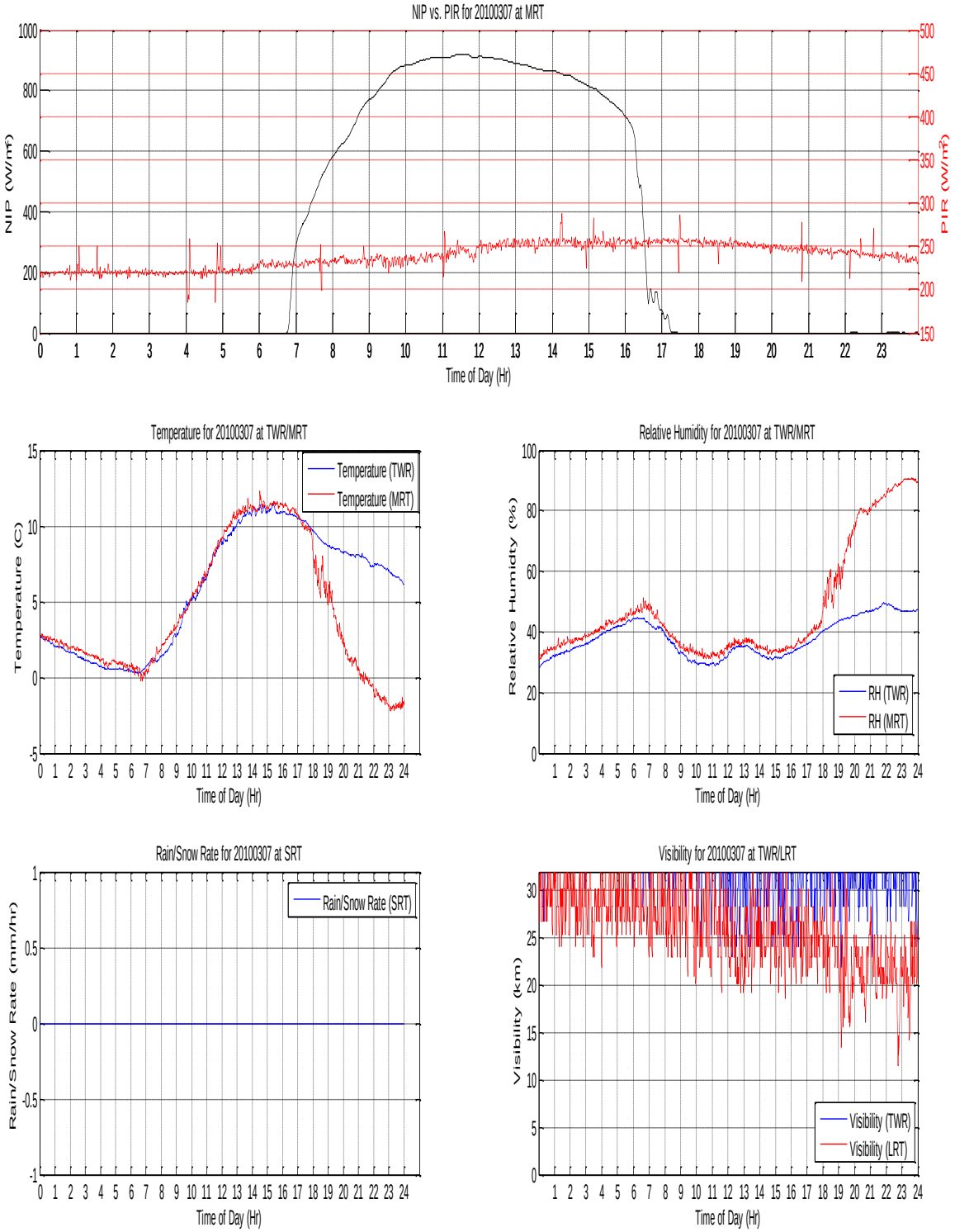

Figure 4.15 Meteorological information for 7 MAR 2010 captured by the data collection facility located in Northern NJ.

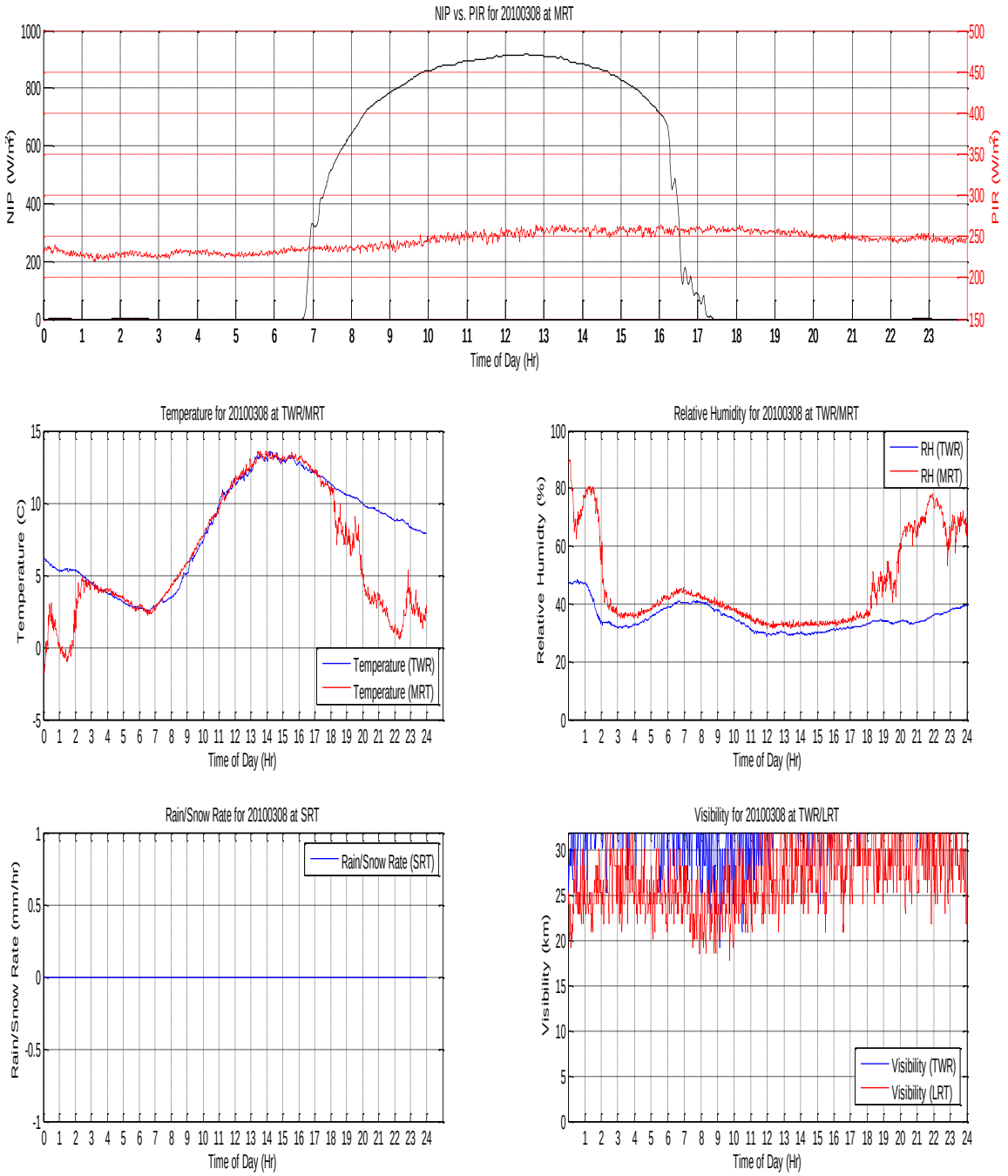

Figure 4.16 Meteorological information for 8 MAR 2010 captured by the data collection facility located in Northern NJ.

Regarding the polarimetric data, the spatial area of all images used for this study is 256 rows by 320 columns, with a pixel resolution of approximately 1.47 m; the primary targets in the scene consist of 75 pixels (surrogate posed at 0° aspect angle), 102 pixels (surrogate posed at 90° aspect angle), and 96 pixels (surrogate posed at 135° aspect angle). According to the ground truth information, in day 1, the heating engines of T_0, T_{90}, and T_{135} were turned *off*; in day 2, the engines of T_0 and T_{90} were turned *on*, while T_{135} remained *off*; in day 3, all three surrogates were *off* again.

4.8 Conclusions

Chapter 4 presented details on the SPICE data collection effort, the testing facility, the specifications of the LWIR polarimetric cameras used, the meteorological information captured by the data collection tower, examples of the imagery collected using the autonomous data collection system, and finally a brief description of the dataset used in the dissertation. Example images from SPICE were shown earlier in Chapters 2 and 3, and additional images representing other complex events and their implications to algorithm performance are shown and discussed in Chapter 5.

CHAPTER 5

POLARIMETRIC IMAGERY EXPLOITATION ALGORITHMS

5.1 Introduction

This chapter introduces several contributions to the field of PI exploitation for the specific topic of autonomous manmade object detection using imagery spatially dominated by natural background clutter (forest canopy, etc.); the topic has applicability to commercial and surveillance systems. These contributions fall into two very different fields of mathematics, the first contribution is based on set theory called mathematical morphology and the second contribution is based on multivariate statistics. Regardless of the methodology chosen, both methods attempt to enhance the ability of identifying locations of interest where manmade objects may be present in the scene. The first method, presented in Section 5.2, proposes the use of morphological operators to enhance manmade object features found in conventional Stokes imagery while reducing natural clutter features. Its performance, relative to conventional Stokes, demonstrates that morphological operations play an important role in PI exploitation allowing for the development of more-effective manmade object detectors relative to conventional polarimetric methods, with the added benefit of easy implementation into existing graphic processing unit (GPU) cards, using data from polarimetric sensors available in today's the market.

The second method, presented in Section 5.3, is based on multivariate statistics by using the raw polarimetric angle measurement imagery as input information, where each image, representing one of the angles (0°, 45°, 90°, and 135°), is stacked upon others to create a polarimetric data cube. By using higher order statistics data analysis on the

newly proposed polarimetric data cube, an anomaly detection algorithm based on covariance difference test is proposed capable of discriminating manmade objects from natural clutter background over a variety of weather patterns. Since higher order statistics between manmade objects and natural clutter change dramatically from long to short range PI, two variations of the proposed algorithm are recommended in order to make it range invariant.

Finally, Section 5.4 conveys the conclusions and summarizes key important points discussed in Sections 5.2 and 5.3.

5.2 Morphological Operators for Polarimetric Imagery

5.2.1 Introduction to Mathematical Morphology

Mathematical morphology (MM) was introduced in 1964 from the collaborative work between Matheron and Serra [43-46] to quantify mineral characteristics from thin cross sections. During the 1960s and early 70s, MM focused essentially on binary imagery, commonly known as sets, with work by Serra on "Texture Analyser", which allowed the analysis of binary images using any type of *structuring element* (SE) based on straight lines. In 1964, Matheron defined the set addition, commonly known as dilation in MM, which is based on *Minkowski algebra* from 1903, and is today one of the basic MM operators or filters. The work of both Matheron and Serra led to other developments in MM during this period of time, which included the hit-or-miss transform, erosion, opening, closing, granulometry, thinning, skeletonization, between many others. Until then, all the work accomplished in MM was only applicable to binary images, when in 1978 Nakagawa and Rosenfeld [47] were able to demonstrate that erosion and dilation in

binary imagery was linked to the maximum and minimum filters applied to grayscale imagery.

Heijmans [48], for example, demonstrated how binary morphological operators and thresholding techniques could be used to build grayscale morphological operators. Their implementation in terms of minimum and maximum filters proved impossible to be implemented into systems that required real time computation. Shih and Mithcell [49] came up with an innovative approach to process grayscale morphology efficiently by threshold decomposition of grayscale morphology into binary morphology by decomposing grayscale signals into multiple binary ones, therefore, allowing them to be processed using binary morphology operators. This innovative idea allowed for the real time implementation of morphological operations on grayscale imagery with the same output as grayscale MM.

Since then, the scope of MM applications has evolved to include image enhancement, segmentation, edge detection, restoration, texture analysis, compression, shape analysis, skeletonization, between many other applications. MM is often referred as a geometrically based image processing because the basic idea of MM is the probing of a test image using a structuring element, see Figure 5.1, in order to quantify how well the structuring element fits (or not) within the image.

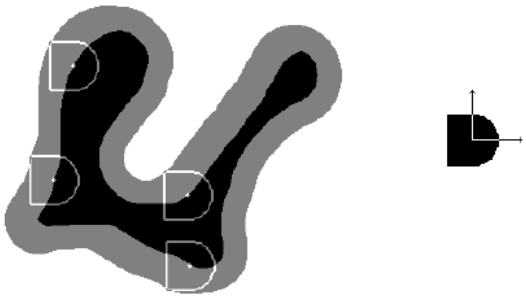

(a) (b)

Figure 5.1 Original input image (black) and the resulting image (gray) using the SE in (b)
Source: [50]

The use of a SE implies that the size and shape of the structuring element used to probe the test image has a direct effect on the output of the MM process, therefore, using a different probing element would then yield a different result as shown in Figure 5.2. Consequently the choice of structuring element is dependent on the information one wishes to observe or desire as an output. Such can be seen in target recognition systems where the SE's, often called "chips", are used to probe potential anomalies found in the imagery based on known target shapes.

The use of morphological operators for image enhancement has not been widely used in PI for anomaly detection or feature extraction of manmade objects. In fact, a search of the literature on the usage of MM in PI yielded a small number of results such as [51], which used MM to remove isolated pixels, fill holes, and object extraction if the shape was known *a priori* by fusing conventional and polarimetric LWIR imagery and [52], where morphological operators were used in S_0, S_1, and ψ (polarization angle) imagery to enhance and extract shape information in order to identify landmines in the field.

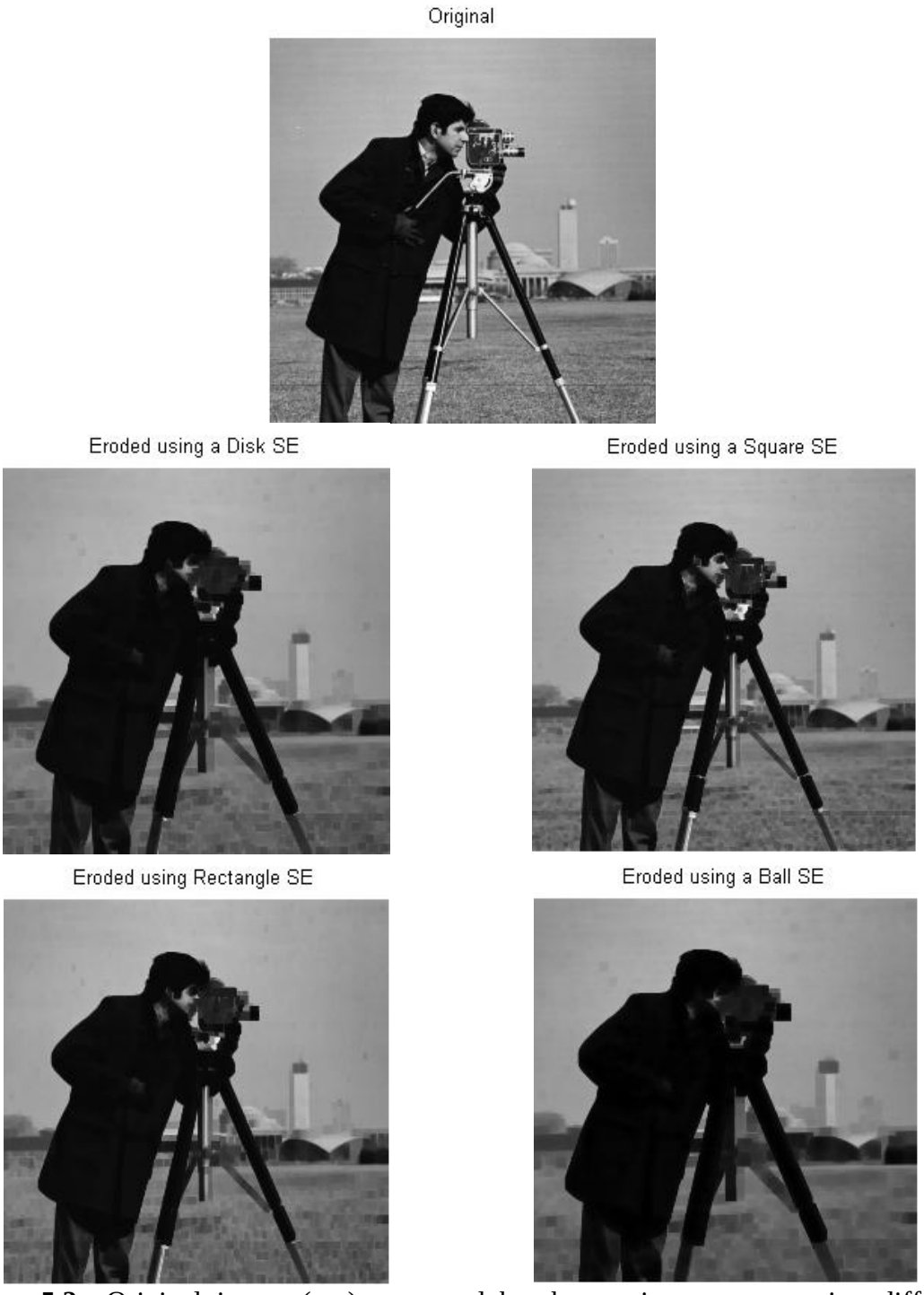

Figure 5.2 Original image (top) processed by the erosion operator using different structuring element shapes and their effect on the original image.

Unlike the above mentioned work, this dissertation proposes an algorithm based on MM operators that takes as an input any Stokes vector imagery (S_0, S_1, or S_2) or

DoLP, enhances the manmade object features present in the image while mitigating clutter effectively, therefore, yielding an enhanced version of the input imagery suitable for anomaly detection. To demonstrate the effectiveness of the proposed algorithm relative to the original input imagery, ROC curves, output surfaces, and 72-hour probability of detection curves will be presented (Subsection 5.2.4) for heated and cold targets for Stokes/DoLP and Morphology-based Stokes/DoLP where no *a priori* information (shape or structure) about the targets is used to help discriminate the objects from natural clutter. Rather, a small 3×3 pixel square element was used as the SE of choice since, for the ranges presented in this dissertation (at about 550m), the targets should be partially or fully covered by the SE. The work presented in Subsection 5.2 clearly demonstrates the effectiveness of the proposed algorithm in enhancing the SCR of manmade structures relative to the background as its performance is tested and evaluated over 300 images of different weather patterns, temperature, low and high contrast imagery, without any *a priori* knowledge on the background or targets that may be present in the scene.

The remainder of Section 5.2 is organized as follows; Subsection 5.2.2 introduces MM as applied to grayscale imagery, representing the type of imagery used as input to the proposed set of morphological operators, followed by Subsection 5.2.3, which proposes the morphology-based anomaly detection algorithm for PI imagery. Subsection 5.2.4 illustrates an in depth study of the algorithm by presenting ROC curves for selected times of the day for 6 MAR 2010, their respective output surfaces, and a 72-hour probability of detection performance of each conventional metric (S_0, S_1, S_2, and DoLP)

compared to its morphology-based version for the different manmade objects present in the scene. Finally, Subsection 5.2.5 summarizes the results and concludes Section 5.2.

5.2.2 Morphological Operations on Grayscale Imagery

A grayscale image can be represented as a function $f(r,c)$ where r and c represent the coordinates of the test image, and $f(r,c)$ represents the grayscale value of the pixel at location (r,c). As with the case of binary morphology, grayscale morphology is defined over two images: the input image, $f(r,c)$, and the SE denoted as $k(r,c)$ with both as grayscale images.

5.2.2.1 Grayscale Dilation. The *grayscale dilation* of an input image by a SE is defined as,

$$f \oplus_g k = max\{f(r-m, c-n) + k(m,n)\}, \tag{5.1}$$

$\forall(m,n) \in K(r-m, c-n) \in F$, where $\oplus$ denotes the dilation operator, the subscript g defines the operation for a grayscale image, K is the SE N-dimension feature space, and F is defined as the input image N-dimension feature space. Grayscale dilation is accomplished by taking the maximum value of $f + k$ in the neighborhood of the SE where the goal effect of such operation is to brighten the image by expanding the light objects while at the same time reducing or eliminating dark details by shrinking dark tones. The effect of dilation on an input image, as with binary MM, it is highly dependent on the values and shape of the SE.

Figure 5.3 illustrates an example of grayscale dilation by a 3×3 square SE which resulted in the brightening of the original image (from Matlab-cameraman.tif) while shrinking dark tones. Notice the tripod legs for example, where portions of the legs are clearly brighter and the dark tones shrunk.

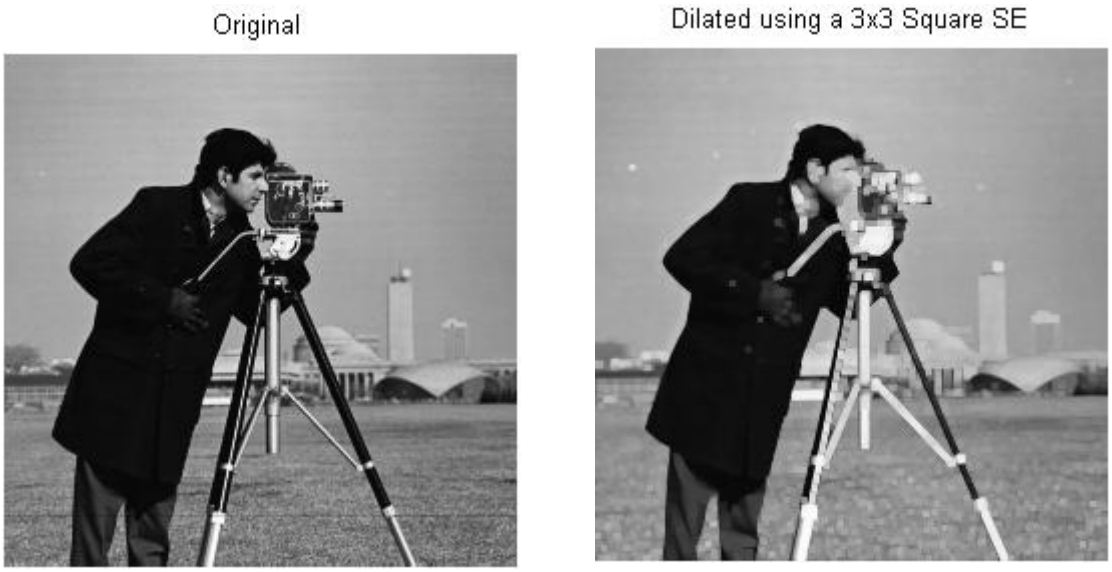

Figure 5.3 Grayscale dilation of original image (left) by a 3×3 square SE (right). Notice how the image became brighter relative to the original image on the left.

5.2.2.2 Grayscale Erosion. *Grayscale erosion* is defined as

$$f \ominus_g k = min\{f(r-m, c-n) - k(m,n)\}, \tag{5.2}$$

and is accomplished by taking the minimum value of $f - k$ in a neighborhood defined by the shape of the SE. In contrary to grayscale dilation, erosion darkens the input image while reducing bright details and once again the effect is directly affected by the shape and values of the SE. Figure 5.4 illustrates an example of grayscale erosion using 3×3

square SE which resulted in darkening the input imagery while reducing bright pixels found in the image.

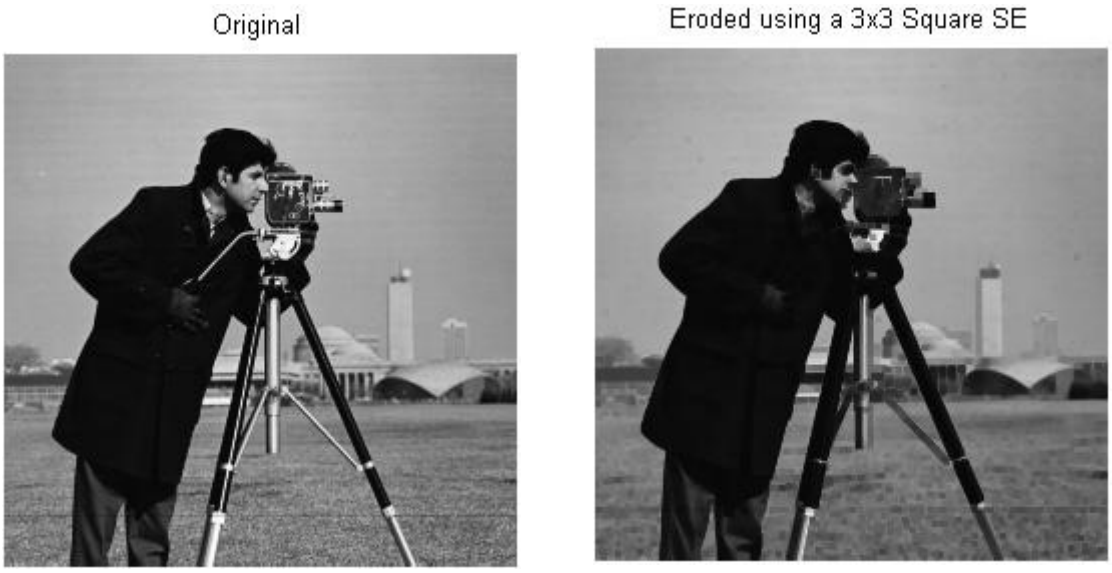

Figure 5.4 Grayscale erosion of original image (left) by a 3×3 square SE (right). By eroding the original image the result is a darker image.

5.2.2.3 Grayscale Opening. The *opening operator* ($\circ_g$) for grayscale imagery by a SE is the result of eroding an input image by a SE, followed by dilating the result with the same SE,

$$f \circ_g k = \left(f \ominus_g k\right) \oplus_g k. \tag{5.3}$$

The effect of opening is to diminish the intensity of all bright features found in f while having a negligible effect on the dark features as well as the background as it is shown in Figure 5.5.

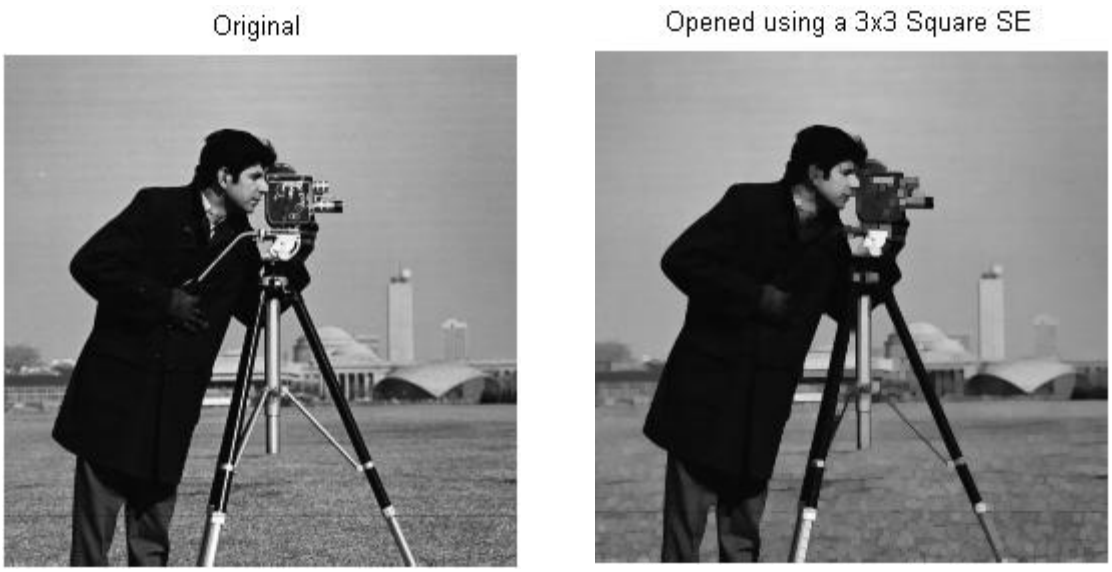

Figure 5.5 Grayscale opening operator on original image (left) by a 3×3 square SE (right). By opening the original image one can observe the brightness of bright pixels are diminished while dark pixels are negligibly unaffected.

5.2.2.4 Grayscale Closing. *Grayscale closing* ($\cdot_g$) is the dual of opening.

Grayscale Closing is defined by the dilation of f by k, followed by erosion operator with the same SE,

$$f \cdot_g k = \left(f \oplus_g k\right) \ominus_g k, \tag{5.4}$$

and the effect of closing a grayscale image is the attenuation of dark features while bright pixels and the background are negligibly affected. Figure 5.6 demonstrates the original cameraman image (left) and the output when the closing operator is applied to the original image using a 3×3 square SE.

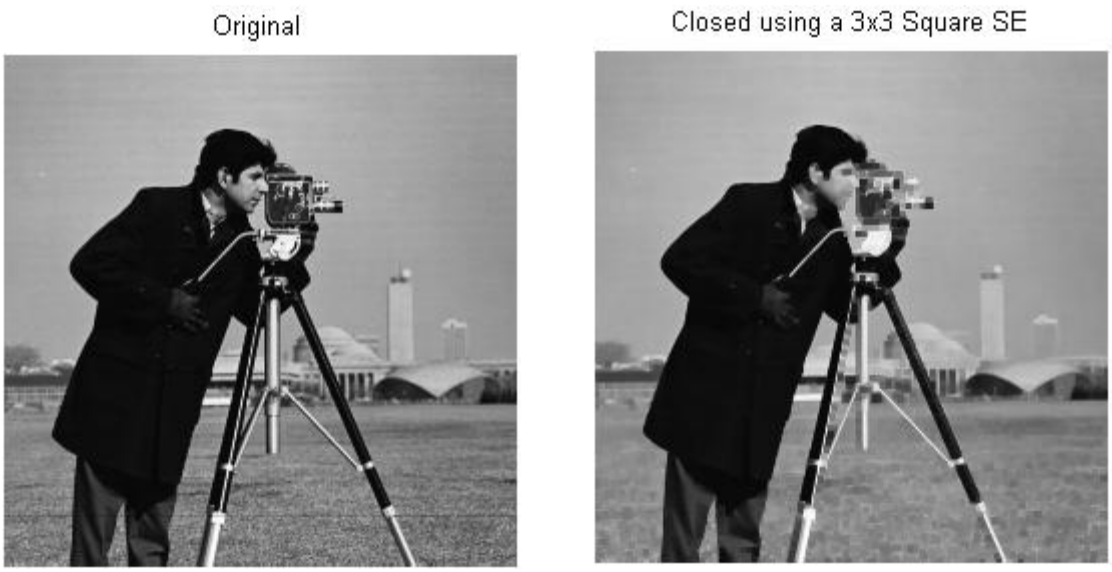

Figure 5.6 Grayscale closing operation on original image (left) by a 3×3 square SE (right). The closing operator, the dual of opening, has the opposite effect where dark pixels are darken while bright pixels are negligibly unaffected by the operator.

5.2.2.5 Applications of Grayscale Operations. Having discussed some of the most fundamental operators in grayscale MM, a set of examples of MM as applied to grayscale imagery for various applications such as filtering, smoothing, and edge detection will be shown in the following subsections.

5.2.2.5.1 Top-Hat Transform. *Morphological Top-Hat transform*, denoted by $\hat{\circ}_g$, for a grayscale image, is one of the most widely used MM transform for edge detection. As previously mentioned, the choice and size of the SE will have an effect on the final output image relative to a different choice or size of SE. The Top-Hat transform is expressed at the subtraction of the original image f with opening of f by a SE.

$$f \,\hat{\circ}_g\, k = f - \left(f \circ_g k\right). \tag{5.5}$$

The top-hat transform can also be very useful as a pre-processing step in order to correct for uneven illumination that may be found in the test image prior to thresholding. Figure 5.7 illustrates the use of the Top-Hat transform for edge detection using a 3×3 square SE.

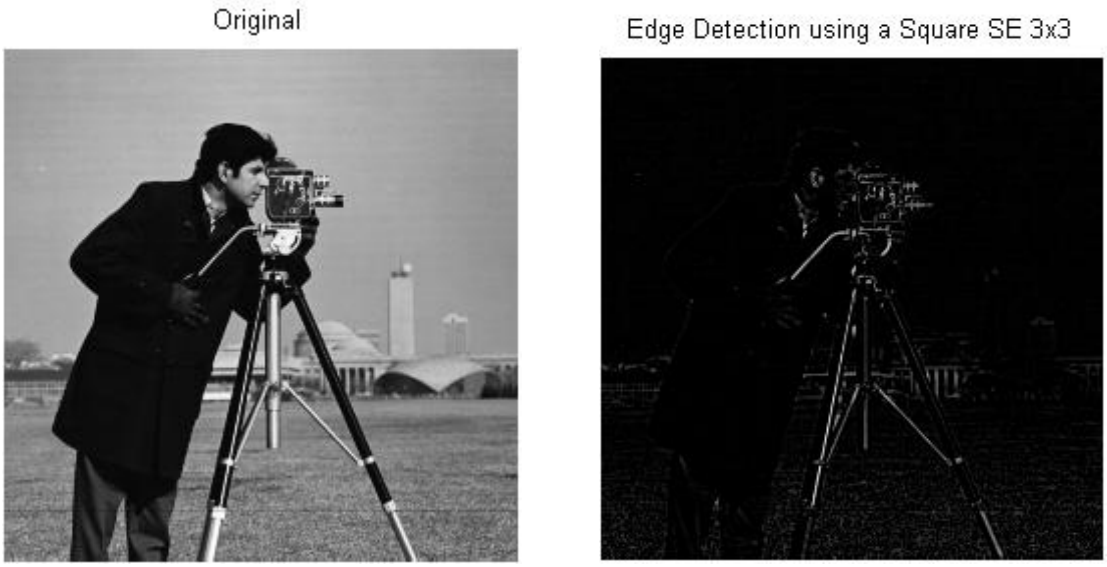

Figure 5.7 Edge detection using the top-hat transform for a square SE of 3×3 pixels.

5.2.2.5.2 Smoothing. *Morphological smoothing* allows the removal or attenuation of both bright and dark artifacts and noise by performing a morphological opening followed by a closing operator using the same SE as follows,

$$f_o = \left(f \circ_g k\right) \cdot_g k. \tag{5.6}$$

Figure 5.8 demonstrates the result of smoothing (right image) the original image using a 3×3 square SE. Notice how both bright and dark tones are smoothed out and detail once found in the original image (left) is eroded in the output (right).

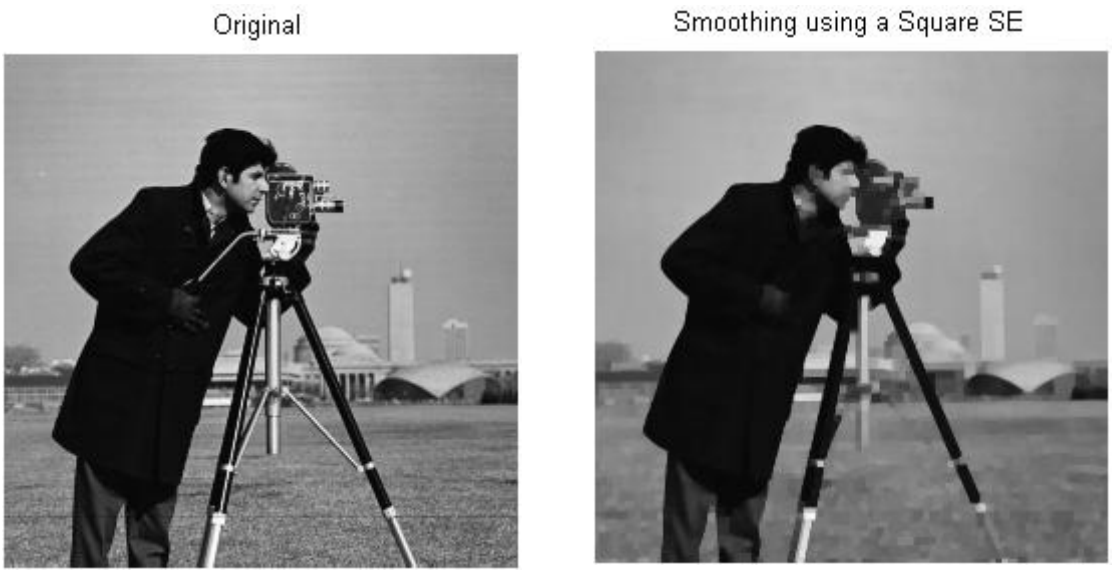

Figure 5.8 Illustration of image smoothing using the opening operation followed by the closing operator using a square SE of 3 × 3 pixels.

5.2.2.5.3 Gradient. *Morphological gradient* is highly used to highlight sharp gray-level transitions in the input image and is defined as

$$grad_{k_e,k_i}(f) = \left(f \oplus_g k_e\right) - \left(f \ominus_g k_i\right), \tag{5.7}$$

where k_e and k_i are the external and internal SE. Equation (5.7) can be decomposed into the sum of two partial gradients. The *external gradient* denoted as,

$$grad_{k_e}(f) = \left(f \oplus_g k_e\right) - f, \tag{5.8}$$

and the *internal gradient*

$$grad_{k_i}(f) = f - \left(f \ominus_g k_i\right). \tag{5.9}$$

The morphological gradient can also be used as a grayscale edge detector once a threshold is applied to the output image of Equation (5.7). Figure 5.9 illustrates the

outputs of Equation (5.8) using a 5 × 5 square SE (top right), Equation (5.9) using a 3 × 3 square SE (bottom left) and the subtraction of the two as per Equation (5.7) (bottom right). One can conclude that the output of morphological gradient, Equation (5.7), clearly defines edges or transitions in the image better than the Top-Hat transform.

Figure 5.9 Illustration of using the gradient operator as a combination of the internal (upper right) and the external gradient (lower left) resulting on an effective edge detector (lower right) compared to top-hat transform.

5.2.3 Morphological Image Enhancement for PI Anomaly Detection

It is nontrivial to assemble a sequence of basic MM operators geared toward addressing a particular image processing problem as shown previously by combining dilation and erosion MM operators in order to achieve different results where the effectiveness of the different combinations will vary, significantly, depending on the purpose one is trying to achieve and the SE used with each operation. The procedure proposed in this subsection for anomaly detection in PI has several stages of computing dilation and gradients or edges of the image within a morphological framework, together with region growing; the framework is consistent with other works in the literature involving the development of a multistage morphological procedure for prescreening large numbers of broadband infrared image data (see, for instance, [53-54]). Specifically, this dissertation proposes the application of the following seven-step MM algorithmic sequence, shown in Table 5.1, to the Stokes and DoLP parameters imagery for anomaly detection as follows:

Step 1 is only applied to S_1 imagery where the end result is to emphasize the vertical polarization component since it is the dominant component emitted by optically smooth surfaces. Step 2, dilation, is applied to the input image with the objective of: (1) brightening the original image by expanding light objects while (2) reducing dark tones, which are usually associated to natural clutter, and (3) expanding small objects (by use of the SE), so they become more noticeable. The SE chosen for this experiment was a square of width 3, which ensures that all manmade objects in the scene are either partially or fully covered by the SE of choice.

Grayscale dilation of the input image f by the structuring element k is denoted as $f \oplus_g k$ and expressed as,

$$f_1 = f \oplus_g k = max\{f(r-m, c-n) + k(m,n)\}, \quad (5.10)$$

$\forall (m,n) \in K(r-m, c-n) \in F.$

Table 5.1 Proposed Morphological Operations on Stokes and DoLP Imagery

Step	Operation	Reasoning
1*	Invert S_1 imagery	To emphasize the vertical component that will be exploited by the dilation operator. See Chapter 3 for more information on the reasoning for the dominance of the vertical component in manmade objects.
2	Morphological Dilation	Brighten the image by expanding the bright pixels while reducing or eliminating dark details by shrinking dark tones
3	Morphological Gradient	Used to detect the edges where there is a rapid light-(target) to-dark (background) change
4	Hole Filling	Fill in the internal area bound by edges with bright pixels
5	Morphological Closing	Attenuation of dark features (background) while bright pixels (target) are unaffected
6	Adaptive Cutoff Threshold Estimation	Threshold based on image-dependent estimated parameter values making it robust, since a robust criterion (δ) can be imposed *a priori* for all of the incoming images
7	High Intensity (anomaly) Region Detection	

*Step 1 is only required for S_1 image to emphasize the vertical component, which is the dominant component emitted by optically smooth surfaces.

The next step employs a morphological gradient (see Subsection 5.2.2.5.3), the key is to capitalize any rapid light-to-dark (or dark-to-light) changes often associated with transitions from clutter to target or vice versa, or

$$f_2 = \left(f_1 \oplus_g k\right) - \left(f_1 \ominus_g k\right). \tag{5.11}$$

This edge detection defines closed or semi-closed shapes, which, in theory, should be related to objects present in the scene while the result of performing Equation (5.11) in clutter, which is often shapeless, returns open lines that do not form closed shapes.

The region-filling process, step 4, uses an average filtering method to join the detached nearby edges and fill closed and semi-closed regions with representative values of the nearby edges with the objective of filling and accentuating regions of interests where targets may be present. The region-filling process, denoted as f_3 is defined as,

$$f_3 = \frac{\sum_{m=-a}^{a}\sum_{n=-b}^{b} w(m,n) f_2(r-m, c-n)}{\sum_{m=-a}^{a}\sum_{n=-b}^{b} w(m,n)}, \tag{5.12}$$

where, w is a filter mask of size 3×3 just like the SE and $a = \ b = \frac{n-1}{2}$ and the result is an image of size $f_3 \in \boldsymbol{R}^{R-2a,C-2b}$.

Finally, in step 5, the morphological closing operation is applied to f_3 with a 3×3 pixel square SE k. The closing operation attenuates dark features, often associated with clutter, while at the same time, bright pixels, associated with manmade objects, are negligible affected, or

$$f_4 = \left(f_3 \oplus_g k\right) \ominus_g k, \tag{5.13}$$

where the symbols $\oplus_g$ and $\ominus_g$ denote dilation and erosion, respectively.

In step 6, the dissertation proposes a simple but effective approach to determine the detected locations in f_4, i.e., a cutoff threshold (δ) obtained via,

$$f_{std} = \frac{f_4 - \hat{\mu}_{f_4}}{\hat{\sigma}_{f_4}} \geq \delta, \tag{5.14}$$

where $\hat{\mu}_{f_4}$ and $\hat{\sigma}_{f_4}$ are the estimated sample average and standard deviation, respectively, using all of the pixel values in f_4. The resulting image from Equation (5.14) is an image with positive and negative values in terms of the number of standard deviations from the estimated mean of f_4.

In order to find anomalous objects in the test scene a robust criterion (δ) can be imposed a priori for all the incoming images (f_{std}), where $\delta > 0$ is the number of standard deviations above the estimated mean as shown in Equation (5.15).

$$T_{th} = f_{std} \geq \delta. \tag{5.15}$$

Equation (5.15) yields a binary image, where the spatial locations of all pixels in f_{std}—having values greater than δ—are represented by 1 in the final image, or 0 otherwise. It is desired that only pixels belonging to manmade objects in a scene dominated by natural clutter are represented by 1's in the final image. Notice that Equation (5.15) is both *adaptive*, since f_{std} will vary—accordingly—due to the image-dependent estimated parameter values; and also *robust*, since a robust criterion (fixed δ e.g., $\delta = 5$) is imposed *a priori* for all of the incoming images. For convenience, from

here forth, one shall refer to the proposed overarching approach as the Morph anomaly detector.

Figures 5.10 through 5.13 illustrate each of the steps from Table 5.1 on the Stokes and DoLP imagery and the effect each morphologic operation has on the input image. The first image (top left) of each figure demonstrates the input imagery, with the exception of S_1 where one inverts the surface ($-S_1$) prior of applying any of the MM operators. The input image is dilated (top right) using a 3×3 square SE resulting in retaining the maximum values seen by the SE when superimposed on f for a given location (r, c).

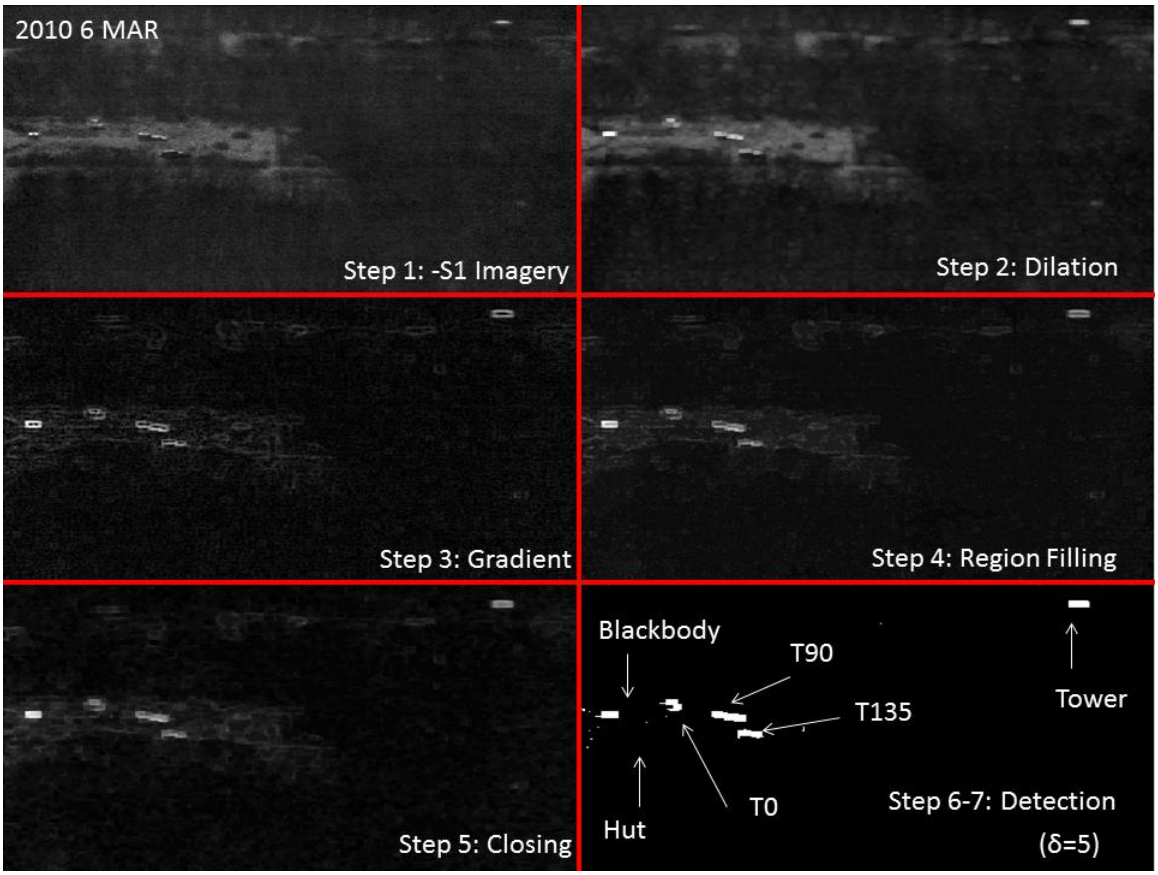

Figure 5.10 Illustration of each of the steps proposed for using morphological operators on Stokes S_1 imagery.

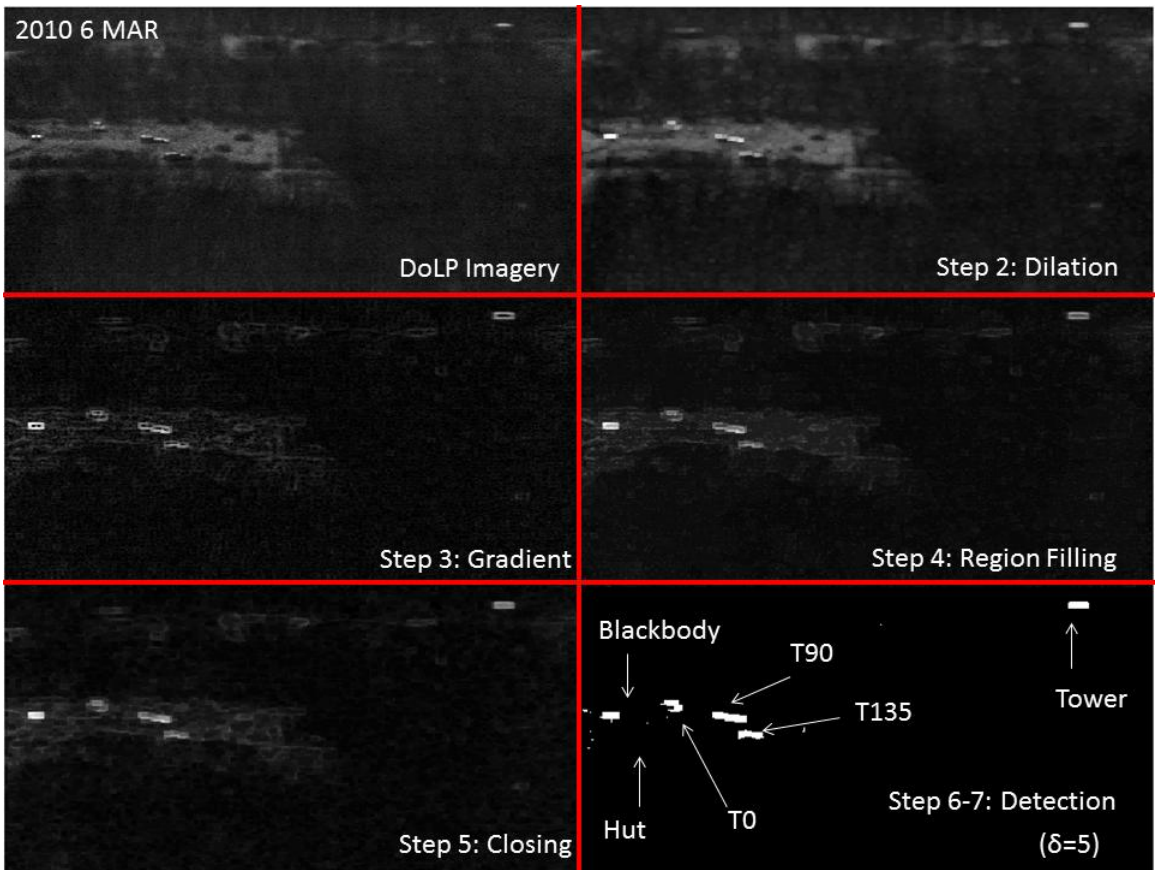

Figure 5.11 Illustration of each of the steps 2-7 proposed for using morphological operators on DoLP imagery.

The dilation operation, as previously described, brightens the image by expanding bright pixels, often associated with manmade objects, and reducing dark details, which are often linked to natural clutter. A gradient is then applied to f_1 by subtracting the dilated with the eroded input image (f_1) using the same SE (middle left), see Equation (5.11). This operation allows for the isolation of edges where there is a rapid light-(target) to-dark (background) changes, often associated with deviations from clutter to clutter or target to clutter. Edges that form fully or semi-closed areas are then filled using the hole-filling operator (middle right), which fills up the area composed of closed and semi-close loops. A closing operator is then applied to the image with the objective of further attenuating the background (dark pixels) while leaving bright pixels (potential

anomalies) unaffected (lower left image), thus in practice increasing the signal-to-noise ratio between dark and light pixels. Finally, a threshold $(\delta = 5)$ is applied to the standardized image in order to identify potential areas where manmade objects may be present (lower right image). These areas can then be further interrogated using other modalities or specialized algorithms (e.g., classifiers) in order to identify potential targets and/or reject anomalies. As one can observe in Figures 5.10 through 5.13, there is a clear advantage in using morphological operators to extract and enhance manmade object features for effective identification of anomalies (manmade objects).

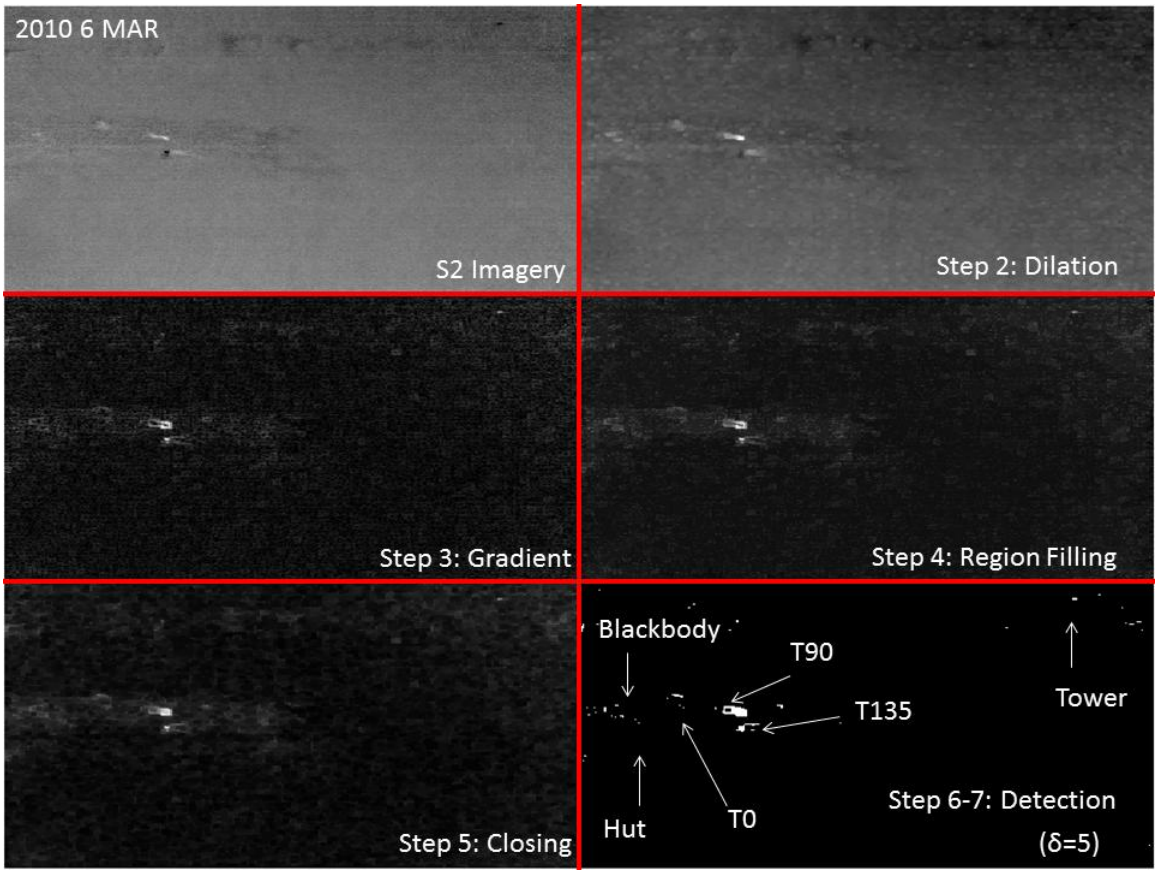

Figure 5.12 Illustration of each of the steps 2-7 proposed for using morphological operators on Stokes S_2 imagery.

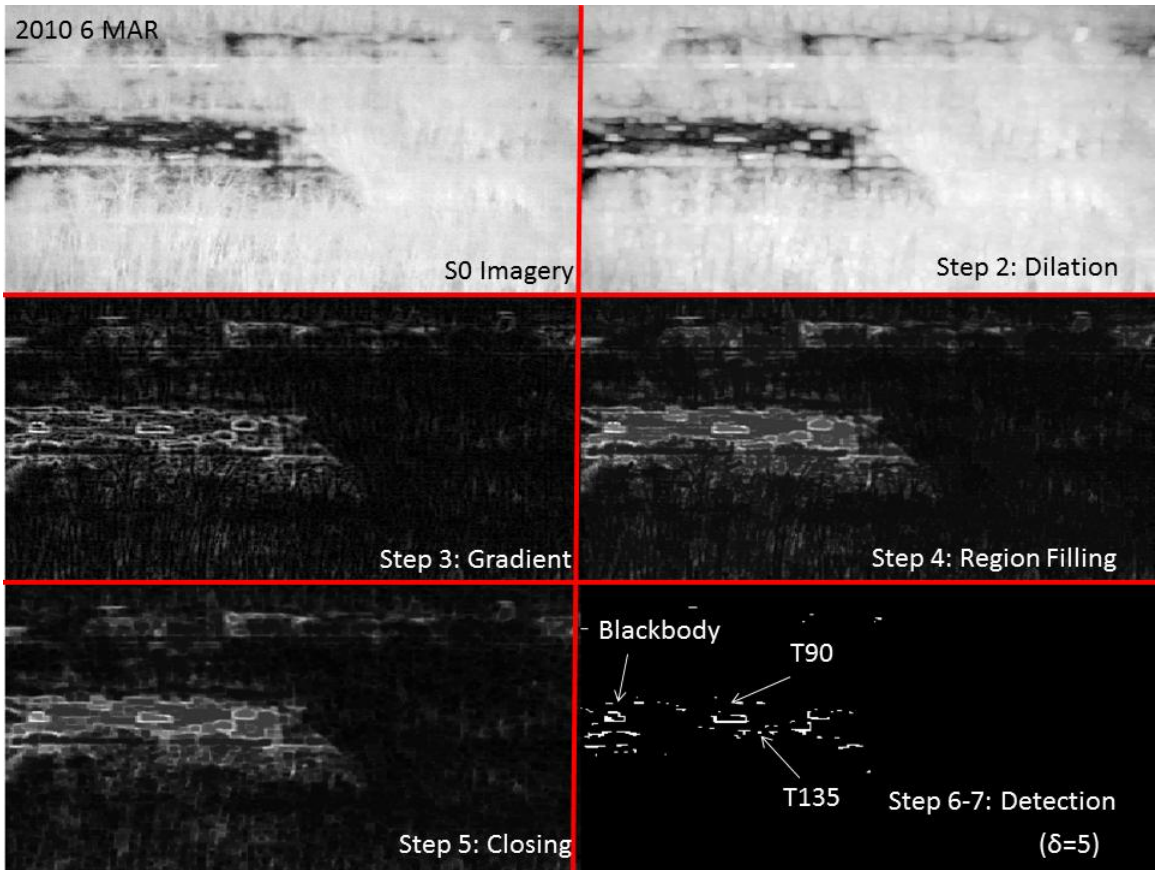

Figure 5.13 Illustration of each of the steps 2-7 proposed for using morphological operators on Stokes S_0 imagery.

In summary, this subsection introduced the use of morphological operators as a polarization feature extraction and enhancement that can be used for effective manmade object detection in images where natural clutter is the dominant class. The proposed method, along with the chosen SE, demonstrated the capability of retrieving not only additional target spatial information than what was present in the original image; but also increased the SNR between the extracted features and natural clutter. Figures 5.10 through 5.13 demonstrated how the same morphological procedure could be used in all Stokes and DoLP imagery, and demonstrated the ability of enhancing manmade objects features while reducing the number of false alarms present relative to the original images. In the following Subsection 5.2.4, a performance comparison between the morphology-

based Stokes/DoLP detectors and the conventional Stokes parameters and DoLP will be presented using ROC curves, output surfaces, and a 72-hour probability of detection curve for all conventional and morphology-based Stokes/DoLP metrics.

5.2.4 Performance Assessment of Morphologic Based Stokes/DoLP Imagery

In this subsection a comparison between conventional and morphology enhanced Stokes/DoLP parameters will be presented for the time period between 6 and 8 MAR 2010. Several key points will be made throughout this section:

1) Applying the morphological filters on Stokes and DoLP increases the probability of detection of all manmade objects in the scene relative to the conventional Stokes and DoLP metrics.

2) Morphology-based S_1 and DoLP performances were very stable regardless of diurnal or target state changes using this particular dataset.

3) ROC curves demonstrate that morphology-based Stokes exhibit high detection rates at very low false alarm rates, making them useful for unmanned and aided systems.

Figures 5.14 through 5.19 illustrate the ROC curves for the Stokes/DoLP and Morph-Stokes/DoLP for each of the manmade objects separately as well as the overall detection when all manmade objects are combined into a single class. The plots on the left side of each figure illustrates a plot representative of the full ROC curve where the probability of detection (P_d) and the probability of false alarm (P_{fa}) range from 0 to 1, while the right side of the figure illustrates a zoomed in version of the left side plot with the P_d still ranging from 0 to 1 and the P_{fa} ranging only from 0 to 0.01. The reason why 0.01 was chosen is because any false alarm rate above 0.01 results in an output surface that is unusable by any autonomous or aided system due to the high number of false alarms present, diminishing the system's ability to correctly discriminate any potential

targets from natural clutter. Finally, the rows in each figure represent the different timestamps chosen for this comparison: 0710h, 0910h, 1310h, and 2010h.

To further aid the reader in comparing the performance difference between the different ROC curves, probability of detection tables for each Stokes parameter and its morphological counterpart are given in Tables 5.2 through 5.5, while holding a more restrictive false alarm probability, i.e., $P_{fa} = 0.005$.

Observing Figure 5.14 for manmade object T_0 and timestamp 0710h, the P_d difference between S_0 and Morph-S_0 is greater than 0.10 for a $P_{fa} = 0.01$. By P_{fa} = 0.20, Morph-S_0 has reached full detection or P_d = 1 while conventional S_0 only achieved a P_d = 0.92.

Two hours later, 0910h, Morph-S_0 achieves full detection at a P_{fa} = 0.05 while conventional S_0 only achieves a P_d of about 0.10 for the same false alarm rate. By observing the zoomed in ROC curve on the right side of the figure, one notices that Morph-S_0 clearly outperforms its conventional counterpart even at low false alarm rates where for a $P_{fa} = 0.005$ Morph-S_0 achieves a P_d of about 0.90 and S_0 a $P_d = 0.00$. At 1310h, where high contrast imagery can be found, Morph-S_0 achieves full detection at about P_{fa} = 0.001 with S_0 measuring only a $P_d \approx 0.20$. By 2010h, S_0 and Morph-S_0 P_d values drop significantly to approximately the same levels found in timestamp 0710h with Morph-S_0 once again outperforming S_0 greater than 0.10 for a $P_{fa} = 0.01$.

The impact of morphological operators can be felt more profoundly when used with Stokes parameters S_1, S_2, and DoLP, for example, observing timestamps 0710h, 0910h, 1310h, and 2010h, the P_d, for a $P_{fa} = 0.005$, for conventional S_1 for manmade object T_0 is 0.32, 0.24, 0.23, and 0.33 respectively, while for Morph-S_1 the P_d values are

0.96, 0.85, 0.87, and 0.88. DoLP P_d values for the same probability of false alarm and timestamps are 0.28, 0.23, 0.12, and 0.27; while Morph-DoLP P_d yielded 0.96, 0.87, 0.67, and 0.85. Finally, for Stokes parameter $S_{2,}$ the performance achieved was 0.12, 0.05, 0.28, and 0.21; while Morph-S_2 attained 0.27, 0.13, 0.76, and 0.36 for the same timestamps and false alarm rate.

The average probability of detection given a $P_{fa} = 0.005$ for S_0, S_1, S_2, and DoLP for the four timestamps in detecting T_0 was $P_d = 0.06, 0.28, 0.17, \text{and } 0.22$ respectively; while Morph-S_0. Morph-S_1, Morph-S_2, and Morph-DoLP had an average probability of detection of $P_d = 0.49, 0.89, 0.38, \text{and } 0.79$, correspondingly.

6 MAR 2010 – T_0
0710h

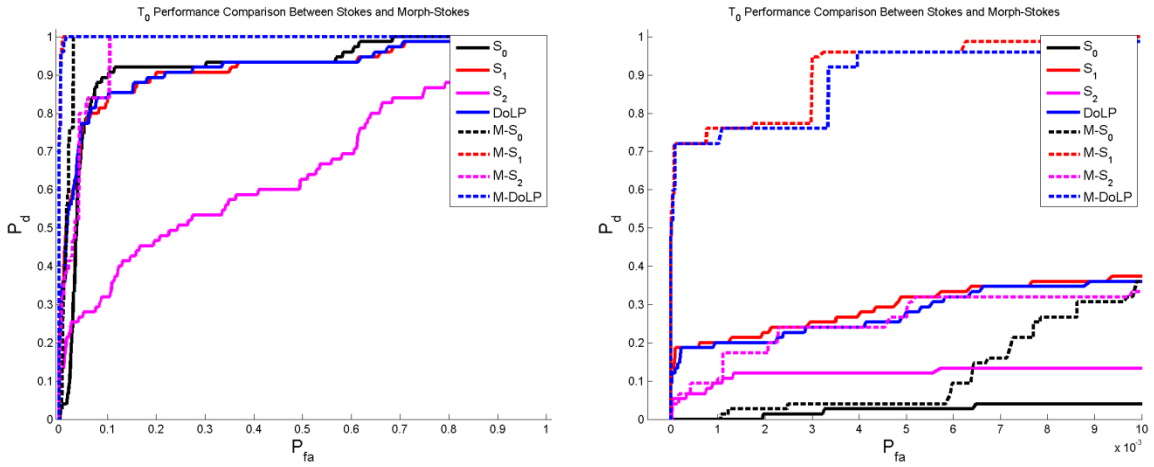

0910h

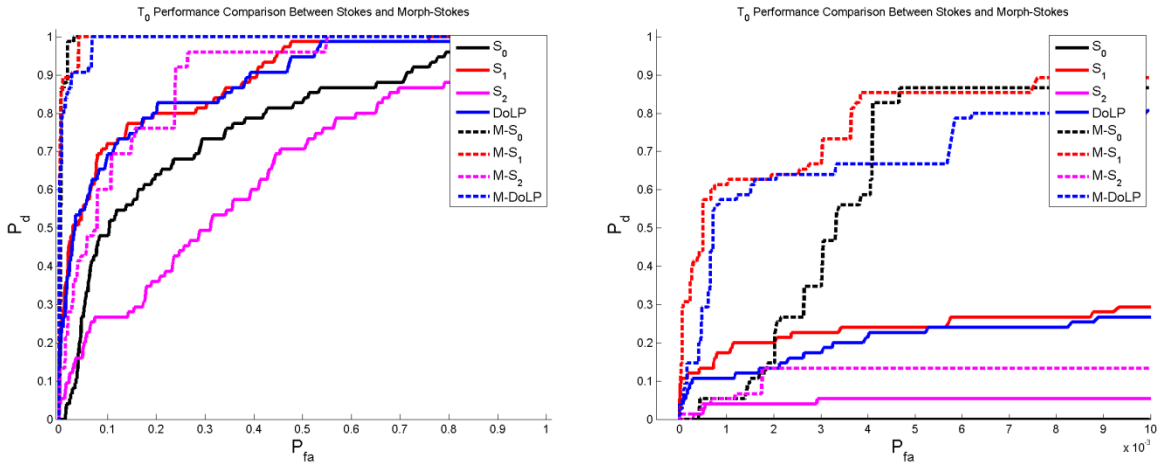

Figure 5.14 ROC curves comparing the performance between conventional and morphologic operator-based Stokes vector and DoLP when detecting T_0. The average probability of detection given a $P_{fa} = 0.005$ for S_0, S_1, S_2, and DoLP for the four timestamps in detecting T_0 was $P_d = 0.06, 0.28, 0.17, \text{and } 0.22$, respectively; while Morph-S_0. Morph-S_1, Morph-S_2, and Morph-DoLP had an average probability of detection of $P_d = 0.49, 0.89, 0.38, \text{and } 0.79$, correspondingly.

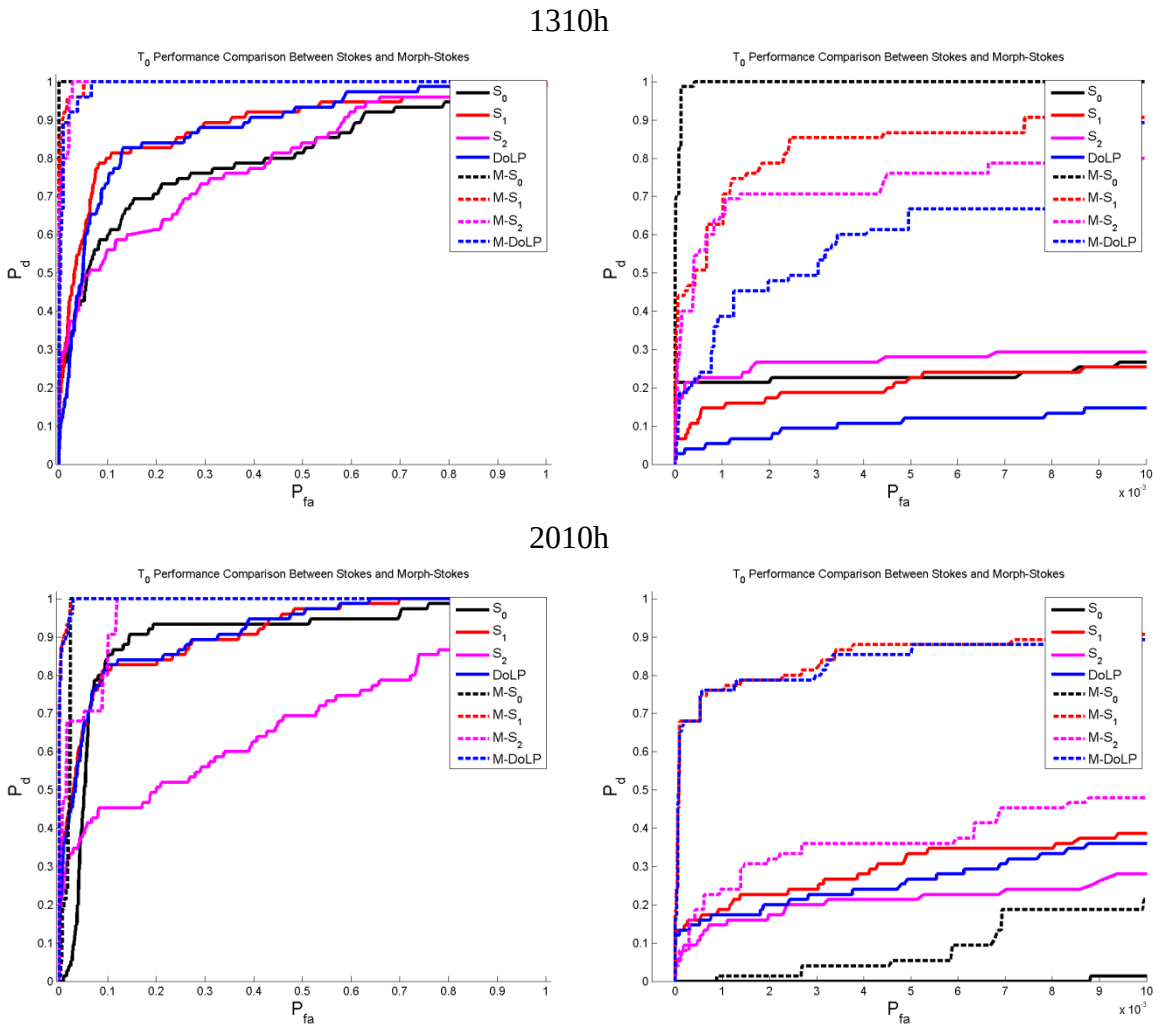

Figure 5.14 ROC curves comparing the performance between conventional and morphologic operator-based Stokes vector and DoLP when detecting T_0. The average probability of detection given a $P_{fa} = 0.005$ for S_0, S_1, S_2, and DoLP for the four timestamps in detecting T_0 was $P_d = 0.06, 0.28, 0.17, \text{and } 0.22$, respectively; while Morph-S_0. Morph-S_1, Morph-S_2, and Morph-DoLP had an average probability of detection of $P_d = 0.49, 0.89, 0.38, \text{and } 0.79$, correspondingly. (Continuation)

Figure 5.15 illustrates the ROC curves for T_{90} for the Stokes parameters and DoLP as well as their morphological counterparts. Once again one can observe that the morphological operators increased the probability of detection relative to their conventional counterparts. For example, for a $P_{fa} = 0.005$, see the plots on the right side of the figure, S_0 probability of detection for all timestamps was about 0.0, 0.05, 0.20, and 0.0 with Morph-S_0 achieving a P_d of about 0.20, 0.60, 1.00, and 0.20 for 0710h, 0910h, 1310h, and 2010h, respectively. S_1 performed better than S_0 in detecting the T_{90} with a probability of detection of 0.30, 0.28, 0.23, and 0.19 while Morph-S_1 performed better than S_1 with a probability of detection of 0.91, 0.81, 0.82, and 0.72 for the same timestamps. For this target set one observes that DoLP performed very closely to S_1 and as a result the performance of Morph-DoLP was very similar to Morph-S_1 as well. The Stokes parameter S_2 had a probability of detection of 0.21, 0.15, 0.30, and 0.24 with Morph-S_2 performing better than its counterpart with a probability of detection of 0.65, 0.44, 0.74, and 0.59. As with T_0, Morph-S_1 and Morph-DoLP are the best metrics for detecting T_{90}.

The average detection probability for a $P_{fa} = 0.005$ over all timestamps in detecting T_{90} for conventional Stokes and DoLP was $P_d = 0.07, 0.14, 0.23, \text{and } 0.23$ for S_0, S_1, S_2, and DoLP, respectively. On the other hand, Morphology-based Morph-S_0, Morph-S_1, Morph-S_2, and Morph-DoLP demonstrated an enhanced detection capability relative to their conventional equivalents with a $P_d = 0.51, 0.82, 0.60, \text{and } 0.82$, respectively.

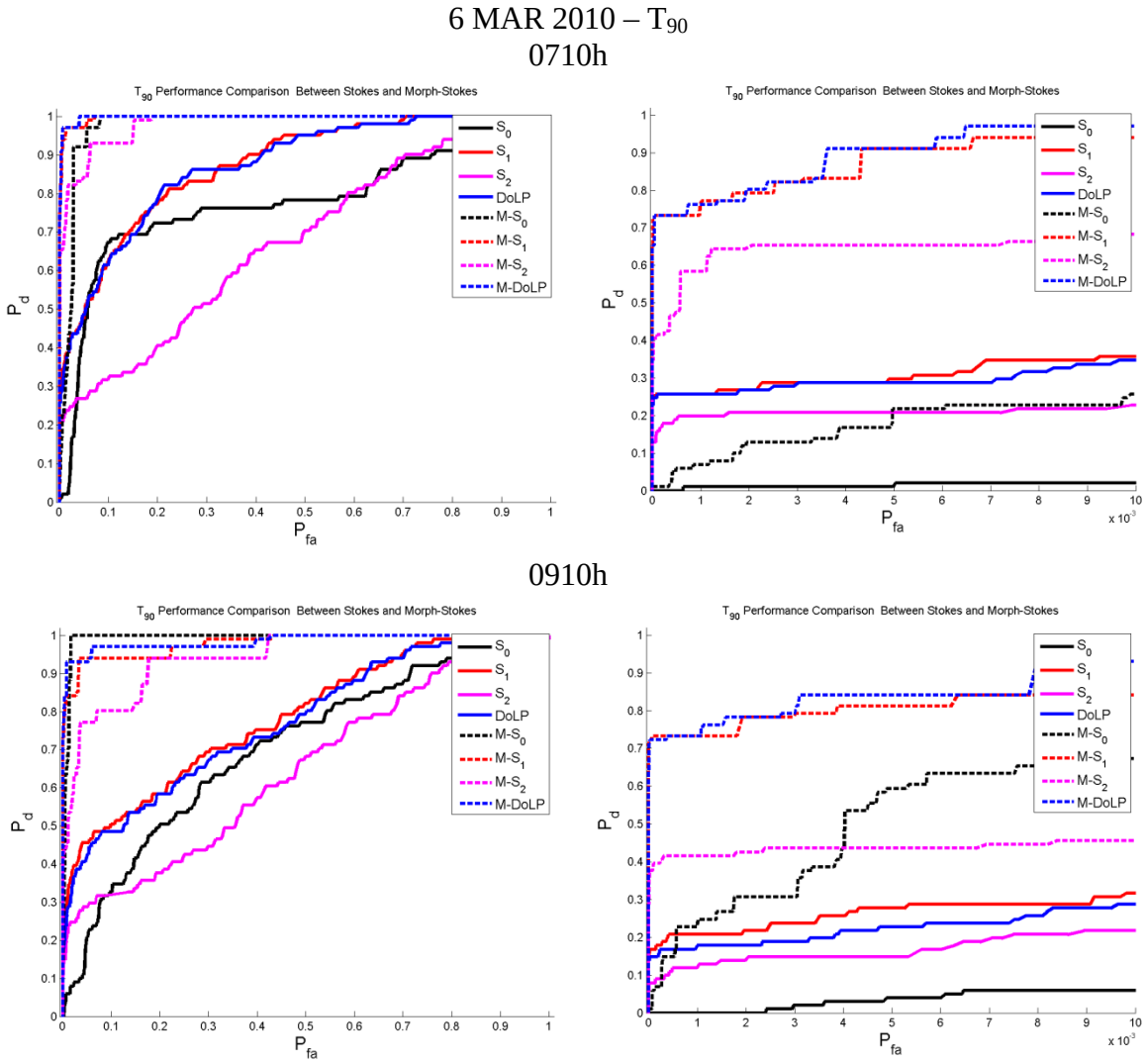

Figure 5.15 ROC curves comparing the performance between conventional and morphologic operator-based Stokes vector and DoLP when detecting T_{90}. The average detection probability given a $P_{fa} = 0.005$ over all timestamps in detecting T_{90} for conventional Stokes and DoLP was $P_d = 0.07, 0.14, 0.23, \text{and } 0.23$ for S_0, S_1, S_2, and DoLP, respectively. On the other hand, Morphology-based Morph-S_0, Morph-S_1, Morph-S_2, and Morph-DoLP demonstrated an enhance detection capability relative to their conventional equivalents with a $P_d = 0.51, 0.82, 0.60, \text{and } 0.82$, respectively.

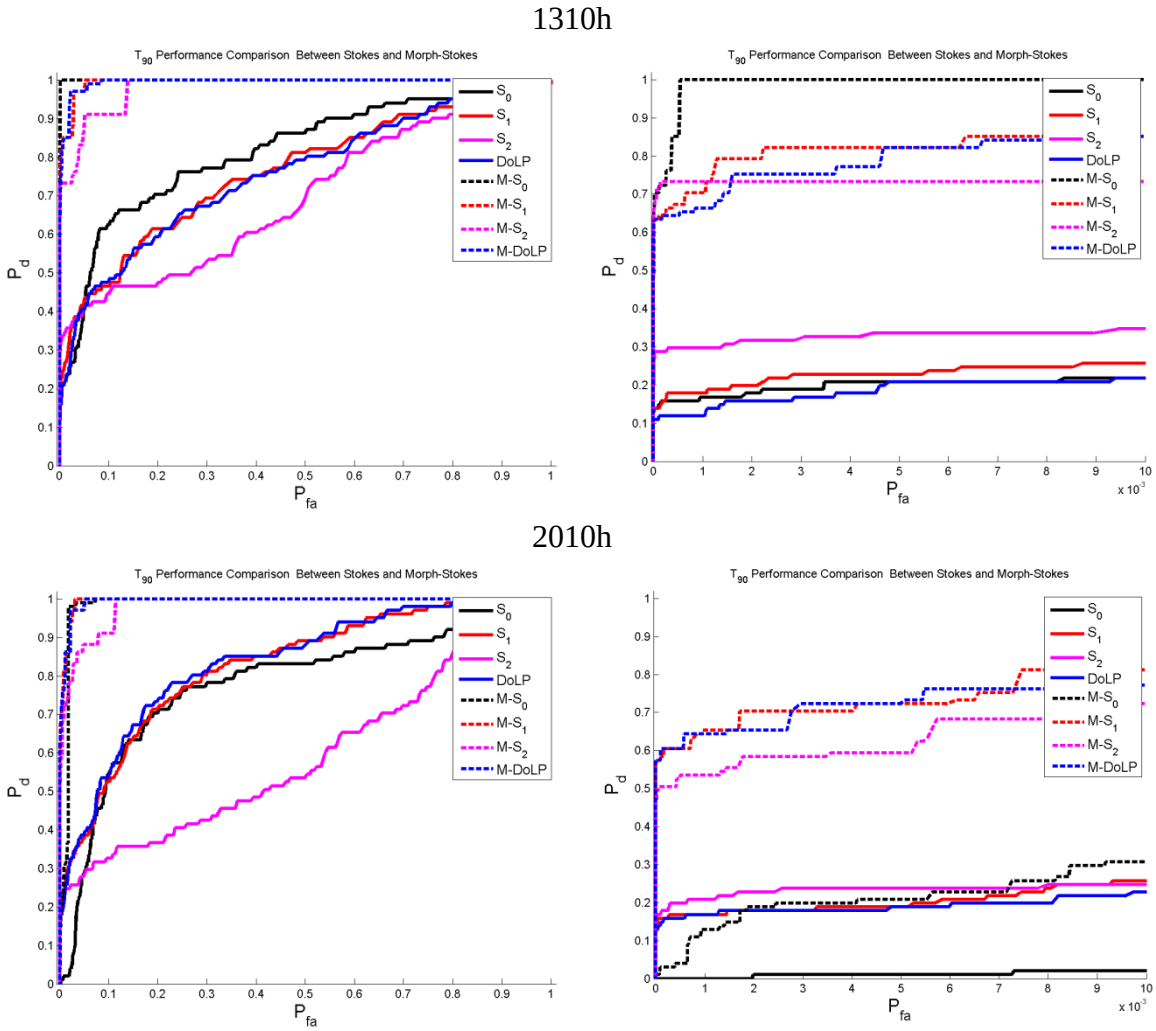

Figure 5.15 ROC curves comparing the performance between conventional and morphologic operator-based Stokes vector and DoLP when detecting T_{90}. The average detection probability given a $P_{fa} = 0.005$ over all timestamps in detecting T_{90} for conventional Stokes and DoLP was $P_d = 0.07, 0.14, 0.23, \text{and } 0.23$ for S_0, S_1, S_2, and DoLP, respectively. On the other hand, Morphology-based Morph-S_0, Morph-S_1, Morph-S_2, and Morph-DoLP demonstrated an enhance detection capability relative to their conventional equivalents with a $P_d = 0.51, 0.82, 0.60, \text{and } 0.82,$ respectively. (Continuation)

Figure 5.16 illustrates the ROC performance curves for T_{135} with the full range ROC curves on the left side of the figure and the zoomed in version on the right side. Here again, the plots demonstrate the effectiveness of the morphological operators in discriminating T_{135} from the background relative to conventional metrics. Observing the plots on the right side, Morph-S_1 and Morph-DoLP demonstrated an increased performance relative to their conventional counterparts and the remaining metrics for timestamps 0710h, 0910h, and 2010h. As expected, Morph-S_0 performed better than all other metrics at 1310h as a result of the solar loading effect on the targets. Furthermore, one can find Morph-S_1 outperforming Morph-DoLP at 1310h with a significant advantage at very low false alarm rates, while Morph-S_2 and Morph-DoLP perform very similarly to each other but underperforming relative to Morph-S_1. Given the same $P_{fa} = 0.005$, S_0 detection rate for the four timestamps was as follows: 0.02, 0.02, 0.26, and 0.0, while Morph-S_0 achieved a P_d of 0.22, 0.53, 1.00, and 0.18 for the respective timestamps. S_1 achieved a P_d of 0.16, 0.16, 0.11, and 0.14 with Morph-S_1 outperforming its counterpart with a detection rate of 0.76, 0.67, 0.71, and 0.69. DoLP and Morph-DoLP performed very similarly to S_1 and Morph-S_1, respectively. DoLP achieved a P_d of 0.15, 0.14, 0.10, and 0.14 and Morph-DoLP outperformed DoLP with a P_d of 0.79, 0.66, 0.72, and 0.74 for timestamps 0710h, 0910h, 1310h, and 2010h, correspondingly. S_2 was the worst performing metric compared to S_1 and DoLP with a P_d of 0.16, 0.08, 0.31, and 0.24, while Morph-S_2 outperformed S_2 with a detection rate of 0.47, 0.19, 0.72, and 0.75. As a clarification, when using "outperformed by" term denotes $|P_{\text{d of detector A}} - P_{\text{d of detector B}}|$. Finally, the average detection probability given a $P_{fa} = 0.005$ for S_0, S_1, S_2, and DoLP was $P_d = 0.07, 0.25, 0.20, \text{and } 0.13$, respectively; while Morph-S_0, Morph-S_1,

Morph-S_2 and Morph-DoLP achieved a $P_d = 0.48, 0.71, 0.53, \text{and } 0.73,$ correspondingly.

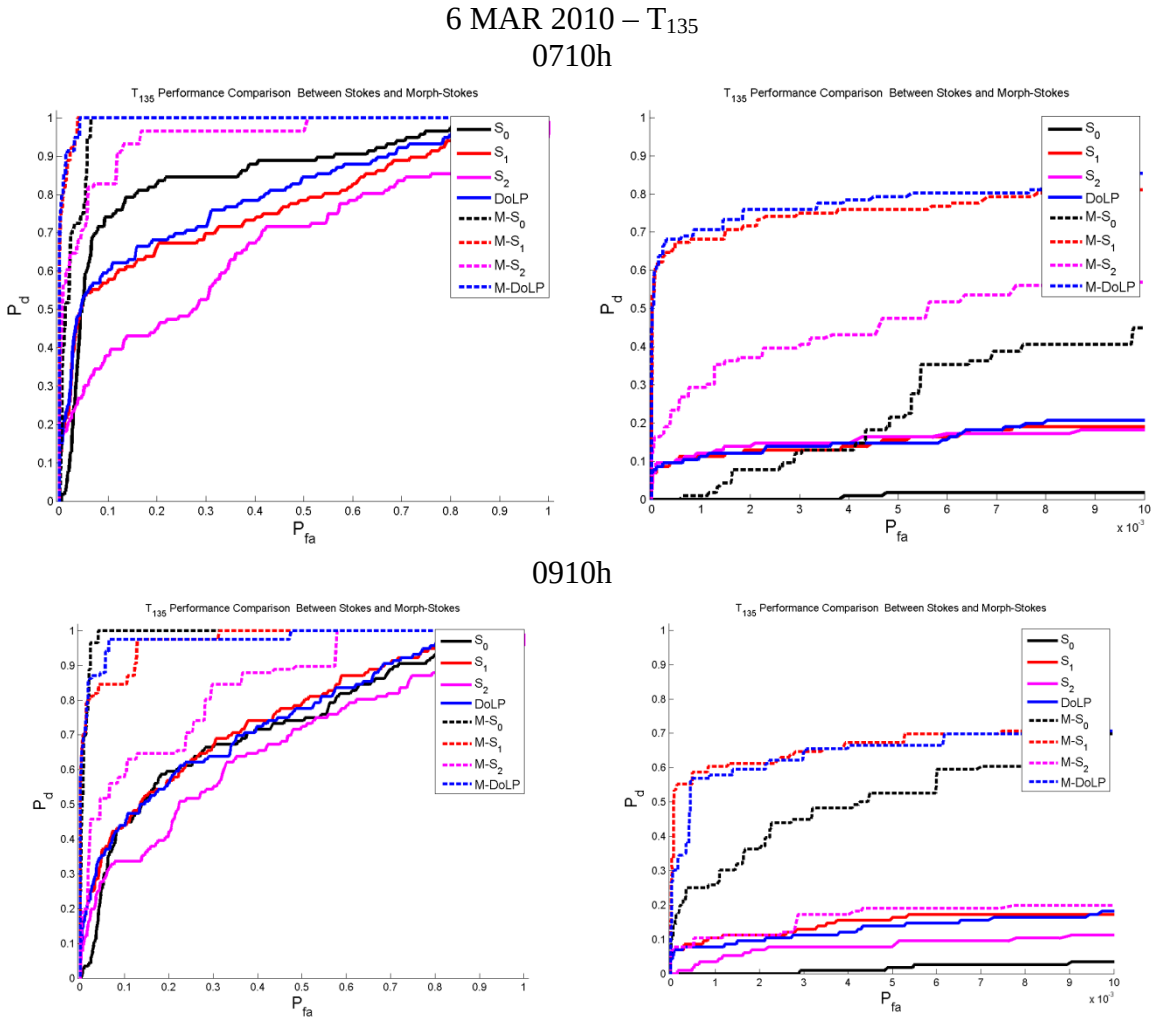

Figure 5.16 ROC curves comparing the performance between conventional and morphologic operator-based Stokes vector and DoLP when detecting T_{135}. The average detection probability given a $P_{fa} = 0.005$ for S_0, S_1, S_2, and DoLP was $P_d = 0.07, 0.25, 0.20, \text{and } 0.13,$ respectively; while Morph-S_0, Morph-S_1, Morph-S_2 and Morph-DoLP achieved a $P_d = 0.48, 0.71, 0.53, \text{and } 0.73,$ correspondingly.

1310h

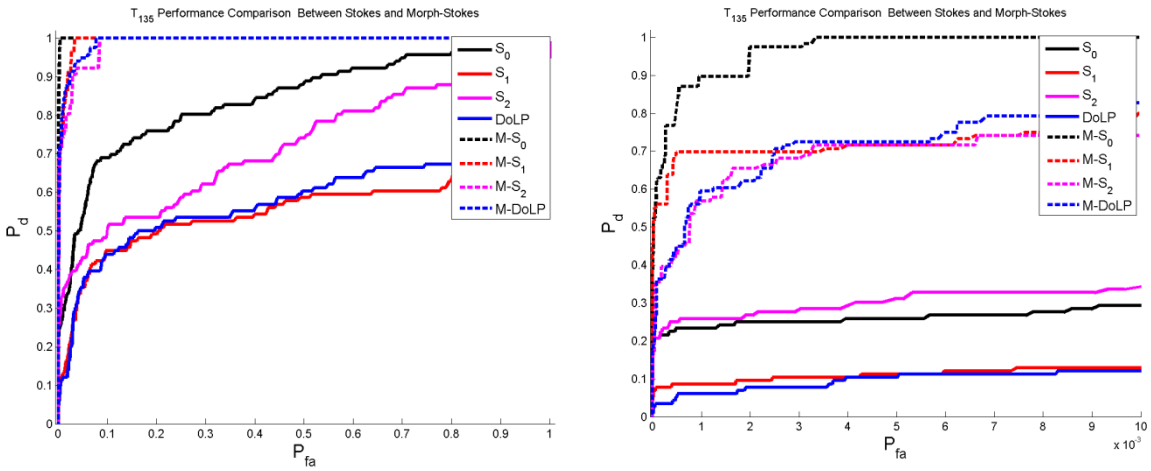

2010h

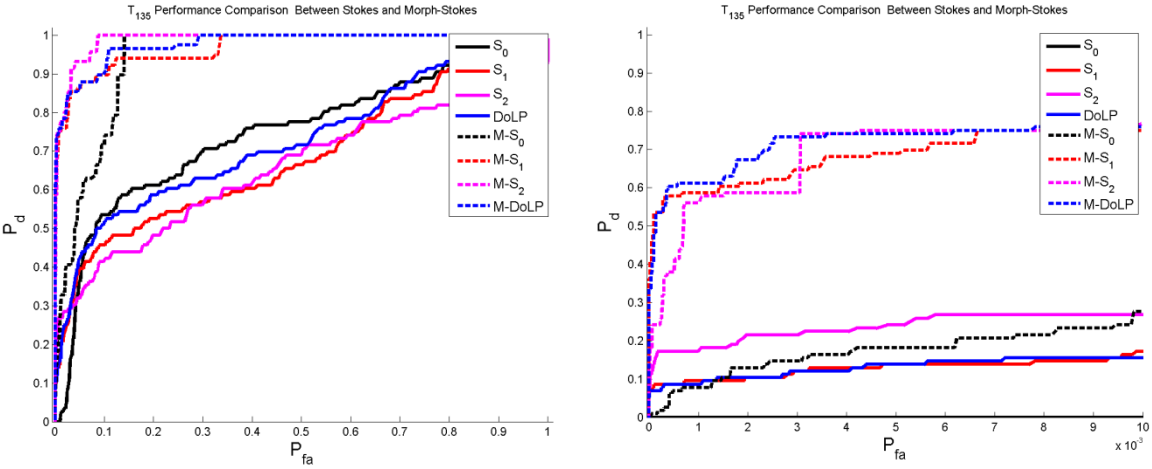

Figure 5.16 ROC curves comparing the performance between conventional and morphologic operator-based Stokes vector and DoLP when detecting T_{135}. The average detection probability given a $P_{fa} = 0.005$ for S_0, S_1, S_2, and DoLP was $P_d = 0.07, 0.25, 0.20, \text{and } 0.13$, respectively; while Morph-S_0, Morph-S_1, Morph-S_2 and Morph-DoLP achieved a $P_d = 0.48, 0.71, 0.53, \text{and } 0.73$, correspondingly. (Continuation)

The ROC curves for the external blackbody can be found in Figure 5.17. In the plots shown on the right side of the figure illustrate S_0 as a non-performing metric for the detection of the blackbody in the desired low false alarm rate region of the ROC curve. In contrast to previous figures, Morph-S_0 only performed considerably better than S_0 for timestamps 0710h, 1310h, and 2010h. For the remaining timestamp 0910h, neither S_0 nor Morph-S_0 detected the blackbody for a $P_{fa} = 0.005$. Morph-S_1 and Morph-DoLP

performed very well relative to their respective conventional Stokes metrics with both Morph-S_1 and Morph-DoLP performing very similarly to each other for 0710h and 0910h. However, for the remainder of the timestamps Morph-S_1 performed considerably better than Morph-DoLP with a probability of detection difference of about 0.30 for 1310h and 0.25 for 2010h for the P_{fa} range between 0.001 and 0.003. Also interestingly, S_2 performed better than Morph-S_2 for the low false alarm rate region at around 0.001, with Morph-S_2 outperforming S_2 for the remainder of the ROC curve.

Considering a constant P_{fa} rate of 0.005 for all metrics, S_0 was unable to detect any portion of the blackbody for all timestamps, while S_1 achieved a P_d of 0.19, 0.21, 0.14, and 0.17, S_2 probability of detection was 0.17, 0.02, 0.21, and 0.24, and finally DoLP had a probability of detection of 0.19, 0.21, 0.12, and 0.14. Morph-S_0 probability of detection, for the $P_{fa} = 0.005$, was as follows: 0.38, 0.0, 0.50, and 0.17, Morph-S_1 and Morph-DoLP probability of detection was about 0.90 for all timestamps, and finally Morph-S_2 probability of detection was 0.62, 0.0, 0.40, and 0.38.

For the detection of the blackbody, the average probability of detection given a $P_{fa} = 0.005$ for S_0, S_1, S_2, and DoLP was $P_d = 0.00, 0.18, 0.16, \text{and } 0.17$ respectively, and $P_d = 0.26, 0.91, 0.35, \text{and } 0.91$ for Morph-S_0, Morph-S_1, Morph-S_2, and Morph-DoLP, correspondingly.

6 MAR 2010 – Blackbody
0710h

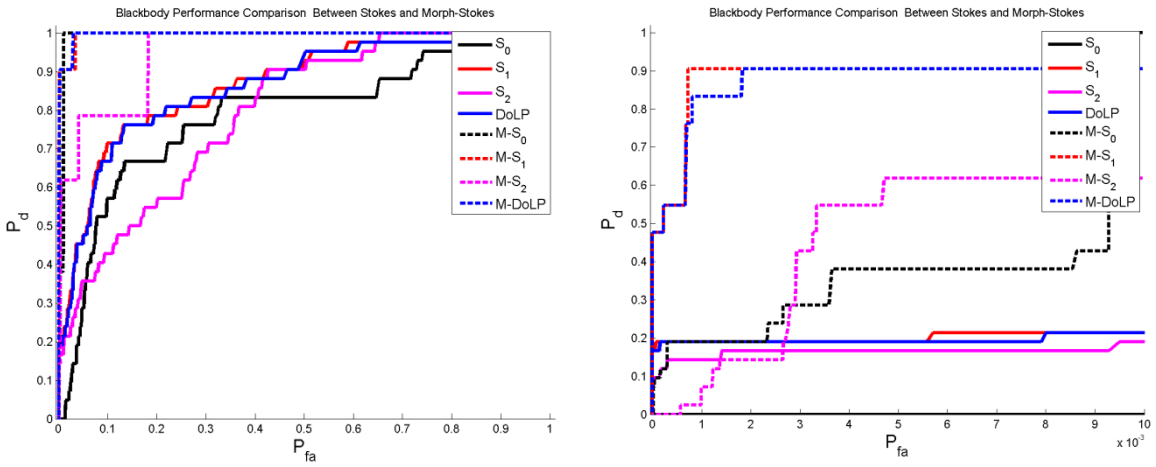

0910h

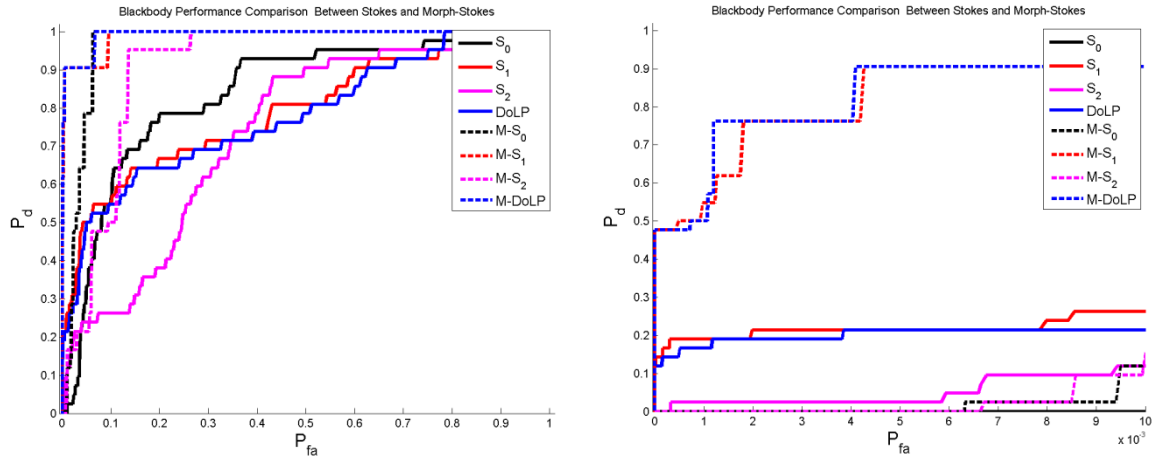

Figure 5.17 ROC curves comparing the performance between conventional and morphologic operator-based Stokes vector and DoLP when detecting the external blackbody. The average detection rate given a $P_{fa} = 0.005$ for S_0, S_1, S_2, and DoLP was $P_d = 0.00, 0.18, 0.16, \text{and } 0.17$, respectively and $P_d = 0.26, 0.91, 0.35, \text{and } 0.91$ for Morph-S_0, Morph-S_1, Morph-S_2, and Morph-DoLP, correspondingly.

1310h

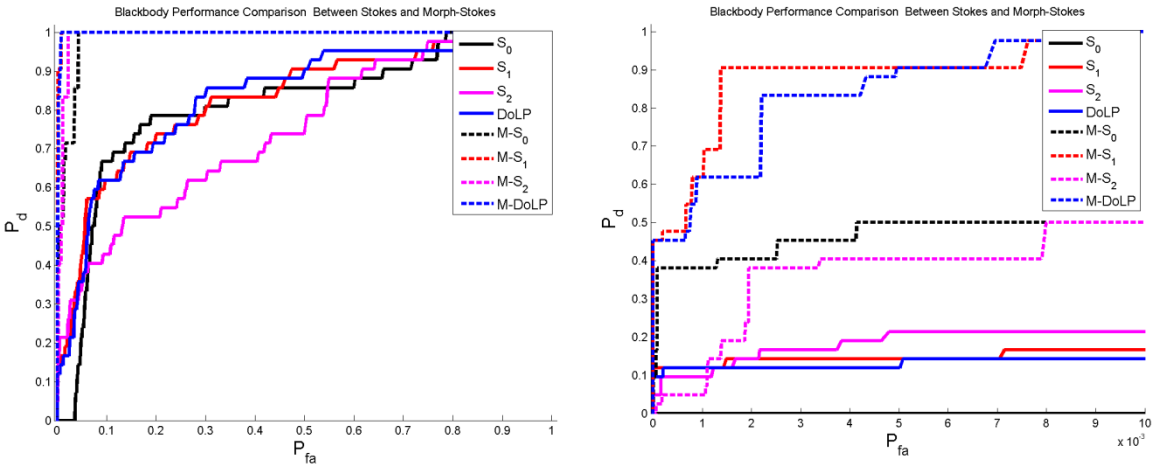

2010h

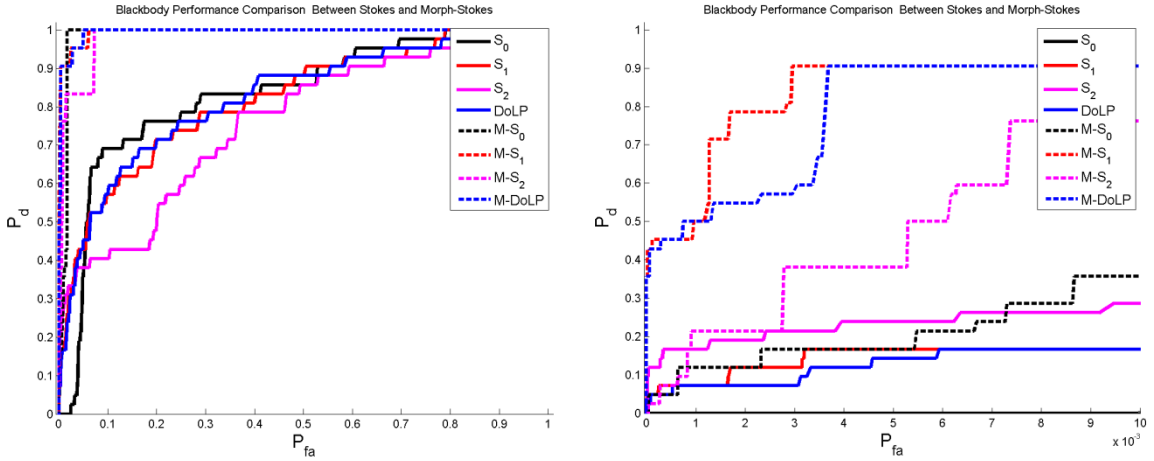

Figure 5.17 ROC curves comparing the performance between conventional and morphologic operator-based Stokes vector and DoLP when detecting the external blackbody. The average detection rate given a $P_{fa} = 0.005$ for S_0, S_1, S_2, and DoLP was $P_d = 0.00, 0.18, 0.16, \text{and } 0.17,$ respectively and $P_d = 0.26, 0.91, 0.35, \text{and } 0.91$ for Morph-S_0, Morph-S_1, Morph-S_2, and Morph-DoLP, correspondingly. (Continuation)

The performance curves between conventional and morphology-based Stokes/DoLP for the observation tower can be found in Figure 5.18. One observes that Stokes parameters S_0 and S_2 were unable to detect the observation tower for the low false alarm rate region for all timestamps while S_1 and DoLP once again performed very similarly to each other with an average probability of detection of about 0.30 for timestamps 0710h, 0910h, and 1310h, and 0.20 for 2010h. As with its conventional

metrics, Morph-S_0 was unable to detect the observation tower for all the timestamps however, Morph-S_2 was able to detect small portions of the observation tower relative to S_2. Morph-S_1 and Morph-DoLP performed very similarly to each other for all timestamps, with the exception of timestamp 2010h, with an average probability of detection of 0.80 throughout the low false alarm region of the ROC curve. For 2010h, Morph-S_1 performed slightly better than Morph-DoLP for the very low false alarm region ($P_{fa} < 0.002$) with Morph-DoLP converging on Morph-S_1 detection rate at around $P_{fa} = 0.005$.

Using a constant false alarm rate of 0.005, S_0, S_2, Morph-S_0, and Morph-S_2 were unable to detect the observation tower, while S_1 and DoLP had similar performance of about 0.33, 0.30, 0.33, and 0.18 for the respective timestamps. Morph-S_1 and Morph-DoLP performed similarly with a constant detection rate of about 0.80 for all timestamps.

The average detection probability given a $P_{fa} = 0.005$ in discriminating the tower from natural clutter for all timestamps for S_0, S_1, S_2, and DoLP was $P_d = 0.00, 0.28, 0.00, \text{and } 0.28$ respectively, while for Morph-S_0, Morph-S_1, Morph-S_2, and Morph-DoLP was $P_d = 0.00, 0.80, 0.08, \text{and } 0.80$, correspondingly.

6 MAR 2010 – Observation tower
0710h

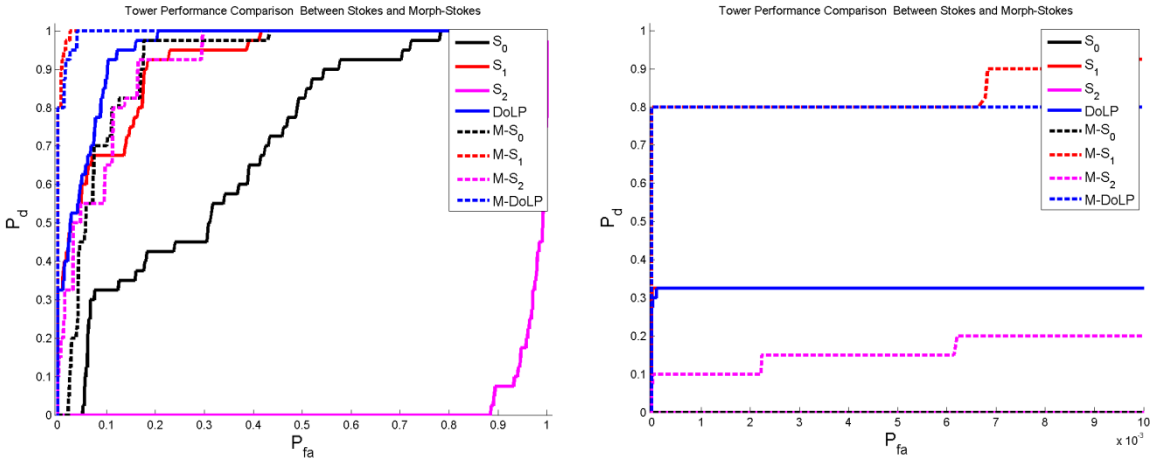

0910h

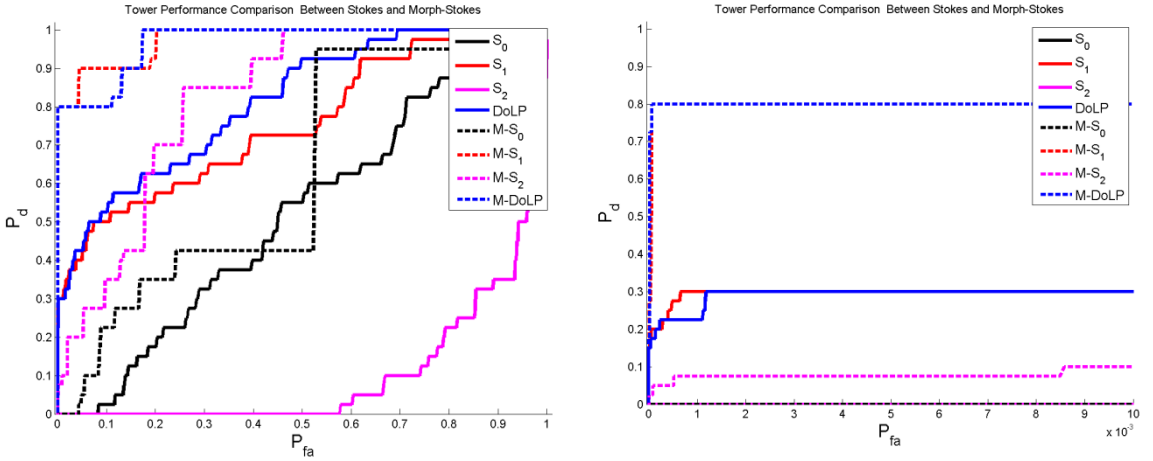

Figure 5.18 ROC curves comparing the performance between regular and morphologic operator-based Stokes vector and DoLP when detecting the observation tower. The average detection probability given a $P_{fa} = 0.005$ for all timestamps for S_0, S_1, S_2, and DoLP was $P_d = 0.00, 0.28, 0.00,$ and 0.28 respectively, while for Morph-S_0, Morph-S_1, Morph-S_2, and Morph-DoLP was $P_d = 0.00, 0.80, 0.08,$ and 0.80, correspondingly.

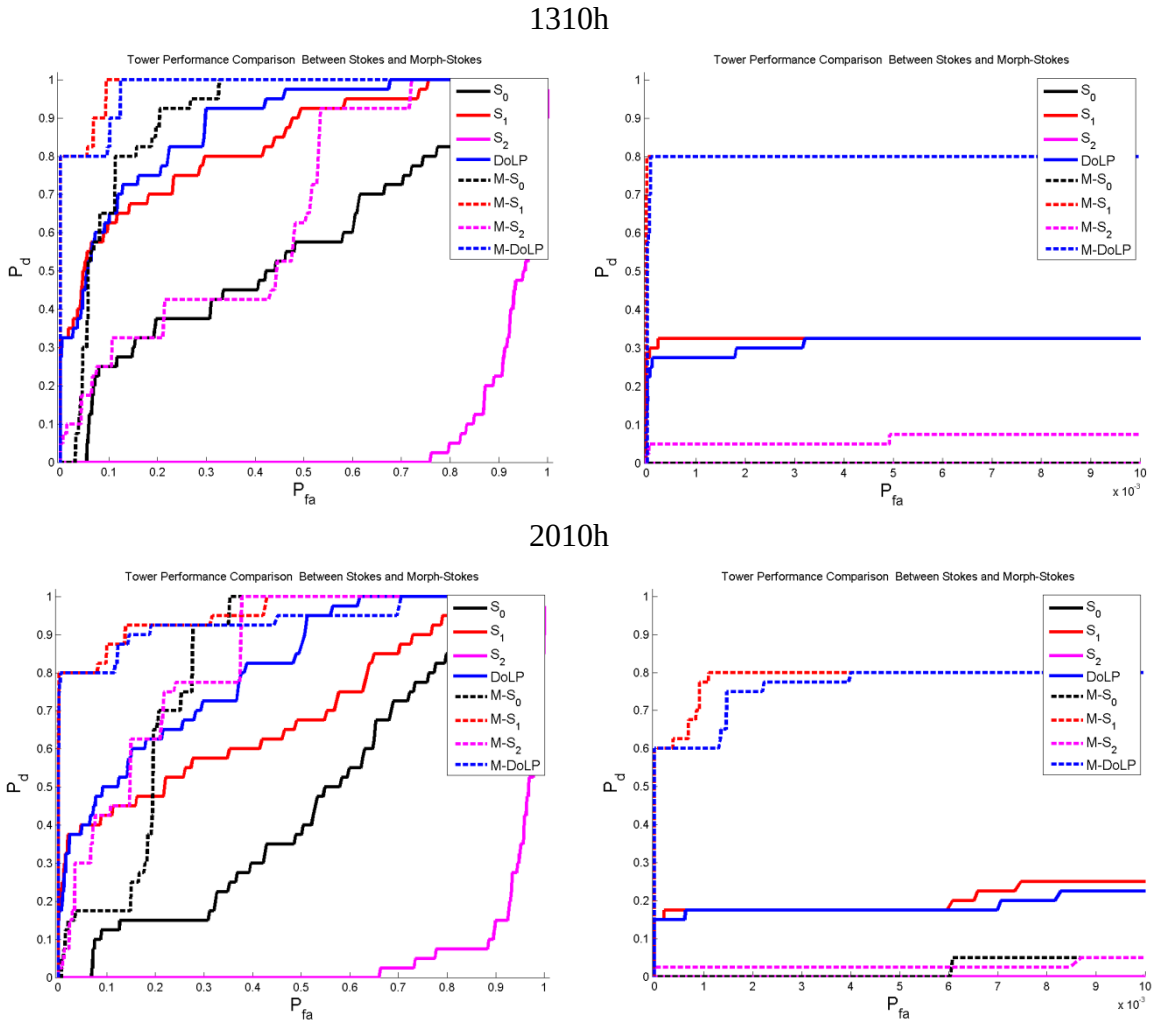

Figure 5.18 ROC curves comparing the performance between regular and morphologic operator-based Stokes vector and DoLP when detecting the observation tower. The average detection probability given a $P_{fa} = 0.005$ for all timestamps for S_0, S_1, S_2, and DoLP was $P_d = 0.00, 0.28, 0.00,$ and 0.28 respectively, while for Morph-S_0, Morph-S_1, Morph-S_2, and Morph-DoLP was $P_d = 0.00, 0.80, 0.08,$ and 0.80, correspondingly. (Continuation)

Finally, Figure 5.19 illustrates the performance of all metrics in detecting all manmade objects as a single class. Once again, focusing on the right side of Figure 5.19, S_0 performed very poorly for all timestamps with the exception of 1310h where the average probability of detection was about 0.15 of all manmade object pixels in the scene. Morph-S_0 outperformed S_0 detection rate by 0.17, 0.48, 0.64, and 0.14 for the respective timestamps for a $P_{fa} = 0.005$. As expected, Morph-S_1 outperformed S_1 by as

much as 0.61, 0.54, 0.61, and 0.57 for the respective timestamps and for $P_{fa} = 0.005$. The probability of detection difference between Morph-DoLP and its conventional metric, DoLP, was 0.63, 0.54, 0.61, and 0.60 and the difference between Morph-S_2 and S_2 was calculated as 0.31, 0.13, 0.37, and 0.30 for the same false alarm rate and timestamps.

The average probability of detection given a $P_{fa} = 0.005$ of all manmade objects for S_0, S_1, S_2, and DoLP was $P_d = 0.05, 0.22, 0.18, \text{and } 0.20$ correspondingly, and for the morphology-based Stokes and DoLP; Morph-S_0, Morph-S_1, Morph-S_2, and Morph-DoLP the average detection rate was $P_d = 0.41, 0.81, 0.45, \text{and } 0.79$, respectively.

Observing Figures 5.14 through 5.19, one can, therefore, conclude that the implementation of morphology-based filters on conventional Stokes parameters yields a significant increase in the probability of detection for the same false alarm rate. Furthermore, the increase in probability of detection achieved by Morph-S_1 and Morph-DoLP at low false alarm rates makes them good contenders as anomaly detectors for both aided and unmanned operational systems.

6 MAR 2010 – Overall Performance
0710h

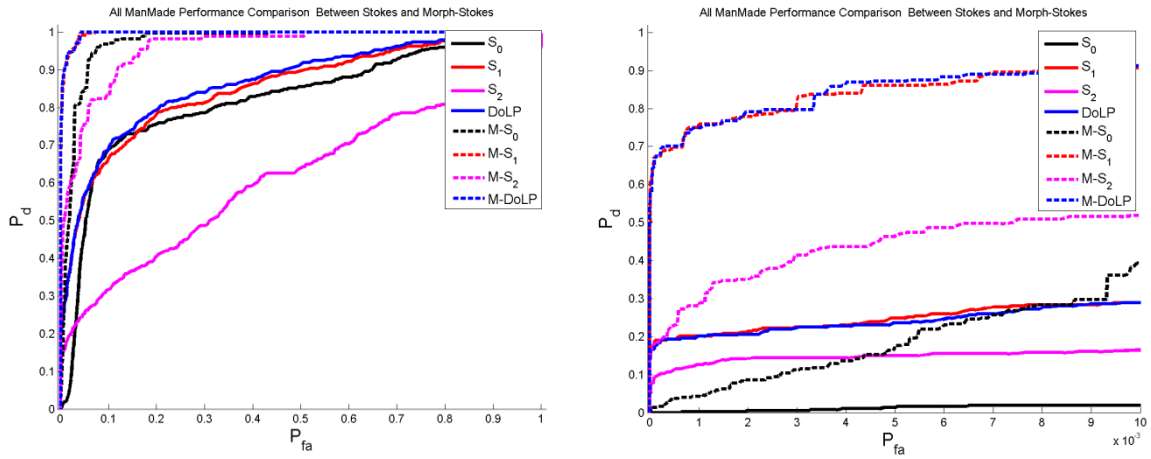

0910h

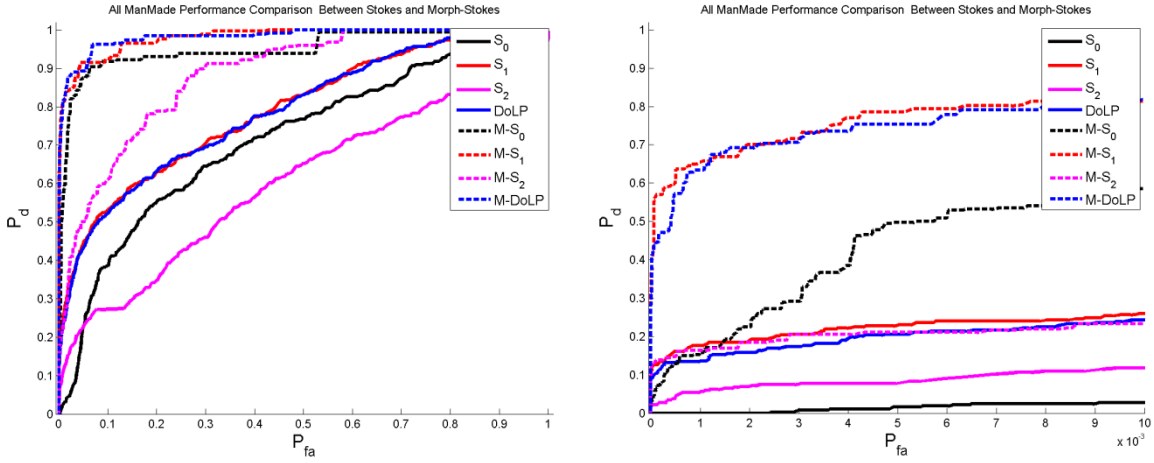

Figure 5.19 ROC curves comparing conventional and morphologic operator-based Stokes vector and DoLP when all manmade objects are combined into one class. The average probability of detection given a $P_{fa} = 0.005$ for S_0, S_1, S_2, and DoLP was $P_d = 0.05, 0.22, 0.18, \text{and } 0.20$ correspondingly, and for the morphology-based Stokes and DoLP; Morph-S_0, Morph-S_1, Morph-S_2, and Morph-DoLP the average detection rate was $P_d = 0.41, 0.81, 0.45, \text{and } 0.79$, respectively.

1310h

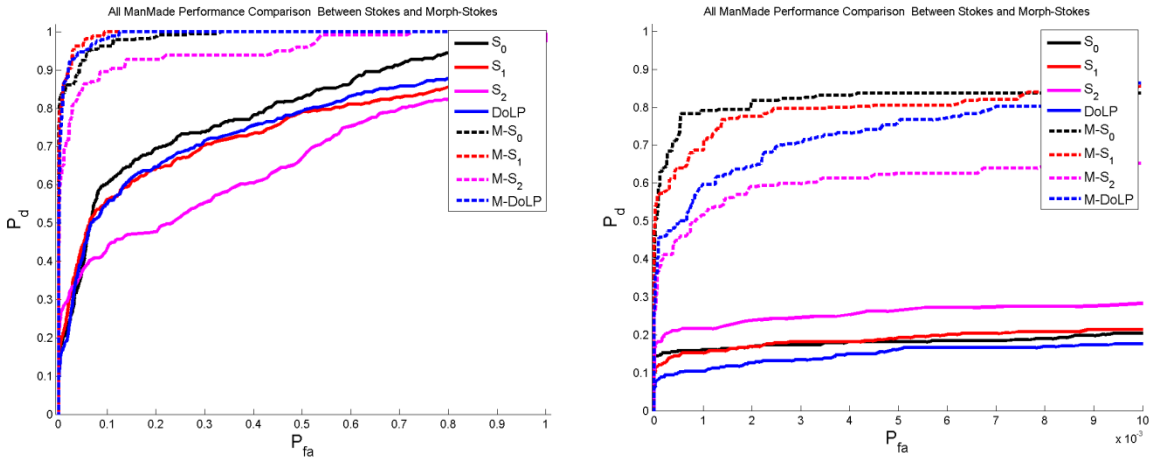

2010h

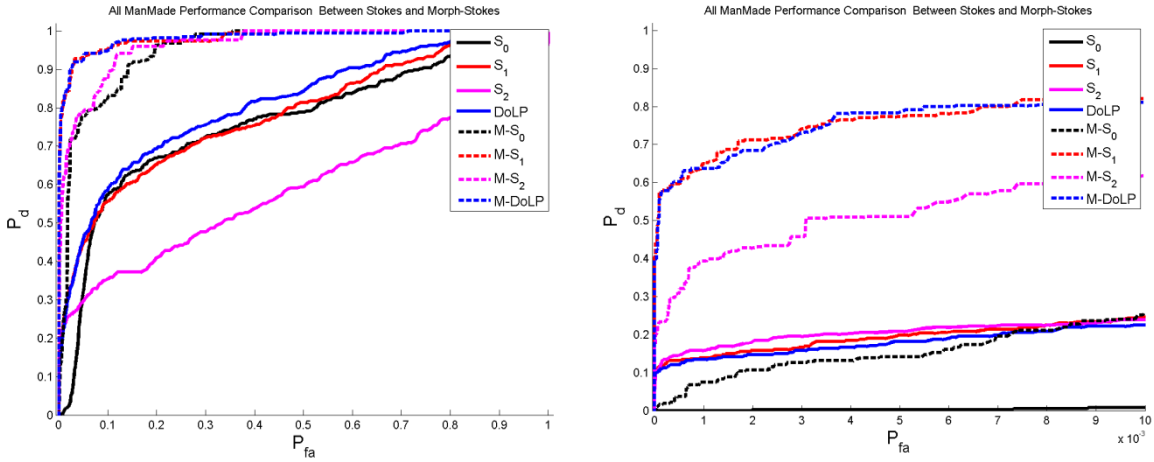

Figure 5.19 ROC curves comparing conventional and morphologic operator-based Stokes vector and DoLP when all manmade objects are combined into one class. The average probability of detection given a $P_{fa} = 0.005$ for S_0, S_1, S_2, and DoLP was $P_d = 0.05, 0.22, 0.18, \text{and } 0.20$ correspondingly, and for the morphology-based Stokes and DoLP; Morph-S_0, Morph-S_1, Morph-S_2, and Morph-DoLP the average detection rate was $P_d = 0.41, 0.81, 0.45, \text{and } 0.79$, respectively. (Continuation)

Tables 5.2 through 5.5 demonstrate the probability of detection for all manmade objects for a constant $P_{fa} = 0.005$ for timestamps 0710h, 0910h, 1310h, and 2010h, as well as 0210h and 2310h where conventional Stokes/DoLP P_d is shown in black and morphology-based Stokes/DoLP in red. The intent of each of the tables is to compare the effectiveness of morphology-based Stokes/DoLP to conventional Stokes for each of the timestamps and manmade objects in an easy to read table format.

The tables demonstrate that, in general, applying the morphology-based filters to conventional Stokes/DoLP increases the probability of detection for all manmade objects regardless of which Stokes/DoLP parameter is used as input to the filters. However, certain anomalies can be found, for example in Table 5.4, the performance of Morph-S_2 at timestamps 0210h and 0910h was inferior to conventional S_2 but regardless, on average, the morphology-based Stokes (in red) parameters are consistently and considerably better performers than conventional Stokes (in black).

From Table 5.2, the average probability of detection of S_0 over the six timestamps for each of the targets was as follows: 0.04, 0.05, 0.05, 0.0, 0.0, and 0.04 for T_0, T_{90}, T_{135}, blackbody, observation tower, and overall, respectively. Conversely, Morph-S_0 average performance for the same targets was 0.37, 0.40, 0.39, 0.31, 0.0, and 0.34. As per Table 5.3, the probability of detection difference between S_1 and Morph-S_1 was quite significant with S_1 exhibiting an average probability of detection of 0.28, 0.24, 0.14, 0.16, 0.27, and 0.21 for T_0, T_{90}, T_{135}, blackbody, observation tower, and overall respectively, while Morph-S_1 demonstrated an average probability detection of 0.87, 0.79, 0.70, 0.89, 0.80, and 0.79 for the same target set. On the other hand, observing Table 5.4, S_2 exhibited poor performance relative to S_1 and DoLP with an average probability of detection of 0.19, 0.23, 0.18, 0.19,0.0, and 0.18 while Morph-S_2 demonstrated an enhanced detection performance relative to conventional S_2 with a probability of detection of 0.34, 0.59, 0.51, 0.31, 0.10, and 0.43 for T_0, T_{90}, T_{135}, blackbody, observation tower, and overall, correspondingly. Finally, DoLP and Morph-DoLP performed similarly to S_1 and Morph-S_1 respectively, with DoLP exhibiting an average probability of detection, as per the values in Table 5.5, of 0.23, 0.22, 0.13, 0.15, 0.25, and

0.19 while Morph-DoLP demonstrated an average probability of detection of 0.80, 0.78, 0.72, 0.88, 0.79, and 0.78.

Table 5.2 S_0 (black) and Morph-S_0 (red) Probability of Detection for Different Timestamps for a $P_{fa} = 0.005$

	T_0		**T_{90}**		**T_{135}**		**Blackbody**		**Observation Tower**		**Overall**	
0210h	0.01	0.16	0.02	0.22	0.02	0.22	0	0.57	0	0	0.01	0.22
0710h	0.03	0.04	0.01	0.22	0.02	0.22	0	0.38	0	0	0.01	0.18
0910h	0	0.87	0.04	0.59	0.02	0.53	0	0	0	0	0.02	0.50
1310h	0.23	1.00	0.20	1.00	0.26	1.00	0	0.50	0	0	0.18	0.84
2010h	0	0.05	0.01	0.21	0	0.18	0	0.17	0	0	0.003	0.14
2310h	0	0.07	0.01	0.17	0	0.18	0	0.24	0	0.03	0.003	0.14

Table 5.3 S_1 (black) and Morph-S_1 (red) Probability of Detection for Different Timestamps for a $P_{fa} = 0.005$

	T_0		**T_{90}**		**T_{135}**		**Blackbody**		**Observation Tower**		**Overall**	
0210h	0.23	0.79	0.22	0.71	0.14	0.65	0.07	0.88	0.18	0.80	0.17	0.73
0710h	0.32	0.96	0.30	0.91	0.16	0.76	0.19	0.90	0.33	0.80	0.25	0.86
0910h	0.24	0.85	0.28	0.81	0.16	0.67	0.21	0.90	0.30	0.80	0.23	0.77
1310h	0.23	0.87	0.23	0.82	0.11	0.71	0.14	0.90	0.32	0.80	0.19	0.80
2010h	0.33	0.88	0.19	0.72	0.14	0.69	0.17	0.90	0.18	0.80	0.20	0.77
2310h	0.31	0.85	0.21	0.77	0.11	0.72	0.17	0.86	0.28	0.80	0.20	0.78

Table 5.4 S_2 (black) and Morph-S_2 (red) Probability of Detection for Different Timestamps for a $P_{fa} = 0.005$

	T_0		T_{90}		T_{135}		Blackbody		Observation Tower		Overall	
0210h	0.15	0.9	0.19	0.51	0.15	0.51	0.26	0.12	0	0.08	0.16	0.33
0710h	0.12	0.27	0.21	0.65	0.16	0.47	0.17	0.62	0	0.15	0.15	0.46
0910h	0.05	0.13	0.15	0.44	0.08	0.19	0.02	0	0	0.08	0.08	0.21
1310h	0.28	0.76	0.34	0.74	0.31	0.72	0.21	0.40	0	0.08	0.26	0.63
2010h	0.21	0.36	0.24	0.59	0.24	0.75	0.24	0.38	0	0.03	0.21	0.51
2310h	0.31	0.41	0.24	0.63	0.20	0.39	0.26	0.31	0	0.15	0.22	0.43

Table 5.5 DoLP (black) and Morph-DoLP (red) Probability of Detection for Different Timestamps for a $P_{fa} = 0.005$

	T_0		T_{90}		T_{135}		Blackbody		Observation Tower		Overall	
0210h	0.21	0.79	0.20	0.63	0.14	0.68	0.07	0.88	0.18	0.75	0.17	0.72
0710h	0.28	0.96	0.29	0.91	0.15	0.79	0.19	0.90	0.33	0.80	0.24	0.87
0910h	0.23	0.67	0.23	0.84	0.14	0.66	0.21	0.90	0.30	0.80	0.21	0.75
1310h	0.12	0.67	0.21	0.82	0.10	0.72	0.12	0.90	0.33	0.80	0.16	0.77
2010h	0.27	0.85	0.19	0.72	0.14	0.74	0.14	0.90	0.18	0.80	0.18	0.78
2310h	0.25	0.88	0.19	0.73	0.12	0.71	0.14	0.80	0.20	0.80	0.17	0.76

Figures 5.20 through 5.21 illustrate the output surfaces (top) obtained from conventional (left) and morphology-based Stokes (right) and their respective thresholded outputs on the bottom image. The two images chosen illustrate a low contrast scenario observed at 0210h and a high contrast scenario captured at 1310h. The output surfaces were normalized from 0 to 1 so to accurately compare each metric and the bottom image

was thresholded using a δ=5 threshold value. In order to aid the reader, pixels belonging to the three surrogate targets that were above the threshold are represented by the color white, other manmade objects such as the observation tower and blackbody are represented by the color green, false alarms are represented by the color red, and finally all pixels with values below the threshold are represented by the color black.

Observing the performance between S_0 and Morph-S_0 for Figure 5.20, one notices that S_0 is unable to detect any of the manmade objects in the scene, while for timestamp 1310h (Figure 5.21), T_0, T_{90} and T_{135} are partially visible with a small false alarm at the top of the output surface. Alternatively, Morph-S_0 was only able to detect the edges of T_0, T_{90}, T_{135}, and the blackbody for the low contrast scene (Figure 5.20) as well as a high number of false alarms making Morph-S_0 not a useful discriminator. Conversely, in high contrast imagery Figure 5.21, Morph-S_0 was able to detect a significant portion of the targets' area with a small number of false alarms present in the binary image.

Both Morph-S_1 and Morph-DoLP performed quite well relative to conventional S_1 and DoLP for both timestamps (Figures 5.20 and 5.21) and for all of the targets present in the scene. The morphological operators were able to significantly reduce the number of false alarms present in conventional imagery while enhancing the manmade targets' features, increasing the number of pixels found for each of the manmade objects. A good example is Figure 5.21 for S_1 and DoLP where the number of false alarms present clearly hinders any possibility of discriminating the surrogate targets or the blackbody from natural clutter. After the morphological filters are applied to conventional S_1 or DoLP, the number of false alarms present in the original imagery is reduced significantly, while the manmade objects are clearly identified.

The Stokes parameter S_2 performed very poorly in detecting all of the manmade objects present in the scene given the 5σ threshold for Figures 5.20 and 5.21. Only portions of T_{90} are continuously detected throughout the two timestamps, while for the remainder of the surrogate targets, only small portions could be successfully detected at timestamp 1310h. Once again, when the morphological operators are applied to the S_2 imagery, one can observe an increase in the detection of T_{90}'s surface area relative to S_2 for all timestamps; portions of T_{135} are successfully detected in all timestamps, even when conventional S_2 was not able to detect it.

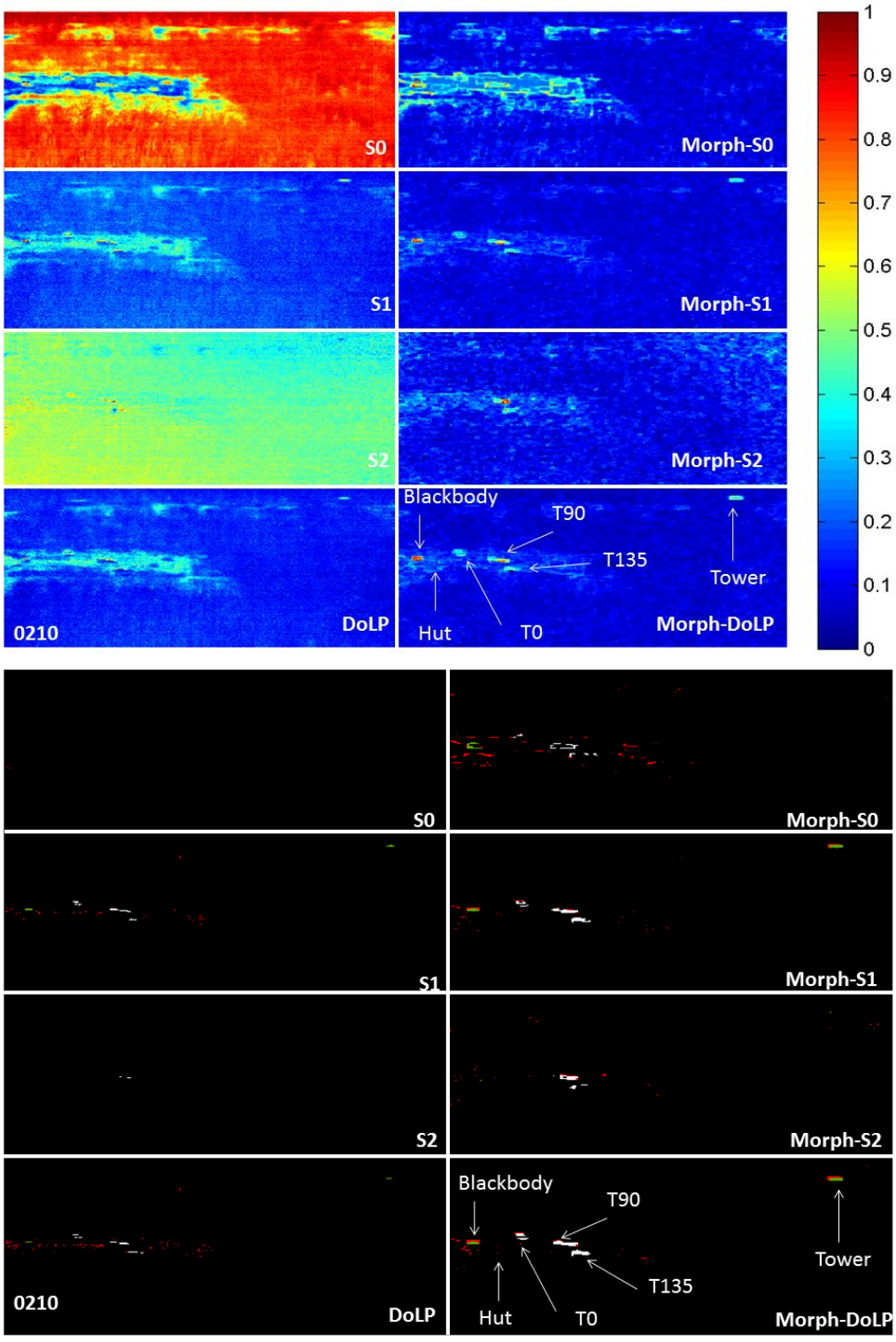

Figure 5.20 Output surfaces (above image) for conventional and morphologic operator-based Stokes and DoLP at 0210h and the respective thresholded outputs for a $\delta = 5$ (bottom image). White pixels represent the surrogate targets, the green pixels represent the blackbody and observation tower, while the red pixels represent the false alarms found in the image.

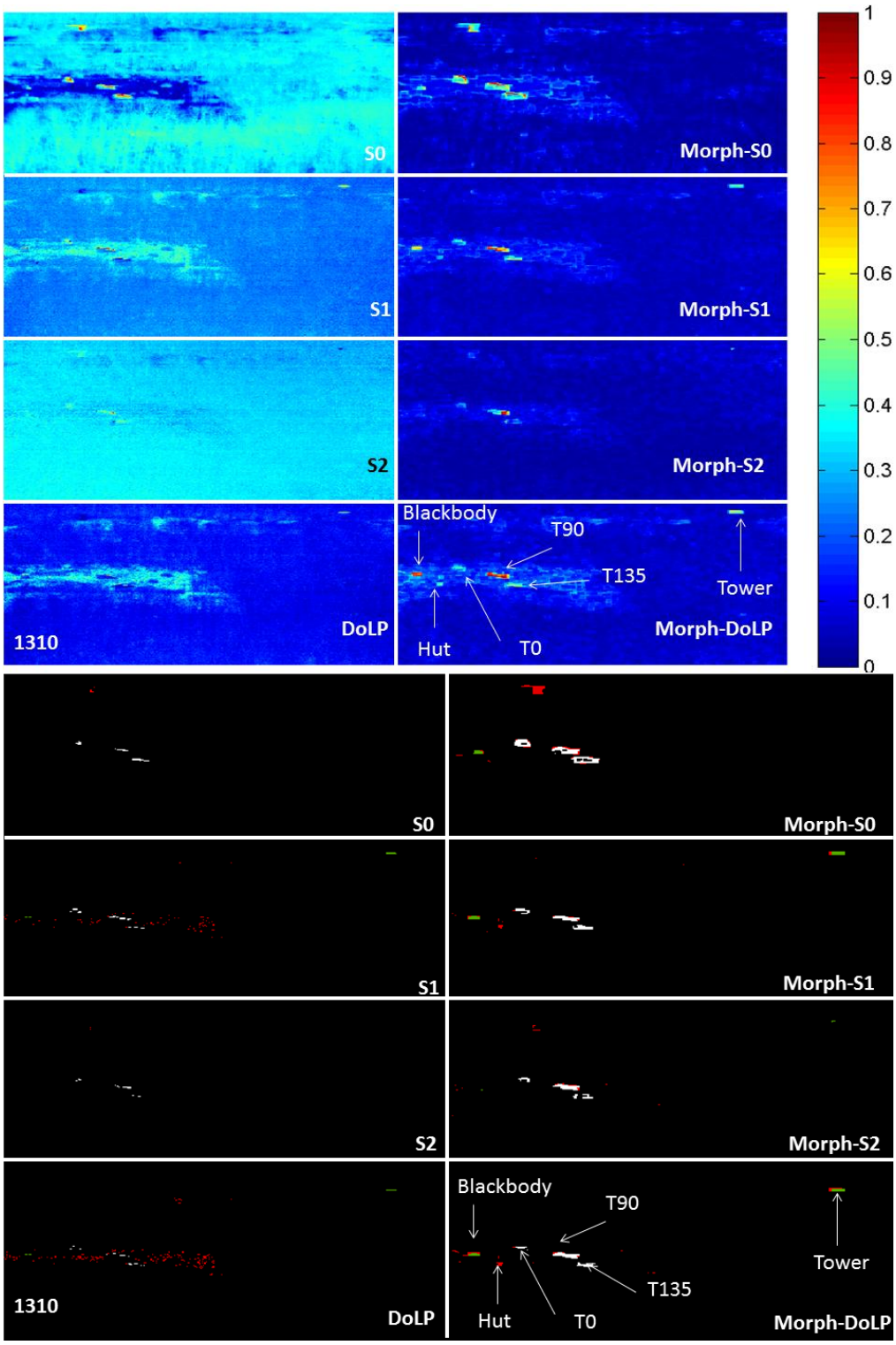

Figure 5.21 Output surfaces (above image)for conventional and morphologic operator-based Stokes and DoLP at 1310h and the respective thresholded outputs for a $\delta = 5$ (bottom image). White pixels represent the surrogate targets, the green pixels represent the blackbody and observation tower, while the red pixels represent the false alarms found in the image.

Figure 5.22 illustrates the probability of detection of S_0 and Morph-S_0 for each of the targets in the scene for a full 72-hour performance period starting on 6 MAR 2010 at 0000h and ending on 8 MAR 2010 at 2350h for a constant false alarm rate of $P_{fa} = 0.005$. One should remember that for the first and third day (6 and 8 MAR) T_0 and T_{90} were turned *off* while on the second day the heating elements under the targets fuselage were turned *on* mimicking an operating vehicle. T_{135}, on the other hand, remained *off* for the full three days.

One can readily observe that Morph-S_0 was more effective in discriminating all surrogate targets, under low contrast situations when compared to conventional S_0. During the periods of high humidity, starting around 2300h on day 2 through 0300h on day 3 and 1900h through 2359h on day 3, one can observe that the performance of Morph-S_0 for T_0 degraded significantly, however its performance was still slightly higher or similar to conventional S_0. For periods of low contrast and low humidity (early hours of 6 MAR 2010), the probability of detection difference between Morph-S_0 and S_0, $P_{d(morph\text{-}S0)}$-$P_{d(S0)}$, was $P_d \sim 0.15$ for T_0, where ~ denotes approximately, and $P_d \sim 0.20$ for T_{90} and T_{135}, $P_d \sim 0.58$ for the blackbody, and $P_d \sim 0.0$ for the observation tower. Alternatively, for high contrast imagery (e.g., 1100h-1600h for day 1, 2 and 3), the P_d difference between Morph-S_0 and S_0 is $P_d \sim 0.70$ for T_0, $P_d \sim 0.80$ for $T_{90,}$ and $P_d \sim 0.60$ for T_{135}. Interestingly, one can observe that the blackbody P_d difference between Morph-S_0 and S_0 is a decreasing function with respect to time, where similar performance to S_0 can be observed during the time periods where high humidity was prevalent in the scene. The observation tower, although visible in the output surfaces did not fair too well for the false alarm rate chosen, $(P_{fa} = 0.005)$ where the P_d difference between the two metrics

(S_0 and Morph-S_0) was very similar ($P_d \sim 0.0$) over the 72 hours except for the periods of high contrast. During the periods of high contrast, the P_d difference between the two metrics around 1300h was on average $P_d \sim 0.50$. Finally, observing the trend in Figure 5.22 for the overall performance, one can conclude that during the periods of no solar loading, Morph-S_0 exhibited a $P_d \sim 0.20$ higher than conventional S_0, while for the periods of solar loading, this difference reached a maximum of 0.60 on average. In summary, one can conclude that the Morph-S_0 outperformed conventional S_0 for the full 72 hours regardless of the timestamps and target set, with the exception of the observation tower, where the probability of detection was very similar for both metrics during the periods of low contrast.

The average 72-hour probability of detection for T_0, T_{90}, T_{135}, blackbody, observation tower, and overall was $P_d = 0.07, 0.04, 0.07, 0.00, 0.03, \text{and } 0.05$ respectively, for S_0; while Morph-S_0 achieved a $P_d = 0.62, 0.49, 0.46, 0.23, 0.13, \text{and } 0.44$. The P_d difference between Morph-S_0 and S_0 was measured to be $0.55, 0.45, 0.39, 0.23, 0.10, \text{and } 0.39$ for T_0, T_{90}, T_{135}, blackbody, observation tower, and overall, correspondingly.

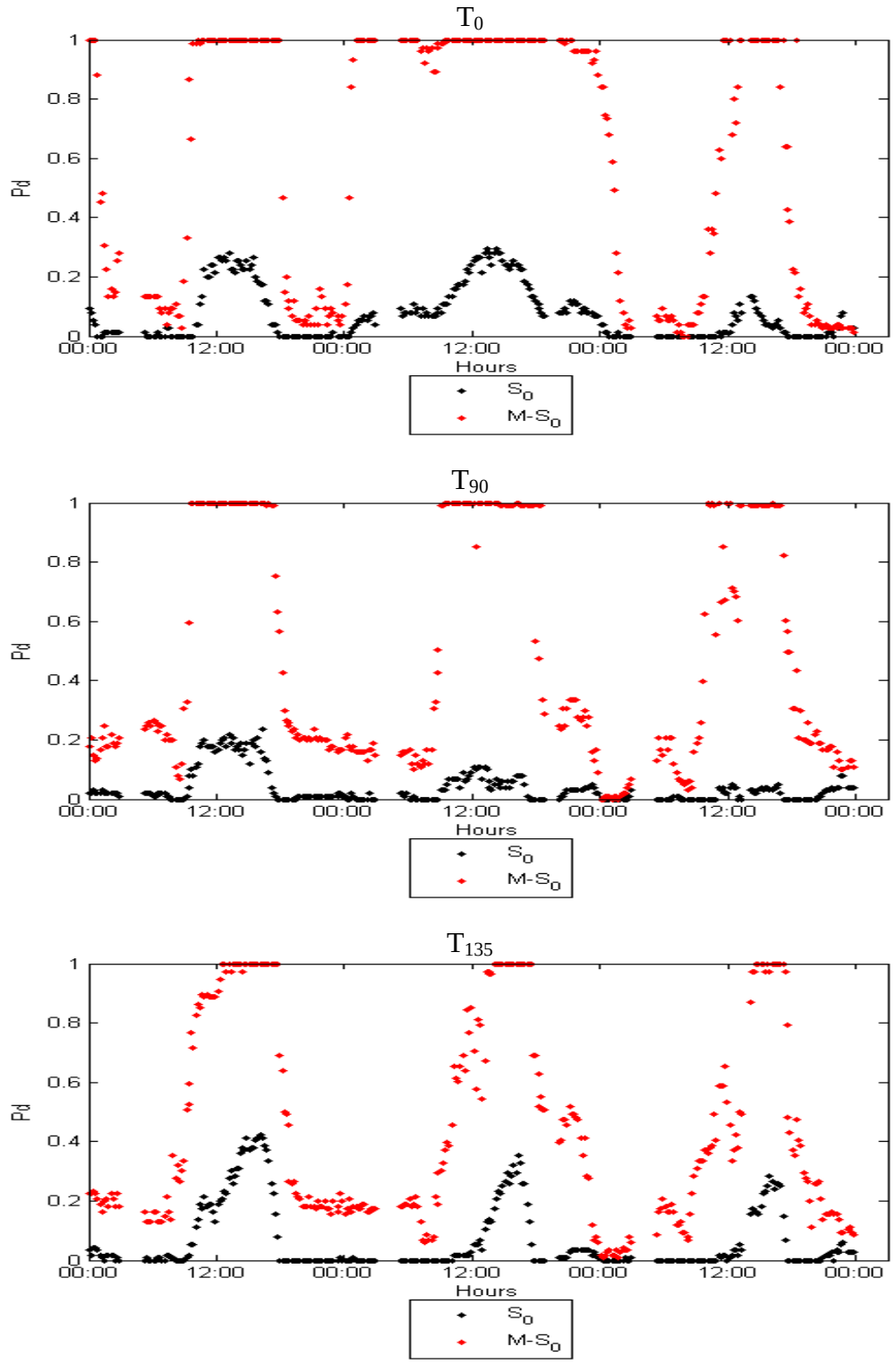

Figure 5.22 72-hour probability of detection curves comparing Stokes parameter S_0 and Morph-S_0.

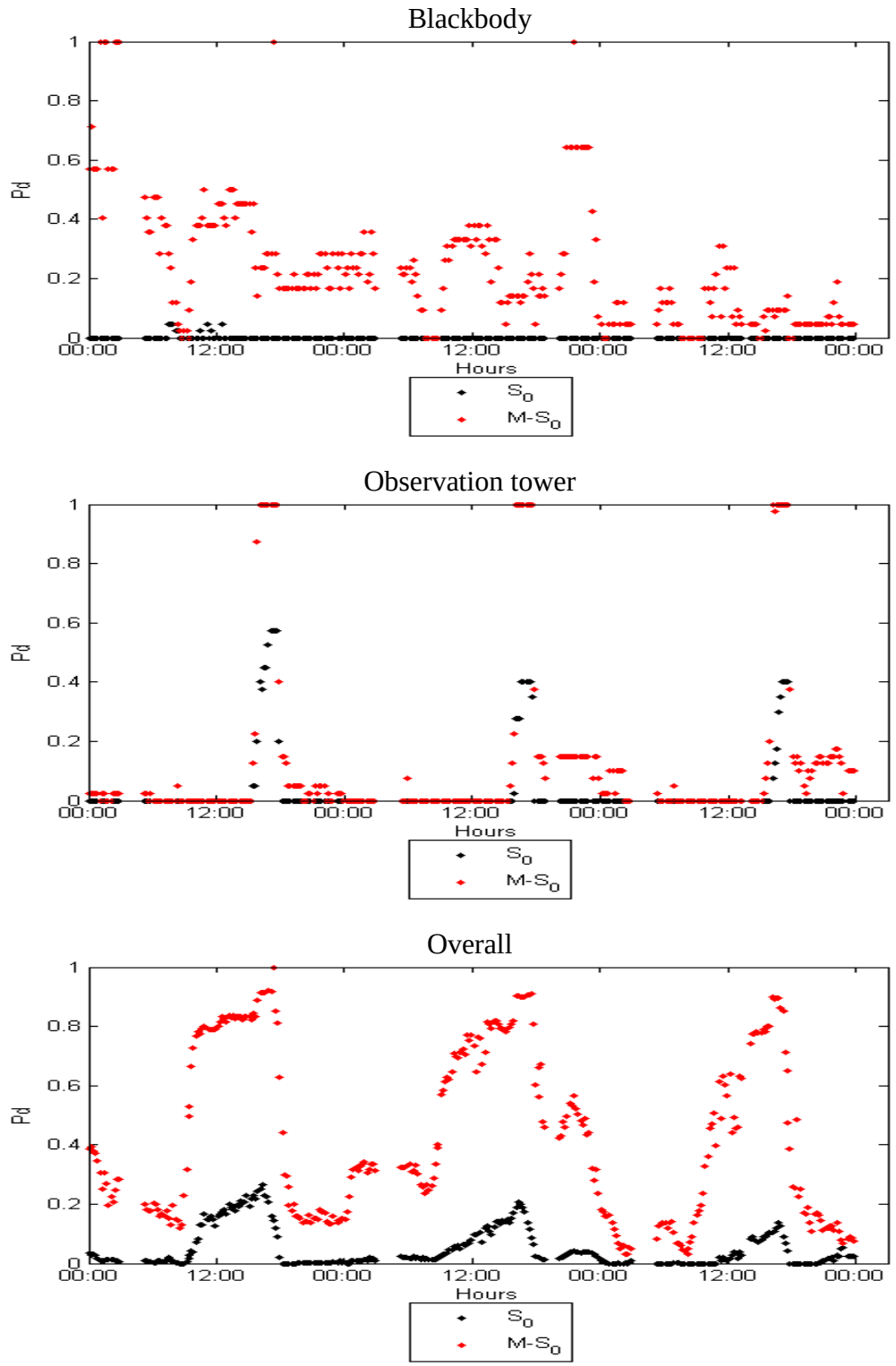

Figure 5.22 72-hour probability of detection curves comparing Stokes parameter S_0 and Morph-S_0. (Continuation)

Morph-S_1 and Morph-DoLP, Figures 5.23 and 5.24, performed very similarly to each other with an average probability of detection for all manmade objects of $P_d \sim 0.75$ compared to S_1 ($P_d = 0.23$) and DoLP ($P_d = 0.22$). Morph-S_1 and Morph-DoLP average probability of detection for the entire 72-hour period were as follows: 0.87 (Morph-S_1) and 0.84 (Morph-DoLP) for T_0, 0.74 (Morph-S_1 and Morph-DoLP) for T_{90}, 0.66 (Morph-S_1 and Morph-DoLP) for T_{135}, 0.82 (Morph-S_1) and 0.76 (Morph-DoLP) for blackbody, and finally 0.80 (Morph-S_1) and 0.75 (Morph-DoLP) for the observation tower. As one can observe, only the probability of detection for T_0, blackbody, and the observation tower were slightly different between Morph-S_1 and Morph-DoLP. In contrast, the 72-hour average probability of detection for S_1 and DoLP were as follows: 0.35 (S_1) and 0.30 (DoLP) for T_0, 0.24 (S_1) and 0.23 (DoLP) for T_{90}, 0.15 (S_1 and DoLP) for T_{135}, 0.16 (S_1) and 0.15 (DoLP) for blackbody, and finally 0.32 (S_1) and 0.30 (DoLP) for the observation tower. In the case of conventional S_1 and DoLP only T_0 exhibits a higher discrepancy in performance between the two metrics of $P_d = 0.05$ as a result of S_2 influence. Another interesting observation is that S_1, DoLP, Morph-S_1 and Morph-DoLP have stable performances even in high humidity (day 2 and day 2) for T_0, T_{90}, blackbody, and observation tower. The exception happens with T_{135} where performance degradation is highly visible in the early hours of day 3, especially for Morph-S_1 and Morph-DoLP.

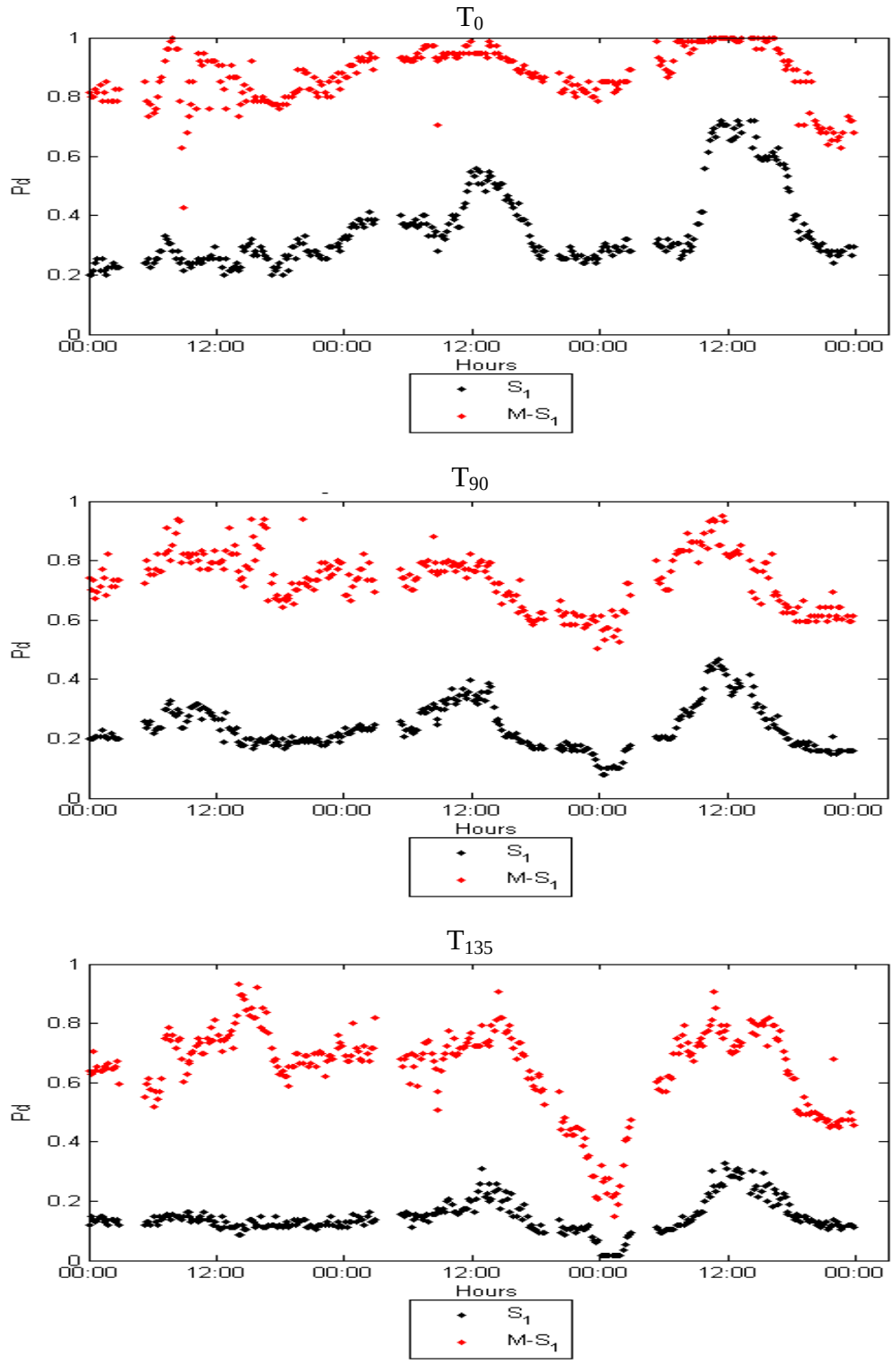

Figure 5.23 72-hour probability of detection curves comparing Stokes parameter S_1 and Morph-S_1.

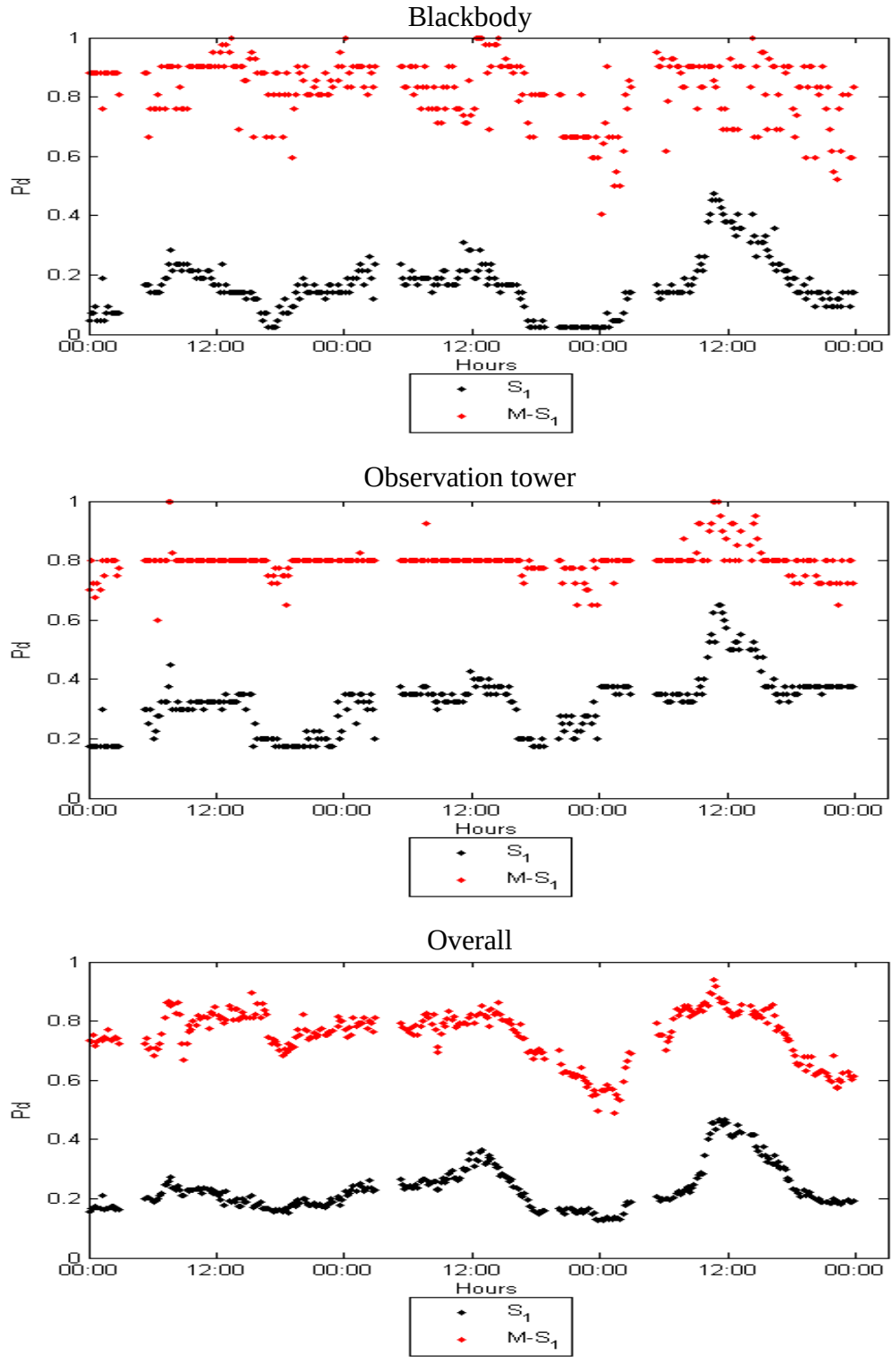

Figure 5.23 72-hour probability of detection curves comparing Stokes parameter S_1 and Morph-S_1. (Continuation)

Furthermore, from the probability of detection values shown above, one can calculate the 72-hour average probability of detection difference between Morph-S_1 and conventional S_1 was as follows: 0.53 for T_0, 0.49 for T_{90}, 0.50 for T_{135}, 0.66 for the blackbody, and 0.48 for the observation tower. On the other, hand the 72-hour average probability of detection difference between Morph-DoLP and DoLP was measured as 0.54 for T_0, 0.51 for T_{90}, 0.51 for T_{135}, 0.61 for the blackbody, and 0.45 for the observation tower. The 72-hour average probability of detection difference between morphology-based and conventional S_1 and DoLP parameters was greater or equal to 0.50, which clearly demonstrates the power of using morphological filters to enhance the Stokes imagery for anomaly detection purposes.

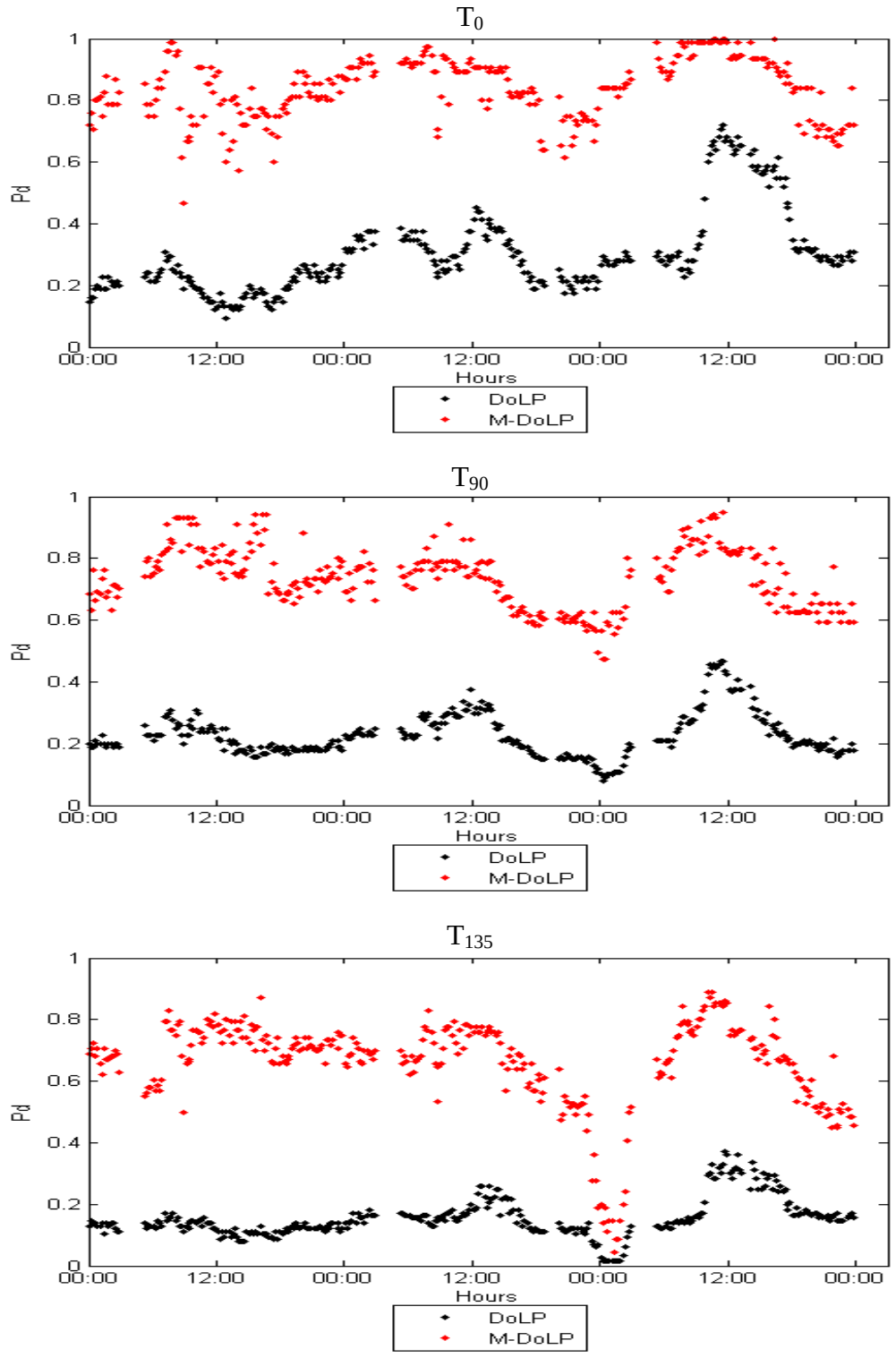

Figure 5.24 72-hour performance curves comparing DoLP and Morph-DoLP.

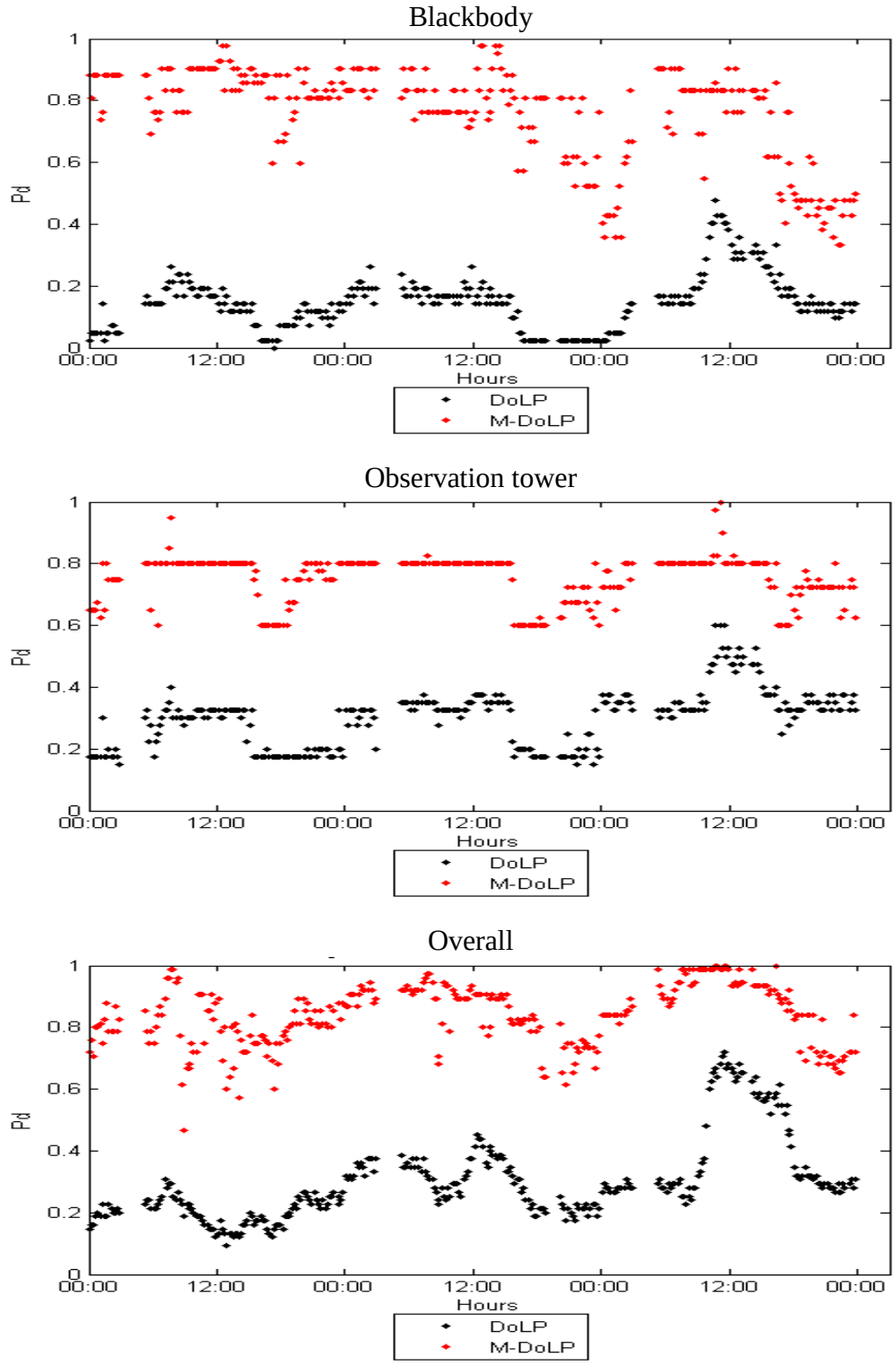

Figure 5.24 72-hour performance curves comparing DoLP and Morph-DoLP. (Continuation)

As briefly hinted in the previous paragraph and shown in the previous output surfaces as well as in Figure 5.25, the features present in S_2 imagery were as stable compared to S_1 and DoLP as shown by the large variability in S_2's probability of detection curve throughout the 72 hours. Remarkably, even with so much variability as well as poor performance (see blackbody and observation tower plots) by S_2 imagery, the morphological operators proposed in Subsection 5.2.3 when applied to S_2 demonstrated an increased in detection relative to the original image as seen in the plot for all surrogate targets. For example, the 72-hour average probability of detection for S_2 and Morph-S_2 are as follows: 0.25 (S_2) and 0.52 (Morph-S_2) for T_0, 0.25 (S_2) and 0.68 (Morph-S_2) for T_{90}, and 0.25 (S_2) and 0.58 (Morph-S_2) for T_{135}.

However, when discriminating the blackbody, S_2 and Morph-S_2 at times performed very similarly, while during other periods S_2 performed better than Morph-S_2 or vice-versa. Interestingly, one can observe a tremendous amount of variability in Morph-S_2 compared to a more stable performance by conventional S_2. This can be the result of the enhancement procedure which magnifies target features and/or false alarms in S_2 imagery depending of the available features. The 72-hour average probability of detection for the blackbody was calculated as 0.22 for S_2 and 0.39 for Morph-S_2. On the other hand, Morph-S_2 was able to discriminate the observation tower from the natural clutter better than S_2, with a 72-hour average probability of detection of 0.14 versus 0.00 from conventional S_2. Overall, when all targets are combined into a single class, S_2 average probability of detection was $P_d = 0.22$ compared to Morph-S_2 with a $P_d = 0.52$.

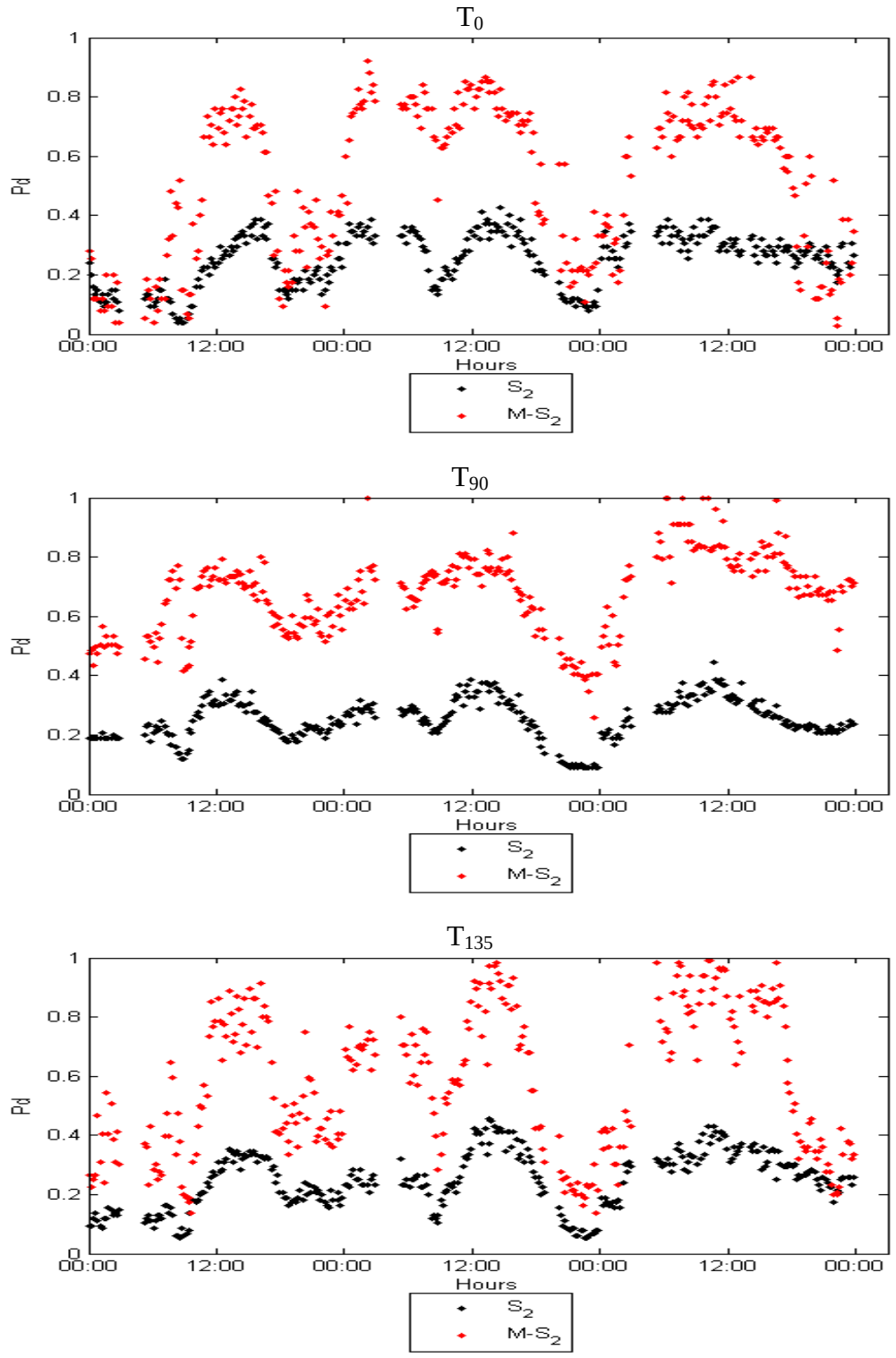

Figure 5.25 72-hour probability of detection curves comparing Stokes parameter S_2 and Morph-S_2.

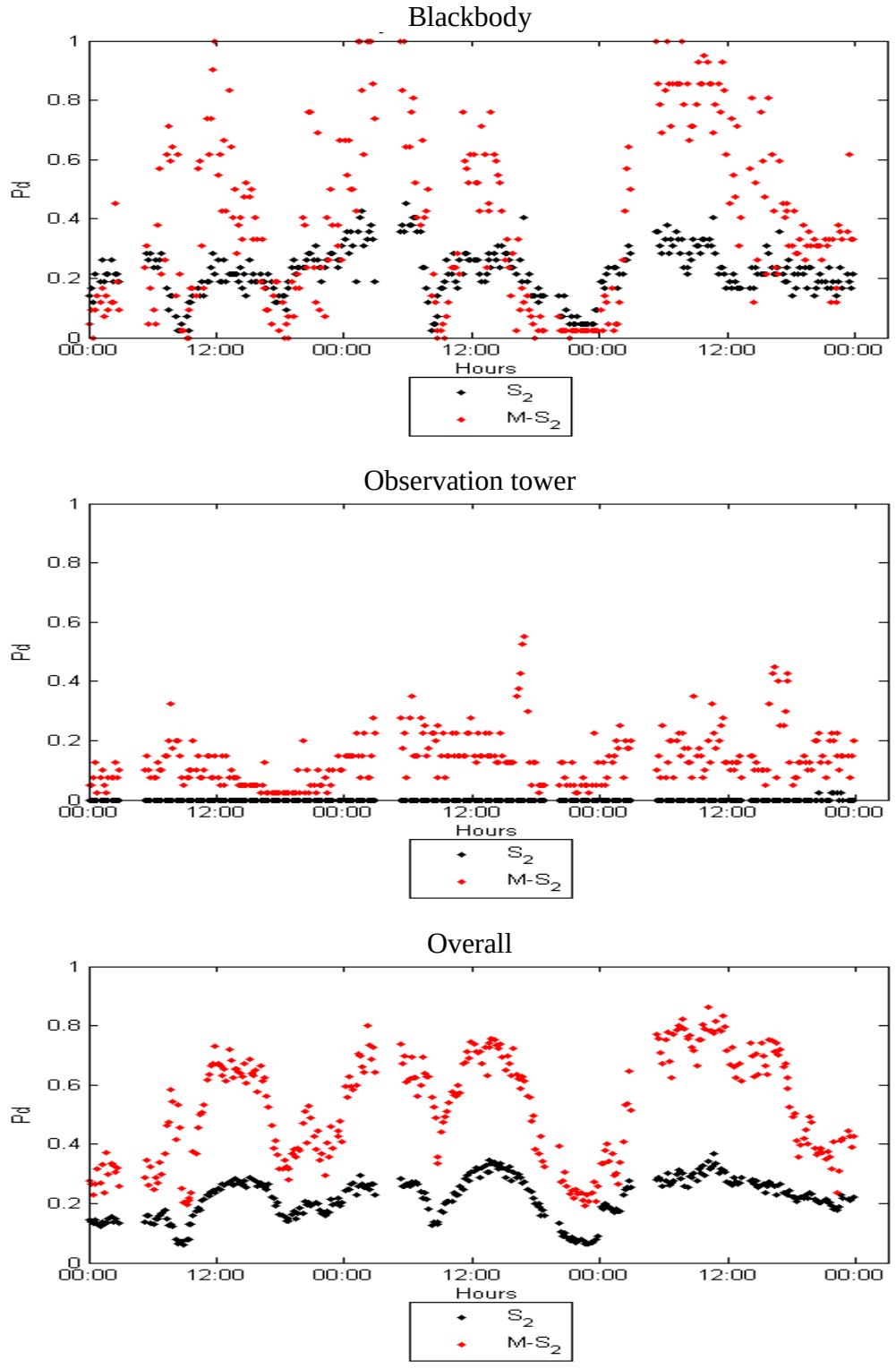

Figure 5.25 72-hour probability of detection curves comparing Stokes parameter S_2 and Morph-S_2. (Continuation)

Subsection 5.2.4 presented a performance comparison between conventional and morphology-based Stokes and DoLP metrics using individual ROC curves, output surfaces, and a 72-hour P_d comparison for a constant false alarm rate of 0.005. The comparison demonstrated the following key points:

1) Applying the morphological filters on Stokes and DoLP increased the probability of detection of all manmade objects in the scene relative to the conventional Stokes and DoLP.

2) The morphology-based S_1 and DoLP performances were very similar regardless of diurnal changes or target state for this particular dataset. Furthermore, these two parameters were the most effective of all the metrics tested in Subsection 5.2.4 as per the average probability of detection over the 72-hour period.

3) The individual ROC curves, Figures 5.14 through 5.19, demonstrated that morphology-based Stokes had a higher detection rate at low false alarm rates making them highly desirable for autonomous as well as aided system to detect manmade objects in natural clutter backgrounds.

5.2.5 Summary and Conclusions

In Section 5.2 an efficient image enhancement technique based on morphological operators was presented with the capability of enhancing target features present in Stokes and DoLP imagery while significantly reducing potential false alarms found in the original imagery. On contrary to other morphology-based algorithms presented in previous work where the objective was either to eliminate single pixels from a threshold image or object extraction using *a priori* information, the focus of this section was on the problem of anomaly detection by improving the signal-to-noise ratio between manmade objects and clutter, demonstrating that one could detect manmade objects with very low false alarm rates when compared to their conventional equivalent imagery. The new method, as discussed in Subsection 5.2.4, demonstrated an enhanced capability in not only extracting the spatial features of the target but also dramatically reducing the false

alarms present in the original image. Another very important aspect of the proposed algorithm is its ability to enhance the performance of all input imagery regardless of the metric used, making the proposed algorithm input image invariant for Stokes parameters or DoLP.

5.3 Covariance Based Anomaly Detectors for Polarimetric Imagery

5.3.1 Introduction

Section 5.2 introduced a new image enhancement algorithm for Stokes vector based on morphological operations and presented a comparison between Morph-Stokes and conventional Stokes, see Subsection 5.2.4. The results demonstrated that the morphological filters successfully enhanced manmade object features while mitigating natural clutter features which then translated into higher probability of detection compared to conventional Stokes/DoLP. Section 5.3 introduces, to the best of the committee's knowledge, the first set of anomaly detectors based on multivariate statistics using the independent individual polarization components captured by a polarimetric sensor (i.e., 0°, 45°, 90°, and 135°) as input to the proposed algorithms. Unlike the previous algorithm presented in Section 5.2 where the input imagery was a 2-dimensional image (e.g., Stokes and DoLP), in this chapter the goal is to use the individual polarization angle imagery to create a polarimetric data cube (PC) of p-dimensional space where each pixel represents the spatial and polarization information characterizing the material(s). Using the PC, one can take advantage of the variability found in the polarization bivariate space, which happens to be discriminant between two general

classes of material (manmade and natural clutter background) to introduce novel concepts for anomaly detection applications in the PI community.

The word "*anomaly detection*" has been previously introduced in applications employing hyperspectral sensors for discrimination of signatures that do not lend themselves as part of the overall composition of the scene. This chapter introduces the same concept of anomaly detection for polarimetric imagery by demonstrating how certain features when properly exploited can be used to determine if a test pixel does or not belong to the overall statistical representation of the natural clutter present in the imagery. In using these new features, a polarimetric anomaly detection algorithm based on multivariate statistics is presented for the first time to discriminate manmade objects from natural clutter environment over a variety of weather conditions, diurnal cycle, as well as hot and cold objects significantly better than conventional Stokes/DoLP metrics can.

Subsection 5.3.2 introduces the concept of polarimetric data cube, followed by an introduction to the hypothesis test for anomaly detection algorithms in Subsection 5.3.3. Subsection 5.3.4 presents some key results from data analysis using PI, where some novel features are proposed that potentially discriminate manmade from natural objects. An algorithm capable of exploiting these key features will be presented in Subsection 5.3.5 followed by, in Subsection 5.3.6, the implementation and performance analysis that also include contrasting it with performances of conventional Stokes and DoLP parameters. Subsection 5.3.7 analyses the potential limitations of the proposed algorithm. In Subsection 5.3.8 a variation of the proposed anomaly algorithm called RS-M is offered, which removes three major limitations of the approach presented in Subsection 5.3.5

involving order statistics on covariance determinants, sample size equality requirements, and range dependency. A performance analysis and implementation of the RS-M is shown in Subsection 5.3.9 and finally Subsection 5.3.10 presents the limitations of the RS-M algorithm. Subsection 5.3.11 presents a more generalized anomaly detector called the PRS-M. This new proposed variation has the same benefits as the two previous detectors found in Subsections 5.3.5 and 5.3.8, with the added benefit that it is able to identify anomalous objects under more difficult and ambiguous sample cases. A performance evaluation of the proposed algorithm is shown in Subsection 5.3.12 followed by a discussion on the PRS-M limitations in Subsection 5.3.13. Finally Subsection 5.3.14 concludes the chapter with a summary, conclusions, and emphasis on the contributions made in Section 5.3.

5.3.2 Polarimetric Cube and Window Sampling

As discussed in Chapter 2, polarimetric imagery is produced by a sensor that rotates a polarizer in front of the lens in order to produce four images at different angles (0°, 45°, 90°, and 135°). Each pixel in these images corresponds to a ground sampling area at the different polarization angles which can be expressed as follows:

$$\boldsymbol{x} = [L_0, L_{45}, L_{90}, L_{135}], \tag{5.16}$$

where the scalars L_U, $(U = 0, 45, 90, 135)$, are the radiances in units W/cm^{-2}sr^{-1} for a particular pixel for each of the polarization states. If a pixel represents a polarizing surface, the combinations of radiances of L_0 with L_{90} and L_{45} with L_{135} are found to be highly positively or negatively correlated. For example, if a polarizing surface has a preferred vertical polarization, then one expects that all pixels in the surface to have a

higher L_{90} value compared L_0 resulting in negative correlation between L_0 and L_{90}. In contrast, if the surface has a preferred horizontal polarization, then L_0 will have higher values than L_{90}, resulting in positive correlation between the two components. The same is true for surfaces that exhibit $\pm 45°$ polarization. The only exception to the rule is if the material in the scene is completely unpolarized, then in theory, $L_0 = L_{45} = L_{90} = L_{135}$, therefore, all polarization component measurements would be uncorrelated (see Section 3.2 and 3.3 for more information).

Using Equation (5.16), a PC can be built where $\mathbf{X} \in \mathbf{R}^{R \times C \times p}$, representing a spatial area of $R \times C$ pixels by p polarization components , or

$$\mathbf{X} = \begin{bmatrix} \boldsymbol{x}_{11} & \cdots & \boldsymbol{x}_{1C} \\ \vdots & \ddots & \vdots \\ \boldsymbol{x}_{R1} & \cdots & \boldsymbol{x}_{RC} \end{bmatrix}, \tag{5.17}$$

where, $\boldsymbol{x}_{\boldsymbol{rc}}$ is an observation vector located at row r ($r = 1, \ldots, R$) and column c ($c = 1, \ldots, C$).

Anomaly detectors are used to find outliers in a given image using small windows (also known as blocks of data) that move across test image $\mathbf{X}$ and it is customary to model the background clutter with a known distribution, so, if local observations fall outside the range of the known distribution, that spatial location will be designated as an anomaly (outlier).

Therefore, a moving window of size $n \times n$ (where $n \ll R$ and $n \ll C$, and $\ll$ indicates much less than) moving across $\mathbf{X}$ can be represented as follows,

$$\boldsymbol{X} = \begin{Bmatrix} \boldsymbol{x}_{11} & \boldsymbol{x}_{11} & \cdots & & \boldsymbol{x}_{1C} \\ \boldsymbol{x}_{21} & \boldsymbol{x}_{22} & & & \\ \boldsymbol{x}_{31} & \boldsymbol{x}_{ij} & \boldsymbol{x}_{i(j+1)} & \cdots \cdots & \boldsymbol{x}_{i(j+n)} \\ & \boldsymbol{x}_{(i+1)(j)} & \boldsymbol{x}_{(i+1)(j+1)} & & \vdots \\ \vdots & \vdots & \vdots & \ddots & \vdots \\ & \boldsymbol{x}_{(i+n)(j)} & \boldsymbol{x}_{(i+n)(j+1)} & \cdots & \boldsymbol{x}_{(i+\boldsymbol{n})(j+n)} \\ \boldsymbol{x}_{R1} & \boldsymbol{x}_{R2} & \cdots & & \boldsymbol{x}_{RC} \end{Bmatrix} \quad (5.18)$$

Moving window of size $n \times n$ pixels

The moving window reference pixel starts at the index i and j and spans n pixels in both r and c directions relative to the rows and columns of **X**. Equation (5.18) represents an $n \times n$ window at the pixel location i = 3, j = 2 in **X**. As the moving windows slides across **X** it will observe different classes of materials in the scene represented by the vector information in $\boldsymbol{x}$ until all the polarization vectors in **X** are observed through the $n \times n$ window.

Typically, prior to any type of processing or modeling, the data is rearranged in column or row vector format as follows,

$$\begin{aligned} \mathbf{W} &= \left[\mathbf{x_{ij}}, . . , \mathbf{x_{i(j+n-1)}}, \mathbf{x_{(i+1)j}}, \cdots, \mathbf{x_{(i+1)(j+n-1)}}, \cdots, \mathbf{x_{(i+n-1)j}}, \cdots, \mathbf{x_{(i+n-1)(j+n-1)}}\right] \\ &= [\mathbf{w_1}, \ldots, \mathbf{w_m}], \end{aligned} \quad (5.19)$$

where $\mathbf{W} \in \mathbf{R}^{m \times p}$, $m = n \times n$ pixels, and $\mathbf{w_l} \in \mathbf{R}^p, (l = 1, \ldots, m)$. Once the data is in a suitable format, various statistical parameters (e.g., mean, covariance, kurtosis, etc.) can be estimated in order to extract intricate relationships within the vectors of the moving window.

5.3.3 Hypothesis Test for Anomaly Detection

Unlike the composite hypothesis test where one tries to classify an unknown sample to one of L classes, anomaly detectors are considered a simple hypothesis test. Simple hypothesis tests are often used when one class is well defined while the other(s) is(are) not [56,p. 67]. Such a test involves measuring the "distance" between an unknown sample and a known reference sample, where a cutoff threshold is attained (through a PDF assumed for the reference sample) and applied as part of the test to determine whether the test sample is also controlled by the same PDF; if the latter is not true, the test sample is labeled as an anomaly relative to the reference sample. Although this technique is quite useful and widely used, its performance suffers as the dimensionality of the data increases. For example, it has been shown in [56,p. 67-73] that as the number of dimensions increases, the error of the simple hypothesis test increases as well, independently of whether the assumption given to the reference sample is satisfied or not. This error is the result of mapping the original p-dimensional feature space onto a one dimensional feature space as this transformation destroys valued information otherwise available in the original feature space, where potential discriminant information contained in the original data is lost after the transformation.

When using any hypothesis test, it is imperative that a distribution is defined for the reference samples to which a test sample will be tested against. By determining or assuming the distribution of the input samples, the output of the employed discriminant function test itself is modeled by a resulting distribution where a fixed criterion based on error probability can be used to attain the cutoff threshold.

As an example, let us assume that a reference and test sample, denoted as $\mathbf{W}^{(r)} \in \boldsymbol{R}^{m\times p}$ and $\mathbf{W}^{(t)} \in \boldsymbol{R}^{m\times p}$ respectively, are captured from the scene in question, where $\mathbf{W}^{(t)}$ is defined by the samples within the moving window as it slides across **X**, as specified in Equations (5.18) and (5.19) and $\mathbf{W}^{(r)}$ the reference sample is denoted by all the information in **X** in the form of Equation (5.19). One will also assume that the spatial area of the moving window $(n \times n)$ is much smaller in relation to the area of **X**, (i.e., $n \times n \ll R \times C$) and that the vectors of **X** are multivariate normally distributed with p-dimensions with mean $\boldsymbol{\mu_X}$ and covariance matrices $\boldsymbol{\Sigma}$, or

$$\mathbf{W}^{(r)} \sim N_p(\boldsymbol{\mu_X}, \boldsymbol{\Sigma}). \tag{5.20}$$

Since the pixel area occupied by potential anomalies in **X** is very small compared to the size of **X**, their effect on the overall distribution of **X** would be negligible. The hypothesis test for this example is as follows,

$$\begin{aligned} &\mathrm{H}_0: \boldsymbol{\mu}_X = \boldsymbol{\mu}_{\mathbf{W}^{(t)}} \\ &\mathrm{H}_1: \boldsymbol{\mu}_X \neq \boldsymbol{\mu}_{\mathbf{W}^{(t)}} \end{aligned} \quad , \tag{5.21}$$

where $\boldsymbol{\mu}_X$ represents the mean vector of **X** and $\boldsymbol{\mu}_{\mathbf{W}^{(t)}}$ the mean of a test window of size $n \times n$ pixels. Equation (5.21) states that if $\boldsymbol{\mu}_X = \boldsymbol{\mu}_{\mathbf{W}^{(t)}}$ then the spatial location where data are observed through the test window is labeled as not being anomalous to the reference data; otherwise, the reverse is declared as per the alternative hypothesis H_1.

Because the distribution of **X** is assumed multivariate normal with mean vector $\boldsymbol{\mu_X}$ and covariance matrix $\boldsymbol{\Sigma}$, the PDF of a block of data taken from **X** is given by

$$g\left(\boldsymbol{\mu}_{\mathbf{W}(t)}\right) = \frac{1}{\left(\sqrt{2\pi}\right)^{2}|\boldsymbol{\Sigma}|^{1/2}} e^{-\frac{\left(\boldsymbol{\mu}_{\mathbf{W}(t)}-\boldsymbol{\mu}_{\boldsymbol{X}}\right)\boldsymbol{\Sigma}^{-1}\left(\boldsymbol{\mu}_{\mathbf{W}(t)}-\boldsymbol{\mu}_{\boldsymbol{X}}\right)^{T}}{2}}. \quad (5.22)$$

It is worth mentioning, in Equation (5.22), that the term $\left(\boldsymbol{\mu}_{\mathbf{W}(t)} - \boldsymbol{\mu}_{\boldsymbol{X}}\right)\boldsymbol{\Sigma}^{-1}\left(\boldsymbol{\mu}_{\mathbf{W}(t)} - \boldsymbol{\mu}_{\boldsymbol{X}}\right)^{T}$ is a generalized distance measure also known as the *Mahalanobis distance test* [56-58], where using the same notation of Equation (5.22),

$$d^2 = \left(\boldsymbol{\mu}_{\mathbf{W}(t)} - \boldsymbol{\mu}_{\boldsymbol{X}}\right)\boldsymbol{\Sigma}^{-1}\left(\boldsymbol{\mu}_{\mathbf{W}(t)} - \boldsymbol{\mu}_{\boldsymbol{X}}\right)^{T}. \quad (5.23)$$

The parameter d^2 increases as the dissimilarity between the two vectors also increases. The output d^2 follows a Chi-Square distribution (χ_K^2) [56-58], with K degrees of freedom, where one can test the null hypothesis H_0 by specifying a criterion based on the desired probability of error. Some notes follow about Equation (5.23) and H_0:

1) The best one can claim is that H_0 cannot be rejected, which indicates that it would be better to accept H_0 than to accept H_1. The reason is that only the Type I Error is taken into account as the criterion to determine the cutoff threshold; Type II Errors are not taken into account; which is usually the case for most if not all of the hypothesis test used in practice. [59 and 60]

2) Under H_0, Equation (5.23) follows a chi-square distribution; this statement would not be true under H_1.

3) In this example, the output of the discriminant function d^2 under the null hypothesis is a $\chi_{K,\alpha}^2$ distribution with α the Type I Error (or the probability of missing the correct detection of a value under Equation (5.23), given that H_0 is true) and K the number of degrees of freedom. Given that the test yields values of a known distribution, under the assumption that the data are normally distributed, the user then can set a statistical threshold of, for instance, $\chi_{(2,0.05)}^2 = 6$ where all the values below six do not reject H_0, and any value above or equal to six rejects H_0, according to tables in [61].

For illustration, Figure 5.26 depicts the shapes of a χ^2_K distribution with $K = 1, 2, 3, 5, \text{and } 8$.

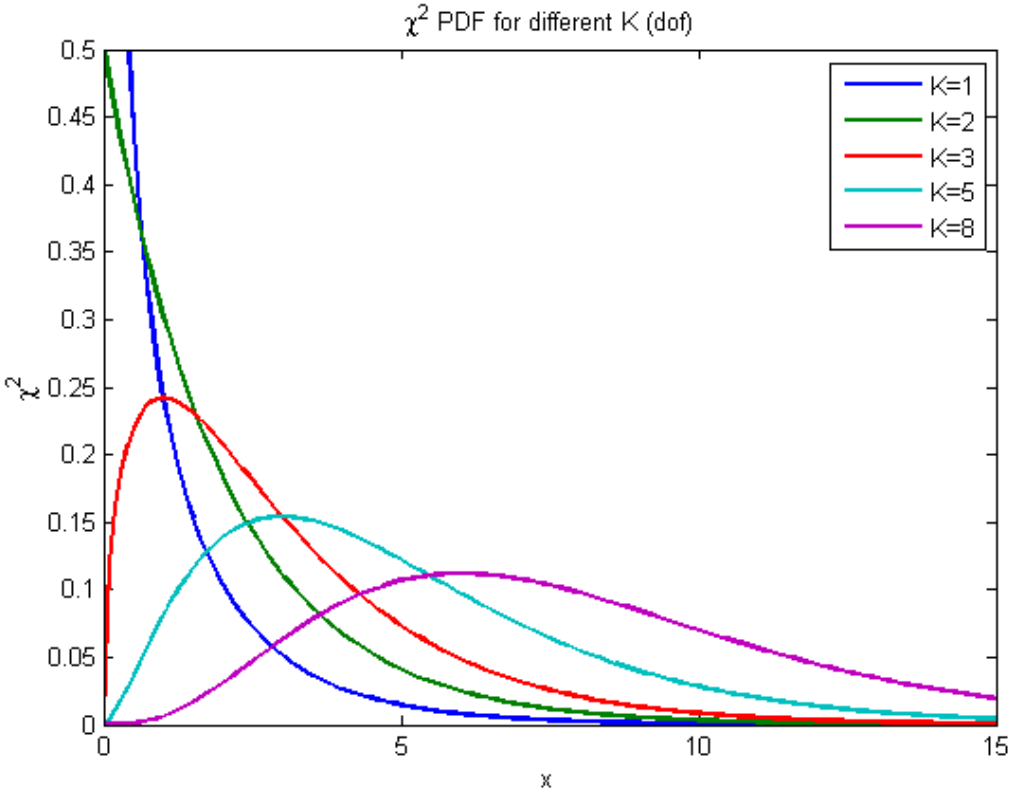

Figure 5.26 χ^2_K PDF for different degrees of freedom.

Under H_0 and assuming that the data are normally distributed, notice that as the degree of freedom increases, the variability of the PDFs shown in Figure 5.26 increases as well; the same requested Type I Error yields significantly higher cutoff thresholds as a function of increasing degrees of freedom, especially as the dimensionality of the data increases. Nonetheless, even when the data is clearly not normal, the assumption of normality is often used (even for high dimensionality data) because of its analytical tractability [57,p.30]; scholars argue that "the simplicity and robustness of the linear classifier more than compensate for the loss in performance" [56, p.131].

5.3.4 Feature Determination for PI Exploitation

In order to define a useful hypothesis test for an anomaly detector for PI, one must first determine the features that will be effective in discerning potential manmade objects from clutter. This subsection accomplishes this goal by analyzing a novel construct - bivariate polarimetric data cubes - in the form of $\boldsymbol{X} \in \boldsymbol{R}^{R\times C\times 2}$ such that a vector $\boldsymbol{x}$ is composed of $\boldsymbol{x} = [L_0, L_{90}]$, see Equation (5.16).

As mentioned earlier, samples to be tested are observed using the moving window $\mathbf{W}^{(t)}$ that slides across the entire test image $\mathbf{X}$ where the mean and covariance of the samples are often calculated for each location in $\mathbf{X}$. The reference sample is usually defined as the statistical distribution of the materials in the scene excluding the potential targets that may be present. In a practical sense, since one often does not know where the object(s) of interest is(are) located in the scene, it is customary to build the reference distribution in one of three ways:

1) Global information –in this framework, the unknown parameters, such as mean and variance/covariance, of the assumed reference PDF are estimated from the entire image. This method is only valid when the spatial area of all objects of interest is much smaller than the total image spatial area. This method is widely used in the HS community as no *a priori* information about range or target size is needed.

2) Local Information (Inside and Outside window) - in this method two windows simultaneously move across the image centered at a pixel location i and j. The inside window is defined as the test window while the outside window is designated as the reference window. The main concern of using such method is that the user needs to know *a priori* the physical scale of the target in the ground and altitude of the airborne platform carrying the employed sensor, since the unknown scale of an example target in the imagery may either cause both windows (reference and test) to cover the same target or cause the test window to partially cover both target and background material types; in both cases, the anomaly detection test will be compromised.

3) Quasi Global Information (Random Sampling) – In this construct, the reference sample is assembled by randomly taking a number of observations

from the scene in order to represent the background clutter; however, for this purpose, the author finds the use of the Parallel *Random Sampling* (PRS) discussed in [62-66], to be noticeably more effective, as it will be demonstrated later on in this dissertation (Subsections 5.3.8 and 5.3.11).

For the data analysis performed in this subsection, due to the size of the objects of interest compared to the image size and the fact that the scene is dominated by natural clutter, the global information should be a particular good fit as a reference distribution because natural clutter is often weakly polarized, imposing that all material types composing the scene background fall under a single class.

In order to determine the features needed to discriminate manmade objects from clutter, random blocks representing both classes (clutter and target) will be collected from the imagery and the mean and covariance of the samples estimated. The mean and covariance parameters will also be estimated using data from the entire imagery (global information). The strategy here is to use individually estimated parameters from random blocks of data and from global information, as reference, and test against the estimated parameters from target data in order to determine the particular parameter that will best separate the two object classes, using the results from the proposed bivariate polarization feature space.

Figure 5.27 illustrates the locations of blocks of data of size 7 x 7 pixels of background clutter used for the experiment. In contrast, due to the limitation of available target pixels, all target pixel information is used to determine the mean and covariance for each manmade object, as shown in Figure 5.28

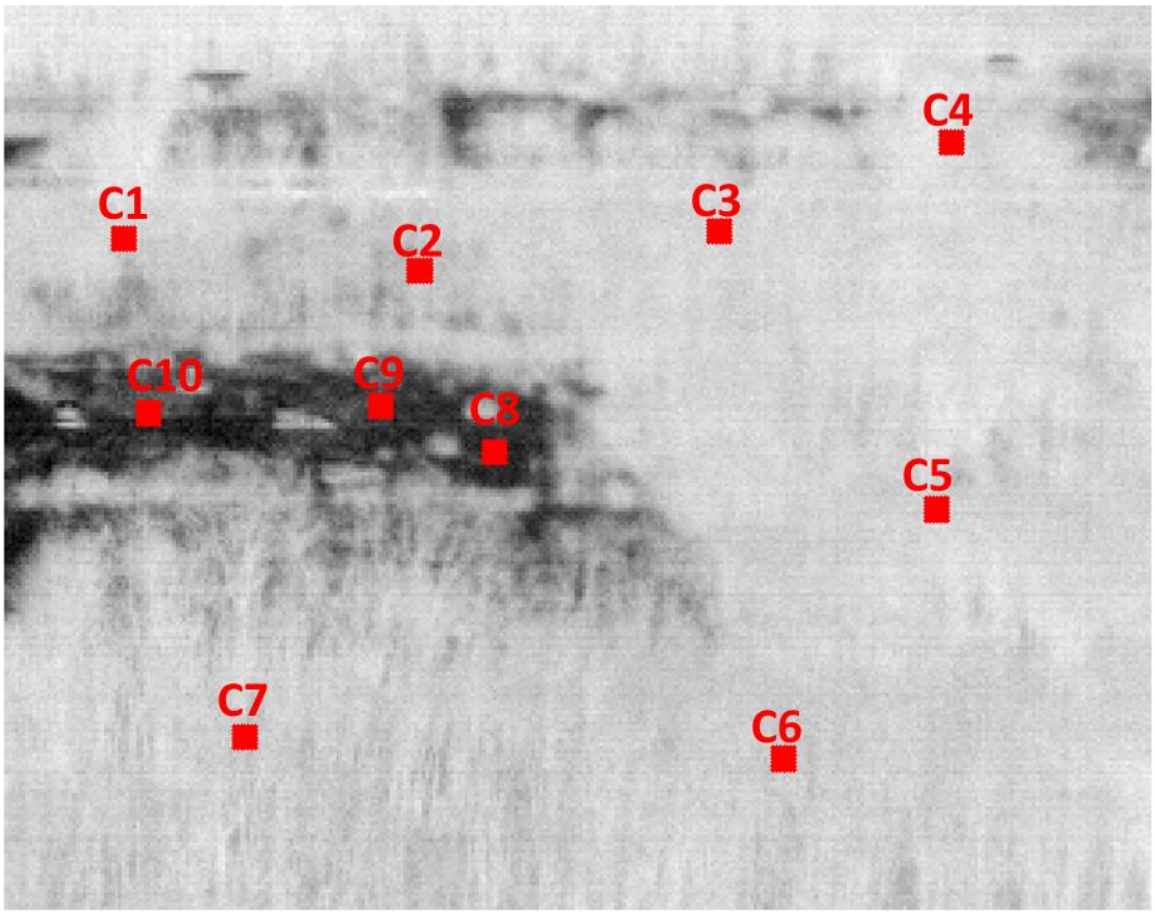

Figure 5.27 Location of the ten random blocks used for data analysis representing natural background material types, each block having 7 x 7 pixels. Blocks of data C1 through C7 correspond to trees while C8 through C9 correspond to grass. A gravel road, not visible, leads to one of the targets where C10 is sampled from. C10 is in essence a combination of samples of both grass and gravel stone where grass is the predominant class.

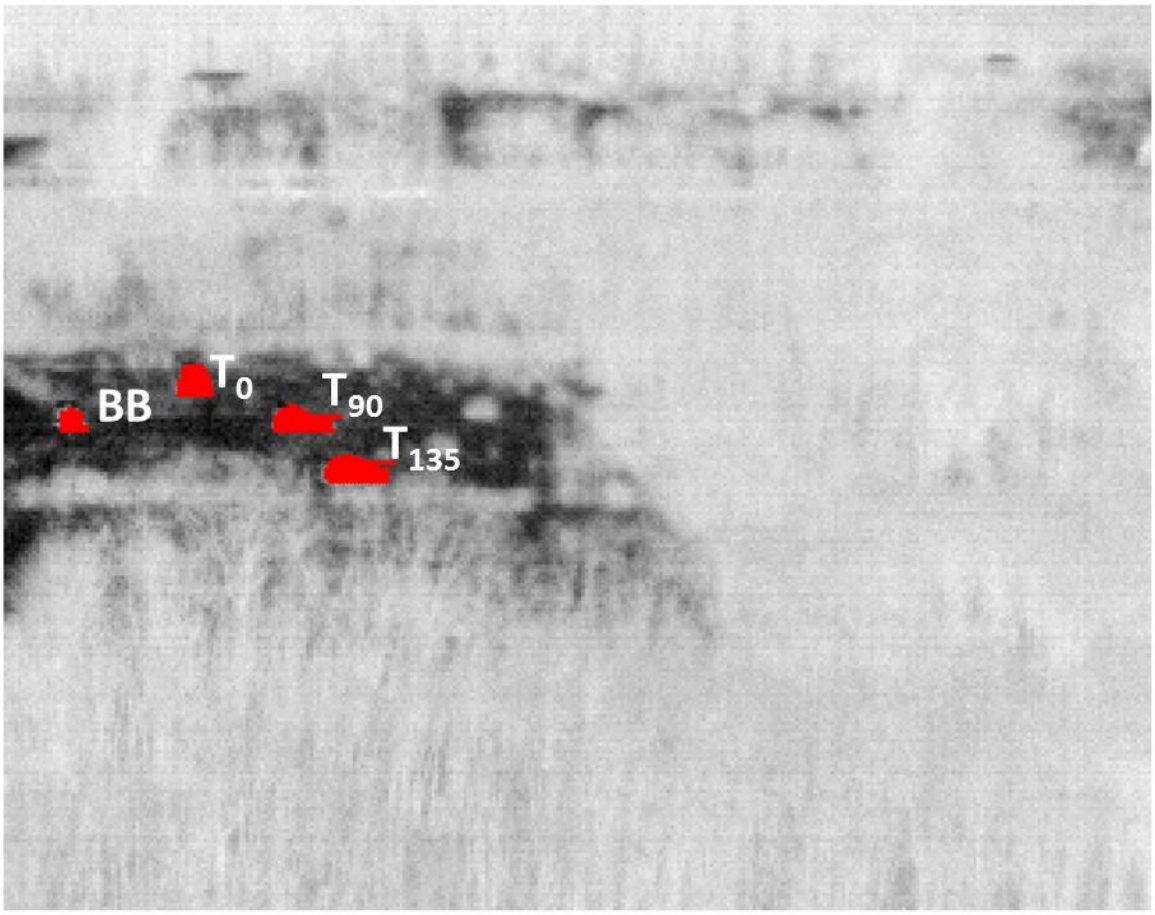

Figure 5.28 Locations of the four manmade objects used for the data analysis. The red color depicts the pixels taken from each manmade object where each manmade object is a separate class for the data analysis.

For each target and background sample, the mean and covariance were estimated and used to plot the ellipsoids, shown in Figure 5.29 and 5.30, using the Gaussian PDF as a model only for the purpose of visual appreciation. Where y-axis and x-axis are labeled as I_{90} and I_0 respectively, representing the two polarization components composing **X.** In particular, the plots shown in Figures 5.29 and 5.30 represent four distinct times of the day, 0710h, 0910h, 1310h, and 2010h chosen to represent low and high contrast imagery. Figures 5.29 and 5.30 show the estimated parameters in terms of the normal distribution model set to a 3σ (standard deviations) boundary for each of the individual material samples as well as for the global information. The plotting of the data using normal

distribution was done in order for the reader to easily compare the different material classes to the global reference class. Using the normal distribution plots does not imply, in any shape or form, that the data in **X** is Gaussian distributed.

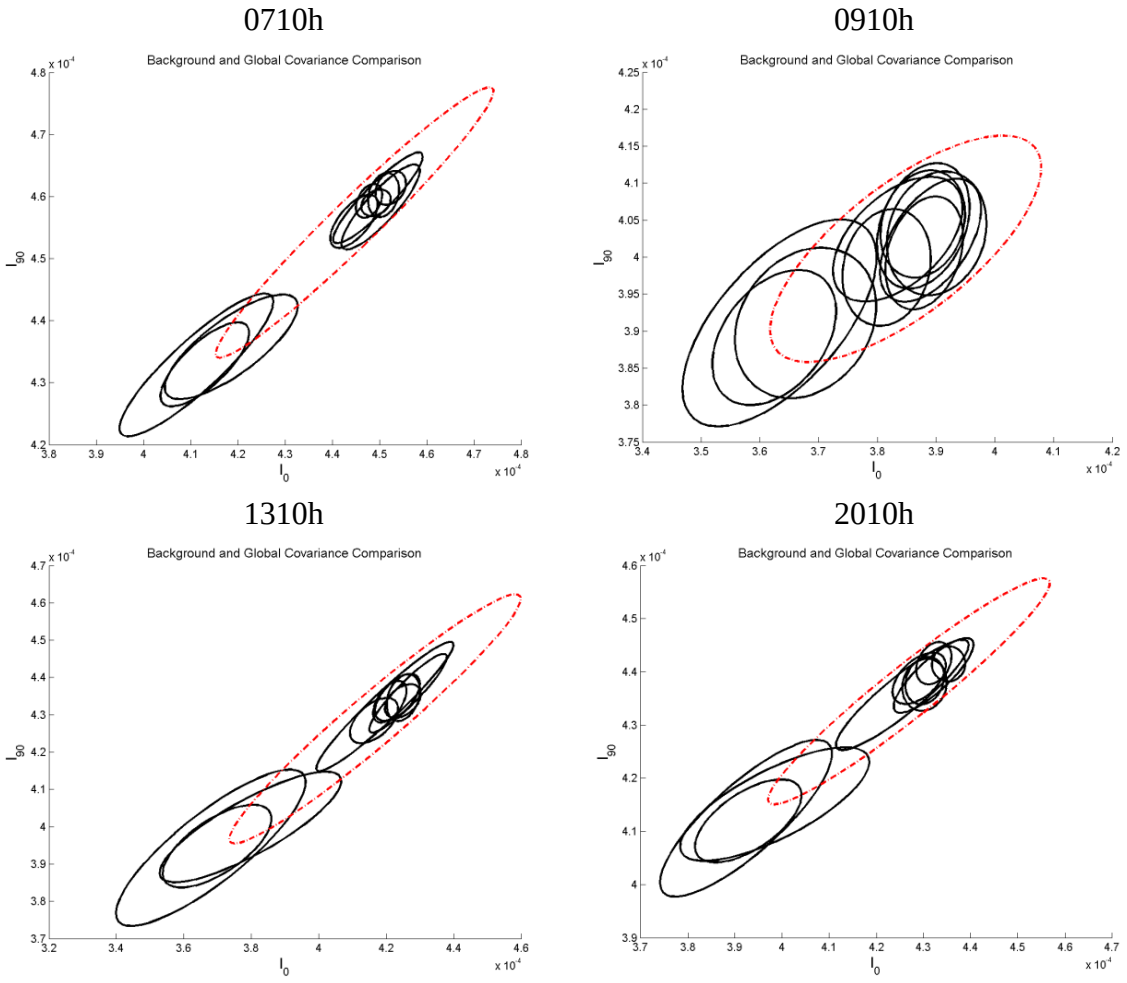

Figure 5.29 Distribution of ten (10) random background samples (in black) and the global distribution of **X** (red). The ellipsoids in black plotted inside the ellipsoid in red represent the seven blocks of data from the tree class in this feature space. Conversely, the ellipsoids representing grass and mixed materials samples (grass and gravel) can be found outside the one in red implying that the temperature of the grass was cooler than the trees.

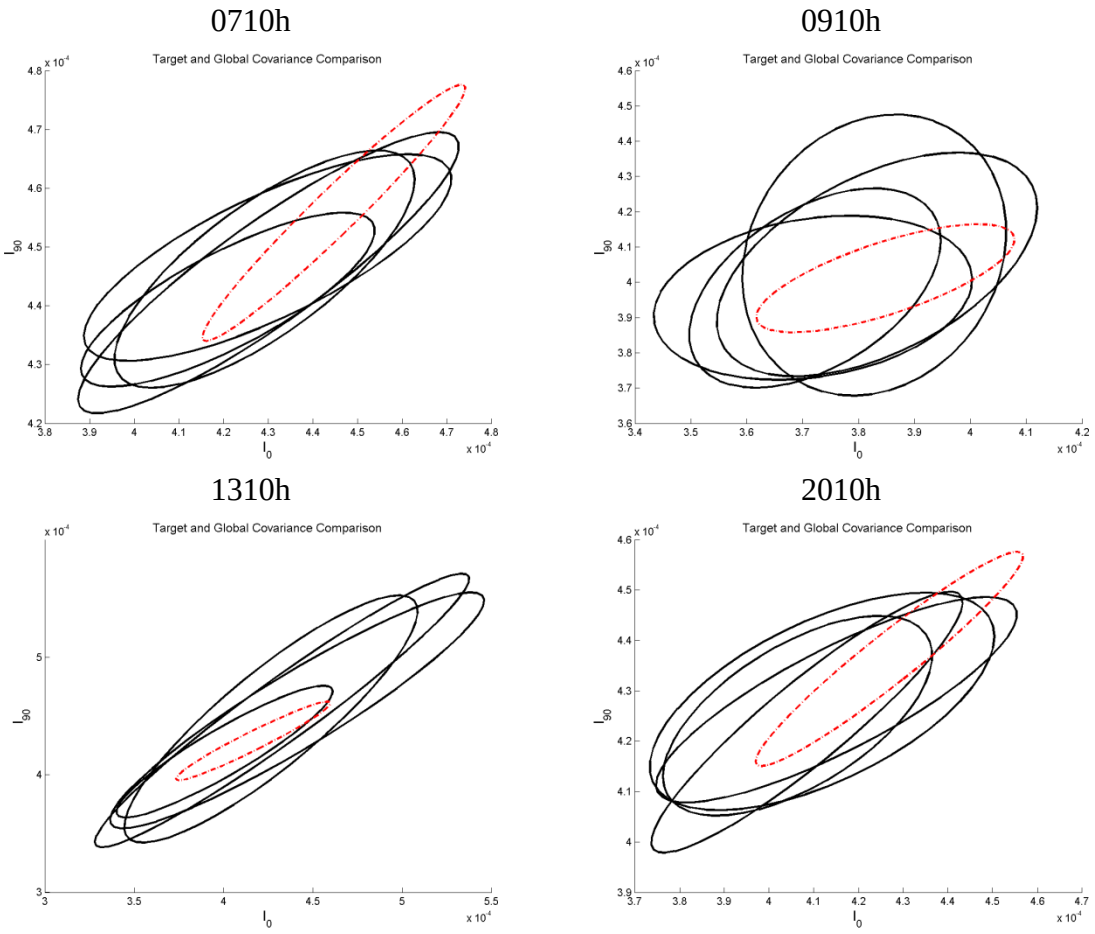

Figure 5.30 Distribution of eight (8) target samples (black) and the global distribution of **X** (red). Notice that the distributions of the target samples include samples of the global distribution. This implies that the mean of the target samples may not be very discriminant relative to the mean using the entire data cube (the global information). But, in contrast, notice also that the variability of targets in this feature space is significantly higher than that of the global information.

Figures 5.29 and 5.30 illustrate the distribution of the random samples of background and target classes (both in black) in contrast to the global distribution of **X** in red, being used here as an empirical reference. From these figures, one may draw the following important conclusions:

1) Figure 5.30 demonstrates that the target sample variability seems to be higher than the global sample variability, indicating that this feature ought to be exploited for discriminating manmade objects from natural objects, where the latter dominates the global information of **X**. Moreover, this desired characteristics is consistent over different times of the day. On the

other hand, the mean value of the target samples distribution lies close or within **X** distribution.

2) In Figure 5.29, where local natural objects are compared to the global information (again, spatially dominated by natural objects in the scene), the tree class distribution (mean and variance of the class) is included in the global distribution of **X**, while the distribution of the grass (located around the targets) is different from the distribution of **X** due to a mean shift (lower radiance values both in I_0 and I_{90} for all the four timestamps). However the variability of grass seems to be similar to the variability of the global information of **X**.

In order to quantify some of these preliminary conclusions one can compare the amount of variability in each of the target and background samples with respect to the global distribution by taking the determinant [67, Chapter 5] of the covariance matrix of each of the samples and divide them by the determinant of the global covariance,

$$\mathrm{D} = \frac{\det(\mathbf{\Sigma}_i)}{\det(\mathbf{\Sigma}_{global})}, \tag{5.24}$$

where $\mathbf{\Sigma}_i$ represents the covariance matrix for each test sample i, $\mathbf{\Sigma}_{global}$ the global covariance matrix of data cube **X**, and $\det(.)$ denotes the determinant.

Examining Equation (5.24), if the covariance of a test sample is greater than the reference then $D > 1$, otherwise $D \leq 1$. In the context of anomaly detection, it is desired that $D > 1$ when the test sample represents a manmade object in the scene spatially dominated by natural clutter; otherwise, $D \leq 1$ when the test sample represents a subset of the background clutter.

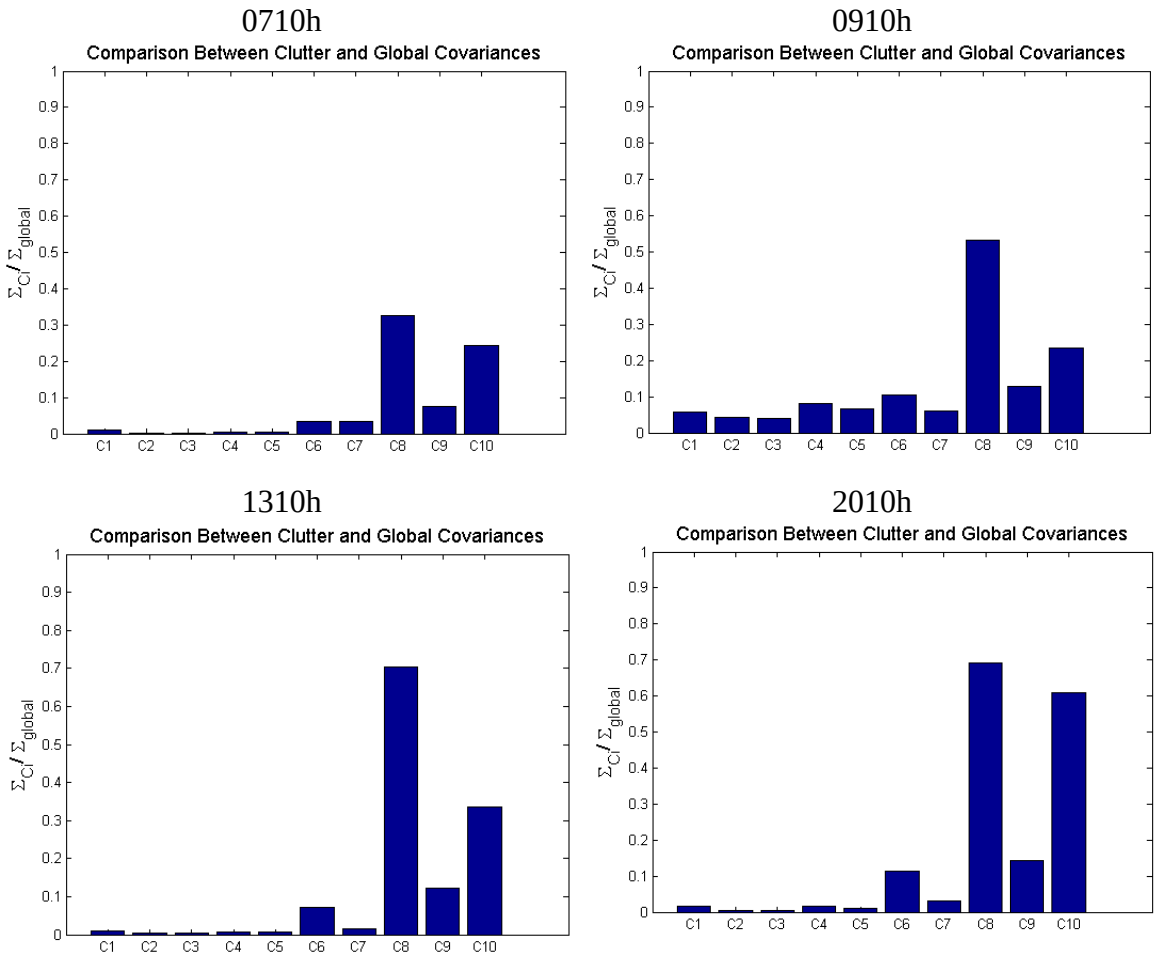

Figure 5.31 Comparison of covariance determinants between each random block of data and the global information, using Equation (5.24). The figure demonstrates that the global covariance has significantly more variability than any individual covariance estimated for this analysis.

Figure 5.31 illustrates the result of Equation (5.24) when each of the clutter samples covariance matrices is compared to the global covariance of **X**, where the horizontal axis represents the sample and the vertical axis represents the covariance determinant ratio of a sample relative to the global. One can clearly observe that all clutter classes, regardless of grass or tree, have less variability than the global reference irrespective of the mean value of each of the samples. One may conclude from this

finding that when $D \leq 1$ the individual samples taken from a spatially dominating natural background ought to be declared as a non-anomaly.

Figure 5.32 illustrates the result of Equation (5.24) for each of the different manmade objects in the scene, where the horizontal axis represents the samples drawn from the manmade objects from the test image and the vertical axis represents the covariance determinant ratio of the manmade object samples and the global data. Right away one can observe that the amount of variability encountered within the target (T_0, T_{90}, T_{135} and the external blackbody) distribution is significantly larger than the variability in the natural background clutter. As such, D values for the manmade objects in question varied substantially higher, $3 \leq D \leq 14$, in contrast to the realization of D observed for natural clutter, shown in Figure 5.31, $0.01 \leq D \leq 0.7$.

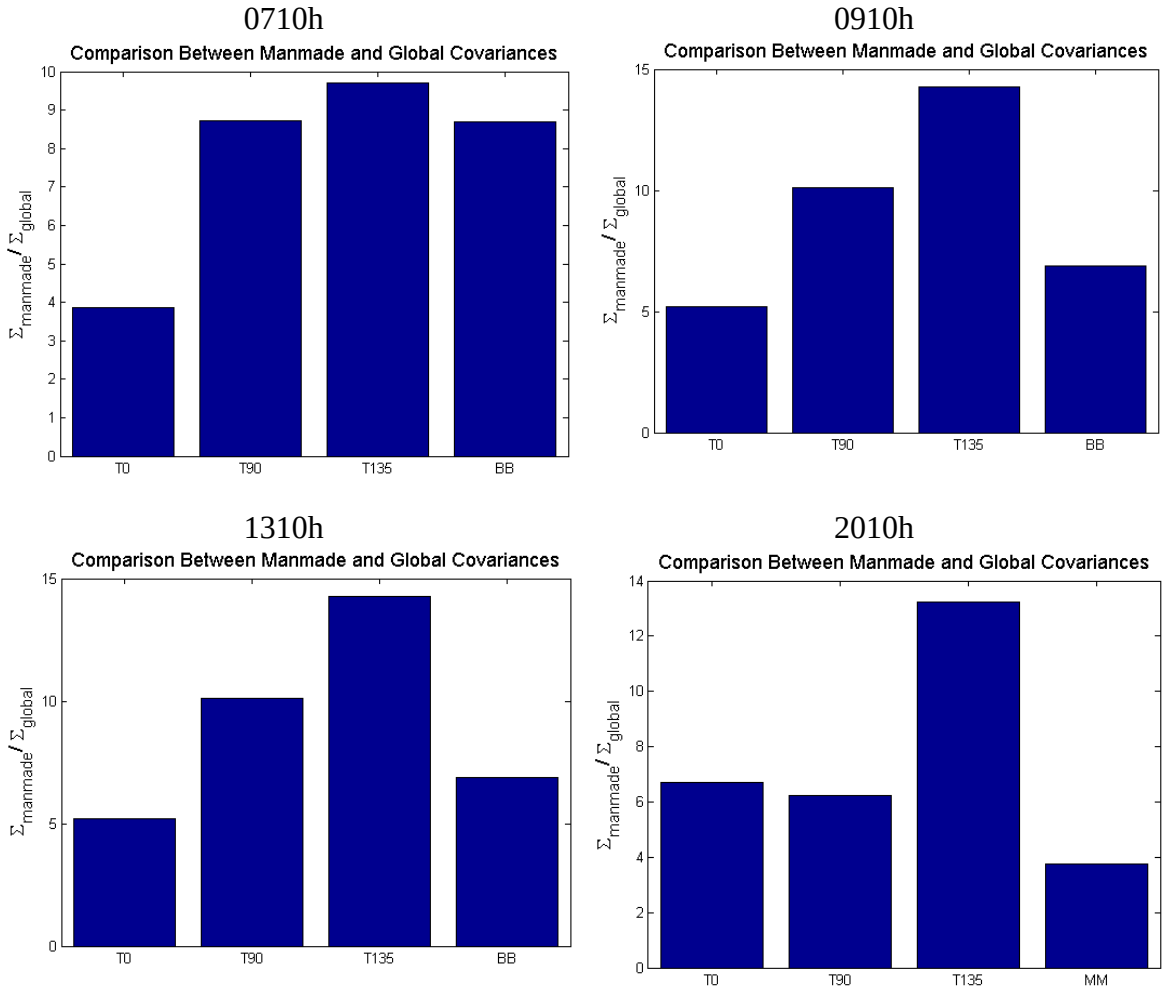

Figure 5.32 Comparison of covariance determinants between each random block of data and the global information, using Equation (5.24). In contrast to the Figure 5.31, the power (the determinant) of the covariance matrix for each manmade object is significantly larger than the global covariance.

Figure 5.33 demonstrates the *Euclidean distance* between the mean value of **X**, and the mean value of each block of clutter $C_i, i = 1, \ldots, 10$, where the Euclidean distance between two dimensional vectors $\boldsymbol{g} = [g_1, g_2]^T$ and $\boldsymbol{e} = [e_1, e_2]^T$, where T denotes the transpose operator [67, p. 96], is as follows,

$$\|\boldsymbol{g} - \boldsymbol{e}\| = \sqrt{(g_1 - e_1)^2 + (g_2 - e_2)^2}. \tag{5.25}$$

The horizontal axis of plots in Figure 5.33 represents the labeled samples and the vertical axis represents the Euclidean distance between each estimated sample mean per C_i and the global mean, using Equation (5.25).

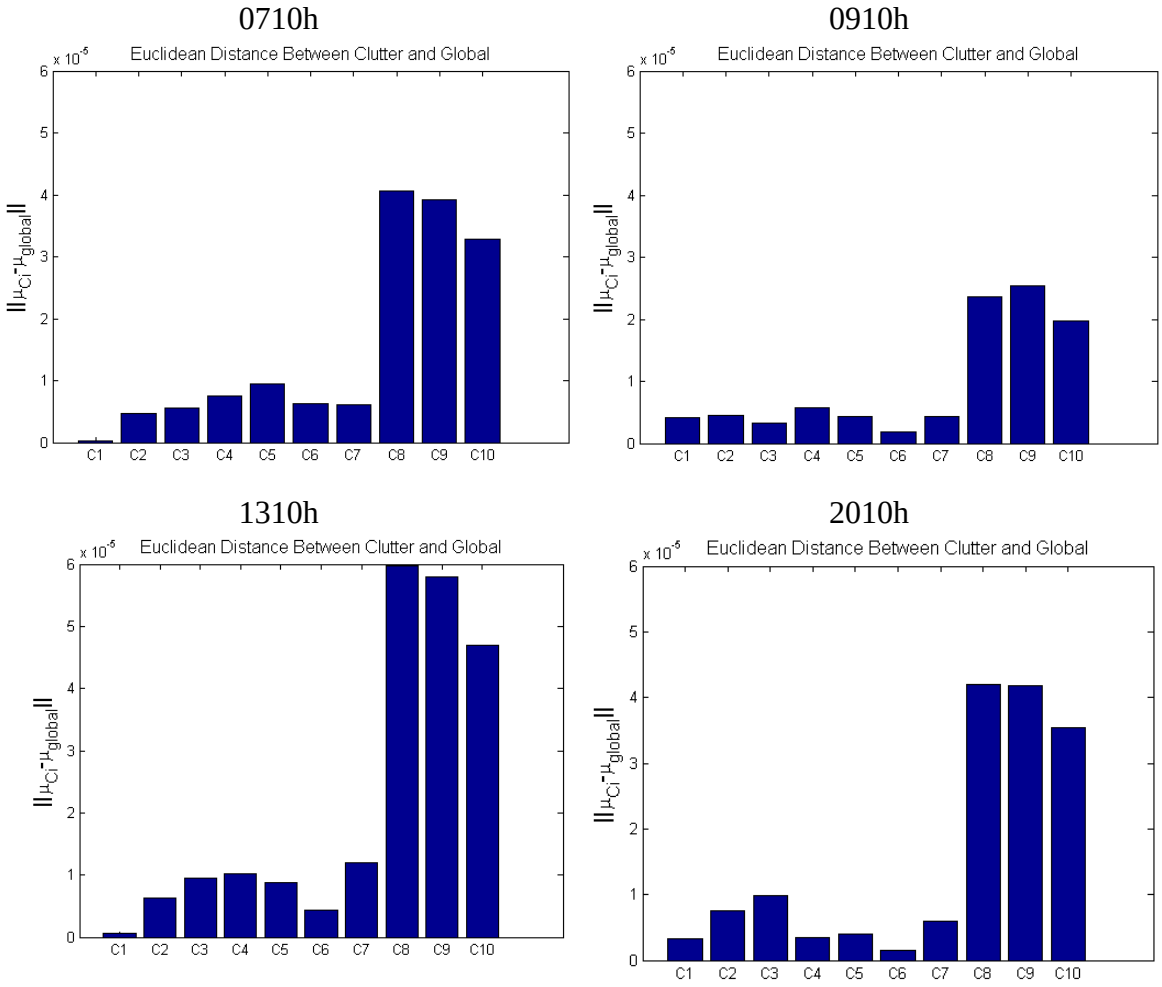

Figure 5.33 Euclidean distance between the mean of each clutter sample collected from the scene using a 7 × 7 window and the global mean of the test scene, **X**. As expected from Figure 5.29 the samples collected from trees have a smaller distance than the samples from grass. The high Euclidean distance between the global mean and the grass samples were a result of the significantly lower temperature found in the grass samples with respect to the overall scene temperature.

The results in Figure 5.33 are quite interesting because there seems to be a higher variability in the Euclidean distance results between the trees and grass classes, where grass exhibits higher values than trees. This result is expected since Figure 5.29

demonstrated that grass was at a lower temperature (low radiance values) with respect to the overall scene temperature. Moreover, since most of the scene is dominated by trees and only a small portion of the image is dominated by a grass field one also expects that the tree samples taken from the image exhibit similar values relative to the global information. Although, one can observe that the Euclidean distance difference between the grass and trees is reduced around timestamp 0910h, by 1310h when the air temperature is at its highest value, this difference is actually more accentuated with the tree canopy having higher temperature than grass.

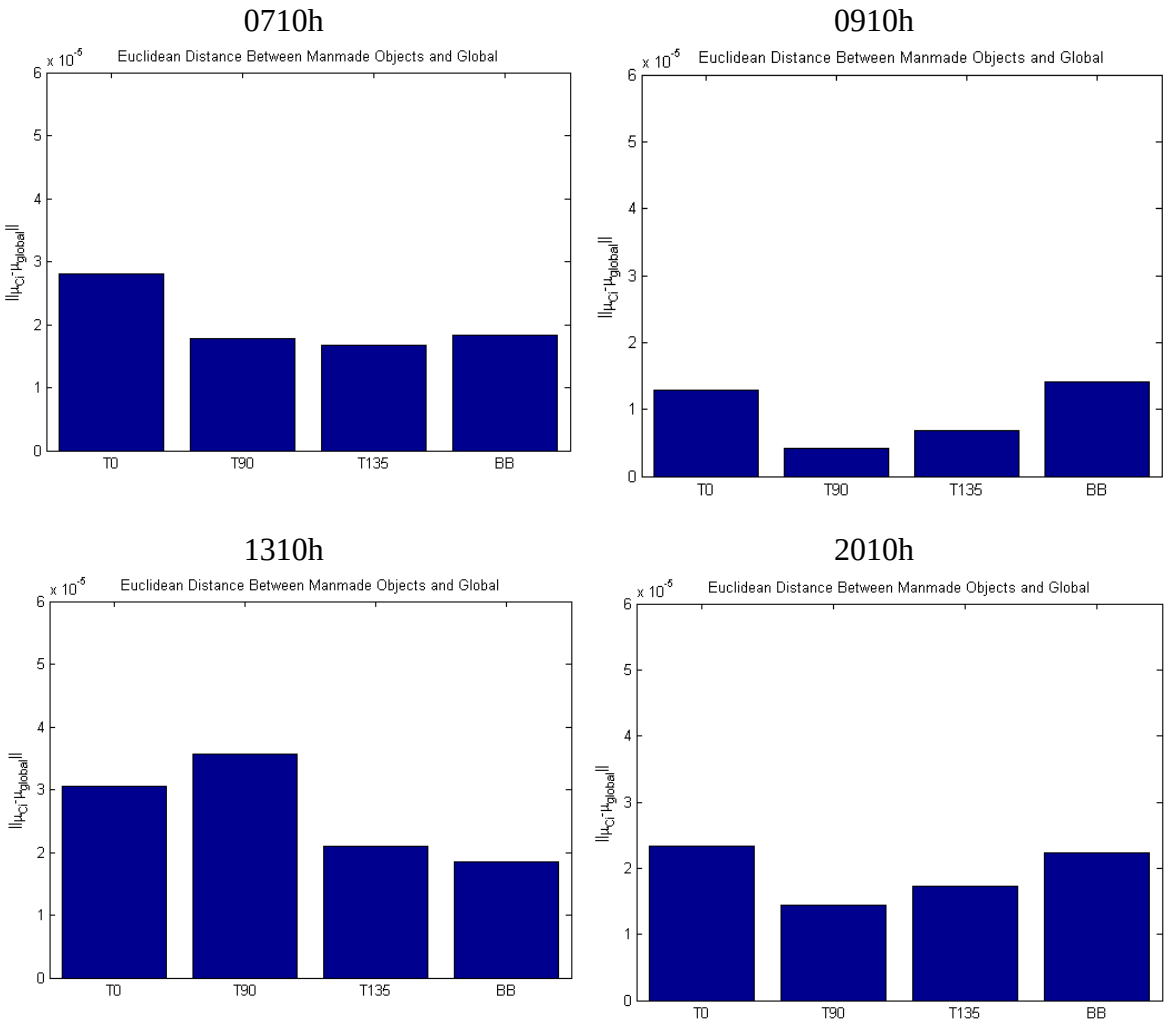

Figure 5.34 Euclidean distance between the mean of each of the targets and the global mean of the test scene, **X**. Contrary to Figure 5.33, the plots in this figure show less variability between the different manmade objects with T_0 having the highest Euclidean values for 0710h and 2010h, the blackbody for 0910h, and T_{90} at 1310h.

Figure 5.34 illustrates the Euclidean distance between each of the manmade objects in the scene and the global mean of **X** using Equation (5.25). Contrary to Figure 5.33, one can observe less variability in the results among the manmade objects. Although some differences can be observed, for example, T_0 seems to have a higher result at timestamp 0710h and 2010h, T_{90} for 1310h, and the blackbody at 0910h, their differences are minimum with respect to the other objects.

Comparing the plots in Figures 5.33 and 5.34, reveals that the mean-difference between manmade objects and the global mean of **X** is not very discriminatory as seen from the results between the tree and grass relative to the global mean. A conclusion that can be drawn from results in this subsection is that the data analysis clearly indicates a hypothesis test focused on discriminant functions that take advantage of covariance-difference methodologies should be suitable for the application of distinguishing manmade objects from natural objects using PI, as proposed in this dissertation.

Before moving on to a hypothesis test, it is important to describe to the reader, in polarization terms, the reasoning of why the variability of a moving window when sampling a 3-dimensional manmade object is more discriminatory relative to the global information than its mean value.

Manmade objects like the targets in the test scene are complex 3-dimensional object. Complex, in this case, implies multiple facets at different angles and as described in Section 3.4 their polarization values can vary dramatically as a function of the viewing angle of the camera relative to the normal of a dielectric surface. Referring to Figure 5.35, when a sliding window moves across the target, each pixel is observing different values of polarization as a result of the different orientation of each of the plates with respect to the sensor angle. Therefore, the values of observables I_0 and I_{90} within the inside window vary significantly, which in turn implies high variability within the covariance matrix. On the other hand, natural objects, as discussed earlier, are expected to emit EM in an unpolarized fashion or at best, weakly polarized. When the moving window moves across natural clutter, in principle, it will only collect weakly polarized signals and as a result one should expect for the variability of a test window when

capturing natural clutter to be lower than the samples of 3-dimensional manmade objects. From these facts one can conclude that in the context of anomaly detection an effective covariance based test is a suitable means to distinguish manmade objects from natural clutter.

Figure 5.35 Illustration on how the variability of a window superimposed on manmade objects and natural clutter differs from each other. In this situation, the test window exhibits higher variability when sampling the target because each pixel in the test window samples different surfaces at different angles with respect to the sensor.

This subsection presented a data analysis of polarimetric imagery which allowed for the identification of features that could be used to develop an effective discriminant function for manmade object detection using PI as input. As seen from the data analysis, one can conclude that a covariance-difference based methodology will potentially be highly effective in discriminating the targets from natural clutter. It was also determined that using the global distribution of **X** as a reference seemed to be appropriate since natural clutter dominated the scene and the variability of the background samples collected were similar or smaller than the variability in the reference (global) distribution while manmade objects exhibited higher variability in its observables than the reference. Finally, it was described in simple terms why one would expect the observations on

variability to be true by referencing some of the lessons learned on polarization from Section 3.4.

5.3.5 Covariance Equality Test for PI Anomaly Detection

This subsection presents a hypothesis test based on the conclusions of the Subsection 5.3.4 and proposes an effective discriminant function for anomaly detection using PI as input; the discriminant function is based on the M-Box covariance equality test proposed by Bartlett [68] and Box [69]. The equations found in this subsection are based on information found in [70].

Subsection 5.3.4 demonstrated that a covariance test approach seemed to be adequate to discriminate potential manmade objects from a scene dominated by natural clutter. Subsection 5.3.4 also concluded that the global covariance is an effective reference to which a local window can be tested against in order to determine whether the data observed through the local window are anomalous to the spatially dominant data composing the background scenery. It was shown that samples from natural clutter exhibited similar or less variability than the global reference, while targets on the other hand exhibited higher variability compared to the reference.

From the conclusions in Subsection 5.3.4 one would like to test if the variability of a window moving across an image $\mathbf{X}$ with p observables exhibits the same variability as the reference sample. If the variability is the same, then there is a strong likelihood that the local sample is from a natural object, given that Subsection 5.3.4 showed that manmade objects are expected to yield a higher variability from that of natural objects.

Let one assume $\mathbf{F}$ is a $m \times p$ matrix where each row is independently drawn from a p-variate normal distribution with zero mean and covariance matrix $\mathbf{\Sigma}$, such that

$$\mathbf{F} = (\boldsymbol{f}_1, \dots, \boldsymbol{f}_m)^T \sim N_p(0, \boldsymbol{\Sigma}), \tag{5.26}$$

where m represents the number of samples and p the number of dimensions in **F.**

A Chi square random variable, χ^2, is defined as the sum of squares of independent normal random variables, for example Equation (5.26), such that

$$\mathbf{U} = \boldsymbol{F}\boldsymbol{F}^T. \tag{5.27}$$

The resulting **U** is a $p \times p$ matrix with a Wishart distribution in the form of

$$\mathbf{U} \sim W_p(v, \mathbf{V}), \tag{5.28}$$

Where v is the degrees of freedom and $v \geq p - 1$, and **V** is the scale matrix.

The likelihood of Equation (5.28) is then

$$\mathcal{L}(\mathbf{U}, \mathbf{V}) = |\mathbf{V}|^{-v/2} e^{-\frac{1}{2} trace(\mathbf{V}^{-1}\mathbf{U})}. \tag{5.29}$$

It has been shown in [70, page 185] that the maximum likelihood estimator for Equation (5.29) is equivalent to the estimated sample covariance of the data in **F** or $\widehat{\boldsymbol{\Sigma}} = \frac{\mathbf{U}}{v}$. Therefore, as a result, the maximum likelihood of Equation (5.29) is

$$\mathcal{L}\left(\mathbf{U}, \widehat{\boldsymbol{\Sigma}}\right) = \left|\frac{\mathbf{U}}{v}\right|^{-v/2} e^{-1/2vp}. \tag{5.30}$$

Let one assume that there are two groups ($\boldsymbol{F_1}$ and $\boldsymbol{F_2}$) and one would like to test if their scale matrices are equal. Assuming that $\mathbf{U_1}$ and $\mathbf{U_2}$ are independent where

$$\begin{aligned}\mathbf{U}_1 &\sim \mathrm{W}_p(v_1, \mathbf{V}_1)\\ \mathbf{U}_2 &\sim \mathrm{W}_p(v_2, \mathbf{V}_2)\end{aligned} \tag{5.31}$$

The hypothesis to test if the two scale matrices are equal can be formulated as follows,

$$\begin{aligned}\mathrm{H}_0&: \mathbf{V}_1 = \mathbf{V}_2 \sim \left(\widehat{\boldsymbol{\Sigma}}_1 = \widehat{\boldsymbol{\Sigma}}_2\right)\\ \mathrm{H}_1&: \mathbf{V}_1 \neq \mathbf{V}_2 \sim \left(\widehat{\boldsymbol{\Sigma}}_1 \neq \widehat{\boldsymbol{\Sigma}}_2\right).\end{aligned} \tag{5.32}$$

It will be shown that testing the scale matrices is equivalent to testing the estimated covariance matrices belonging to groups $\boldsymbol{F_1}$ and $\boldsymbol{F_2}$.

The likelihoods for both H_0 and H_1 can be defined as Equation (5.33) for H_1 (because $U_i's$ are independent), or

$$\begin{aligned}&\mathcal{L}(\mathbf{V}_1, \mathbf{V}_2;\ \boldsymbol{U}_1, \boldsymbol{U}_2)\\ &= |\mathbf{V_1}|^{-v_1/2} \exp\left(-\frac{1}{2} tr\{\mathbf{V_1^{-1}U_1}\}\right) \cdot |\mathbf{V_2}|^{-\frac{v_2}{2}} \exp\left(-\frac{1}{2} tr\{\mathbf{V_2^{-1}U_2}\}\right),\end{aligned} \tag{5.33}$$

but in the special case of H_0, Equation (5.33) becomes Equation (5.34), or

$$\mathcal{L}(\mathbf{V}, \mathbf{V};\ \boldsymbol{U}_1, \boldsymbol{U}_2) = |\mathbf{V}|^{-(v_1+v_2)/2} \exp\left(-\frac{1}{2} tr\{\mathbf{V^{-1}}(\mathbf{U_1} + \mathbf{U_2})\}\right), \tag{5.34}$$

where under the null hypothesis $\mathbf{V} = \mathbf{V_1} = \mathbf{V_2}$. [70, page 186] demonstrates that the ratio of the maximum likelihood estimate of Equations (5.33) and (5.34) is,

$$M = \frac{\left|\boldsymbol{U}_1/v_1\right|^{-v_1/2}\left|\boldsymbol{U}_2/v_2\right|^{-v_2/2}}{\left|(\boldsymbol{U}_1+\boldsymbol{U}_2)/(v_1+v_2)\right|^{-(v_1+v_2)/2}}. \tag{5.35}$$

Notice that by using the maximum likelihood of H_0 and H_1, Equation (5.35) is no longer dependent on the scale matrix **V**, rather it is dependent on $\boldsymbol{U}_i$ and $\boldsymbol{v}_i$.

Finally, by taking the $-2log(M)$,

$$-2\log(M) = v_1 log\left|\frac{\boldsymbol{U}_1}{v_1}\right| + v_2 log\left|\frac{\boldsymbol{U}_2}{v_2}\right| - (v_1+v_2) log\left|\frac{\boldsymbol{U}_1+\boldsymbol{U}_2}{v_1+v_2}\right|. \tag{5.36}$$

Previously, $\widehat{\boldsymbol{\Sigma}}_{\boldsymbol{i}}$ was defined as $\widehat{\boldsymbol{\Sigma}}_{\boldsymbol{i}} = \frac{\mathbf{U}_i}{v_i} = \frac{\boldsymbol{F_i F_i}^T}{v_i}$, as the estimated covariance matrix of the samples in $\boldsymbol{F}$, which was based on the fact that $\widehat{\boldsymbol{\Sigma}}_{\boldsymbol{i}}$ is the maximum likelihood estimator of Equation (5.29).

Therefore, Equation (5.36) can be re-written in terms of covariance estimates, or

$$\begin{aligned} -2\log(M) = {} & v_1 log\left|\widehat{\boldsymbol{\Sigma}}_{\mathbf{1}}\right| + v_2 log\left|\widehat{\boldsymbol{\Sigma}}_{\mathbf{2}}\right| \\ & - (v_1+v_2) log\left|\frac{v_1}{v_1+v_2}\widehat{\boldsymbol{\Sigma}}_{\mathbf{1}} + \frac{v_2}{v_1+v_2}\widehat{\boldsymbol{\Sigma}}_{\mathbf{2}}\right|. \end{aligned} \tag{5.37}$$

where Equation (5.37) is the well-known Bartlett test of equality for covariance matrices for $k = 2$. Under the null hypothesis, Equation (5.37) approaches a Chi square distribution $\chi^2_{(k-1)p(p+1)/2}$ with $(k-1)p(p+1)/2$ degrees of freedom, where k is defined as the number of covariance matrices being tested and p the number of

observables.Furthermore, if $v_1 = v_2$ Equation (5.37) can be further simplified as shown below,

$$\frac{-1}{(v)}\log(M) = \frac{1}{2}log\left|\widehat{\boldsymbol{\Sigma}}_1\right| + \frac{1}{2}log\left|\widehat{\boldsymbol{\Sigma}}_2\right| - log\left|\left(\widehat{\boldsymbol{\Sigma}}_1 + \widehat{\boldsymbol{\Sigma}}_2\right)\Big/_2\right|. \tag{5.38}$$

Barlett demonstrated that Equation (5.37) is approximated by the limiting χ^2 distribution given by $-2log(M)$ while Lee et al. [71] presented the exact upper 5% points of Equation (5.38) for the special case where $v = v_1 = v_2 =, \dots, = v_k$.

$$-2log(M) = v\left(k \cdot ln\left|\widehat{\boldsymbol{\Sigma}}_{pl}\right| - \sum_{i=1}^{k} \ln\left|\widehat{\boldsymbol{\Sigma}}_i\right|\right), \tag{5.39}$$

where the pooled covariance matrix ($\widehat{\boldsymbol{\Sigma}}_{pl}$) is defined as

$$\widehat{\boldsymbol{\Sigma}}_{pl} = \frac{\sum_{l=1}^{k} v_l \widehat{\boldsymbol{\Sigma}}_l}{\sum_{l=1}^{k} v_l}. \tag{5.40}$$

In the cases where the χ^2 distribution is not sufficiently accurate, Anderson [72] proposed two improvements known as "Barlett improvement", where the first improvement divides $2log(M)$ by a constant C such that the mean of $\frac{2log(M)}{C}$ is closer to the mean of the limiting χ^2 distribution and the second is obtained by adding an extra term to the limiting χ^2 distribution of order $O(n^{-2})$.

In 1949 and 1950, Box [69], also proposed a χ^2 approximations for the distribution of Equation (5.37), also referred as M-Box's tests. For the χ^2 distribution, Box proposed

$$-2(1-c_1)log(M) \rightarrow \chi^2_{\frac{1}{2}(k-1)p(p+1)}, \tag{5.41}$$

Where

$$c_1 = \left(\sum_{l=1}^{k} \frac{1}{v_l} - \frac{1}{\sum_{l=1}^{k} v_l}\right)\left(\frac{2p^2+3p-1}{6(p+1)(k-1)}\right). \tag{5.42}$$

In this subsection the Bartlett's test of equality for covariances is proposed as an anomaly detector for polarimetric imagery; implementation details of this approach using a relevant dataset are shown in Subsection 5.3.6. The use of covariance-different tests is based on the covariance and mean data analysis presented in the previous Subsection 5.3.4. If possible, it is desirable to have the search window to be the same size as the test window in order to simplify Equation (5.37) into (5.38) as well as to mitigate any sample size differences between the two covariance matrices. In the next subsection, the implementation of the algorithm, which for the remainder of the dissertation will be referred as M-Box, is presented and a comparison of its performance against the Stokes vector and DoLP is shown.

5.3.6 Performance Assessment of M-Box

This subsection presents the implementation of the covariance test proposed in Subsection 5.3.5 to the application of anomaly detection using polarimetric imagery as input data. The polarimetric input data is a data cube **X**, where $\boldsymbol{X} \in \boldsymbol{R}^{R\times C\times p}$ where R by C pixels define the spatial information in the x- and y-axis and $p = 2$ the polarization

measurements of I_0 and I_{90}. A performance analysis comparing the M-Box algorithm to Stokes and DoLP imagery using the SPICE database is also presented.

5.3.6.1 Algorithm Implementation. Let $\boldsymbol{X}$ be an R×C image of p observables s.t. $\boldsymbol{X} \in \boldsymbol{R}^{\boldsymbol{R}\times\boldsymbol{C}\times\boldsymbol{p}}$. The implementation of the proposed anomaly detector algorithm is twofold: (1) Find a reference covariance matrix to which all moving window locations will be compared to and (2) apply Equation (5.38) using the reference covariance and the test window sliding as it moves across the spatial area of **X**.

In order to find the reference covariance matrix from **X**, one could use all of the polarization signatures to estimate the global distribution parameters such as the mean and covariance. However, one must be aware of some potential complications that may reduce the effectiveness of the proposed test. For example, the M-Box algorithm is a very sensitive covariance test where its robustness suffers as a result of its high sensitivity to different sample sizes [73]. A significant difference in sample sizes between the reference and test covariance matrices increases the power of the output of the test significantly where the resulting output deviates from the desired $\chi^2_{\frac{1}{2}(k-1)p(p+1)}$ distribution of the null hypothesis.

In order to mitigate sample size differences between the reference and locally estimated covariance matrices, this dissertation proposes to keep the sample size for the moving and reference covariance matrix identical as follows: the data analysis in Subsection 5.3.4 concluded that the natural clutter variability was significantly lower than any of the manmade objects in the scene, as a result, one could safely deduce that there is a location in the test scene where a covariance matrix with the smallest variance should

be representative of natural clutter. By using a search window of the same size as the test window to search for a location in **X** with the smallest variability, one would be able to: (1) find an effective reference covariance matrix for the M-Box test and (2) eliminate any sample size difference between the reference and test window as required for the M-Box test.

Let's start by using a window in the form of Equation (5.18) to collect samples as shown in Equation (5.19) across the image for each (i, j). For the first location $(i, j) = (1,1)$, the determinant of the covariance of the sliding window is estimated and stored in a temporary variable, where (using the notation employed in Equation (5.19))

$$\mathbf{W}^{(i,j)} = [\mathbf{w}_1, .., \mathbf{w}_m] \in \mathbf{R}^{m \times p}, \tag{5.43}$$

and $\mathbf{w}_k \in \mathbf{R}^p$.

The covariance of $\boldsymbol{W}^{(i,j)}$ is calculated as

$$\boldsymbol{\Sigma}_{\boldsymbol{W}^{(i,j)}} = \mathrm{E}\left(\left(\mathbf{w}_k - \boldsymbol{\mu}_{\boldsymbol{W}^{(i,j)}}\right)\left(\mathbf{w}_k - \boldsymbol{\mu}_{\boldsymbol{W}^{(i,j)}}\right)^T\right). \tag{5.44}$$

In this dissertation the PC is composed of I_0 and I_{90} measurements or $p = 2$, therefore, the determinant of the $\boldsymbol{\Sigma}_{\boldsymbol{W}^{(i,j)}} \in \boldsymbol{R}^{2\times 2}$ is given by,

$$D^{(i,j)} = \det\left(\boldsymbol{\Sigma}_{\boldsymbol{W}^{(i,j)}}\right) = \left(\sigma_{I_0}^2 \times \sigma_{I_{90}}^2\right) - \left(2\sigma_{I_0 I_{90}}\right). \tag{5.45}$$

For the first location, $(i, j) = (1,1)$, the result of Equation (5.45) is used as the initial reference value $D^{\boldsymbol{r}} = D^{(1,1)}$. Subsequent locations in the polarimetric data cube **X** are estimated using Equations (5.44) and (5.45). The result of 5.45 for each combination (i, j) where $i > 1$ and $j > 1$ is compared to $D^{\boldsymbol{r}}$ and if the result of $D^{(i,j)}$ for any location

in $\mathbf{X}$ is smaller than the current $D^{\boldsymbol{r}}$, then the new smaller value becomes the new reference.

The $\boldsymbol{\Sigma}_{\boldsymbol{W}^{(i,j)}}$ which estimates the smallest $D^{\boldsymbol{r}}$ in data cube $\mathbf{X}$ becomes the reference covariance matrix $\left(\boldsymbol{\Sigma}_r = \boldsymbol{\Sigma}_{\boldsymbol{W}^{(i,j)}}\right)$ by which all other covariances in the image shall be tested against using the covariance test (Equation (5.38)) proposed Subsection 5.3.5.

The next step in the implementation is to test the covariance matrix $\boldsymbol{\Sigma}_{\boldsymbol{W}}{}^{(i,j)}$ for all locations (i, j) in data cube $\mathbf{X}$ to the reference covariance $\boldsymbol{\Sigma}_r$ using Equation (5.38). The output of Equation (5.38) for all combinations of (i, j) yields an output surface in the form of,

$$\boldsymbol{Z} = \begin{bmatrix} \mathrm{Z}^{(\mathbf{1},\mathbf{1})} & \cdots & \mathrm{Z}^{(\mathbf{1},\boldsymbol{C}-\mathrm{n}+1)} \\ \vdots & \ddots & \vdots \\ \mathrm{Z}^{(\boldsymbol{R}-\mathrm{n}+1,\mathbf{1})} & \cdots & \mathrm{Z}^{(\boldsymbol{R}-\mathrm{n}+1,\boldsymbol{C}-\mathrm{n}+1)} \end{bmatrix}. \tag{5.46}$$

The spatial size of $\mathbf{Z}$ is $\boldsymbol{Z} \in \boldsymbol{R}^{(R-n+1)\times(C-n+1)}$ is a result of using a sliding window across $\mathbf{X}$ in the form of Equation (5.18) to test a center location in $\boldsymbol{W}^{(\boldsymbol{i},\boldsymbol{j})}$ of size $n \times n$ pixels. Since not all the pixel locations close to the boundaries of image $\mathbf{X}$ are tested due to window size, $\boldsymbol{Z}$ output surface size will be smaller than $\mathbf{X}$ by $R - n + 1 \times C - n + 1$.

Once the output surface is complete for all possible locations of $\boldsymbol{Z}$, if pixels in $\mathbf{Z}^{(i,j)}$ fall under the null hypothesis, then their distribution is $\mathbf{Z}^{(i,j)} \sim \chi^2_{(k-1)p(p+1)/2}$, and as a result one can calculate the Type I error given $\chi^2_{(k-1)p(p+1)/2,\alpha}$ by specifying α. Figure 5.36 illustrates the $\chi^2_{(k-1)p(p+1)/2}$ for two observables $(k = 2)$ using a Type I error of α = 0.05 or $z = 7.9$ and α = 0.01 or $z = 11.4$. The y-axis corresponds to the χ^2 probability given a value z, and the x-axis represents the values that span the distribution. Although

most texts use x as a variable in the x-axis, it was decided to use z for easy correspondence to the values from the output surface in Equation (5.46).

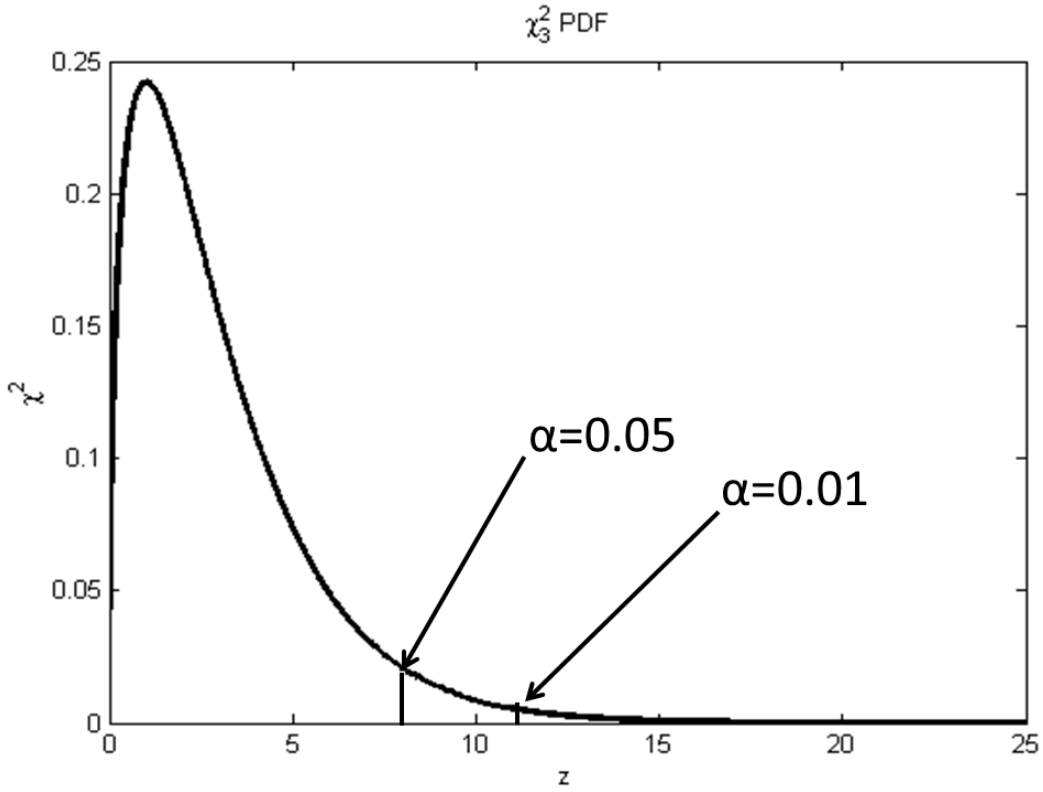

Figure 5.36 Illustration of a χ^2 distribution with three degrees of freedom. Probability of miss (α) = 0.05 (z = 7.9) and α = 0.01 (z = 11.4) are shown in the figure.

Figure 5.37 illustrates the use of the $\chi^2_{(k-1)p(p+1)/2}$ on **Z** using the proposed M-Box as the anomaly algorithm for α = 0.05, 0.01, and 0.001. The output surface **Z** is shown on the top left of the figure. The binary surfaces for different α are shown in the top right (α = 0.05), bottom left (α = 0.01), and bottom right (α = 0.001) and the manmade objects present in the scene are specified in the bottom left image.

As previously explained, under the construct of the anomaly algorithm when setting a desired probability of miss, the user is fixing the probability of missing the incorrect rejection of the null hypothesis. However, from a user/system perspective the probability of missing is usually referred as the probability of false alarms (what the user

does not want to detect) and the intended targets, in this case manmade objects, are considered the true detections. From this point on, the dissertation will refer to pixels related to the TYPE I errors (natural clutter that was incorrectly rejected by the null hypothesis) as false alarms.

One can observe when using $\alpha = 0.05$, the number of false alarms allowed to pass through is quite high, but as the Type I error decreases to $\alpha = 0.01$, the number of false alarms are greatly reduced while preserving the anomalies of interest. If one is to further decrease the Type I error to $\alpha = 0.001$, only T_0, T_{90} and the blackbody are retained but the ability to detect the observation tower and T_{135} successfully is lost.

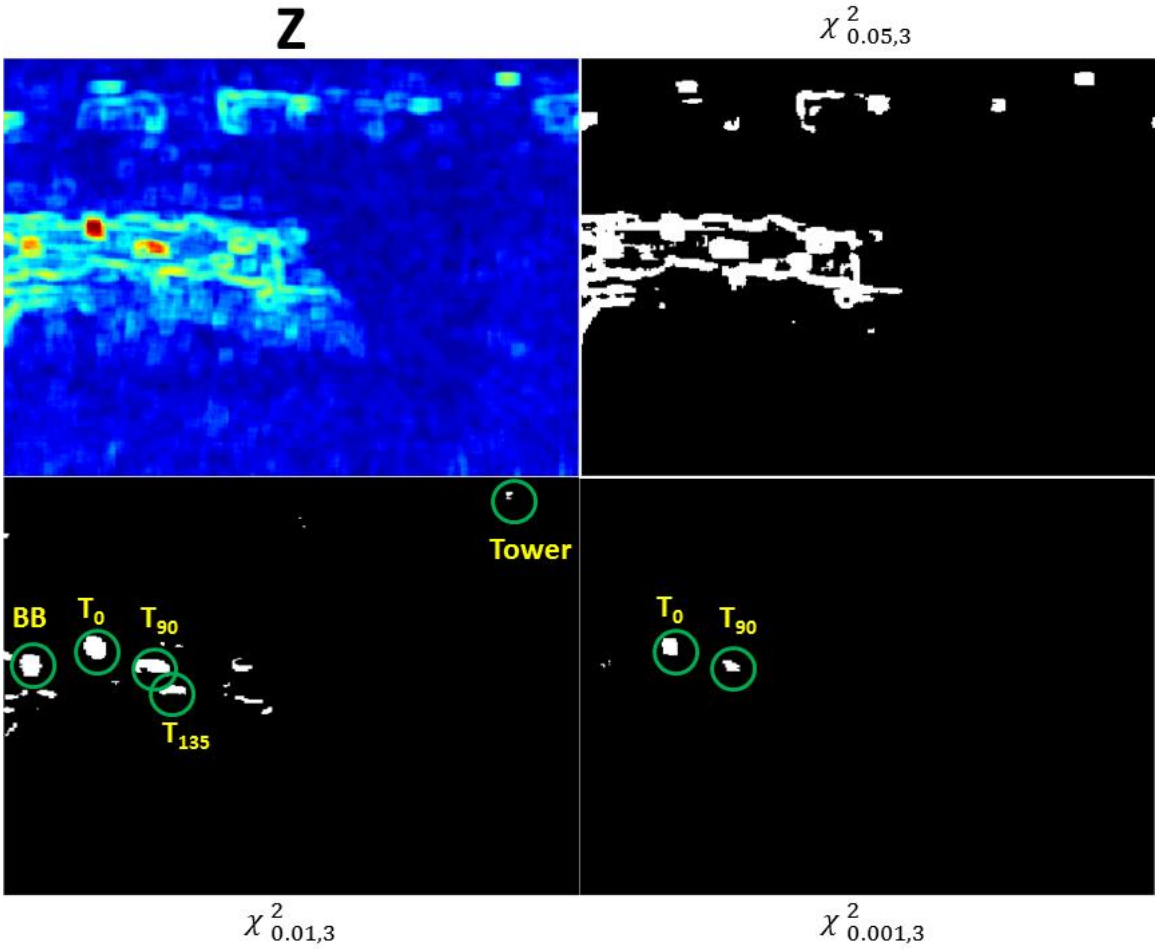

Figure 5.37 Illustration of an example of output surface Z and the threshold imagery given different values of α for a χ_3^2 distribution. The output surface **Z** is located on the top left of the figure for reference. The **Z** surface thresholded using a $\alpha = 0.05$ is shown on the top right, $\alpha = 0.01$ is on the bottom left, and finally $\alpha = 0.001$ is shown on the bottom right of the figure. Using a $\alpha = 0.01$ demonstrates the ability to detect all manmade objects with very few false alarms.

In this subsection the implementation of the anomaly detection algorithm proposed in Subsection 5.3.5 was presented by using a two-step approach to first find the reference covariance matrix and then process small pixel neighborhoods in the data cube **X** using Equation (5.38). Finally, since the null hypothesis values follow a $\chi^2_{(k-1)p(p+1)/2}$, one can determine a probability of miss (α) that can be used to estimate the threshold value using the number of degrees of freedom in the data. Finally, an

example of an output surface **Z** thresholded by different values of α was also presented to the reader.

5.3.6.2 Performance Analysis. A performance comparison between the proposed detector and the different Stokes parameters and DoLP metrics is now presented.

This performance comparison will use ROC curves and output surfaces for the data collection period of 6 MAR 2010, and a 72-hour detection performance for a P_{fa}= 0.005 to demonstrate the effectiveness of the proposed algorithm. The intent of this subsection is to demonstrate:

1) The proposed M-Box algorithm greatly surpasses the detection performance of the Stokes and DoLP parameters for all manmade objects with the exception of the observation tower.

2) At low false alarm rates there is a significant performance difference between the Stokes/DoLP and the proposed algorithm.

3) The M-Box algorithm performed very well for the entire 72-hour data collection regardless of the targets state or perspective angle, with only reduced performance during the periods of high humidity (>80%) and only affecting the performance of T_{135} more than any other object in the scene.

The ROC curves for the four timestamps (Figures 5.38-5.43) demonstrate how each of the metrics performs in discriminating the different manmade objects present in the scene. Reiterating an important key point previously mentioned, the manmade objects are at the same temperature or colder than the background for timestamps 0710h, 0910h, and 2010h, while for timestamp 1310h the manmade objects are hotter than the background. These situations are commonly found in surveillance applications where target temperature varies widely depending of their state (engine *on* or *off*).

For each timestamp there are two ROC plots. The first plot (on the left side of each figure) spans the full range of the P_{fa} ($0 \leq P_{fa} \leq 1$) to show the reader the full performance of the algorithms over the entire probability of false alarm. The ROC plot on the right side focuses on the low P_{fa} region where most systems and users desire to operate.

Figure 5.38 illustrates the performance of the Stokes vector parameters, DoLP, and the M-Box algorithm for T_0 for 0710h, 0910h, 1310h, and 2010h. For the remainder of this subsection, the focus will be on the low P_{fa} range, right side plots, although the full-range ROC curve (left side) is available to the reader if interested.

Referencing Figure 5.38, one can observe that the performance of conventional infrared (S_0) at the operating false alarm range ($P_{fa} \leq 0.01$) is extremely poor for all timestamps with the exception of the high contrast scenario (1310h). During this timestamp, S_0 probability of detection increases at a faster rate to about 0.20 for a $P_{fa} \leq 0.001$ relative to S_1 and DoLP and by $P_{fa} = 0.01$, S_0 performs similarly to S_1. S_2, on the other hand, does not perform very well in discriminating T_0 from the background except for timestamp 1310h where its performance is better than S_0, S_1, and DoLP for a $0.005 \leq P_{fa} \leq 0.01$. For the remainder to the timestamps, S_2 performance can be characterized as somewhat in the middle of S_1 and S_0. S_1 performs the best when compared to the remaining metrics for all timestamps except for 1310h. As it was demonstrated in Section 3.5.2, in high contrast scenarios a significant number of false alarms were usually detected, which in turn degraded the performance of S_1 compared to other metrics. Conversely, the M-Box algorithm performed very well in discriminating T_0 regardless of its state relative to the background. Its probability of detection in the low

false alarm rate for a $P_{fa} = 0.001$ was in excess of 0.35 for 0710h, about 0.15 higher than S_1, P_d =0.68 for 0910h with a probability of detection difference (e.g., $P_{d_{M-Box}} - P_{d_{2nd\ hihgest\ metric}}$) of 0.48 relative to S_1, P_d =1.00 for timestamp 1310h, once again with a probability of detection difference of 0.77 higher performance than S_2, and finally, P_d =0.93 for 2010h, which translated into 0.76 probability of detection difference from S_1.

By fixing the reference P_{fa} to 0.005, the M-Box algorithm had the best average probability of detection for the four timestamps with a $P_d = 0.87$, followed by S_1 ($P_d = 0.28$), DoLP ($P_d = 0.23$,), S_2 ($P_d = 0.19$,), and finally S_0 ($P_d = 0.04$).

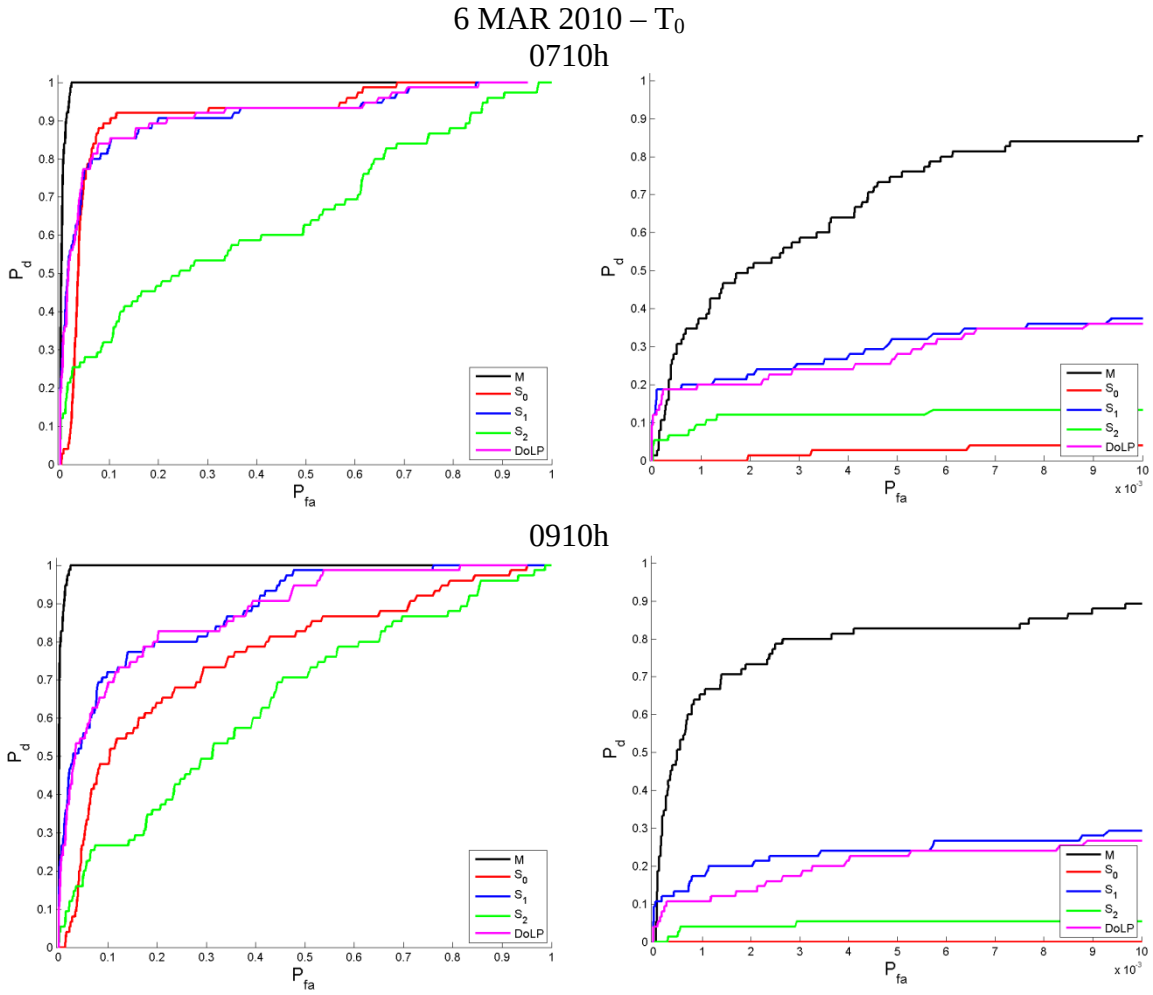

Figure 5.38 ROC curves for T_0 comparing the probability of detection between M-Box detector and conventional Stokes vector and DoLP. The M-box algorithm had the best average probability of detection over the four timestamps with a $P_d = 0.87$ for a reference $P_{fa} = 0.005$, followed by S_1, DoLP, S_2, and S_0 with a $P_d = 0.28, 0.23, 0.19, \text{and } 0.04$, respectively.

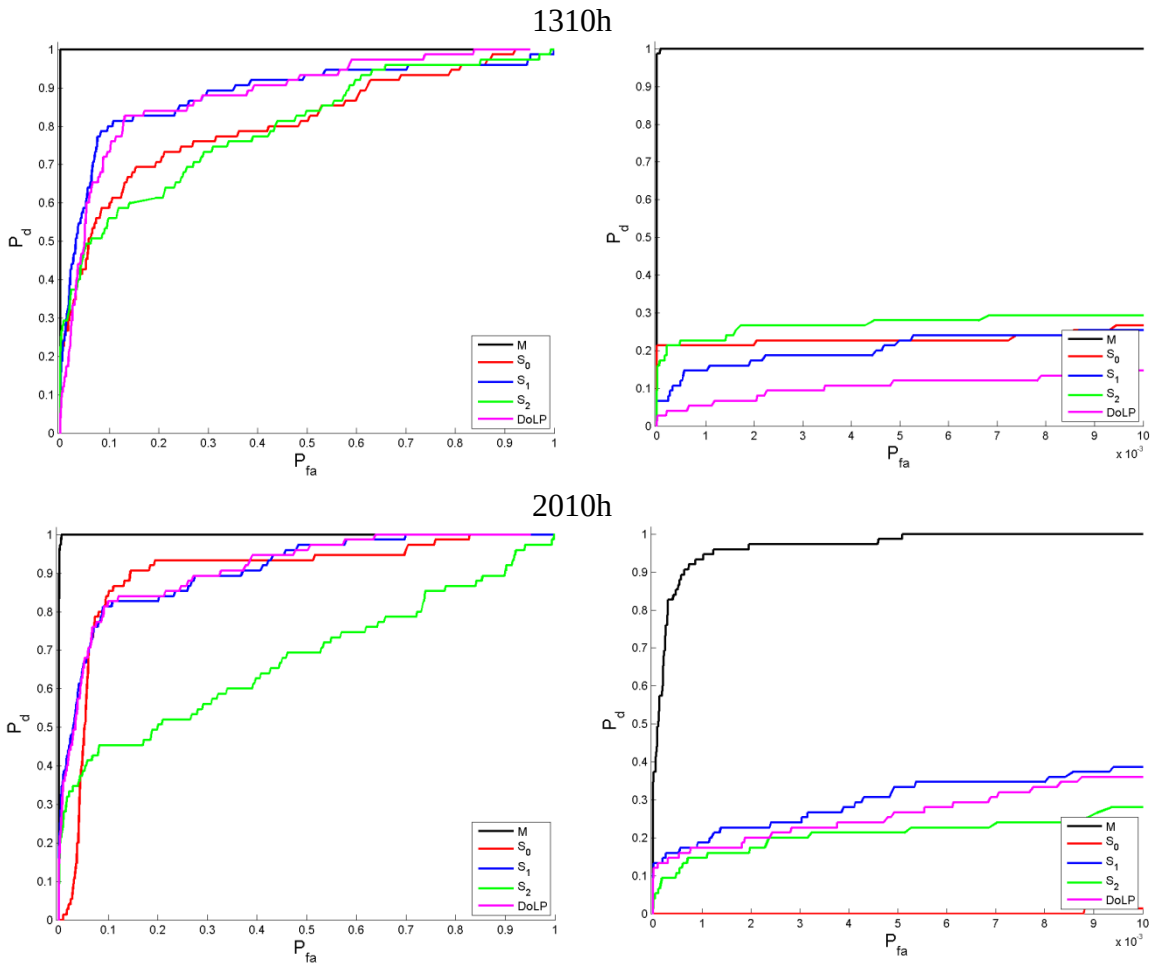

Figure 5.38 ROC curves for T_0 comparing the probability of detection between M-Box detector and conventional Stokes vector and DoLP. The M-box algorithm had the best average probability of detection over the four timestamps with a $P_d = 0.87$ for a reference $P_{fa} = 0.005$, followed by S_1, DoLP, S_2, and S_0 with a $P_d = 0.28, 0.23, 0.19, \text{and } 0.04$, respectively. (Continuation)

By observing the Stokes performance in detecting T_{90} (Figure 5.39 right side plot) one can find a few differences relative to the previous Figure 5.38. One can still observe that S_0 performs very poorly, as expected, during the times of low contrast while demonstrating better performance during the high contrast scenario. The main difference relative to Figure 5.38 is that S_0 is not the highest performing metric for the high contrast scenario when compared to the remaining metrics, rather S_2 performed very well for timestamps 1310h and 2010h, with a probability of detection difference of almost 0.10

(for a $P_{fa} = 0.001$) at timestamp 1310h when compared to Stokes parameter, S_1. S_1 was once again the best performing Stokes/DoLP metric for timestamps 0710h and 0910h, however as previously mentioned S_2 outperformed S_1 for the remaining timestamps. The M-Box algorithm once again performed very well relative to all metrics. For $T_{90,}$ its probability of detection for timestamp 0710h, 0910h, 1310h, and 2010h was 0.92, 0.97, 1.00, and 0.86, respectively. The probability of detection difference between the M-Box and the second highest performing metric for a $P_{fa} = 0.001$ was: 0.67 (for S_1 at 0710h); 0.76 (for S_1 at 0910h); 0.70 (for S_2 at 1310h); and 0.65 (for S_2 at 2010h). Finally, the average probability of detection for each metric over timestamps 0710h, 0910h, 1310h, and 2010h in Figure 5.39 using a reference $P_{fa} = 0.005$ was measured as: $P_d = 0.05, 0.24, 0.23, 0.22, \text{and } 0.94$ for S_0, S_1, S_2, DoLP and the M-Box algorithm, respectively.

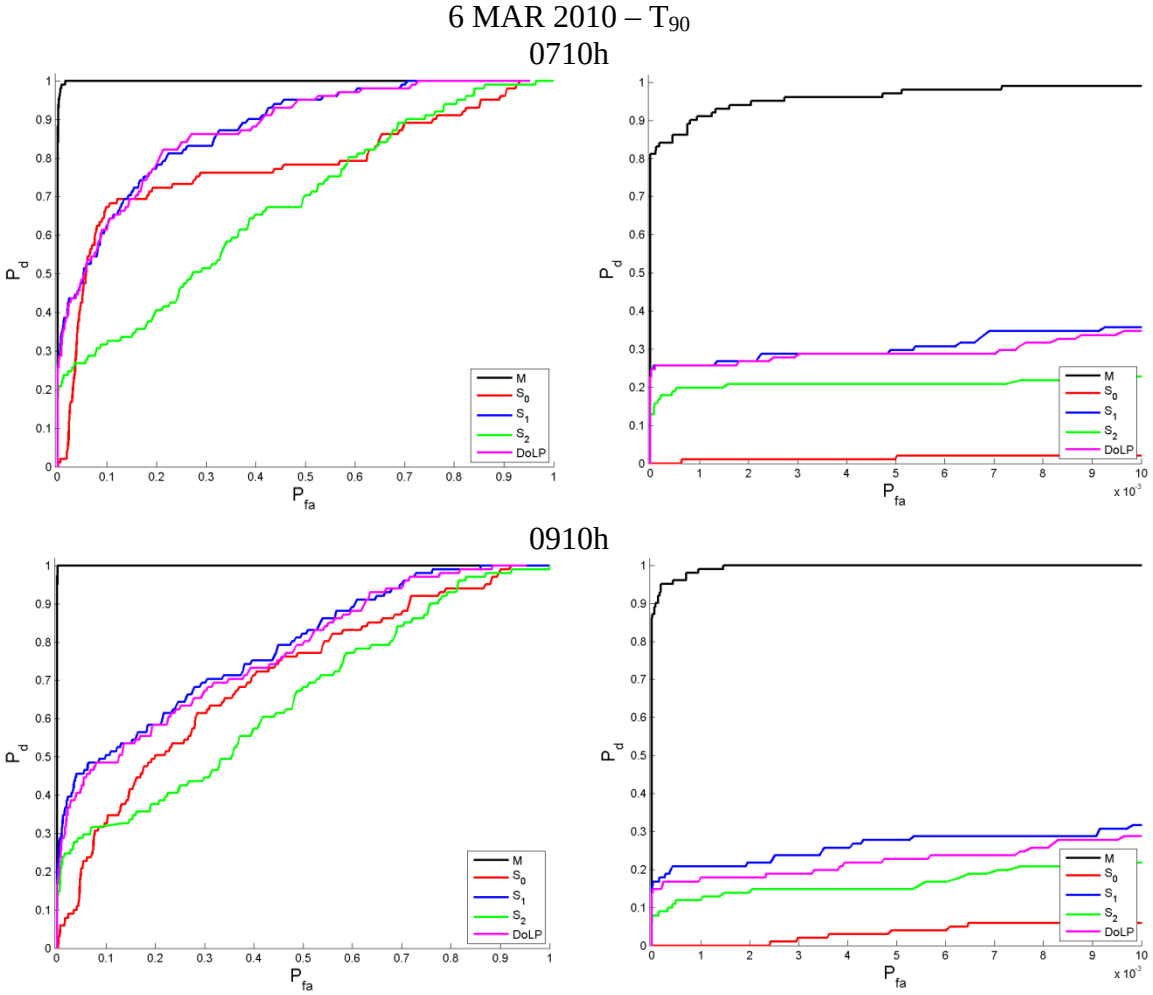

Figure 5.39 ROC curves for T_{90} comparing the probability of detection between M-Box and conventional Stokes vector and DoLP. The probability of detection difference between the M-Box and the second highest performing metric for each timestamp using a reference $P_{fa} = 0.001$ was: 0.67 (for S_1 at 0710h); 0.76 (for S_1 at 0910h); 0.70 (for S_2 at 1310h); and 0.65 (for S_2 for 2010h). The average probability of detection of each metric over the four timestamps and using a reference $P_{fa} = 0.005$ was calculated as $P_d = 0.05, 0.24, 0.23, 0.22,$ and 0.94 for S_0, S_1, S_2, DoLP and M-Box algorithm, respectively.

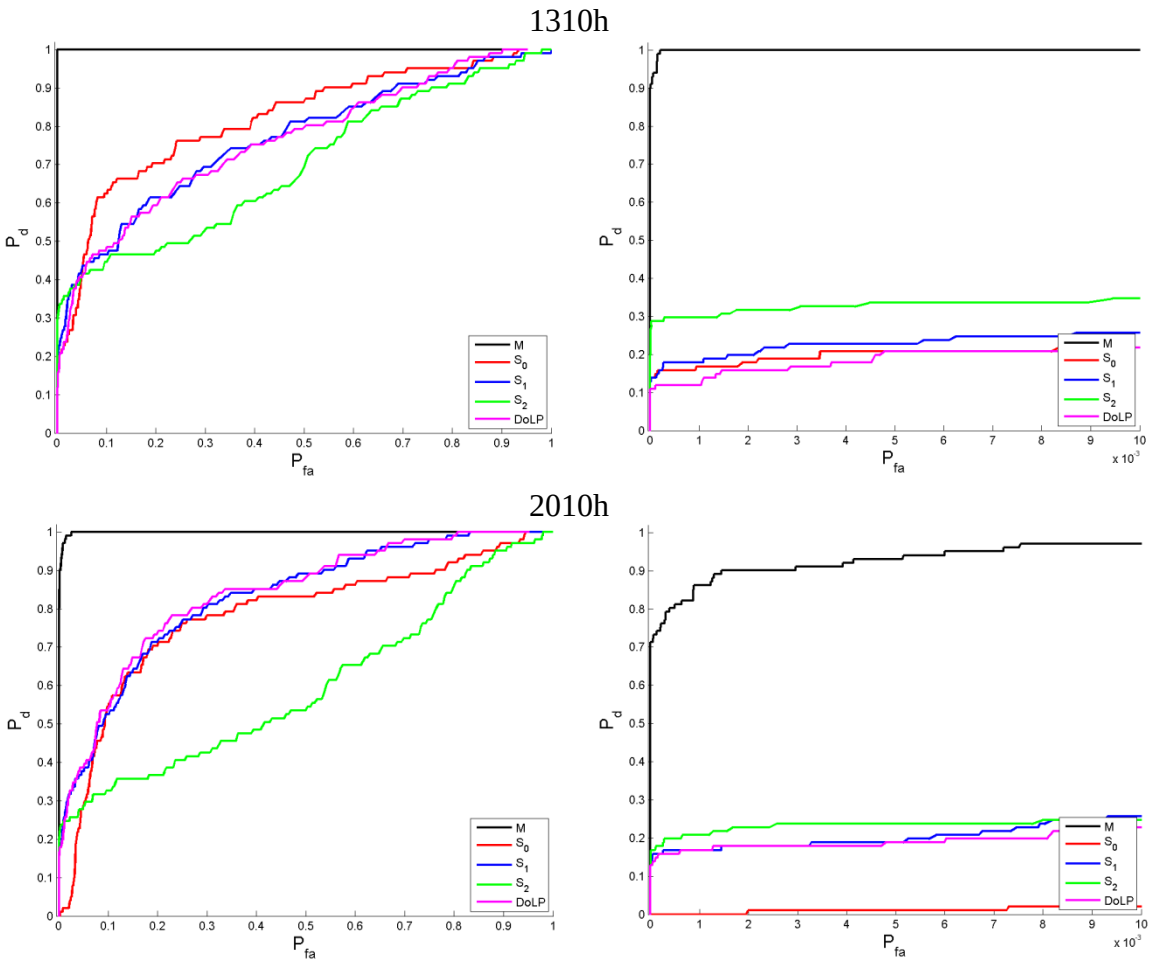

Figure 5.39 ROC curves for T_{90} comparing the probability of detection between M-Box and conventional Stokes vector and DoLP. The probability of detection difference between the M-Box and the second highest performing metric for each timestamp using a reference $P_{fa} = 0.001$ was: 0.67 (for S_1 at 0710h); 0.76 (for S_1 at 0910h); 0.70 (for S_2 at 1310h); and 0.65 (S_2 for 2010h). The average probability of detection of each metric over the four timestamps and using a reference $P_{fa} = 0.005$ was calculated as $P_d = 0.05, 0.24, 0.23, 0.22,$ and 0.94 for S_0, S_1, S_2, DoLP and M-Box algorithm, respectively. (Continuation)

One can observe the same trend as found in Figure 5.39 when examining the performance of the Stokes and DoLP parameters in discriminating T_{135}. S_1 performed the best, relative to the remaining Stokes and DoLP metrics, for timestamp 0910h while S_2 performed very well for timestamps (1310h and 2010h). Furthermore, S_1, S_2, and DoLP performed similarly for timestamp 0710h throughout the low false alarm rate of the ROC

curve (see right side ROC plot). As expected, the M-Box algorithm performed better than the Stokes and DoLP with a probability of detection of $P_d \sim 0.70, 0.90, 0.99, \text{and } 0.67$, where ~ denotes approximately, for all timestamps using a reference $P_{fa} = 0.001$. Finally, the probability of detection difference between the M-Box algorithm and the second best performing metric for the same reference $P_{fa} = 0.001$ was $P_d = 0.58, 0.79, 0.73, \text{and } 0.48$ for timestamps 0710h, 0910h, 1310h, and 2010h, correspondingly. Overall, when averaging the probability of detection over the four timestamps using a reference $P_{fa} = 0.005$, the M-Box algorithm performed the best with an average probability of detection $P_d = 0.79$, followed by S_2, S_1, DoLP, and S_0 with a $P_d = 0.19, 0.14, 0.13, \text{and } 0.05$, respectively.

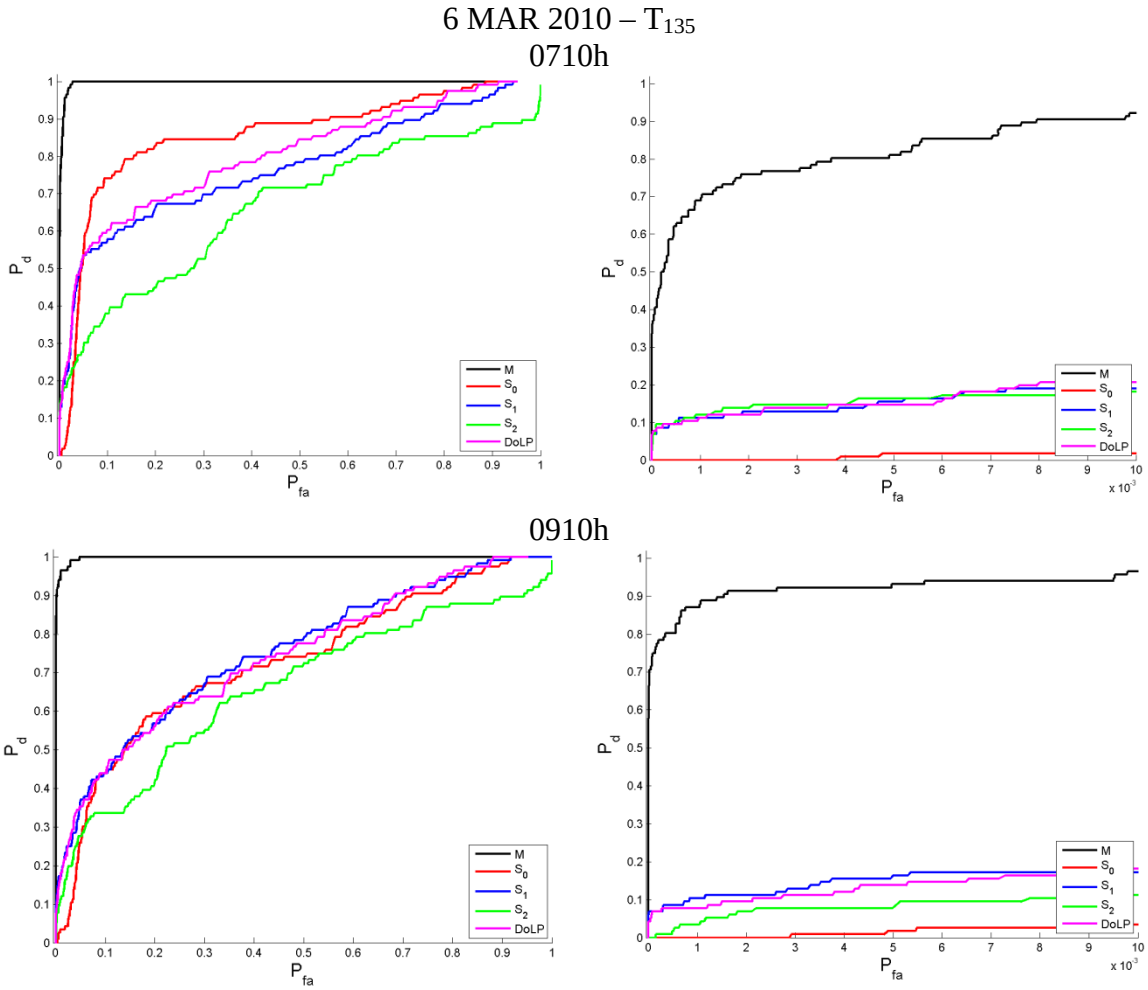

Figure 5.40 ROC curves for T_{135} comparing the probability of detection between M-Box and conventional Stokes vector and DoLP metrics. The best performing metric was the M-Box algorithm with an average probability of detection over the four timestamps with a $P_d = 0.79$ for a $P_{fa} = 0.005$, followed by S_2, S_1, DoLP, and S_0 with a $P_d = 0.19, 0.14, 0.13,$ and 0.05, respectively.

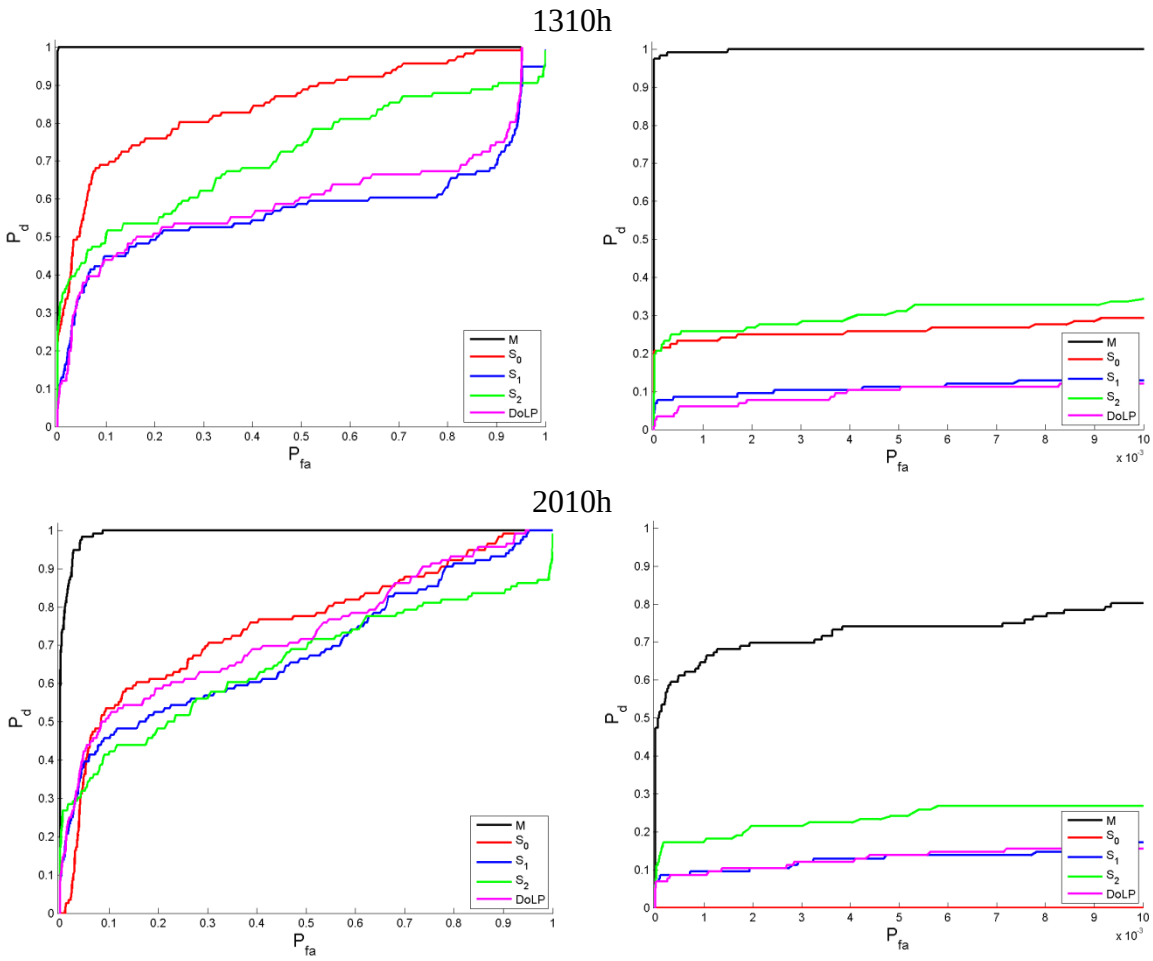

Figure 5.40 ROC curves for T_{135} comparing the probability of detection between M-Box and conventional Stokes vector and DoLP metrics. The best performing metric was the M-Box algorithm with an average probability of detection over the four timestamps with a $P_d = 0.79$ for a $P_{fa} = 0.005$, followed by S_2, S_1, DoLP, and S_0 with a $P_d = 0.19, 0.14, 0.13,$ and 0.05, respectively. (Continuation)

Figure 5.41 illustrates the performance of all the metrics in discriminating the blackbody from natural clutter background. Once again, the following discussion will focus entirely on the ROC plot on the right side of Figure 5.41. For this manmade object the performance of S_0 was very poor regardless of timestamp with a probability of detection of nearly zero while the remaining Stokes parameters performed as follows:

1) S_1 once again performed better than S_2 for timestamps 0710h and 0910h, while at the same time, matching its performance to DoLP.

2) S_2 performed better than S_0, S_1, and DoLP for timestamp 2010h.

3) For timestamp 1310h both S_1 and DoLP had slightly higher probability of detection than S_2 for a $P_{fa} \leq 0.002$ while for the remaining false alarm operating range, $0.002 \leq P_{fa} \leq 0.01$, S_2 performed better than S_1 and DoLP.

Once more, the M-Box algorithm performed very well for all the timestamps exhibiting a probability of detection of 0.94, 0.79, 0.98, and 0.98 for 0710h, 0910h, 1310h, and 2010h respectively. The probability of detection difference between the M-Box and the next best metric for a $P_{fa} = 0.005$ was calculated as 0.75, 0.59, 0.86, and 0.81 for 0710h, 0910h, 1310h, and 2010h, respectively. The average probability of detection over the four timestamps for a $P_{fa} = 0.005$ was as follows: $P_d = 0.99$ for M-Box, followed by S_2 with a $P_d = 0.19$, S_1 and DoLP with a $P_d = 0.16$, and finally S_0 with a $P_d = 0.0$.

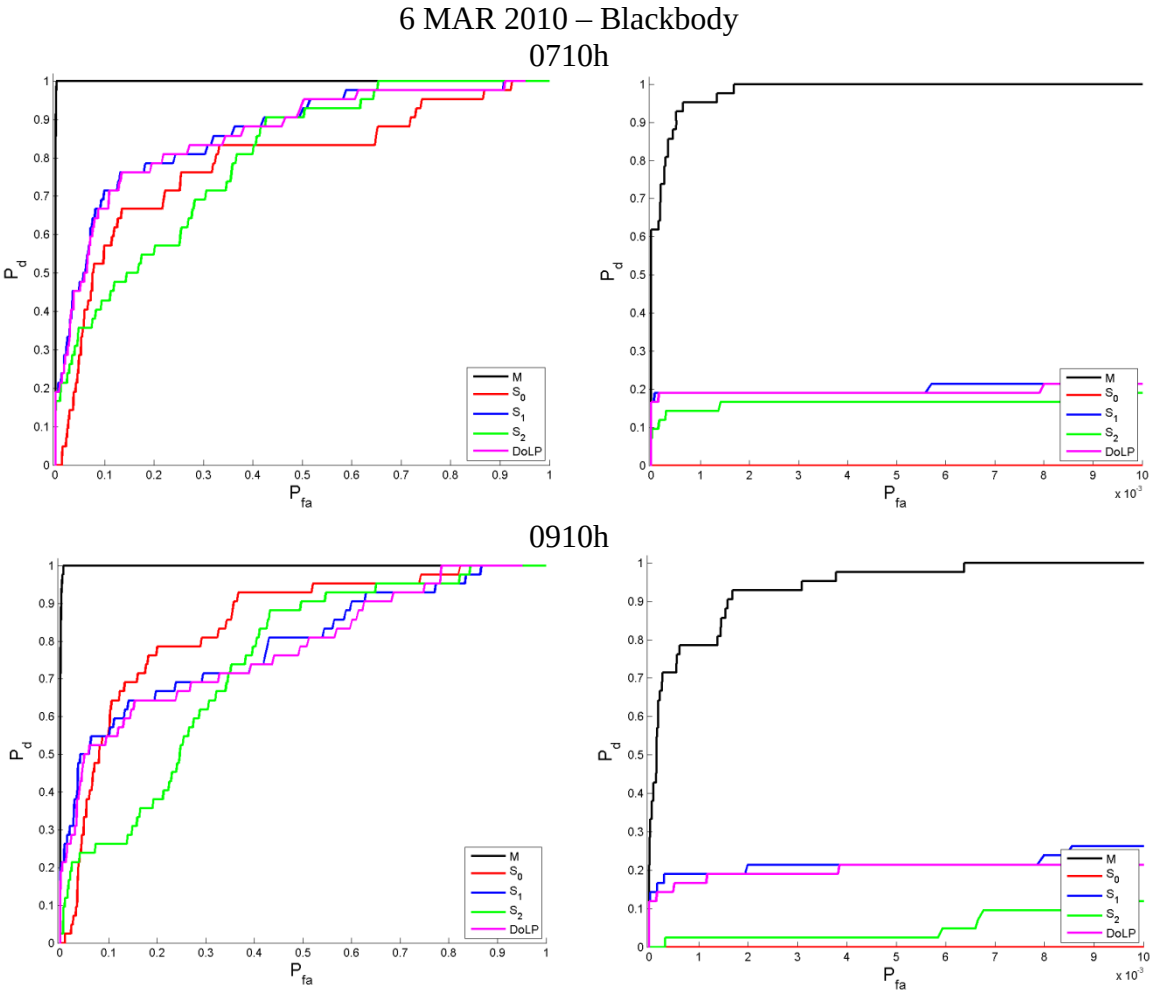

Figure 5.41 ROC curves for Blackbody comparing the probability of detection between M-Box and conventional Stokes vector and DoLP. The average probability of detection over all timestamps using a reference $P_{fa} = 0.005$ was as follows: M-Box with a $P_d = 0.99$, followed by S_2 with a $P_d = 0.19$, S_1 and DoLP with a $P_d = 0.16$, and finally S_0 with a $P_d = 0.0$.

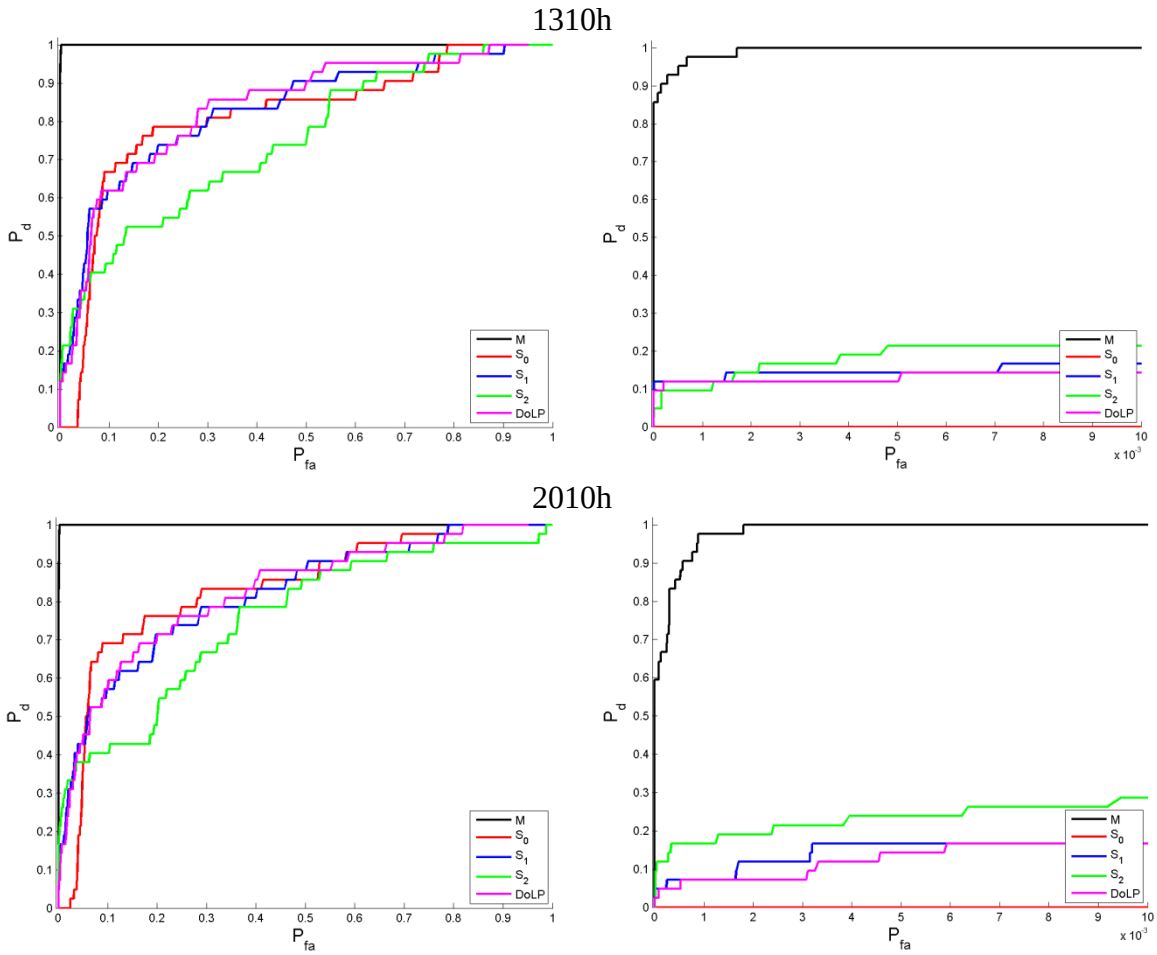

Figure 5.41 ROC curves for Blackbody comparing the probability of detection between M-Box and conventional Stokes vector and DoLP. The average probability of detection over all timestamps using a reference $P_{fa} = 0.005$ was as follows: M-Box with a $P_d = 0.99$, followed by S_2 with a $P_d = 0.19$, S_1 and DoLP with a $P_d = 0.16$, and finally S_0 with a $P_d = 0.0$. (Continuation)

Figure 5.42 illustrates the probability of detection of all the metrics in discriminating the observation tower from the natural clutter background. As one can observe from the ROC plot on the right side of Figure 5.42, S_0 and S_2 performed very poorly with a probability of detection of nearly zero for the P_{fa} range between $0.0 \leq P_{fa} \leq 0.01$. On the other hand, the probability of detection of the M-Box relative to S_1 or DoLP varies tremendously depending of the false alarm rate chosen. For example, for timestamp 0710h, both S_1 and DoLP perform better than the M-Box throughout the low false alarm range (see right side plot of Figure 5.42), while for the remainder of the timestamps: (1) S_1 and DoLP perform better than the M-Box for extremely low false alarm rates only, e.g., $P_{fa} \leq 0.005$ for 0910h, $P_{fa} \leq 0.0025$ for 1310h, and $P_{fa} \leq 0.004$ for 2010h; (2) the proposed algorithm performs better than the Stokes and DoLP parameters for a $P_{fa} > 0.005$. For the four timestamps shown in Figure 5.42, the M-Box algorithm demonstrated an average probability of detection relative to Stokes and DoLP with an average $P_d = 0.21$ for a $P_{fa} = 0.005$. S_1 and DoLP performed slightly better than M-Box with an average probability of detection of $P_d = 0.26$ and 0.25 respectively, and finally S_0 and S_2 exhibited an average probability of detection of $P_d = 0.0$. One can observe in Figure 5.42, depending of the P_{fa} chosen, the P_d difference between S_1 and M-Box can be more or less accentuated.

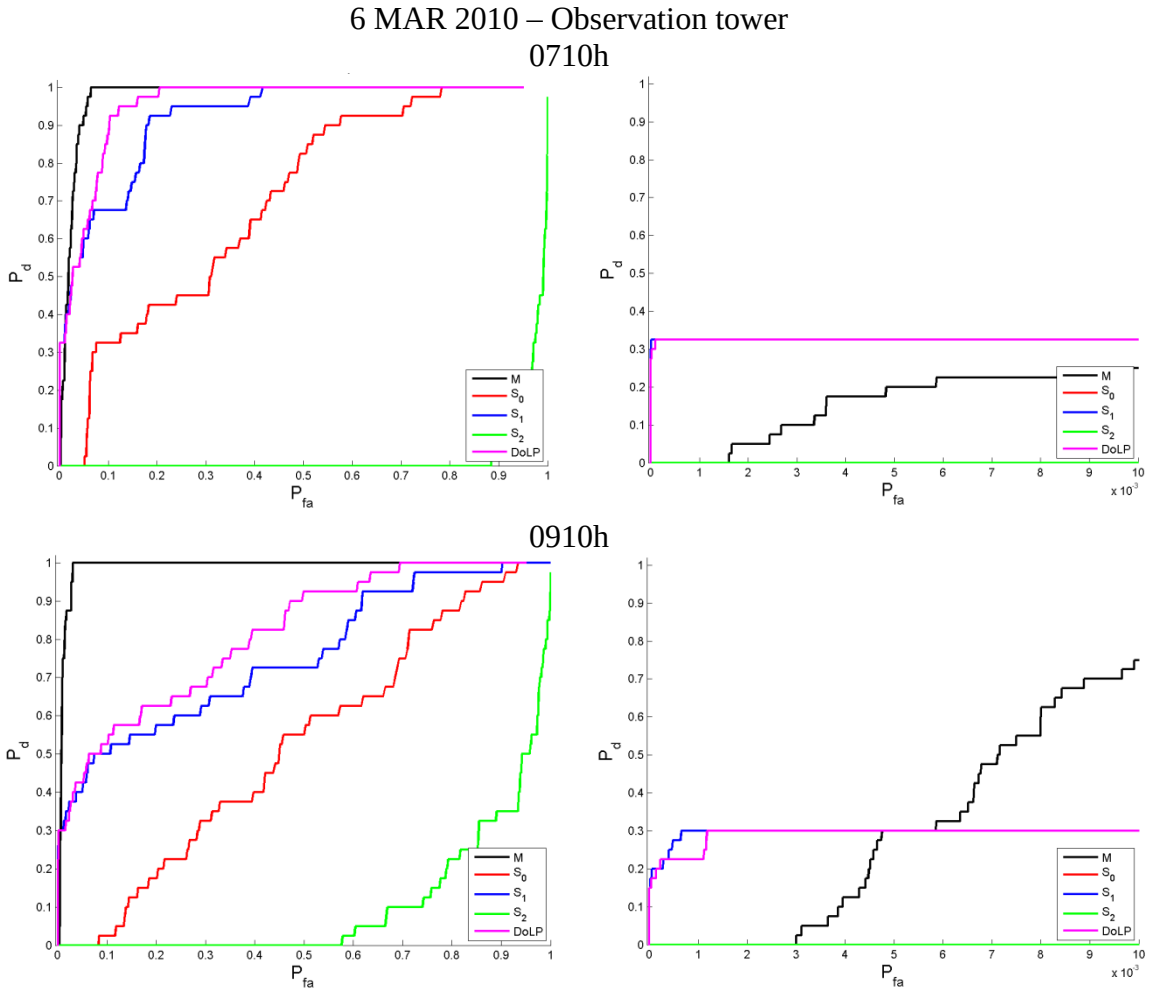

Figure 5.42 ROC curves comparing the probability of detection of the observation tower between M-Box and conventional Stokes vector and DoLP. S_1 and DoLP demonstrated the best average probability of detection (over the four timestamps and for a $P_{fa} = 0.005$) with a $P_d = 0.26$ and 0.25 respectively, followed by the M-Box algorithm with an average $P_d = 0.21$, and finally S_0 and S_2 with a $P_d = 0.0$.

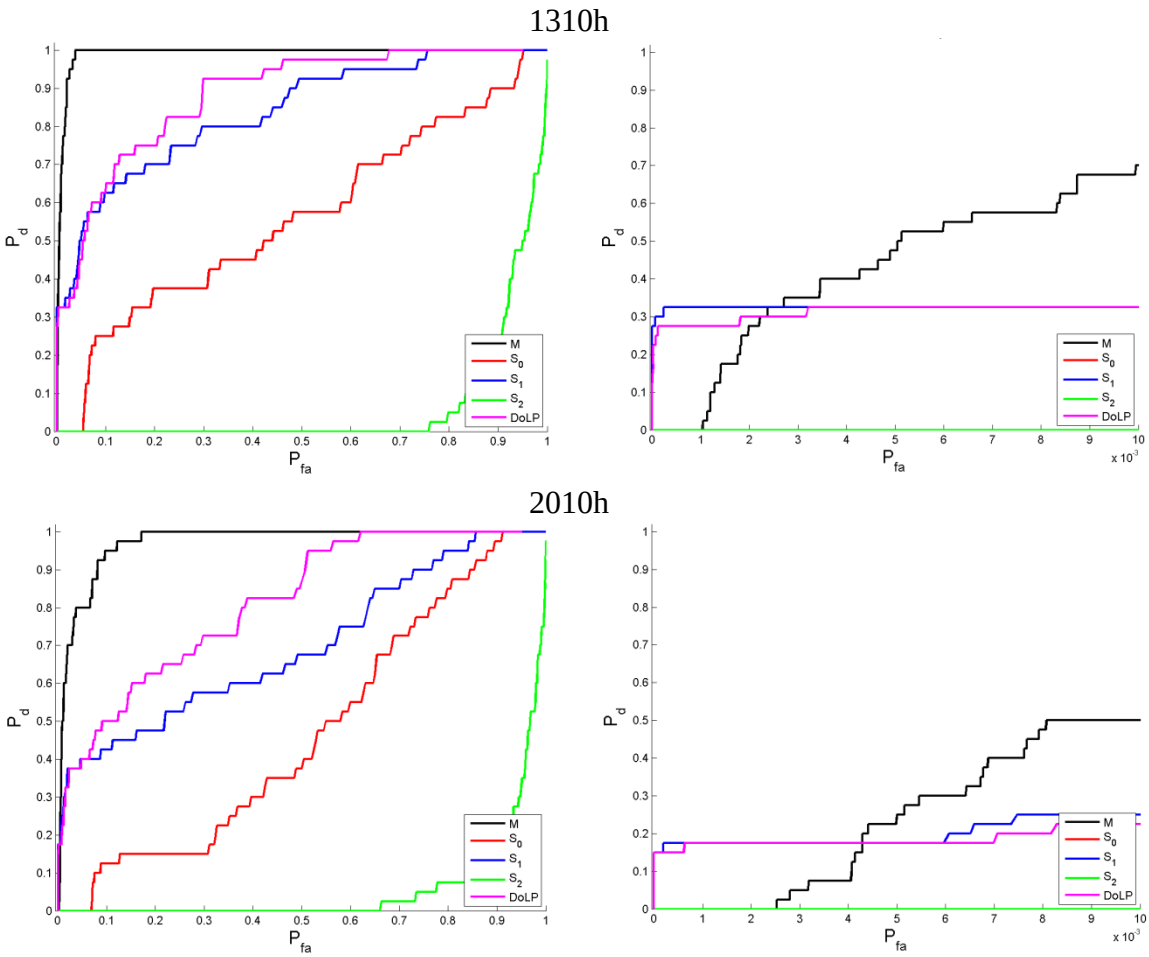

Figure 5.42 ROC curves comparing the probability of detection of the observation tower between M-Box and conventional Stokes vector and DoLP. S_1 and DoLP demonstrated the best average probability of detection (over the four timestamps and for a $P_{fa} = 0.005$) with a $P_d = 0.26$ and 0.25 respectively, followed by the M-Box algorithm with an average $P_d = 0.21$, and finally S_0 and S_2 with a $P_d = 0.0$. (Continuation)

Figure 5.43 demonstrates the probability of detection when all manmade objects are grouped into a single class. As expected, from previous ROC figures shown in this subsection, the proposed algorithm (M-Box) performs very well compared to the Stokes or DoLP metrics. Even with the low probability of detection in discriminating the tower from clutter, the probability of detection of the M-Box algorithm in Figure 5.43 using a $P_{fa} = 0.001$ can be measured as 0.62, 0.74, 0.89, and 0.72 for 0710h, 0910h, 1310h, and 2010h, respectively. The probability of detection difference between the M-Box and the

subsequent higher performing metric was measured as 0.42, 0.56, 0.67, and 0.56 for the respective timestamps. The average probability of detection over the four timestamps and using a reference $P_{fa} = 0.005$ was measured as: $P_d = 0.81$ for the M-Box, followed by S_1, S_2, and DoLP with a $P_d = 0.21, 0.19,$ and 0.19 respectively, and finally S_0 with a $P_d = 0.04$.

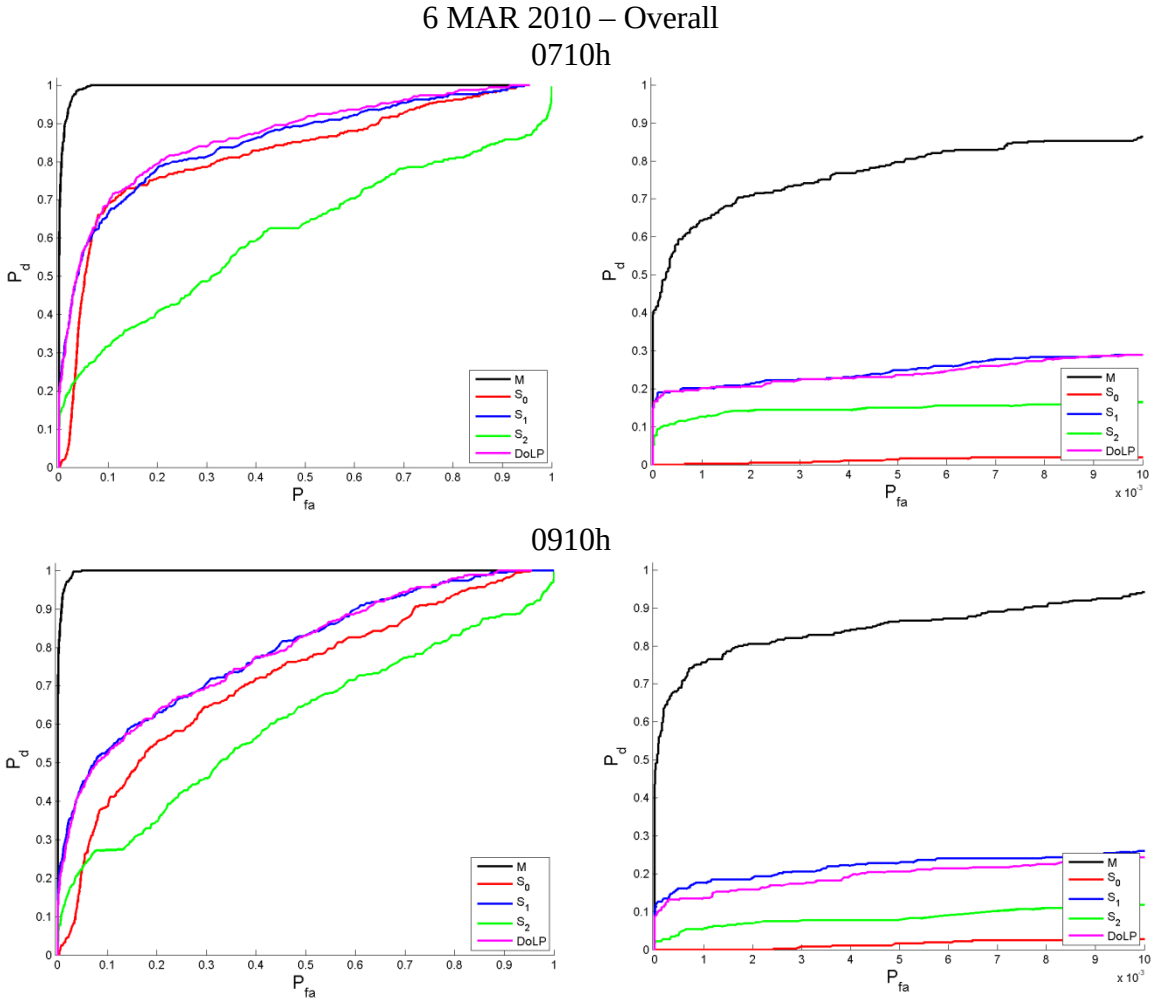

Figure 5.43 ROC curves comparing the probability of detection of all manmade objects as a single class between the M-Box and conventional Stokes vector and DoLP. The average probability of detection over the four timestamps for a $P_{fa} = 0.005$ was measured as: $P_d = 0.81$ for M-Box, followed by S_1, S_2, and DoLP with a $P_d = 0.21, 0.19,$ and 0.19 respectively, and finally S_0 with a $P_d = 0.04$.

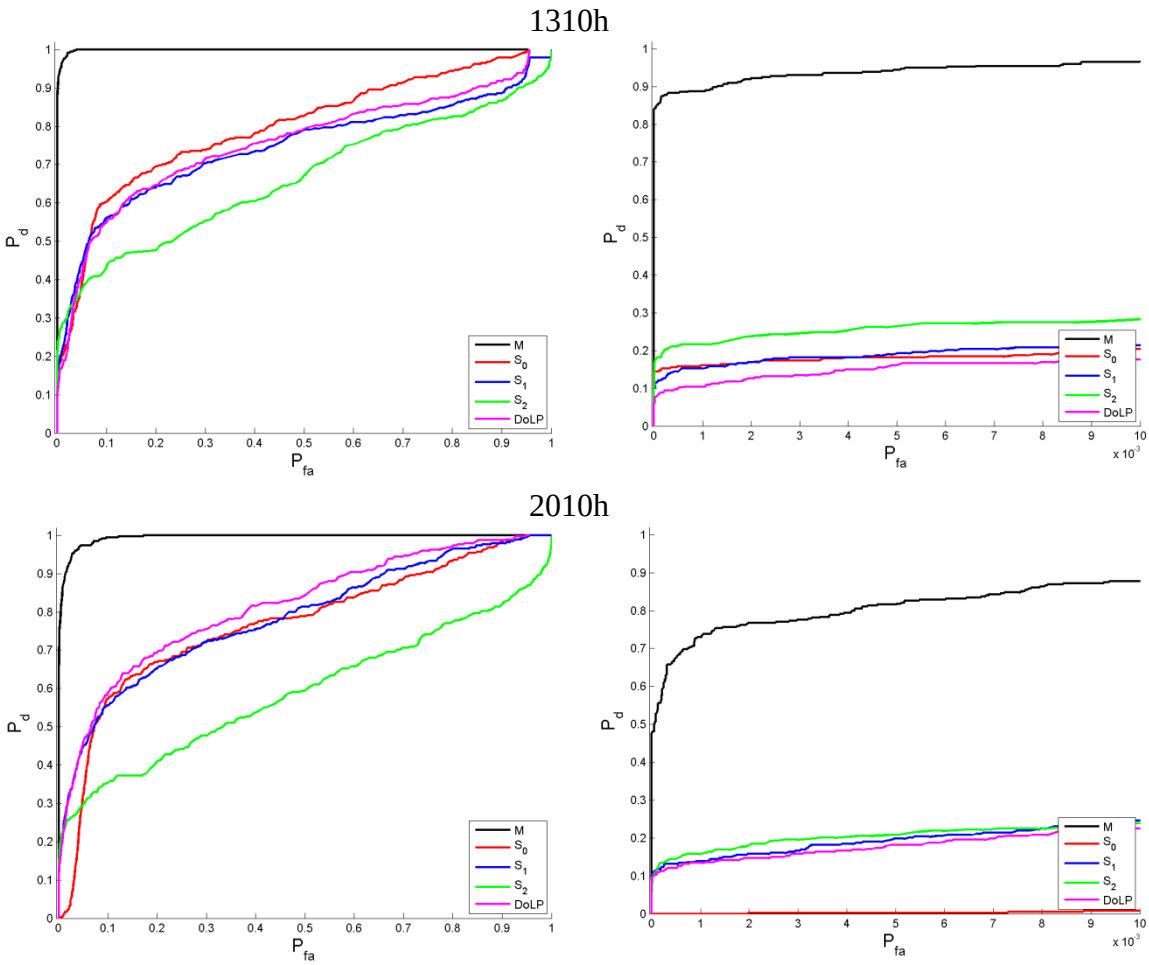

Figure 5.43 ROC curves comparing the probability of detection of all manmade objects as a single class between the M-Box and conventional Stokes vector and DoLP. The average probability of detection over the four timestamps for a $P_{fa} = 0.005$ was measured as: $P_d = 0.81$ for M-Box, followed by S_1, S_2, and DoLP with a $P_d = 0.21, 0.19,$ and 0.19 respectively, and finally S_0 with a $P_d = 0.04$. (Continuation)

Table 5.6 represents the probability of detection of each target separately as well as all manmade objects grouped into a single class for a $P_{fa} = 0.005$ where the proposed algorithm is referenced by the color red to distinguish from conventional Stokes and DoLP metrics. The timestamps chosen for this performance comparison were 0210h, 0710h, 0910h, 1310h, 2010h, and 2310h for 6 MAR 2010. For the chosen P_{fa} the M-Box algorithm performed very well compared to the Stokes parameters for T_0, T_{90}, T_{135}, and the blackbody for all of the timestamps, with the exception of the observation tower

where the M-Box either performed better or similarly to S_1 or DoLP for three out of the six timestamps. From the tables below, one can measure the following average probability of detection for a $P_{fa} = 0.005$ over all timestamps, 0210h, 0710h, 0910h, 1310h, 2010h, and 2310h, as follows: S_0 probability of detection for T_0, T_{90}, T_{135}, blackbody, observation tower, and combined was measured as 0.04, 0.05, 0.05, 0.0, 0.0, and 0.04, respectively. S_1 and DoLP had similar average probability of detection of 0.28, 0.24, 0.14, 0.16, 0.27, and 0.21 for T_0, T_{90}, T_{135}, blackbody, observation tower, and combined, correspondingly. S_2 exhibited an average probability of detection of 0.19, 0.23, 0.18, 0.19, and 0.0, and 0.18. Finally, M-Box algorithm performed extremely well compared to conventional Stokes and DoLP with an average probability of detection measured as 0.94, 0.79, 0.99, 0.21, and 0.76.

In conclusion, the M-Box algorithm demonstrated an enhanced capability in detecting most of the manmade objects better than the Stokes parameters over the six timestamps, with the exception of the observation tower, where its performance was found to be similar to S_1 and DoLP parameters.

Table 5.6 Probability of Detection Comparison Between Stokes and M-Box for Different Timestamps for a $P_{fa} = 0.005$

	T_0				**T_{90}**				**T_{135}**			
	S_0	**S_1**	**DoLP**	**M**	**S_0**	**S_1**	**DoLP**	**M**	**S_0**	**S_1**	**DoLP**	**M**
0210h	0.01	0.23	0.21	**0.87**	0.02	0.22	0.20	**0.87**	0.02	0.14	0.14	**0.56**
0710h	0.03	0.32	0.28	**0.75**	0.01	0.30	0.29	**0.97**	0.02	0.16	0.15	**0.81**
0910h	0.00	0.24	0.23	**0.83**	0.04	0.28	0.23	**1.00**	0.02	0.16	0.14	**0.93**
1310h	0.23	0.23	0.12	**1.00**	0.20	0.23	0.21	**1.00**	0.26	0.11	0.10	**1.00**
2010h	0.00	0.33	0.27	**0.99**	0.01	0.19	0.19	**0.93**	0.00	0.14	0.14	**0.74**
2310h	0.00	0.31	0.25	**0.79**	0.01	0.21	0.19	**0.89**	0.00	0.11	0.12	**0.69**

Table 5.6 Probability of Detection Comparison Between Stokes and M-Box for Different Timestamps for a $P_{fa} = 0.005$ (Continuation)

	Blackbody				**Observation tower**				**Overall**			
	S_0	**S_1**	**DoLP**	**M**	**S_0**	**S_1**	**DoLP**	**M**	**S_0**	**S_1**	**DoLP**	**M**
0210h	0.00	0.07	0.07	**1.00**	0.00	0.18	0.18	**0.05**	0.01	0.17	0.17	**0.55**
0710h	0.00	0.19	0.19	**1.00**	0.00	0.33	0.33	**0.20**	0.01	0.25	0.24	**0.71**
0910h	0.00	0.21	0.21	**0.98**	0.00	0.30	0.30	**0.30**	0.02	0.23	0.21	**0.87**
1310h	0.00	0.14	0.12	**1.00**	0.00	0.32	0.33	**0.48**	0.18	0.19	0.16	**0.94**
2010h	0.00	0.17	0.14	**1.00**	0.00	0.18	0.18	**0.25**	0.003	0.20	0.18	**0.82**
2310h	0.00	0.17	0.14	**1.00**	0.00	0.28	0.20	**0.00**	0.003	0.20	0.17	**0.69**

Figure 5.44 illustrates the broadband images on the left (for visual appreciation) and the output surfaces for M-Box (top left), S_0 (top right), S_1 (bottom left), and DoLP (bottom right). The output surfaces are normalized so they can be easily compared. For

this particular example it is desirable to have manmade locations with the color red and natural clutter as the color blue.

One can readily observe that the M-Box algorithm is able to discriminate manmade objects very well as evident by their large red and yellow areas, which unlike the remainder of the metrics the target locations are not as noticeable. For example, S_0 is only useful at 1310h due to high contrast between the manmade objects and natural clutter, while for the remainder of the timestamps the manmade objects have similar temperature to natural clutter and as a result S_0 is unable to discriminate them at all. S_1 and DoLP have similar performance in discriminating the manmade objects from within the natural clutter. As a result of the angle dependency between the target surfaces and the sensor only a small number of pixels are clearly visible for each of the manmade objects while the remainder of the targets is within the natural clutter background distribution (blue color). The M-Box performed very well throughout the six timestamps shown in Figure 5.44 by identifying the locations where the manmade objects are present relative to conventional Stokes and DoLP. Furthermore, one can also observe an interesting characteristic when using the M-Box algorithm; in low contrast scenarios the M-Box can identify manmade objects as a result of their polarimetric variability with respect to the background. However, during the high contrast periods, the M-Box performance increases as a result of the polarimetric diversity as well as the temperature difference between the manmade objects and clutter.

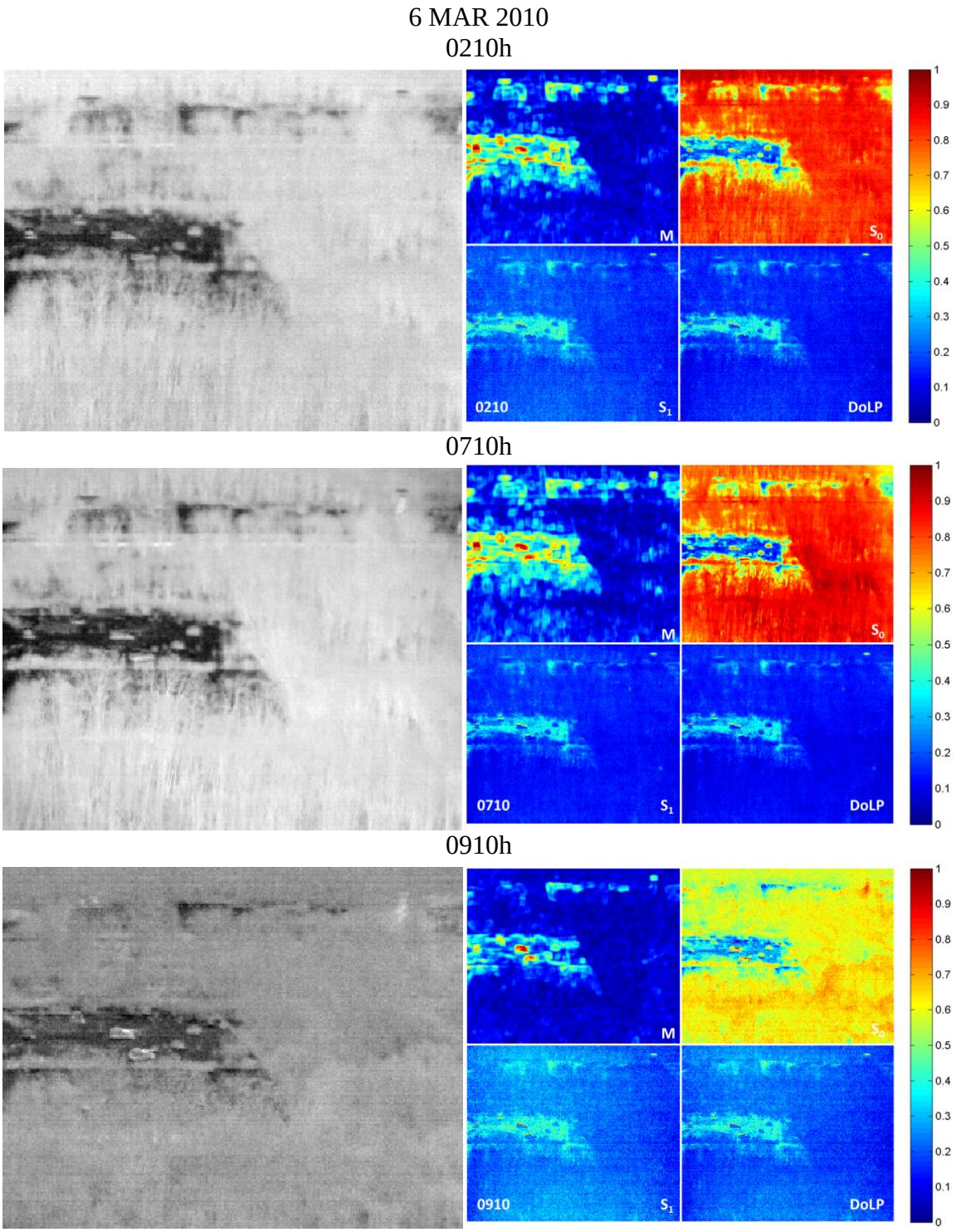

Figure 5.44 Output surfaces for the proposed M-Box algorithm and S_0, S_1, and DoLP.

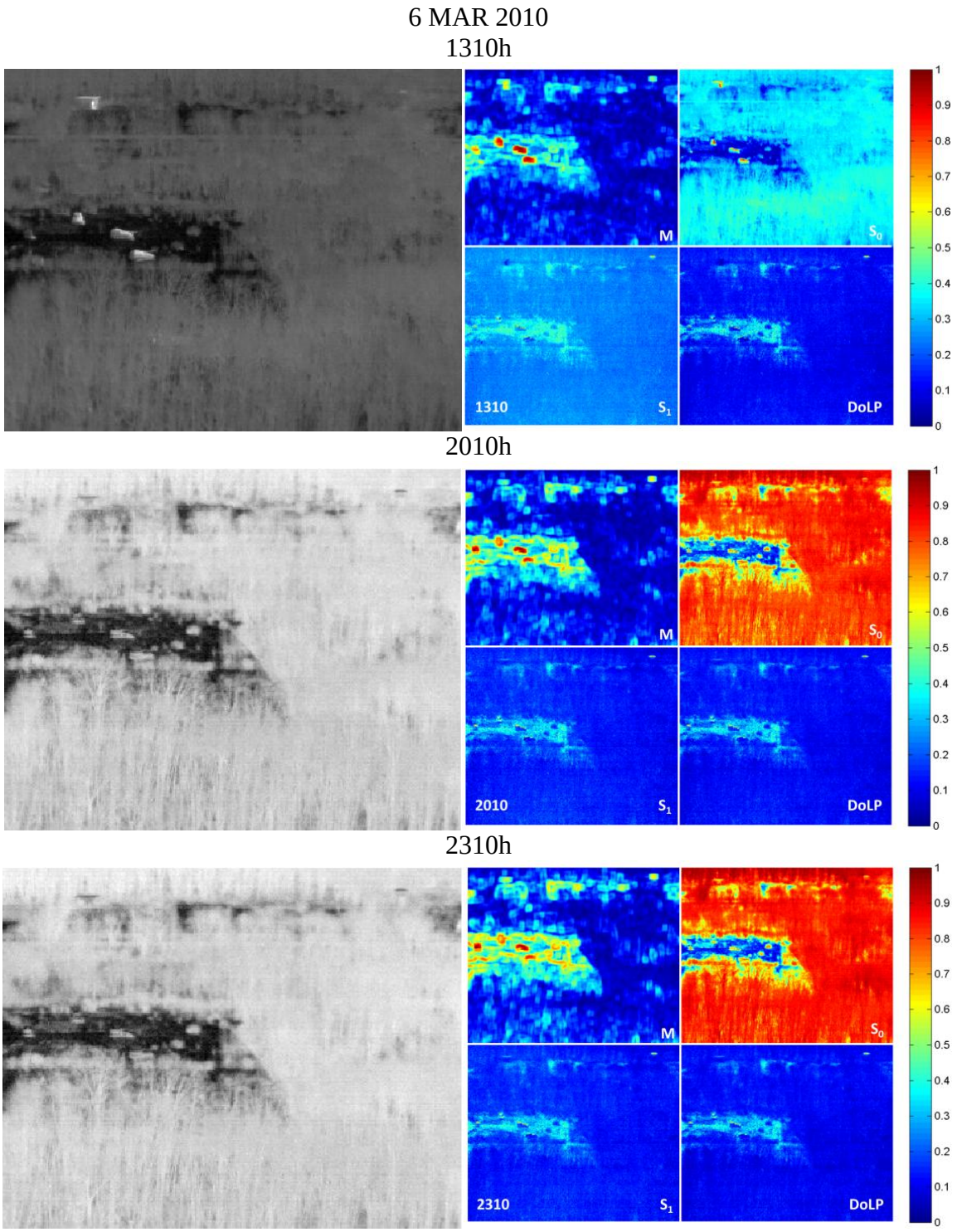

Figure 5.44 Output surfaces for the proposed M-Box algorithm and S_0, S_1, and DoLP.(Continuation)

Figures 5.45 through 5.49 illustrates the probability of detection of all metrics for a 72-hour performance period from 6 through 8 MAR, 2010 for each of the individual manmade objects in the scene for a $P_{fa} = 0.005$, while Figure 5.50 illustrates the probability of detection when all the manmade objects are grouped into a single class.

As expected, the probability of detection plots vary significantly over the 72 hours regardless of the metric used since the output surfaces for each algorithm also vary as a consequence of diurnal cycles, weather events, and target states. As mentioned before, for each of the figures, a common $P_{fa} = 0.005$ was chosen to fairly compare the performance of each algorithm independent of threshold.

Figure 5.45 demonstrates the probability of detection of all the metrics for T_0 for the 72-hour performance period. As anticipated, S_0 only performed well in situations where the target is either in a solar loaded state, during the day time (1st and 3rd day), or when the target is internally heated (day 2). As previously observed, S_1 and DoLP exhibited similarly probability of detection; however one can notice some significant differences in their performances that are worth mentioning. In day 1, there is a probability of detection difference between DoLP and S_1, where DoLP lagged in performance between 1100h and 2300h, finally catching up to S_1 after 2330h on the same day. This lagging effect can be observed once again in day 2, while in day 3, both the DoLP and S_1 behave quite similarly to each other for the full 24 hours. S_1, on average, is the best performing metric (highest average probability of detection over the 72-hour period) relative to the remaining Stokes parameters and DoLP in discriminating T_0 from natural clutter background. S_2 performs better than S_1 during some periods but such occurrences are rare and only for brief moments. In general, S_2 underperforms both S_1

and DoLP over the 72-hour period. The M-Box algorithm, on the other hand, demonstrates a tremendous capability in discriminating T_0 from natural clutter in comparison to the remaining metrics. Two extreme performance degradations during the 72-hour data can be observed. For example, the first occurs on the first day at around 0600h while the second happens during the last few hours of day 3. The first performance degradation can be contributed, to the best of the author's knowledge, to a considerable change in T_0's polarization diversity relative to the background, which in turn affected the output of the M-Box algorithm, while the second, is a direct consequence of extremely high humidity values (>80%). During these two situations, the performance of the M-Box algorithm, for the most part, performed better than the Stokes or DoLP metrics. As expected, the M-Box algorithm had the best 72-hour average probability of detection of all metrics with a $P_d = 0.92$, followed by S_1, DoLP, S_2, and S_0 with a $P_d = 0.35, 0.30, 0.25, \text{and } 0.07$, correspondingly.

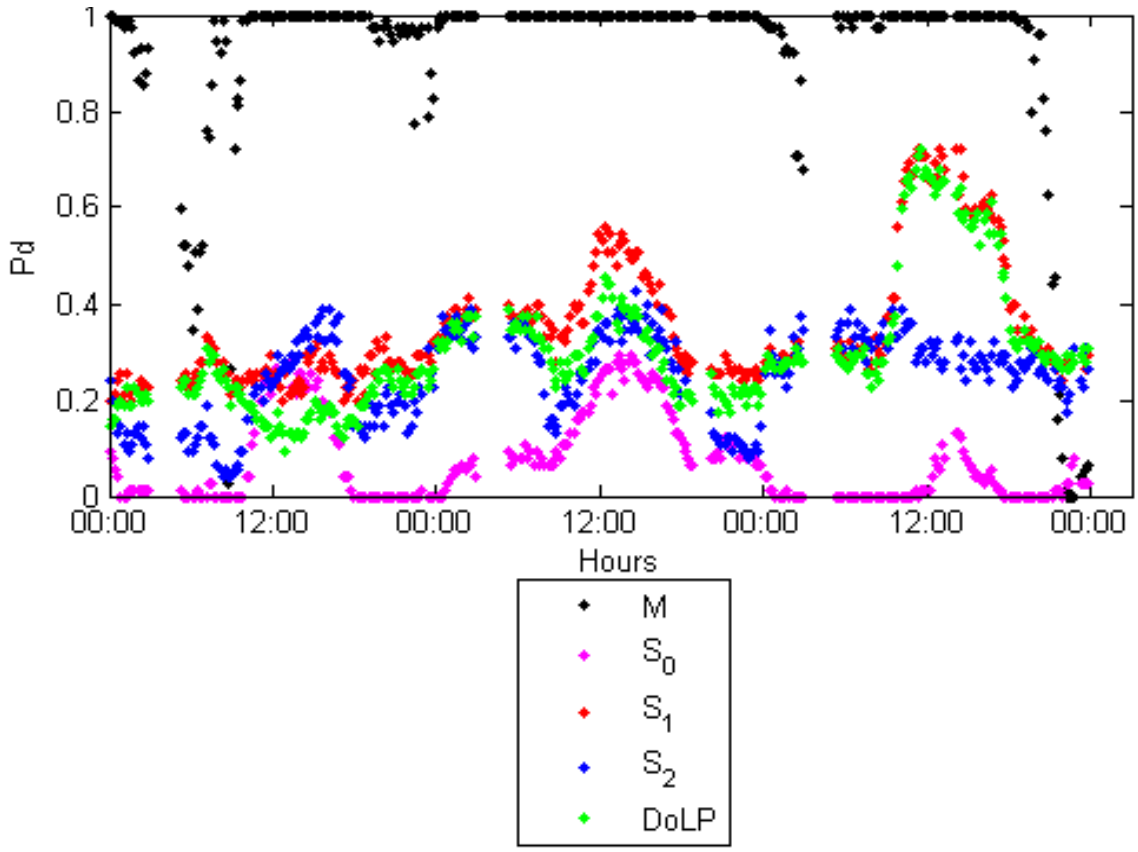

Figure 5.45 72-hour probability of detection comparison between Stokes parameters, DoLP, and M-Box algorithms in discriminating T_0 from natural clutter. The M-Box algorithm demonstrated the best 72-hour average probability of detection with a $P_d = 0.92$, followed by S_1, DoLP, S_2, and S_0 with a $P_d = 0.35, 0.30, 0.25, \text{and } 0.07$, correspondingly.

Figure 5.46 illustrates the 72-hour probability of detection of all metrics in discriminating T_{90} from natural clutter background. In this figure, one observes some interesting dissimilarities relative to the previous Figure 5.45 that are important to comment. In Figure 5.45, one could clearly observe S_1 as the best performing Stokes/DoLP metric for the full 72 hours, although S_2, at times and very rarely, performed slightly better than S_1. In Figure 5.46, there's a clear back and forth between S_1 and S_2 as the best performing metric for the 72-hour data in discriminating T_{90}. For example, between 0000h and 1200h in day 1, one observes a good S_1 performance

relative to S_2. Conversely, between 1200h in day 1 and 1000h in day 2, S_2 becomes the best performing metric, when compared to S_0, S_1, and DoLP. Then once again S_1 performs better than S_2 for a brief moment in day 2 between 1100h and 1200h. S_2 once more performed better than S_1 between the hours of 1200h and 1900h, and finally S_1 performed better than S_2 for the remaining of day 2. Finally in day 3, S_2 appears to be the best performing metric compared to the remaining Stokes and DoLP parameters. DoLP, unlike previous Figure 5.45, also performed quite well, demonstrating similar performance to S_1. S_0, as expected, did not perform as well when compared to the remaining metrics, demonstrating extremely poor performance results for day 2 and 3 regardless of high or low contrast scenarios, while for day 1, its probability of detection was quite comparable to S_1, S_2, and DoLP but only for high contrast scenarios and for brief periods of time.

The M-Box algorithm, see Figure 5.46, performed quite remarkably compared to the remaining metrics with two extreme performance degradations at the end of day 2 and day 3. These two degradation events, as explained in the previous Figure 5.45, are a result of high humidity (>80%) encountered during these two periods of time. The performance degradation that occurs at the end of day 2 is more pronounced for T_{90} than T_0 while for the third day, the degradation encountered is lesser than shown in the previous Figure 5.45. Nonetheless, the M-Box algorithm was still the best performing metric with an average probability of detection over the 72 hours with a $P_d = 0.93$, followed by S_1, S_2, and DoLP performing similarly to each other with a $P_d = 0.24$, and finally S_0 with a $P_d = 0.04$.

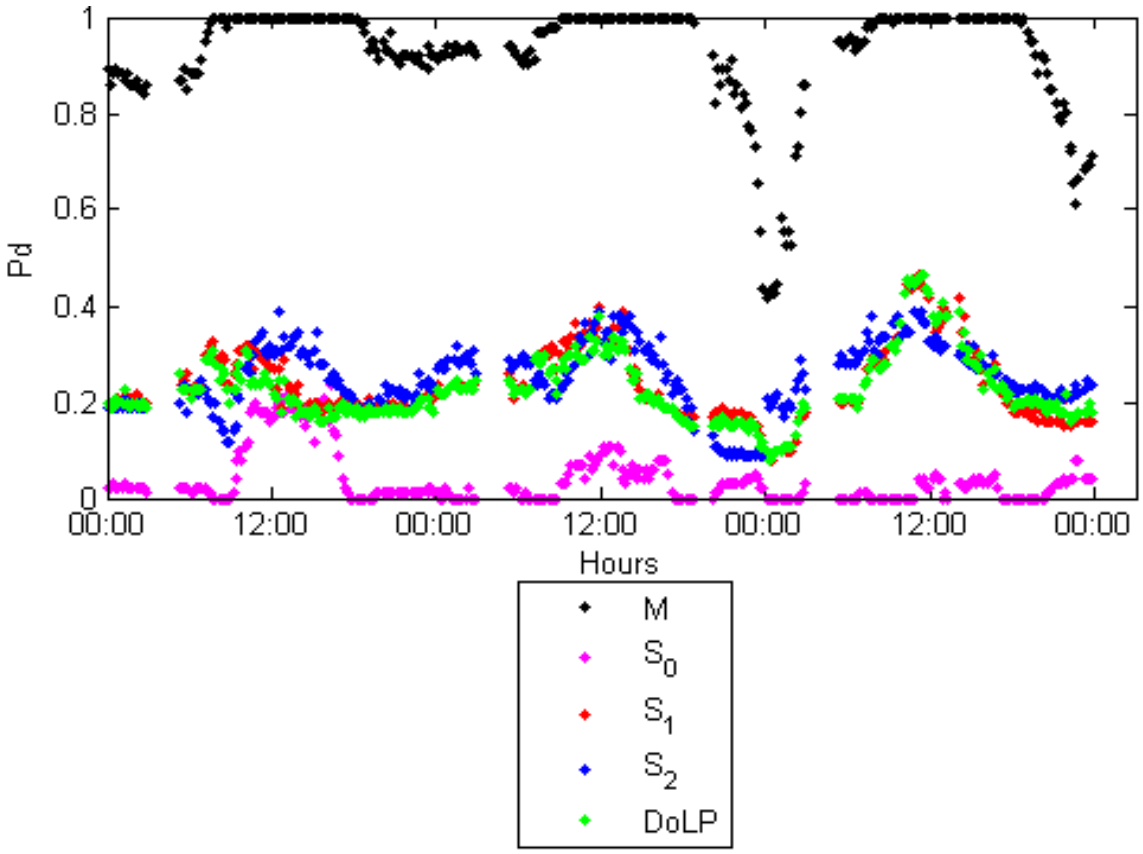

Figure 5.46 72-hour probability of detection comparison between Stokes parameters, DoLP, and M-Box algorithms in discriminating T_{90} from natural clutter. The M-Box algorithm demonstrated the best 72 hour average probability of detection with a $P_d = 0.93$, followed by S_1, S_2, and DoLP with a $P_d = 0.24$, and finally S_0 with a $P_d = 0.04$.

Figure 5.47 demonstrates the probability of detection of Stokes, DoLP, and M-Box for the 72-hour period for T_{135} discrimination from natural clutter background. Once again, there are certain performance dissimilarities shown in T_{135} relative to previous targets (T_0 and T_{90}). For example, S_2 in this case, exhibits the best average probability of detection throughout the 72-hour period with some rare periods where one finds similar detection rates for S_1 and DoLP. These periods can be found during the first hours of day 1 as well as some underperforming periods close to the end of day 2. S_2 probability of detection was highly variable throughout the three days, however one can observe that for

high contrast periods S_2 performs better compared to low contrast scenes. During high contrast periods, S_2 probability of detection hovered between 0.30 and 0.40, while during low contrast periods, S_2 probability of detection was measured to be between 0.15 and 0.30. S_1 and DoLP 72-hour average probability of detection was about 0.15 with some periods of better performance found in day 3 as well as periods of low performance found at the end of day 2 as a consequence of high humidity. During this event all metrics, including the M-Box algorithm, were adversely affected.

S_0 in Figure 5.47, surprisingly, performed much better compared to the previous two targets (T_0 and T_{90}) where during the high contrast periods the S_0 performance was higher or similar to the other Stokes metrics, while during the periods of low contrast, S_0 once again performed very poorly.

The proposed algorithm, M-Box, demonstrated once more its ability to discriminate T_{135} successfully from natural clutter background relative to the remaining metrics. On the contrary to what was observed with T_0 and T_{90}, there's a tremendous amount of variability in the 72-hour probability of detection measurements, where high probability is synonymous to high contrast scenarios as low probability is to low contrast. Nonetheless, the measured probability of detection for the M-Box algorithm was considerably higher relative to Stokes and DoLP parameters by a significant margin for most of the 72-hour period, with some probability of detection degradation found during the periods of high humidity at the end of day 2 and day 3. For the detection of T_{135} the M-Box average 72-hour probability of detection was measured to be $P_d = 0.79$, followed by S_2 with a $P_d = 0.25$, then S_1 and DoLP with a $P_d = 0.15$, and finally S_0 with a $P_d = 0.04$.

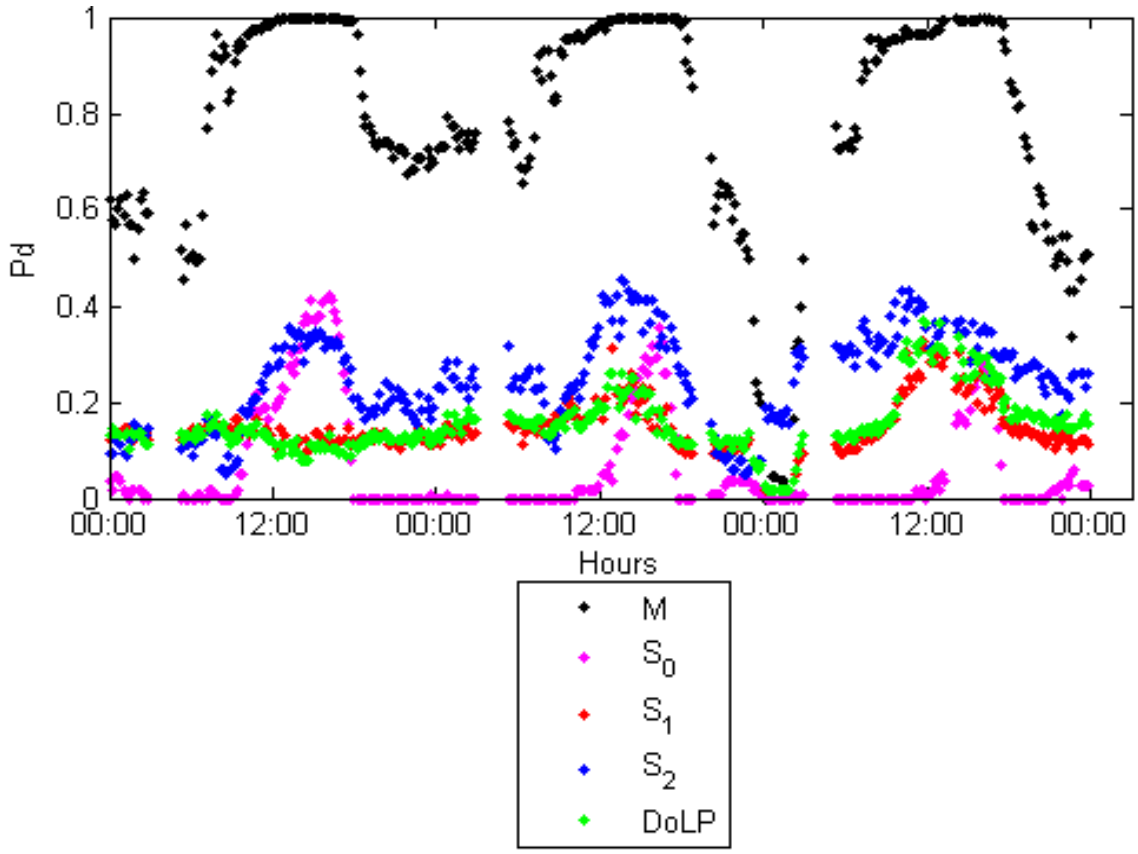

Figure 5.47 72-hour probability of detection comparison between Stokes parameters, DoLP, and M-Box algorithms in discriminating T_{135} from natural clutter. The M-Box average 72-hour probability of detection was measured to be $P_d = 0.79$, followed by S_2 with a $P_d = 0.25$, then S_1 and DoLP with a $P_d = 0.15$, and finally S_0 with a $P_d = 0.04$.

Figure 5.48, which demonstrates the 72-hour probability of detection of all metrics in discriminating the blackbody from natural clutter, illustrates some of the trends shown in previous Figure 5.47. For this manmade object, S_2 once again performs very well in discriminating the blackbody from natural clutter compared to S_1 and DoLP for the 72-hour period. S_1 and DoLP only demonstrate better probability of detection during the periods of high contrast more specifically around 1200h. S_0 performed the worst of all metrics with absolutely no detection whatsoever for the chosen probability of false alarm. The M-Box algorithm on the other hand, had almost perfect detection rate (P_d~1.00) for most of the 72 hours with very few periods where the probability of

detection fell below 0.90 which, as stated before, are due to the adverse conditions found in those periods of time. In sum, the M-Box was the best performing metric with an 72-hour average probability of detection of $P_d = 0.96$, followed by S_2, S_1, DoLP, and S_0 with a $P_d = 0.22, 0.16, 0.15, \text{and } 0.0$.

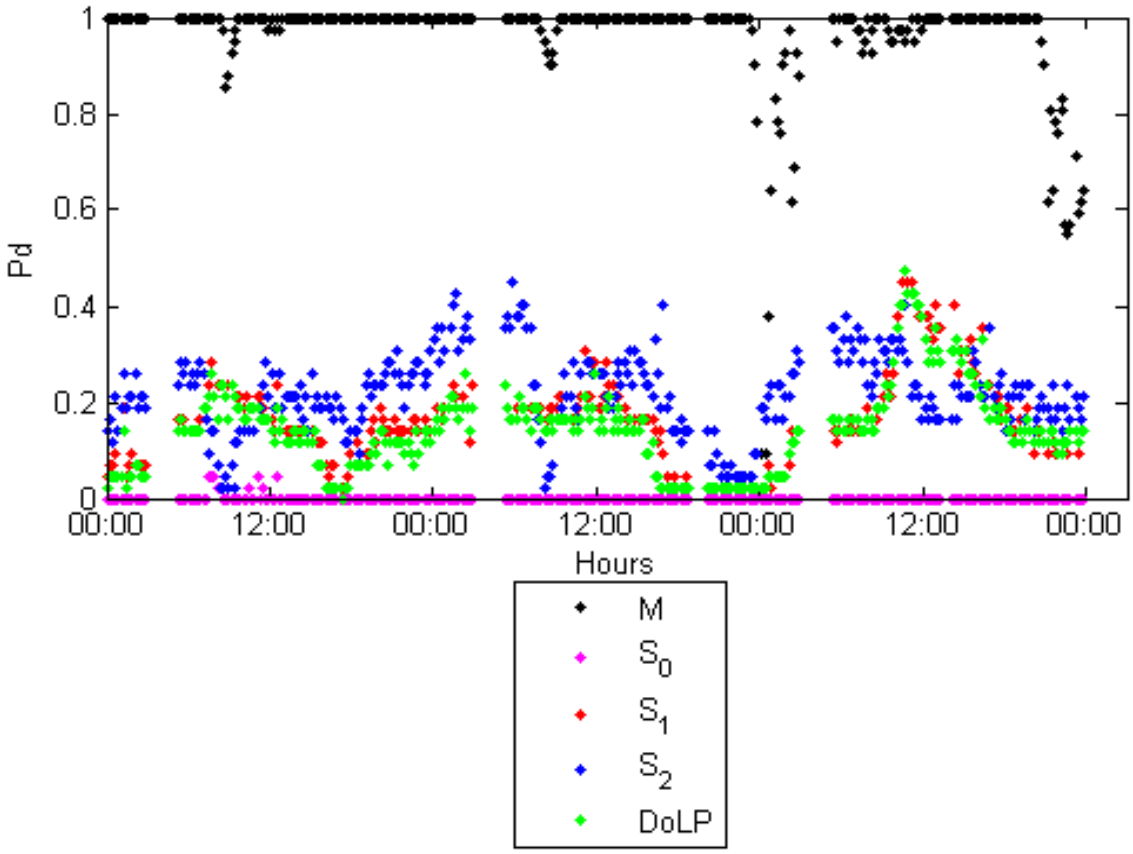

Figure 5.48 72-hour probability of detection comparison between Stokes parameters, DoLP, and M-Box algorithms in discriminating Blackbody from natural clutter. The M-Box exhibited the best 72-hour average probability of detection with a $P_d = 0.96$, followed by S_2, S_1, DoLP, and S_0 with a $P_d = 0.22, 0.16, 0.15, \text{and } 0.0$.

Figure 5.49 illustrates the 72-hour probability of detection of all metrics for the discrimination of the observation tower from natural clutter background. The plot demonstrates some interesting differences not seen in previous figures that must be acknowledged. For starters S_2 is unable to discriminate the observation tower throughout

the whole 72-hour period given the false alarm rate chosen. Furthermore, S_0 is only effective in detecting portions of the observation tower in high contrast periods, more specifically around 1400h. Surprisingly, S_1 and DoLP are quite efficient in discriminating the observation tower from natural clutter; however their probability of detection varies depending if it is a high or low contrast scene, where high probability of detection equates to high contrast and vice versa.

Although the M-Box performed quite well for most of the manmade objects in the scene, the measured probability of detection for the observation tower is less than desirable with a probability of detection of less than 0.10 for the low contrast periods while higher detection rates were found during periods of high contrast. One of the reasons for the low discrimination is the result of the size of the test window relative to the number of observation tower pixels available in the image.

The observation tower demonstrates the first encounter where the assumption that manmade objects always have larger covariance matrices than natural clutter fails. The reason is as follows, let us refer back to Figure 5.34 where it was reasoned that in order to observe high variability in manmade objects one must collect samples of facets at different angles thus demonstrating a variety of polarizing features. Since only one facet of the observation tower is available, the amount of variability encountered is actually less than found in the other objects where more facets and, therefore, higher polarization diversity, is available. In subsequent subsections, this dissertation will demonstrate how to detect such objects when the variability is less than that of natural clutter.

Nonetheless, the 72-hour average probability of detection for the M-Box was measured to be $P_d = 0.36$, followed by S_1 and DoLP with a $P_d = 0.30$, and S_0 and S_2 with a $P_d = 0.05$.

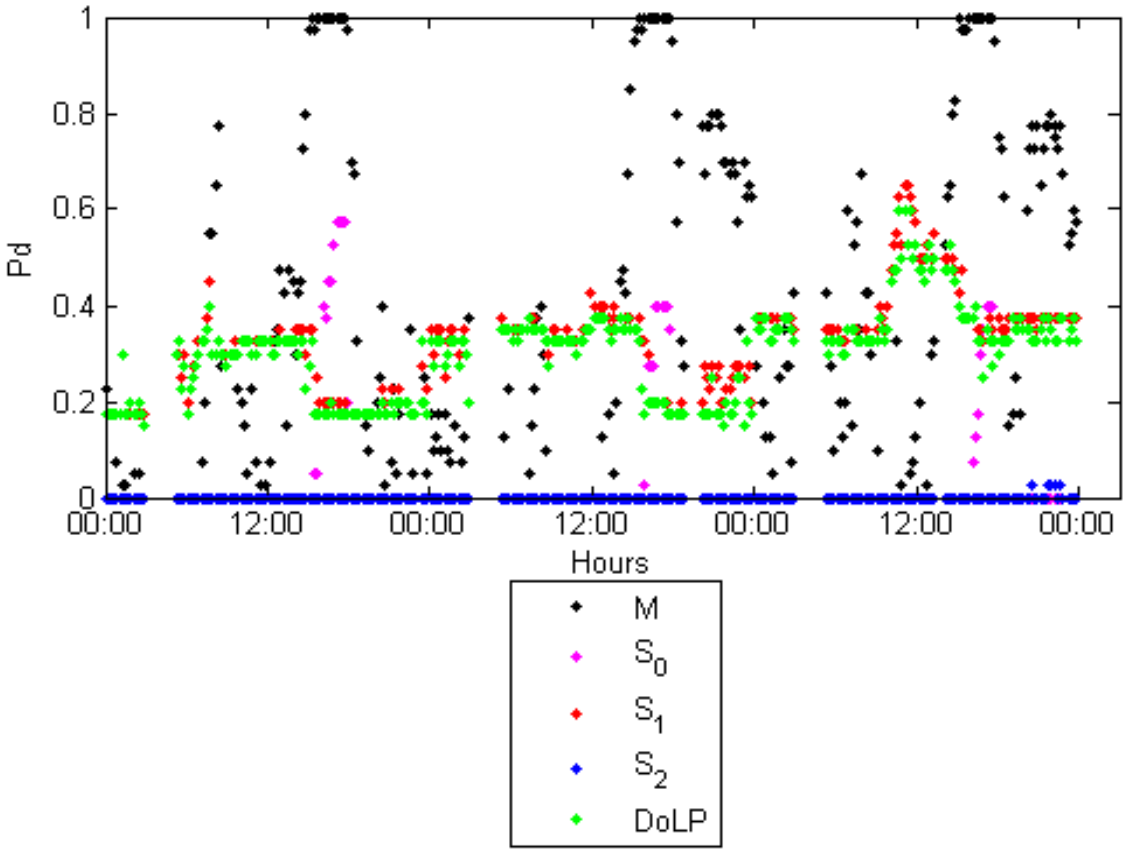

Figure 5.49 72-hour probability of detection comparison between Stokes parameters, DoLP, and M-Box algorithms in discriminating observation tower from natural clutter. For the observation tower, the 72-hour average probability of detection of the M-Box algorithm was significantly lower than previous figures measured as $P_d = 0.36$, followed by S_1 and DoLP with a $P_d = 0.30$, and S_0 and S_2 with a $P_d = 0.05$.

Finally, Figure 5.50 represents the probability of detection for all metrics when considering all manmade objects as a single class. In this figure, one can conclude the following:

1) S_1, S_2, and DoLP performed very similarly to each other with some of the metrics doing better than others for certain periods of times.

2) S_0 only performed well during periods of high contrast while during the periods of low contrast its performance was less than desirable.

3) The M-Box algorithm demonstrated good overall discrimination performance throughout the 72-hours with some performance degradation as a result of adverse weather conditions, however its performance was still higher than the Stokes or DoLP detection rate.

The M-Box algorithm was proposed as a covariance based discriminant function for polarimetric imagery in Subsection 5.3.5 based on the results of Subsection 5.3.4. In Subsection 5.3.6, the performance results of the M-Box algorithm against the Stokes parameters and DoLP for a full 72-hour performance period were presented as well as ROC curves and output surfaces results for specific timestamps. From the results shown in this subsection, the M-Box algorithm clearly demonstrated enhanced detection capability at very low false alarm rates $\left(P_{fa} = 0.005\right)$ compared to the Stokes and DoLP metrics. The best metric for detecting all the manmade objects in a single class was the M-Box algorithm with an 72-hour average probability of detection of 0.81, followed by S_1, S_2, and DoLP with similar performance ($P_d = 0.22$), and finally S_0 with a $P_d = 0.05$.

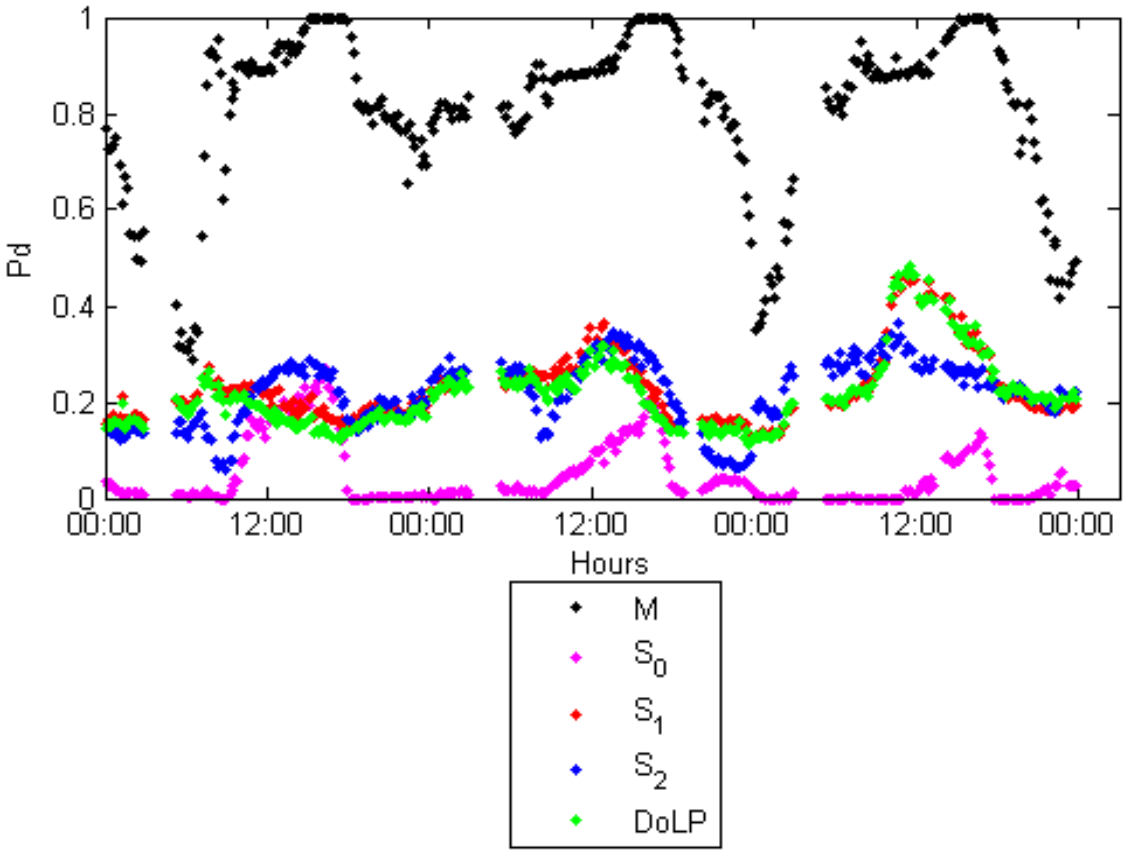

Figure 5.50 72-hour all manmade object detection comparison between Stokes parameters, DoLP, and M algorithms. M-Box algorithm exhibited a 72-hour average probability of detection of 0.81, followed by S_1, S_2, and DoLP with a $P_d = 0.22$, and finally S_0 with a $P_d = 0.05$.

In conclusion, this subsection demonstrated that:

1) The proposed M-Box algorithm greatly surpasses the detection performance of the Stokes and DoLP parameters for all manmade objects with the exception of the observation tower, which as a result of the tower's spatial resolution relative to the moving window area created some difficulties for the algorithm to differentiate the manmade object from other natural clutter samples.

2) At low false alarm rates the M-Box algorithm clearly shows a tremendous improvement relative to Stokes/DoLP metrics.

3) The M-Box algorithm performed very well for the entire 72-hour data collection regardless of the surrogate target state or perspective angle, with only reduced performance during the periods of high humidity (>80%) and

only affecting the performance of T_{135} more than any other object in the scene.

5.3.7 Limitations of the M-Box Anomaly Detector

As shown in Subsection 5.3.4, covariance tests are an efficient method in discriminating potential anomalies (manmade objects) from natural cluttered backgrounds by testing the hypothesis,

$$\begin{aligned} \mathrm{H}_0&: \boldsymbol{\Sigma}_{\boldsymbol{t}}^{(\boldsymbol{i},\boldsymbol{j})} = \boldsymbol{\Sigma}_r \\ \mathrm{H}_1&: \boldsymbol{\Sigma}_{\boldsymbol{t}}^{(\boldsymbol{i},\boldsymbol{j})} \neq \boldsymbol{\Sigma}_r, \end{aligned} \tag{5.47}$$

where $\boldsymbol{\Sigma}_r$ is the reference covariance matrix that may be known *a priori* or collected from the image as per the proposed implementation in Subsection 5.3.6.1, and $\boldsymbol{\Sigma}_{\boldsymbol{t}}^{(\boldsymbol{i},\boldsymbol{j})}$ is the estimated covariance matrix of a moving window at location (i, j) in the test scene, $\mathbf{X}$. Equation (5.47) was used in Subsection 5.3.5 as a two sample test ($k = 2$) between the reference and test covariance. It is worth noting that the reference covariance matrix was specified *a priori* as the covariance with the smallest variability in the scene based on the data analysis in Subsection 5.3.4, which suggested that the determinant of a covariance estimated from manmade objects in the bivariate space I_0 and I_{90} yielded larger values than any corresponding covariance matrices representative of natural objects. However, what if the determinant of manmade objects' covariances yielded smaller values than the ones found in natural clutter background? How would the proposed M-Box implementation in Subsection 5.3.6.1 behave under such situations?

The goal of this subsection is to demonstrate the limitations of the M-Box implemented as per Subsection 5.3.6.1. In that construct, the following key points will be presented:

1) Not all manmade covariance matrices yield larger determinant values than natural clutter. Data analysis on a previously shown dataset will be presented here where the determinant of manmade objects' covariance yields smaller values than natural clutter.

2) Under such circumstances, the implementation of M-Box algorithm as proposed in Subsection 5.3.6.1 will not correctly discriminate manmade objects from natural clutter.

5.3.7.1 Data Analysis. Up to now, long range imagery of manmade objects has been presented geared towards surveillance applications. Under these situations the implementation proposed in Subsection 5.3.6.1 demonstrated that the M-Box algorithm was robust in discriminating manmade objects from natural clutter backgrounds.

However, the assumption that the determinant of a manmade covariance is always greater than the determinant of natural clutter covariance matrix is not very robust.

The intent of this subsection is to present a dataset which demonstrates that in certain conditions, the variability found in manmade objects can be smaller than encountered in natural clutter.

Figure 5.51 has been shown previously Subsection 3.5.1, where the goal was to demonstrate how S_1, S_2, and DoLP measurements varied as the test plate (center) angle changed from 0°, normal, to 90°, parallel to the camera's viewing perspective. The data from Figure 5.51 was collected from a plate about 20 meters from the sensor, while the data from Figure 5.35 was collected from surrogates at about 550m from the sensor.

Figure 5.51 illustrates the locations of ten random blocks of size 11×11 pixels collected from the image representative of natural clutter class.

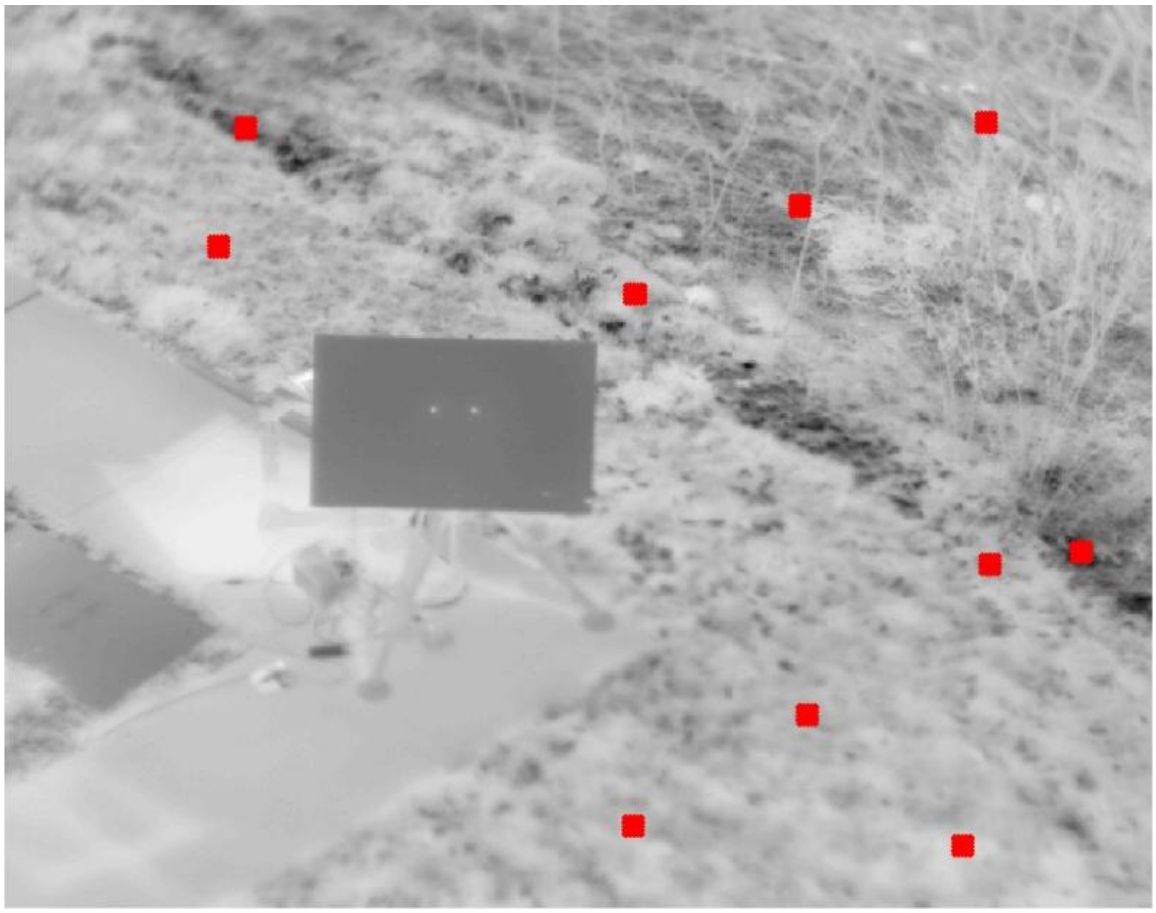

Figure 5.51 Locations of blocks of data collected of natural clutter using a 11×11 blocks of data size.

Figure 5.52 assumes that the data distribution controlling each block is multivariate Gaussian (for illustration purposes only), where the mean and covariance were estimated of each block. The distribution of each natural clutter random block is represented black lines, while the global distribution is shown in red for the periods where the test plate was angled at 5°, 25°, 50°, and 75° degrees from the camera viewing perspective. The y-axis and x-axis are labeled as I_{90} and I_0, respectively, representing the two polarization components composing **X**. Once again, as previously mentioned in Subsection 5.3.4, the plotting of the data using a normal distribution was done in order

for easy comparison between the different material classes and the global reference class, and that using the normal distribution plots does not imply, in any shape or form, that the data in **X** is Gaussian distributed.

In contrast to what has been suggested in Subsection 5.3.4 where clutter had always a smaller spread than the reference, Figure 5.52 demonstrates that the clutter sample distributions spread are shown to be wider, equal, or smaller than the global reference. Another way to visualize the results from Figure 5.52 is to take the ratio of the determinant of each of the natural clutter covariance matrices relative to the global using Equation (5.24) as it was done in Subsection 5.3.4. If $D > 1$ then the variability encountered in the random block of data is higher than the reference, otherwise $D < 1$. It is also important to note that Subsection 5.3.4 suggested that for manmade objects $D > 1$ and natural clutter $D \leq 1$.

Figure 5.53 illustrates the ratio of the determinant of the covariance for each block of data representative of natural clutter relative to the determinant of the global covariance. Right away some interesting results can be observed that defy previous results shown in Subsection 5.3.4. In Figure 5.53 for example, the determinant of the covariance samples shown in the 5° imagery are smaller than the determinant of global covariance matrix ($D < 1$), however for images 25°, 50°, and 75° clutter samples four and five exhibit larger variability relative to the reference global covariance matrix, while the remaining samples still exhibit lesser variability relative to the reference. For the time being, one can conclude that in this dataset not all natural clutter samples demonstrate lesser variability relative to the global distribution.

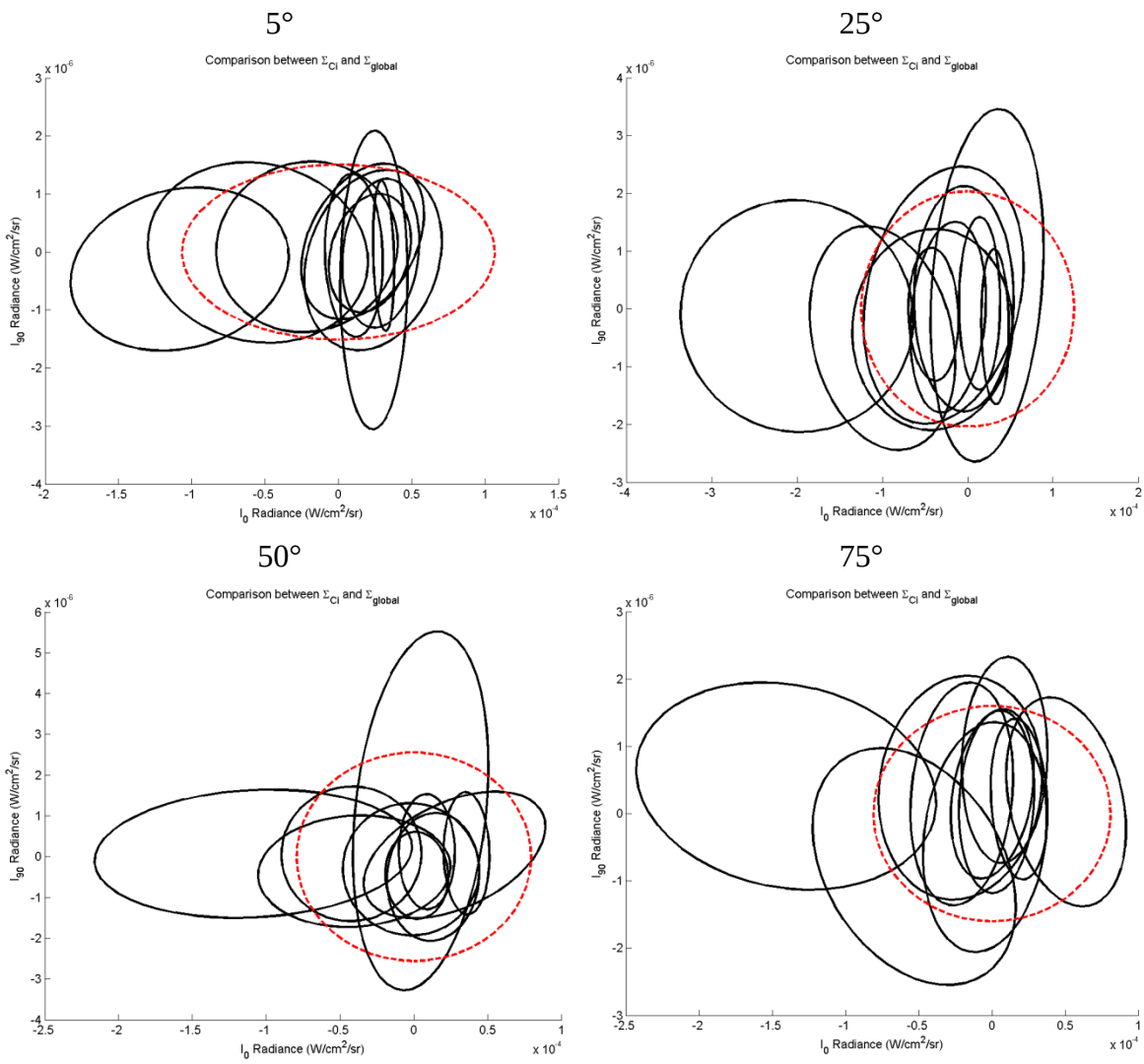

Figure 5.52 Comparison between the distribution of each natural clutter block of data (black) and global distributions (red dashed) for 5°, 25°, 50°, and 75°. Although most clutter distributions demonstrate smaller variability relative to the global reference, there are some outliers that exhibited larger variability relative to the global.

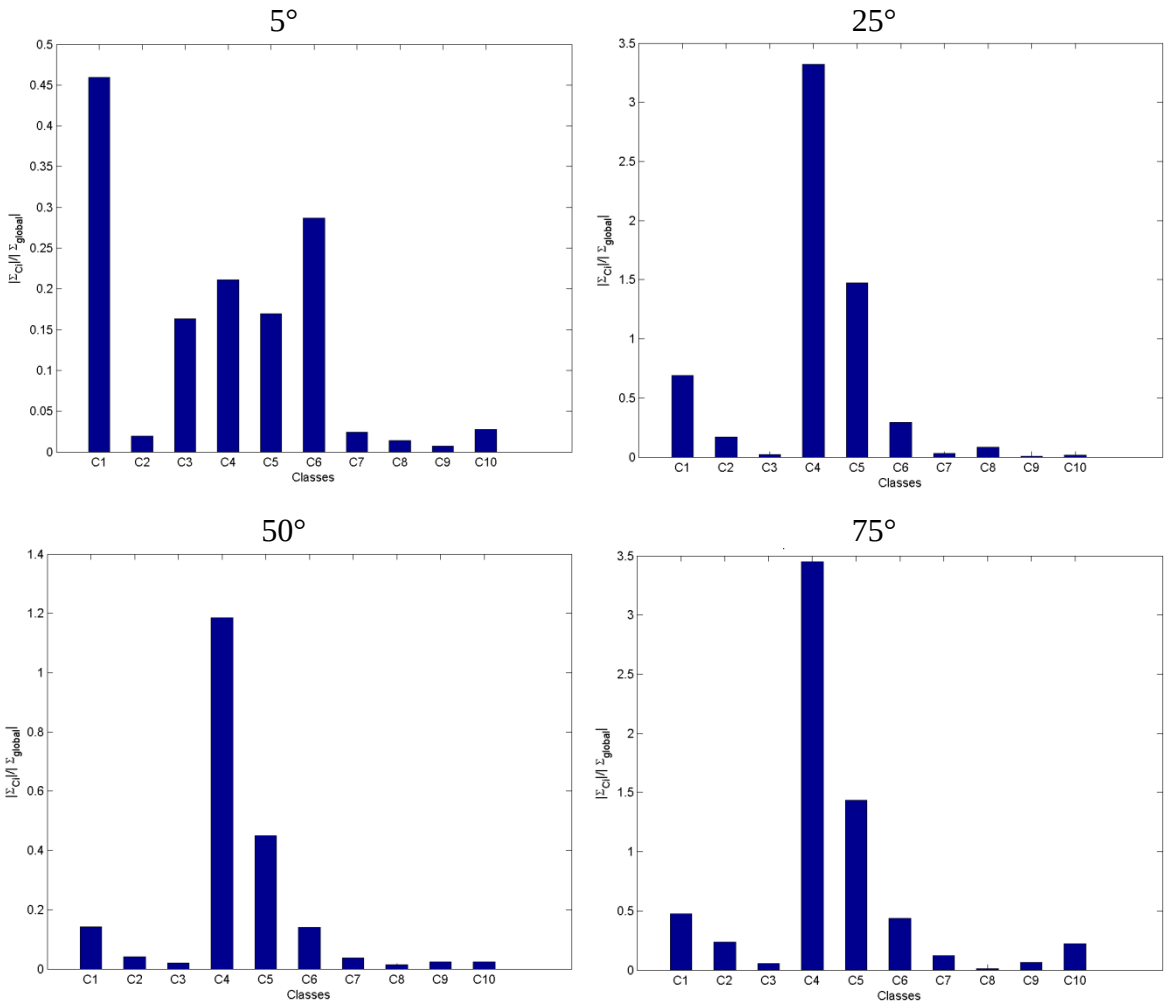

Figure 5.53 Ratio of determinant of each manmade covariance matrix ($\boldsymbol{\Sigma_{C_i}}$) and the global reference ($\boldsymbol{\Sigma_g}$) using Equation (5.24) for 5°, 25°, 50°, and 75°. In contrast to what was demonstrated in Subsection 5.3.4 there are some outliers in clutter where their variability was larger than the reference matrix. Nonetheless, for most of the clutter samples collected still exhibited smaller variability relative to the global covariance.

Focusing on the manmade objects present in the scene, Figure 5.54 illustrates ten blocks of data, denoted as $\boldsymbol{W}_{MM_i}$, representative of the different manmade objects present in the scene where three blocks of data represent the test plate (MM1-3), five represent the concrete slab (MM4-8), and two represent the reference plate (MM9 & 10). It is important to note that each of the blocks of data are extremely smaller relative to the

surfaces of each manmade object, which is in contrast to Subsection 5.3.4 where each block of data covered at least two or more surfaces at different orientation angles.

The Figure 5.55 illustrate the sinusoidal plots of $\boldsymbol{\Sigma}_{\boldsymbol{MM}_i}$ and $\boldsymbol{\Sigma}_{\boldsymbol{g}}$ using a normal distribution model as reference while Figure 5.56 illustrates the ratio $D = \frac{\det(\boldsymbol{\Sigma}_{\boldsymbol{MM}_i})}{\det(\boldsymbol{\Sigma}_{\boldsymbol{g}})}$.

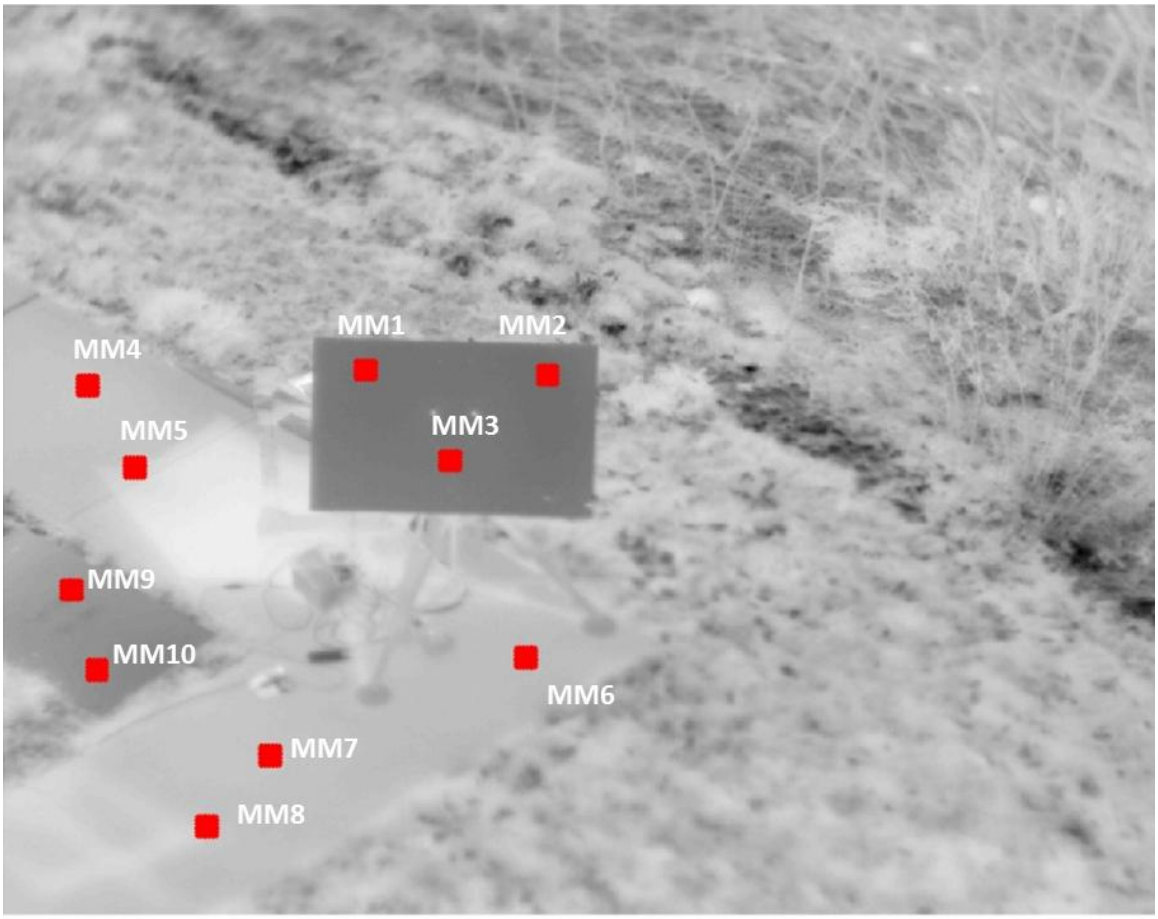

Figure 5.54 Locations of blocks of data collected from manmade objects where three blocks of data were collected from the test plate (MM1-3), five from the concrete slab (MM4-8), and two from the reference plate (MM9 & 10).

Right away one can observe an interesting phenomenon unlike previously seen in Subsection 5.3.4; Figures 5.55 and 5.56 demonstrate that all manmade objects distributions, regardless of material, can also exhibit smaller variability in the I_0 and I_{90} bivariate space when compared to the global distribution or the clutter samples shown in

Figures 5.52 and 5.53. Although at a glance these results may be somewhat contradictory, the reasoning on why such happens is simple to explain. In Subsection 5.3.4 a block of data representative of a manmade object collected information of several surfaces oriented at different angles relative to the camera (see Figure 5.35), which as explained in Subsection 5.3.4, the result of a moving window in observing different manmade surfaces yielded higher variability than what was measured from the clutter. In this case, however, one has quite the opposite. At closer range the polarization information is based on smooth and homogeneous surfaces yielding less variability than natural clutter, but at longer ranges and using more complex manmade objects in the scene the variability is dominated by orientation diversity than any other phenomena.

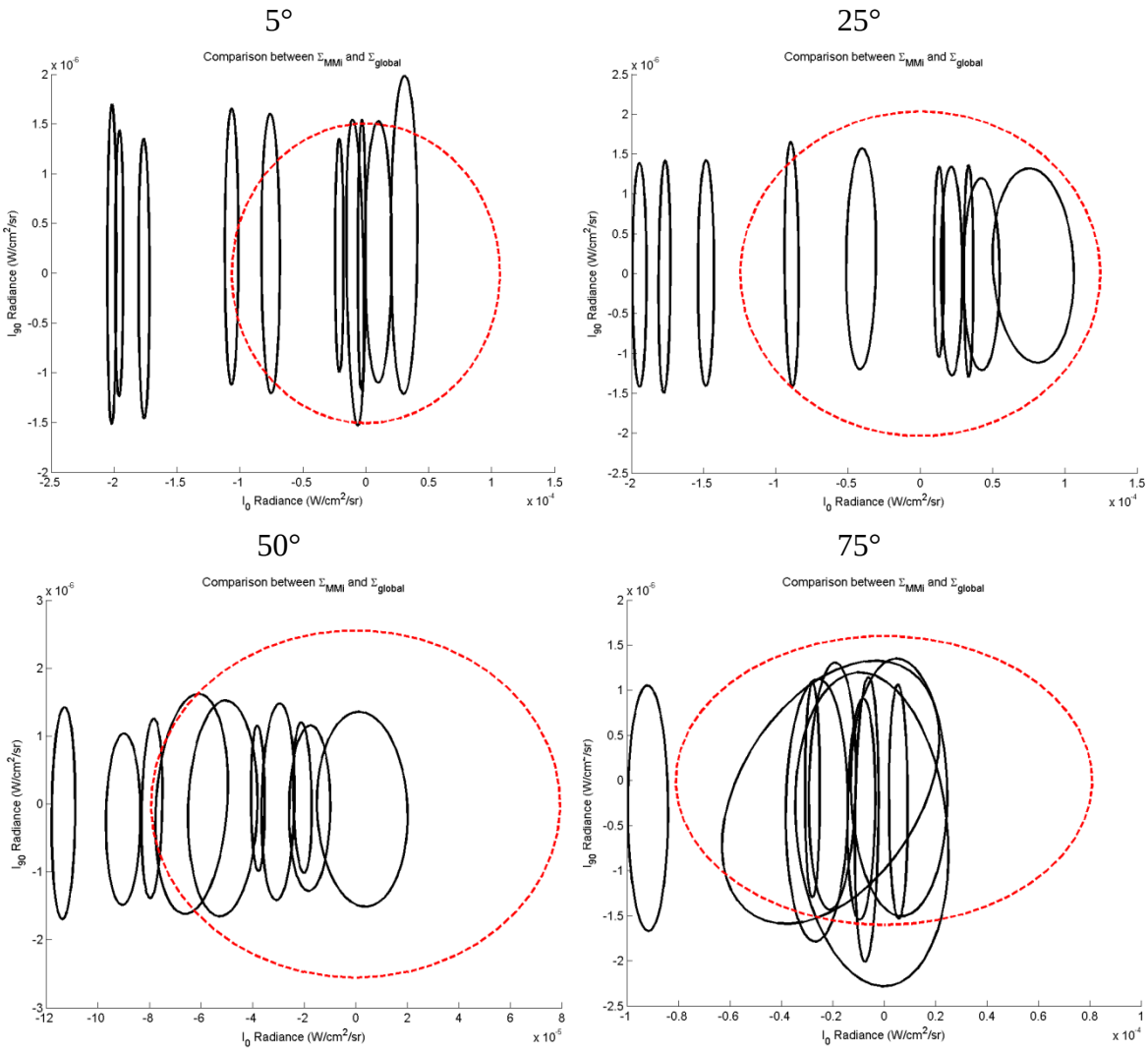

Figure 5.55 Comparison between the distribution of each block of data representative of a manmade object (black) and the global distribution (red dashed) for 5°, 25°, 50°, and 75°. In contrast to the results in Subsection 5.3.4 the manmade materials in this experiment exhibit smaller variability relative to the global distribution or the individual clutter samples from Figures 5.52 and 5.53.

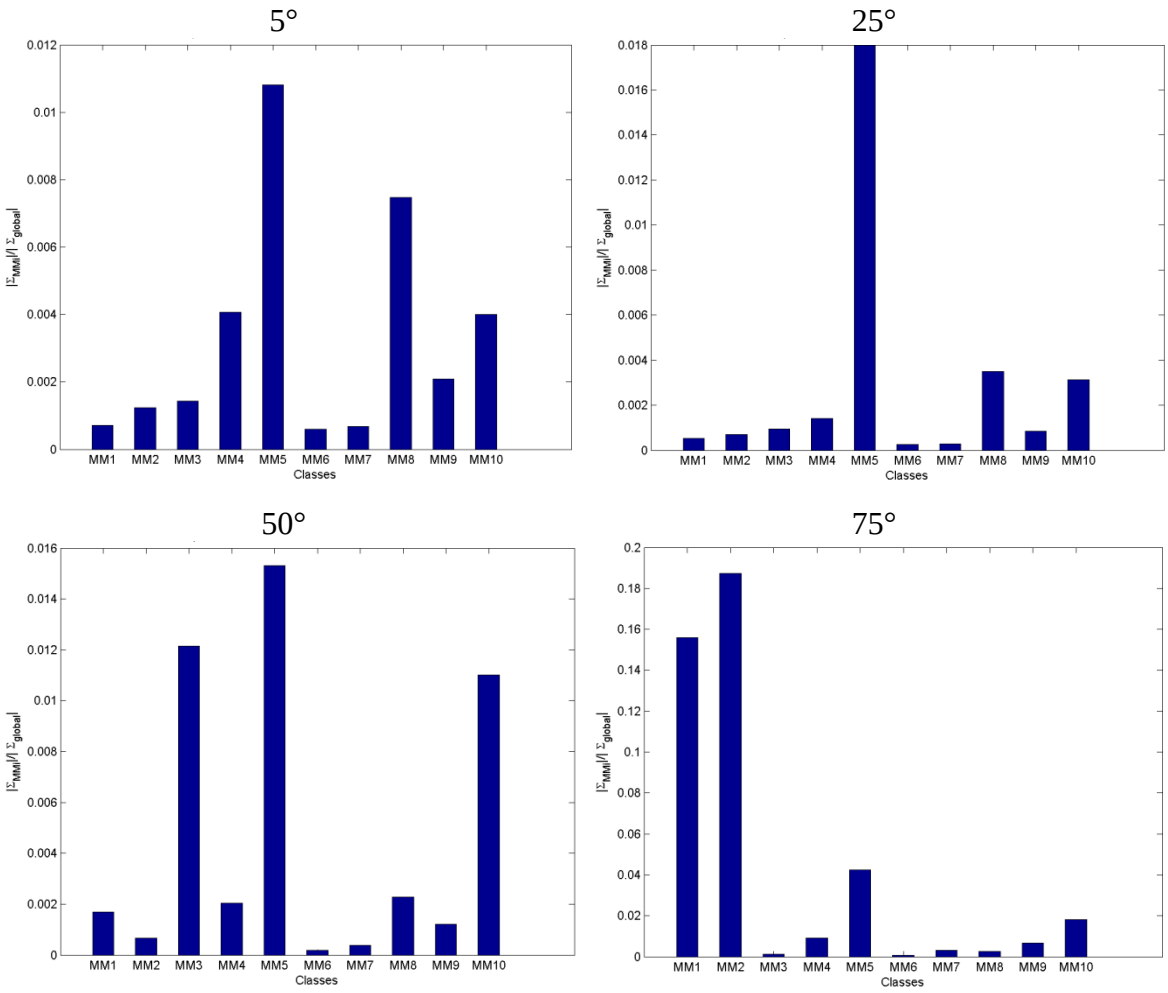

Figure 5.56 Ratio between the determinant of each $\boldsymbol{\Sigma_{MM_i}}$ relative to the determinant of $\boldsymbol{\Sigma_g}$ for 5°, 25°, 50°, and 75°. As a result of collecting polarization information from homogeneous surfaces the variability exhibited in the test window was extremely smaller ($D < 1$) than the global reference and clutter information.

In summary, by comparing figures 5.53 and 5.56, the following conclusions can be reached:

1) The distribution of manmade objects was, in contrast to earlier drawn conclusions from Subsection 5.3.4, smaller than the global distribution and the background samples for the 5°, 25°, 50° and 75°images.

2) The reason for low variability is the result of collecting data at close range where each block of data size is smaller than any single manmade surface and, therefore, the information captured by the block of data of a smooth homogeneous surface yields small variability.

3) Because natural clutter surface is more heterogeneous (e.g., different materials or same material at different angles) the value from Equation (5.24) is higher than that of manmade objects for close range PI.

4) One can conclude that for close proximity or zoomed in polarimetric where the test window is smaller than any surface of a manmade material, the variability captured by the window will be less than that of a clutter sample.

As per the conclusions above, one can predict that the M-Box algorithm, proposed in Subsection 5.3.5, and as currently implemented as per Subsection 5.3.6.1, will not operate as expected when processing close range PI. Because the smallest determinant is now representative of a manmade object, one can expect that most of the samples (clutter) that one would like to accept under $H_0|\chi^2_{\alpha=\varphi}$ will now be rejected, (φ represents the desired probability of miss) and vice versa.

5.3.7.2 M-Box Anomaly Detector Results. The implementation of the M-Box anomaly detector in Subsection 5.3.6.1 assumes that the reference covariance matrix, $\boldsymbol{\Sigma_r}$, is the covariance matrix with the smallest variability found in the test image representative of natural clutter in the scene. In other words, to successfully detect a manmade object in the test image the assumption $|\boldsymbol{\Sigma_{manmade}}| > |\boldsymbol{\Sigma_r}|$, where $|.|$ denotes the determinant, must be satisfied in order to accept or reject H_0 successfully. As seen in the previous Subsection 5.3.7.1, such assumption is definitely not satisfied since the smallest determinant value in the scene may be in fact representative of one of the manmade objects in the scene. Therefore, since $|\boldsymbol{\Sigma_{manmade}}| > |\boldsymbol{\Sigma_r}|$ cannot be satisfied, one can predict from the implementation proposed in Subsection 5.3.6.1 that all manmade object locations will be represented with very low scores (e.g., close to zero, accepting H_0)

while background clutter will be represented with high scores (rejecting H_0), which is clearly an undesirable result as shown in Figures 5.57 and 5.58.

Figure 5.57 illustrates the output surfaces from the M-Box algorithm implemented using the instructions in Subsection 5.3.6.1. The output surfaces were normalized for visual appreciating and comparison by the reader and the angles on the top right of each sub-image represent the angle at which the test plate was oriented relative to the sensor's viewing perspective. The dark blue color represents low values which for the sake of argument will be accepted under H_0, the red color represents high values illustrating pixels which will be rejected under H_0. At a glance, one can observe that all manmade objects are represented by the color blue, which will be accepted under the null hypothesis, conversely, there are portions of the clutter which will definitely be rejected under the null hypothesis as shown by the color red.

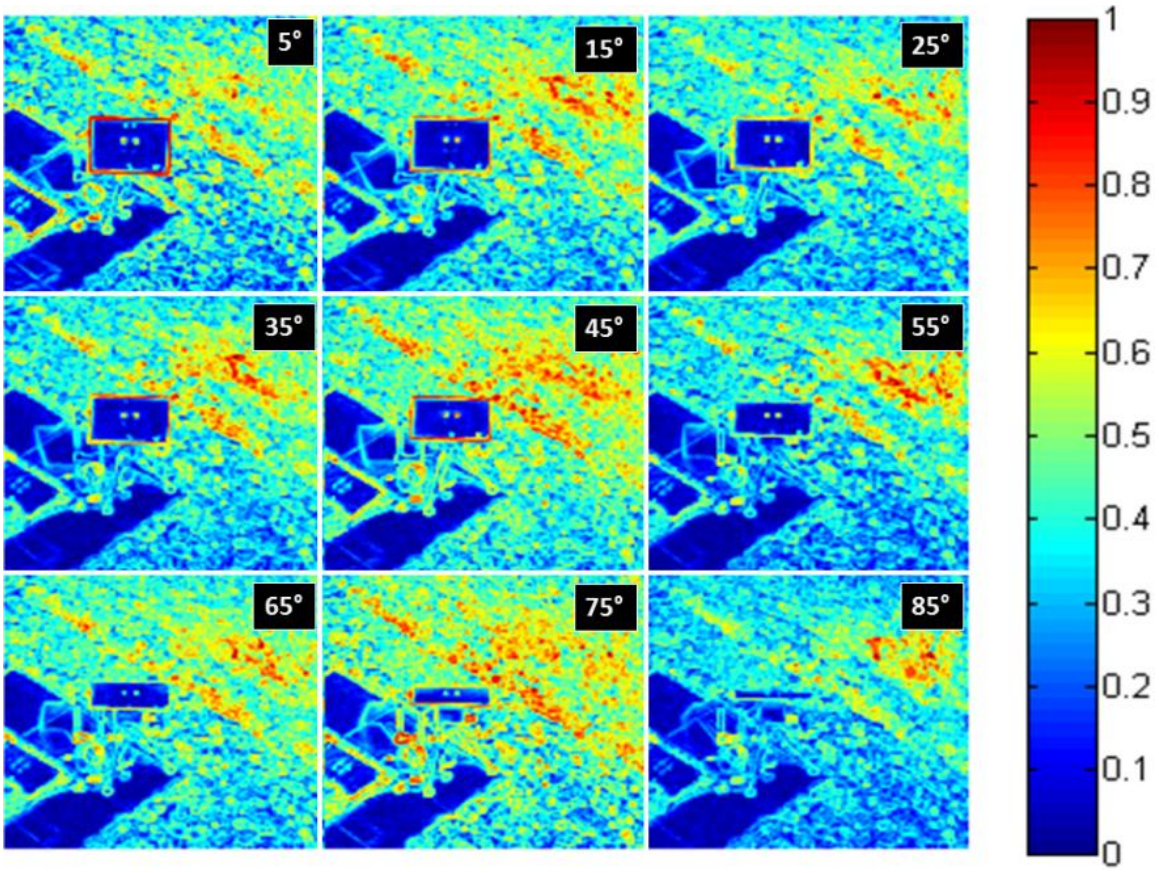

Figure 5.57 Output surface of the M-Box algorithm for the close-range polarimetric imagery. Note that all manmade objects are in dark blue color, these locations will be not be rejected under the H_0 while the red color are locations that will be rejected by the null hypothesis, in this case clutter.

Figure 5.58 illustrates corresponding binary images after cutoff threshold were applied to the output surfaces in Figure 5.57 under $H_0|\chi^2_{\alpha=0.01}$. In this figure, the black pixels represent locations below the cutoff threshold and white pixels represent locations above the same cutoff threshold. All the pixels representing manmade objects were accepted under $H_{0,\alpha=0.01}$ meaning the decision making process accepted those locations as being representative of natural clutter per the algorithm implementation in Subsection 5.3.6.1, while at the same time the clutter was rejected under the null hypothesis; an undesirable result.

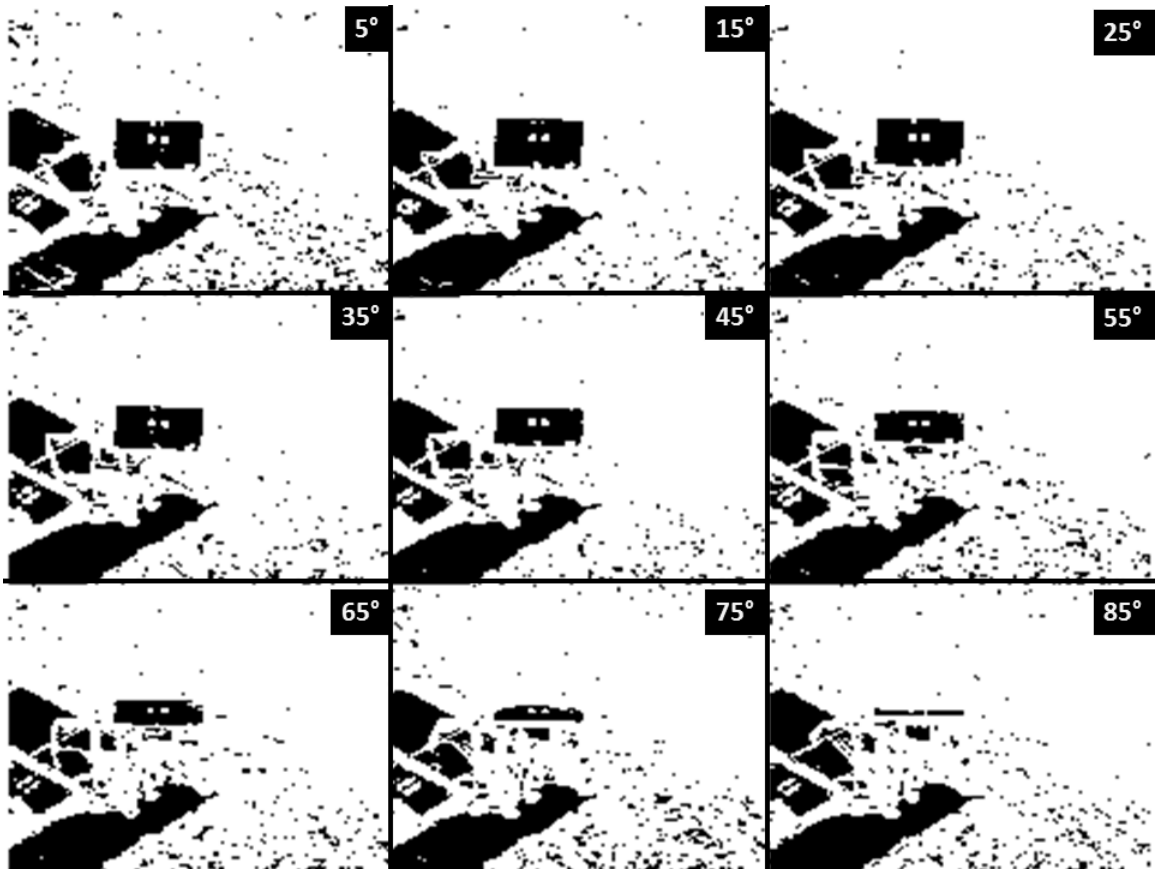

Figure 5.58 Binary surface of each output surface of the M-Box algorithm for close range imagery for $H_0|\chi^2_{\alpha=0.01}$. All manmade objects values are below the cutoff threshold chosen while a very large part of the clutter values is above the threshold.

Figure 5.59 represents the PDF of each of the output surfaces shown in Figure 5.57 with normalized x- and y-axis. As shown, the first peak (on the left side of each plot) represents the manmade object pixels in the image, while the wider peak represents locations representative of natural clutter. In the M-Box implementation in Subsection 5.3.6.1, clutter is represented by the smallest $|\mathbf{\Sigma}|$ and one expects that H_1 should represent manmade objects and H_0 clutter. However, when using the implementation in Subsection 5.3.6.1 in close range PI the manmade objects are represented by H_0 while clutter is represented by H_1. This result is in contrast to what was shown in Subsection 5.3.5.

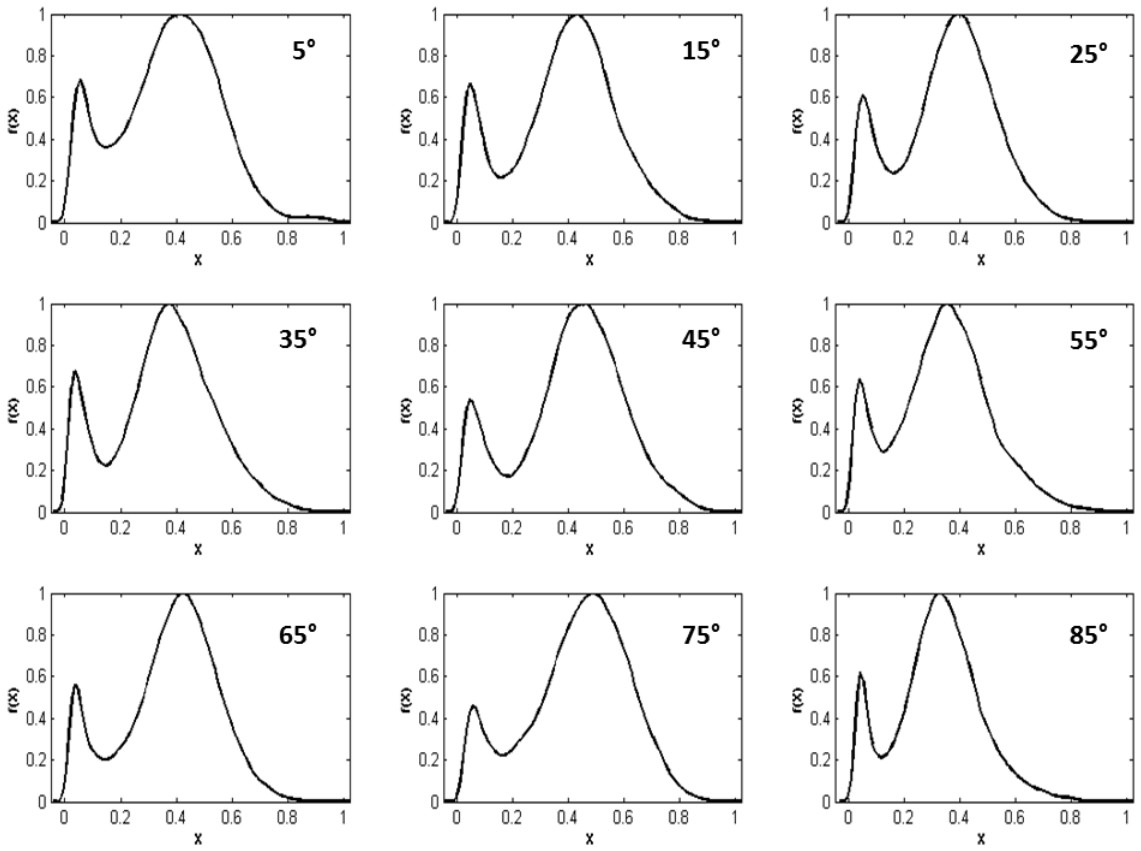

Figure 5.59 PDF plots for all output surfaces shown in Figure 5.57.

One can conclude that the implementation of the M-Box algorithm as proposed in Subsection 5.3.6.1 has a clear limitation when used in close proximity or zoomed in polarimetric imagery since the location with the smallest variability will be representative of a manmade object rather than natural clutter.

5.3.7.3 Data Analysis on the Observation Tower. Figure 5.49 demonstrated that the M-Box algorithm performed extremely poor in discriminating the observation tower from natural clutter with some exceptions during high contrast time periods between 1100h and 1500h.

Figure 5.60 illustrates the distribution of T_{90}, the observation tower, and natural clutter from a polarimetric data cube collected at 0710h on 6 MAR 2010. The remainders

of the manmade objects' distributions are not important to show as they bring little to the overall discussion. What is important to note from this figure is twofold: 1) as expected the T_{90} (as well as T_0, T_{135}, and the blackbody not shown) distribution demonstrates large variability in the I_0 and I_{90} bivariate space relative to the natural clutter and 2) Most importantly, the observation tower exhibits less variability relative to the global distribution, or similar to that of natural clutter, defying the conclusions in Subsection 5.3.4.

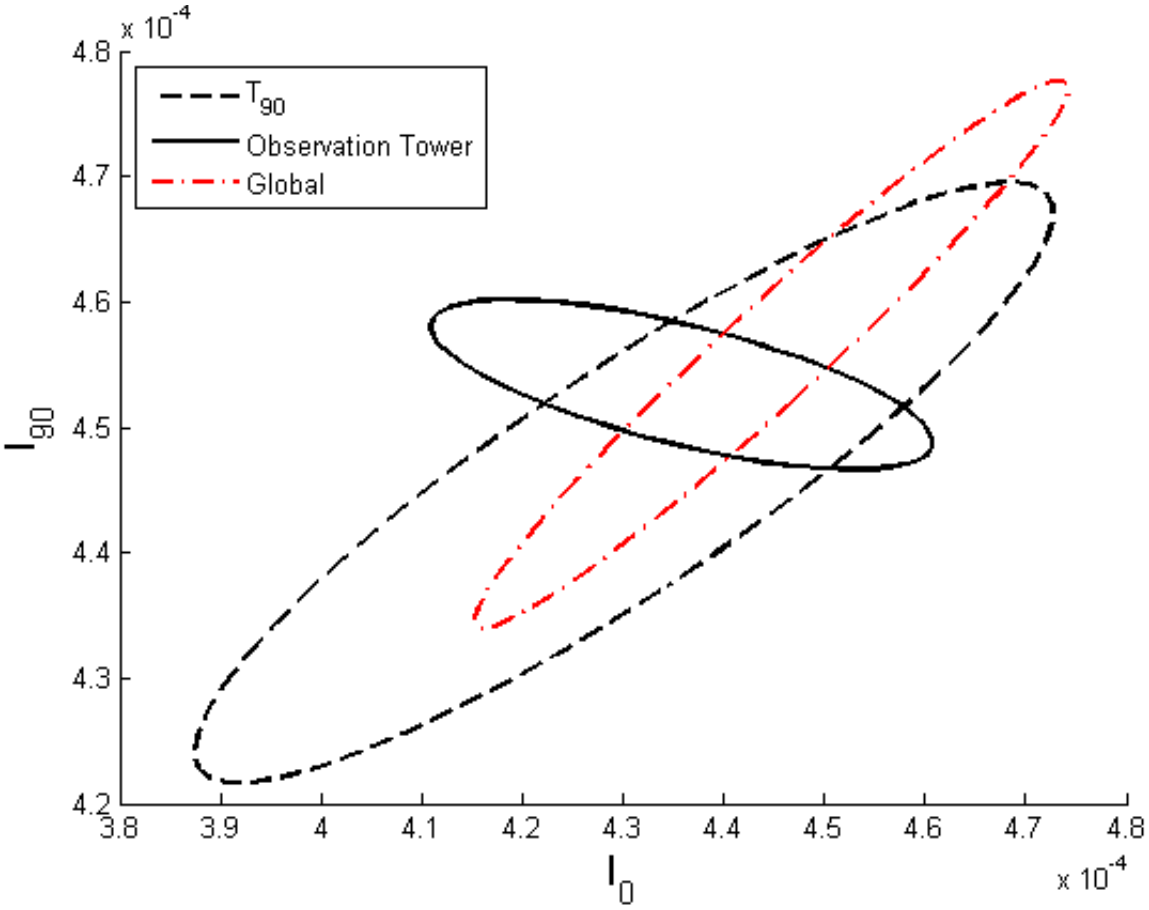

Figure 5.60 Statistical distribution of T_{90}, observation tower, and global information. As expected from Subsection 5.3.4 the surrogate target exhibited higher variability relative to the global distribution. Conversely, the observation tower, another manmade object, exhibited lesser variability relative to the global.

The principal reason on why the variability of the observation tower is similar to natural clutter is because: (1) only one facet, belonging to the observation tower, can be seen from the sensor's viewing perspective and (2) the facet may not be very polarized as a consequence of its angle relative to the sensor. Referring to the results shown in Subsection 5.3.7.1, observing only one facet with very little polarization diversity in the bivariate space severely limits the amount of variability that can be collected from the manmade object, which validates the results shown in Figure 5.60.

Furthermore, the spatial resolution of the tower was much smaller relative to the moving window area (about 17% the size of the moving window), the distribution of the moving window when centered on the observation tower yielded a distribution with significantly smaller variability than natural clutter distribution, and as a result the M-Box could not successfully discriminate from natural clutter as shown in Figure 5.49.

In the following Subsection 5.3.8, a variant of the M-Box anomaly detector will be presented which: (1) removes the assumption that the smallest $|\mathbf{\Sigma}|$ is representative of natural clutter and (2) allows for the M-Box to be range invariant, and as a result of these two features, the M-Box will be able to discriminate the tilting plane (Figure 5.51) and the observation tower from natural clutter successfully.

5.3.8 Random Sampling M-Box (RS-M) Anomaly Detector

Subsection 5.3.7 demonstrated a concerning limitation of the M-Box algorithm, when implemented as proposed by Subsection 5.3.6.1, where it restricted the use of the M-Box algorithm to long range imagery only or in situations where the determinant value of a manmade object covariance matrix was always larger than any covariance matrix determinant representing natural clutter.

This subsection proposes the implementation of a random sampling process with the M-Box algorithm to remove the above mentioned assumption, therefore, allowing the M-Box anomaly detection algorithm to become range invariant, while at the same time retaining equal sample sizes for both the reference and test windows.

The goal of this subsection is to demonstrate that by using the a random sampling process together with the M-Box algorithm allows to:

1) Keep both the reference and test with equal samples size. Such is desirable because the M-Box covariance test is very sensitive to sample size differences.

2) Make the M-Box algorithm range invariant, thus eliminating the limitations presented in Subsection 5.3.7.

Furthermore, as a result of the random sampling process, the possibility of contamination has limited effect on the overall output of the algorithm as long as the number of random samples representing clutter far exceeds the number of contaminated samples.

5.3.8.1 Random Sampling Approach. In Subsection 5.3.5, the M-Box algorithm was proposed as a two covariance test where one of the covariance matrices was defined as the reference and the other the test. In summary, Equation (5.30) sets the possible hypothesis where H_0 represents the occurrence when both the test and reference sample are drawn from the same distribution while H_1 (the alternative) represents when both the test and reference samples come from difference distributions. The reference covariance matrix was estimated from the test image by using a search algorithm to find the smallest determinant in the scene (e.g., covariance with the smallest variability) as presented in Subsection 5.3.4. This search algorithm was included in this particular implementation to

impose sample size equality of both samples (test and reference), therefore, removing any sample size differences that can adversely influence the result of the M-Box algorithm. However, this implementation made an assumption that the determinants of the manmade object covariance matrix always exhibited larger values than that of natural clutter, and as it was shown in Subsection 5.3.7, it also limited the use of the M-Box algorithm to data acquisitions at long ranges only.

This subsection proposes a background characterization methodology based on a random sampling process to characterize the test scene. As a result, it removes any assumption on the spread of background and manmade objects' distribution allowing the M-Box to work in both short and long range imagery (range invariant), while at the same time retaining similar sample size between the reference and test windows.

In a very simplistic explanation, the proposed random sampling scheme consists of N $n \times n$ (pixel) blocks of data that are randomly collected from spatial locations in the polarimetric data cube **X** with the objective of characterizing the background. Each random block is automatically designated as a reference clutter sample; however there might be a possibility that a random sample could also represent other than natural clutter (this will be discussed later). These clutter samples are then used as reference by the M-Box algorithm to test if an unknown sample collected from the scene using the test window is similar (or not) to that of the reference samples. Since the knowledge of both the number and locations of anomalies in the scene is unknown, the test window is expected to slide across the entire spatial area of **X** in order to test all possible locations in the imagery.

A quick example can be explained as follows, if one were to sample Figure 5.61 with 20 random blocks of data (N=20) of size 7×7 pixels, one could safely assume that from the data analysis in Subsection 5.3.4, the distribution of all the clutter samples would have a smaller spread (variability) than any of the surrogate targets on the scene, or (see Figure 5.62)

$$\left|\boldsymbol{\Sigma}_{clutter}^{i}\right| < |\boldsymbol{\Sigma}_{manmade}|, i = 1, \dots, 20 \tag{5.48}$$

where $|.|$ designates the determinant, $\boldsymbol{\Sigma}_{clutter}^{i}$ defines the random reference sample covariance matrices, and $\boldsymbol{\Sigma}_{manmade}$ the manmade covariance matrix.

Figure 5.62 illustrates the Gaussian distribution of the 20 random blocks of clutter and the manmade object T_{90} as an example. As previously stated for similar plots, the data blocks are assumed to be Gaussian for illustration purposes. The covariance was estimated from each of the random blocks of data and T_{90} pixels and used to plot the Gaussian distribution shown in Figure 5.62. The mean of each block was removed so that visual comparison can be focused on the data variability.

The results from Figure 5.62 validate the results found in Subsection 5.3.4 where all of the random blocks representative of clutter exhibit smaller spread relative to T_{90}. Therefore, one can then conclude that random sampling the background as shown in Figure 5.61 would reach, to a certain extent, the same reference covariance spread as the implementation proposed in 5.3.6.1.

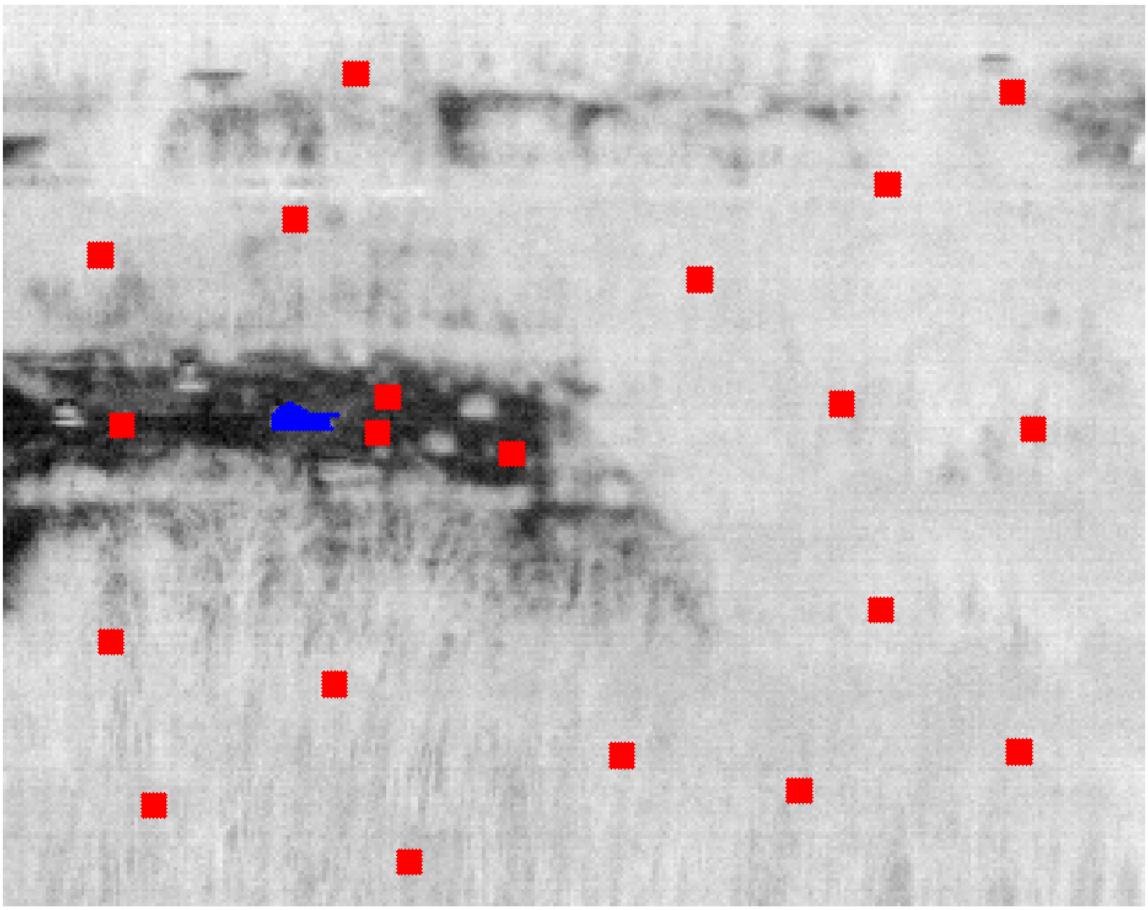

Figure 5.61 Illustration of 20 blocks of clutter randomly collected from the scene represented by the color red. The reference surrogate target is represented by the color blue, also known in this dissertation as T_{90}.

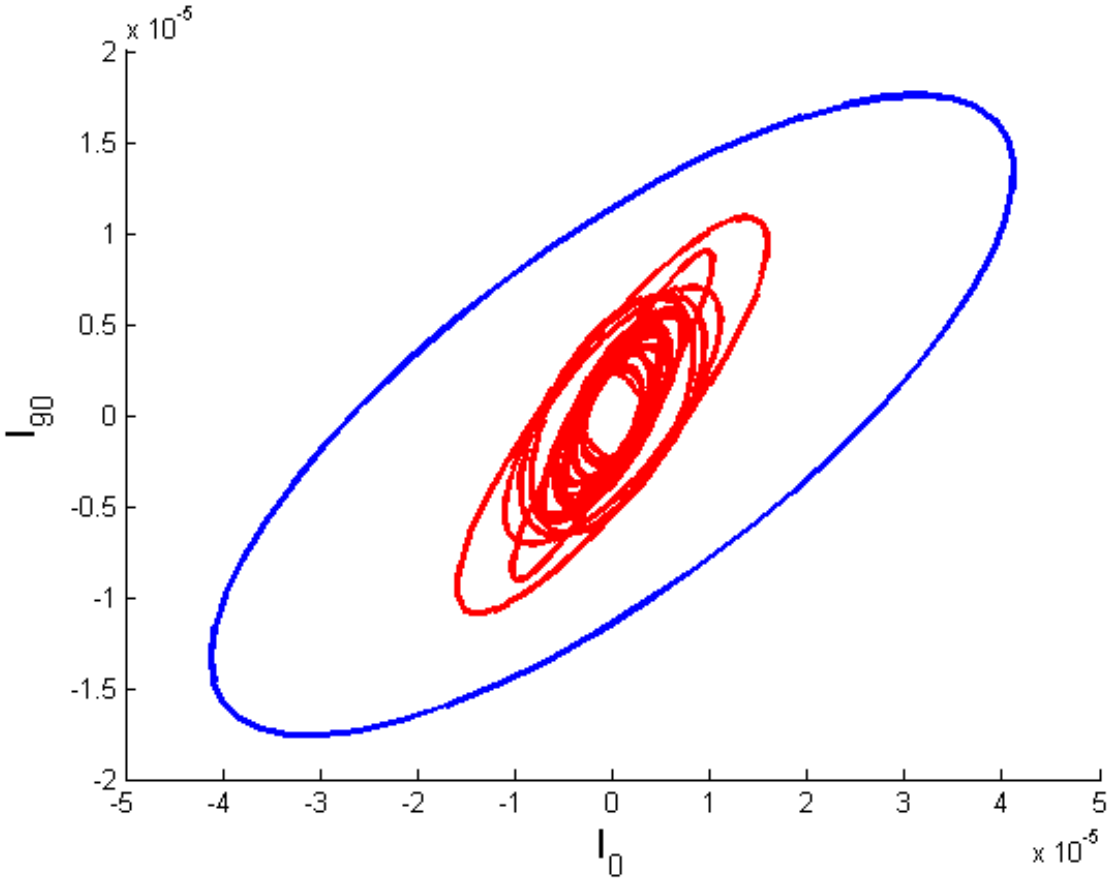

Figure 5.62 Gaussian distribution representation of the 20 random samples in red and T_{90} in blue. As expected, the data once again validates the results shown in Subsection 5.3.4 where all clutter samples distribution exhibited smaller spread relative to the target surrogate.

Figure 5.63, on the other hand, illustrates close range PI, where ten and five blocks of data were randomly collected from clutter (red) and manmade objects (blue), respectively. Figure 5.64 presents the Gaussian distribution for each of the clutter and manmade samples centered at zero for visual appreciation and comparison.

Figure 5.64, as expected from the conclusions from Subsection 5.3.7.1, demonstrates that each clutter sample distribution exhibits larger spread relative to the manmade objects' distribution.

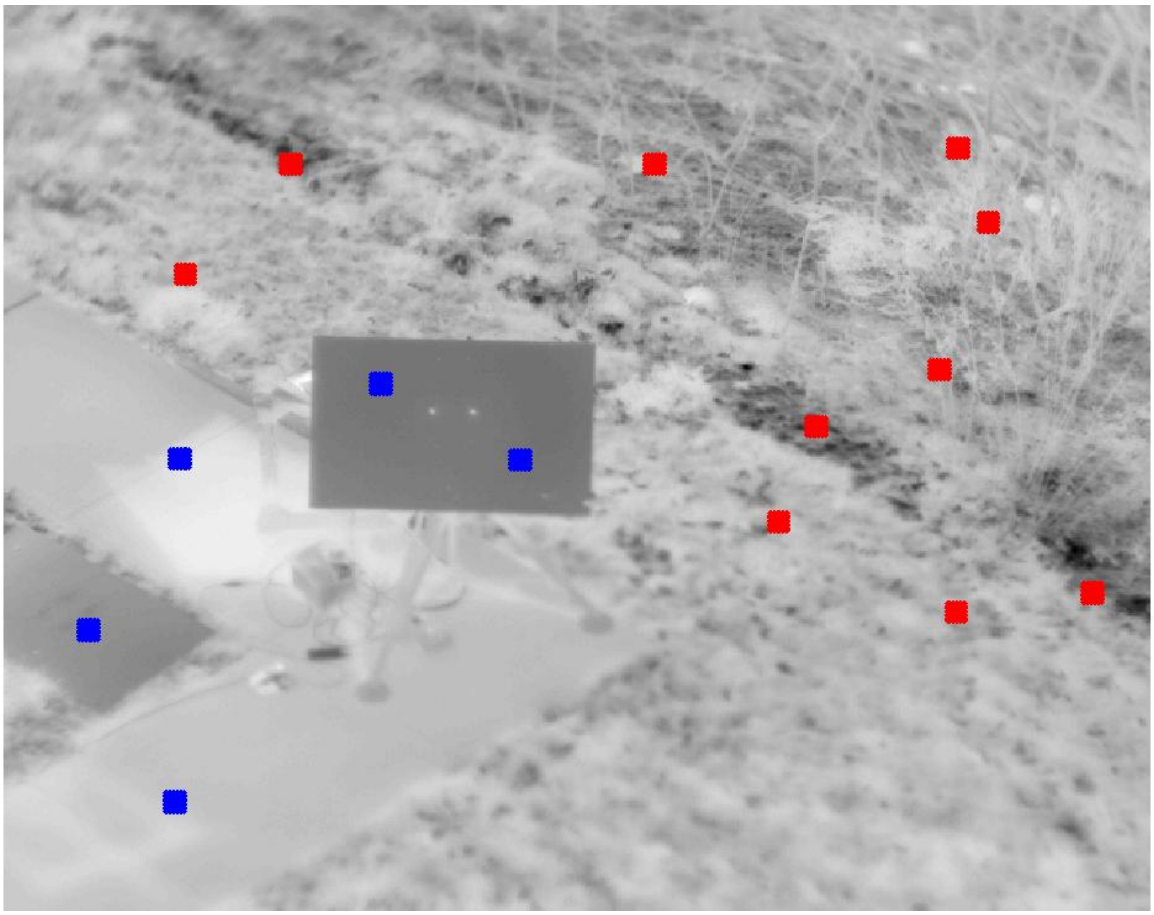

Figure 5.63 Ten random samples were collected from the natural clutter (red) and five random samples were collected from the difference manmade objects present in the scene (blue).

Therefore, for close proximity PI, each of the clutter samples exhibit the following relationship relative to the manmade objects,

$$\left|\boldsymbol{\Sigma}_{clutter}^{i}\right| > \left|\boldsymbol{\Sigma}_{manmade}\right|, i = 1, \ldots, 10 \tag{5.49}$$

In this experiment, the use of the random sampling approach was successful in characterizing the background for short range PI, whereas the assumption from Subsection 5.3.6.1 would have failed. Therefore, the implementation of random sampling methodology has shown the ability to characterize the two extreme cases (short and long range data acquisitions). Therefore, combining the random sampling with the

M-Box covariance test results in a more generalized detector that could be used in situations where the manmade object and clutter spread is not readily defined.

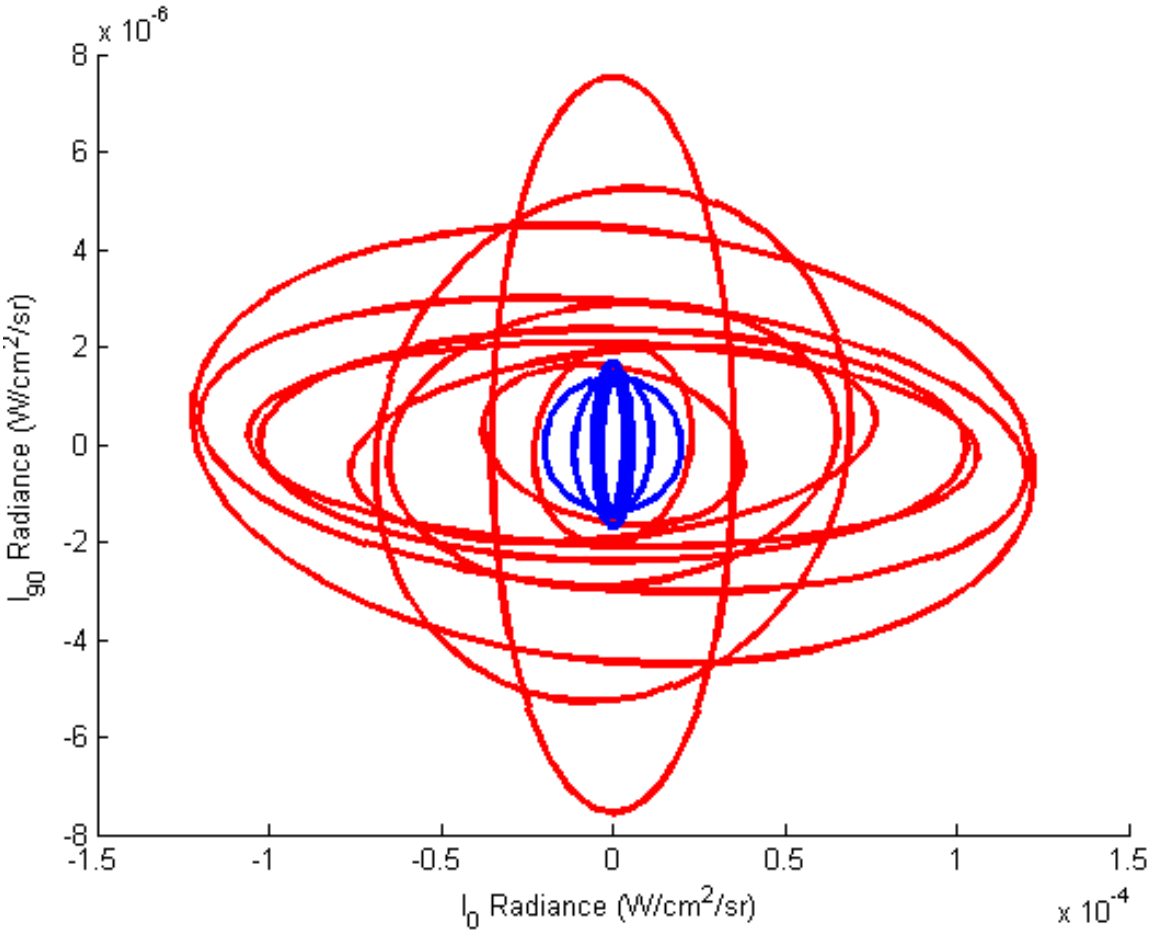

Figure 5.64 As expected from the conclusions in Subsection 5.3.7. 1, the distribution spread of the manmade objects is smaller than that of the natural clutter when the area of the moving window is smaller than any of the manmade objects surfaces.

The focus now turns to the adaptation of the M-Box algorithm with the random sampling technique. Equation (5.38), shown in Subsection 5.3.5, was used to test two covariance matrices (k=2) where the first covariance matrix was the reference and the other the test. The hypothesis test for the M-Box algorithm can be easily extended to k>2 as shown in Equation (5.50).

$$\begin{aligned} \mathrm{H}_0&: \boldsymbol{\Sigma}_1 \ = \cdots = \boldsymbol{\Sigma}_k \\ \mathrm{H}_1&: \boldsymbol{\Sigma}_1 \ \neq \cdots \neq \boldsymbol{\Sigma}_k \end{aligned} \tag{5.50}$$

The random sampling methodology can be easily adapted with Equation (5.39) by taking, for the time being, a test image and (1) random sampling it with N blocks of data and automatically designating them as clutter information (regardless if they are or not). Each of the N blocks of data uses a window size of $n \times n$ pixels, which is the same size as the test window. Since the number of target pixels present in the scene is usually lesser than the available spatial area in **X**, for the time being, one assumes that no manmade object is sampled during the random sampling procedure. (2) All N blocks of data are automatically designated as the reference library set $\{\boldsymbol{W}_r^d\}_{\boldsymbol{d=1}}^{\boldsymbol{N}}$, where $d = 1, \ldots, N$ and each $\boldsymbol{W}_r^d$ is rearranged into a sequence of vectors, see Equation (5.19), of size $n_2 = n^2$ in the form of $\boldsymbol{W}_r^d = \left(\boldsymbol{x}_1^d, \ldots, \boldsymbol{x}_{n_2}^d\right)$ where $\left\{\boldsymbol{x}_i^d\right\}_{i=1}^{n_2}$. (3) The covariance matrix is calculated for each individual location in $\boldsymbol{W}_r^d$ to yield N covariance matrices $\{\boldsymbol{\Sigma}_r^d\}_{d=1}^{N}$, which are used as reference to the M-Box detector.

(4) Once all $\boldsymbol{\Sigma}_r^d$ are calculated for all N reference samples, a moving window $\boldsymbol{W}_t^{(i,j)}$ of size $n_2 = n^2$ slides across **X** at every location (i, j) for all possible locations in **X**, see Equation (5.18), calculating $\boldsymbol{\Sigma}_t^{(\boldsymbol{i,j})}$. (5) The M-Box covariance test compares $\boldsymbol{\Sigma}_t^{(\boldsymbol{i,j})}$to all reference $\boldsymbol{\Sigma}_r^d$ using Equation (5.39) to either reject (or not) the null hypothesis as follows,

$$\begin{aligned} \mathrm{H}_0&: \boldsymbol{\Sigma}_r^{\boldsymbol{1}} = \cdots = \boldsymbol{\Sigma}_r^{\boldsymbol{N}} = \boldsymbol{\Sigma}_t^{(\boldsymbol{i,j})}, \\ \mathrm{H}_1&: \boldsymbol{\Sigma}_r^{\boldsymbol{1}} \neq \cdots \neq \boldsymbol{\Sigma}_r^{\boldsymbol{N}} \neq \boldsymbol{\Sigma}_t^{(\boldsymbol{i,j})}. \end{aligned} \tag{5.51}$$

Now to understand how this all comes together with the hypothesis test (Equation (5.51)), let's assume that all of the blocks of data randomly collected from the scene are representative of natural clutter only, such that $\boldsymbol{\Sigma_r^1 \approx \cdots \approx \Sigma_r^N}$.

If the moving window, $\boldsymbol{W_t^{(i,j)}}$, as it moves across **X**, collects clutter samples only, then $\boldsymbol{\Sigma_r^1 \approx \cdots \approx \Sigma_r^N \approx \Sigma_t^{(i,j)}}$ and one can conclude that H_0 would not be rejected. On the other hand, if $\boldsymbol{W_t^{(i,j)}}$ happens to sample a manmade object, then $\boldsymbol{\Sigma_r^1 \approx \cdots \approx \Sigma_r^N \neq \Sigma_t^{(i,j)}}$ and as a result H_0 is likely to be rejected.

Given that N reference blocks of data are available to test the hypothesis (Equation (5.51)), as previously mentioned the M-Box equation can be extended to a $k = N + 1$ covariance matrices test as follows, [68] and [69]

$$\begin{aligned} -2log(M) &= v\left((k+1)\cdot ln\left|\Sigma_{pl}\right| - \ln|\boldsymbol{\Sigma}_r^1| - \ln|\boldsymbol{\Sigma}_r^2| - \cdots - \ln|\boldsymbol{\Sigma}_r^N| - \ln\left|\boldsymbol{\Sigma}_t^{(i,j)}\right|\right) \\ &= v\left((k+1)\cdot ln\left|\boldsymbol{\Sigma}_{pl}\right| - \sum_{d=1}^{N}\ln|\boldsymbol{\Sigma}_r^d| - \ln\left|\boldsymbol{\Sigma}_t^{(i,j)}\right|\right), \end{aligned} \tag{5.52}$$

where $v = v_d = v_t$, N is the number of random samples collected from the scene, $\boldsymbol{\Sigma}_r^d$ is the covariance matrix for each block of data randomly collected from **X**, $\boldsymbol{\Sigma}_t^{(i,j)}$ is the test covariance for location (i,j) in **X**, and $\boldsymbol{\Sigma}_{pl}$ is the pooled covariance defined as $\boldsymbol{\Sigma}_{pl} = \frac{\sum_{d=1}^{k} v_d\boldsymbol{\Sigma}_r^d + v_t\boldsymbol{\Sigma}_t^{(i,j)}}{\sum_{d=1}^{k} v_d + v_t}$ for $\boldsymbol{\Sigma}_r^d, \forall d$ and $\boldsymbol{\Sigma}_t^{(i,j)}$. Note that using the random sampling technique allowed to keep the test and reference window sample size the same, which was one of the goals in this subsection.

The reason for $k = N + 1$, is that the M-Box algorithm test determines if all covariance matrices are equal or not, which now includes the N random blocks of data and the test window. Equation (5.52) when used with the random sampling scheme will be known from now on as the Random Sampling M-Box or RS-M for short. The null hypothesis distribution of Equation (5.52) is defined by a χ^2 distribution with $(k-1)p(p+1)/2$ degrees of freedom, where $k = N + 1$, the N random blocks collected from the image plus the test window. The degrees of freedom can be further simplified in terms of random blocks only as $Np(p+1)/2$ when substituting k with $N + 1$.

In conclusion, this subsection demonstrated the following:

1) Random sampling technique is highly beneficial for characterizing an unknown test scene eliminating the need to define *a priori* the clutter spread relative to that of manmade objects.

2) The M-Box can be easily implemented with the random sampling technique since it is able to test multiple covariance matrices simultaneously.

3) The random sampling technique allows for the reference and the test blocks to have the same sample size, which is desirable since the M-Box covariance test is highly sensitive to unequal sample sizes.

5.3.8.2 Short Range PI Results using RS-M. The goal of this subsection is to quantify the performance of the RS-M using close range PI. Figure 5.65 illustrates a simple example where the intent is to show the effectiveness of the random sampling technique when implemented with the M-Box equation in the form of Equation (5.52) as an effective manmade object discriminator. In this example four clutter samples, in red, were manually collected from the test scene and used as reference samples. Ten test samples were collected from the scene where five are representative of manmade objects,

shown in blue from one through five, and the remaining five samples from clutter, shown in yellow from six through 10. The intent of this example is to understand how effective Equation (5.52) is in rejecting, or not, the null hypothesis when the test sample is representative of natural clutter or rejecting the null hypothesis when the test sample is from a manmade object.

Figure 5.66 illustrates the Gaussian distributions of all the reference and test samples, where the reference samples are shown in color red, manmade test samples are shown in blue, and the clutter test samples in black. As one can observe in Figure 5.66 the manmade objects distribution has a smaller spread than any of the clutter samples (reference and test). Therefore, when using the reference clutter samples to test if a block of data is from a manmade object or not, one expects that the result of Equation (5.52) should yield a high score if the test sample is from a manmade object and a low score if it is from clutter.

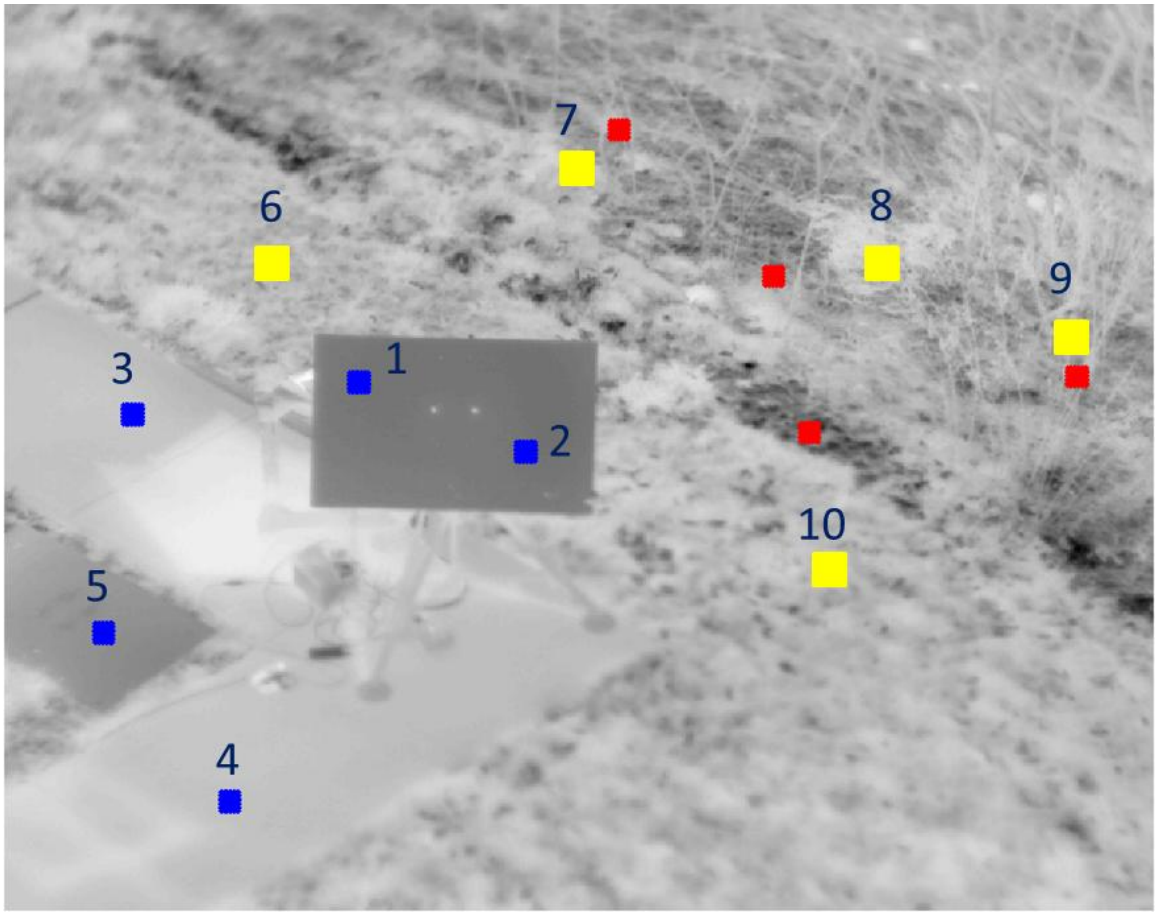

Figure 5.65 Four clutter samples were collected from image (red) to be used as reference and ten samples, five from manmade objects (1 through 5) in blue and five from natural clutter (6 through 10) in yellow will be used for testing.

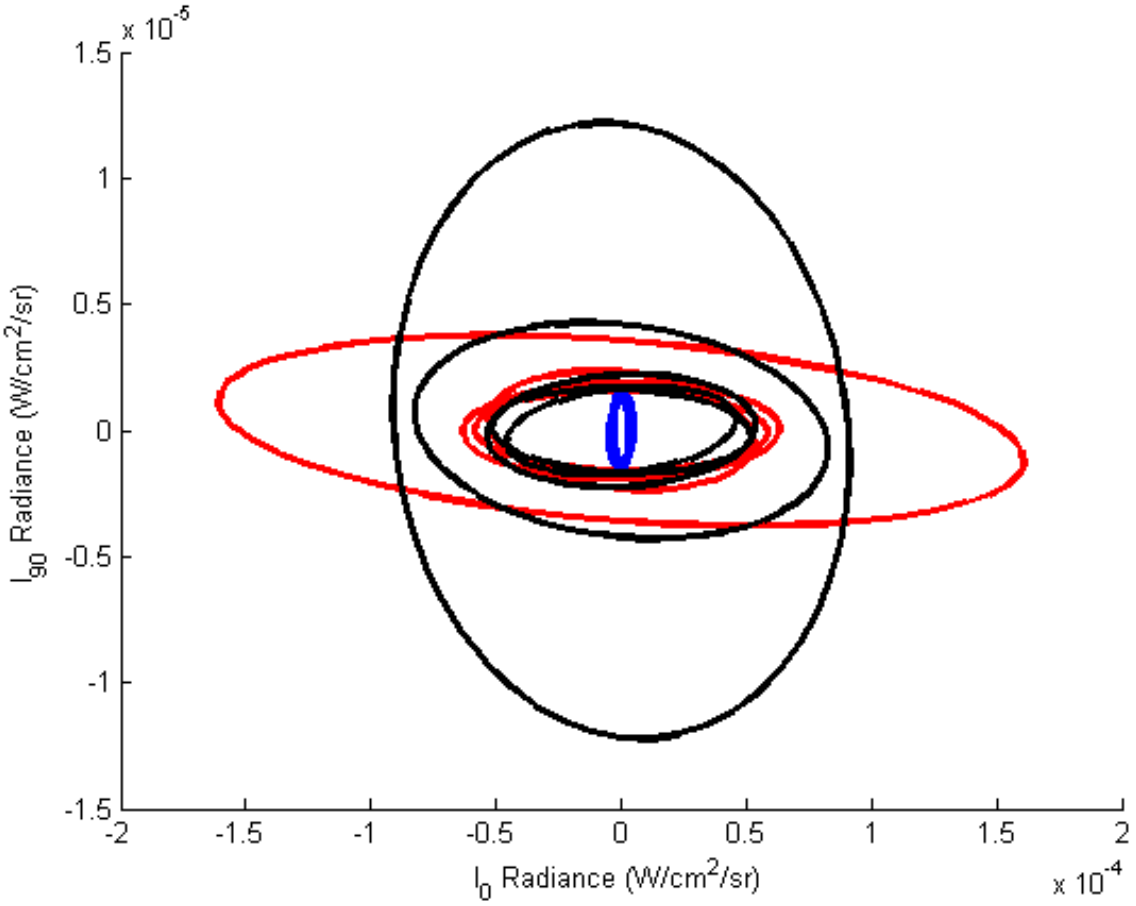

Figure 5.66 Gaussian distribution of the reference clutter samples (red), manmade objects (blue), and natural clutter (black). Notice that the natural clutter test samples are in black instead of yellow so they can be easily discriminated from the white background.

Figure 5.67 presents the χ^2 distribution with 12 degrees of freedom for different probabilities of miss and their respective thresholds, $\alpha = 0.10$ ($z = 18.6$), $\alpha = 0.05$ ($z = 21.1$) and $\alpha = 0.01$ ($z = 26.3$). These thresholds allow to determine if the results of Equation (5.52) reject or not the null hypothesis.

Figure 5.68 illustrates the results of Equation (5.52) where the x-axis represent the test samples; MM1 through MM5 are for blocks of data representative of manmade while BKG represents natural clutter. The y-axis represents the equation output score for each

of the test and the manually picked samples from Figure 5.65. Two horizontal lines are also shown in this plot that depict different cutoff thresholds for $\chi^2_{12,\alpha=0.10}$ and $\chi^2_{12,\alpha=0.05}$.

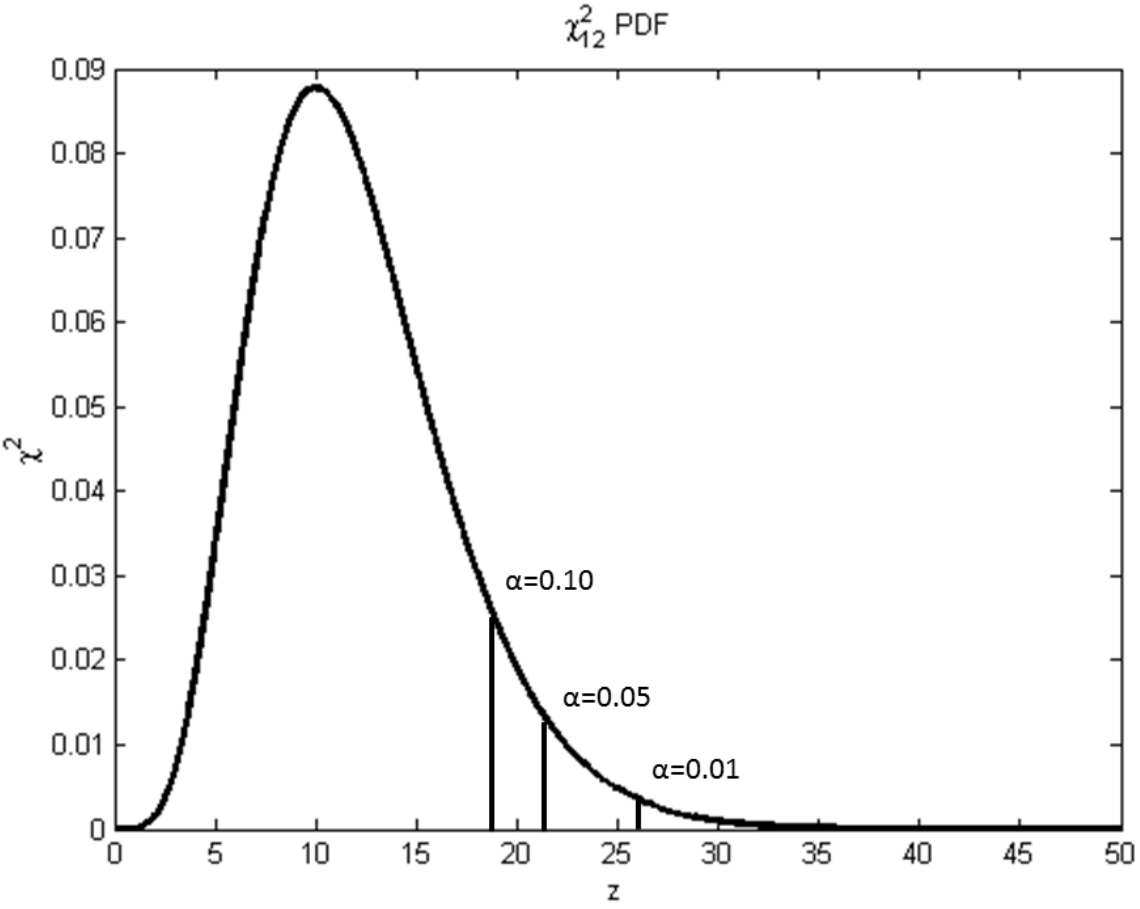

Figure 5.67 χ^2 distribution with 12 degrees of freedom for α = 0.10 (z = 18.6), α = 0.05 (z = 21.1) and α = 0.01 (z = 26.3).

Overall, the results of the RS-M shown in Figure 5.68 seem quite promising since all of the five samples representing manmade objects were rejected by the null hypothesis with a cutoff threshold of z=21.1 ($\alpha = 0.10$). Conversely, when the test sample came from a natural clutter, the null hypothesis could not be rejected using the same threshold.

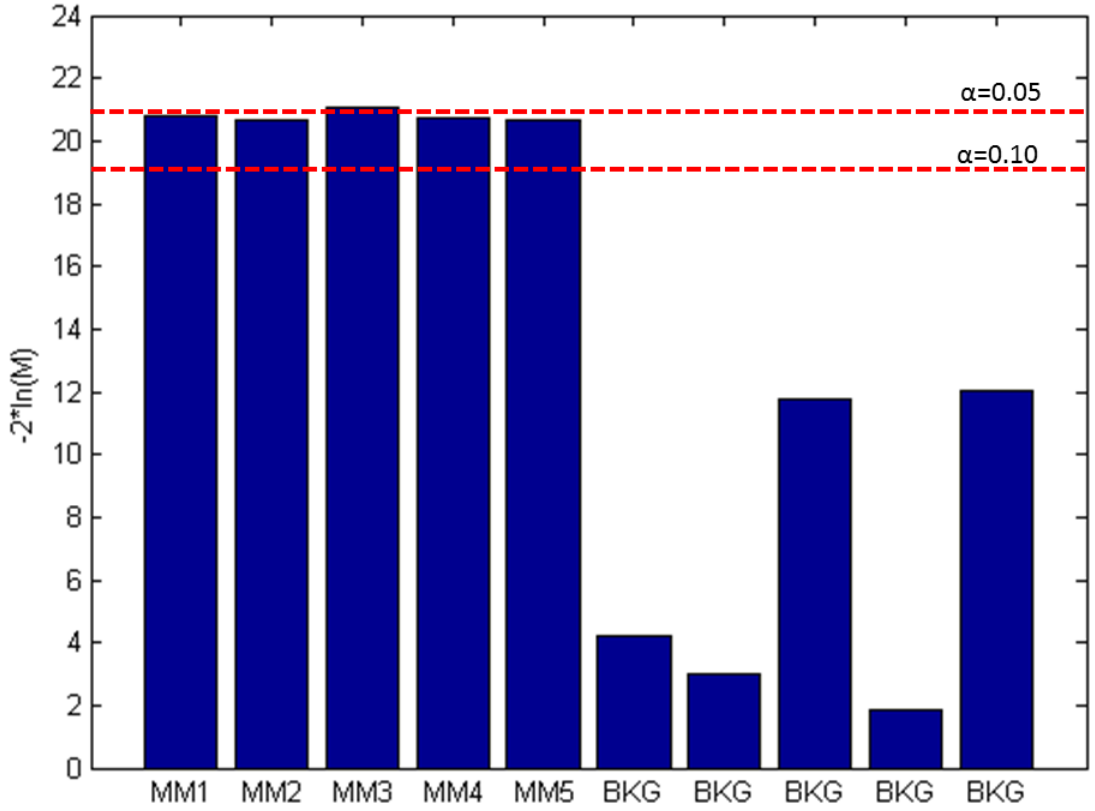

Figure 5.68 Results from Equation (5.52) using the four samples (red) shown in Figure 5.65 as reference and the blue and yellow blocks of data as test. MM1 through MM5 represent the blue blocks of data from manmade objects one through five, while the BKG represent the five clutter samples. It is clear that using the reference blocks in Equation (5.52) to test the unknown samples demonstrated the ability to discriminate the manmade objects from natural clutter using a $\alpha = 0.10$.

In conclusion, from this limited example results, one can suggest that using random samples collected from clutter as reference and used with the M-Box algorithm, one was successful in discriminating the manmade object samples from natural clutter samples.

In the following example, the RS-M will be used to process the images, shown in Figure 3.15, with the objective to show that (1) the random sampling technique is effective in characterizing the background, resulting in successful discrimination of all manmade objects from natural clutter backgrounds, and (2) as the number of samples, N,

increase so does the ability of the M-Box algorithm in discriminating the manmade objects from clutter with a lesser number of false alarms.

Clutter samples were manually collected from each of the test images for the different angles. The first experiment manually sampled the background 20 times or $N = 20$, while the second experiment manually sampled the background 30 times or $N = 30$. All sampled blocks of data are reference samples to be used with the M-Box algorithm in Equation (5.52) and the resulting output surfaces are shown in Figures 5.69 and 5.70. From here on out the RS-M will be defined as RS-20 or RS-30 when N = 20 or 30.

Figure 5.69 illustrates the output surfaces for the M-Box and RS-M, where the RS-M used 20 and 30 reference samples to characterize the test imagery. All of the output surfaces are normalized for visual appreciation. However, it is important to note that Figure 5.69 can be quite little misleading since there are several pixels (especially for RS-M algorithm) that display extremely high scores and as a result of the normalization the output surface reveals very low contrast between manmade objects and clutter.

More importantly, Figure 5.70 illustrates the binary output surfaces for a probability of miss of 0.05 for the M-Box and RS-20 and 30. One can clearly observe the RS-M anomaly detector working very well when the output surfaces are thresholded.

For example, Figure 5.70 demonstrates that the ability in discriminating the manmade objects relative to natural clutter was very similar for both $N = 20$ and 30 reference samples. On the other hand, the number of false alarms actually decreased significantly as a function of increasing N, which should be expected since more samples (usually) imply better background characterization.

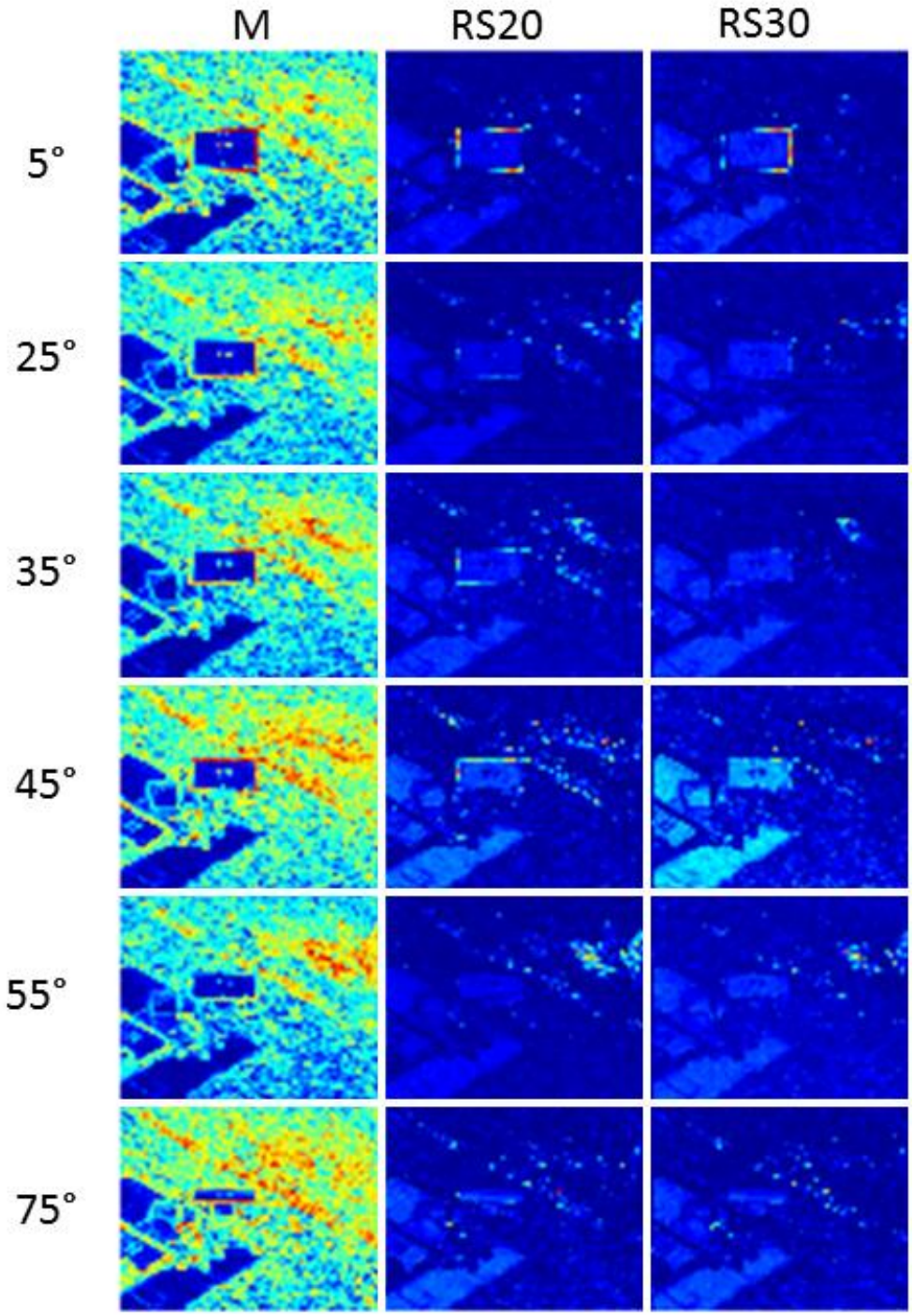

Figure 5.69 Output surface comparison between the M-Box, RS-20, and RS-30.

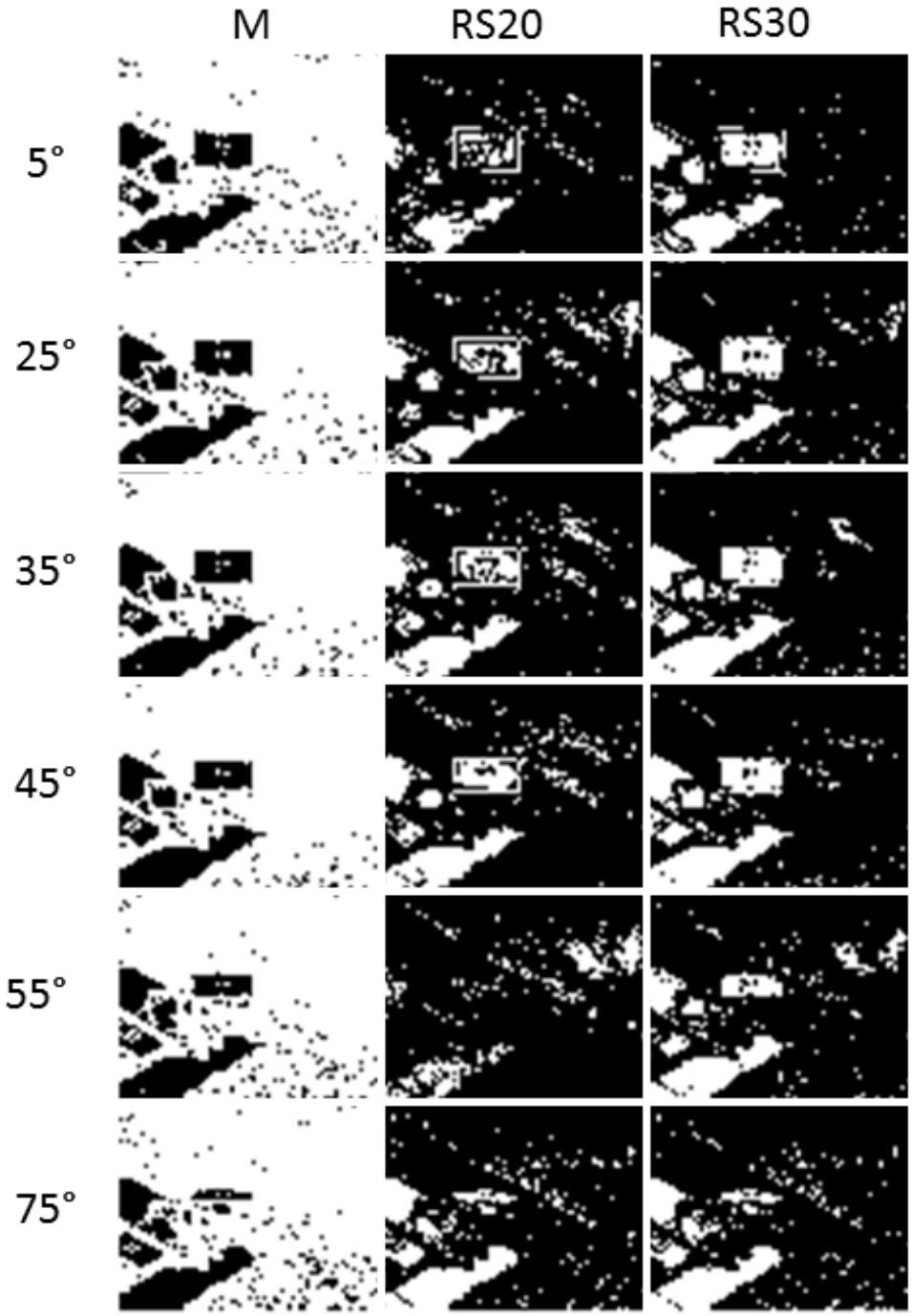

Figure 5.70 Threshold binary images for each of the input images in Figure 5.69 for $H_0 | \chi^2_{\alpha=0.05}$.

The following trends can be observed in Figure 5.70:

1) As explained in Subsection 5.3.7, the M-Box algorithm, when implemented as per Subsection 5.3.6.1 only rejected natural clutter while in contrast RS-M successfully rejected the manmade objects.

2) As the number of reference samples increased from 20 to 30, the number of false alarms decreased significantly as a result of better background characterization.

Figure 5.71 illustrates the PDF plot for the RS-20 output surfaces in Figure 5.69. In this image the higher peak (left) in each of the distributions represents the clutter and the lower peak (right) the manmade objects in the scene. The PDF plots for RS-30 are not shown due to the redundancy.

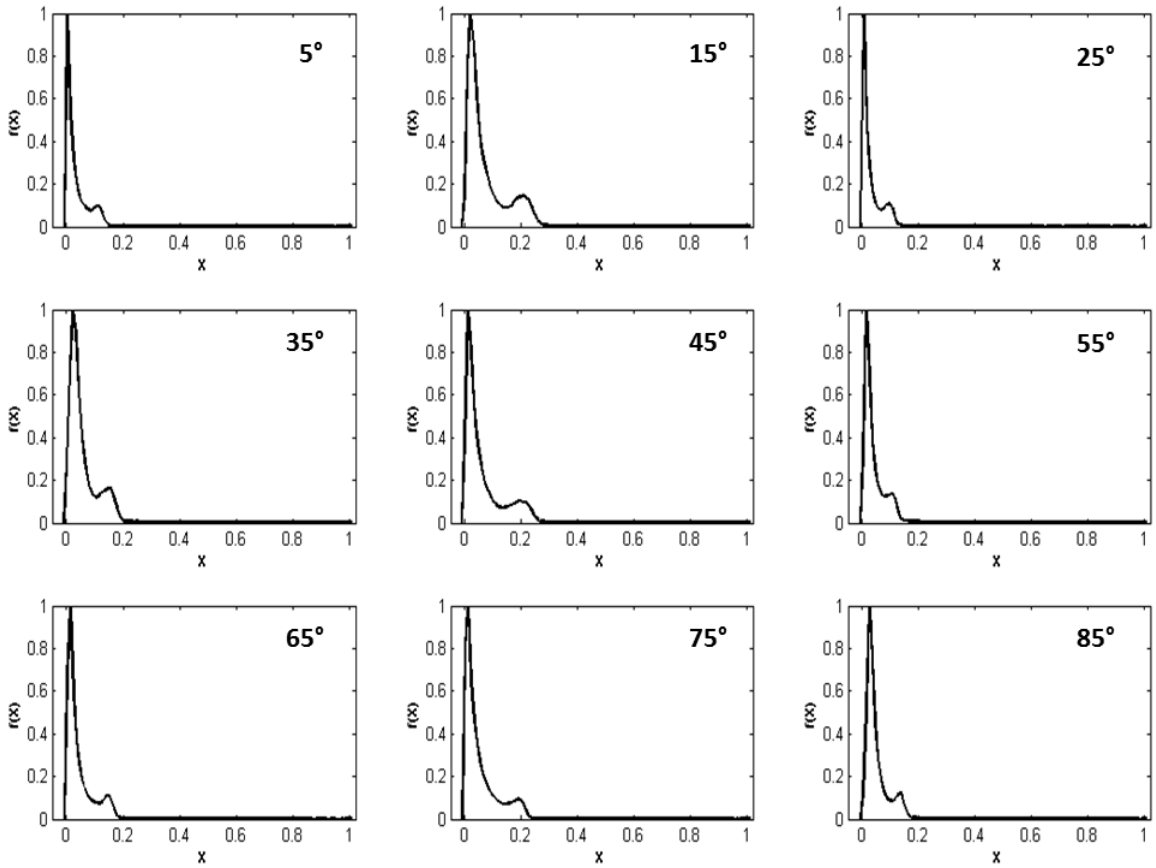

Figure 5.71 PDF plots of the output surfaces of RS-20 from 5° to 85°.

The important point to stress from Figure 5.71 is that the output surface for the RS-M seems to achieve the shape and form of what is expected from the PDF under H_0,

where in this context natural objects respond with values far left toward zero and manmade objects respond with values far right toward large numbers. This desired outcome justifies putting a high cutoff threshold far right, based on a χ^2distribution, and rejecting H_0 for values above the threshold. From the M-Box limitations discussed earlier in Subsection 5.3.7, the PDF plots shown in Figure 5.59 for the M-Box output surfaces do not show the desired features depicted in Figure 5.71.

5.3.8.3 Long Range PI Results using RS-M. In Subsection 5.3.8.2, the RS-M demonstrated the capability in discriminating manmade objects in close proximity PI, unlike the M-Box implementation presented in Subsection 5.3.6.1. This subsection evaluates the RS-M methodology in discriminating manmade objects in natural clutter background for long range (550m) PI.

The goal of this subsection is to demonstrate that, using the RS-M to test imagery collected at long range:

1) The RS-M is a versatile anomaly detection algorithm that is able to characterize the background successfully using the random sampling approach.

2) The RS-M is as effective as the M-Box algorithm in detecting the surrogate targets and external blackbody.

3) The RS-M is able to successfully discriminate the observation tower from natural clutter unlike the M-Box algorithm from Subsection 5.3.6.1.

Figure 5.72 illustrates a broadband image of a scene collected on 6 MAR, 2010 at 0710h. In this figure, all manmade objects have similar temperature relative to the natural clutter. Five random samples ($N = 5$) were manually collected from natural clutter shown in red and used by the RS-M as reference clutter blocks.

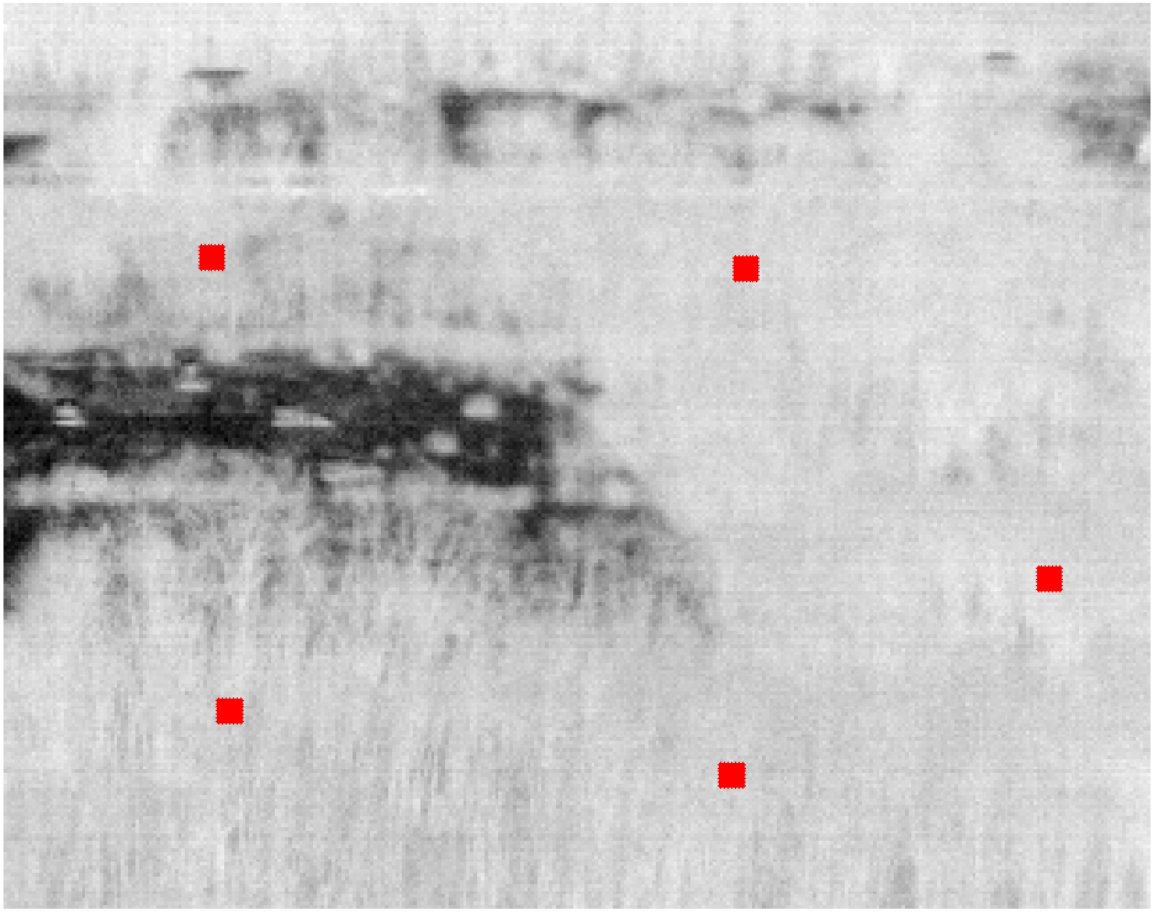

Figure 5.72 Broadband image collected on 6 MAR 2010 at 0710h. The manmade objects had similar temperature as the natural background. Five clutter samples were manually collected from the scene and used as reference blocks for the RS-M.

Using Equation (5.52), the reference covariance matrices estimated from each block of data are represented by $\{\boldsymbol{\Sigma}_r^d\}_{d=1}^5$ while the covariance test matrix estimated from the samples of the test window of size 7×7 for each location (i, j) is represented by $\boldsymbol{\Sigma}_t^{(i,j)}$. In order to test the whole image, the test window has to cover all possible locations (i, j) resulting in an output surface of size $\boldsymbol{Z} \in \boldsymbol{R}^{R-n+1,C-n+1}$. In this experiment, both the reference blocks of data and the test window have identical sample sizes.

Figure 5.73 demonstrates the output surface $-2 \cdot \ln(\boldsymbol{Z})$, where dark red color indicates pixels that are very likely to be rejected by the null hypothesis and dark blue represents pixels that are very likely to accepted by the null hypothesis. In this framework, it is desired to have all manmade objects in yellow-red color so they can be rejected by the null hypothesis (for a given probability of miss). What is important to emphasize in Figure 5.73 is that not only the surrogates and the blackbody were successfully discriminated from the background, the tower was also successfully discriminated unlike the results shown earlier in Subsection 5.3.6.2 for the M-Box.

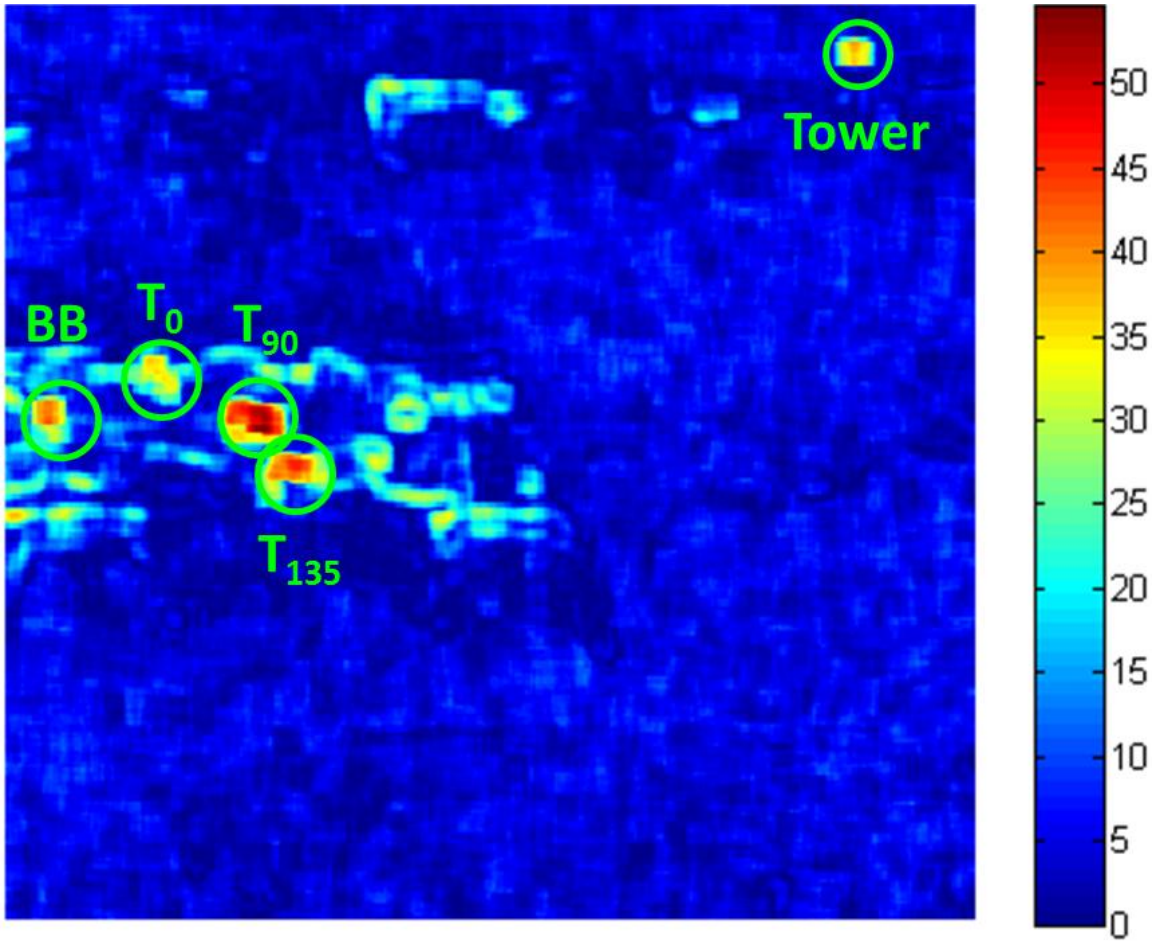

Figure 5.73 Output surface of Equation (5.52) using five clutter samples shown in Figure 5.72. All manmade objects are shown in the desired yellow-red color indicating that there is a high probability that their locations will be deemed as anomalies when a desired probability of miss (α) is applied.

Figure 5.74 presents the binary output surfaces for different probability of miss, $0.10\ (22.31), 0.05(25.00), \text{and } 0.01(30.58)$, shown on the top left, top right, and bottom images, respectively.

Figure 5.74 shows that as the number of false alarms diminishes as a function of decreasing probability of miss (incorrectly rejecting H_0), all pixels representing manmade objects were successfully rejected by the null hypothesis, a highly desirable outcome. More importantly, the pixels representing the observation tower were also successfully

discriminated using the RS-M anomaly detector, unlike the M-Box algorithm discussed in Subsection 5.3.6.1.

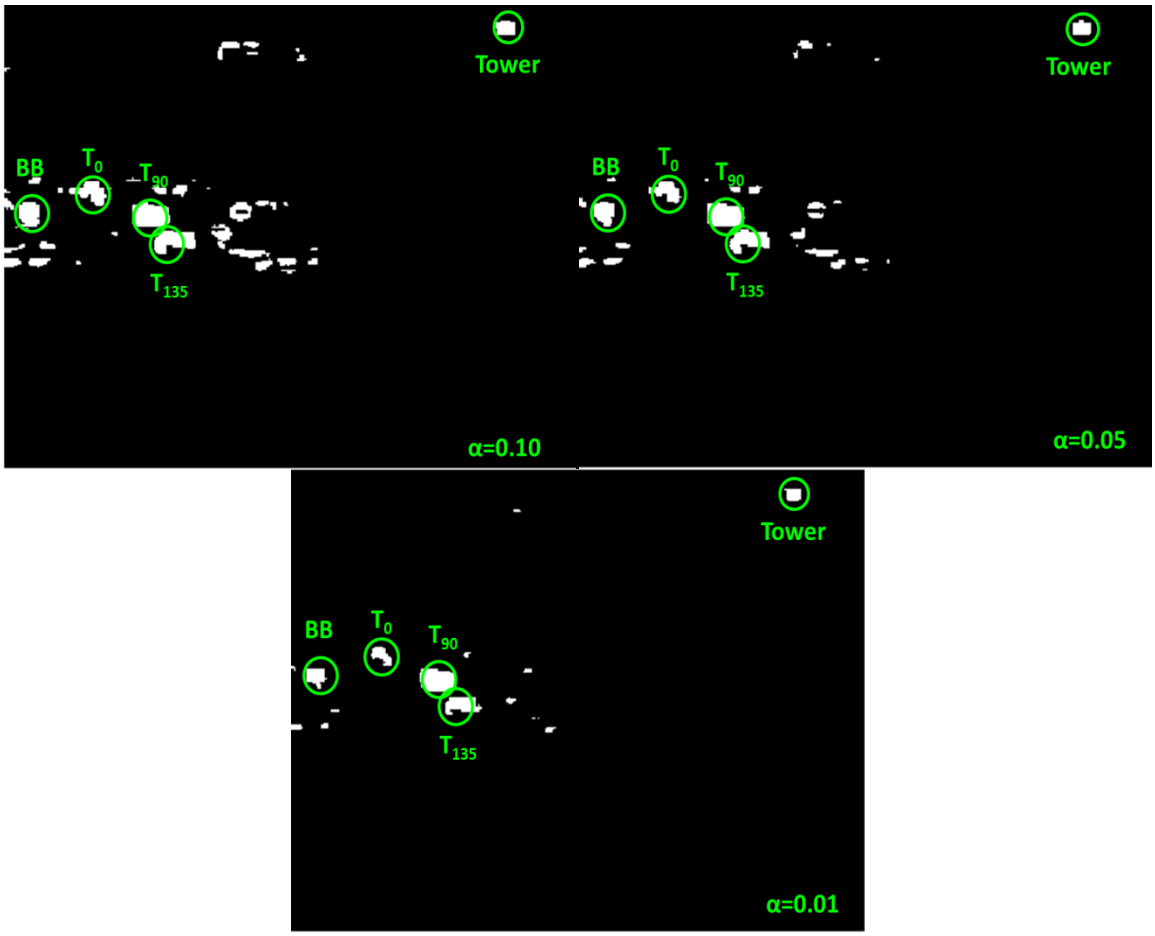

Figure 5.74 Threshold output surfaces of Figure 5.73 using a probability of miss of 0.10, 0.05, and 0.01. In this example, the surrogates and the external blackbody are clearly detected, performing similarly to the M-Box algorithm. In addition, unlike the M-Box, RS-M was also able to discriminate the observation tower successfully.

This subsection presented results on the RS-M in discriminating manmade objects from natural clutter background using long range PI. The conclusions one can draw from this subsection are as follows:

1) By using a random sampling technique to characterize the background, the RS-M is able to discriminate manmade objects in both close range

(Subsection 5.3.8.2) and long range (Subsection 5.3.8.3) PI unlike the M-Box anomaly algorithm.

2) The RS-M demonstrated that is as effective as the M-Box algorithm in detecting the surrogate targets and external blackbody.

3) The RS-M is able to successfully detect the observation tower from natural clutter unlike the M-Box algorithm.

5.3.8.4 Contamination Effects on the RS-M Performance. The case of contamination of target pixels in $\boldsymbol{W_r^d}$ as a result of the random sampling process is now addressed. Contamination in this framework indicates that one or more blocks of data randomly collected from **X**, captured information from a manmade object present in the scene.

Let one assume as an example that N blocks of data are randomly collected from a test scene where N-1 blocks are representative of natural clutter and their covariance matrices estimated from the blocks of data are similar to each other, or $\boldsymbol{\Sigma_r^1 \approx \Sigma_r^2 \approx \Sigma_r^3 \approx \cdots \approx \Sigma_r^{N-1}}$. The remaining Nth block of data collects information of a manmade object (contamination) present on the scene and the covariance matrix estimated from that same block of data is represented by $\boldsymbol{\Sigma_r^N}$. Let one also assume that the location of the test window $\boldsymbol{W_t^{(i,j)}}$ is identical to the location of the Nth random block of data such that, $\boldsymbol{\Sigma_r^N = \Sigma_t^{(i,j)}}$, where both $\boldsymbol{\Sigma_r^N}$ and $\boldsymbol{\Sigma_t^{(i,j)}}$ represent the same manmade object. An important question follows: what happens to the RS-M ability in discriminating that same manmade object when contamination occurs?

The goal of this subsection is twofold:

1) Rationalize the reason why as the number of random blocks of data (N) collected from the test scene increases (which as a result also

increases the probability of contamination), the overall adverse effect on the discriminant power of the RS-M is insignificant.

2) Present data analysis and quantify the RS-M capability of discriminating manmade objects from natural clutter when contamination occurs.

Let one assume that a test scene is random sampled using N blocks of data to be used as reference to the RS-M. As expected, increasing N would also increase the probability that one or more random blocks of data can sample manmade objects present in the test scene. Although such contamination issue seems quite problematic at first, the truth is that as the number of random blocks of data (N) increases, a large number of those N blocks of data should represent only clutter. In other words, for each block of data that is representative of a manmade object, chances are there are many more blocks of data representative of natural clutter.

In order to appreciate how the RS-M may be robust to contamination one must understand the impact of the pooled covariance on the overall result of the M-Box algorithm.

Examining Equation (5.40), the pooled covariance by definition is the sum of all covariance matrices (reference and test), each multiplied by the respective sample size and the result is then divided by the total number of samples of all the covariance matrices. Under this scenario, one would expect that the determinant of the pooled covariance matrix $\left|\boldsymbol{\Sigma}_{pl}\right|$ would lie somewhere between the determinant values of $\{\boldsymbol{\Sigma}_r^d\}_{\boldsymbol{d=1}}^{\boldsymbol{N}}$ and $\left|\boldsymbol{\Sigma}_{\boldsymbol{t}}^{(\boldsymbol{i},\boldsymbol{j})}\right|$, [58,p. 256], since the pooled estimation is the average of the individual estimations.

Since $\mathbf{\Sigma}_{pl}$ is the average of all N reference and test covariance matrices, as the number of blocks of data random sampled from the scene increase, the probability that a significant large percentage of all N blocks of data is representative of natural clutter should be quite high. If such is true, then $\mathbf{\Sigma}_{pl}$ would be inclined to bear the values of representatives of natural clutter only. Using this rationale, one would expect that contamination should have little effect on the overall result of Equation (5.40) with increasing N. The following figures check its validity.

In order to visualize this effect on the pooled covariance, let one assume that ten random samples, red blocks shown in Figure 5.75, are collected from a test scene where all random samples are representative of natural clutter only. At the same time, a test sample is collected from the test plate (blue).

Figure 5.76 illustrates the distributions of the ten reference samples (red), the manmade object sample (blue), and the pooled covariance (black). Notice that all clutter samples distributions are wider than the manmade object distribution. Since, the pooled distribution, as mentioned earlier, is the average of all the reference and test distributions, the pooled covariance distribution lies closer to the reference samples distribution. Therefore, one can conclude that the pooled and the ten reference samples distributions are very different from the test sample.

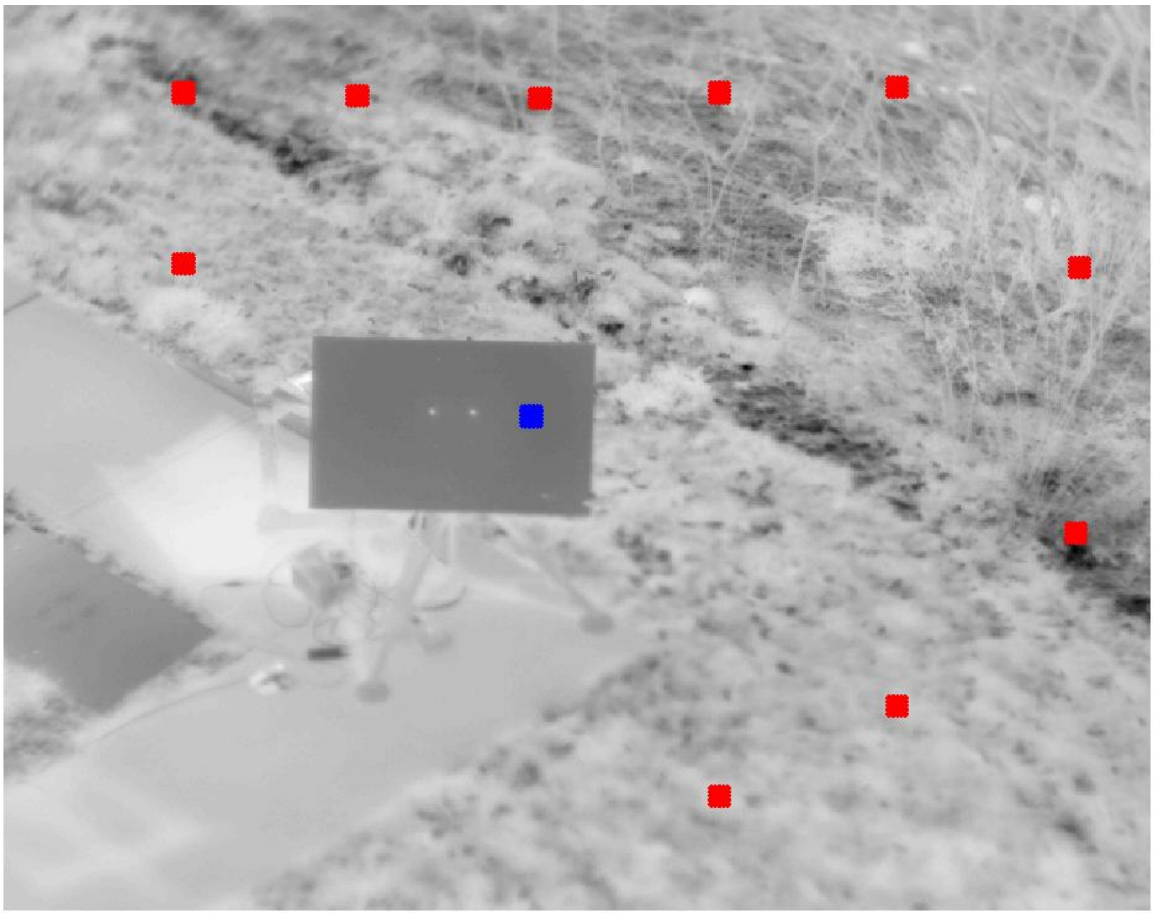

Figure 5.75 Ten clutter samples were manually collected from the image shown in red to be used as reference blocks for the RS-M. One manmade object sample, in blue, was collected to be compared to the reference samples in Figure 5.76.

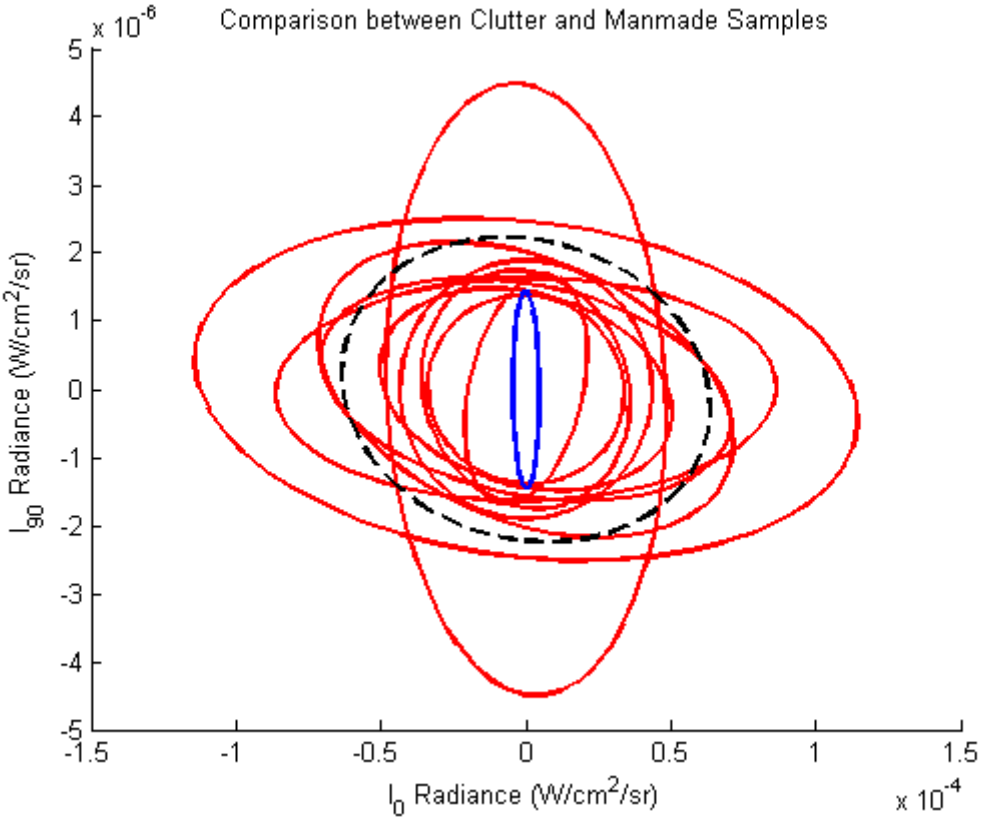

Figure 5.76 The ten clutter samples distributions from Figure 5.75 are shown in red, the manmade sample distribution is shown in blue, and the pooled distribution is shown by a dashed black line. The pooled distribution is shown to be the average of all the clutter distributions which, as expected, is very different from the manmade distributions. All distributions are centered at zero for visual appreciation.

Conversely, Figure 5.77 illustrates the concept of contamination. In this figure, nine reference samples are collected from natural clutter and one reference sample from the tilting plate (red) as the contaminated sample, and the same manmade sample, as in Figure 5.75, was collected again (blue).

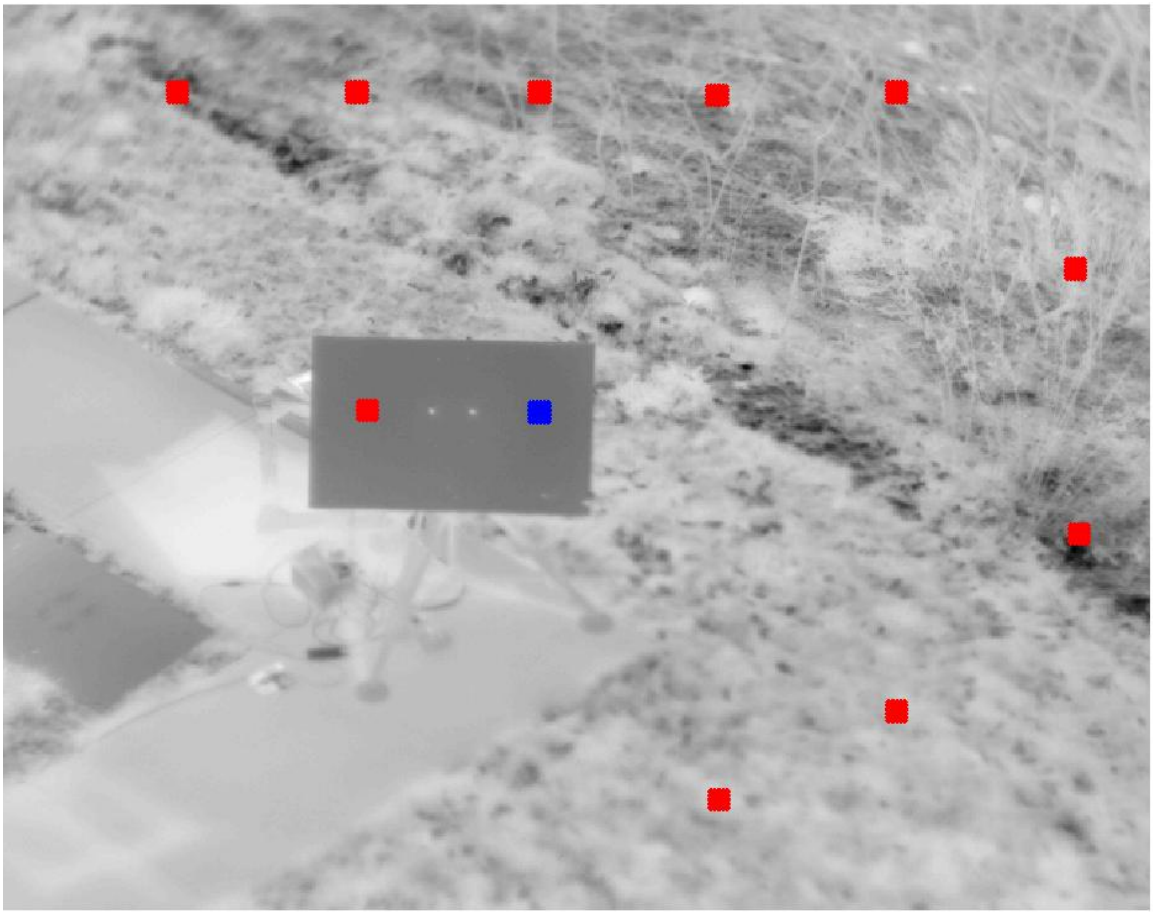

Figure 5.77 Illustration of contamination where nine out of the ten reference samples are taken from clutter and the remaining one from the test plate. As with Figure 5.75 the same manmade sample (blue) was once again to be compared to the reference samples in Figure 5.78.

Figure 5.78 illustrates the reference samples distribution in red, the manmade object in blue, and the pooled covariance in black. In contrast to Figure 5.76, Figure 5.78 presents the situation of contamination where one of the reference samples collected information from the same manmade object. As a result, one can observe that the distribution of the manmade object (in blue) and the contaminated sample are similar to each other. Comparing the distributions of the pooled covariance from Figure 5.76 and 5.78 one can observe both to be very similar to each other as well.

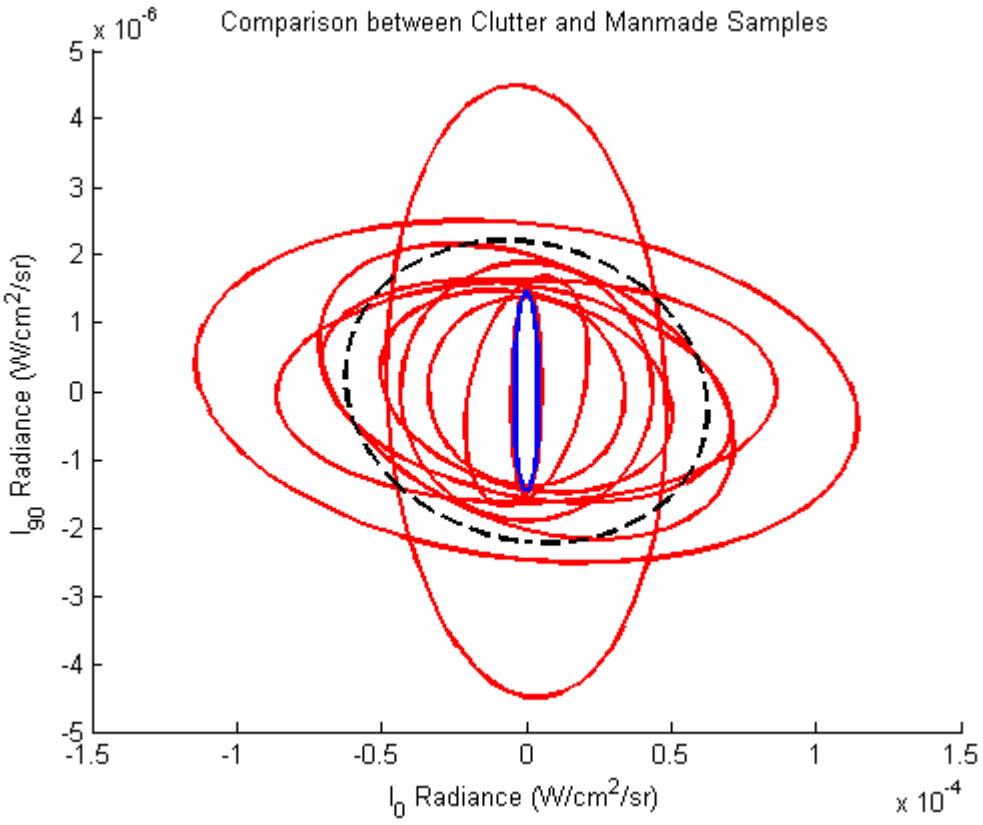

Figure 5.78 Distribution of all the reference samples (red), manmade sample (blue), and the pooled distribution (dashed black line). In this example, the contaminated sample has the same distribution as the blue distribution. Since nine of the samples are representative of the background, the pooled covariance is similar to the one found in Figure 5.76.

In order to compare the pooled covariances, Figure 5.79 compares the distribution of the pooled covariance when no contamination is present (black line) and when contamination is present (dashed black line). The left plot shows both pooled covariances plotted on Figure 5.78 and the right plot demonstrates a zoomed in version of the left plot for visual appreciation. What is interesting to note is that even with the one sample of contamination present, the difference between the spread of the pooled covariance relative to the uncontaminated pooled covariance was minimum, which is desirable.

For a situation such as in Figure 5.72 where the RS-M algorithm will be applied to, as N, the number of random blocks collected from the scene, increases, the probability that one or more blocks will sample a manmade object will increase as well. However, the probability that most of the random samples will be representative of the natural clutter is also very high, and as a result, the pooled covariance will be representative of the natural clutter and the contamination will have little effect on the overall distribution of the pooled statistics.

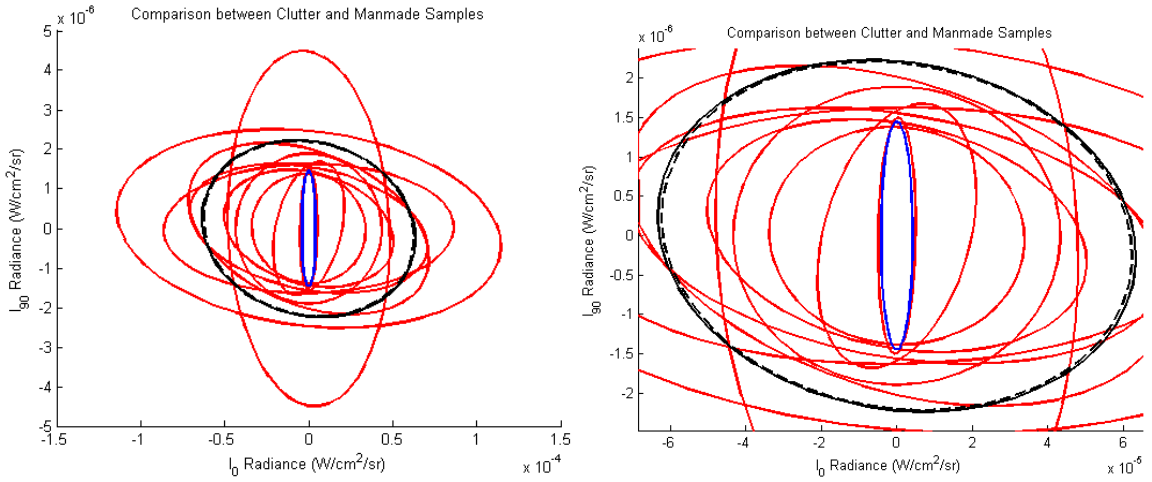

Figure 5.79 Comparison between the uncontaminated (black line) and contaminated (dashed black line) pooled distributions. The left plot illustrates the two pooled distribution plotted on the Figure 5.78 while the right plot is zoomed in for visual appreciation. One can clearly observe that both the contaminated and uncontaminated distributions yield similar spread.

Finally, Figure 5.80 illustrates the output surfaces when using the reference samples from Figure 5.75 (top) and Figure 5.77 (bottom). It is important to note that for the top image in Figure 5.80, all reference samples were collected from clutter while for the bottom image one of the ten reference samples was collected from the tilting plate while the remaining nine samples were collected from natural clutter. In comparing the

top and bottom images in Figure 5.80, one readily notices that the manmade objects in the top image have a higher contrast relative to the surrounding clutter compared to the bottom image where contamination occurred. One also notices that the same false alarms located at the top right of the image can be seen in both output surfaces. This could be the result where that precise location exhibits a very different distribution from the surrounding clutter and since no random sample was collected from that location, it showed up as an anomaly.

Figure 5.81 illustrates the binary output surfaces using a cutoff threshold of 22.31 for a probability of miss of $\alpha = 0.10$. The top image represents the binary cutoff image for the uncontaminated output surface (Figure 5.81 top image) and the bottom image represents the binary cutoff image for the contaminated surface (Figure 5.81 bottom image).

At a glance, one can observe that for both binary surfaces all manmade objects were successfully detected, however the bottom image, where contamination occurred, one can find a few more false alarms than in the top image. The main key point to take from these images (and subsection) is that contamination although a possibility has limited effect on the final output of the RS-M as long as the number of contaminated blocks of data is much less than the number of blocks of data representing clutter.

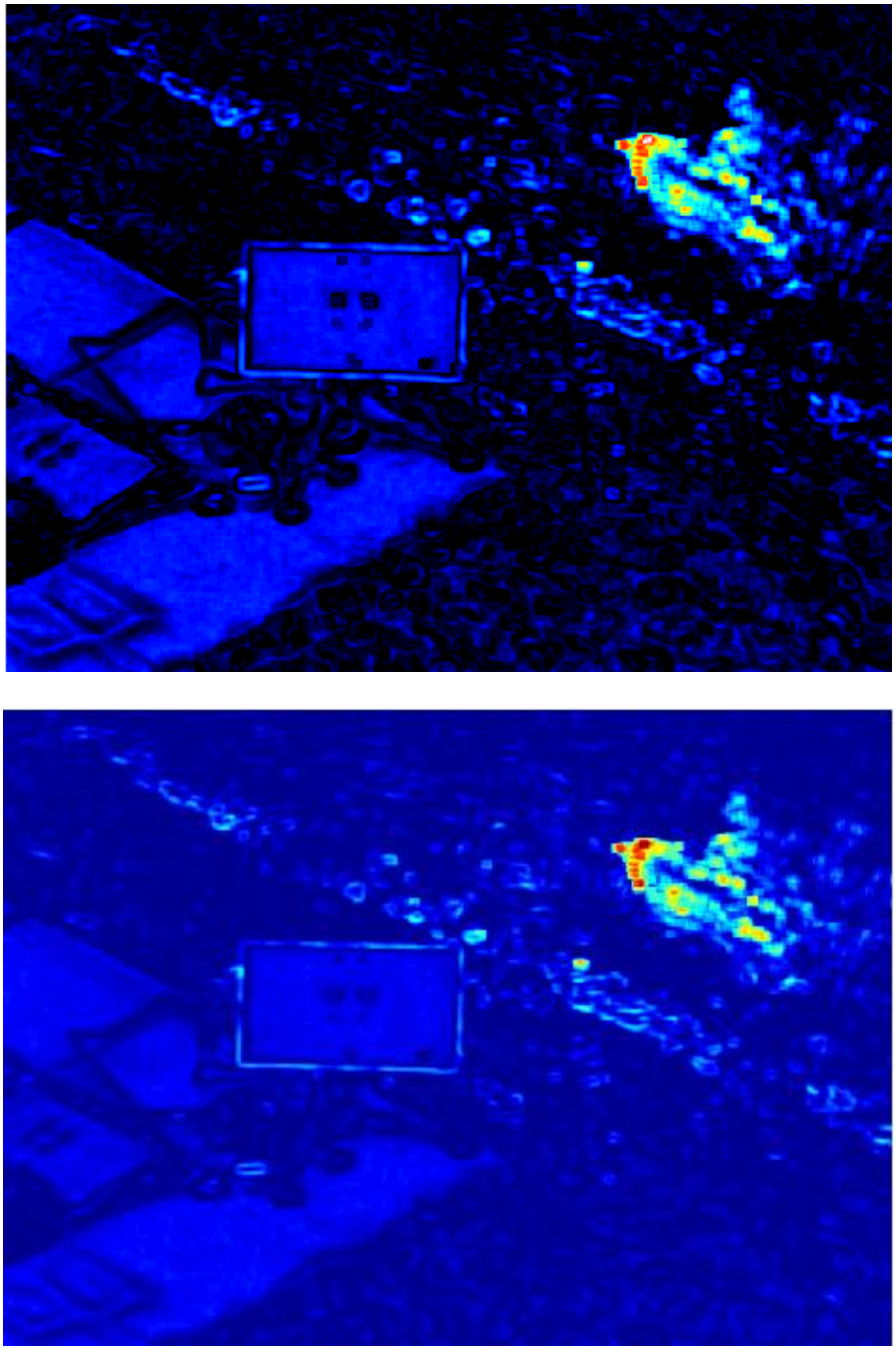

Figure 5.80 Output surfaces for Figures 5.75(top) and 5.77 (bottom). Both figures demonstrate the ability to discriminate all manmade objects from natural clutter background.

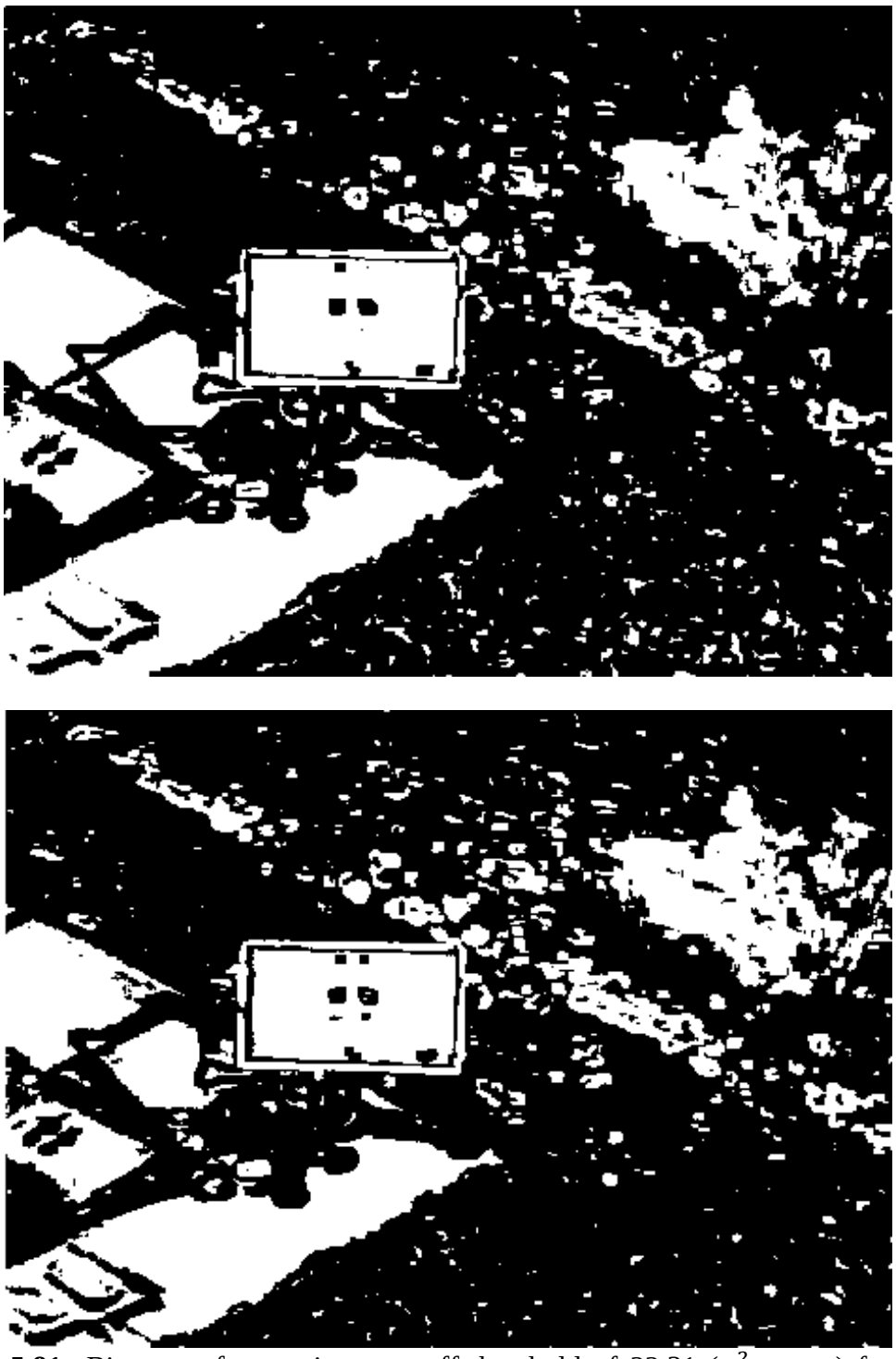

Figure 5.81 Binary surfaces using a cutoff threshold of 22.31 ($\chi^2_{30,\alpha=0.10}$) for Figure 5.80. The top image had no contamination in the reference samples unlike the bottom figure. All manmade objects are clearly discriminated from natural clutter, however one can find a few more false alarms present in the bottom image relative to the top image.

In conclusion, the RS-M algorithm is a more versatile algorithm which can be used for a variety of situations where manmade distribution spread may fluctuate between being larger or smaller than natural clutter and there is no need for *a priori* knowledge of the background as described in Subsection 5.3.7 and tested in this subsection with short and long range imagery. Finally, this subsection demonstrated some key facts worth mentioning again:

1) The random sampling was proposed as a background characterization methodology to be implemented with the M-Box algorithm, known as RS-M.

2) The RS-M was able to discriminate manmade objects from natural clutter background for both short and long range PI.

3) Increasing the number of random samples increases the ability to characterize the background very well, resulting in fewer false alarms detected.

4) A certain level of contamination in the randomly chosen data blocks from the testing imagery, although a potential problem, has little adverse effect on the RS-M discriminant output.

In the next subsection, the RS-M performance will be compared to the M-Box algorithm using long range PI as input.

5.3.9 Performance Assessment of RS-M

The implementation of the RS-M detector and its performance against the baseline algorithm, the M-Box detector, is presented in this subsection.

5.3.9.1 Algorithm Implementation. Let **X** be an R×C image of p observables such that $\boldsymbol{X} \in \boldsymbol{R}^{\boldsymbol{R}\times\boldsymbol{C}\times\boldsymbol{p}}$.

The first step in implementing the RS-M is to collect N number of blocks of data in the form of $\{\boldsymbol{W}_r^d\}_{\boldsymbol{d=1}}^{\boldsymbol{N}}$ where $\boldsymbol{W}_r^d \in \boldsymbol{R}^{n_2\times p}$ for any given d, and all N blocks of data are automatically designated as reference clutter signatures. Figure 5.82 illustrates a polarimetric test image randomly sampled with different N, e.g., five (red), 10 (green), 15 (blue), and 20 (yellow).

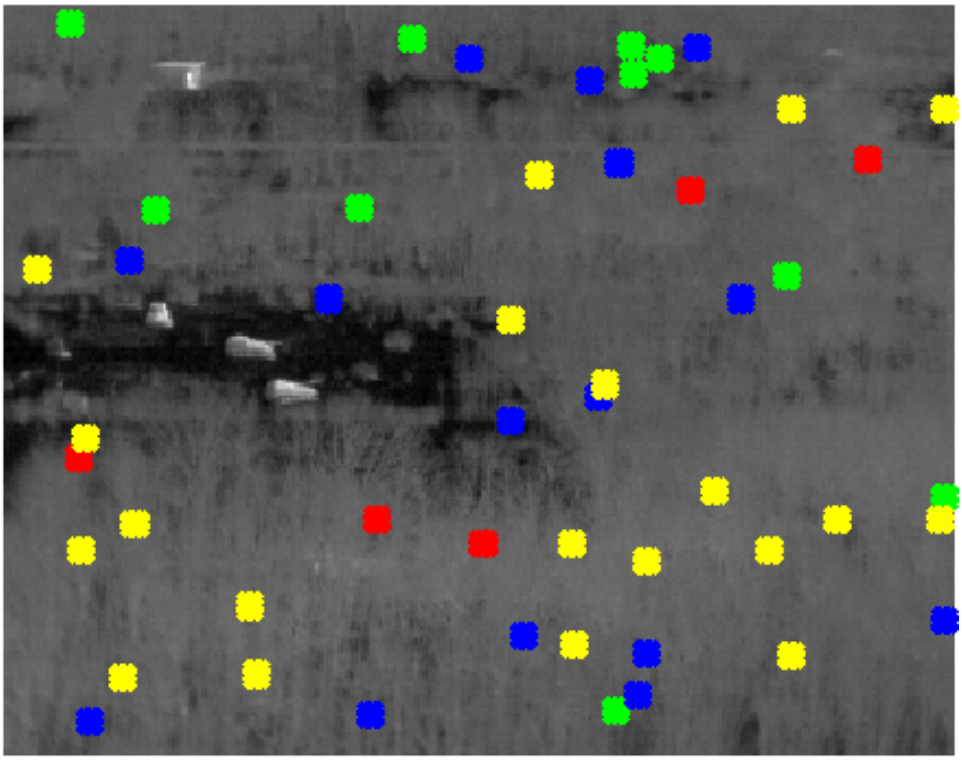

Figure 5.82 Locations of random blocks collected from the scene for the M algorithm for $N = 5, 10, 15, \text{and } 20$ without any *a priori* knowledge on the locations of manmade objects in the scene.

The covariance of each random block of data, $\boldsymbol{W}_r^d$, is given by

$$\boldsymbol{\Sigma}_r^d = \mathrm{E}\left[\left(\boldsymbol{W}_r^d - \boldsymbol{\mu}_{\boldsymbol{W}_r^d}\right)\left(\boldsymbol{W}_r^d - \boldsymbol{\mu}_{\boldsymbol{W}_r^d}\right)^T\right], \tag{5.53}$$

where $\boldsymbol{\mu}_{\boldsymbol{W}_r^d}$ is the mean of $\boldsymbol{W}_r^d$, and the determinant of $\boldsymbol{\Sigma}_r^d \in \boldsymbol{R}^{p\times p}$ is calculated as,

$$D_r^d = \det(\boldsymbol{\Sigma}_r^d). \tag{5.54}$$

Once the determinant of the covariance for each N block of data is calculated, a sliding test window moves across image $\mathbf{X}$ for every possible location (i, j) in $\mathbf{X}$ where $\boldsymbol{\Sigma}_{\boldsymbol{t}}^{(\boldsymbol{i},\boldsymbol{j})}$, the covariance matrix of $\boldsymbol{W}_t^{(\boldsymbol{i},\boldsymbol{j})}$, is calculated. Given the N reference covariance matrices $(\boldsymbol{\Sigma}_r^d)$ and $\boldsymbol{\Sigma}_{\boldsymbol{t}}^{(\boldsymbol{i},\boldsymbol{j})}$, Equation (5.55) is used to test the null hypothesis shown in Equation (5.51).

$$\mathrm{Z}^{(i,j)} = -2log(M) = v\left((N+1)\cdot \ln\left|\boldsymbol{\Sigma}_{pl}\right| - \sum_{d=1}^{N} \ln|\boldsymbol{\Sigma}_r^d| - \ln\left|\boldsymbol{\Sigma}_{\boldsymbol{t}}^{(\boldsymbol{i},\boldsymbol{j})}\right|\right), \tag{5.55}$$

where $\boldsymbol{\Sigma}_r^d$ represents the covariance matrices of the observed data for each of the random blocks of data, $\boldsymbol{\Sigma}_{\boldsymbol{t}}^{(\boldsymbol{i},\boldsymbol{j})}$ the covariance matrix calculated from the observed data in the moving window, $|.|$ represents the determinant, v the sample size for both the test and reference matrices, $\boldsymbol{\Sigma}_{pl}$ the pooled covariance matrix.

$\boldsymbol{Z}$ is the output surface of Equation (5.55) for all possible combinations of (i, j) in $\mathbf{X}$ of the moving window, such that

$$\boldsymbol{Z} = \begin{bmatrix} \mathrm{Z}^{(\mathbf{1},\mathbf{1})} & \cdots & \mathrm{Z}^{(\mathbf{1},\boldsymbol{C}-\mathrm{n}+1)} \\ \vdots & \ddots & \vdots \\ \mathrm{Z}^{(\boldsymbol{R}-\mathrm{n}+1,\mathbf{1})} & \cdots & \mathrm{Z}^{(\boldsymbol{R}-\mathrm{n}+1,\boldsymbol{C}-\mathrm{n}+1)} \end{bmatrix}, \tag{5.56}$$

where $\boldsymbol{Z} \in \boldsymbol{R}^{(R-n+1)\times(C-n+1)}$, as a result of using a moving window size of $n > 1$ across **X** in the form of Equation (5.18) to test a center location in $\boldsymbol{W}_t^{(\boldsymbol{i},\boldsymbol{j})}$ of size $n \times n$ pixels. It is important to note that $v = v_r^d = v_t$ in order to keep the sample size between the reference and test samples equal to each other.

Once **Z** is computed, local results (using samples from $n \times n$ spatial locations across **X**) that fall under H_0 are expected to follow the χ^2 distribution, which in turn allows to specify a cutoff threshold based on a desired probability of miss (α).

5.3.9.2 Performance Analysis This section reviews the performance of the RS-M algorithm for different number of N = 5, 10 and 15 blocks of data randomly collected from a test scene with no *a priori* information on the location of the manmade objects.

The results will be compared to the baseline M-Box algorithm proposed in Subsection 5.3.5 using ROC curves, output surfaces, and a 72-hour performance comparison for each of the manmade objects. The performance between the RS-M and the Stokes vector parameters and DoLP are not shown here since it was previously demonstrated, Subsection 5.3.6.2, that the proposed M-Box algorithm performed far better than the Stokes vector parameters or DoLP. Therefore, subsequent subsections in Chapter 5 will consider the M-Box algorithm as the baseline by which new algorithms will be compared to.

Figure 5.83 illustrates the probability of detection of T_0 for the standard timestamps (0710h, 0910h, 1310h, and 2010h) for 6 MAR 2010 for a P_{fa} range between 0.000 and 0.005 for the M-Box and RS-M. The full ROC curve is not shown because the RS-M and the baseline perform similarly to each other as the P_{fa} value increases. One can readily observe that both RS-5 and RS-10 perform poorly with respect to the baseline for all timestamps with the exception of timestamp 1310h. Interestingly, one can also observe that the performance of RS-5 was actually better than RS-10 for timestamps 0710h and 0910h. Such performance difference can be explained as follows, because one is collecting random samples from the test imagery and use them as reference points, the locations of the random samples and, therefore, their "quality" have a direct influence in how well the background is characterized. This ability to characterize the background well has a direct impact on the algorithm's ability in detecting manmade objects in the scene. It is important to note that in this frame work the term "quality" is used loosely to convene how valuable is the information collected by each sample relative to the remaining random samples. It is important to remind the reader that increasing the number of samples does not always imply a significant improvement in performance as demonstrated by RS-5 and RS-10 performances. At the same time, as demonstrated by RS-15, by increasing the number of random samples from 10 to 15 the probability of detection rate, using a reference $P_{fa} = 0.005$, for T_0 relative to the baseline was considerably better with a $P_d = 0.92$ compared to the baseline of $P_d = 0.75$ for 0710h. For timestamp 0710h, RS-15 exhibited higher probability of detection relative to the baseline for the entire ROC curve, shown in Figure 5.83, and with similar detection rate for 1310h ROC curves. The probability of detection of RS-15

was reduced slightly relative to the baseline for 0910h and 2010h with the RS-15 performing very well for extreme low false alarm rates, $(P_{fa} < 0.0005)$, while the baseline performed better for the remaining P_{fa} values. The average probability of detection for all timestamps for each metric in discriminating T_0 using a reference $P_{fa} = 0.005$ was $P_d = 0.88$ for RS-15 and the baseline, and RS-5 and RS-10 with a $P_d = 0.70$ and 0.66, respectively.

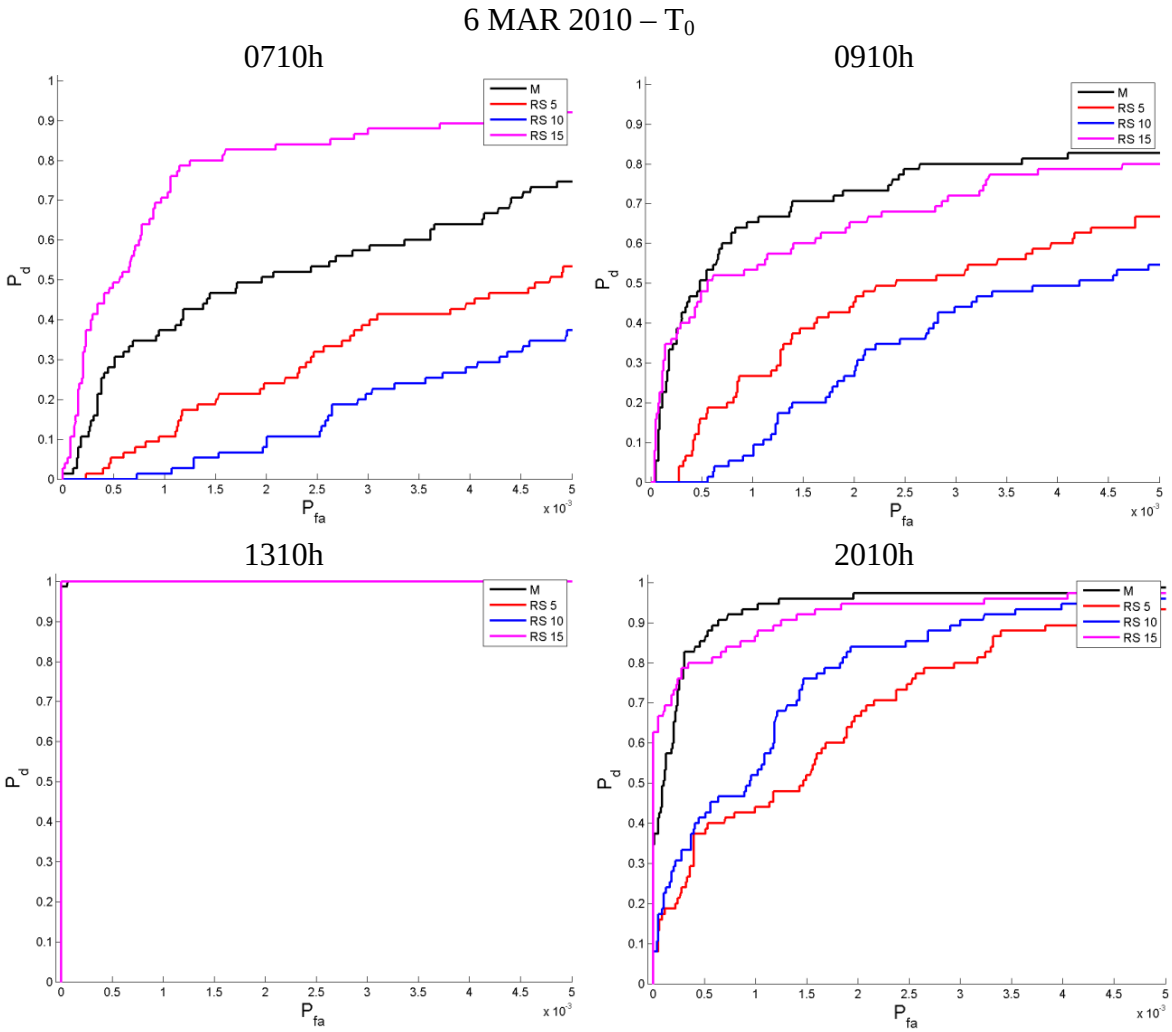

Figure 5.83 ROC curves for T_0 comparing the performance between the baseline and RS-M for different random sample locations. The P_{fa} axis of the ROC curves shown is limited to very small numbers 0.000 and 0.005. The average probability of detection for all timestamps for T_0 using a reference $P_{fa} = 0.005$ for all metrics was $P_d = 0.88$ for RS-15 and the baseline, and RS-5 and RS-10 with a $P_d = 0.70$ and 0.66, respectively.

Figure 5.84 shows the performance comparison in detecting T_{90}. One can observe that for 0710h RS-10 once again underperformed RS-5 for most of the ROC curve, while RS-15 exhibited a higher probability of detection relative to RS-5 and RS-10 for the full false alarm range. Interestingly, as shown in Figure 5.83, RS-15 outperforms the baseline for a $P_{fa} < 0.0005$, whereas for the remainder of the P_{fa} range, the baseline once again becomes the best performing metric with RS-15 catching up to the baseline P_d at around $P_{fa} = 0.005$. Conversely, all metrics had similar probability of detection for timestamps 0910h and 1310h with the exception of the baseline which performs slightly poorly for low false alarm rates $(P_{fa} < 0.0004)$ for timestamp 1310h. Timestamp 2010h demonstrates the same trend found in 0710h with the baseline having better probability of detection than RS-M for $P_{fa} > 0.00025$ while RS-10 and RS-15 exhibit a better detection rate for $P_{fa} < 0.00025$. Nonetheless, by $P_{fa} = 0.005$ the RS-M catches up to the baseline with a $P_d = 0.92, 0.94, \text{and } 0.92$ for RS-5, RS-10, and RS-15, respectively, compared to the baseline with a $P_d = 0.93$. Finally, the average probability of detection of all detectors for a $P_{fa} = 0.005$ and the four timestamps was relatively the same with a $P_d = 0.93$.

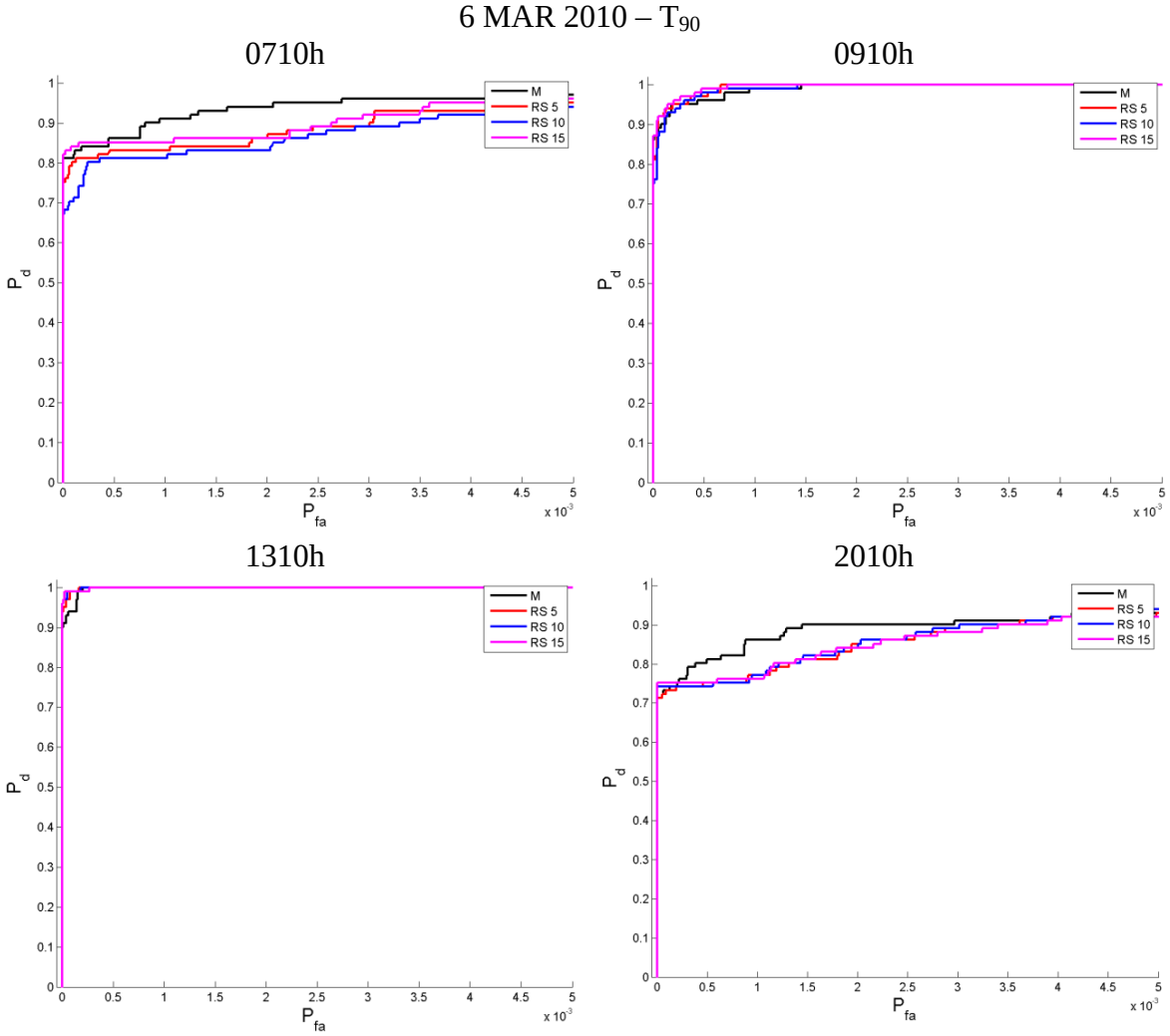

Figure 5.84 ROC curves for T_{90} comparing the performance between the baseline and RS-M for different random sample locations. The P_{fa} axis of the ROC curves shown is limited to very small numbers 0.000 and 0.005. The average probability of detection of all detectors for the four timestamps was relatively the same with a $P_d = 0.93$ for a $P_{fa} = 0.005$.

Figure 5.85 illustrates the probability of detecting T_{135} for the M-Box and RS-M. As seen in the previous figure, once again RS-10 trails all the other metrics for 0710h and 0910h while demonstrating similarly P_d rate for the remaining timestamps. RS-5 exhibits better probability of detection over the P_{fa} range relative to RS-10 for the first two timestamps and similarly to it for timestamp 2010h. RS-15 once again exhibits better probability of detection relative to the baseline for very small $P_{fa} < 0.0004$ which is

highly desirable, while for higher P_{fa} values, the M-Box algorithm performs better as shown in timestamps 0710h and 2010h. Finally, for the remainder two timestamps the baseline performs very similarly to RS-15. RS-10 once again demonstrates a lesser detection rate than RS-5, RS-15, and the baseline for the low false alarm rate, $P_{fa} < 0.001$, but it quickly catches up to the other algorithms as the P_{fa} increases close to 0.005.

As such for a $P_{fa} = 0.005$, both the RS-M and the baseline have similar detection rate, for example, for 0710h RS-15 and the baseline have a detection rate of $P_d = 0.80$ and $P_d = 0.81$, respectively. For timestamp 0910h, RS-5, RS-10, RS-15, and the baseline have similar probability of detection, $P_d = 0.94, 0.94, 0.95, \text{and } 0.93$, and for timestamp 1310h a $P_d = 1.00$ was measured for all metrics. Finally, for timestamp 2010h, a probability of detection of $P_d = 0.74, 0.70, 0.71, \text{and } 0.72$ can be found for the baseline, RS-5, RS-10, and RS-15, respectively. The average probability of detection for the four timestamps using a reference $P_{fa} = 0.005$ was $P_d = 0.79, 0.74, 0.73, \text{and } 0.78$ for the baseline, RS-5, RS-10, and RS-15, respectively.

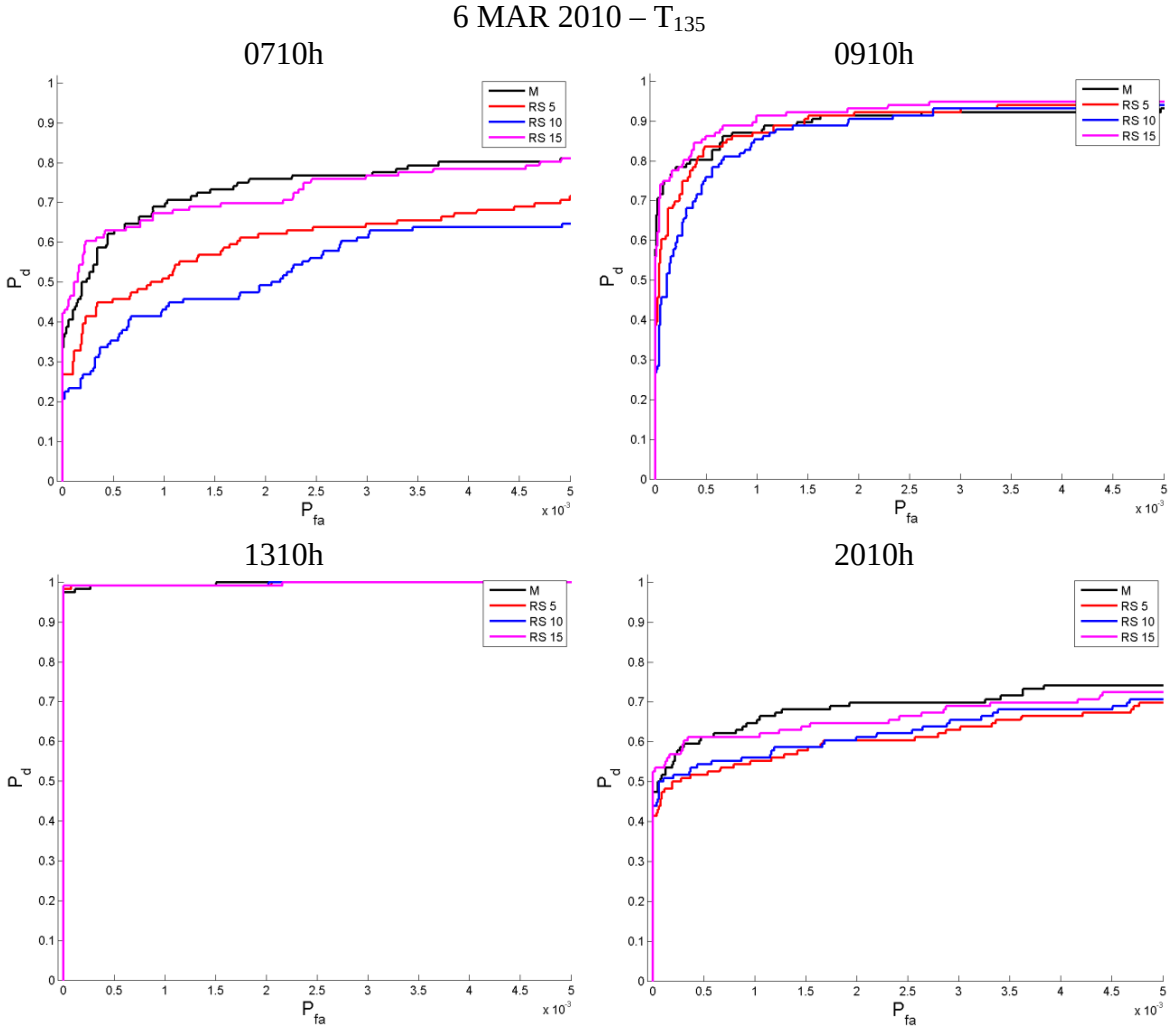

Figure 5.85 ROC curves for T_{135} comparing the performance between the baseline and RS-M for different random sample locations. The P_{fa} axis of the ROC curves shown is limited to very small numbers 0.000 and 0.005. The average probability of detection for the four timestamps using a reference $P_{fa} = 0.005$ was $P_d = 0.79, 0.74, 0.73,$ and 0.78 for the baseline, RS-5, RS-10, and RS-15, respectively.

Unlike what has been demonstrated in the previous ROC curves, the baseline revealed to be quite effective in discriminating the blackbody from natural clutter at low false alarm rates relative to the other metrics as shown in Figure 5.86. This trend is illustrated in all timestamps where the baseline performs very similarly to RS-M, regardless of the number of samples, within the very low false alarm rate of $P_{fa} < 0.0002$. For $0.0002 \leq P_{fa} \leq 0.005$ the baseline performs better than the RS-M for

0710h, 0910h, and 2010h, and as the false alarm rate approaches $P_{fa} = 0.005$, all metrics have a similar P_d. The divergences between the M-Box and RS-M are shown to be in timestamps 0710h, 0910h, and 2010h, while for high contrast scenes (1310h), all metrics perform very similarly regardless of P_{fa}. The average probability of detection for all timestamps given a $P_{fa} = 0.005$ were measured as follows; the baseline had the best performance with a $P_d = 0.99$, followed by RS-5 and 15 with a $P_d = 0.98$, and finally RS-10 with a $P_d = 0.96$.

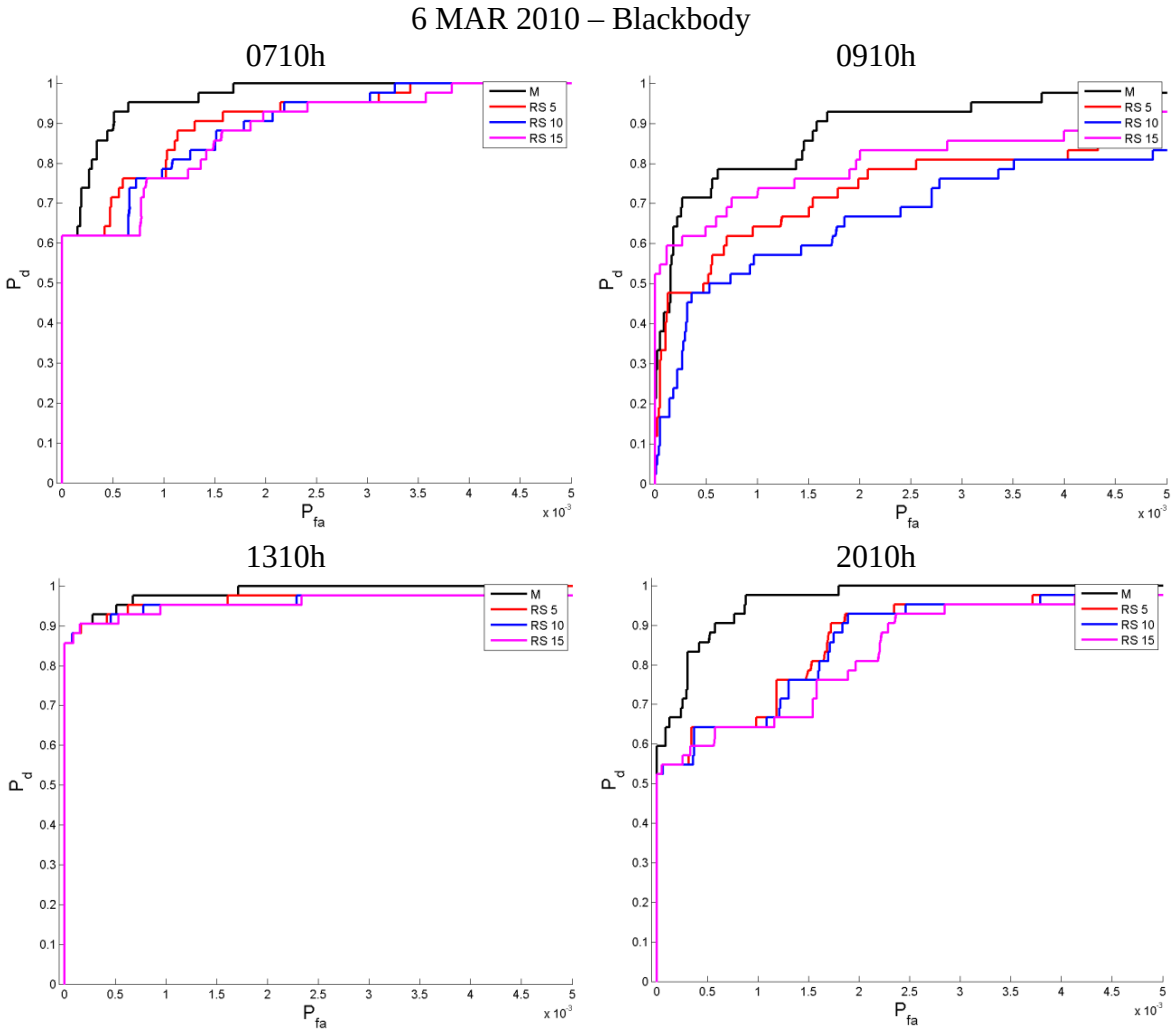

Figure 5.86 ROC curves for the external blackbody comparing the performance between the baseline and RS-M for different random sample locations. The P_{fa} axis of the ROC curves shown is limited to very small numbers 0.000 and 0.005. The average probability of detection for all timestamps given a $P_{fa} = 0.005$ were measured as follows; the baseline had the best performance with a $P_d = 0.99$, followed by RS-5 and 15 with a $P_d = 0.98$, and finally RS-10 with a $P_d = 0.96$.

As demonstrated in Subsection 5.3.6.2, the M-Box algorithm performed extremely poorly in discriminating the observation tower from natural clutter. Figure 5.87 once more validates those results by zooming in further than previously shown in Subsection 5.3.6.2. As expected, from the limited results shown in Subsection 5.3.8.3, the RS-M algorithm performs extremely well in discriminating the observation tower

from natural clutter. In Figure 5.87 one observes that RS-15 clearly exhibits a better detection rate than all other metrics at extremely low false alarm rates for all timestamps with RS-5 performing as the second best metric for timestamps 1310h and 2010h and RS-10 for 0710h and 0910h. Once again, the M-Box probability of detection is less than 0.30 for a $P_{fa} = 0.005$. The average probability of detection for all timestamps using a reference $P_{fa} = 0.005$ for the observation tower was $P_d = 0.95$ for RS-15, followed by RS-5, RS-10, and the baseline with a $P_d = 0.73, 0.68, \text{and } 0.21$, respectively.

Figure 5.88 illustrates the overall performance as if all manmade objects were combined into a single class. Overall, for a $P_{fa} = 0.001$, one concludes that the RS-15 performed very well in discriminating all the manmade objects in the scene with a $P_d = 0.77, 0.83, 0.99, \text{and } 0.73$ for 0710h, 0910h, 1310h, and 2010h, respectively. The M-Box was measured as the second best performing metric with a $P_d = 0.77, 0.76, 0.89, \text{and } 0.73$, followed by RS-5 with a $P_d = 0.55, 0.67, 0.97, \text{and } 0.60$, and finally RS-10 with a $P_d = 0.46, 0.61, 0.99, \text{and } 0.63$. Interestingly, the ranking changes dramatically if one changes the reference to be $P_{fa} = 0.005$. For example, for a $P_{fa} = 0.005$, RS-15 still remains the best performing metric with a $P_d = 0.91, 0.94, 1.00, \text{and } 0.87$, followed by RS-5 with a $P_d = 0.77, 0.83, 0.99, \text{and } 0.73$, then RS-10 with a, $P_d = 0.73, 0.79, 1.00, \text{and } 0.86$, and finally the M-Box algorithm with a $P_d = 0.71, 0.87, 0.94, \text{and } 0.82$. In conclusion, depending of the P_{fa} chosen, the 2nd, 3rd, and 4th ranking changes while RS-15 still remains the best performing metric for the chosen timestamps.

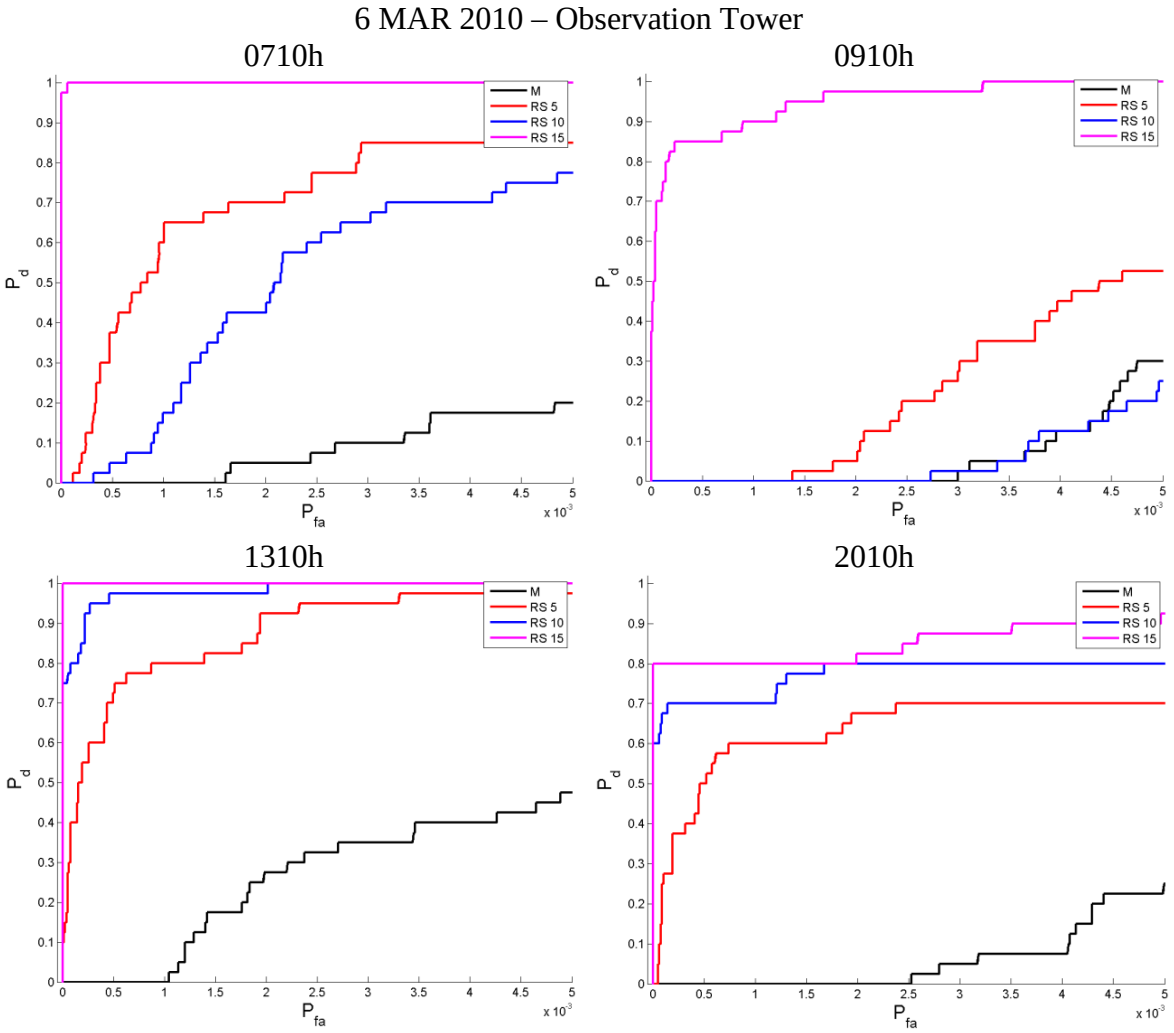

Figure 5.87 ROC curves for the observation tower comparing the performance between the baseline and RS-M for different random sample locations. The P_{fa} axis of the ROC curves shown is limited to very small numbers 0.000 and 0.005. The average probability of detection for all timestamps for the observation tower was $P_d = 0.95$ for RS-15, followed by RS-5, RS-10, and the baseline with a $P_d = 0.73, 0.68, \text{and } 0.21$, respectively.

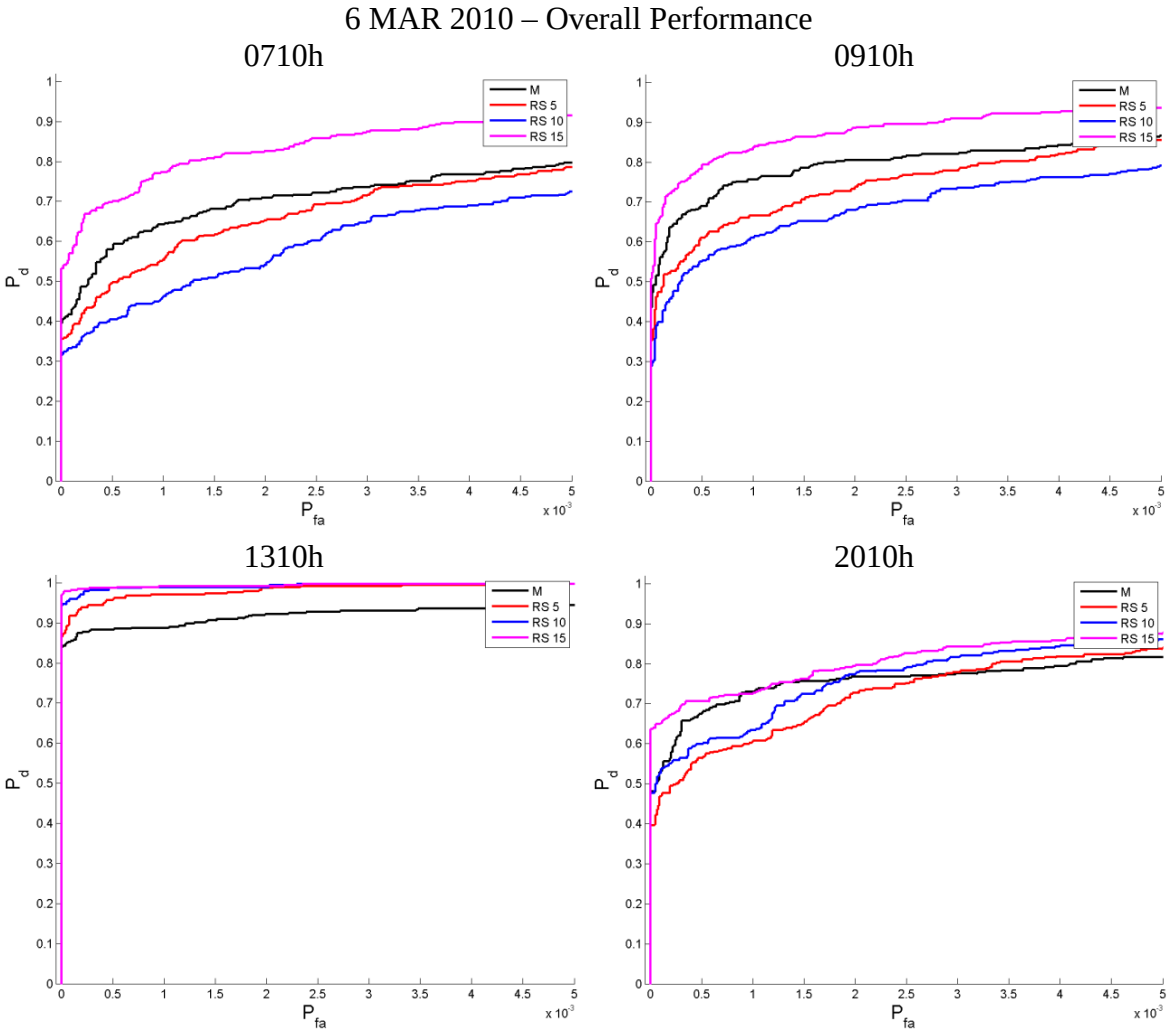

Figure 5.88 ROC curves for all manmade objects in the scene comparing the performance between the baseline and RS-M for different random sample locations. The P_{fa} axis of the ROC curves shown is limited to very small numbers 0.000 and 0.005. For a $P_{fa} = 0.005$ RS-15 is the best performing metric with a $P_d = 0.91, 0.94, 1.00,$ and $0.87,$ followed by RS-5 with a $P_d = 0.77, 0.83, 0.99,$ and $0.73,$ then RS-10 with a, $P_d = 0.73, 0.79, , 1.00,$ and $0.86,$ and finally the M-Box algorithm with a $P_d = 0.71, 0.87, 0.94,$ and $0.82.$

Table 5.7 illustrates a performance comparison between the M-Box algorithm proposed in Subsection 5.3.6.1 and RS-M for N = 5, 10, and 15 random samples for a $P_{fa} = 0.005$. The color scheme used for Table 5.7 represents the following: 1) Red – the algorithm(s) with the best probability of detection $(P_{d\,best})$ for a specific timestamp; 2) Green – represents any algorithm where the difference in probability of detection from

the highest $P_{d\ best}$ is less than 0.03 per object for a given timestamp; 3) black – algorithms that performed outside the previous two parameters.

For T_0, RS-15 performed the best by exhibiting both the best P_d (red) or similarly to $P_{d\ best} \leq 0.03$ five out of the six timestamps, while the M-Box algorithm performed better or similarly four out of the six timestamps. On T_{90}, all metrics performed similarly to each other, within the 0.03 P_d difference tolerance, with M-Box algorithm achieving the best probability of detection for all timestamps, except for 2010h where RS-10 demonstrated a better P_d value than all other metrics by a 0.02 difference. For the T_{135}, the M-Box algorithm once again performed very well with six out six timestamps with either the best or similar detection rate, followed by the RS-15 with five out the six timestamps, and finally RS-5 and 10 with four out of the six timestamps, respectively. The M-Box algorithm once again had the best probability of detection for the blackbody for all six timestamps, followed by RS-5, 10, 15 with five out of the six timestamps. However, the proposed RS-M algorithm has a clear advantage over the M-Box algorithm in detecting the observation tower. For this manmade object, RS-15 was able to outperform all of the other algorithms by a significant margin regardless of timestamp. Overall, the RS-15 had the best detection rate for all timestamps than the M-Box detector, RS-15, and RS-10. However, it is important to emphasize the differences between the RS-M and the baseline is because the RS-M algorithm was able to detect the observation tower with a very high probability of detection, which the M-Box could not. Therefore, it more than compensated for any P_d degradation the RS-M had for any of the other manmade objects in the scene.

Table 5.7 Performance Comparison Between M-Box and RS-M for Different Timestamps for a $P_{fa} = 0.005$

	T_0				T_{90}				T_{135}			
	M	**RS-5**	**RS-10**	**RS-15**	**M**	**RS-5**	**RS-10**	**RS-15**	**M**	**RS-5**	**RS-10**	**RS-15**
0210h	**0.87**	0.48	0.31	0.65	**0.87**	**0.85**	**0.84**	**0.85**	**0.56**	0.47	0.42	0.50
0710h	0.75	0.53	0.37	**0.92**	**0.97**	**0.95**	**0.94**	**0.96**	**0.81**	0.72	0.65	**0.81**
0910h	**0.83**	0.67	0.55	**0.80**	**1.00**	**1.00**	**1.00**	**1.00**	**0.93**	**0.94**	**0.94**	**0.95**
1310h	**1.00**	**1.00**	**1.00**	**1.00**	**1.00**	**1.00**	**1.00**	**1.00**	**1.00**	**1.00**	**1.00**	**1.00**
2010h	**0.97**	0.88	0.91	**0.96**	**0.93**	**0.94**	**0.95**	**0.93**	**0.74**	0.66	0.67	0.70
2310h	0.79	0.60	0.77	**0.96**	**0.89**	**0.86**	**0.88**	**0.87**	**0.69**	0.62	0.65	**0.70**

Table 5.7 Performance Comparison Between M-Box and RS-M for Different Timestamps for a $P_{fa} = 0.005$ (Continuation)

	Blackbody				**Observation tower**				**Overall**			
	M	**RS-5**	**RS-10**	**RS-15**	**M**	**RS-5**	**RS-10**	**RS-15**	**M**	**RS-5**	**RS-10**	**RS-15**
0210h	**1.00**	**1.00**	**1.00**	**1.00**	0.05	0.68	0.53	**0.80**	0.55	0.65	0.59	**0.71**
0710h	**1.00**	**1.00**	**1.00**	**1.00**	0.20	0.85	0.78	**1.00**	0.71	0.79	0.73	**0.91**
0910h	**0.98**	0.93	0.83	0.93	0.30	0.53	0.25	**1.00**	0.87	0.86	0.79	**0.94**
1310h	**1.00**	**1.00**	**0.98**	**0.98**	0.48	**0.98**	**1.00**	**1.00**	0.94	**1.00**	**1.00**	**1.00**
2010h	**1.00**	**0.98**	**0.98**	**0.98**	0.40	0.70	0.80	**0.93**	0.83	0.82	**0.84**	**0.87**
2310h	**1.00**	**1.00**	**1.00**	**1.00**	0.00	0.65	0.70	**0.95**	0.69	0.73	0.78	**0.86**

Figure 5.89 illustrates the 72-hour performance for 6-8 MAR 2010 between the baseline (M-Box algorithm) and RS-M for different number of random blocks of samples collected from the test scene for a $P_{fa} = 0.005$. Examining the RS-M performance for

RS-M for different N, one can readily observe that overall, RS-15 demonstrated comparable probability of detection to RS-5 and RS-10 for the 72-hour period excluding the periods of adverse weather, where RS-15 performance was very similar to RS-10 during the high humidity period in the last few hours of day 3 or better for the remaining periods. The baseline performed remarkably well for most of the 72 hours matching the RS-15 probability of detection with some differences worth mentioning. For example, during the beginning hours of day 1, the M-Box algorithm actually performed reasonable well compared to RS-M while during the last hours of day 3, the baseline performed very poorly relative to RS-10 and RS-15 but exhibiting better detection rate than RS-5. During the high contrast periods, all metrics performed similarly to each other. The best average probability of detection over the 72-hour period was RS-15 and the baseline with a $P_d = 0.92$, followed by RS-10 ($P_d = 0.89$), and finally RS-5 ($P_d = 0.86$).

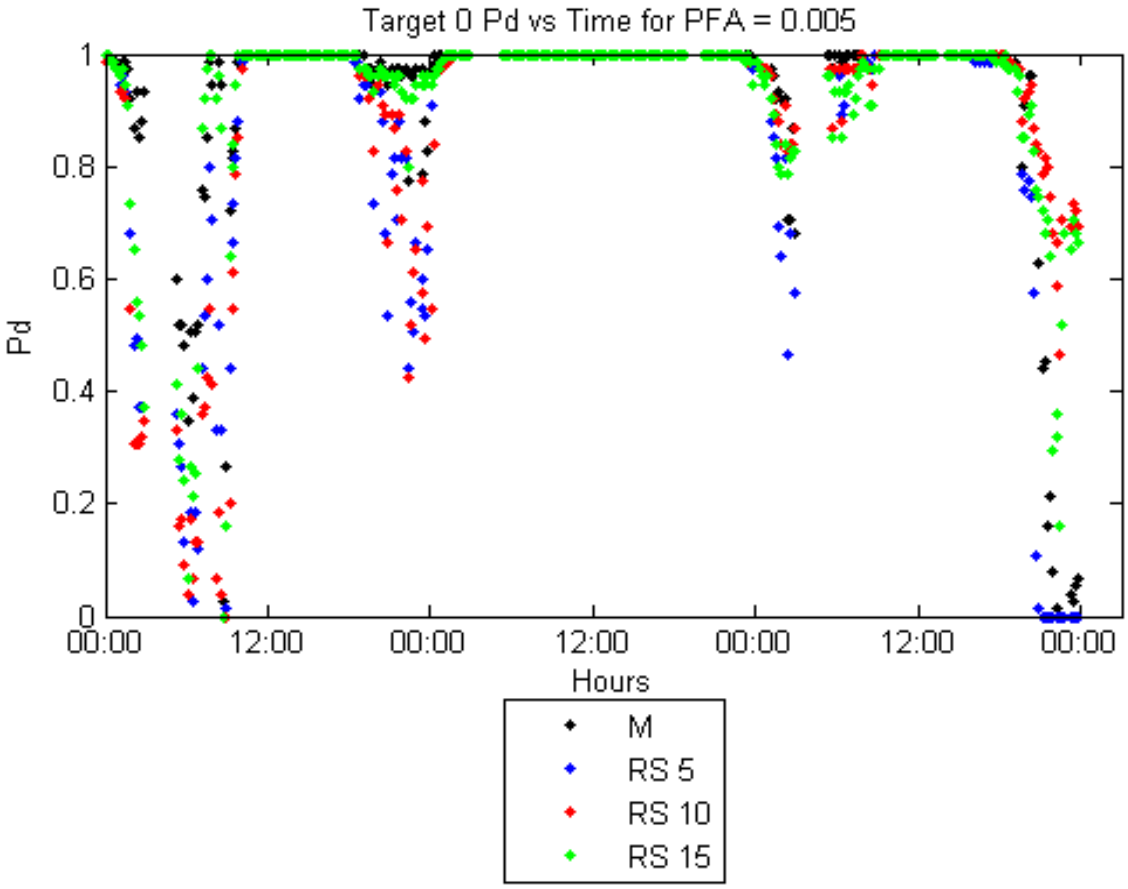

Figure 5.89 72-hour performance comparison between RS-M and M algorithm in discriminating T_0 from natural clutter. The best average performing metric over the 72-hour period was RS-15 and the baseline with a $P_d = 0.92$, followed by RS-10 ($P_d = 0.89$), and finally RS-5 ($P_d = 0.86$).

Figure 5.90 illustrates the 72-hour probability of detection of T_{90} for the baseline and the different RS-M. The RS-M, regardless of number of samples collected, performed comparably well to the baseline for most of the 72-hour period of performance with the exception for the periods of high humidity found in day 2 and 3. In the first adverse weather period, RS-10 and RS-15 exhibited degraded performance relative to the baseline and RS-5, while for the second period, RS-5 performed very poorly compared to the remaining metrics. During the periods of high contrast all metrics performed

similarly to each other, while during the periods of low contrast RS-M performed slightly worse than the baseline.

Regardless of the performance differences, on average, all metrics performed very similarly to each other, with the best average performing metric as the M-Box algorithm with a $P_d = 0.93$, followed by RS-10 and RS-15 with a $P_d = 0.91$, and finally RS-5 with a $P_d = 0.90$.

For the detection of T_{135}, Figure 5.91, the baseline demonstrated better probability of detection than RS-M for the 72 hours where one can find a maximum P_d divergence of 0.10 during the early hours of 6 MAR 2010. During the time periods where the target is solar loaded or high humidity is present, both RS-5 and RS-10 display similar probability of detection as the baseline. It is interestingly to notice that during the periods of high contrast scenarios all metrics performed quite similarly, while during the periods of low contrast scenarios the baseline performs better than RS-M. For the period of high humidity in day 2, all metrics performed very poorly in discriminating T_{135} from natural clutter with no or very low detection probability, while for the next high humidity period found at the end of day 3, all metrics, with the exception of RS-5, had similarly probability of detection. The best performing metric in discriminating T_{135} over the 72-hour period was once again the M-Box algorithm with an average detection rate of $P_d = 0.79$, followed by RS-15 ($P_d = 0.75$), and RS-5 and RS-10 with a $P_d = 0.73$.

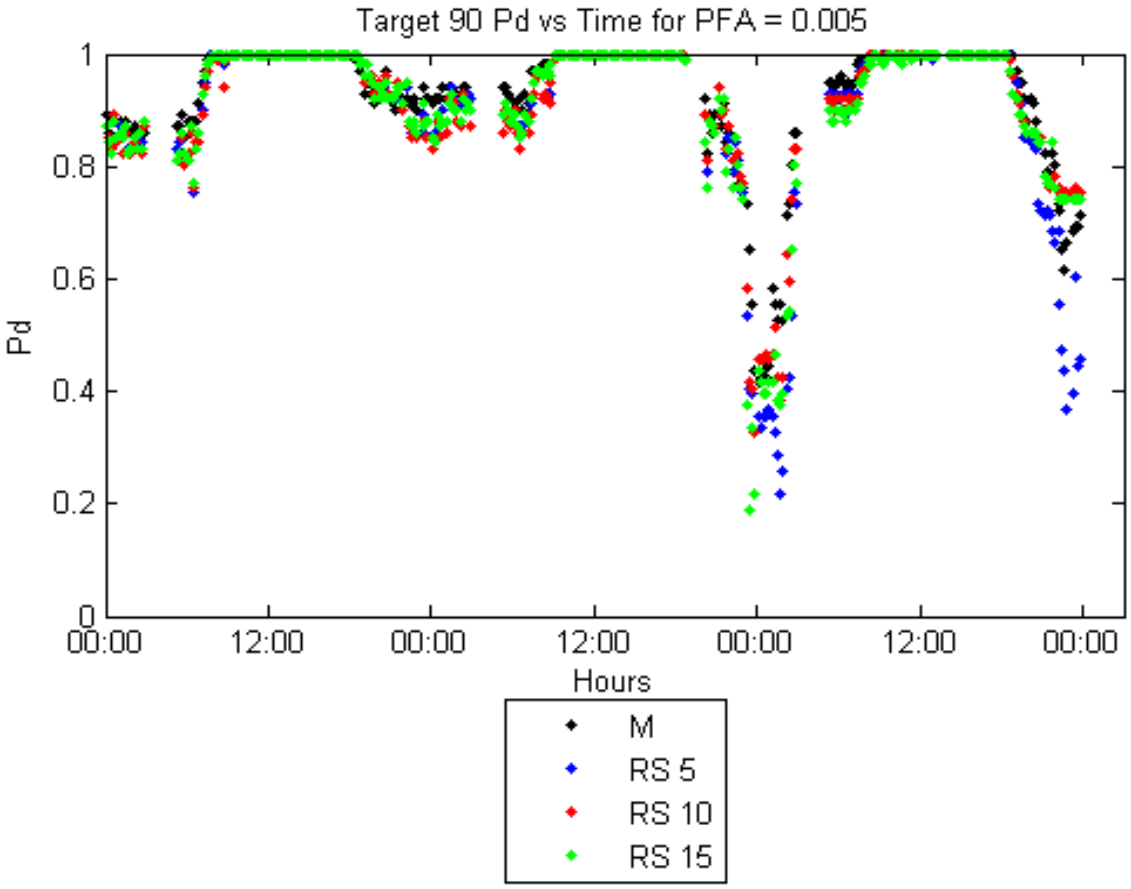

Figure 5.90 72-hour performance comparison between RS-M and M algorithm in discriminating T_{90} from natural clutter. The best average performing metric for T_{90} was the M-Box algorithm with a $P_d = 0.93$, followed by RS-10 and RS-15 with a $P_d = 0.91$, and finally RS-5 with a $P_d = 0.90$.

Figure 5.92 illustrates the probability of detection comparison between the baseline and the different RS-M for the blackbody. In this figure, RS-15 demonstrated similar probability of detection relative to the baseline and at the same time outperforming both RS-5 and RS-10 for most of the timestamps. During the periods where high humidity was present, RS-15 demonstrated a very slight decrease in the detection rate compared to the baseline. Conversely, RS-5 performed similarly to the baseline and RS-10 throughout the 72-hour period with the exception of the last hours in

day 3 where RS-5 performed slightly worse than the baseline, RS-10, and RS-15. The baseline performed better than the remaining metrics during this same period. Furthermore, observing the period of high humidity at the beginning of day 3, one observes that the baseline performs better in detecting the blackbody compared to the RS-M with a probability of detection difference of about 0.20 at certain times. Therefore, it is with no surprise that in detecting the blackbody the M-Box algorithm demonstrated the best a 72-hour average probability of detection with a $P_d = 0.96$, followed by RS-10 ($P_d = 0.89$), RS-15 ($P_d = 0.88$), and RS-5 ($P_d = 0.87$).

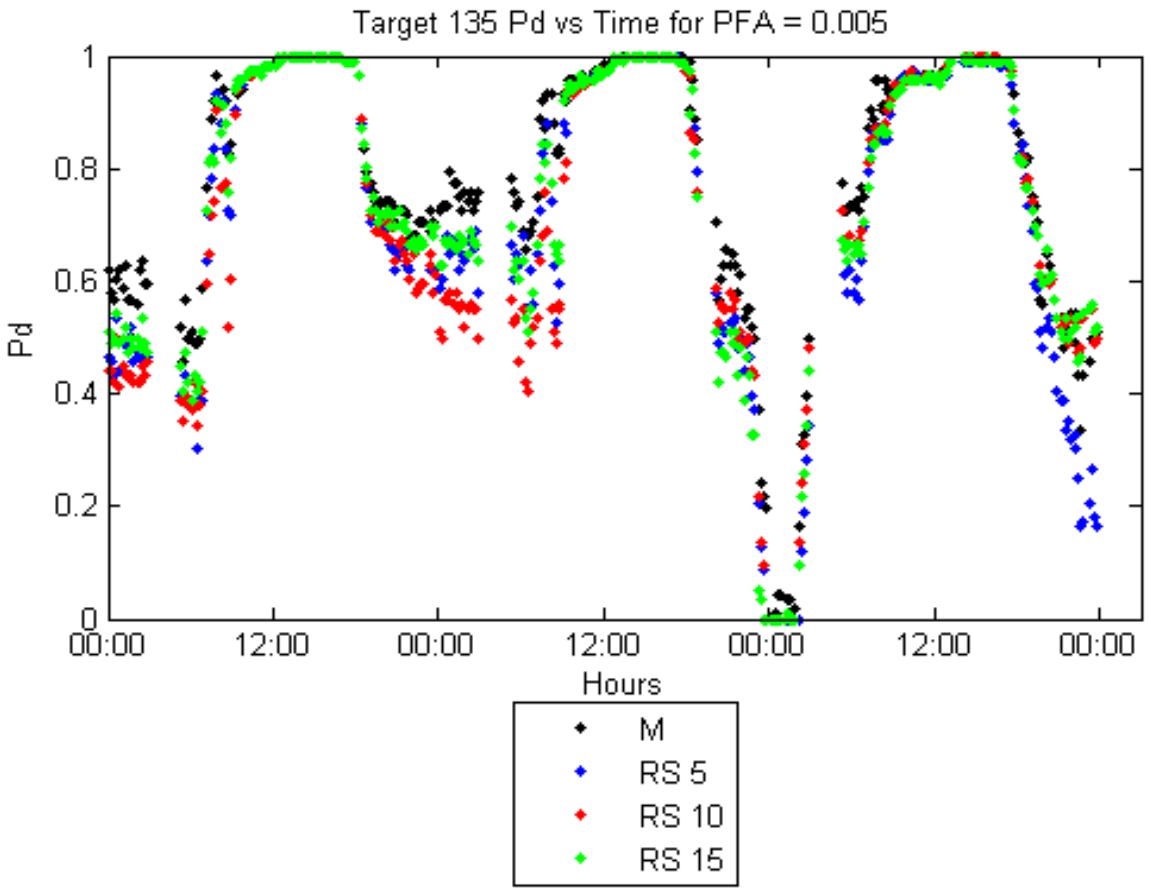

Figure 5.91 72-hour performance comparison between RS-M and M algorithm in discriminating T_{135} from natural clutter. For T_{135} target set the best performing metric was the M-Box algorithm with an average detection rate of $P_d = 0.79$, followed by RS-15 ($P_d = 0.75$), and RS-5 and RS-10 with a $P_d = 0.73$.

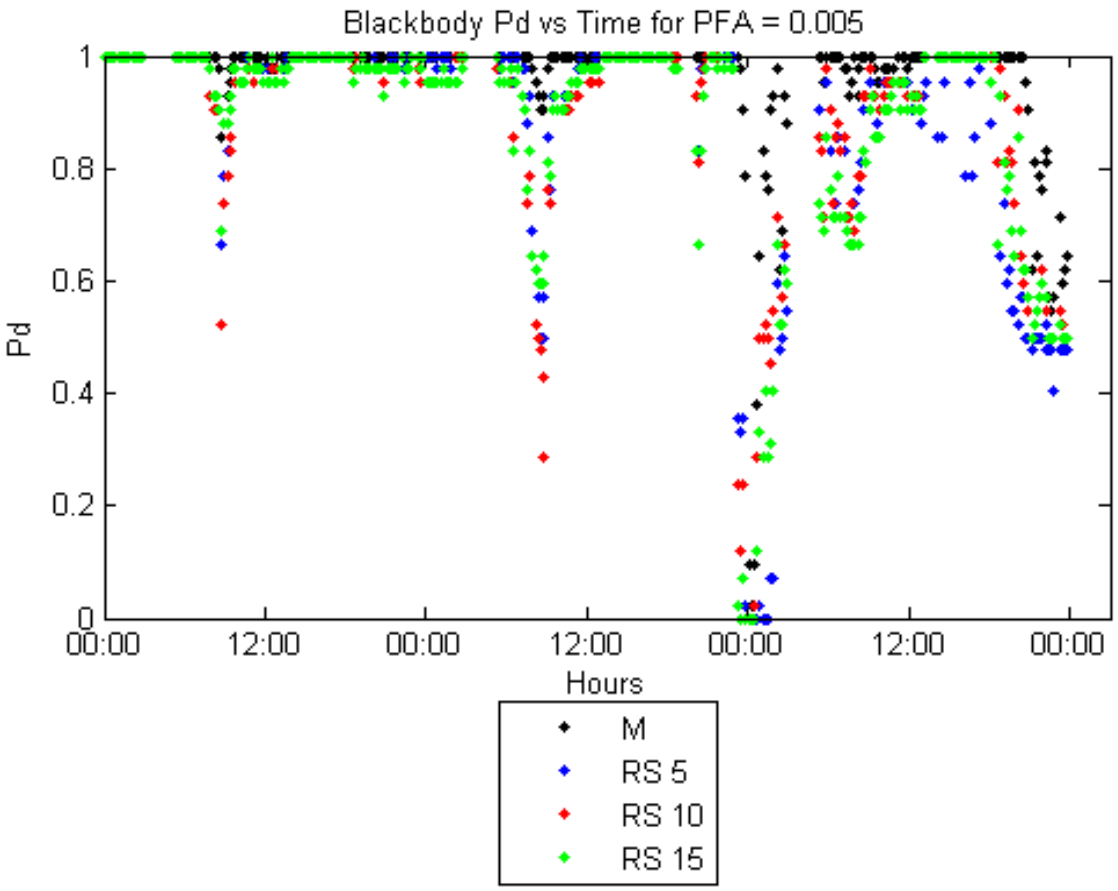

Figure 5.92 72-hour performance comparison between RS-M and M algorithm in discriminating the blackbody from natural clutter. For the blackbody target set, the M-Box algorithm clearly outperforms all other metrics with a $P_d = 0.96$, followed by RS-10 ($P_d = 0.89$), RS-15 ($P_d = 0.88$), and RS-5 ($P_d = 0.87$).

As shown in previous ROC curves for the observation tower, Figure 5.87, the RS-M performed very well over the entire 72-hour performance period, Figure 5.93, with the baseline demonstrating some relatively good detection rates during the periods of high contrast only. One also observes that both RS-5 and RS-10 exhibit higher variability in the probability of detection throughout the 3 days, especially during the periods of adverse weather found in day 2 and 3. In contrast, the probability of detection of RS-15 was far more stable throughout the 72-hour relative to the other metrics as a result of

better background characterization. For Figure 5.93 the metric with the best average probability of detection over the 72-hours was RS-15 ($P_d = 0.90$), followed by RS-5 and RS-10 ($P_d = 0.80$), and finally M-Box ($P_d = 0.36$).

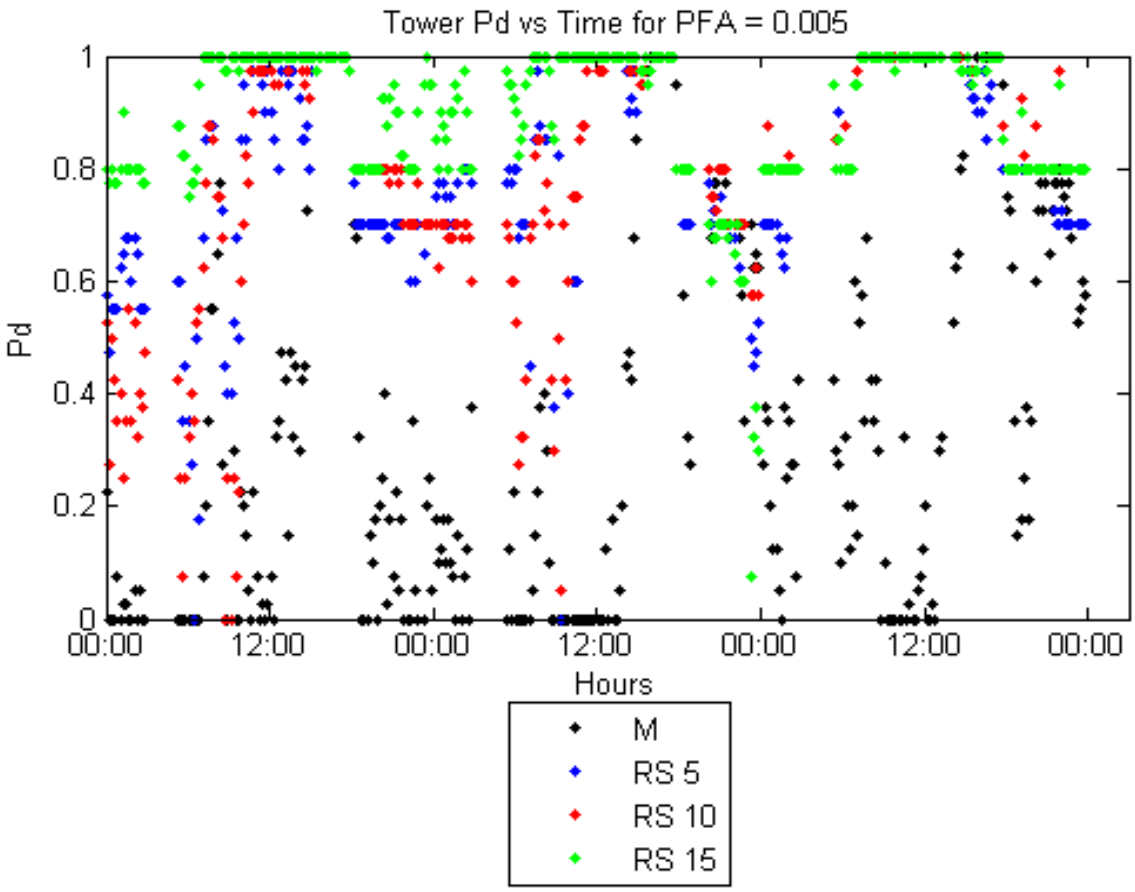

Figure 5.93 72-hour performance comparison between RS-M and M algorithm in discriminating the observation tower from natural clutter. The best average probability of detection for the 72-hours was achieved by RS-15 ($P_d = 0.90$), followed by RS-5 and RS-10 ($P_d = 0.80$), and finally M-Box ($P_d = 0.36$).

Finally, Figure 5.94 represents the overall probability of detection for the 72-hour period of performance when all manmade objects are placed into a single class. From Figure 5.94 one observes that the RS-M had similar or better detection rate than the baseline during the late morning hours of each day, while during the periods of high

humidity both RS-10 and RS-15 exhibited better probability of detection compared to the baseline. On average, the probability of detection for the 72-hour period was measured as follows: RS-15 was the best performing metric with an average detection rate of $P_d = 0.86$, followed by RS-10 ($P_d = 0.84$), RS-5 ($P_d = 0.82$), and finally M-Box ($P_d = 0.81$).

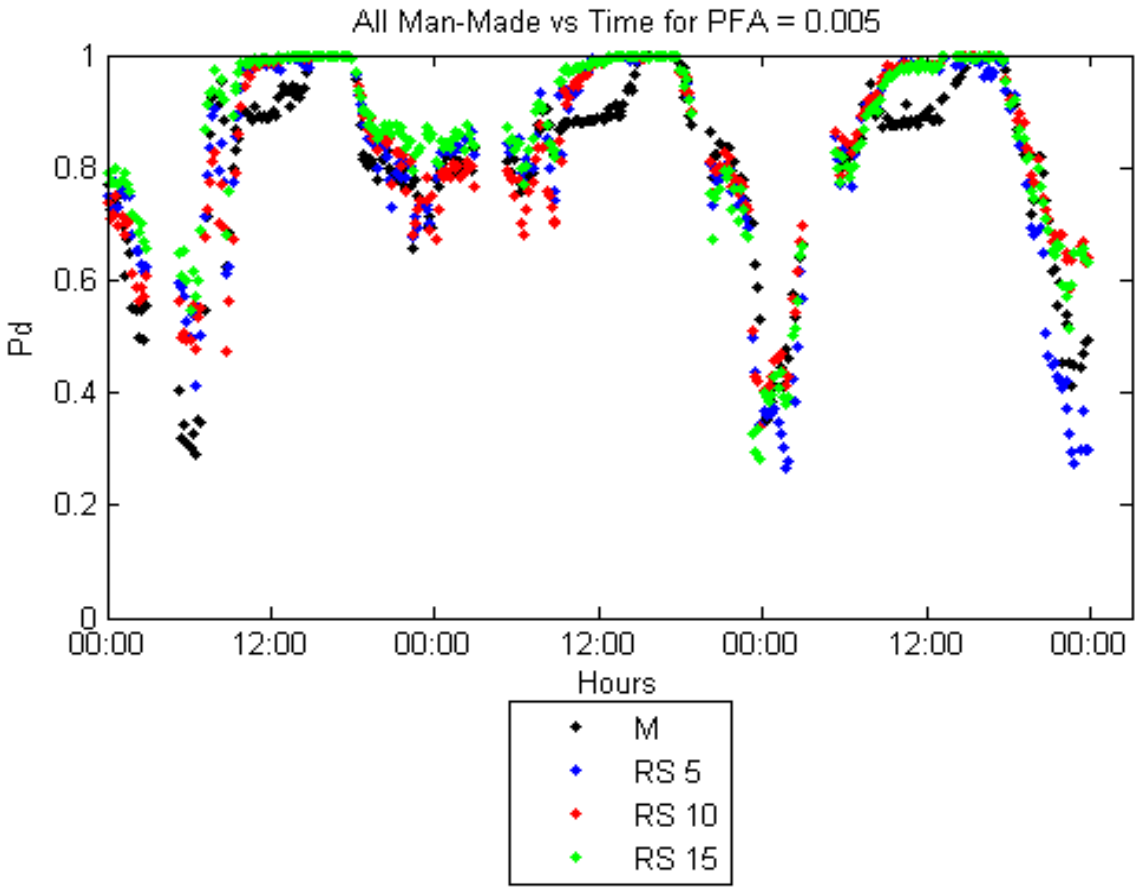

Figure 5.94 72-hour performance comparison between RS-M and M algorithm for all manmade objects in the scene. The average probability of detection for the 72-hour period was measured as follows: RS-15 was the best performing metric with an average detection rate of $P_d = 0.86$, followed by RS-10 ($P_d = 0.84$), RS-5 ($P_d = 0.82$), and finally M-Box ($P_d = 0.81$).

The above Figures 5.89 through 5.94 demonstrated some key points worth emphasizing:

1) The RS-M demonstrated a tremendous capability in discriminating the observation tower from natural clutter relative to the baseline.

2) For the chosen $P_{fa} = 0.005$ the RS-15 demonstrated similar 72-hour average probability of detection compared to the baseline for most manmade objects with some few exceptions:

    a. The baseline exhibited better detection rate than RS-15 for the external blackbody.

    b. The RS-M demonstrated better detection rate than the baseline for the observation tower.

3) RS-M using $N = 15$ had the best 72-hour average probability of detection compared to RS-M using $N = 5$ or 10.

4) There was very little difference in the 72-hour average probability of detection between RS-5 and RS-10.

Figure 5.95 presents the broadband images on the left (for visual appreciation) and the output surfaces for the baseline, RS-5, RS-10, and RS-15 for timestamps 0210h, 0710h, 0910h, 1310h, 2010h, and 2310h on 6 MAR 2010. These output surfaces are normalized for visual appreciation and ease of comparison.

Right away one observes that all metrics are capable of discriminating most of the manmade objects successfully, with the exception of the baseline which cannot discriminate the observation tower.

The number of false alarm regions shown in the M-Box algorithm is higher than the ones found in the RS-M. In fact, as the number of N increases, the width and number of false alarms tend to decrease significantly.

In conclusion, Figure 5.95 demonstrates that as N increases from five to 15 random samples, the output surfaces of the RS-M algorithm seem to be more visually appealing to an operator than the one provided by the baseline.

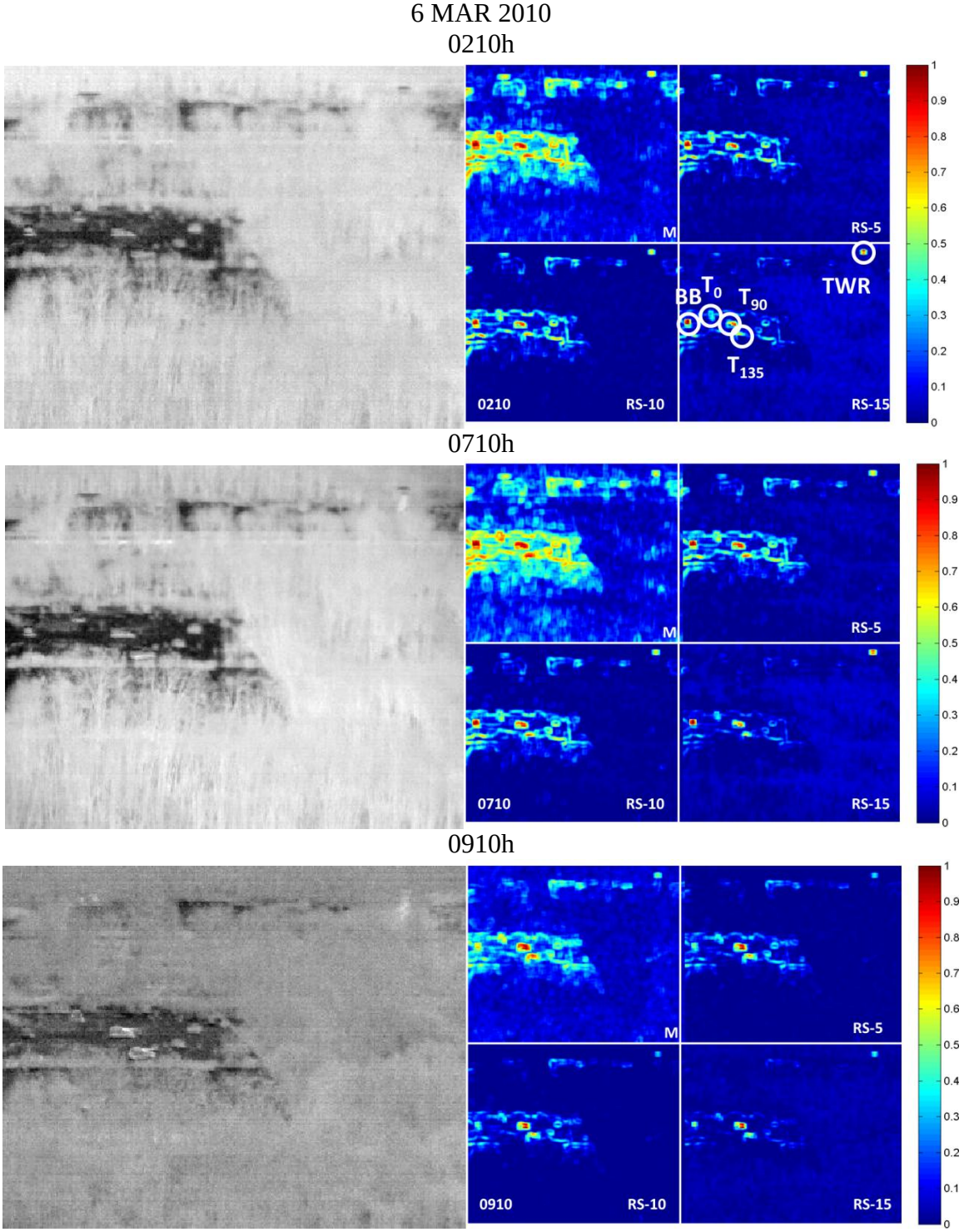

Figure 5.95 Output surfaces for M-Box and RS-M algorithm for N = 5, 10, and 15 random samples.

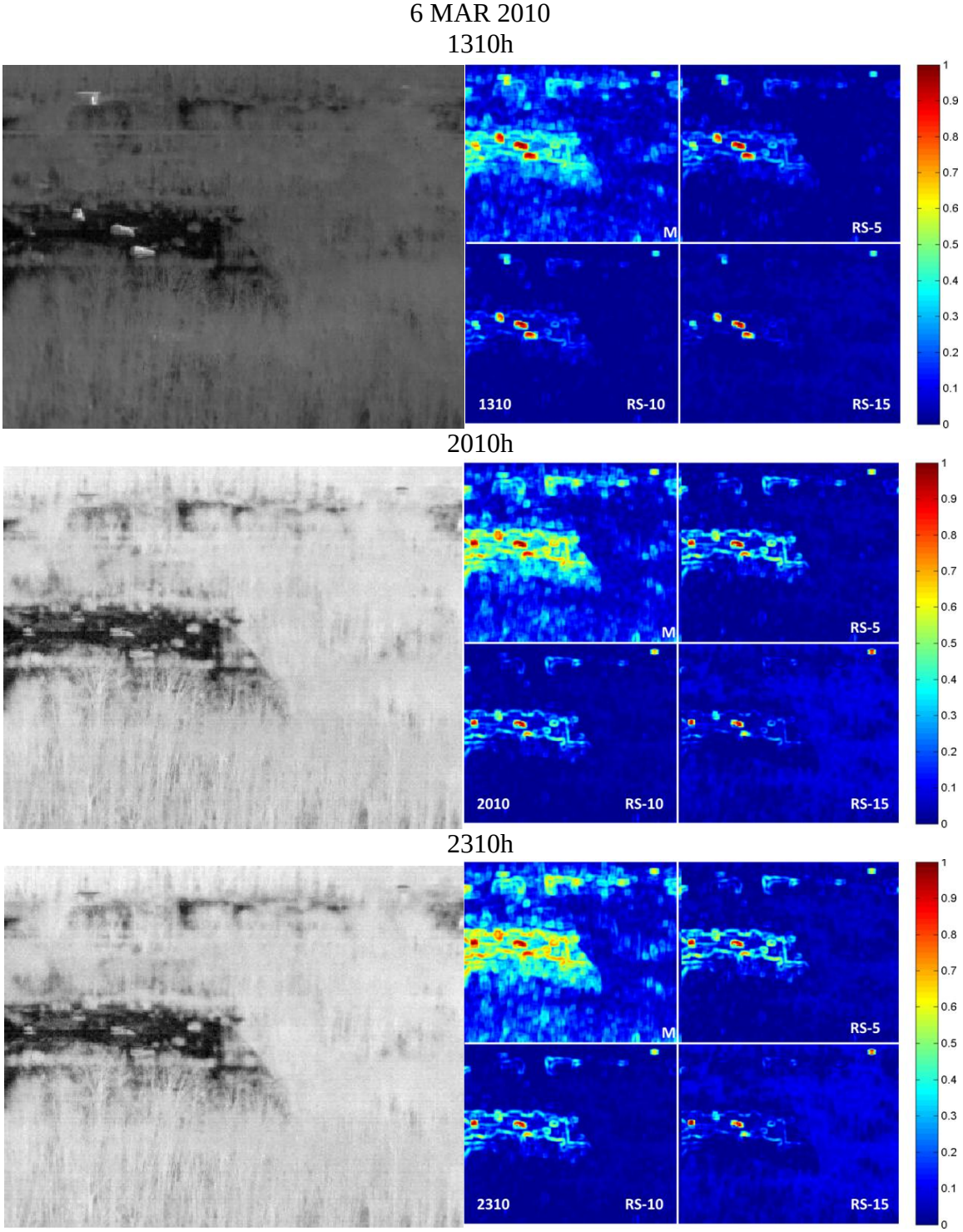

Figure 5.95 Output surfaces for M-Box and RS-M algorithm for N = 5, 10, and 15 random samples.(Continuation)

In this subsection the performance of the RS-M was presented and compared to the baseline, M-Box. The following key points can be summarized from this subsection as follows:

1) The ROC curves demonstrated that the baseline performed better than the RS-M for very low false alarm rates $P_{fa} < 0.005$, however by $P_{fa} = 0.005$ both the RS-M and the baseline demonstrated similar performances.

2) The RS-M was capable of detecting the observation tower better than the baseline for the ROC curves and the 72-hour performance period.

3) The ROC curves demonstrated that, in general, the RS-5 displayed better detection rate than RS-10 at low false alarm rates, and as the false alarm rate reached 0.005 both RS-5 and RS-10 performed very similarly. Consequently, one could find little difference in the 72-hour average probability of detection between RS-5 and RS-10. One can conclude that for the low false alarm rate region, the locations or "quality" of samples collected from the scene directly influenced the algorithm's ability to discriminate the manmade objects.

4) For the chosen $P_{fa} = 0.005$, the RS-15 demonstrated similar or better 72-hour average probability of detection for T_0, T_{90}, T_{135} and the observation tower relative to the baseline. Conversely, its detection rate was inferior to the baseline in discriminating the external black body.

5) RS-M using $N = 15$ had the best 72-hour average probability of detection compared to RS-5 and RS-10. Therefore, increasing the number of random samples enhanced the algorithm's ability in discriminating the manmade objects from the natural clutter.

6) As the number of samples increased, the output surface from the RS-M became more visually appealing compared to the baseline.

Finally, the limitations of the RS-M will be presented in the next subsection.

5.3.10 Limitations of the RS-M Anomaly Detector

Subsection 5.3.8 demonstrated that by implementing a background characterization methodology based on a random sampling scheme with the M-Box test the newly proposed algorithm, the RS-M, became range invariant. This range invariance was validated using close and long range imagery (Subsection 5.3.8.2 and 5.3.8.3) and the results demonstrated that the RS-M was highly successful in discriminating the manmade objects from natural clutter background regardless of the range. Furthermore, Subsection 5.3.8.4 confirmed that there was limited adverse effect from potential manmade sample contamination as a result of the random sampling scheme, a highly desirable robustness. Subsection 5.3.9 presented a performance analysis between the M-Box and the RS-M and demonstrated that the RS-M not only exhibited similar performance to the M-Box algorithm for a $P_{fa} \geq 0.005$ but it was also capable of detecting the observation tower, which the M-Box algorithm could not. Also, as the number of random samples collected from the scene (N) increased from five to 15 random samples, the RS-M ability in discriminating the target at very low false alarm rates increased as well.

This subsection will present a significant limitation of the RS-M in situations where the scene's manmade objects covariance determinant value lies in between clutter values or $|\boldsymbol{\Sigma}_{clutter\ A}| < |\boldsymbol{\Sigma}_{manmade}| < |\boldsymbol{\Sigma}_{clutter\ B}|$. In such situation, the RS-M will not be able to detect the manmade object, in fact, as it will be shown later on, all test samples regardless if they come from natural clutter or not will be deemed as anomalies making the output surface unusable for anomaly detection applications.

Before showing any results, it is important to emphasize that until this day the SPICE data collection effort has not collected any dataset that specifically shows

manmade objects covariance determinant values in between two clutter classes. The fact that any analysis performed for this work has not found this particular subtle case in the SPICE dataset does not mean it cannot be manifested in real data, as a result it was decided to further investigate this particular limitation. In order to present scenarios where the RS-M limitation is evident, clutter samples from short and long range PI were collected and their Gaussian distributions estimated for the following examples.

Figure 5.96 illustrates a synthetic scene made up of three distributions, Clutter A, Clutter B, and manmade. Clutter A and manmade signatures were generated using the Matlab© multivariate random generator (mvnrnd) [74] using the estimated mean and covariance from clutter and manmade samples, respectively, collected from close range PI, whereas Clutter B signatures were generated using estimated mean and covariance using clutter samples collected from long range PI. Different shades of red exemplify a hot object while shades of blue a cold object. The estimated mean and covariance matrices of the clutter and manmade samples are shown in Table 5.8 and their distributions are plotted in Figure 5.97 where distribution Clutter A is plotted as a black solid line, distribution Clutter B as a dashed black line, and the manmade distribution as a red solid line.

In the next set of examples, five and ten samples ($N = 5$ or 10) from distribution Clutter A and/or Clutter B are manually collected from the image. Test samples are then collected from either distribution Clutter A, Clutter B, or manmade to assess if the RS-M test rejects or not the null hypothesis.

It is important to note that the first experiment does not illustrate the limitation of the RS-M per say, rather is used as a precursor to the introduction of the limitation. The

first experiment entails the collection of ten random samples from distribution A only, which will be used as reference, and three test samples are collected from each of the distributions Clutter A, Clutter B, and manmade.

Table 5.8 Estimated Statistical Parameters for Manmade and Clutter Classes

	μ	Σ
Manmade	[**0.0007439 0.0007386**]	$\begin{bmatrix} \mathbf{0.4162} & \mathbf{0.2152} \\ \mathbf{0.2152} & \mathbf{0.3074} \end{bmatrix} \times 10^{-10}$
Clutter A	[**0.0007143 0.0007121**]	$\begin{bmatrix} \mathbf{0.1089} & \mathbf{0.0852} \\ \mathbf{0.0852} & \mathbf{0.0732} \end{bmatrix} \times 10^{-9}$
Clutter B	[**0.0004456 0.0004564**]	$\begin{bmatrix} \mathbf{0.4416} & \mathbf{0.2369} \\ \mathbf{0.2369} & \mathbf{0.2400} \end{bmatrix} \times 10^{-11}$

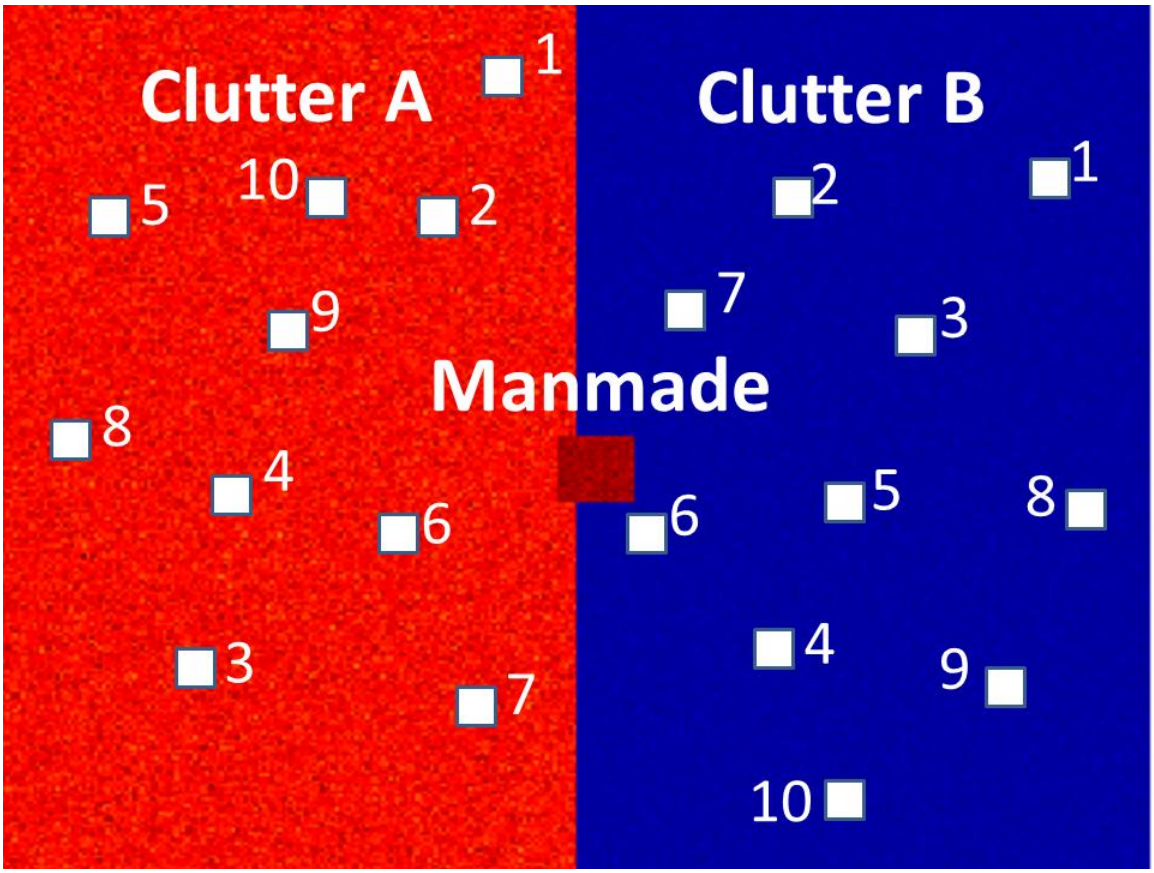

Figure 5.96 Synthetic image illustrating two clutter classes (Clutter A and Clutter B) and a manmade class. Each of the areas were randomly generated by Matlab© multivariate random generator using estimated mean and covariance matrices from real data. Clutter A and manmade statistics were estimated from close range PI while Clutter B statistics were estimated from long range PI.

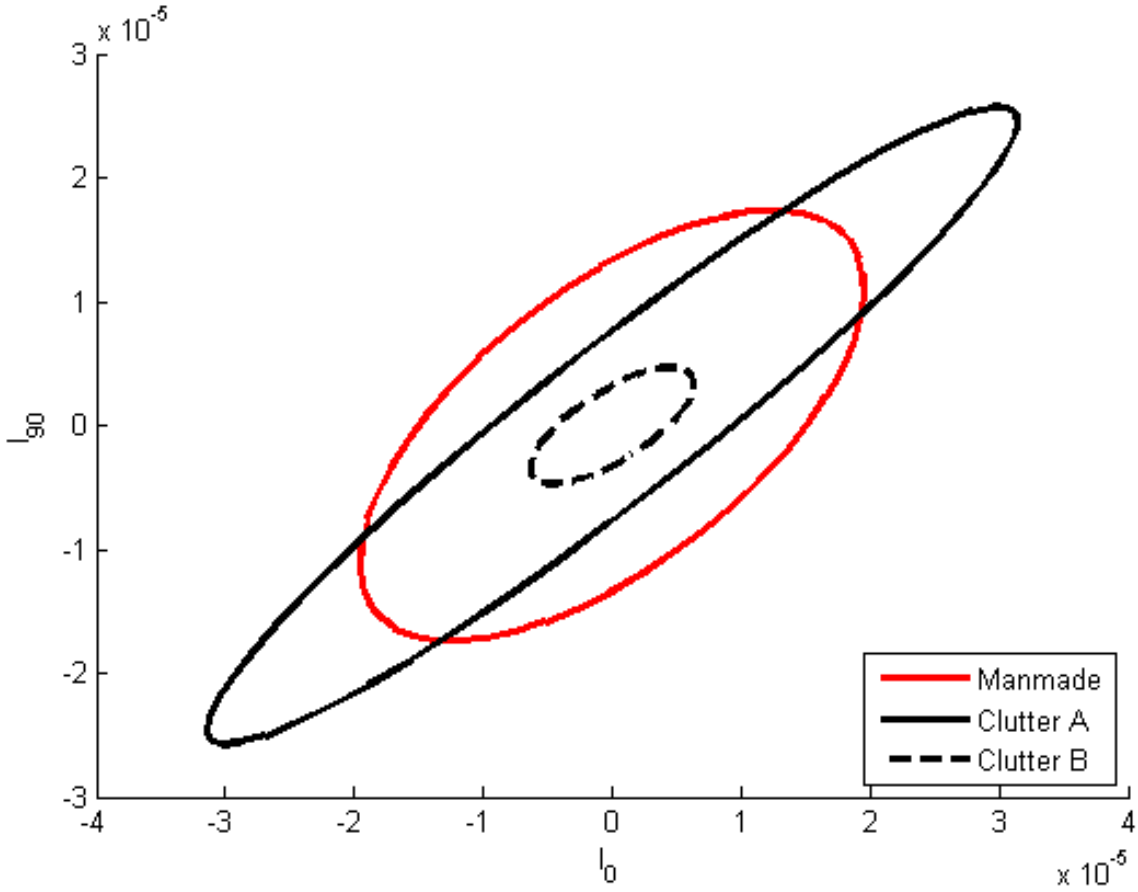

Figure 5.97 Distribution of all three classes, manmade and Clutter A and Clutter B. Clutter A exhibits a larger spread relative to manmade object while Clutter B exhibits a smaller spread.

The first example entails the collection of ten reference blocks of data from Clutter A only. Figure 5.98 illustrates the distribution of Clutter A, Clutter B, and manmade, as shown in Figure 5.97, with the addition of the pooled distribution when all reference samples are taken from Clutter A only. As expected, since all ten reference samples are collected from distribution Clutter A and only one test sample is collected from either one of the three distributions, the pooled distribution follows the distribution Clutter A very closely, which is expected. One can then conclude that if a test sample is taken from Clutter A, one would expect that the output of the RS-M should yield a very

low score; otherwise if the test sample is collected from Clutter B or manmade object, the RS-M should yield a high score.

Figure 5.99 presents the RS-M output values when the ten reference samples are taken from Clutter A and compared to test samples taken from all distributions (three from each distribution). As shown in Figure 5.99, if the test sample is collected from distribution Clutter A, the output of the RS-M yields a very low score (9.96, 11.34, 9.81), therefore, not rejecting the null hypothesis, for $\alpha = 0.10$ or 22.31, $\alpha = 0.05$ or 25.00, and $\alpha = 0.01$ or 30.57. If the test samples are taken from distribution Clutter B or manmade then the RS-M yields very high scores (86.22, 85.53, 106.75, 49.09, 48.60, 36.11), therefore, rejecting the null hypothesis. Although not shown here, if one collects ten random samples from distribution B only, then the RS-M output scores for any test sample from distribution B yields a low score (8.5, 5.12, 13.91) while any test sample from either manmade or distribution A yields a high RS-M output value (331.22, 375.68, 322.06 for distribution A, 398.25, 307.57, 337.38 for manmade). Table 5.9 illustrates the results from the experiments for both cases when the reference samples were collected from distribution Clutter A or Clutter B only.

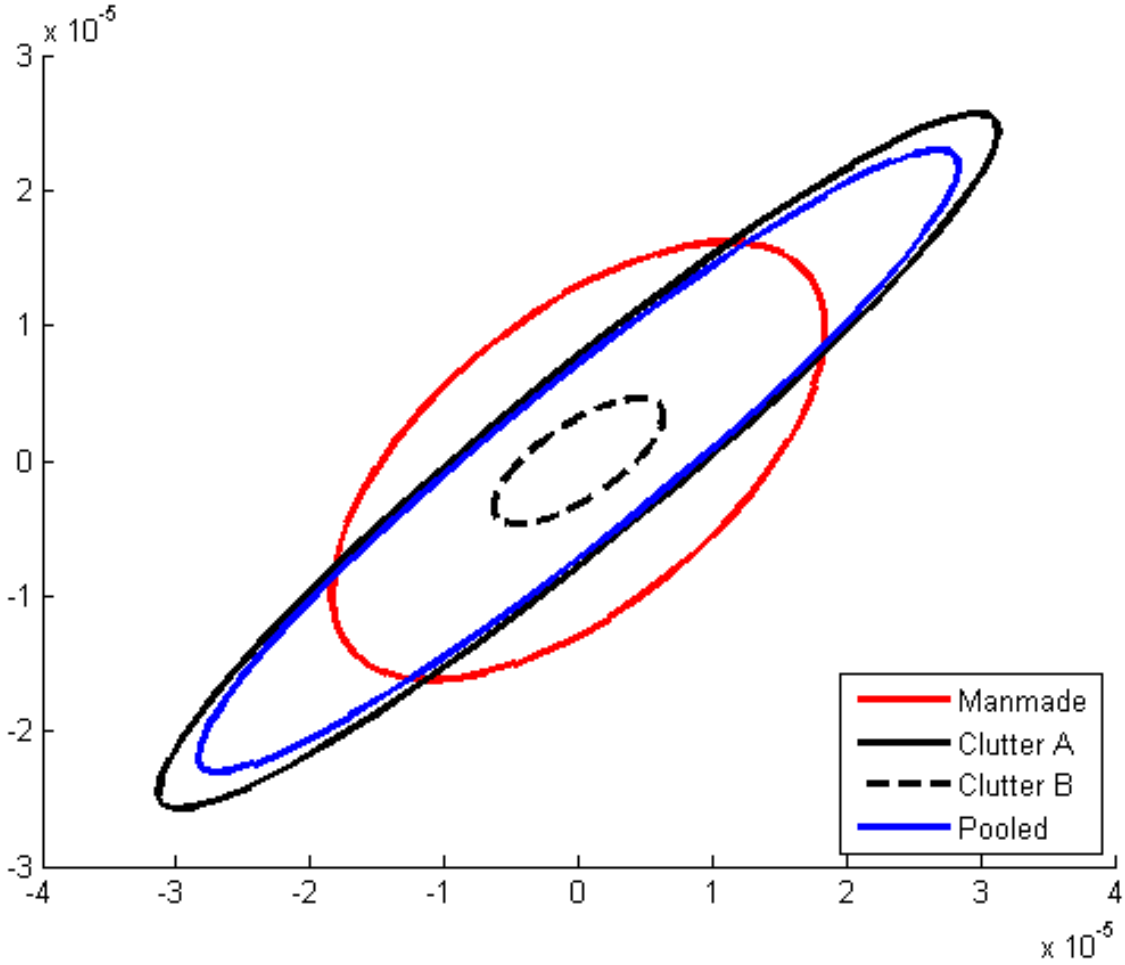

Figure 5.98 By collecting all ten reference samples from Clutter A only the pooled distribution is similar to that of Clutter A distribution. Therefore, any test sample taken from distribution Clutter A the result of the RS-M will yield a small value, otherwise it will yield a high value.

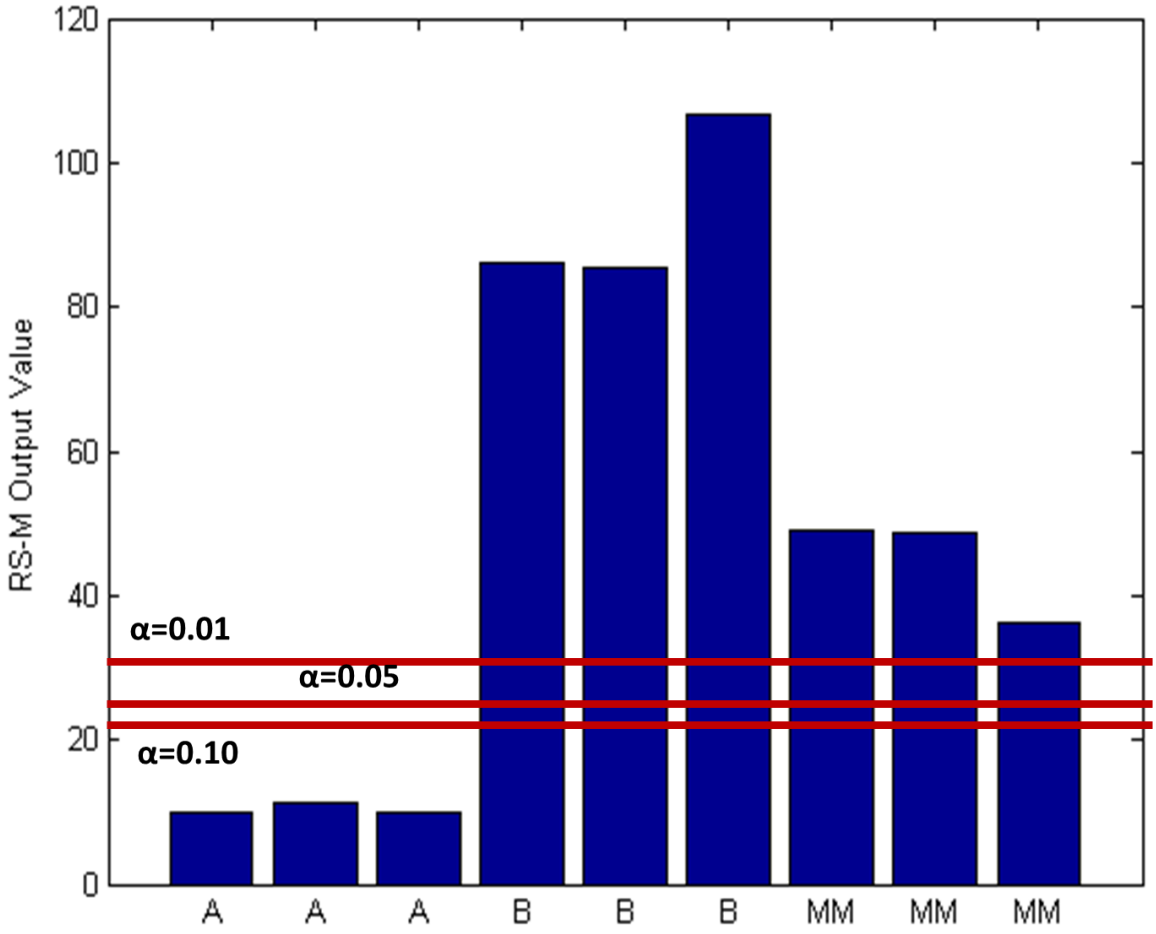

Figure 5.99 Since all reference samples were taken from distribution Clutter A, the result of the RS-M when a test sample is taken from Clutter A yield very small values compared to test samples from distribution Clutter B or manmade.

Table 5.9 compares the output of the RS-M for the different test samples and the reference samples when collected from Clutter A or Clutter B only. Table 5.9 shows, as expected, that collecting reference samples from distribution Clutter A or Clutter B demonstrates that the RS-M does not reject the null hypothesis if test samples come from the same reference distribution, otherwise it rejects the null hypothesis for any test sample collected from other distributions based on the threshold values shown above for a probability of miss of $\alpha = 0.10, 0.05, \text{and } 0.01$..

Table 5.9 RS-M Results for Reference Samples Taken from Clutter A or B

	Clutter A Only			Clutter B Only		
	T_1	T_2	T_3	T_1	T_2	T_3
Manmade	49.09	48.60	36.11	398.25	337.38	307.67
Clutter A	9.96	11.34	9.81	331.22	375.68	322.06
Clutter B	49.09	48.60	36.11	8.5	5.12	13.91

Now let's consider the case when the reference values are collected from both distributions controlling Clutter A and Clutter B. For example, let two sets of five reference samples be manually collected from distribution Clutter A and Clutter B for a total of ten reference samples. The distributions of Clutter A, Clutter B, manmade, and the pooled distribution are shown in Figure 5.100. In this example, because the distribution spreads of Clutter A and Clutter B is larger and smaller, respectively, relative to the manmade object distribution, the pooled distribution of all samples lies close to the distribution of the manmade object somewhere between the two clutter distributions. However, the result of the RS-M test yields very high scores for all test samples, virtually rejecting the null hypothesis (values are above $\alpha = 0.01$ or 30.57) regardless of where the test samples are collected from, see Figure 5.101. Although counterintuitive at first, one should remember that the RS-M hypothesis test (Equation (5.50)) is comparing all covariance matrices to see if they are equal to each other or not. This is accomplished by Equation (5.52), which compares the individual covariance matrices to the pooled covariance. As a result, when the test sample is from a manmade object, ten (reference samples from Clutter A and B) of the eleven distributions are highly different from the pooled distribution, and the output of the RS-M test yields extremely high scores. If the

test sample is collected from either Clutter A or Clutter B then five of the eleven distributions are significantly different from the pooled distribution and once again the RS-M yields a high score. Therefore, one can conclude that in situations where clutter distribution spread is both larger and smaller compared to manmade object distribution and the number of random samples collected from both distributions is also similar, the RS-M will reject the hypothesis for any test sample in the scene making it unusable as an effective anomaly detector.

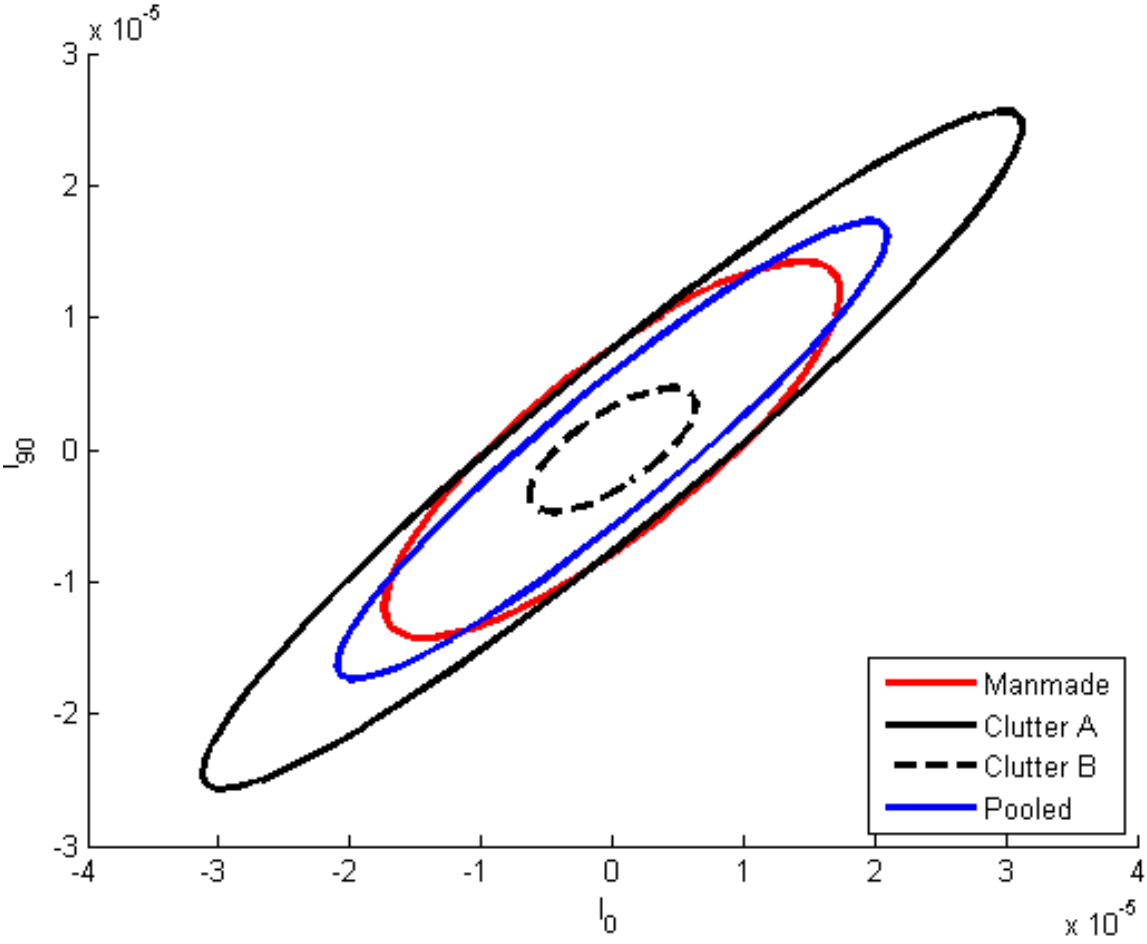

Figure 5.100 Two sets of five random samples were manually collected from Clutter A and B, respectively. In this case the pooled distribution lies somewhere between the two clutter distributions, in this case similar to the manmade object distribution. Unlike Figure 5.98 the pooled distribution is not representative of any of the clutter classes.

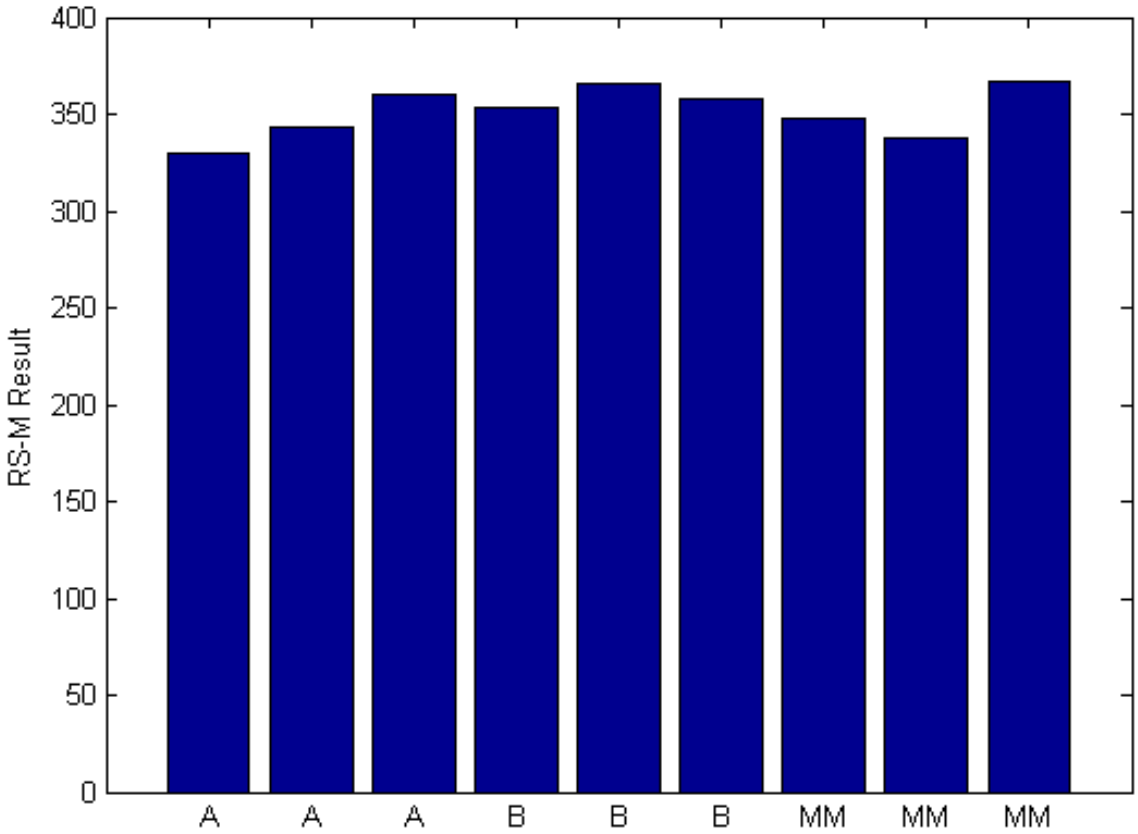

Figure 5.101 Since ten of the eleven distribution spreads (all clutter reference samples) are highly different from the pooled covariance the output of the RS-M yields an extremely high result, ensuing that the hypothesis is rejected (all values are above 30.57 for $\alpha = 0.01$) regardless if the sample is from clutter or not.

In the previous example the same number of samples, five, were collected from each of the clutter and the RS-M output values shown in Figure 5.101. Table 5.10 presents the RS-M output values as the number of samples collected from Clutter A increases relative to Clutter B. In this example, as expected, the RS-M output values for test samples belonging to Clutter A decreased as function of increasing the number reference samples collected from Clutter A. The same is true for reference samples and test samples taken from Clutter B.

Nonetheless, what is important to emphasize from this table is that even as the number of samples collected from Clutter A increase to nine out of the ten collected

samples the spread of the distribution from Clutter B still influences significantly the result of the RS-M to reject the null hypothesis (using a threshold of 30.57) regardless if the samples come from Clutter A or not.

Therefore, one must conclude that the RS-M is not a reliable algorithm for situations where the manmade covariance determinant values are found in between two different clutter values.

Table 5.10 Experiment to Show the RS-M Limitation Using a Threshold of 30.57

Clutter A Samples	Clutter B Samples	Test Sample	Result
5	5	Clutter A	330.27
5	5	Clutter B	365.98
5	5	Manmade	366.60
6	4	Clutter A	315.04
6	4	Clutter B	347.79
6	4	Manmade	338.12
7	3	Clutter A	265.88
7	3	Clutter B	301.78
7	3	Manmade	288.66
9	1	Clutter A	95.98
9	1	Clutter B	311.18
9	1	Manmade	129.45

In conclusion, the RS-M is a very versatile algorithm in discriminating manmade objects from natural clutter backgrounds as previously shown for close and long range PI where these two situations the spread of the distribution of the clutter was either smaller

than manmade distribution (long range) or larger (short range). Conversely, as presented in this subsection, if a test scene exhibits clutter that has both larger and smaller distribution spread relative to the manmade objects the RS-M will fail to discriminate the manmade object from natural clutter.

Again, the specific problematic case described in this subsection was not found in the dataset presented in other subsections in this dissertation and the results present here used distribution samples from several close and long range test images to demonstrate the potential limitation of the RS-M in a practical environment.

The next subsection will present a new variation of the RS-M algorithm called Parallel Random Sampling M-Box anomaly detector and this new variation is both range invariant as the RS-M without the limitation shown in this subsection.

5.3.11 Parallel Random Sampling M-Box (PRS-M) Anomaly Detector

Subsection 5.3.5 proposed the M-Box covariance test as an anomaly detector for manmade objects in natural clutter backgrounds based on the discriminant features found in Subsection 5.3.4. The implementation proposed for the M-Box algorithm in Subsection 5.3.6.1 demonstrated exceptional performance compared to Stokes and DoLP parameters; however, as a result of the proposed implementation, the M-Box algorithm was limited to long range PI (see Subsection 5.3.7 for details). Subsection 5.3.8 proposed the Random Sampling M-Box anomaly detector, which much like the M-Box from Subsection 5.3.6.1 excelled in discriminating manmade objects from natural clutter backgrounds with the added benefit that the RS-M could be operated in both close and long range PI with no *a priori* information about the test scene. Nonetheless, the RS-M performance could be adversely affected if a test scene exhibited a manmade distribution

where its spread lies in between two clutter distributions spreads. In such situation, as shown in Subsection 5.3.10, any test sample, regardless if it would come from clutter or not, the output from the RS-M yielded high values that were prone to be rejected by the null hypothesis, thus making the RS-M an ineffective anomaly detector.

Before diving into the PRS-M, it would be beneficial to describe how some of the features previously individually implemented into the M-Box and RS-M from Subsections 5.3.6.1 and 5.3.8 are now implemented conjointly into the PRS-M.

As shown previously, the implementation of the M-Box from Subsection 5.3.6.1 suffered from range limitations (Subsection 5.3.7) and one way to bypass this limitation was the introduction of the random sampling methodology, which was used as a background characterization method for the M-Box test in the RS-M anomaly algorithm, thus making the RS-M range invariant. Therefore, to keep the M-Box covariance test still range invariant the random sampling technique still needs to be incorporated.

On the other hand, the RS-M had difficulty in discriminating manmade objects from natural clutter in situations where the manmade covariance determinant value lies in between two or more clutter covariance determinant values. In this situation the test rejected the hypothesis regardless if the test sample was representative from clutter or manmade objects making the RS-M impractical as an anomaly detector. This limitation was directly influenced by the pooled distribution when the covariance test compared all N reference and test samples to the pooled covariance in a single equation. Therefore, it isn't practical to use the M-Box to test k samples, where $k > 2$; as shown in Subsection 5.3.8. Instead, for situations where the clutter distributions change dramatically with respect to the manmade object, the test should remain between each of the reference

samples and the test sample only or $k = 2$. In this case, by keeping $k = 2$, the pooled covariance will be influenced only by the test sample and each individual reference sample.

In conclusion, for the reasons mentioned in the previous paragraphs, the proposed algorithm should retain the random sampling approach presented in Subsection 5.3.8 and at the same time keep the number of covariance matrices tested by the M-Box as $k = 2$ as discussed in Subsection 5.3.5.

This subsection proposes to combine the powerful test statistic presented in Subsection 5.3.5 (M-Box algorithm) with an existing autonomous background characterization method known as *Parallel Random Sampling* (PRS) that has been previously proposed as a highly efficient background characterization method for HS imagery [62-66]. This methodology demonstrated the ability to increase an algorithm's performance for a variety of adverse weather conditions. In this subsection the PRS and the M-Box are combined to yield an even more effective anomaly detector when compared to the M-Box and RS-M detectors while preserving the range invariance needed for close and long range PI as well as mitigating the RS-M limitation introduced in Subsection 5.3.10.

The parallel random sampling methodology, as the name implies, uses the random sampling technique to collect information about the scene (scene characterization) that will be used by the detector to discriminate potential manmade objects from the scene. The parallel term is added because each set of random sampling and image processing is repeated multiple times independently of each other and the output surfaces from all the parallel outputs are then fused together to yield a final output surface.

5.3.11.1 Using the Random Sampling Approach with the PRS-M. As shown in Subsection 5.3.8, by random sampling the scene with N blocks (windows) of data and designate them as clutter allowed for the RS-M to be range invariant. The same concept is again used for the PRS-M by implementing the random sampling method to characterize the test scene.

The difference between what was proposed in Subsection 5.3.8 and in this subsection is that M-Box compares the distance between each individually randomly selected reference samples with the test sample, and for reasons to be explained shortly, keep the result with the lowest score out of all N scores.

For example, let one assume that a PC **X**, such that $\boldsymbol{X} \in \boldsymbol{R}^{R\times C\times P}$, is to be tested and N blocks of data of size $(n \times n)$ are randomly collected from the image and used as reference in the background library set, such that each reference block is represented by $\left\{\boldsymbol{W_r^d}\right\}_{\boldsymbol{d=1}}^{\boldsymbol{N}}$ and $d = 1,2, \dots, N$, where each $\boldsymbol{W_r^d}$ contains the polarization vector information collected from **X** in the form of,

$$\boldsymbol{W_r^d} = \left[\boldsymbol{x}_{r,1}^{d}, \dots, \boldsymbol{x}_{r,n_2}^{d}\right], \tag{5.57}$$

where $n_2 = n^2$ is the number of total pixels collected by each block of data and $\boldsymbol{x}_r^d \in \boldsymbol{R}^{1\times p}$ is a p-dimensional vector. From each $\boldsymbol{W_r^d}$, $\boldsymbol{\Sigma_r^d}$ is calculated for each individual random block. As the moving window moves across the image in **X,** collecting a block of data of size $n \times n$ pixels, at a given location (i, j) denoted as $\boldsymbol{W_t^{(i,j)}}$ where,

$$\boldsymbol{W_t^{(i,j)}} = \left[\boldsymbol{x_1^{(i,j)}}, \ldots, \boldsymbol{x_{n_2}^{(i,j)}}\right], \tag{5.58}$$

and the covariance of $\boldsymbol{W_t^{(i,j)}}$ is given by $\boldsymbol{\Sigma_t^{(i,j)}}$. Since there are N reference covariance matrices, one needs to test if

$$\begin{aligned} \mathrm{H}_0&: \boldsymbol{\Sigma}_t = \boldsymbol{\Sigma_r^d}, \\ \mathrm{H}_1&: \boldsymbol{\Sigma}_t \neq \boldsymbol{\Sigma_r^d}, \end{aligned} \tag{5.59}$$

for all N blocks of data and produce a final output value for each location (i, j), such that $\tilde{\mathbf{Z}}_d^{(i,j)} \geq 0$. Therefore, for each location (i, j), the hypothesis test (Equation (5.59)) will be tested N times, yielding N results in the form of $\left\{\tilde{\mathbf{Z}}_d^{(i,j)}\right\}_{d=1}^{N}$. $\tilde{\mathbf{Z}}_d^{(i,j)}$ is represented as,

$$\begin{aligned} \tilde{\mathbf{Z}}_d^{(i,j)} &= -2\log(M) \\ &= v_t log\left|\boldsymbol{\Sigma_t^{(i,j)}}\right| + v_d log\left|\boldsymbol{\Sigma_r^d}\right| \\ &- (v_d + v_t) log\left|\frac{v_d}{v_d + v_t}\boldsymbol{\Sigma_r^d} + \frac{v_t}{v_d + v_t}\boldsymbol{\Sigma_t^{(i,j)}}\right|, \end{aligned} \tag{5.60}$$

for all $d = 1,2, \ldots, N$ and $v_d = v_t = n^2$. Then,

$$\tilde{Z}^{(i,j)} = \min_{1 \leq d \leq N} \tilde{\mathbf{Z}}_d^{(i,j)}, \tag{5.61}$$

where $\tilde{Z}^{(i,j)}$ is the final value at location (i, j) in the output surface.

The reason for taking the minimum of all N results is as follow, let one assume that all N blocks of data that were randomly collected from the image are representative of background only. If the moving window collects samples representative of clutter then

one could predict that all N results would yield small scores since the reference and the test samples come from the same class (natural objects), in other words one would not reject H_0 for all N results. Therefore, taking the minimum of all N scores one would still not reject H_0. Conversely, if the moving window collects a sample representative of a manmade object, then in principle all N results would yield high scores, rejecting H_0, and once again if the minimum score were to be taken it would still reject the null hypothesis.

Furthermore, by calculating the score between each individual random sample and the test sample the RS-M limitation is removed. To validate this statement let's take the same example shown in Subsection 5.3.10 in Figures 5.96 and 5.97 using the estimated distributions of Clutter A and Clutter B and manmade from Table 5.8. For this experiment each clutter distribution will be manually sampled once (Figure 5.96) and used as reference and a test sample from each clutter and manmade distribution will be used in Equation (5.60), respectively, to determine if one should reject (or not) the null hypothesis.

For the first example, a test sample is collected from Clutter A and compared to both Clutter A and Clutter B distributions as shown in Figure 5.102. As seen in the top plot of Figure 5.102, both the distribution of the test sample, Clutter A, and the pooled covariance are extremely similar. However, as shown in the bottom plot, the test sample is very different from Clutter B and consequently the pooled covariance is also different from the two distributions. When testing Clutter A reference sample to the test sample the M-Box result was 0.6918 while when testing Clutter B reference sample to the test sample yielded 1338. In this example, taking the minimum of $\tilde{\mathbf{Z}}_d$, it is obvious that the test sample came from Clutter A distribution, therefore, one should not reject H_0.

The next example illustrates the opposite where a test sample from Clutter B was collected and tested in Equation (5.60) for each of the reference samples. As shown in the top plot of Figure 5.103, the test sample distribution is very different from the Clutter A distribution and as a result the pooled covariance is also different from both the test and Clutter A distribution. Conversely, since the test sample comes from Clutter B distribution, the pooled covariance is also similar to the two distributions. For this scenario, the M-Box yielded the following values; 1277 (when comparing Clutter A reference samples to the test sample) and 3.08 (when the reference samples were taken from Clutter B). Once again, one can conclude that the test sample was taken from Clutter B and by taking the minimum of $\tilde{\mathbf{Z}}_d$ one would not reject H_0.

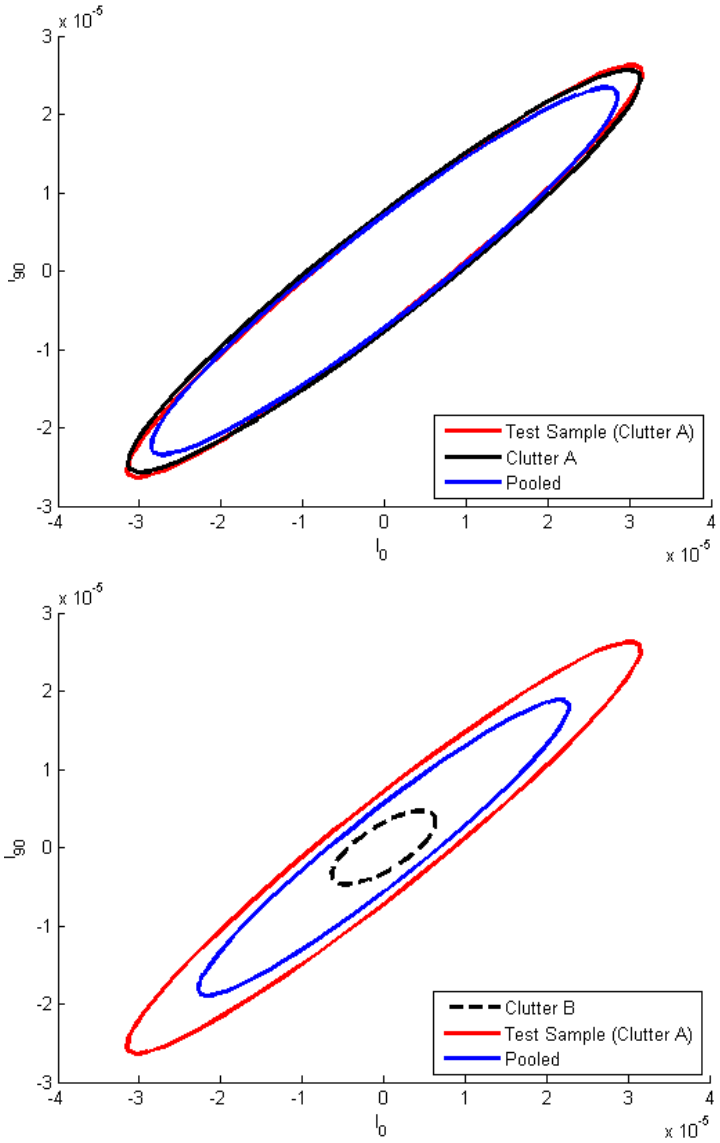

Figure 5.102 Illustration of the pooled covariance when the test sample comes from the same distribution as the reference sample. In this case the test sample is collected from the same distribution as the Clutter A reference sample. As a result the pooled covariance is similar to the test and reference sample. On the other hand, since the test sample is different from Clutter B distribution the pooled covariance is also very different from the test and the reference sample.

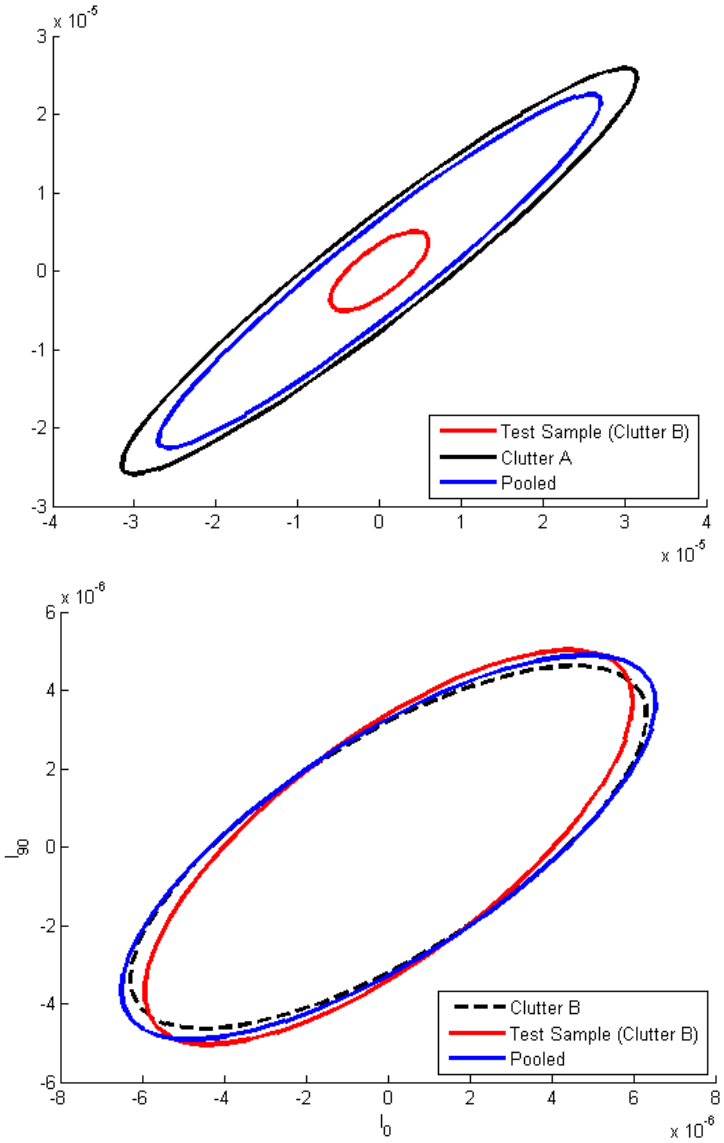

Figure 5.103 In this example the test sample is drawn from the same distribution as the reference sample (Clutter B). As shown previously, the pooled covariance is similar only to the reference and test samples when the latter are both from the same distribution.

So what happens when the test samples come from a manmade object? As shown in Figure 5.104, the manmade distribution is very different from Clutter A (top plot) and Clutter B (bottom plot) distributions resulting on a M-Box score of 17.72 when taking Clutter A as the reference sample and 71.84 when Clutter B was used the reference

sample. By taking the minimum of the two values, one could still reject H_0 with a very low probability of miss of 0.01.

Figure 5.105 illustrates a summary of the results as a bar graph. The x-axis references where test sample was taken from, the y-axis the M-Box result between the reference and test covariance matrices, while the bar illustrates the reference samples (dark tone for Clutter A and light tone for Clutter B). The y-axis is topped at 90 for visual appreciation for the manmade sample results. As shown in Figure 5.105 when the test sample is from clutter A, the dark tone bar (using Clutter A as reference) is close to zero while light tone bar displays a very high score. Conversely, when the test sample is taken from Clutter B, the dark tone bar shows a very high score while the light tone bar yields a value very close to zero. Finally, when the test sample is from a manmade object both the dark and light tone bar yield a high score greater than 17, therefore, rejecting the null hypothesis with a probability of miss of 0.01.

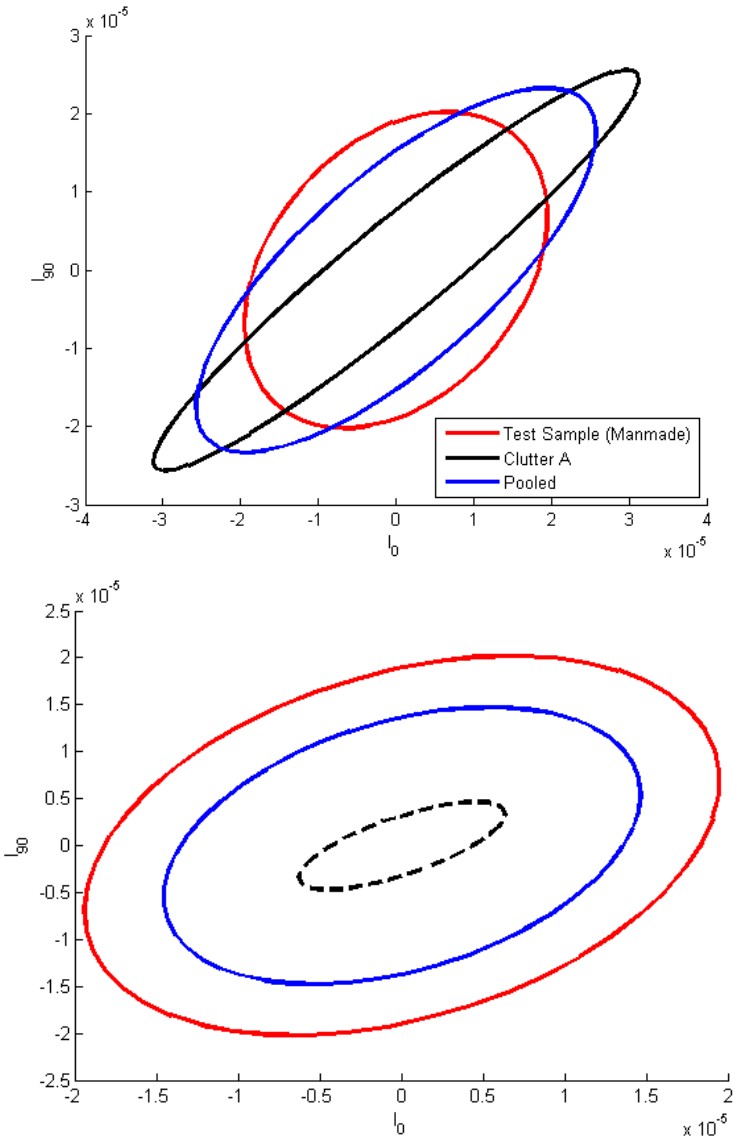

Figure 5.104 When a test sample is different from any of the reference samples, all the distributions (test, reference, and pooled) are highly different from each other. As a result the M-Box algorithm has a high probability of deeming the test sample as an anomaly.

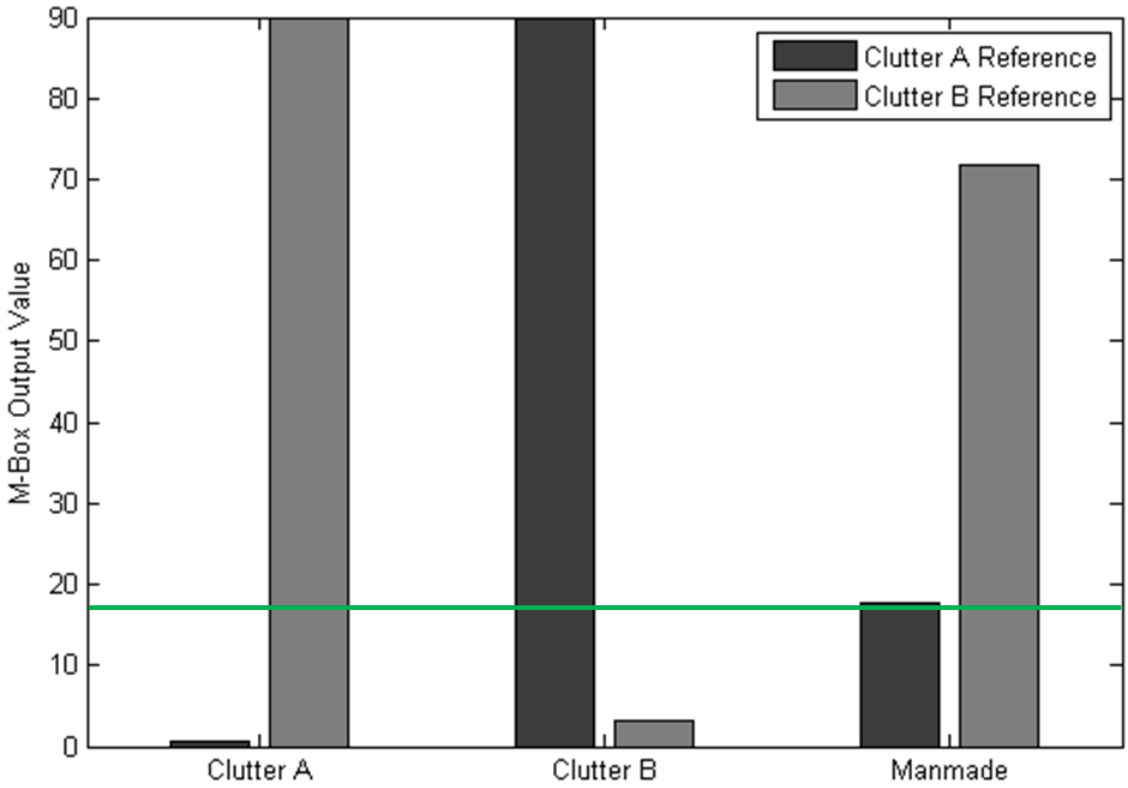

Figure 5.105 M-Box covariance test results. The x-axis defines which distribution the test sample was drawn from, the y-axis displays the output of the M-Box test, and finally the bar in red delineates if the reference sample is from distribution Clutter A (dark tone) or Clutter B (light tone).

In conclusion, unlike the RS-M, which wasn't able to discriminate clutter from manmade for the same example, the proposed implementation for the PRS-M was capable of distinguishing each of the test samples as clutter or anomaly successfully for the same example which RS-M failed. By taking the minimum of $\tilde{\mathbf{Z}}_d$ one is capable of successfully rejecting (or not) H_0 as shown in this example.

5.3.11.2 The Effect of Contamination in the PRS-M as a Result of the Random Sampling.

When random blocks of data are collected from a test scene there is a probability that a manmade object may be sampled as well, also known as contamination.

Contamination is a more serious incident for the PRS-M than it was for the RS-M (i.e., one of the reference blocks of data includes target pixels) because it is assumed that all reference samples represent natural objects. If this assumption is violated then the presence of manmade objects could potentially not be detected. To illustrate this problem, let one randomly collect N blocks of data from an image where N-1 reference blocks belong to clutter and the N^{th} block represents a manmade object. Under the PRS method, if the test sample came from the same manmade object one would expect high output scores from Equation (5.60) for the first N-1 reference samples and a very low score for the last reference sample (manmade). By retaining the minimum value of all N results, it would specify that specific location where the manmade object is located as a non-anomaly, which is a highly undesirable result.

To demonstrate the severity of the problem let one assume that the reference samples are taken from the three distributions in Figure 5.97, i.e., Clutter A, Clutter B, and manmade and a test sample from the same manmade distribution is also collected and tested against all reference samples using Equation (5.60). Figure 5.106 illustrates the distribution of the reference samples relative to the test sample, in this particular case manmade, and the pooled distribution. All distributions are centered at zero for visual appreciation. The top left plot illustrates the distribution of Clutter A, test sample and its respective pooled distribution, while the top right illustrates the distribution of Clutter B, test sample, and its corresponding pooled distribution, and finally the bottom picture illustrates the distribution of manmade, test sample, and its equivalent pooled distribution.

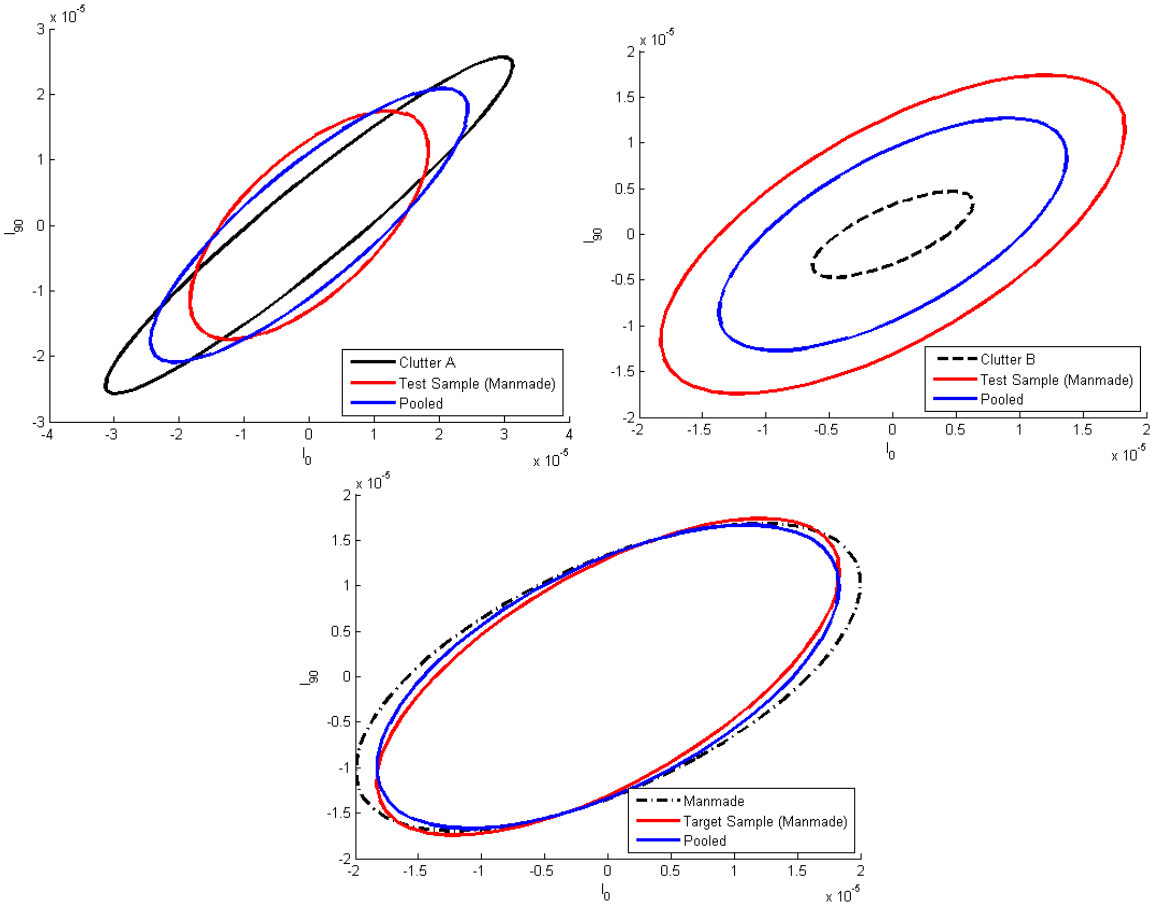

Figure 5.106 Example illustrating a case of contamination. Contamination is a problem because it is assumed that all reference samples randomly selected from the imagery represent natural objects, so if this assumption is violated then the presence of manmade objects could potentially not be detected. In this example three reference samples were collected from the scene but one of the reference samples was collected from the manmade object itself. Consequently, the manmade location will be deemed as a non-anomaly because the test sample is similar to one of the reference samples.

As shown in Figure 5.106 because the test sample came from a manmade distribution only the bottom image demonstrates the reference, test sample, and the pooled sample with similar distributions, while for the remainder of the plots the test distribution is very different from the reference distribution.

As a result, see Table 5.11, if contamination occurs (labeled reference sample - Manmade) and a test sample comes from the same manmade object, Equation (5.60)

yielded a result of 10.40, 65.12, and 0.68 when the reference sample represents Clutter A, Clutter B, and Manmade distributions, respectively. By taking the minimum of the third row of the test samples (test sample – Manmade) one would retain 0.68, therefore, not rejecting the null hypothesis and labeling the manmade test sample as a non-anomaly. Moreover, as shown from the results in Table 5.11, if the image was composed of only Clutter A and Clutter B as the natural background clutter and the manmade object had been sampled during the random sampling process, one can very easily see that all pixels in the output surface would be accepted by the null hypothesis.

Table 5.11 M-Box Output for Difference Combination of Reference and Test Samples

		Reference Samples			$\min_{1\le d\le N} \tilde{\mathbf{Z}}_d$
		Clutter A	Clutter B	Manmade	
Test Samples	Clutter A	2.73	73.14	27.12	2.73
	Clutter B	52.95	2.70	55.24	2.70
	Manmade	10.40	65.12	0.68	0.68

The top image of Figure 5.107 illustrates an example using long range PI where out of the five random samples collected from the test image, one sampled T_0. The output surface of Equations (5.60) and (5.61) is shown at the bottom image of Figure 5.107. As shown in the previous examples, since one of the reference samples came from T_0, this manmade object is completely mitigated from the output surface. Conversely T_{90} and T_{135} are slightly discriminated from most of the background although one can still find many false alarms around the area where the surrogate targets are located in. The blackbody on the other hand is slightly more discriminated (red color) than the surrogate

targets. One can then conclude that the distribution of T_0 is to some extent similar to T_{90} and T_{135} but different from the external blackbody distribution. Nonetheless, the key message from this experiment is that contamination will have a serious impact on the algorithm's performance.

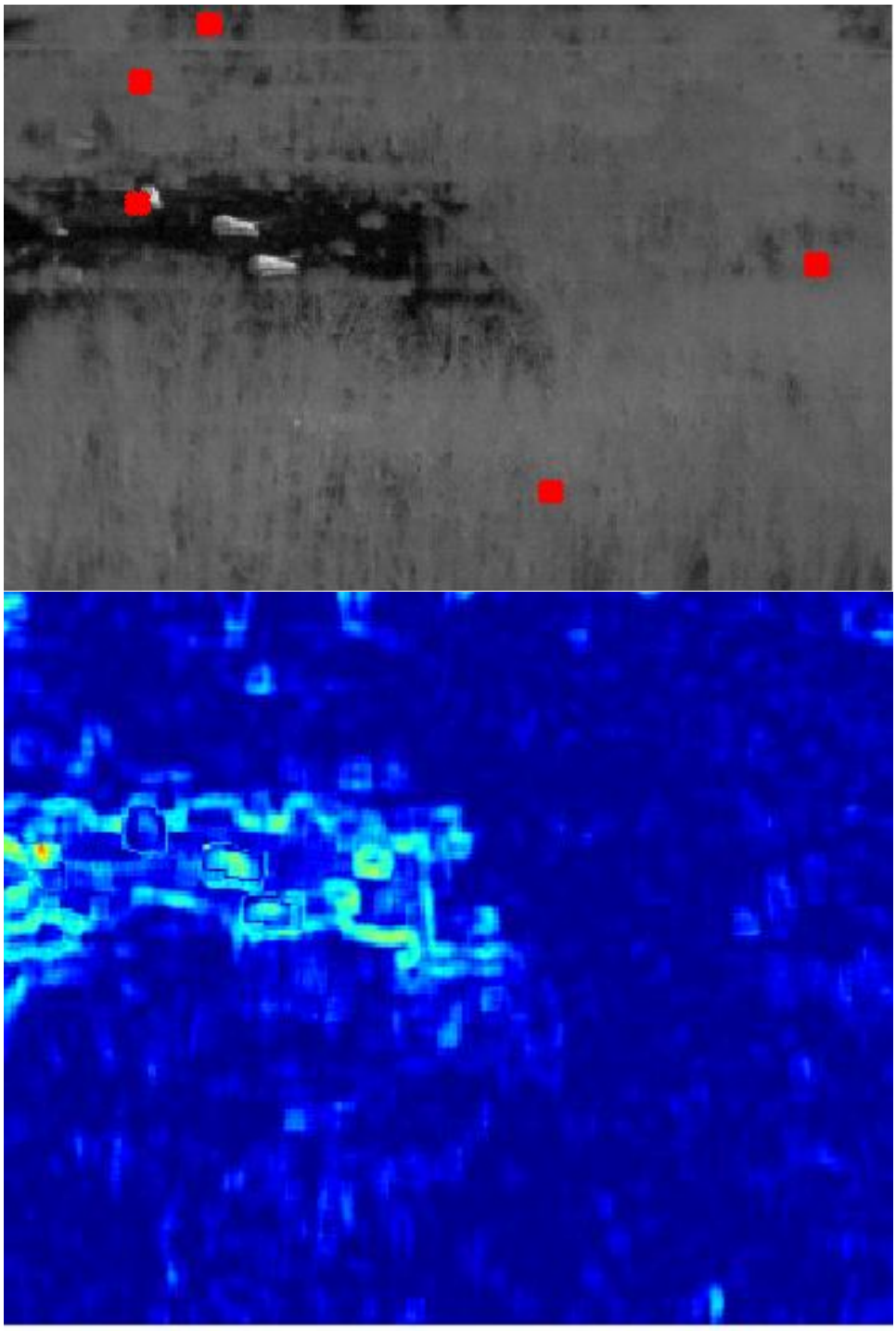

Figure 5.107 Example demonstrating the effects of contamination. In the top image because one of the reference samples collected samples from T_0, the manmade object is completely omitted from the output surface. The other surrogates although visible, their output values are very similar to false alarms present in the scene which one may deduce that the distribution of T_0 is similar but not equal to the other surrogate targets.

So, how often can contamination occur during the random sampling process? Let's assume that manmade pixels are present in a $R \times C$ spatial area of a PC cube **X** where $\boldsymbol{X} \in \boldsymbol{R}^{R \times C \times p}$ such that their total spatial area in **X** is denote by a. Let us denote q as the probability of sampling a manmade pixel out of all the pixels $(A = R \times C)$ in image **X**, such as

$$\mathrm{q} = \frac{a}{A}. \tag{5.62}$$

Let N blocks of data of size n^2 such that $(n^2) \ll (R \times C)$ be randomly selected from **X**. Assuming $(n^2) = 1$ and that all manmade pixels in **X** are disjoint and randomly scattered across the image area, the probability P where at least one block of data samples a manmade pixel is

$$\begin{aligned} \mathrm{P}(m \geq 1) &= P(m = 1) + P(m = 2) + \cdots + P(m = N), \\ &= 1 - P(m = 0), \end{aligned} \tag{5.63}$$

where parameter m represents the number of random blocks of data containing target pixels and P is the Binomial density function given by

$$\mathrm{P}(m|q, N) = \frac{N!}{m!\,(N-m)!} q^m (1-q)^{N-m}, \tag{5.64}$$

where q and N were previously defined as probability of sampling a manmade pixel and the number of random blocks of data collected from the image, respectively. Before continuing it must be noted that the assumption that manmade pixels are disjoint and scattered throughout the imagery is usually not met in practice. Nonetheless, the

assumption allows for a baseline approach to understand the implications of choosing different N and the probability of contamination as a result of the random sampling process.

Figure 5.108 illustrates the theoretical probability of contamination $\left(P(m \geq 1)\right)$ of one or more blocks of data for different q and different number of random samples N. It is obvious that, given a constant q, as the number of random blocks of data collected from **X** increase, so does the probability that one or more random blocks of data sample target pixels. At the same time, if the number of random blocks collected from the imagery is unchanged, but q increases, the probability of contamination also increases since the total number of available target pixels in the image increases with respect to the image spatial area. In summary, Figure 5.108 illustrates the trade-off between characterizing the background well with a large number of blocks of data, which is a desired outcome (better background characterization), and the probability of contamination, an undesirable consequence. One must remember, as per the examples shown previously, that the inclusion of target samples into one of the reference blocks of data would result on the target being suppressed since the algorithm defines each random block of data as being representative of clutter.

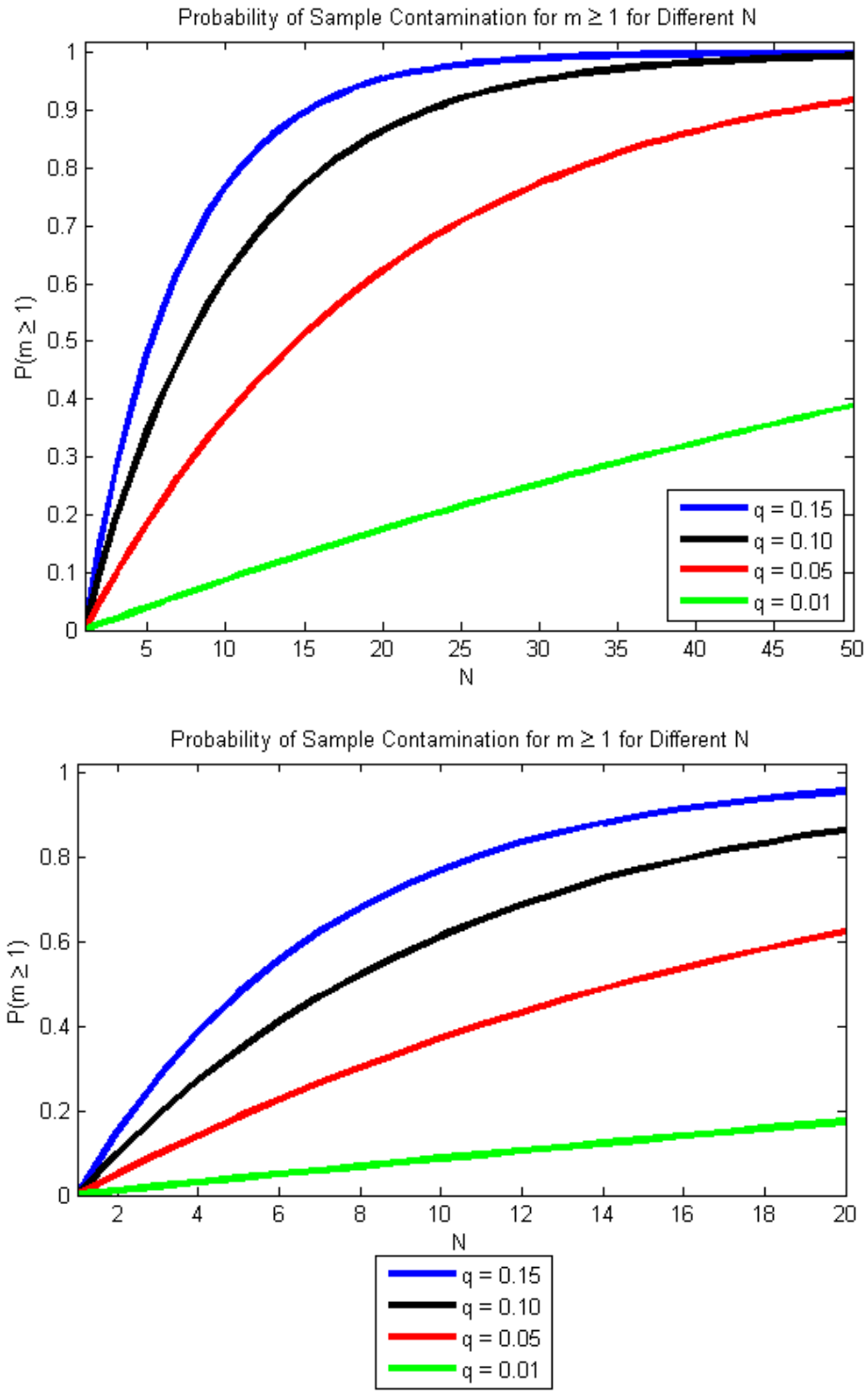

Figure 5.108 Probability of contamination curve for different values of N for $m \geq 1$ for $q = 0.01, 0.05, 0.10, \text{and } 0.15$. The probability of contamination increases as a function of increasing manmade object area and/or number of blocks of data collected.

From the ground truth available for the long range test scenes, a $q \sim 0.01$ was calculated which, from Figure 5.108, the probability of contamination $\left(P(m \geq 1)\right)$ when collecting N = 10 is $P(m \geq 1) \approx 0.10$, while for N = 20 the $P(m \geq 1) \approx 0.19$. As previously stated one must remember that these probability values are to be used as a guide as the real probabilities can fluctuate higher or lower depending on the number of targets present in the image.

In conclusion, when randomly collecting N blocks of data from an image where manmade objects may be present there is a probability of random sampling those same manmade objects as shown previously in Figure 5.108. If such happens, under the PRS method, one would eliminate the target from ever being discriminated since its information, as a result of the random sampling process, is by design designated as background clutter. Therefore, the result of Equation (5.60) between the test and any reference blocks of data, which are contaminated with target information would yield (when taking the minimum of the all the results) a very low score (e.g., close to zero), resulting on not rejecting the null hypothesis, as shown in Figure 5.107 bottom image.

In summary, contamination in the PRS-M is highly problematic because:

1) If a manmade object is sampled by chance and denoted as a reference natural object sample by design, it will not be discriminated as shown in Figures 5.106 and 5.107, and Table 5.11.

2) The probability of contamination, as shown in Figure 5.108, increases as a function of:

    a. Increasing manmade object area, or

    b. Decreasing scene spatial area, or

    c. Increasing N, the number of random samples collected from the image.

5.3.11.3 Mitigating Contamination in the PRS-M. The previous subsection demonstrated the adverse effect of contamination in the PRS-M. In order to mitigate the probability of inclusion of manmade object pixels into the reference blocks of data, [62] proposes repeating each *trial* (random sampling process plus the processing of the test image) M number of times. By repeating each trial M times the probability that the same target is sampled by chance on all trials can be easily modeled by the Binomial distribution as a decreasing function of increasing M (number of trials). As described in [62], all M output surfaces are fused (summed) together to yield a final output surface. The reasoning for the fusing is as follows; let one assume that a number of M trials' output surfaces (>2 and <M) eliminated a specific manmade object as a result of contamination while at the same time at least one or more remaining output surfaces successfully discriminated the same manmade object. By fusing all M parallel outputs one assures that the desired manmade object is retained in the final output surface, as it will be shown very briefly.

To understand how repeating each trial M number of times can mitigate contamination in the final output surface let one assume that the random sampling process together with the algorithm of choice is denoted as a *trial*. If each trial operates on the same image M times for a given q and N, knowing that $0 < P(m \geq 1) < 1$ and $P_1(m \geq 1) = \cdots = P_M(m \geq 1)$, and assuming that each processing block when collecting random samples is entirely independent of all other trials, the probability that all trials sample the same manmade object is a decreasing function of increasing M defined as follows,

$$\mathrm{P}_T = [P_1(m \geq 1)][P_2(m \geq 1)] \dots [P_M(m \geq 1)] = \big(P(m \geq 1)\big)^M. \tag{5.65}$$

Equation (5.65) can also be expressed as a binomial distribution by letting l be the number of trials (or parallel processes) that are contaminated out of M trials. By defining $l \in \{0,1, \dots, M\}$ and using $P(m \geq 1)$ as the probability of contamination per trial, the probability that all trials are indeed contaminated is as follows,

$$\begin{aligned} \mathrm{P}_T(l = M) &= \frac{M!}{l!\,(M-l)!}\big(P(m \geq 1)\big)^l\big(1 - P(m \geq 1)\big)^{M-l}, \\ &= \big(P(m \geq 1)\big)^M. \end{aligned} \tag{5.66}$$

Figure 5.109 illustrates the cumulative probability of having at least one contamination data block per trial as a function of M trials, for a fixed N and four values of q. As expected, as q increases, there is a need to increase M to reduce the probability of contamination in all trials as a result of a higher probability of contamination within each trial. One must remember that if all trials sample the same manmade object the result would be the total suppression of the manmade object in all trials, which is an undesirable result. Although in theory one would like to have a high number of trials, for example $M > 50$, in practice the introduction of unnecessary parallel processes (trials) may increase the number of processing operations and as a consequence processing time, which again would be an undesired effect. Therefore, one must be aware that a tradeoff must be considered when applying the PRS method in real world applications between N and M parameters relative to: (1) the type of background one will encounter; (2) the potential number of target pixels that could be in the test scene (a), and (3) the processing time available for each test scene.

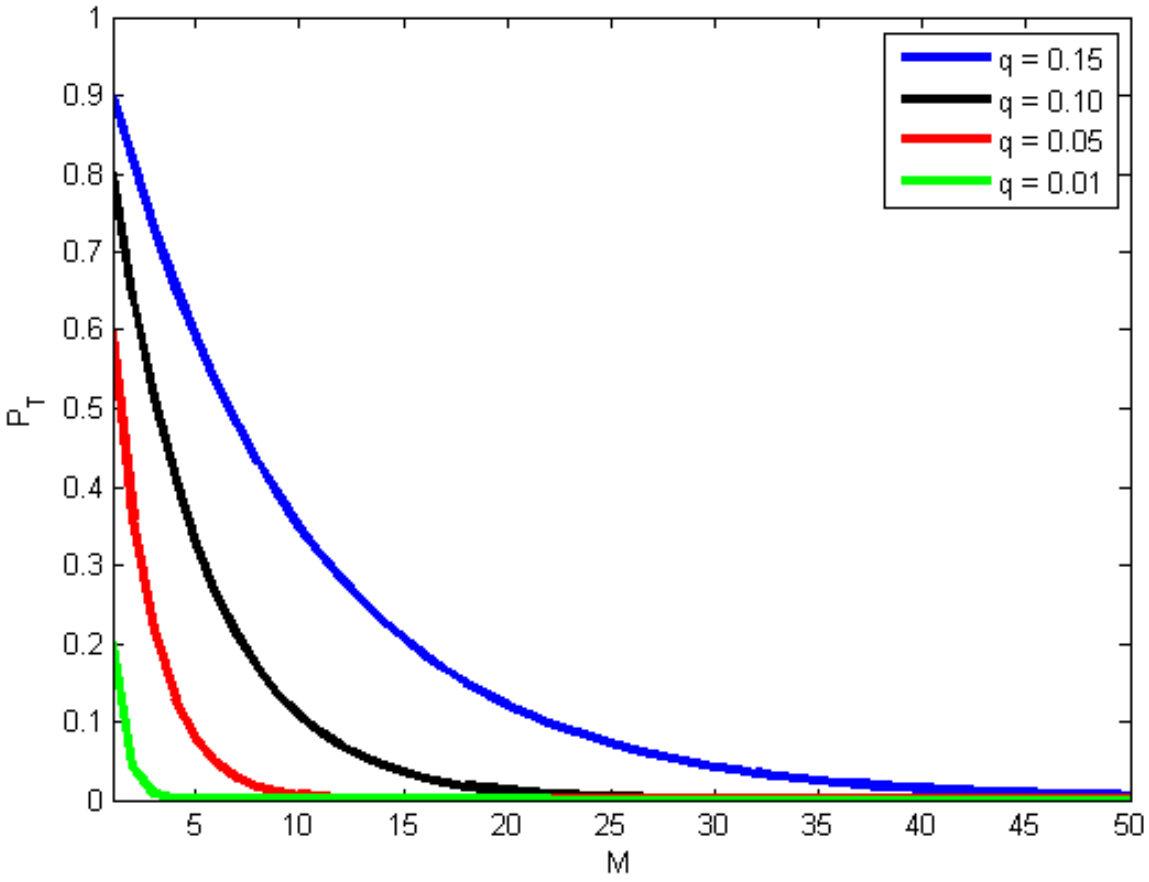

Figure 5.109 Cumulative probability of contamination of having at least a contaminated data block per trial as a function of M trials, for a fixed N and four values of q. The message: as M increases the cumulative probability decreases, which is desired and may be used as a guide by the user to minimize the effect of contamination.

As previously shown, Equation (5.60) represents the M-Box test between each reference sample and the test sample yielding a vector of N output scores. Equation (5.61) places the smallest value from the vector $\tilde{\mathbf{Z}}_d^{(i,j)}$ into the location (i,j) of the output surface.

As the moving window covers all potential locations in **X** for all M processes a 2-dimensional output surface is generated (denoted as $\tilde{\boldsymbol{Z}}^{\boldsymbol{l}}$) as $\tilde{\boldsymbol{Z}}^{\boldsymbol{l}} \in \boldsymbol{R}^{(R-n-1)\times(C-n-1)}$ where l $(l = 1, \ldots, M)$ represents the parallel process number, or

$$\widetilde{\boldsymbol{Z}}^{l} = \begin{bmatrix} \widetilde{Z}^{(1,1)(l)} & \dots & \widetilde{Z}^{(1,C-n-1)(l)} \\ \vdots & \ddots & \vdots \\ \widetilde{Z}^{(R-n-1,1)(l)} & \dots & \widetilde{Z}^{(R-n-1,C-n-1)(l)} \end{bmatrix} \tag{5.67}$$

The spatial area of $\widetilde{\boldsymbol{Z}}^{\boldsymbol{l}}$ is smaller than **X** due to the test window size, $\boldsymbol{W}_{\boldsymbol{t}}^{(\boldsymbol{i},\boldsymbol{j})}$, being greater than one pixel or $n > 1$. From Equation (5.67), $\widetilde{\boldsymbol{Z}}^{l}$ implies that there are M output surfaces representative of all M parallel processes which need to be fused together to yield a final output surface that can be thresholded.

Reference [62] proposed to sum these output surfaces into a single final output surface $\boldsymbol{Z}$. Let's assume as an example, that the same manmade object happens to be sampled in $M-1$ parallel processes, with the last M^{th} parallel process not sampling the target. By using the addition operation as the fusing process the energy of the manmade object detected in the M^{th} output surface would be retained in **Z** output surface.

Therefore, summing all M output surfaces yields a final 2-dimensional output surface represented by $\boldsymbol{Z} \in \boldsymbol{R}^{(R-n-1)\times(C-n-1)}$ as,

$$\boldsymbol{Z} = \begin{bmatrix} \sum_{l=1}^{M} \widetilde{\boldsymbol{Z}}^{(1,1)(l)} & \dots & \sum_{l=1}^{M} \widetilde{\boldsymbol{Z}}^{(1,C-n-1)(l)} \\ \vdots & \ddots & \vdots \\ \sum_{l=1}^{M} \widetilde{\boldsymbol{Z}}^{(R-n-1,1)(l)} & \dots & \sum_{l=1}^{M} \widetilde{\boldsymbol{Z}}^{(R-n-1,C-n-1)(l)} \end{bmatrix} \tag{5.68}$$

Figure 5.110 illustrates the locations of five random blocks of data ($N = 5$) where each color represents a different parallel process when the PRS-M was applied to a SPICE test image. Interestingly, one can observe that on Figure 5.110 one of the samples for $l = 2$ collected information on $T_{0,}$ which as previously shown, it should result on the elimination of that same object from the 2nd parallel process output surface.

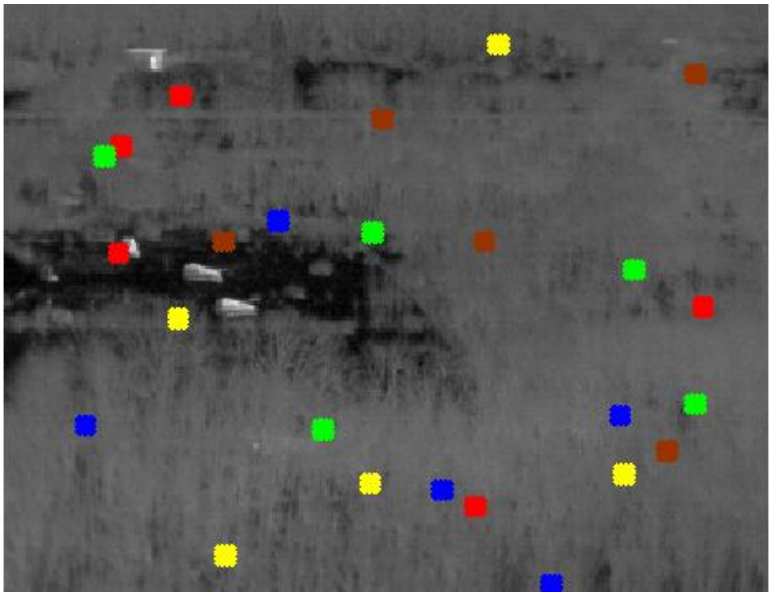

Figure 5.110 Location of random blocks collected from the scene for N = 5 and M = 5, with blue representing l =1, red l = 2, yellow l = 3, green l = 4, and brown l = 5. Notice that in l=2 one of the random blocks collected information on T_0.

Figure 5.111 illustrates the effectiveness of the fusion process when contamination occurs (using the random samples from Figure 5.110) by presenting the output surfaces for each parallel process (denoted as l = 1,..., 5), as well as the final output surface $\boldsymbol{Z}$ (lower right). One can readily observe from Figure 5.110 that T_0 had been sampled during the random sampling process for trial l = 2 and as a result, as shown in Figure 5.111, the output surface l = 2 demonstrates that T_0 is highly suppressed from the output surface with T_{90} and T_{135} also having degraded discrimination with the exception of the tower which still shows up very strongly in the output surface. By fusing (summing) all parallel processes, T_0, T_{90}, and T_{135} are successfully retained in the final output surface and can be easily discriminated as anomalies.

However, one must ask if by summing all the M output surfaces wouldn't that also increase the number of false alarms found in $\boldsymbol{Z}$? It is important to remember that

when each parallel process random samples the background, each set of random locations in each l^{th} process is independent from all the other parallel process. As a result, there is a very high probability that their locations are totally different from trial to trial, see Figure 5.111, therefore, the locations of the false alarms, as well as their energy, are highly different from all of the other trials. In conclusion, summing all M trials should, in principle, keep the false alarms values relatively low, because their spatial locations are random (as a result of the random blocks of data locations for each trial), compared to manmade objects, which are usually detected in the same location over multiple trials, see Figure 5.111.

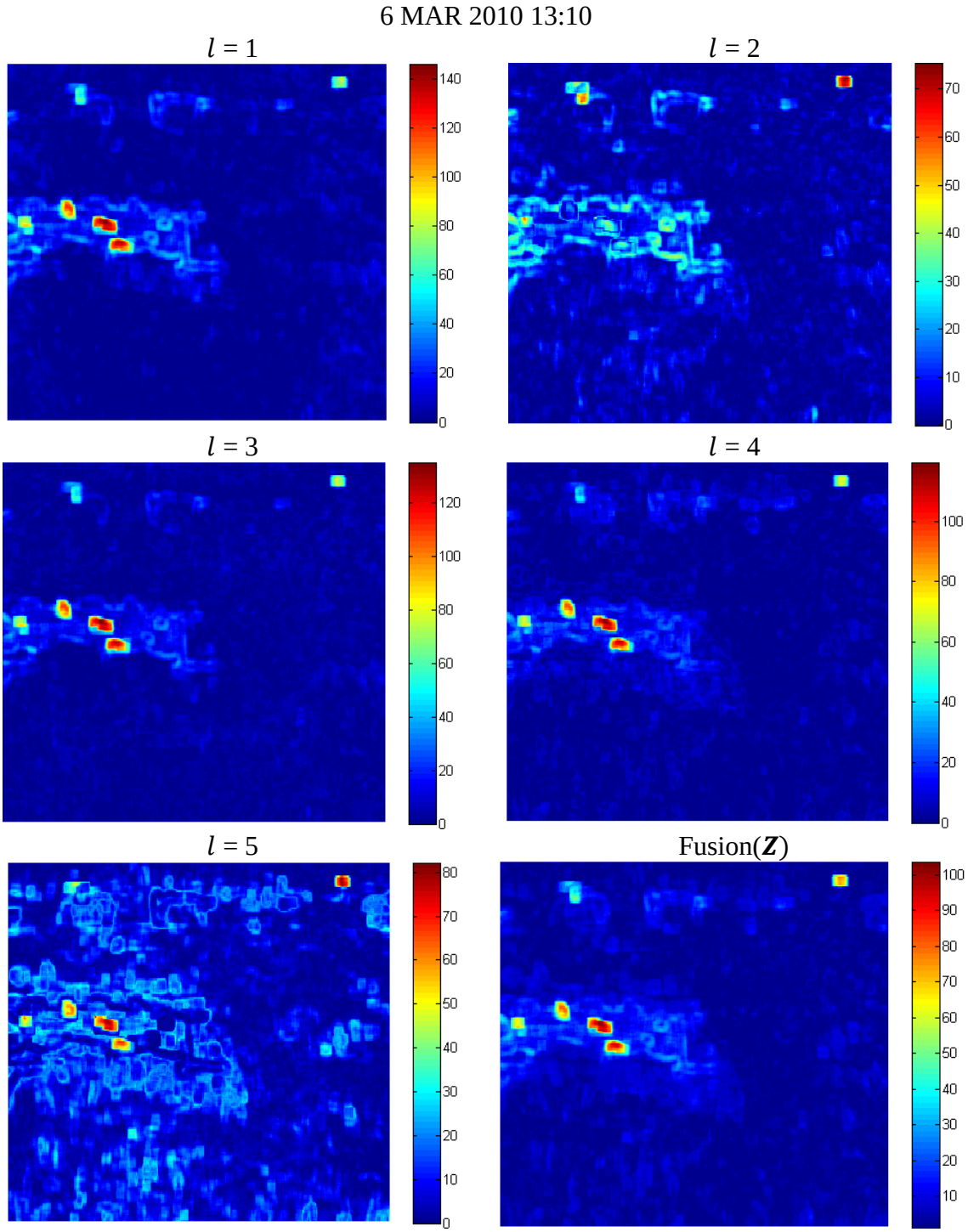

Figure 5.111 Output surfaces for the different trials and the final fused image for 6 MAR 2010 at 1310h. As result of contamination in parallel process 2, T_0 was eliminated from the output surface while the other surrogate targets energy was highly attenuated compared to the other trials. Nonetheless, by summing all M trials all manmade objects were well discriminated from the natural clutter background.

This subsection demonstrated the following key points:

1) The cumulative probability of a trial being contaminated by at least a data block can be modeled by the family of Binomial probability distribution functions.

2) The cumulative probability of contamination decreases as the number of trials (M) increases.

3) The fusion (summing) of all parallel processes introduces two benefits:

    a. It retains anomalies detected in at least one of the M parallel processes.

    b. Mitigates false alarms in the final output surface.

5.3.11.4 Adaptive Threshold for PRS-M. As shown in Subsections 5.3.5 and 5.3.8, the M-Box and the RS-M algorithms null hypothesis were easily modeled by a $\boldsymbol{\chi^2}$ with (k-1)p(p+1) degrees of freedom. Given the degrees of freedom, the user could choose a reasonable probability of miss where the cutoff value to threshold the incoming imagery **Z** is then calculated. The final output surface on the PRS-M (**Z**), however, does not follow such model when M>1 because of the final output surface is the sum of all individual output surfaces $\tilde{\mathbf{Z}}$.

In order to circumvent this problem, an adaptive threshold is proposed much like the one proposed in Subsection 5.2.3 where the cutoff threshold is obtained using Equations (5.14) and (5.15). Once the image is standardized using Equation (5.14), a robust criterion (δ) can then be imposed for all images **Z** where δ represents the number of standard deviations above the estimated mean. In this construct, pixels with values greater or equal to δ are represented by 1 in the binary image (thresholded), or 0 otherwise. It is desired that all manmade objects are represented by 1's.

5.3.11.5 PRS-M Results on Close Range PI. This subsection presents the PRS-M results for close range PI with the objective of discriminating manmade objects from natural clutter background. Figure 5.51 is used as the test scene and it is composed of a test plate placed on a pan and tilt system, a reference plate lying on the floor (right), the sidewalk where the pan and tilt system is located, and natural clutter (grass).

The test scene was processed by the PRS-M using five and 20 manually collected blocks of data with only one parallel process since the user made sure that only background information was collected as reference samples, eliminating the need for multiple parallel processes. Figures 5.112 illustrates the output surfaces for RS-M 20 (RS-20) and 30 (RS-30) reference samples and the PRS-M $(N, M) = (5,1)$ and $(20,1)$. Figure 5.112 illustrates only six out of the ten available angles that were collected due to the page size constrain. As previously stated in Subsection 5.3.8 some pixels located in test plate and/or clutter exhibited very large values and when the RS-M images were normalized, manmade object values were highly attenuated and as a result do not show up in red color as one would like to. However, when thresholded, as one shall see briefly, the manmade objects are successfully discriminated from natural clutter.

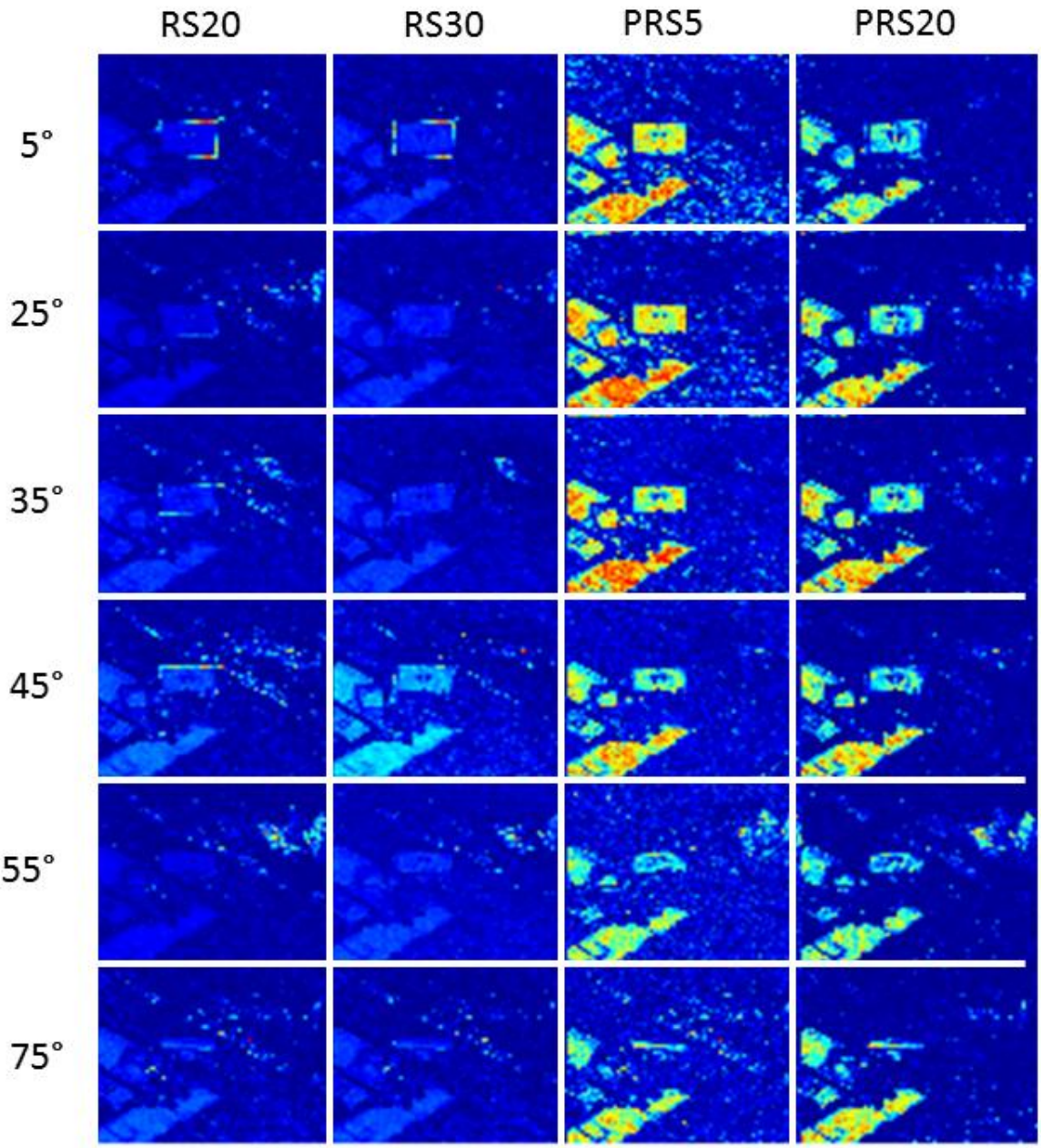

Figure 5.112 RS-20 and RS-30 and PRS-M (5,1) and PRS-M (20,1) output surfaces. Notice that the PRS-M does very well in discriminating (visually) the manmade objects from natural clutter background. In this example all anomalies that exhibited high energy values belong primarily to clutter in the RS-M while for PRS-M the anomalies exhibiting high values were from manmade objects which is highly desired.

Figure 5.113 illustrates a comparison between PRS-M and RS-M thresholded (binary) images using a constant probability of miss of $\alpha = 0.01$. A close examination of both figures demonstrates that both PRS-M $(5,1)$ and PRS-M $(20,1)$ yield similar results

in most images for manmade object discrimination. However, one can also observe that the PRS-M (20,1) has significantly less false alarms relative to PRS-M (5,1), which is directly related to the high number of reference blocks of data manually collected from the test scene (or better background characterization).

Furthermore, Figure 5.113 shows that the PRS-M performs similarly or better than the RS-M in detecting manmade objects while at the same time reducing the number of false alarms significantly.

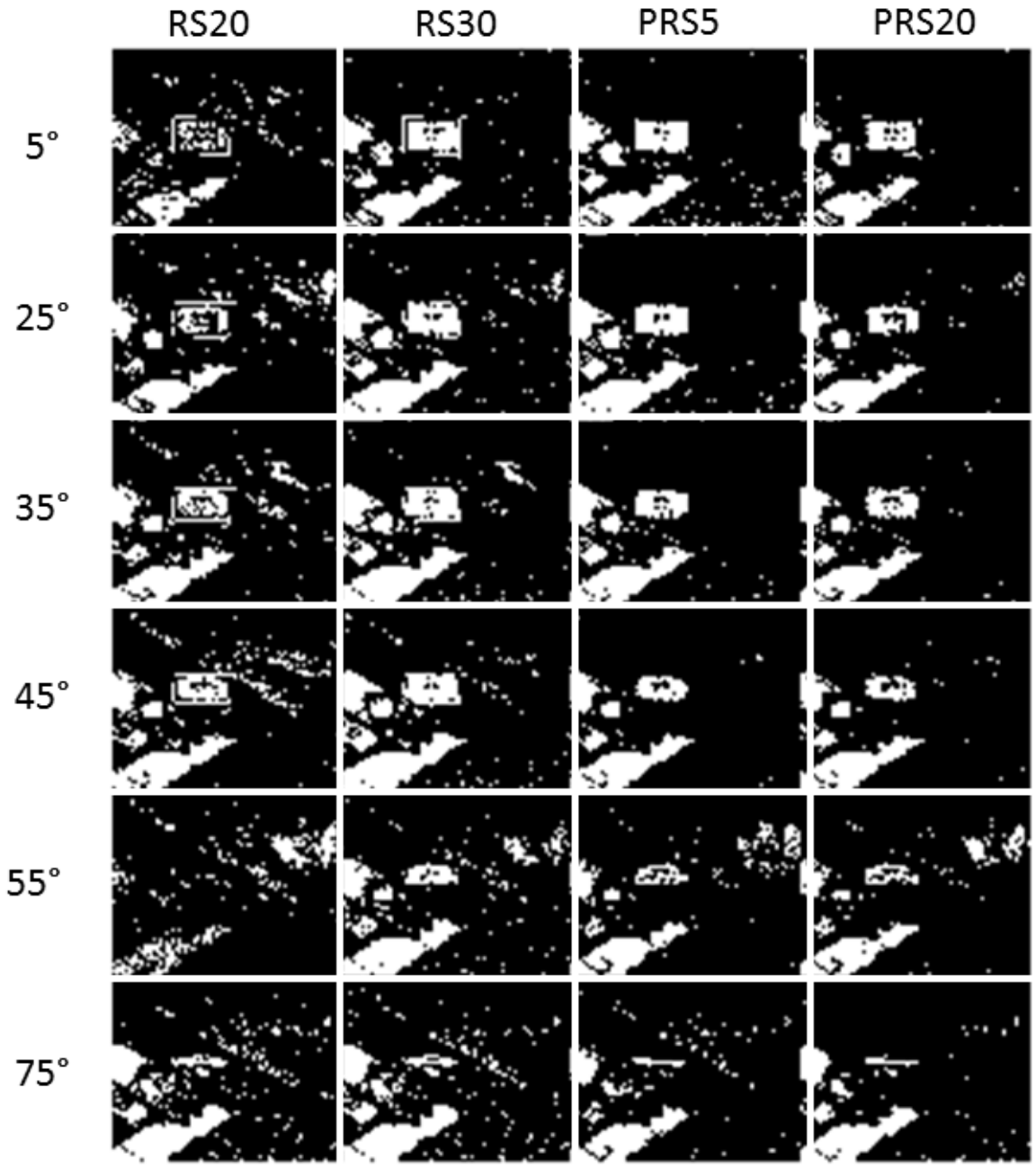

Figure 5.113 RS-M and PRS-M binary output surfaces using a threshold of $H_0|\chi^2_{\alpha=0.01}$. As the number of reference samples collected for the PRS-M increased to 20 one finds that the number of false alarms decreases relative to PRS-M (5,1) while maintaining similar detection rate. Furthermore, one finds that the PRS-M performs significantly better than the RS-M regardless of whether 20 or 30 blocks of data were collected to represent the scene background.

Before getting into performance assessment, let's highlight some key points in the discussion thus far on the PRS-M. The PRS-M detection, similarly to the RS-M detector

relies on random sampling process to characterize the background and as a result the PRS-M is also range invariant as shown in Subsection 5.3.11.4. One significant difference between the RS-M and PRS-M is that the latter performs the covariance test between the test sample and each randomly selected reference block of data (i^{th} block of data out of N blocks), which then solved (see Subsection 5.3.11.1) the limitation characteristic to the RS-M anomaly detector (Subsection 5.3.10). Consequently, this procedure makes contamination a problematic situation for the PRS-M (Subsection 5.3.11.2). Subsection 5.3.11.3 demonstrated that if one is to repeat each trial M number of times, the probability that all M trials are contaminated with at least one random block of data is a decreasing function of M. Furthermore, by fusing all M output surfaces into one single output surface; (1) the final output surface, in principle, retains all of the anomalies detected in at least one of the M parallel processes, and (2) it mitigates false alarms in the final output surface. Finally, Subsection 5.3.11.4 proposed using an adaptive threshold based on the fused output surface statistics for the PRS-M.

In conclusion, the PRS-M is an extremely versatile anomaly detector that retains the benefits of the RS-M anomaly detector while improving over RS-M deficiencies. In the next subsection a performance comparison between the PRS-M and M-Box anomaly detector is presented.

5.3.12 Performance Assessment of PRS-M

This subsection presents the implementation of the PRS-M anomaly detector and a performance comparison between the PRS-M and M-Box detector.

5.3.12.1 Algorithm Implementation. The implementation of the PRS-M is shown in this subsection.

In order to implement the PRS methodology with the M-Box algorithm, one must random sample image **X**, where **X** is a R×C test image of *p* observables s.t. $\boldsymbol{X} \in \boldsymbol{R}^{R\times C\times p}$, using a determined number of blocks of data (N), each of size $n_2=n^2$, as $\left\{\boldsymbol{W_r^{d,l}}\right\}_{\boldsymbol{d=1}}^{\boldsymbol{N}}$ where $\boldsymbol{W_r^{d,l}} \in \boldsymbol{R}^{n_2 X p}$ representing N reference samples (blocks of data) in the l^{th} parallel process (or trial) out of M possible trials.

The estimated covariance for each $\boldsymbol{W}_r^{d,l}$ and $\boldsymbol{W_t^{(i,j)}}$ is calculated as

$$\begin{aligned}\boldsymbol{\Sigma}_r^{d,l} &= \mathrm{E}\left[\left(\boldsymbol{W}_r^{d,l}-\boldsymbol{\mu}_{\boldsymbol{W}_r^{d,l}}\right)\left(\boldsymbol{W}_r^{d,l}-\boldsymbol{\mu}_{\boldsymbol{W}_r^{d,l}}\right)^T\right]\\ \boldsymbol{\Sigma}_t^{(i,j)} &= \mathrm{E}\left[\left(\boldsymbol{W}_t^{(i,j)}-\boldsymbol{\mu}_{\boldsymbol{W}_t^{(i,j)}}\right)\left(\boldsymbol{W}_t^{(i,j)}-\boldsymbol{\mu}_{\boldsymbol{W}_t^{(i,j)}}\right)^T\right],\end{aligned} \tag{5.69}$$

and the determinant for each $\boldsymbol{\Sigma}_r^{d,l} \in \boldsymbol{R}^{p\times p}$ and $\boldsymbol{\Sigma}_t^{(i,j)} \in \boldsymbol{R}^{p\times p}$ is given by

$$\begin{aligned}D_r^{d,l} &= \det\left(\boldsymbol{\Sigma}_r^{d,l}\right)\\ D_t^{(i,j)} &= \det\left(\boldsymbol{\Sigma}_t^{(i,j)}\right).\end{aligned} \tag{5.70}$$

The score between the test covariance matrix, $\boldsymbol{\Sigma_t^{(i,j)}}$, and each reference covariance, $\boldsymbol{\Sigma}_r^{d,l}$, is given by Equation (5.60) yielding a vector of N scores denoted as $\tilde{\mathbf{Z}}_d^{(i,j)}$, where $\tilde{\mathbf{Z}}_d^{(i,j)} \in \boldsymbol{R}^{d\times 1}$. Taking the minimum of $\tilde{\mathbf{Z}}_d^{(i,j)}$ (Equation (5.61)) yields a scalar representing the score of the reference sample (out of the possible N) that is closest to the test sample. When all combinations of (i,j) are taken into consideration an output surface, $\tilde{\boldsymbol{Z}}^{(\mathrm{i=1,\ldots,R-n+1,j=1,\ldots C-n+1})(l)}$, for each l^{th} parallel process is completed (see

Equation (5.67)). Finally, by fusing (summing) all M parallel processes (trials) the result yields the final output image $\boldsymbol{Z}$, Equation (5.68).

Z is then standardized using Equation (5.14) and a cutoff threshold (δ) is applied (see Equation (5.15)) and all pixel locations above the cutoff threshold are represented by 1's are considered anomalies. It is desired that all manmade objects in the scene are represented by 1's in the final thresholded (binary) image.

5.3.12.2 Performance Analysis This subsection presents a comparative performance analysis between the PRS-M and M-Box anomaly detection algorithms.

In order to determine the (N,M) configuration two approaches were taken. The first approach used *a priori* information about the scene such as the total target area (a) and the type of background while for the second approach no *a priori* information was available to the user. For the first approach the area composed of all manmade objects in the scene was calculated to be $q \sim 0.01$. Based on this information, the type of natural clutter background, and referencing Figure 5.108, five random samples seemed to be sufficient to characterize the test scene with a probability of contamination per trial of 0.049. By setting N = 5 and referencing Figure 5.109, the parameter M was set to five trials where the probability of contamination of all trials was calculated as 2.8276×10^{-7}. Although unnecessary to go beyond five trials, the performance of the PRS-M was calculated for different M = 5, 10, 15 (for same N =5) to illustrate any potential performance differences as a function of increasing M. For the second approach, N was set to 20 random samples in order to characterize an unknown scene very well. By setting N = 20 and using a q = 0.01, the probability of contamination per trial, see Figure

5.108, was measured to be 0.18. As a result, a high M was required to mitigate the inclusion of target samples in all trials. Therefore, M, the number of trials, was chosen to be 10 lowering the probability of contamination in all trials to 4×10^{-8}.

This subsection demonstrates the performance of the PRS-M algorithm versus the baseline algorithm (M-Box) using ROC curves (for the standard four timestamps 0710h, 0910h, 1310h, and 2010h for 6 MAR 2010), output surfaces, a table that illustrates the detection rate, and finally a 72-hour performance comparison for $P_{fa} = 0.0005$ for the different targets. Notice that for this comparison the false alarm range is a lot smaller than previously used which demonstrates that the PRS-M can perform extremely better than previously proposed algorithms.

Several key points will be addressed in this subsection:

1) Increasing N, the number of samples, increases the ability in successfully characterizing the test scene, resulting in higher probability of detection.

2) Increasing M, the number of parallel processes, allows for:

    a. Mitigation of the inclusion of manmade samples into the reference library which is believed to be comprised of natural objects' samples only.

    b. Mitigates false alarms in the final output surface $\boldsymbol{Z}$.

3) PRS-M demonstrates exceptionally high performance especially in the low false alarm rate region compared to the baseline for a $P_{fa} \leq 0.001$.

Figure 5.114 illustrates the ROC curves for T_0 by comparing the baseline algorithm (M-Box) with the PRS-M for different combinations of N and M for a $P_{fa} \leq 0.001$. Several key points can be observed in this figure:

1) Increasing the number of random samples (N) increased the PRS-M probability of detection especially in the low false alarm rate region.

2) The baseline was the worst performing metric for all timestamps with the exception of 1310h.

3) PRS-M (20,10) performed the best throughout the four timestamps.

4) The remaining PRS-M metrics performed better than the baseline for all timestamps with the exception of 1310h where (5,5) and (5,15) performed similarly to the baseline.

5) PRS-M (5,15) performed slightly better than (5,5) and (5,10) for 0710h, 0910h, and 1310h.

Observing the T_0 ROC curves in Figure 5.114, the following probability of detection, in the order of best score, for a $P_{fa} = 0.0005$ is as follows: PRS-M (20,10) with a $P_d = 0.97, 0.77, 1.00, \text{and } 0.97$ for timestamps 0710h, 0910h, 1310h, and 2010h, respectively. Followed by PRS-M (5,15) with a $P_d = 0.83, 0.64, 1.00, \text{and } 0.95$, then (5,10) with a $P_d = 0.84, 0.55, 1.00, \text{and } 0.93$, PRS-M (5,5) with a $P_d = 0.81, 0.55, 1.00, \text{and } 0.89$, and finally the baseline with a $P_d = 0.28, 0.51, 1.00, \text{and } 0.87$.

Figure 5.115 illustrates the performance between the two metrics for T_{90}. Once again, in most cases one can observe that the PRS-M performs slightly better than the baseline in the low false alarm region with one exception, shown on 1310h.

PRS-M (5,5) and (5,10) performed very similarly to each other for 0710h and 0910h while trailing PRS-M (5,15) for most of the ROC curves. However, for 1310h and 2010h all combinations of N=5 performed very similarly. In contrast, PRS-M (20,10) demonstrated the best probability of detection of all metrics for 0710h, 0910h, and 2010h, and similar performance for 1310h.

Using the same $P_{fa} = 0.0005$ as reference, all metrics performed similarly to each other with a ± 0.02 detection rate difference of each other with PRS-M (20,10) performing similarly to the baseline with a $P_d = 0.87, 0.98, 1.00, \text{and } 0.77$.

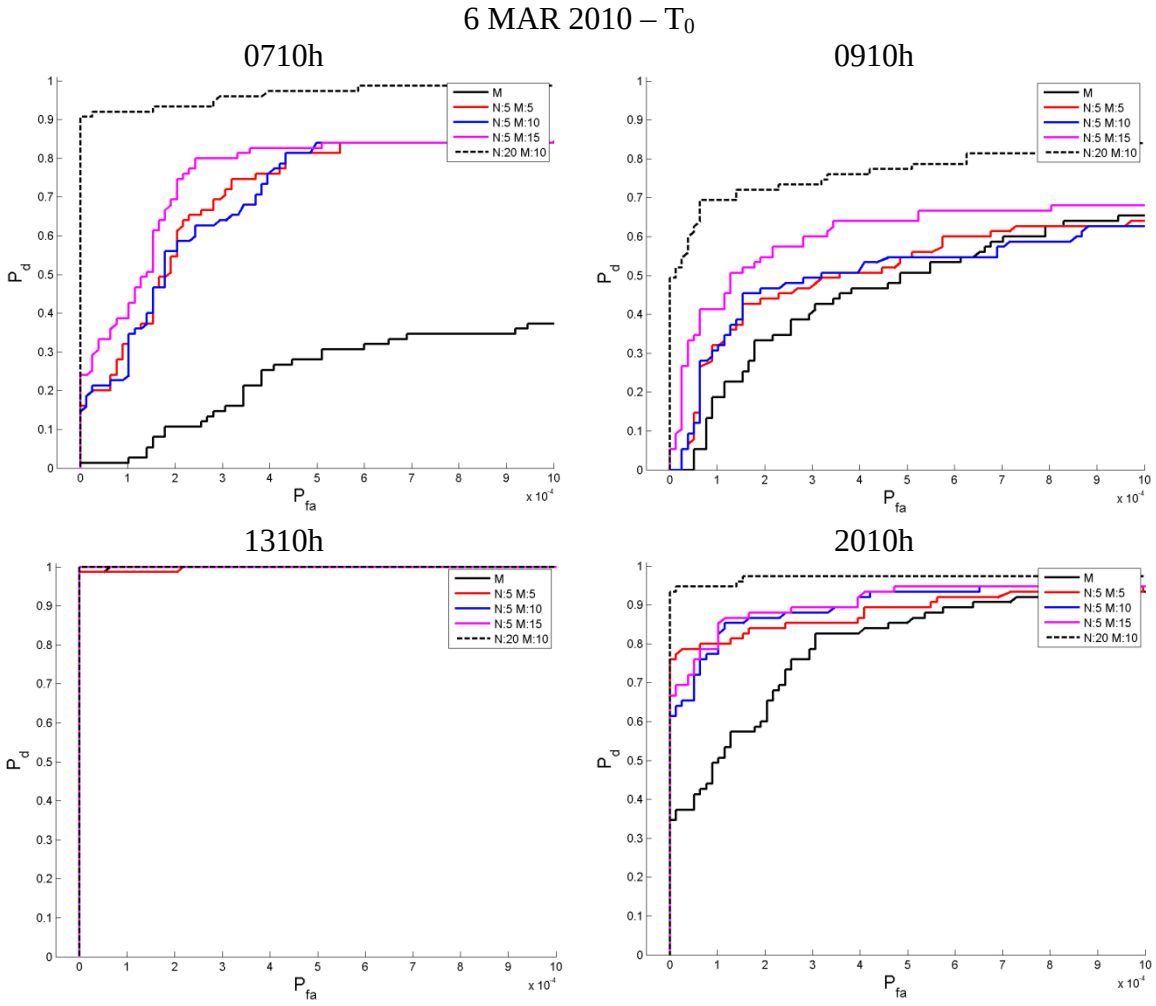

Figure 5.114 ROC curves for T_0 comparing the performance between the baseline and PRS-M for different combinations of (N, M). For a $P_{fa} = 0.0005$ PRS-M (20,10) achieved the best detection rate with a $P_d = 0.97, 0.77, 1.00, \text{and } 0.97$ for timestamps 0710h, 0910h, 1310h, and 2010h, respectively. Followed by PRS-M (5,15) with a $P_d = 0.83, 0.64, 1.00, \text{and } 0.95$, then PRS-M (5,10) with a $P_d = 0.84, 0.55, 1.00, \text{and } 0.93$, next is PRS-M (5,5) with a $P_d = 0.81, 0.55, 1.00, \text{and } 0.89$, and finally the baseline with a $P_d = 0.28, 0.51, 1.00, \text{and } 0.87$.

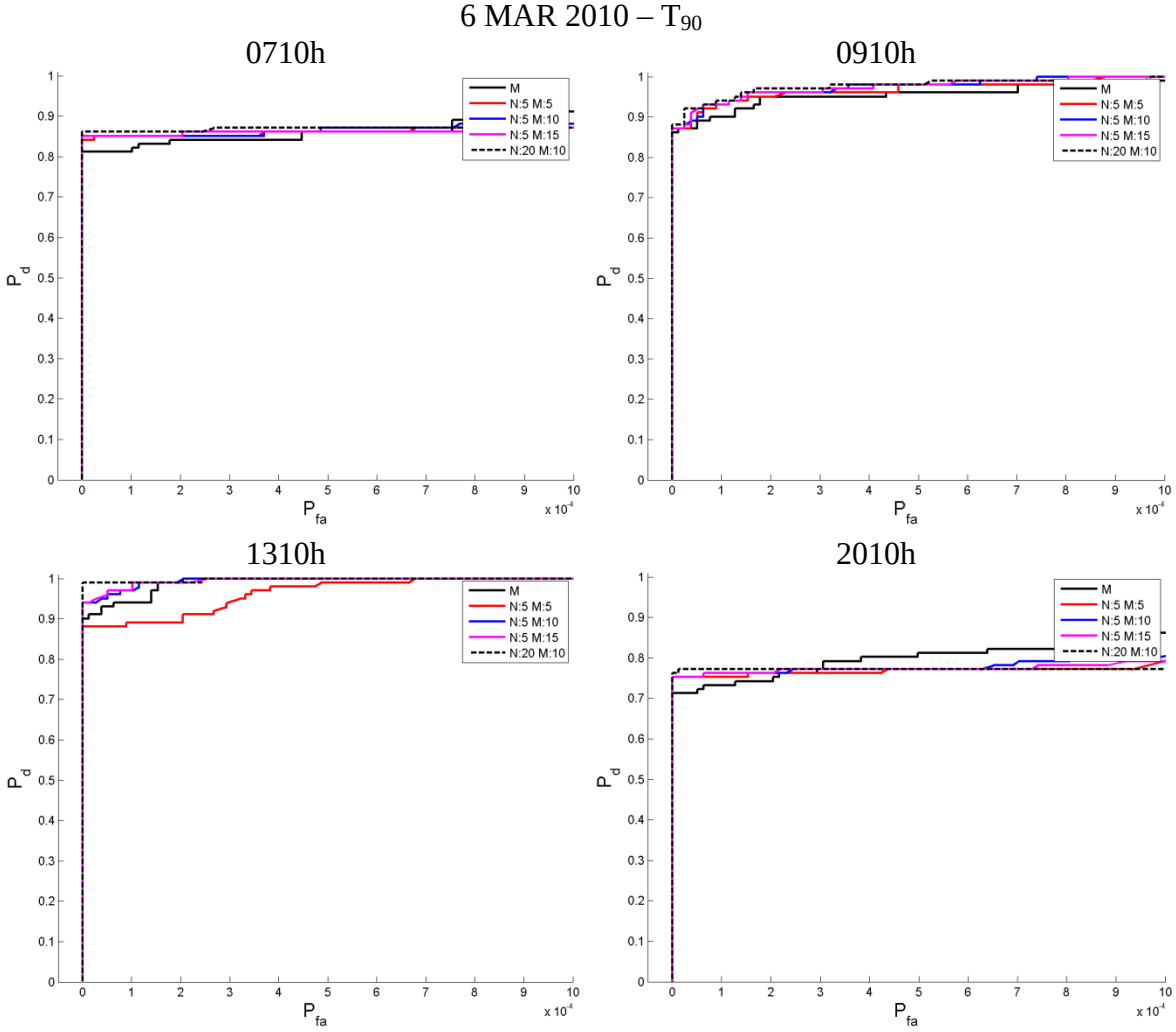

Figure 5.115 ROC curves for T_{90} comparing the performance between the baseline and PRS-M for different combinations of (N, M). PRS-M (20,10) performed the best in the low false alarm region of the ROC curve followed by PRS-M (5,10) and PRS-M (5,15). Using the same $P_{fa} = 0.0005$ as the threshold, all metrics performed similarly to each other with a ± 0.02 detection rate difference of each other with PRS-M (20,10) once again performing the best with a $P_d = 0.87, 0.98, 1.00, \text{and } 0.77$.

The performance of T_{135}, shown in Figure 5.116, demonstrates the same trend that was observed in the previous two figures (Figures 5.114 and 5.115) where the PRS-M in general performs the best relative to the baseline in the low false alarm region of the ROC curve. One particular difference in Figure 5.115 happens at 1310h where PRS-M (5,5) performs slightly worse than all other metrics for $0 \leq P_{fa} \leq 0.0007$.

Nonetheless, on average for a $P_{fa} = 0.0005$, PRS-M (20,10) once again performed very well with a $P_d = 0.75, 0.87, 0.99, \text{and } 0.63$, followed by PRS-M (5,5,), PRS-M (5,10), and PRS-M (5,15) with a ± 0.01 detection rate difference of each other with a $(P_d = 0.72, 0.86, 0.99, \text{and } 0.61)$, and finally the baseline with a $P_d = 0.62, 0.80, 0.99, \text{and } 0.57$.

In Figure 5.117, blackbody ROC curves, some differences occur between the baseline and the PRS-M relative to the previous figures. For example, at the low false alarm rate region ($P_{fa} = 0.0001$) one observes that at timestamp 0710h all metrics have the same performance, however at $P_{fa} = 0.0005$, the baseline starts to perform better than the PRS-M algorithm with PRS-M (20,10) trailing all other. At timestamp 0910h and using $P_{fa} < 0.0002$ as a reference, once again the PRS-M performed better than the baseline. Approaching the level of $P_{fa} = 0.0005$, the baseline performance surpasses the PRS-M (20,10), PRS-M (5,10), and PRS-M (5,15) with PRS-M (20,10) demonstrating the worst performance (probability of detection). For timestamps 0910h and 2010h, the baseline performed worse or similarly to PRS for $P_{fa} < 0.0002$ and as the P_{fa} increased the baseline performed similarly (same probability of detection) to PRS-M (5,10), PRS-M (5,15), and PRS-M (20,10). Finally, one can observe that timestamp 2010h trends very similarly to 0710h with the baseline underperforming at $P_{fa} < 0.0002$ and over

performing the PRS-M for an increasing false alarm rate. In conclusion, the baseline was the best performing metric if the reference false alarm rate remains the same as the previous figures or $P_{fa} = 0.0005$, where the baseline detection rate was measured to be $P_d = 0.91, 0.71, 0.93, \text{and } 0.86$ for timestamps 0710h, 0910h, 1310h and 2010h, respectively. PRS-M (5,10) was second best performing metric with a $P_d = 0.86, 0.74, 0.93, \text{and } 0.67$, followed by PRS-M (5,15) with a $P_d = 0.83, 0.74, 0.93, \text{and } 0.67$, PRS-M (20,10) with a $P_d = 0.74, 0.79, 0.93, \text{and } 0.67$, and finally PRS-M (5,5) with a $P_d = 0.83, 0.64, 0.88, \text{and } 0.64$.

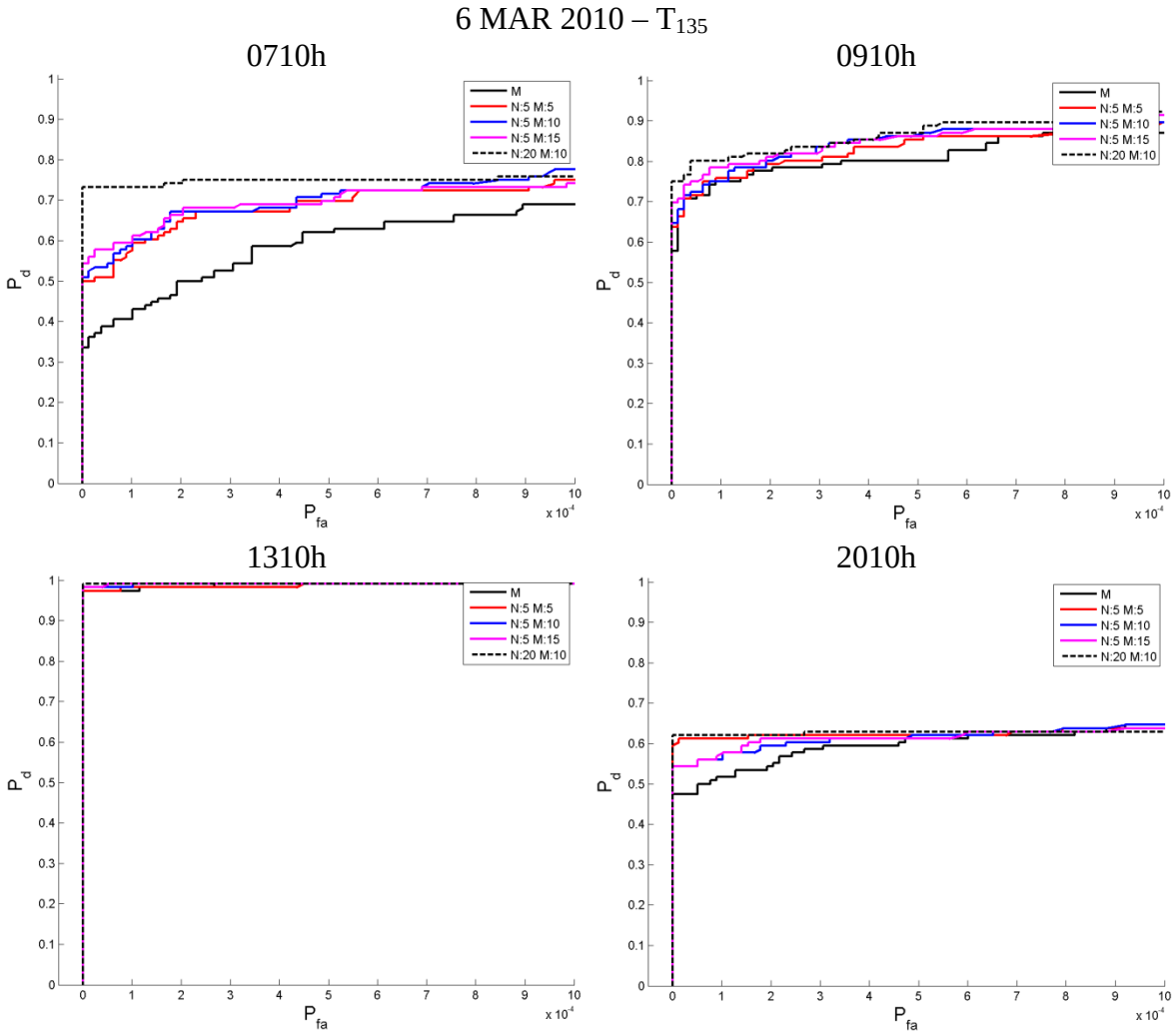

Figure 5.116 ROC curves for T_{135} comparing the performance between the baseline and PRS-M for different combinations of (N,M). PRS performs the best relative to the baseline in the low false alarm region of the ROC curve. For a $P_{fa} = 0.0005$, PRS-M 20,10) once again performed the best with a $P_d = 0.75, 0.87, 0.99,$ and 0.63, followed by PRS-M (5,5), PRS-M (5,10), and PRS-M (5,15) with a ± 0.01 detection rate difference of each other with a ($P_d = 0.72, 0.86, 0.99,$ and 0.61), and finally the baseline with a $P_d = 0.62, 0.80, 0.99,$ and 0.57.

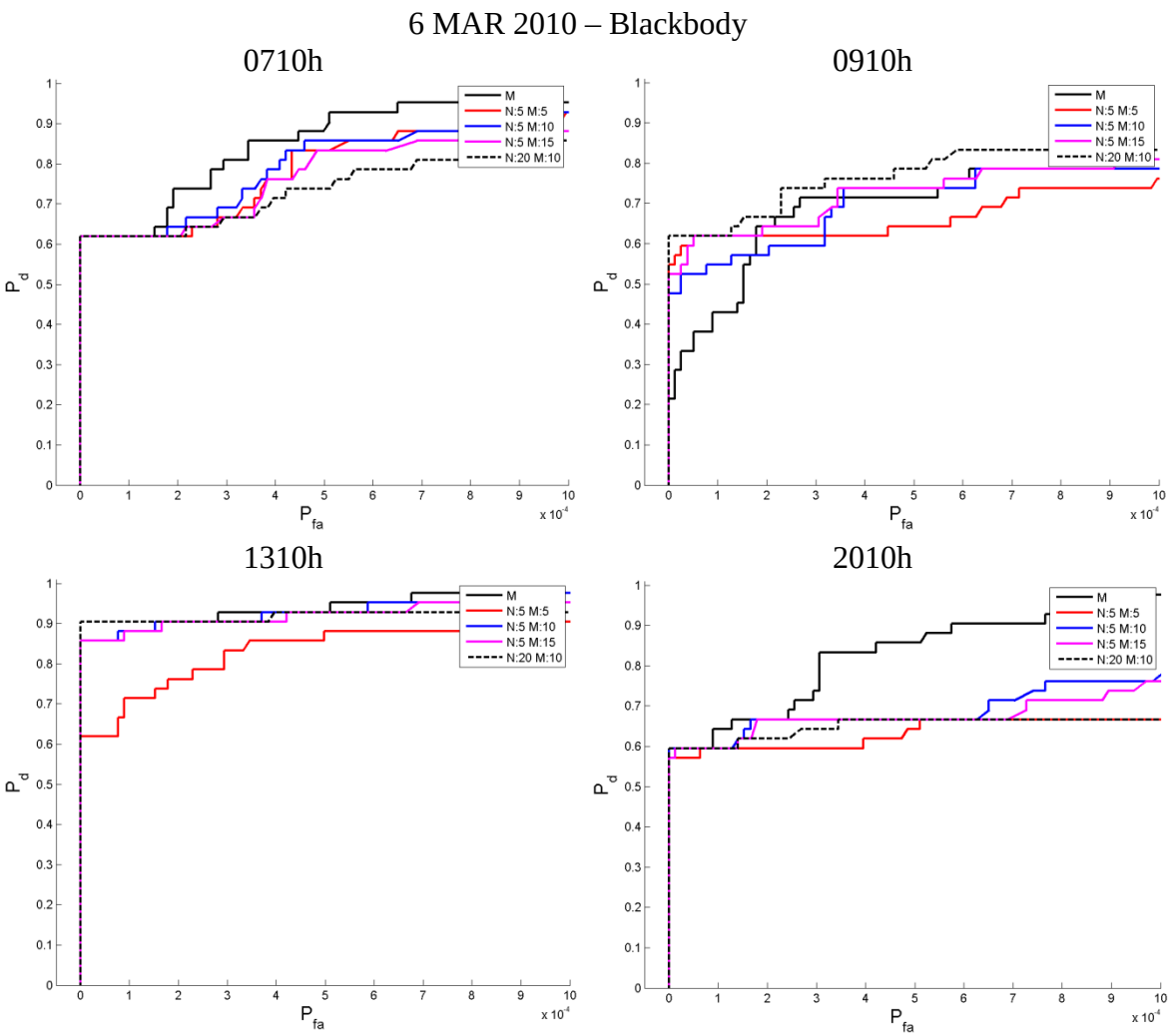

Figure 5.117 ROC curves for Blackbody comparing the performance between the baseline and PRS-M for different combinations of (N,M). For a reference $P_{fa} = 0.0005$, the baseline was the best performing metric with a $P_d = 0.91, 0.71, 0.93,$ and 0.86 for timestamps 0710h, 0910h, 1310h and 2010h, respectively. PRS-M (5,10) was second best performing metric with a $P_d = 0.86, 0.74, 0.93,$ and 0.67, followed by (5,15) with a $P_d = 0.83, 0.74, 0.93,$ and 0.67, (20,10) with a $P_d = 0.74, 0.79, 0.93,$ and 0.67, and finally (5,5) with a $P_d = 0.83, 0.64, 0.88,$ and 0.64.

In Figure 5.118, observation tower ROC curves, the PRS-M performs very well compared to the baseline in discriminating the observation tower in the test scenes, which is similarly to what was observed for the RS-M in Subsection 5.3.9.2. For the reference $P_{fa} = 0.0005$ one can observe that the baseline did not detect the observation tower at all ($P_d = 0.00$) for any of the timestamps, while PRS-M (20,10) was the best performing metric with a $P_d = 1.00$ for all timestamps, followed by PRS-M (5,15) and PRS-M (5,5) with the same probability of detection ($P_d = 1.00, 0.88, 1.00, \text{and } 0.80$) for 0710h, 0910h, 1310h, and 2010h, respectively. Finally, PRS-M (5,10) was the worst performing metric of all PRS-M combinations with a $P_d = 1.00, 0.53, 1.00, \text{and } 0.80$ as a result of a performance degradation on timestamp 0910h potentially due to a set of bad "quality" background samples.

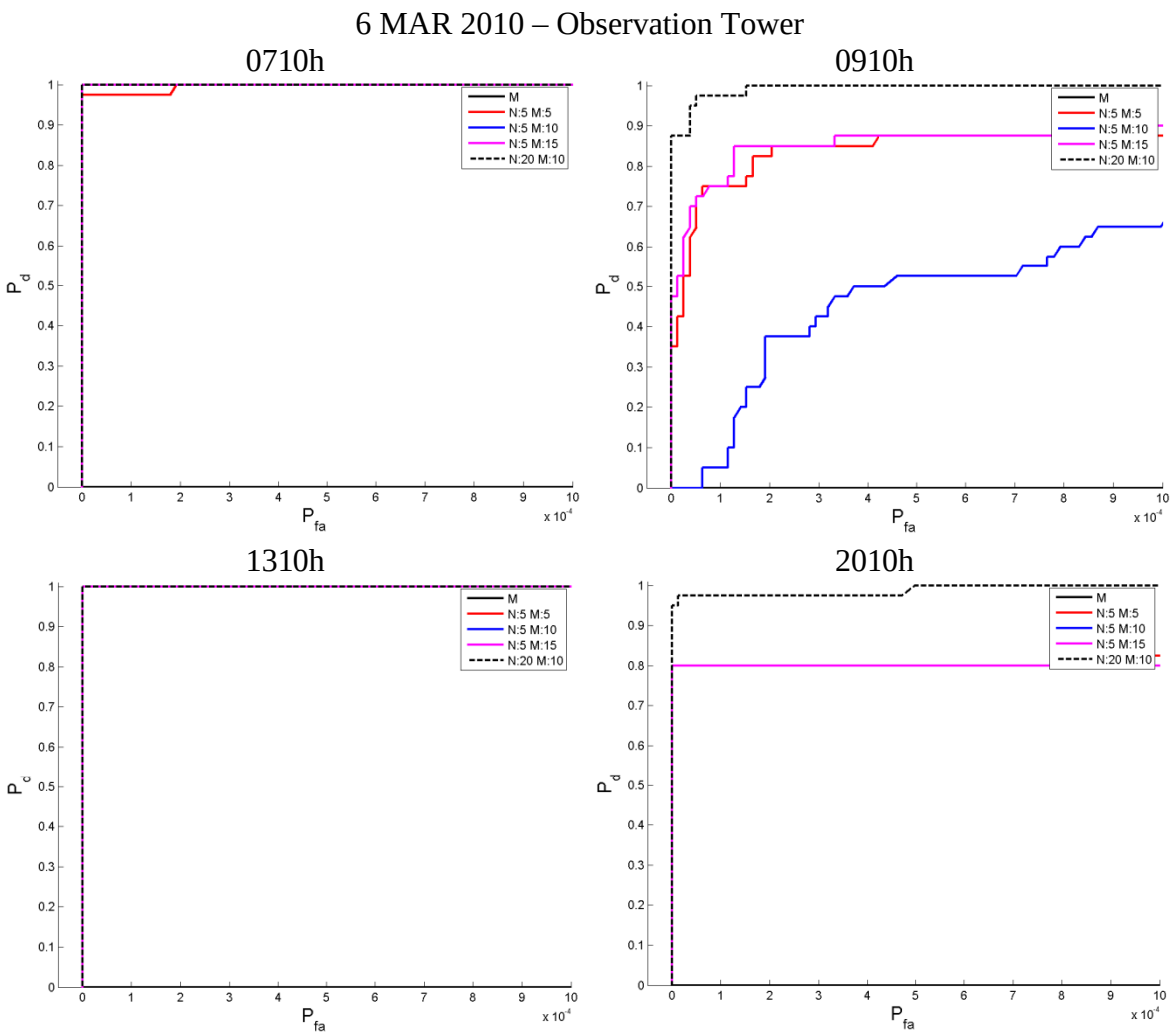

Figure 5.118 ROC curves for observation tower comparing the performance between the baseline and different combination of PRS-M. PRS-M (20,10) was the best performing metric with a $P_d = 1.00$ for all timestamps at $P_{fa} = 0.0005$, followed by PRS-M (5,15) and PRS-M (5,5) with the a probability of detection ($P_d = 1.00, 0.88, 1.00,$ and 0.80) for 0710h, 0910h, 1310h, and 2010h respectively, followed by PRS-M (5,10) with a $P_d = 1.00, 0.53, 1.00,$ and 0.80, and finally the baseline with no detection whatsoever for all timestamps.

Finally, If one combines all objects (T_0, T_{90}, T_{135}, blackbody, and observation tower) into a single class, the performance of each metric is shown in Figure 5.119 where the PRS-M (20,10) was clearly the best performing metric for all timestamps, followed by PRS-M (5,15). There is a clear flip flopping between PRS-M (5,5) and PRS-M (5,10) for the third best performing metric where the former performs better at 0910h and the latter at 1310h. Nonetheless, the baseline is the worst performing metric regardless of timestamp. Again, for a reference $P_{fa} = 0.0005$, PRS-M (20,10) demonstrated a very good probability of detection, $P_d = 0.85, 0.89, 0.99, \text{and } 0.78$, followed by PRS-M (5,15) with a $P_d = 0.82, 0.84, 0.99, \text{and } 0.75$, then PRS-M (5,5) ($P_d = 0.81, 0.81, 0.98, \text{and } 0.74$), next PRS-M (5,10) with a $P_d = 0.83, 0.78, 0.98, \text{and } 0.75$, and finally the baseline with a $P_d = 0.58, 0.69, 0.88, \text{and } 0.67$.

Table 5.12 illustrates the probability of detection for the M-Box algorithm (baseline), and PRS-M (5,5), PRS-M (5,15), and PRS-M (20,10) for a $P_{fa} = 0.0005$ for six different timestamps: 0210h, 0710h, 0910h, 1310h, 2010h, and 2310h for all manmade objects in the scene including the overall performance. For each target (T_0, T_{90}, T_{135}, observation tower, blackbody, and overall), the red color indicates the metrics where the detection rate was the highest (P_{best}) at a given timestamp, green represents performances where the detection rate was within a 0.03 difference of P_{best}, and finally, the color black indicates the detection rates that do not fall in the previous two categories.

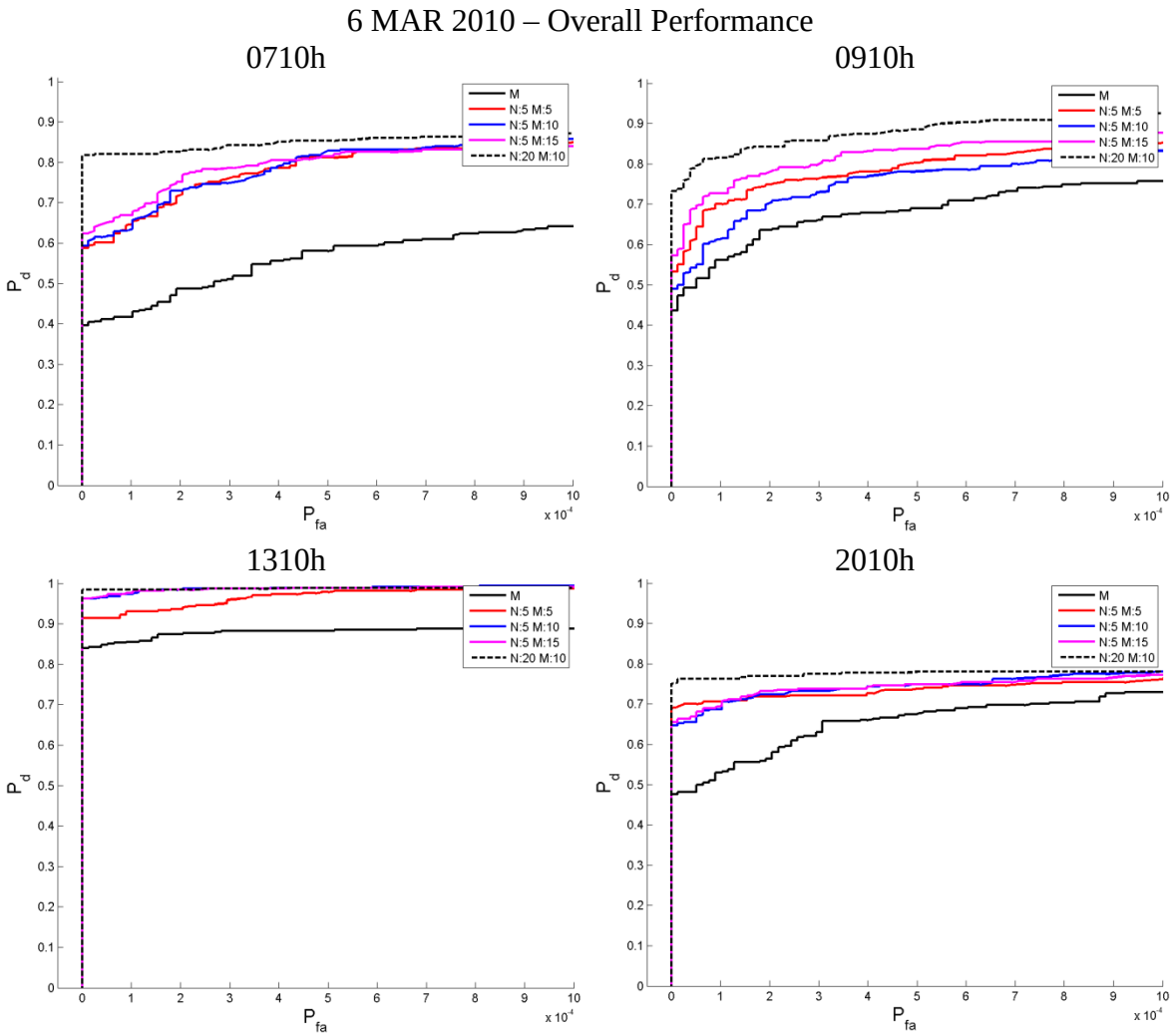

Figure 5.119 ROC curves for overall performance comparing the performance between the baseline and PRS-M for different combinations of (N,M). for the reference $P_{fa} = 0.0005$, PRS-M (20,10) demonstrated a detection performance of $P_d = 0.85, 0.89, 0.99, \text{and } 0.78$, followed by PRS-M (5,15) with a $P_d = 0.82, 0.84, 0.99, \text{and } 0.75$, then PRS-M (5,5) ($P_d = 0.81, 0.81, 0.98, \text{and } 0.74$), next PRS-M (5,10) with a $P_d = 0.83, 0.78, 0.98, \text{and } 0.75$, and finally the baseline with a $P_d = 0.58, 0.69, 0.88, \text{and } 0.67$.

Overall, PRS-M (20,10) clearly outperformed all other metrics for T_0, T_{90}, T_{135}, observation tower, and overall detection for all timestamps, with only the baseline outperforming PRS-M (20,10) for the blackbody. PRS-M (5,5) and PRS-M (5,15) had similar performance for T_0, T_{90}, blackbody, and the observation tower while PRS-M (5,5) performed slightly better for T_{135}, and PRS-M (5,15) performed better for the overall detection rate. Finally, the baseline was the worst performing metric for all manmade objects with the exception of the blackbody where its probability of detection was measured to be the best relative to all the metrics. The best average probability of detection for all timestamps for T_0 was demonstrated by PRS-M (20,10) with a $P_d = 0.90$, followed by PRS-M (5,5) and PRS-M (5,15) with a $P_d = 0.74$, and finally the baseline with a $P_d = 0.53$. For T_{90}, all combinations of the PRS-M performed similarly to each other with a $P_d \sim 0.85$ followed by the baseline with a $P_d = 0.83$. PRS-M (20,10) once again performed the best for T_{135} with an average $P_d = 0.73$ over all timestamps, followed by PRS-M (5,5) with a $P_d = 0.70$, PRS-M (5,15) with a $P_d = 0.68$, and finally the baseline with a $P_d = 0.64$. The baseline had the best probability of detection in discriminating the blackbody from clutter with an average $P_d = 0.83$ over all timestamps, followed by PRS-M (5,15), PRS-M (20,10), and PRS-M (5,5) with a $P_d = 0.75, 0.73, \text{and } 0.71$, respectively. However, for the observation tower PRS-M (20,10) exhibited the best average probability of detection ($P_d = 0.99$), followed by PRS-M (5,5) and PRS-M (5,15) with a $P_d = 0.88$, and finally the baseline with zero detection. Overall, PRS-M (20,10) exhibited the best average probability of detection with a $P_d = 0.93$, followed by PRS-M (5,5) and PRS-M (5,15) with the same detection rate of $P_d = 0.88$, and finally the baseline with a probability of detection of $P_d = 0.62$.

Table 5.12 Performance Comparison Between M-Box and PRS-M for Different Timestamps for a $P_{fa} = 0.0005$

	T_0				T_{90}				T_{135}			
	M	**PRS-M (5,5)**	**PRS-M (5,15)**	**PRS-M (20,10)**	**M**	**PRS-M (5,5)**	**PRS-M (5,15)**	**PRS-M (20,10)**	**M**	**PRS-M (5,5)**	**PRS-M (5,15)**	**PRS-M (20,10)**
0210h	0.13	0.35	0.21	**0.75**	0.63	**0.71**	**0.70**	**0.73**	0.29	0.41	0.35	**0.48**
0710h	0.28	0.81	0.83	**0.97**	**0.86**	**0.86**	**0.86**	**0.87**	0.62	0.70	0.70	**0.75**
0910h	0.51	0.55	0.64	**0.77**	**0.96**	**0.98**	**0.98**	**0.98**	0.80	**0.85**	**0.86**	**0.87**
1310h	**1.00**	**1.00**	**1.00**	**1.00**	**1.00**	**1.00**	**1.00**	**1.00**	**0.99**	**0.99**	**0.99**	**0.99**
2010h	0.87	0.89	**0.95**	**0.97**	**0.81**	0.77	0.77	0.77	**0.61**	**0.62**	**0.61**	**0.63**
2310h	0.41	0.85	0.83	**0.95**	0.73	**0.77**	**0.77**	**0.77**	0.53	**0.62**	0.58	**0.63**

Table 5.12 Performance Comparison Between M-Box and PRS-M for Different Timestamps for a $P_{fa} = 0.0005$ (Continuation)

	Blackbody				**Observation tower**				**Overall**			
	M	**PRS-M (5,5)**	**PRS-M (5,15)**	**PRS-M (20,10)**	**M**	**PRS-M (5,5)**	**PRS-M (5,15)**	**PRS-M (20,10)**	**M**	**PRS-M (5,5)**	**PRS-M (5,15)**	**PRS-M (20,10)**
0210h	**0.71**	0.62	0.62	0.64	0.0	0.78	0.80	**0.95**	0.36	0.54	0.50	**0.67**
0710h	**0.91**	0.83	0.83	0.74	0.0	**1.00**	**1.00**	**1.00**	0.58	0.81	**0.82**	**0.85**
0910h	0.71	0.64	0.74	**0.79**	0.0	0.88	0.88	**1.00**	0.69	0.81	0.84	**0.89**
1310h	**0.93**	0.88	**0.93**	**0.93**	0.0	**1.00**	**1.00**	**1.00**	0.88	**0.98**	**0.99**	**0.99**
2010h	**0.86**	0.64	0.67	0.67	0.0	0.80	0.80	**1.00**	0.67	0.74	**0.75**	**0.78**
2310h	**0.86**	0.67	0.71	0.64	0.0	0.85	0.80	**1.00**	0.54	0.74	0.72	**0.77**

Figure 5.120 illustrates the broadband imagery for each of the timestamps for visual appreciation (left images) and the output surfaces (right quad images) for the M-Box algorithm and the different PRS-M combinations (5,5), (5,15), and (20,10). As shown in the previous figures (ROC curves) as N increased from $N = 5$ to $N = 20$, the ability in discriminating all manmade objects in the scene increased as well. As previously stated anomaly detectors do not need to find the whole target; they need, however, find a portion of the target with the lowest false alarm rate possible for further inquisition by other sensors or algorithms. In this case and shown in previous figures and tables, PRS-M (20,10) performs very well in detecting the necessary regions of interest where manmade objects are located with very few false alarms. One can also observe a reduction of false alarms as N remained the same and M increased from five to 15 parallel processes. This is expected because one is averaging a higher number of parallel processes ($M = 5$ to 15) and the random sampling process within each parallel process is independent of all others, therefore, the locations of the false alarms are also random for each individual trials. As such, the score of all false alarm locations should diminish as M increases, when averaged, while retaining the target information which, when using an effective detector, should always be in a deterministic location.

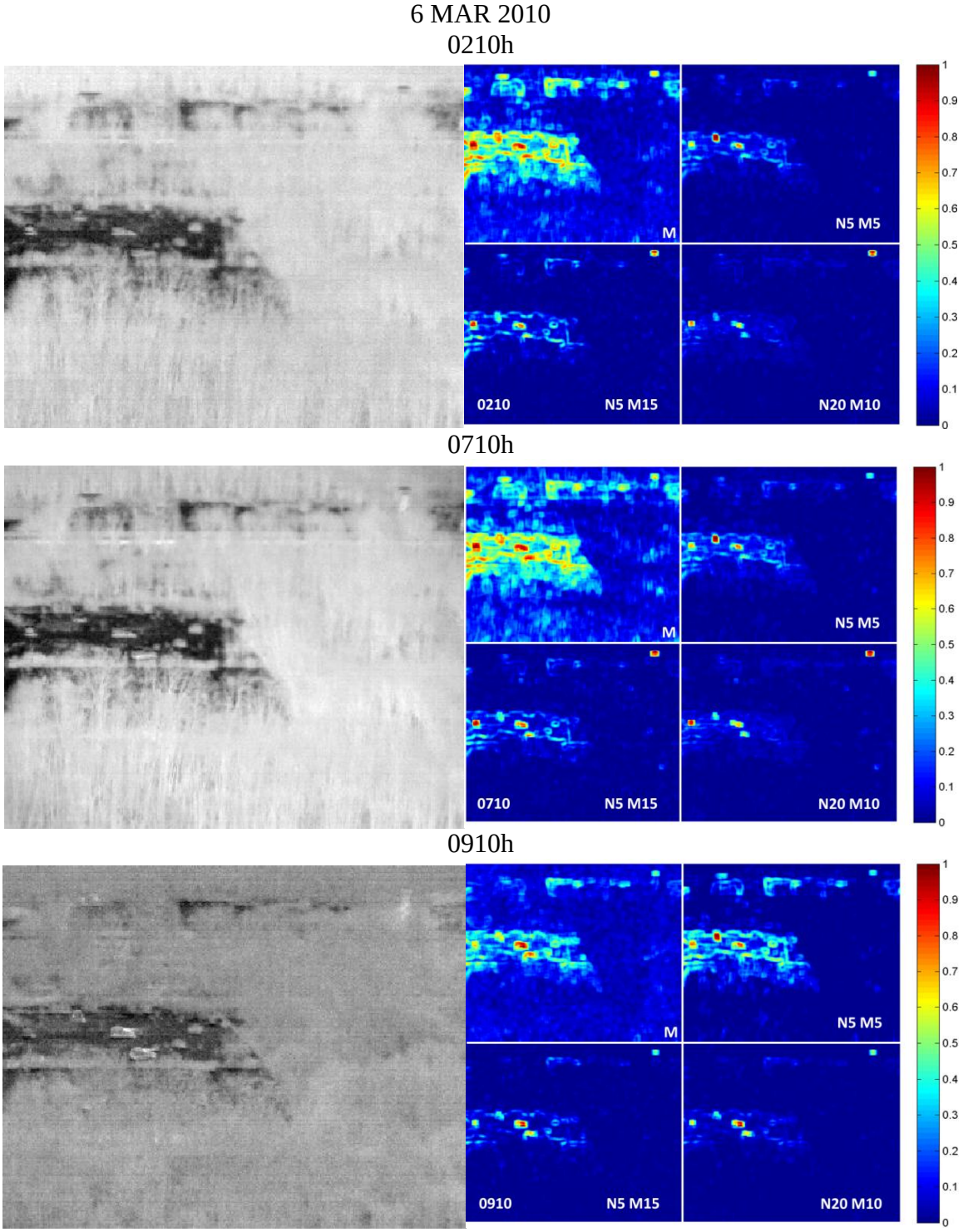

Figure 5.120 Output surfaces for M-Box and PRS-M (5,5), PRS-M (5,15), and PRS-M (20,10) for all six timestamps.

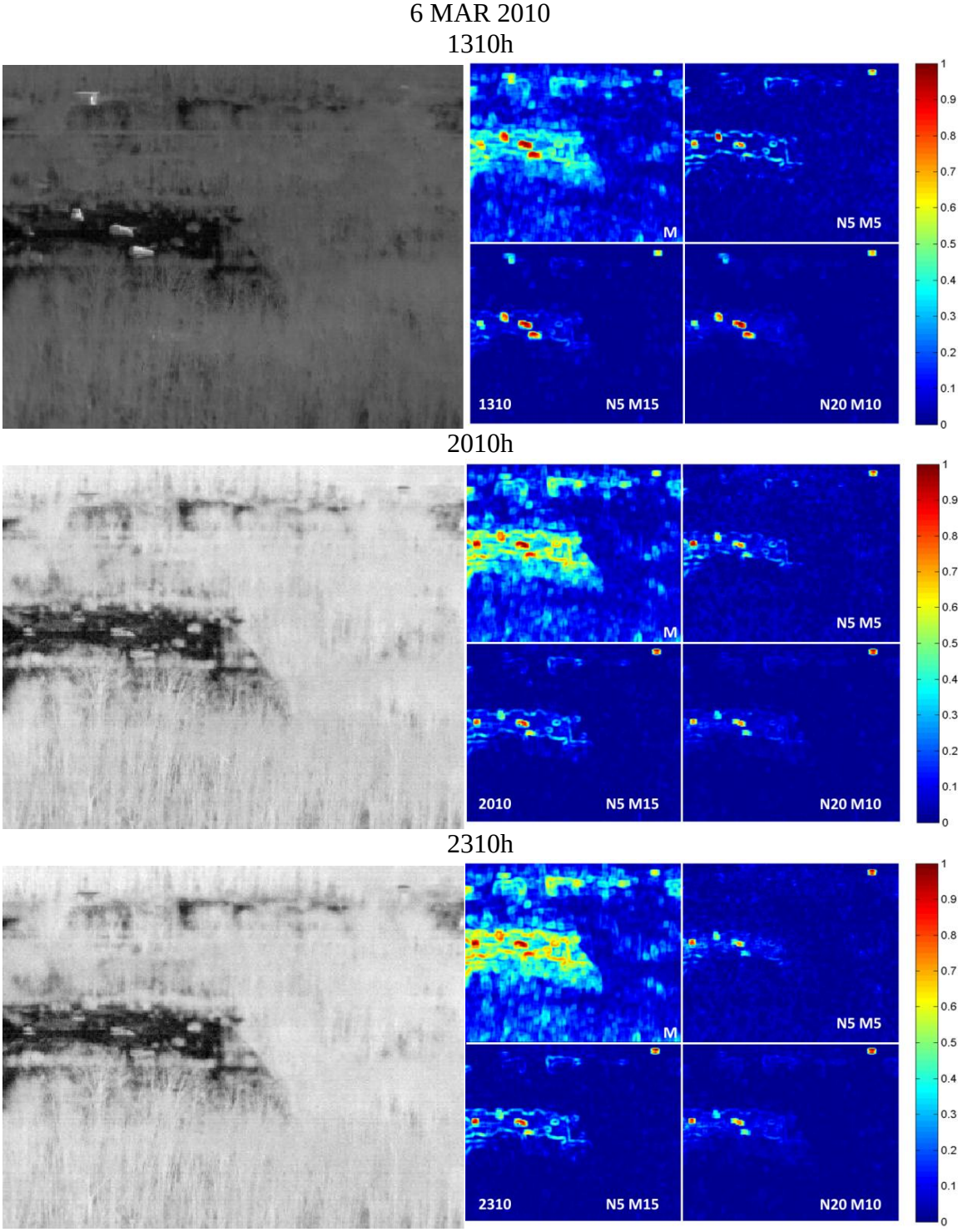

Figure 5.120 Output surfaces for M-Box, PRS-M (5,5), PRS-M (5,15), and PRS-M (20,10) for all six timestamps. (Continuation)

Figures 5.121 through 5.125 examine the 72-hour performance for each of the manmade objects present in the scene as well as the overall performance (Figure 5.126) for the baseline and PRS-M (5,5), PRS-M (5,15), and PRS-M (20,10). Figure 5.121 illustrates the 72-hour performance metric for the detection of T_0 for 6-8 MAR 2010. As explained with previous 72-hour figures, Subsections 5.3.6.2 and 5.3.9.2, there are three periods of high humidity found in the beginning of day 2 and 3 and the last one at the end of day 3. Figure 5.121 demonstrates that PRS-M (20,10) performs very well for most of the degradation periods found in the 72-hour period. The first period of adverse weather, beginning of day 2, the PRS-M (20,10) performs very well compared to the remaining metrics with the baseline clearly performing the worst. Conversely, for the beginning of day 3, although once again PRS-M (20,10) performs very well, the worst performing metric this time was measured to be the PRS-M (5,15). Finally, for the last adverse weather event at the end of day 3 no metric performed very well with the exception of PRS-M (5,5) which exhibited a $P_d \sim 0.05$ of T_0 during this period of time. For the periods of high contrast, all metrics performed very similarly to each other with a probability of detection above 0.97 for all three days. The 72-hour average T_0 probability of detection from highest to lowest was PRS-M (20,10), PRS-M (5,5), PRS-M (5,15), and the baseline with a $P_d = 0.89, 0.85, 0.82,$ and 0.80, respectively. For this target set, PRS-M (20,10) demonstrated almost 0.10 probability of detection difference compared to the baseline.

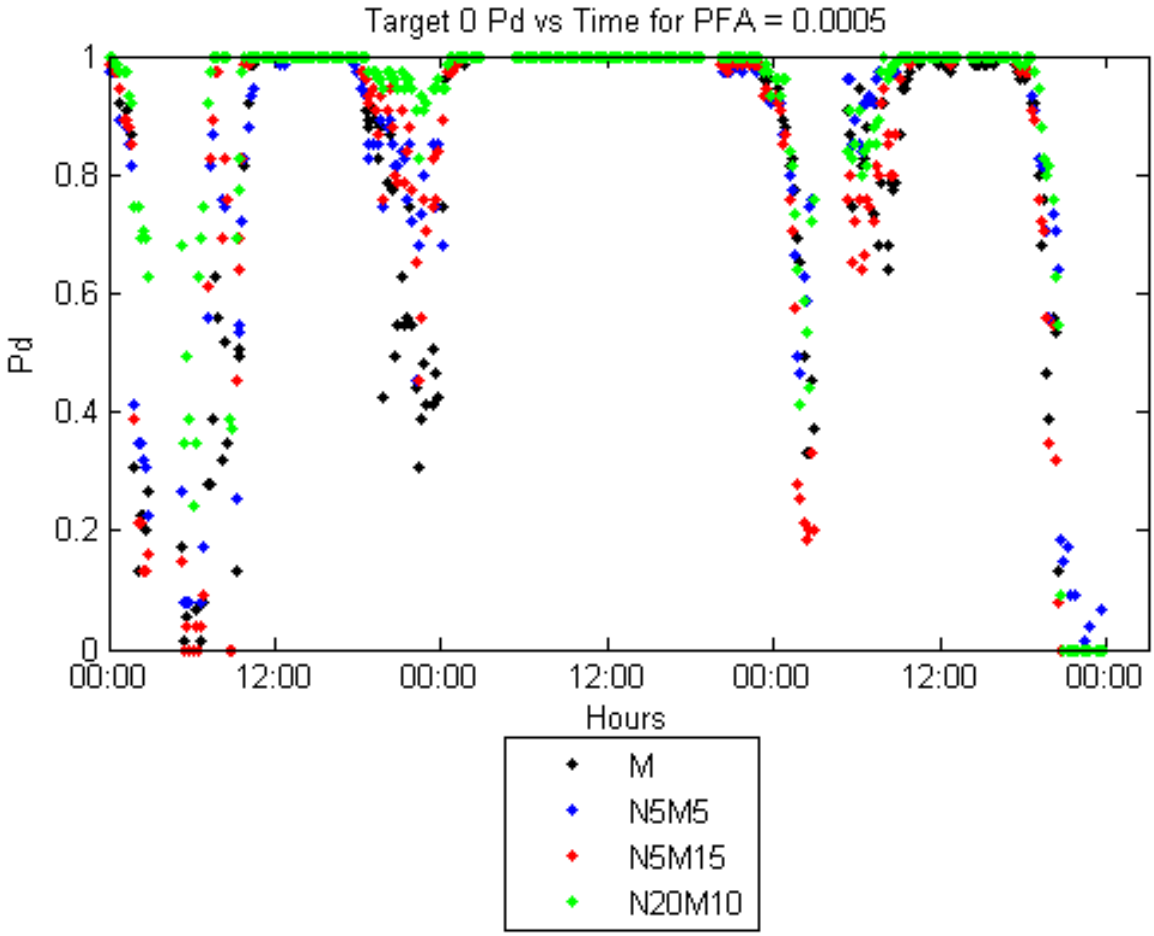

Figure 5.121 72-hour performance comparison between PRS-M and M-Box algorithm in discriminating the T_0 from natural clutter. The 72-hour average probability of detection from highest to lower was PRS-M (20,10), PRS-M (5,5), PRS-M (5,15), and the baseline with a $P_d = 0.89, 0.85, 0.82,$ and 0.80, respectively.

T_{90} 72-hour performance of all metrics is shown in Figure 5.122. In this figure all metrics perform similarly to each other for the first day with the baseline trailing PRS-M during the periods of low contrast. Interestingly, for the first period of high humidity found in the beginning of day 2 all metrics were pretty robust in detecting T_{90} compared to T_0. The PRS-M (20,10) performance dipped a bit compared to all other metrics for the period of high contrast in day 2, nonetheless its detection rate was always above 0.90, which is a highly desirable result for the very low false alarm rate shown here. PRS-M

(20,10) PRS-M (5,5), and the baseline performed similarly to each other for the second period of adverse weather found in the beginning of day 3 with PRS-M (5,15) performing slightly worse with probability of detection difference of 0.15 around 0100 on day 3. Finally, for the last adverse weather period at the end of day 3, both the baseline and PRS-M (5,15) are the worst performing metrics with similar probability of detection. Conversely, PRS-M (20,10) and with PRS-M (5,5) exhibited the best probability of detection during this time period. The average 72-hour probability of detection for T_{90} was very similar for all the metrics with a $P_d = 0.83, 0.84, 0.82,$ and 0.82 for the baseline, (5,5), (5,15), and (20,10), respectively.

Figure 5.123 illustrates the performance of all metrics in detecting T_{135}. For this target set PRS-M (20,10) performs very well from day 1 through the first adverse weather period at the beginning of day 2. Conversely, PRS-M (20,10) trailed all other metrics with a slight performance degradation during the periods of high contrast into the low contrast period during the hours between 1600h and 2359h on day 2. For the second adverse weather event at the beginning of day 3, one finds that none of the metrics were able to discriminate T_{135} between 0000h and 0100h. However, this trend reversed after 0500h with all metrics discriminating significant portions of the T_{135} for the chosen P_{fa}. For the last period of adverse weather, end of day 3, both PRS-M (5,5) and PRS-M (20,10) performed similarly to each other with a P_d difference relative to PRS-M (5,15) and the baseline of about 0.12. Nonetheless, when averaging the 72-hour probability of detection, similar values are measured for the baseline, PRS-M (5,5), PRS-M (5,15), and PRS-M (20,10) with a $P_d = 0.65, 0.67, 0.65,$ and 0.67, respectively.

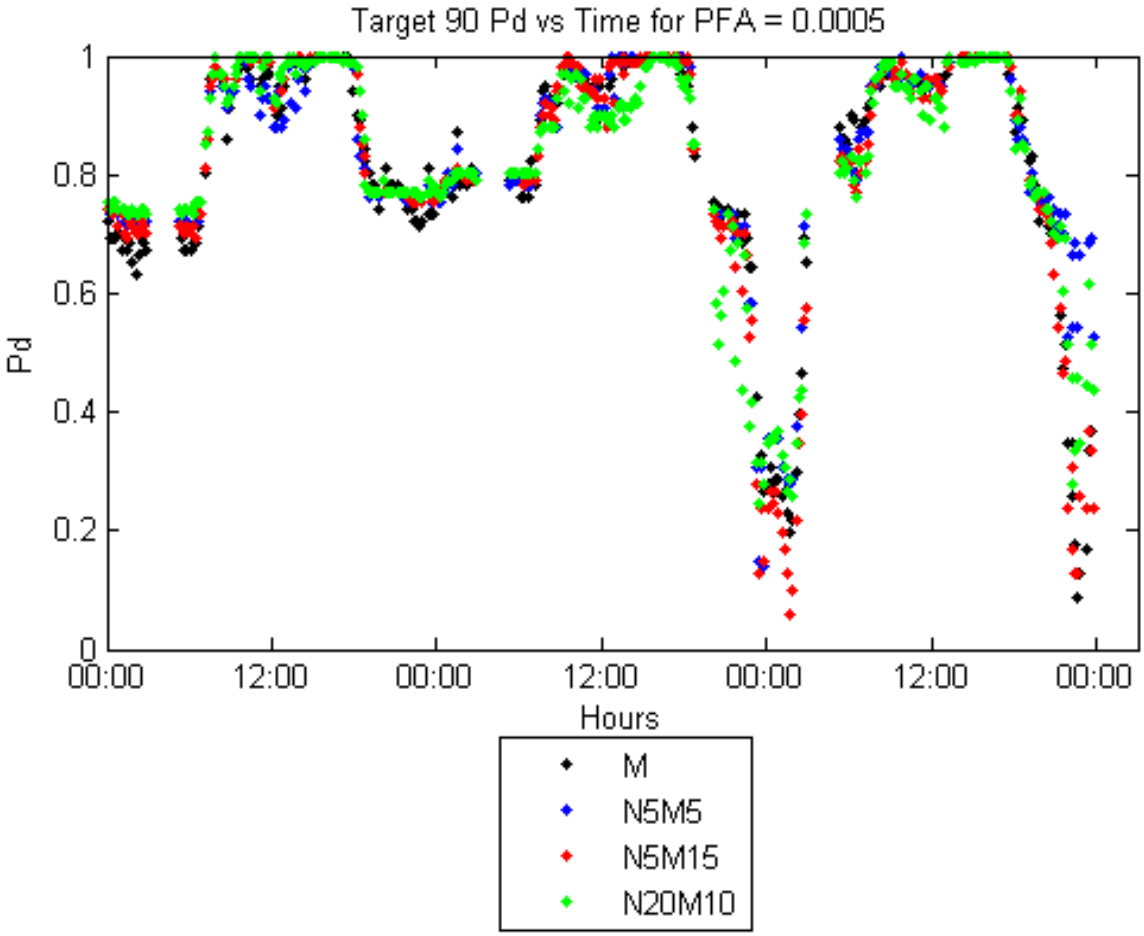

Figure 5.122 72-hour performance comparison between PRS-M and M-Box algorithm in discriminating the T_{90} from natural clutter. The 72-hour average probability of detection was similar for all the metrics with a $P_d = 0.83, 0.84, 0.82,$ and 0.82 for the baseline, PRS-M (5,5) , PRS-M (5,15), and PRS-M (20,10), respectively.

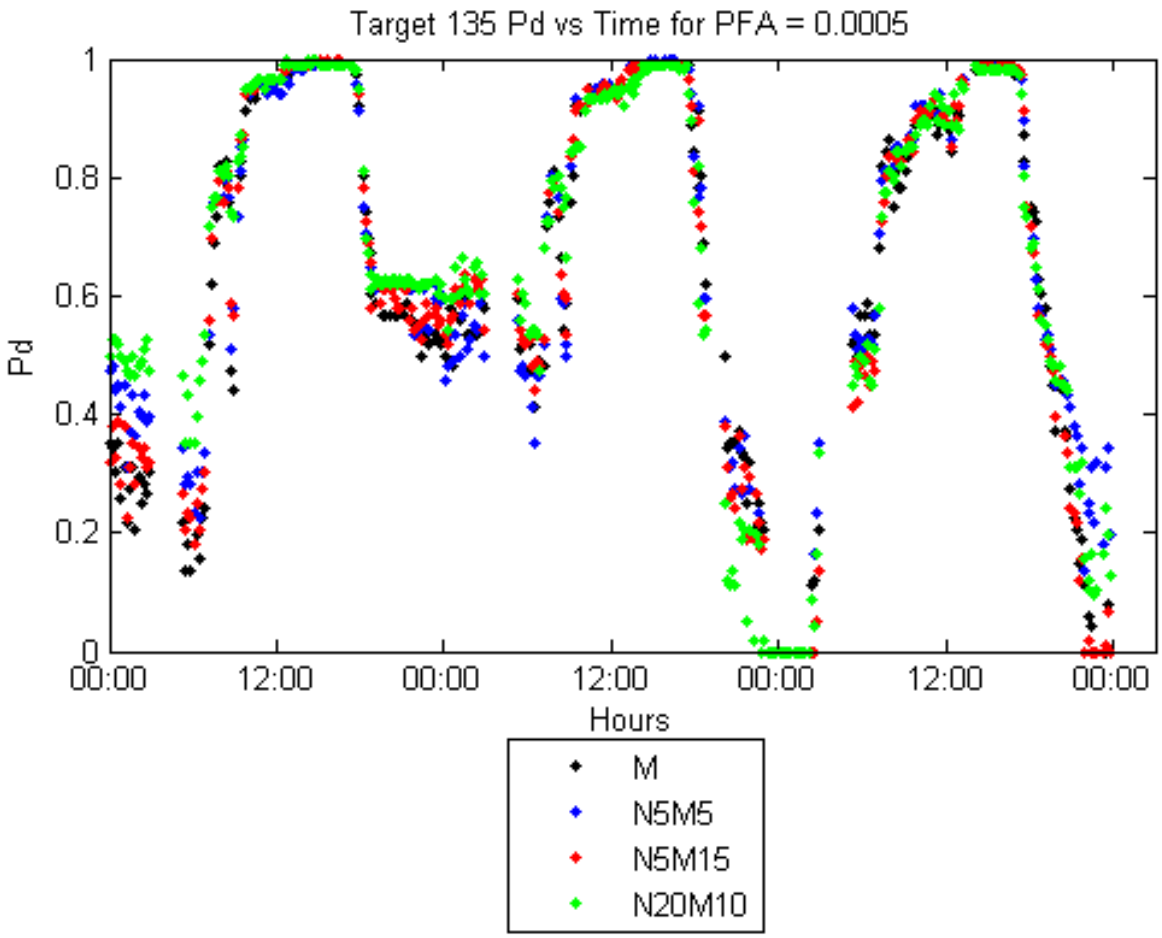

Figure 5.123 72-hour performance comparison between PRS-M and M-Box algorithm in discriminating the T_{135} from natural clutter. The 72-hour average probability of detection were measured to be, from highest to lowest, the baseline, PRS-M (5,5), PRS-M (5,15), and PRS-M (20,10) had a detection rate of $P_d = 0.65, 0.67, 0.65,$ and 0.67, respectively.

From the results in Table 5.12 and Figure 5.117 it is no surprise that the baseline algorithm (M-Box) clearly performed very well when compared to PRS-M in detecting the external blackbody, Figure 5.124. Due to the variability in the probability of detection for both PRS-M and the baseline it is hard to observe a clear trend throughout the 72 hours. However, some interesting tendencies can be discussed, for example, for the low contrast period during day 1 through day 2 the PRS-M (20,10) performs poorly relative to all other metrics, while the baseline performs the best. For the second period

of adverse weather (high humidity), beginning of day 3, none of the metrics were able to discriminate the blackbody, however by 0500h all metrics exhibited a $P_d > 0.50$. For the third adverse weather event, end of day 3, all of the metrics perform similarly to each other with PRS-M (5,15) demonstrating degraded performance in some instances. Nonetheless, the 72-hour average probability of detection demonstrates that all metrics do exhibit similar performances measured as $P_d = 0.79, 0.73, 0.73,$ and 0.73 for the baseline, and PRS-M (5,5), PRS-M (5,15), and PRS-M (20,10), respectively.

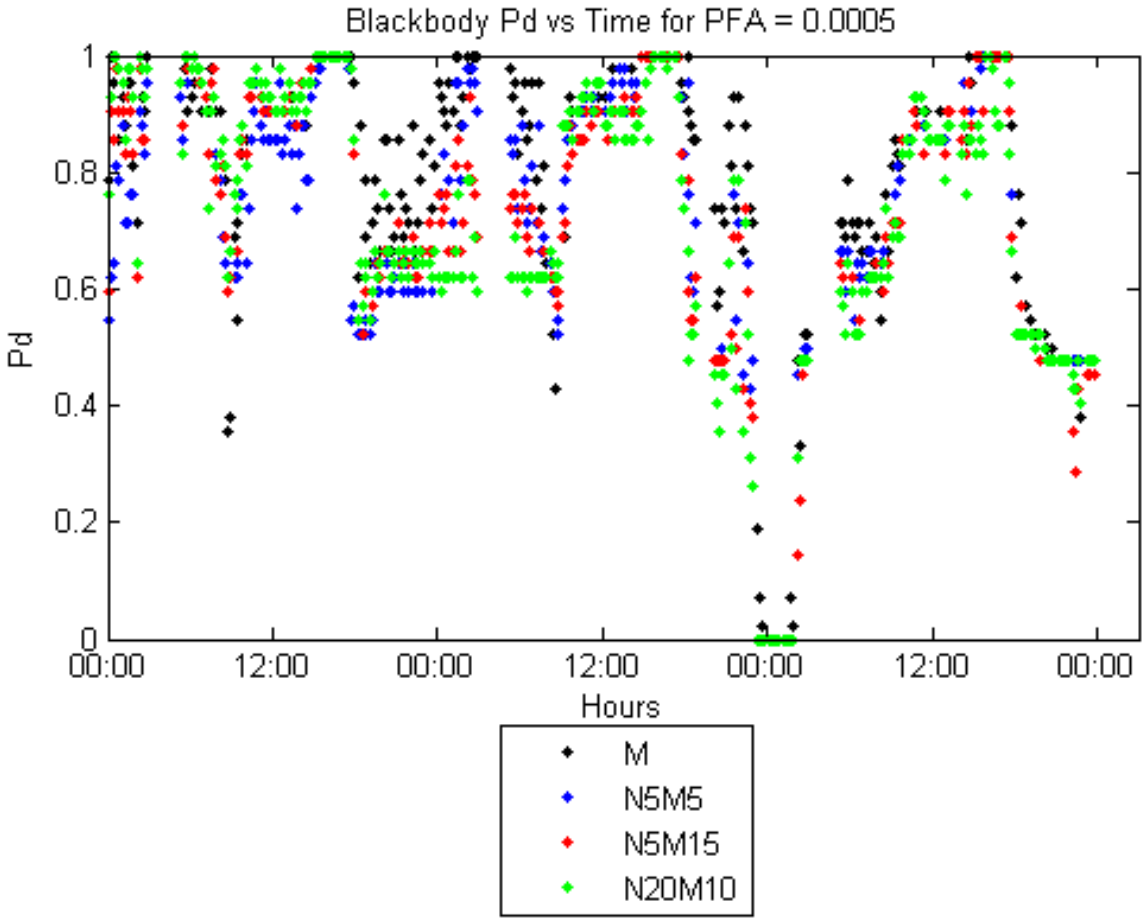

Figure 5.124 72-hour performance comparison between PRS-M and M-Box algorithm in discriminating the blackbody from natural clutter. The 72-hour average probability of detection was measured to be $P_d = 0.79, 0.73, 0.73,$ and 0.73 for the baseline, and PRS-M (5,5), PRS-M (5,15), and PRS-M (20,10), respectively.

Figure 5.125 demonstrates the detection performance of all metrics for the observation tower during the 72-hour performance period. As demonstrated in Table 5.12 and Figure 5.118 the baseline did not perform very well at all during the periods of low contrast. Only during the periods of high contrast the M-Box was able to discriminate the tower from clutter with a probability of detection of above 0.70. Conversely, PRS-M (20,10) demonstrated to be the best performing metric reaching a $P_d > 0.80$ for most of the 72-hour period. During the second adverse weather event, PRS-M (5,5) and PRS-M (20,10) performed very well with PRS-M (5,15) exhibiting degradation sometimes in the excess of 0.60 at some instances relative to PRS-M (20,10). However, for the third period of adverse weather, PRS-M (5,15) exhibited a $P_d \sim 0.60$, PRS-M (20,10) a $P_d \sim 0.70$, PRS-M (5,5) a $P_d \sim 0.80$, and finally the baseline with $P_d \sim 0.0$. The average probability of detection for the 72-hour period was $P_d = 0.17, 0.87, 0.86,$ and 0.92 for the baseline, PRS-M (5,5), PRS-M (5,15), and PRS-M (20,10), respectively.

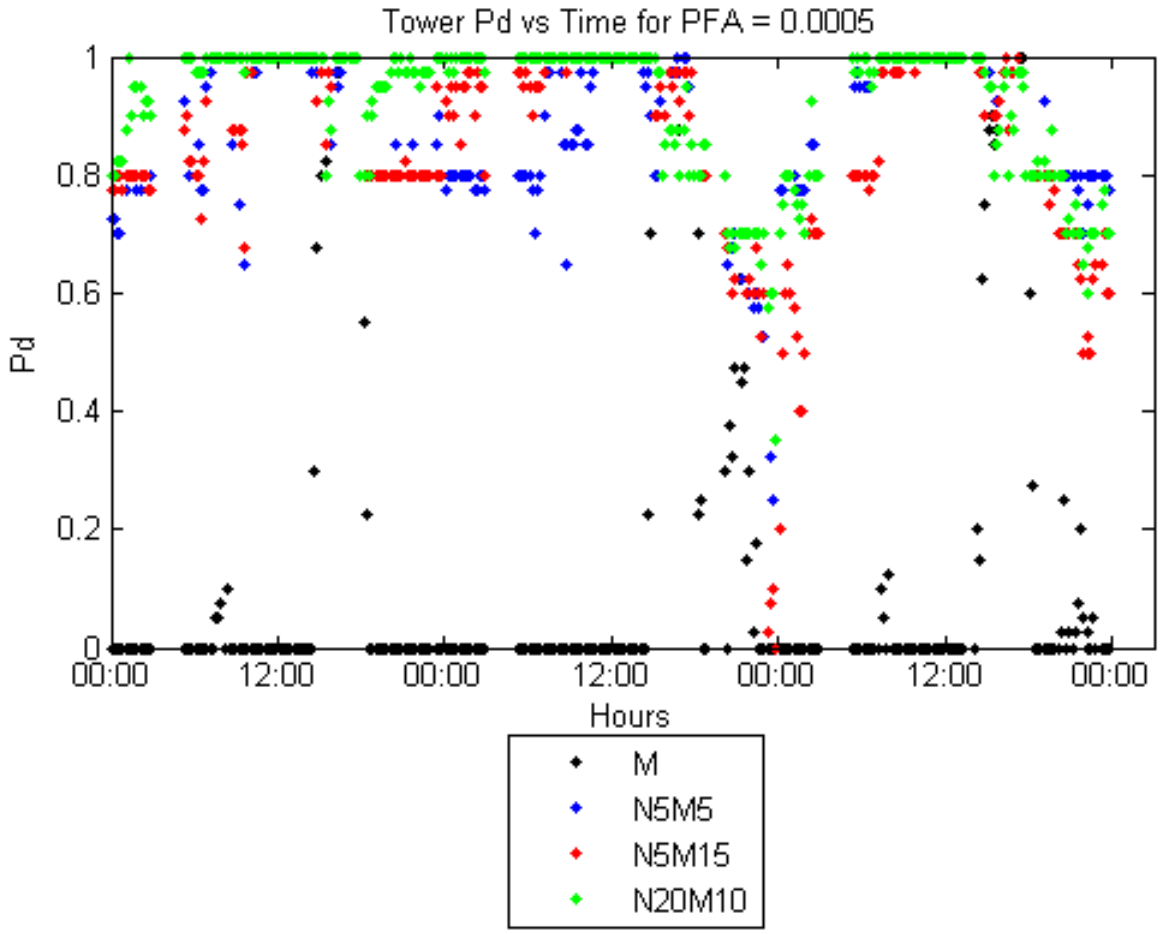

Figure 5.125 72 hour performance comparison between PRS-M and M-Box algorithm in discriminating the observation tower from natural clutter. The 72-hour average probability of detection was $P_d = 0.17, 0.87, 0.86,$ and 0.92 for the baseline, PRS-M (5,5), PRS-M (5,15), and PRS-M (20,10), respectively.

Finally, when all targets are combined into a single class, Figure 5.126, one can clearly observe that the baseline underperforms all combinations of PRS-M for most part of the 72-hour period with the exception of the periods of adverse weather (high humidity) at the beginning and end of day 3 where similar performances between PRS-M and the baseline can be found. During the periods of high contrast, PRS-M exhibits better P_d than the baseline. The average 72-hour probability of detection for Figure 5.126 from highest to lowest metric was PRS-M (20,10) with a $P_d = 0.79$, followed by

PRS-M (5,5) with a $P_d = 0.78$, then PRS-M (5,15) with a $P_d = 0.76$, and finally the baseline with a $P_d = 0.69$.

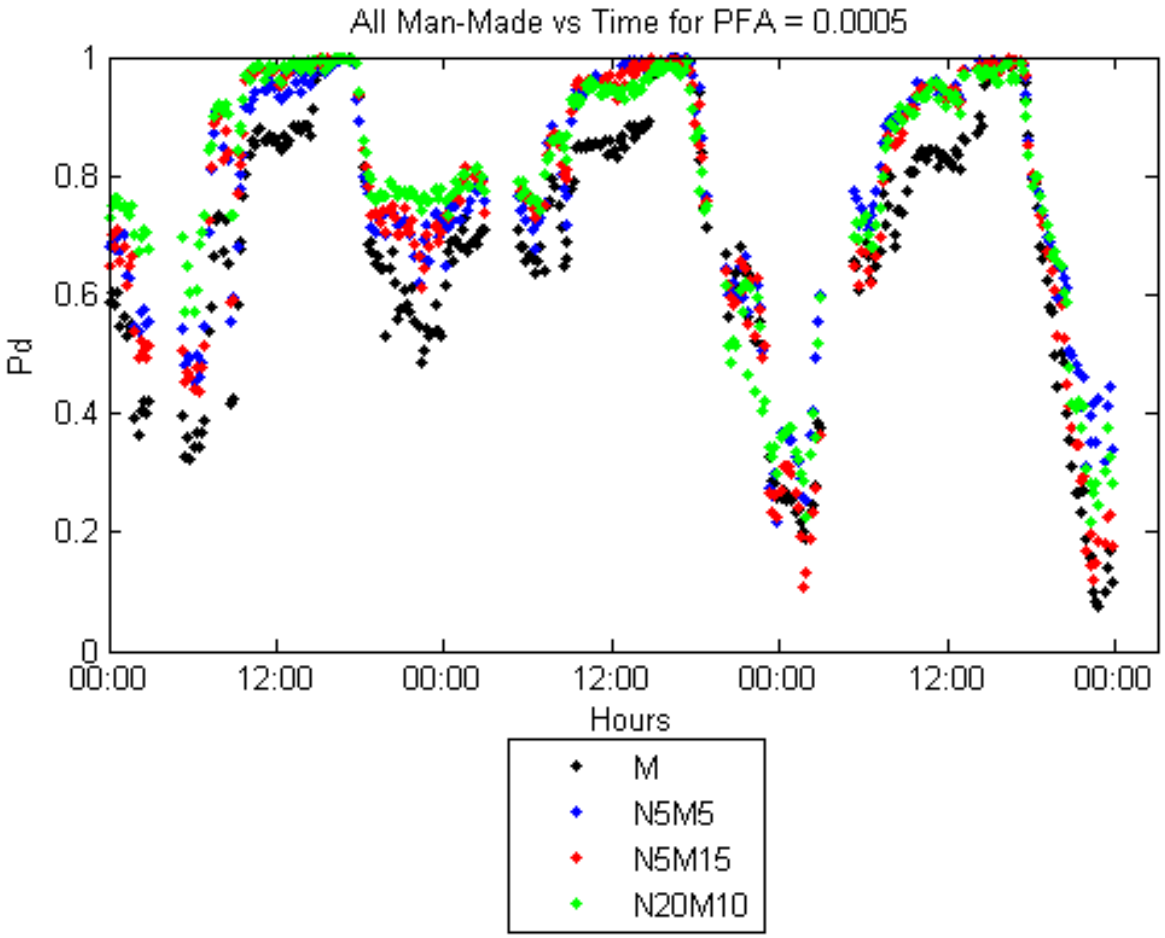

Figure 5.126 72-hour performance comparison between PRS-M and M-Box algorithm for all manmade objects in the scene. The average 72 hour probability of detection from highest to lowest was PRS-M (20,10) with a $P_d = 0.79$, followed by PRS-M (5,5) with a $P_d = 0.78$, then PRS-M (5,15) with a $P_d = 0.76$, and finally the baseline with a $P_d = 0.69$.

From the figures presented in this section, one concludes that for most part increasing N clearly helped the PRS-M in discriminating the manmade objects from natural clutter, which meant the PRS-M was able to characterize the test scene more effectively. By increasing M on the other hand, the performance of the PRS degraded or

improved relative to a lesser number of M but for most part when averaging the performance over a large number of images the performances were relatively similar. As one should remember, increasing the value of M is not done necessarily to increase the performance, that's primarily accomplished by increasing N. Increasing M, decreases the probability that all parallel processes are contaminated with at least one block of data, see for example Figure 5.111 where the PRS methodology was able to successfully discriminate T_0 even though one of the parallel process did not identify T_0 as an anomaly.

This subsection presented a performance comparison between the PRS-M methodology and the baseline algorithm as proposed in Subsection 5.3.5. The following key points can be concluded from the data shown in this subsection:

1) Increasing N, the number of samples, increases the ability in successfully characterizing the test scene very well, which then results in a higher probability of detection for the same P_{fa}.

2) Increasing M, the number of parallel processes, allows for:

    a. Mitigation of the inclusion of manmade samples during the random sampling process in all parallel processes (or trials).

    b. Reduces the false alarms energy relative to manmade objects in the final output surface $\boldsymbol{Z}$.

3) PRS-M demonstrates exceptionally high performance especially in the low false alarm rate region compared to the baseline for a $P_{fa} \leq 0.001$ as shown in the ROC curves.

4) As with the RS-M, PRS-M was able to discriminate the tower very well unlike the baseline.

5) PRS-M performed better or similarly to the baseline for the 72-hour data collection period with two exceptions:

    a. The baseline demonstrated better average probability of detection for the external blackbody. Nonetheless this difference was minimal, 0.06, between the baseline and the PRS-M.

b. PRS-M demonstrated better average probability of detection for the observation tower. In this case, PRS-M (20,10) demonstrated a probability of detection difference relative to the baseline of 0.85.

5.3.13 Limitations of the PRS-M Anomaly Detector

The PRS-M, as well as the RS-M and the M-Box, have a similar limitation, they are all simple anomaly detectors that provide no additional information about the anomalous objects and as a result more sophisticated algorithms and/or sensors are needed to discriminate false alarms from targets. In this dissertation, the background clutter is relatively easy with trees composing most of the scene. One would then expect that more diverse backgrounds consisting of lots of different natural materials could in principle exhibit more false alarms especially in transition areas between the different natural clutter; see Figure 5.120 where transitions (heterogeneous) areas were more accentuated than homogeneous areas. In this construct, a heterogeneous area implies a location where the moving window samples two or more natural clutter class that can, in principle, display different radiance (temperature) values. If such occurs, i.e., different classes exhibiting different radiance values, the variability within the moving window samples may be very high resulting in a potential false alarm.

5.3.14 Summary and Conclusions

Subsection 5.3 presented novel ways to analyze and process polarimetric information that steered away from current polarimetric peer-review research topics. One of the most important key findings demonstrated in Subsection 5.3.4 was the use and analysis of individualized polarization features (I_0 and I_{90}) to separate manmade and natural clutter distributions in the bivariate space, which concluded that the covariance of natural clutter

of a block of data of size $n \times n$ as it moves across the image was smaller than the covariance of manmade objects presented in the scene. This feature was a result of the window observing a large variability in the radiance values when it was place over two or more manmade surfaces at different orientations relative to the camera viewing angle (see Chapter 3 for more information on this phenomenon). Conversely, as the window moved across natural clutter background, the radiance values were found to be more homogeneous, therefore, resulting in lower variability within its pixels.

This information allowed for the proposition of using a covariance-difference multivariate algorithm based on the M-Box covariance test (Subsection 5.3.5), which resulted in an extremely efficient algorithm to pin-point the locations of manmade objects present in the scene compared to conventional Stokes parameters and DoLP (Subsection 5.3.6). However, as shown in Subsection 5.3.7, the implementation proposed in Subsection 5.3.6 assumed that the determinant of manmade objects' covariance matrices were larger than the determinant of background covariance and as a result, the implementation of the M-Box (Subsection 5.3.6) failed in close proximity PI.

In analyzing short range PI, the assumption on the variability exhibited by manmade objects and natural clutter was reversed, i.e., the determinant of natural clutter covariance was actually larger than that of manmade objects. As a result, Subsection 5.3.8 proposed the RS-M which combined a random sampling scheme to characterize the natural clutter background with the M-Box covariance test proposed in Subsection 5.3.5. The implementation of these two methods made the algorithm suite (1) range invariant, now the M-Box covariance test could be used in both short and long range PI, and (2) allowed for both the reference and test windows to have equal sample sizes. The results

in Subsection 5.3.9 demonstrated that RS-M had comparable or better performance to the baseline as a function of increasing N (better background characterization). In addition, the RS-M was able to detect the observation tower, a manmade object, which the M-Box failed to detect as shown in Subsection 5.3.6.2. Subsection 5.3.10 presented a potential limitation of the RS-M in detecting manmade object in PI. This condition arose when a manmade object covariance determinant value was found to be in between two clutter covariance determinants and as a result of this condition, the RS-M could not discriminate a manmade object from clutter. However, although the RS-M limitation is of a concern, as it was noted in Subsection 5.3.10, the data used to highlight the concerning case were fictitious, and examples of similar cases could not be found in the database used for the work described in this dissertation.

Finally, the PRS-M was proposed in Subsection 5.3.11 as a generalized anomaly detector for PI. Just like the RS-M, it implemented a random sampling technique that allowed the M-Box algorithm to remain range invariant. In addition, by keeping the M-Box covariance test to k = 2, eliminated the RS-M limitation as presented in Subsection 5.3.10. On the other hand, unlike the RS-M, contamination was a serious limitation to the PRS-M and as a consequence, the need to parallelize each trial was implemented to mitigate the overall probability of contamination in all trials. Fusing all the trials' output surfaces introduces two benefits: (1) retains anomalies when detected in at least one of the M parallel processes and (2) mitigates false alarms in the final output surface.

All of these features when implemented with the M-Box algorithm, allowed the covariance test to work in any situation, as long as, the variability within a test window

representing manmade objects is significantly different from any of the random samples collected from natural clutter.

Subsection 5.3.12 demonstrated that just like the RS-M, the PRS-M performance increased as a function of increasing N (number of random samples). Moreover, ROC curves demonstrated that the PRS-M performed very well at very low probability of false alarm rates ($P_{fa} \leq 0.0005$) with a minimum $P_d \geq 0.5$ as shown in Table 5.12.

Finally, Subsection 5.3.13 illustrated the limitations posed by the PRS-M. In this case, the PRS-M is a simple anomaly algorithm that provides no additional information about the anomalous objects. Furthermore, the clutter in this database can be viewed as a relatively easy background where trees compose over 90% of the scene. Therefore, as scenes become more diverse (different natural clutter material) the number of false alarms may increase as well if a suitable N is not chosen.

5.4 Conclusions

Chapter 5 introduced two significantly different methodologies for processing PI; the first was based on morphological operations that were capable of enhancing manmade object features with respect to natural clutter, improving manmade object detection over conventional Stokes and DoLP parameters. The first method utilized the conventional Stokes and DoLP imagery as input to the proposed set of MM operators, so in some aspect, its performance was directly influenced by the available features in the original conventional Stokes/DoLP imagery. As it was shown in Section 5.2, if such features were not readily available, the morphological operators would not be able to extract meaningful information needed to enhance the target to clutter contrast.

The second method eliminates the use of Stokes, considered by many as the foundation of PI, and DoLP, focusing on the development of multivariate algorithms that take as input the individual polarization angle imagery captured by the camera as the polarizer changes angles (0°, 45°, 90°, and 135°). Section 5.3 proposed, what this dissertation believes to be, the first multivariate algorithm based on the statistics of the individual angle imagery for anomaly detection applications in PI. By taking into consideration the variance between the pixels of a test window as it moves across the image it was shown that one can take advantage of the covariance difference between manmade objects and natural clutter environments to discriminate one from the other. These analyses resulted in the proposition of using the M-Box algorithm as the covariance difference anomaly detector for PI. As effective as the M-Box was, the algorithm was bounded by a strict assumption, i.e., the determinant of the covariance of a clutter sample was always smaller than the determinant of the covariance of manmade objects, which in some situations could not prevail. Subsections 5.3.8 and 5.3.11 then proposed two variants to the M-Box, called the RS-M and PRS-M anomaly detector. The RS-M is an extension of the M-Box algorithm for N samples using a proposed random sampling scheme, while the PRS-M (which was introduced as the generalized M-Box anomaly detector) used the same random sampling technique found in RS-M coupled with a parallel process to mitigate contamination of manmade samples into the reference signatures. The PRS-M proved to be a more sophisticated algorithm because it was able to remove all assumptions inherent in the M-Box and RS-M anomaly detectors. Finally, the M-Box, RS-M, and PRS-M were tested against an extensive database comprised of three consecutive 24-hour days exhibiting a variety of complex weather conditions and

target states while performing extremely well relative to conventional PI exploitation techniques

CHAPTER 6

CONCLUSION AND FUTURE WORK

6.1 Summarized Conclusions

The objective of this dissertation focused on proposing and evaluating unconventional polarimetry based algorithms for the autonomous detection of manmade objects in the presence of natural background scenes. The aim was set high at significantly improving performance for suitable surveillance applications; both commercial and military. The dissertation supervisory committee sincerely believes the goals of this dissertation were all achieved.

A significant amount of research can be found focused on Stokes imagery as the primary input for polarimetric anomaly detection while at the same time failing to address the underlying problems of angle dependency and, most commonly seen, inseparable clutter-manmade distributions in PI. A key goal in this work was to identify some fundamental challenges characteristic from polarimetric theory which limit the applicability of Stokes imagery. Another goal demonstrated that, in most cases, the manmade distribution is found within the clutter distribution for both S_1 and S_2 images making these images unsuitable for anomaly detection.

An image enhancement algorithm was proposed to improve the signal to noise ratio between manmade objects and natural clutter background by squeezing the clutter distribution while spreading the target distribution further away from clutter as shown in Subsection 5.2. The use of morphological filters on the Stokes imagery demonstrated that the enhanced images could be used as anomaly detection surfaces by applying a

threshold based on the assumption that the null hypothesis could be modeled by a Gaussian distribution.

However, as successful as the morphologic filters were in enhancing manmade features in Stokes imagery, S_1 and S_2 in general provide limited information for the development of more sophisticated anomaly detection algorithms. As a result, the dissertation proposed the notion of using a polarimetric cube composed of individual polarization component imagery captured by the camera as the polarizer changes angles (0°, 45°, 90°, and 135°). This novel idea steered away from common use of polarization information and introduced three benefits, (1) analysis on manmade and clutter distribution using direct polarization measurements; (2) discovery of key features that separate manmade objects from clutter; and (3) the use of multivariate scoring algorithms that take advantage of the key features.

Subsection 5.3.4 demonstrated that by taking into consideration the variance between the pixels of a test window as it moves across the image, one could take advantage of the covariance difference between manmade and natural clutter to distinguish both object classes.

A covariance different test, known as M-Box, was proposed as the anomaly detector of choice demonstrating enhanced detection performance relative to conventional Stokes. However, the implementation proposed in Subsection 5.3.6.1 prevented the M-Box algorithm from working at both short and long range PI, and two more variants of the same algorithm were proposed in Subsections 5.3.8 and 5.3.11, as RS-M and PRS-M, respectively, to remedy those limitations.

The RS-M is an extension of the M-Box algorithm for N samples using a random sampling scheme to characterize the scene. The RS-M performance was similar to the M-Box proposed in Subsection 5.3.6.1 with the added benefit of range invariant performance, not requiring *a priori* information about the distribution spread between the two classes.

The PRS-M on the other hand was introduced as a generalized M-Box anomaly detector using the same random sampling technique found in RS-M, coupled with a parallel process to mitigate contamination of manmade samples into the reference signatures. The PRS-M was able to remove all assumptions inherent to the M-Box and RS-M anomaly detectors and demonstrated the capability of discriminating manmade objects from natural clutter at very low false alarm rates than previously seen in the other proposed algorithms.

6.2 Limitations

The algorithms presented in this dissertation have the following limitations:

1) Anomaly Detection Is Not Target Detection: All of the algorithms proposed in this work merely detect regions of interest that are considerably different from the background clutter. The algorithms provide no additional information on the anomalies and as a result other more sophisticated algorithms need to be deployed to further inquire the regions of interest, having the ability to separate targets from non-targets. It is important to remember that in the construct presented in this work the detected anomalies were usually of manmade objects, however in more complicated backgrounds correct anomaly detection may not always correspond to manmade object detection.

2) Manmade Object Size Restriction: Throughout Section 5.3 the proposed algorithm were successful in detecting manmade objects that were slightly smaller or larger than the sliding window. If the manmade object covers a very small portion of the total area of the moving window, the overall variability of the sliding window may resemble the variability of the clutter and as a result the location may not be deemed anomalous.

3) Higher Dimensional Datacubes: The work presented here focused on bivariate data cube composed of I_0 and I_{90} polarization components. In order to estimate an unbiased covariance matrix of the sliding window samples a 7×7 sampling window was employed. As the number of dimensions increases the sliding window size needs to increase as well to calculate an unbiased estimate of the covariance matrix. An increase in the sliding window size can adversely affect the proposed algorithms ability in detecting potential manmade objects as per the reasoning in point 2.

4) Weather Conditions: Chapter 5 demonstrated very good results of the proposed anomaly algorithms for most of the weather conditions available in the 72-hour database. Nonetheless, the amount of weather variability presented in this work is very limited compared to what surveillance systems actually operate in. As such, these results should not be extrapolated to other more severe weather conditions; and certainly does not imply that by exploiting the same key features similar good results would be expected using sensors operating in other regions of the spectrum, such as SWIR or MWIR where reflectivity properties of the materials play an important role as well.

6.3 Future Work

The work presented in this dissertation can be further developed into the following areas:

1) Multi-Polarimetric Datacube: The work presented in this dissertation focused on a bivariate data cube composed of I_0 and I_{90} polarization components. A natural progression of this work would be to evaluate how the addition of other polarization components can separate manmade objects from natural clutter more effectively and/or create the possibility to go beyond simple anomaly detection applications.

2) Polarization Component Selection: The addition of more information (e.g., polarization components) often comes with a heavy computational price. Therefore, the development of autonomous polarization component selection algorithms promises to add value in reducing computational cost. This type of work can exploit recent accomplishments in the field of hyperspectral imagery exploitation where spectral band selection algorithms and methodologies have been already developed for anomaly and target detection applications, see for example [77-80].

3) Further Evaluation of Proposed Algorithms: All proposed algorithms will be further evaluated using additional PI datasets exhibiting different weather conditions, background clutter, and target sets. Furthermore, additional datasets collected by SWIR and MWIR sensors will be used to evaluate the performance of the propose algorithms in detecting manmade objects in those regions of the spectrum.

6.4 Summary

Anomaly detection algorithms are highly sought after due to their mathematical simplicity and their ability to detect regions of interest where known and unknown targets may be located. Users require such algorithms to work for a variety of target sets of different sizes and shapes under a variety of atmospheric conditions and unknown illumination environments for different ranges and viewing perspectives.

The work presented in this dissertation offers several anomaly detection algorithms capable of detecting the presence of manmade objects in natural clutter backgrounds using LWIR polarimetric imagery. Performance analysis demonstrated that the specific algorithms were capable of discriminating a variety of manmade objects of different sizes, shapes, and/or placed at different aspect angles and ranges, while working under a variety of illumination and atmospheric conditions and holding a high probability of detection as required by the users.

The research community can benefit from the ideas and anomaly detection algorithms presented in this dissertation.

REFERENCES

[1] W. L. Wolfe, *Handbook of Military Infrared Technology*. Michigan University, MI: Ann Arbor, 1965.

[2] J.S.Tyo, D. L. Goldstein, D.B.Chenault, and J.A. Shaw, Review of passive imaging polarimetry for remote sensing applications," *Appl. Opt., vol. 45(22),* pp. 5453-5469, Aug. 2006.

[3] E. Collett, *Polarized Light Fundamentals and Applications*, New York, New York: Marcel Dekker Inc., 1993.

[4] I. S. Reed and X. Yu, "Adaptive multiple-band CFAR detection of an optical pattern with unknown spectral distribution", *IEEE Trans. Acoust., Speech Signal Process.*, vol. 38, no. 10, pp. 1760-1770, 1990.

[5] S. Matteoli, M. Diani; G. Corsini, "A tutorial overview of anomaly detection in hyperspectral images," *Aerospace and Electronic Systems Magazine, IEEE* , vol. 25, no. 7, pp. 5-28, July 2010.

[6] Y. Chen; N.M. Nasrabadi; T.D. Tran, "Sparsity-based classification of hyperspectral imagery," *Geoscience and Remote Sensing Symposium (IGARSS), 2010 IEEE International*, pp. 2796-2799, 25-30 July 2010.

[7] S. Khazai et al., "Anomaly Detection in Hyperspectral Images Based on an Adaptive Support Vector Method," *Geoscience and Remote Sensing Letters, IEEE*, vol.8, no.4, pp.646-650, July 2011.

[8] Sakla, W.; Chan, A.; Ji, J.; Sakla, A, "An SVDD-Based Algorithm for Target Detection in Hyperspectral Imagery," *Geoscience and Remote Sensing Letters, IEEE*, vol. 8, no. 2, pp. 384-388, March 201.

[9] M. Felton; et al., "Comparison of the inversion periods for MidIR and LWIR polarimetric and conventional thermal imagery." *Proc. SPIE 7672, Polarization: Measurement, Analysis, and Remote Sensing IX*, April 2010.

[10] R. Mayer et al., "Detection of camouflaged targets in cluttered backgrounds using fusion of near simultaneous spectral and polarimetric imaging." Navy Research Laboratory, NRL Tech. Rep. 2000.

[11] M. R. Bradley et al. "Detection and tracking of RC model aircraft in LWIR microgrid polarimeter data ", *Proc. SPIE 8160, Polarization Science and Remote Sensing V*, Sept. 2011.

[12] F.A. Sadjadi and C.S.L.Chun, "Passive polarimetric IR target classification," *Aerospace and Electronic Systems, IEEE Transactions on*, vol. 37, no. 2, pp. 740,751, April 2001.

[13] J. Zallat; P. Grabbling; Y. Takakura, "Using polarimetric imaging for material classification," *Image Processing, 2003. ICIP 2003. Proceedings. 2003 International Conference on*, pp. 14-17, Sept. 2003.

[14] V. Thilak; C.D. Creusere; D.G. Voelz, "Passive Polarimetric Imagery Based Material Classification For Remote Sensing Applications," *Image Analysis and Interpretation, 2008. SSIAI 2008. IEEE Southwest Symposium on*, pp. 153-156, 24-26 March 2008.

[15] K. P. Gurton and M. Felton; "Detection of disturbed earth using passive LWIR polarimetric imaging". *Proc. SPIE 7461, Polarization Science and Remote Sensing IV*, Aug. 11, 2009.

[16] J.L. Miller, *Principles of Infrared Technology: A Pratical Guide to the State of the Art*. New York, New York: Van Nostrand Reinhold, 1994.

[17] International Commission on Illumination. (2011). Report: CIE S 017/E:2011

[18] M. Planck, *Theory of heat Radiation*. New York, Dover: Courier Dover, 1959.

[19] R. Hudson, *Infrared System Engineering*. New York, New York: Willey-Blackwell, 1969.

[20] "Wien's law". (2012) Encyclopedia Britannica. Encyclopedia Britannica Online. Encyclopedia Britannica Inc., Available: http://www.britannica.com/EBchecked/topic/643338/Wiens-law.

[21] L.R. Koller, *Ultraviolet Radiation*. 2nd edition. New York, New York: Willey, 1965.

[22] J. R. Schott, *Fundamentals of polarimetric remote sensing*. vol. 26. Society of Photo Optical, 2009.

[23] G.J. Zissis and W.L. Wolfe. *The Infrared Handbook*. Infrared Information and Analysis Center, Ann Arbor, MI: Office of Naval Research Dept., 1978.

[24] M.F. Modest, *Radiative Heat Transfer*. Academic Press, 2003

[25] M. Riedl, *Optical Design Fundamentals for Infrared Systems*, 2nd, Bellingham, WA: SPIE Press, 2001.

[26] B.W. Silverman, *Density estimation for statistics and data analysis*. vol. 26. Chapman & Hall/CRC, 1986.

[27] D.W. Scott, *Multivariate Density Estimation*, New York, New York: Wiley, 1992.

[28] S.J. Sheather and M.C. Jones. "A reliable data-based bandwidth selection method for kernel density estimation." *Journal of the Royal Statistical Society. Series B*, pp. 683-690, 1991.

[29] MATLAB ksdensity. (2013). Available: http://www.mathworks.com/help/toolbox/stats/ksdensity.html

[30] F. Melgani and L. Bruzzone, "Classification of hyperspectral remote sensing images with support vector machines," *Geoscience and Remote Sensing, IEEE Transactions on* , vol.42, no.8, pp. 1778-1790, Aug. 2004.

[31] L.S. Bernstein et. al, "A new method for atmospheric correction and aerosol optical property retrieval for VIS-SWIR multi- and hyperspectral imaging sensors: QUAC (QUick Atmospheric Correction)," *Geoscience and Remote Sensing Symposium, IEEE International*, vol.5, pp. 3549-3552, July 2005.

[32] M.W. Matthew et. al, "Atmospheric correction of spectral imagery: evaluation of the FLAASH algorithm with AVIRIS data," *Applied Imagery Pattern Recognition Workshop, 2002. Proceedings. 31st* , pp. 157-163, Oct. 2002.

[33] T. Krishna. "Exploiting Passive Polarimetric Imagery for Remote Sensing Applications." Dissertation, New Mexico State University, U.S.A., 2008.

[34] J.M. Romano et al. "Spectral and Polarimetric Imagery Collection Experiment," Army Armament Research and Development and Engineering Center, Picatinny Arsenal, NJ, Tech. Rep. No. ARMET-TR-11027., 2011.

[35] V. Thilak; C.D. Creusere; D.G. Voelz, "Material Classification using Passive Polarimetric Imagery," *Image Processing, 2007. ICIP 2007. IEEE International Conference on* , vol.4, pp. 121-124, 2007.

[36] E. Collett, *Field guide to polarization*. SPIE, 2005.

[37] G. G. Stokes, "On the change of refrangibility of light." *Philosophical Transactions of the Royal Society of London*, vol. 142, pp. 463-562, 1852.

[38] K. L. Coulson, *Polarization and Intensity of Light in the Atmosphere*. A Deepak Pub, 1988.

[39] ROC Curves Explanation. Wikipedia. (2013). Available: http://en.wikipedia.org/wiki/Receiver_operating_characteristic.

[40] ImageJ. (2013). Available: http://rsbweb.nih.gov/ij/.

[41] Matlab©. (2013). Available: http://www.mathworks.com.

[42] Microsoft Excel. (2013). Available: http://www.office.microsoft.com.

[43] J. Serra, *Image Analysis and Mathematical Morphology*, London, UK: Academic Press, 1982.

[44] G. Matheron, *Elements pour une Théorie des Milieux Poreux*, Masson, Paris, France, 1967.

[45] G. Matheron, *Random Sets and Integral Geometry*, New York, New York: Wiley, 1975.

[46] G. Matheron and J. Serra, "The Birth of Mathematical Morphology," in *Mathematical Morphology, Proceedings of the VI International Symposium ISMM*, pp. 1-16, Australia, April 2002.

[47] A. Rosenfeld, "Picture Processing by Computer". *ACM Comput. Surv.*, pp. 147-176, 1969.

[48] J.J.A.M. Heijmans, "Theoretical aspects of gray-level morphology,' *IEEE Trans. Patter Analysis and Machine Intelligence*, vol. 13, no.6, pp. 568-582, June 1991.

[49] F.Y. Shih and O.R. Mitchell, "Threshold decomposition of grayscale morphology into binary morphology," *IEEE Trans. Pattern Analysis and Machine Intelligence*, vol. 11, no. 1, pp.31-42, Jan. 1989.

[50] E. R. Dougherty, and A. L. Roberto, *Hands-on morphological image processing*, Belligham, WA: SPIE Press, 2003.

[51] O. G. Merino. Image analysis of Infrared Polarization measurements of landmines.Master thesis. Vrije Universiteit Brussel (VUB)-ETRO department, 2001.

[52] F. Cremer, "Polarimetric Infrared and Sensor Fusion for the Detection of Landmines," Ph.D. dissertation, Delft University, Netherlands, 2003.

[53] V. Tom and T. Joo, "Morphological detection for scanning IRST sensor," Final Report TR-1167-90-1, Atlantic Aerospace Electronics Corporation, 1990.

[54] V. Tom and T. Joo, "Morphological-based front end processing for IR-based ATR systems," Final Report 1992, Atlantic Aerospace Electronics Corporation , 1992.

[55] R.C. Gonzalez and R.E. Woods, *Digital Image Proceesing*. New York, New York: Prentice Hall, 1992.

[56] K. Fukunaga, *Introduction to Statistical Pattern Recognition.* 2nd, New York, New York: Academic Press, 1990.

[57] R. O. Duda, P. E. Hart, and D. G. Stork. *Pattern Classification.* 2nd. Wiley-Interscience.

[58] A. C. Rencher, *Methods of multivariate analysis*. New York, New York: Willey Interscience, 2002.

[59] J. Neyman and E.S. Pearson, "The testing of statistical hypotheses in relation to probabilities a priori". *Joint Statistical Papers*. Cambridge University Press., pp. 186-202, 1967.

[60] D. Sheskin, *Handbook of Parametric and Nonparametric Statistical Procedures*. Boca Raton, Florida: Chapman and Hall/CRC Press, 2004.

[61] R. V. Hogg, J. W. McKean, and A. T. Craig, *Introduction to Mathematical Statistics.* Upper Saddle River, NJ: Pearson Prentice Hall, 2005.

[62] J. M. Romano and D. Rosario, "Random sampling statistical analysis for adaptive target-scale-invariant hyperspectral anomaly detection". *Proc. SPIE 6565, Algorithms and Technologies for Multispectral, Hyperspectral, and Ultraspectral Imagery XIII*, 2007.

[63] D. Rosario and J. Romano, "Wide-area hyperspectral chemical plume detection using parallel random sampling". *Proc. SPIE 6554, Chemical and Biological Sensing VIII*, 2007.

[64] J Romano et al, "Analysis of an autonomous clutter background characterization method for hyperspectral imagery". *Proc. SPIE 6966, Algorithms and Technologies for Multispectral, Hyperspectral, and Ultraspectral Imagery XIV*, 2008.

[65] J.M. Romano; D. Rosario; Luz Roth, "VNIR hyperspectral background characterization methods in adverse weather conditions". *Proc. SPIE 7334, Algorithms and Technologies for Multispectral, Hyperspectral, and Ultraspectral Imagery XV*, 2009.

[66] D. S. Rosario and J.M. Romano, "Ground viewing perspective hyperspectral anomaly detection." US Army Research Laboratory, Maryland, ARL Tech Report 4583 SEP 2008.

[67] G. Strang, *Introduction to linear algebra*. Wellesley, Massachusetts: Wellesley Cambridge Pr, 2003.

[68] M.S. Bartlett, “Properties of sufficiency and statistical tests,” *Proc. R. Soc. Lond.* pp. 268-282, May 1937.

[69] G.E.P. Box, “A general distribution theory for a class of likelihood criteria.” *Biometrika*, vol. 36, pp. 317-346, 1949.

[70] J. Marden. (2012). *Multivariate Statistics Old School* [PDF Online]. Available: http://istics.net/pdfs/multivariate.pdf

[71] J.C Lee; T.C. Chang; P.R. Krishnaiah,”Approximation to the distributions of the likelihood ratio statistics for testing certain structures on the covariance matrices of real multivariate normal distributions. *Multivariate Analysis*, vol. 4, pp. 105-118, 1977.

[72] T.W. Anderson, *An introduction to multivariate statistical analysis.* New York, New York: John Wiley, 2003.

[73] B. G. Tabachnick and L. S. Fidell, *Multivariate analysis of variance and covariance.* Boston, Massachusetts: Allyn and Bacon, 2001.

[74] MATLAB mnvrnd function. (2013). Available: http://www.mathworks.com/help/stats/mvnrnd.html.

[75] J.M. Romano; D. Rosario; J. McCarthy, "Day/Night Polarimetric Anomaly Detection Using SPICE Imagery," *Geoscience and Remote Sensing, IEEE Transactions on*, vol. 50, no. 12, pp. 5014-5023, Dec. 2012.

[76] J. Romano; D. Rosario; N. Nasrabadi, "Covariance trace for polarimetric anomaly detection," *Geoscience and Remote Sensing Symposium (IGARSS), 2012 IEEE International*, pp. 4233-4236, July 2012.

[77] C. Chein-I; S. Wang, "Constrained band selection for hyperspectral imagery," *Geoscience and Remote Sensing, IEEE Transactions on*, vol. 44, no. 6, pp. 1575-1585, June 2006.

[78] D. Hongtao et al., "Band selection using independent component analysis for hyperspectral image processing," *Applied Imagery Pattern Recognition Workshop, 2003. Proceedings. 32nd* , pp. 93-98, Oct. 2003.

[79] L. Paluchowski and P. Walczykowski, "Preliminary hyperspectral band selection for difficult object detection," *Hyperspectral Image and Signal Processing: Evolution in Remote Sensing, 2009. WHISPERS '09. First Workshop on*, pp. 1-4, Aug. 2009.

[80] Y. Yufeng; Y. Jinhua; L. Shijin, "A Fast Approach to Hyperspectral Band Selection Based on Time Series Analysis," *Pattern Recognition (CCPR), 2010 Chinese Conference on*, pp. 1-5, Oct. 2010.